ASME
SETTING THE STANDARD
1880 2005

Journal of Fluids Engineering

Published Bimonthly by ASME

VOLUME 127 • NUMBER 5 • SEPTEMBER 2005

Transactions of the ASME, Journal of Fluids Engineering (ISSN 0098-2202) is published bimonthly (Jan., Mar., May, July, Sept., Nov.) by The American Society of Mechanical Engineers, Three Park Avenue, New York, NY 10016. Periodicals postage paid at New York, NY and additional mailing offices.
POSTMASTER: Send address changes to Transactions of the ASME, Journal of Fluids Engineering, c/o THE AMERICAN SOCIETY OF MECHANICAL ENGINEERS, 22 Law Drive, Box 2300, Fairfield, NJ 07007-2300.
CHANGES OF ADDRESS must be received at Society headquarters seven weeks before they are to be effective. Please send old label and new address.
STATEMENT from By-Laws. The Society shall not be responsible for statements or opinions advanced in papers or ... printed in its publications (B7.1, Par. 3).

EDITORIAL

SPECIAL SECTION ON RANS/LES/DES/DNS: THE FUTURE PROSPECTS OF TURBULENCE MODELING

(Contents continued on inside back cover)

This journal is printed on acid-free paper, which exceeds the ANSI Z39.48-1992 specification for permanence of paper and library materials. ♾™
♻ 85% recycled content, including 10% post-consumer fibers.

Journal of Fluids Engineering Volume 127, Number 5 SEPTEMBER 2005

TECHNICAL PAPERS

TECHNICAL BRIEFS

ERRATA

The ASME Journal of Fluids Engineering is abstracted and indexed in the following:

Applied Science & Technology Index, Chemical Abstracts, Chemical Engineering and Biotechnology Abstracts (Electronic equivalent of Process and Chemical Engineering), Civil Engineering Abstracts, Computer & Information Systems Abstracts, Corrosion Abstracts, Current Contents, Ei EncompassLit, Electronics & Communications Abstracts, Engineered Materials Abstracts, Engineering Index, Environmental Engineering Abstracts, Environmental Science and Pollution Management, Excerpta Medica, Fluidex, Index to Scientific Reviews, INSPEC, International Building Services Abstracts, Mechanical & Transportation Engineering Abstracts, Mechanical Engineering Abstracts, METADEX (The electronic equivalent of Metals Abstracts and Alloys Index), Petroleum Abstracts, Process and Chemical Engineering, Referativnyi Zhurnal, Science Citation Index, SciSearch (The electronic equivalent of Science Citation Index), Shock and Vibration Digest, Solid State and Superconductivity Abstracts, Theoretical Chemical Engineering

Journal of Fluids Engineering

Editorial

RANS/LES/DES/DNS: The Future Prospects of Turbulence Modeling

While we were discussing the rapid increase in Large Eddy Simulation (LES) papers submitted to the Journal of Fluids Engineering (JFE) several years ago, Joe Katz, the editor in chief of JFE, suggested that we needed to organize more in depth symposia to sieve through LES papers as well as to educate the newly emerging large groups of LES users in almost all areas of engineering applications. We also talked about coming up with some sort of a quality assessment criteria to make a judgment of the overall quality of papers that were claimed to be LES. That is where the idea of publishing a special issue on mostly LES applications was started. This special issue is mostly the end result of that discussion. With the hard work of all of the individuals listed in the acknowledgments, we have successfully organized a symposium on "Advances and Applications of LES/DNS." More than 40 papers were submitted. After a thorough review process, 24 papers were accepted to be presented at the symposium held as part of the Joint Fluids Engineering and Heat Transfer Summer Conference, June 11–17, 2004, Charlotte, NC. These papers were further thoroughly reviewed for publication in this special issue according to the standards of JFE. Finally, 13 full papers and one technical brief were recommended for publication.

It was difficult to categorize the papers in this issue into specific classes, though we have tried to order them roughly so that they start with more general review papers and more fundamental topics then proceed towards more applied research papers. Since the fashion for LES was so popular, we wanted to explore first what was going to happen to the good old Reynolds Averaged Navier-Stokes (RANS) models. The first paper by Hanjalic attempts to answer this very question. It should be viewed more as a perspective from a prominent individual who has devoted his carrier spanning close to half a century to development of classical turbulence models. Recent assessments have shown (see, e.g., Rodi [1], Froehlich and Rodi [2], and Temmerman et al. [3]) especially for wall bounded turbulent flows, that a good LES is almost a DNS. That is, a proper resolution of wall layers and prediction of transition to turbulence in boundary layers requires extremely fine grid resolution. For that, one has to resort to some sort of wall functions, and/or a RANS model to save time and perform calculations in an acceptable turn around time for practical engineering applications such as flow around ship hulls. That requires inevitably a hybrid LES/RANS or DES approach. That, in turn, requires a good RANS model. Moreover, even a very crude RANS turbulence model seems to do a good job as a subgrid scale (SGS) model in LES (see Ref. [4]).

SGS models constitute a major component of LES calculations. It is shown by Chen et al. [5] (see also Meneveau et al. [6]) that the balance of predictive capability may change when the stress-strain relationship becomes convoluted under transient rapid straining/destraining conditions. Their a priori analysis indicates that in some cases the dynamic Smagorinsky model does not perform as well as the classical Smagorinsky model, contrary to past experience and expectations. This, therefore, points towards the need to perform more experimental and numerical work to assess the performance of SGS models in more complex engineering flows that exhibit high turbulence Reynolds numbers, rapid straining/destraining, and curvature effects.

LES papers presented in this issue show that, in general, LES results in better agreement with experiments compared to RANS if the grid resolution is sufficiently fine. However, it is difficult to assess without a priori knowledge of the flow characteristics, what grid resolution is actually "sufficient." To this end there need to be some quality assessment measures. Although not part of the special issue, the paper by Celik et al. [7], also printed in this issue, tries to address this question by formulating a LES index of quality (LES_IQ). Some other recent studies (Klein [8], Guerts [9], Meyers et al. [10] and Celik et al. [11]) have also attempted to quantify errors involved in LES calculations. The work by Guerts et al. [9] shows clearly that modeling errors and numerical errors can have opposite signs in some flow regimes, thus indicating a good performance on coarser grid resolutions, but can worsen as the grid is refined while keeping the filter size used in the SGS model fixed.

Several papers fall into the category of detached eddy simulation (DES) or similarly hybrid RANS/LES. The papers by Paterson and Peltier, Wiswanathan and Tafti, and Saric et al., elucidate the critical issues in this approach. The main problem in these applications is related to the control of turbulence inside the so called gray region where transition from RANS to LES takes place. The accuracy of the numerical scheme, as well as the grid resolution and the switching criteria all can influence the quality of the calculations. In particular, the rate of recovery of the unsteady turbulent fluctuations to the level of LES seems to be extremely sensitive to the aforementioned factors in developing flows in wakes or shear layers. In such cases, the loss of upstream turbulence in the transition from RANS to LES may lead to premature turbulence induction or delay separation thus deteriorating the quality of predictions. New criteria would be needed (see, e.g., Temmerman et al. [3]) to make the transition from RANS to LES smooth and controllable.

Another issue that needs further research and consideration and is also closely related to hybrid RANS/LES is the problem of prescribing unsteady boundary conditions at an inlet plane of LES domain in developing flows, for example, at the inlet of a swirling flow turbine combustor. Issues related to validation of such methodologies are addressed in the technical brief by de With et al.

The third paper by Balaras et al. is an example of new frontiers for applications of LES. The two papers by Krajnovic and Davidson illustrate the indispensable problems when LES is applied to a case that closely represents a complex engineering problem such as that of flow past a car model at high Reynolds numbers. These two papers constitute the most thorough study of this particular flow using LES with millions of grid nodes.

Also included in this issue are some DNS examples. While DNS is being expanded to new frontiers such as two-phase, non-Newtonian, reactive flows, the major problem remains not only the computer resources, but the questions and uncertainties related to theory. For example, the question of whether "DNS" of flow

and heat transfer with only a reduced chemical reaction mechanism to simulate turbulent flames is a "true" DNS or not is a matter of debate. Nevertheless, the number of papers that are being published under the classification of "DNS" is also increasing rapidly. It used to be that the acronym DNS was more or less synonymous to an "exact" solution of the physical problem solved with extremely accurate numerical schemes. All relevant time and length scales were resolved so that experiments were not necessary to validate the simulations. Nowadays, nominally second-order schemes on non-structured grids are being used to perform "DNS." In such situations it becomes necessary to verify the so-called "DNS" as well, for example Orozco et al. [12]. The work by Meyers et al. [10], where they apply Richardson extrapolation to determine discretization errors in the predicted length scales of DNS of decaying homogenous isotropic turbulence is a good example of assessment of numerical errors in DNS which seem to appear more pronounced in secondary quantities that are derived by derivation from the primary mean quantities. It seems that this trend will continue and more and more DNS calculations will be performed, albeit with limited grid resolution to more complex flows such as gas turbine flows. The issue of when a DNS is actually DNS must be debated thoroughly.

Jean-Paul Bonnet (The University of Poitiers, France), Peter A. Chang (Naval Surface Warfare Center Carderock Division, USA), and Stephen Jordan (Naval Undersea Warfare Center, USA) have helped in organizing the symposium on LES, reviewing the symposium papers as well as the journal papers. My graduate student Cem Ersahin has worked very hard to put together both the symposium papers and the journal papers. Without their kind help this special issue would not have been possible. Special thanks are due to Laurel Murphy, who as usual, was very forthcoming in handling the web pages and resolving all kinds of problems and hurdles that are common in editorial work.

References

[1] Rodi, W., 2002, "Large-Eddy Simulation of the FLOW Past Bluff Bodies," *Closure Strategies for Turbulent and Transitional Flows*, B. Launder and N. Sandham, eds., Cambridge University Press, Cambridge, pp. 361–391.

[2] Frohlich, J. and Rodi, W., 2002, "Introduction to Large Eddy Simulation of Turbulent Flows," *Closure Strategies for Turbulent and Transitional Flows*, B. Launder and N. Sandham, eds., Cambridge University Press, Cambridge, pp. 267–298.

[3] Temmerman, L., Hadziabdic, M., Leschziner, M. A., and Hajalic, K., 2005, "A Hybrid Two-Layer URANS-LES Approach for Large Eddy Simulation at High Reynolds Numbers," Int. J. Heat Fluid Flow, **26**, pp. 173–190.

[4] Viswanathan, A. K., and Tafti, D. K., 2005, ASME J. Fluids Eng., **127**, pp. 888–896.

[5] Chen, J., et al., 2005, ASME J. Fluids Eng., **127**, pp. 840–850.

[6] Meneveau, C., 2005, "Issues and Case Studies for Experimental Validation of LES in Incompressible Flow," In *Proceedings of Quality Assessment of Unsteady Methods for Turbulent Combustion Prediction and Validation*, Department of Energy and Powerplant Technology, TU Darmstadt, Germany, June 16–17.

[7] Celik, I. B., et al., 2005, ASME J. Fluids Eng., **127**, pp. 951–960.

[8] Klein, M., 2005, "An Attempt to Assess the Quality of Large Eddy Simulations in the Context of Implicit Filtering," Flow, Turbul. Combust. **74**(1), pp. 67–84.

[9] Geurts, B. J., 2005, "Database-Analysis of Interacting Errors in Large-eddy Simulation," In *Proceedings of Quality Assessment of Unsteady Methods for Turbulent Combustion Prediction and Validation*, June 16–17, Department of Energy and Powerplant Technology, TU Darmstadt, Germany

[10] Meyers, J., Geurts, B. J., and Baelmans, M., 2003, "Database Analysis of Errors in Large-Eddy Simulation," Phys. Fluids, **15**(9), pp. 2740–2755.

[11] Celik, I. B., 2005, "Recent Developments on Quantification of Numerical Uncertainty in CFD: Applications to LES/URANS," In *Proceedings of Quality Assessment of Unsteady Methods for Turbulent Combustion Prediction and Validation*, June 16–17, Department of Energy and Powerplant Technology, TU Darmstadt, Germany.

[12] Orozco, C., Claramunt, K., Consul, R., and Oliva, A., 2004, "Finite Volume Computation and Verification of Fluid Flow and Heat Transfer in Domains With Moving Boundaries," European Congress on Comp. Meth. Appl. Sci. Eng., Jyvaskyla, Spain, July 24–28.

Ismail Celik
e-mail: ibcelik@mail.wvu.edu
Mechanical and Aerospace Engineering Department, West Virginia University, Morgantown, WV

Will RANS Survive LES? A View of Perspectives

K. Hanjalic
e-mail: hanjalic@ws.tn.tudeft.nl
Thermal and Fluids Sciences,
Department of Multi-scale Physics,
Delft University of Technology,
Lorentzweg 1, 2628 CJ Delft,
The Netherlands

The paper provides a view of some developments and a perspective on the future role of the Reynolds-averaged Navier-Stokes (RANS) approach in the computation of turbulent flows and heat transfer in competition with large-eddy simulations (LES). It is argued that RANS will further play an important role, especially in industrial and environmental computations, and that the further increase in the computing power will be used more to utilize advanced RANS models to shorten the design and marketing cycle rather than to yield the way to LES. We also discuss some current and future developments in RANS aimed at improving their performance and range of applicability, as well as their potential in hybrid approaches in combination with the LES strategy. Limitations in LES at high Reynolds (Re) and Rayleigh (Ra) number flows and heat transfer are revisited and some hybrid RANS/LES routes are discussed. The potential of very large eddy simulations (VLES) of flows dominated by (pseudo)-deterministic eddy structures, based on transient RANS (T-RANS) and similar approaches, is discussed and illustrated in an example of "ultra-hard" (very high Ra) thermal convection. [DOI: 10.1115/1.2037084]

Keywords: Turbulence Modeling, Convective Heat Transfer RANS, T-RANS, LES, Hybrid RANS-LES

Introduction

Despite their disputable intuitive and empirical rationale, the one-point turbulence closures for Reynolds-averaged Navier-Stokes (RANS) equations have remained for over three decades the mainstay of the industrial computational fluid dynamics (CFD). They are simple to use, computationally affordable, and economical, thus appealing to industry for various applications such as design, optimization, prediction of off-design performances, or for predicting the outcome in situations that are inaccessible to experiment or to other simulation methods. But, as it is well known, the most popular and most widely used linear eddy-viscosity models (EVMs) have serious fundamental deficiencies and cannot be trusted for predicting genuinely new situations of realistic complexity. Various modifications and new modeling concepts have been proposed over the past decades, ranging from ad hoc remedies, complex nonlinear eddy-viscosity approaches to multi-equation and multi-scale second-moment closures (SMCs) (Reynolds stress/flux, algebraic, or differential models). No consensus has ever been reached—and probably it never will—on what should be the optimum model(s) or level of closure. A broad palette of RANS variants are currently used and some models—primarily at the simple EVM level seem to have found niches in different areas of application. However, a general feeling among many CFD users is that the RANS have not met with early expectation. Alternatives have been sought in other approaches, questioning the RANS future and disputing its current role as the only viable tool for industrial and environmental computations of complex turbulent flows and transport phenomena.

The developments in direct and large eddy simulations (DNS, LES) have opened new prospects. While DNS has been viewed as an indispensable research tool, LES has been expected to emerge as the future industrial standard, threatening to eliminate RANS. This excitement did not last for long: while LES proved to be certainly a powerful method, because of formidable demands on grid resolution its application is and will for long be limited to low-to-moderate Re and Ra numbers and relatively simple geometries. Handling the wall-bounded flows, with focus on wall phenomena, friction and heat and mass transfer, especially at high Re and Ra numbers, poses great challenge. For such situations, combining the advantages of RANS and LES seems at present—at least for some flow types—the best option. Because such hybrid approaches imply numerical resolution in time and space of *only* very large eddies (VLES) while the significant portion of turbulence spectrum needs to be modeled, the modeling of the unresolved ("subscale") motion requires a more sophisticated approach than used for common LES subgrid-scale models, opening thus a new niche for the RANS modeling. These prospects, as well as the realization that the grid resolution problem of LES will make this technique long inapplicable to large-scale industrial and environmental problems, have recently renewed the interest in further improvement of RANS and RANS-based methods, as well as their combination with the LES strategy.

We begin with a brief discussion of the current status, limitations, and possible developments of the RANS and related approaches in view of the future increase in the computing power. Some genuine niches for LES, inaccessible to RANS methods (and also for experiments), are then discussed. As an example we discuss the problem of the accurate prediction of distribution and time variation of the surface temperature in configurations encountered in electronics cooling, in internal cooling of gas turbine blades, or other similar applications. Here the local hot spots or strong time variation of the surface temperature and the consequent thermal fatigue are regarded as the major cause of equipment malfunctioning. We move then to discuss some developments in RANS modeling for complex flows and convective heat transfer. By noting some promising progress in numerical treatment of advanced RANS models, primarily at the second-moment level, we show some successful applications of these models to complex flows of industrial relevance, as well as some recent novelties in the model developments originating from the author's group. A new, robust variant of the elliptic relaxation eddy-viscosity model, k-ε-ζ-f, is presented, followed by a new second-moment "elliptic blending" closure. As an example of successful application in the forced convection problem, we consider multiple jets impinging normally on a flat surface, which are used frequently to achieve efficient cooling or heating of solid walls. The attention is then turned to the combination of RANS with LES (hybrid RANS/LES). Several noted controversial issues are

Contributed by the Fluids Engineering Division for publication in the JOURNAL OF FLUIDS ENGINEERING. Manuscript received by the Fluids Engineering Division. Associate Editor: Ismail Celik.

discussed, supported with some illustrations. The paper closes with a brief outline of the potential of VLES based on transient RANS (T-RANS) to applications in flows featured by strong, quasi-deterministic, large-scale structures. The potential of T-RANS is illustrated in "ultra-hard" (very high Ra number) Rayleigh-Bénard convection, which is inaccessible to the conventional LES, with indication of its possible use to solve large-scale real-life engineering and environmental problems.

A Perspective on RANS and its Future Role

Currently, an industrial user is confronted with a very broad palette of the available RANS models. The CFD vendors make the choice more difficult by offering in some cases over 20 different RANS variants, with hardly any suggestions in regard to which models should be used for which application. This is not a happy situation and, paradoxically, despite the obvious need for innovation, there seems to be not much incentive for fundamental research in the conventional RANS modeling. Only a few groups over the globe are seriously engaged in RANS research. Furthermore, because of saturation and earlier numerous disappointments, the novelties are today usually met with distrust among both the CFD vendors and CFD users. In contrast, there seems to be much more activity is researching new approaches, primarily in academia, some seemingly departing from the traditional RANS strategies, in search of better physical justification and expanding the range of model applicability. Among such new developments we can identify the following:

- Unsteady RANS (U-RANS) implying time-solution of the conventional RANS for 3D unsteady problems, with or without special treatment of flow unsteadiness
- Multi-scale RANS (one-point and spectral closures)
- Transient RANS (based on conditional or ensemble averaging of NS equations) with possibly modified RANS model for the subscale (unresolved) motion [1]
- VLES based on T-RANS [1], semi-deterministic modeling (SDM) [2], coherent vortex simulation (CVS) [3], partially averaged NS (PANS) [4], and others
- Hybrid RANS/LES with zonal or seamless coupling of the two strategies [5,6]

It is noted that in most of the approaches one deals with the same form of the momentum and scalar transport equation, of course with different meaning of the variables:

$$\frac{D\langle U_i\rangle}{Dt} = \langle F_i\rangle - \frac{1}{\rho}\frac{\partial\langle P\rangle}{\partial x_i} + \frac{\partial}{\partial x_j}\left(\nu\frac{\partial\langle U_i\rangle}{\partial x_j} - \tau_{ij}\right) \tag{1}$$

$$\frac{D\langle T\rangle}{Dt} = \frac{\langle q\rangle}{\rho c_p} + \frac{\partial}{\partial x_j}\left(\alpha\frac{\partial\langle T\rangle}{\partial x_j} - \tau_{\theta i}\right) \tag{2}$$

where $\langle\ \rangle$ denotes Reynolds (time or ensemble) averaged quantities in RANS, and filtered quantities in LES, and τ_{ij} and $\tau_{\theta i}$ are turbulent stress and scalar flux, respectively, either for the whole turbulence spectrum (RANS) or its parts (multi-scale RANS), or for unresolved motion (VLES, LES), which in all approaches need to be modeled. The identical forms of Eqs. (1) and (2) for RANS, VLES, and LES make it convenient not only to use the same computational code and similar numerics, but also to combine the two approaches in zonal or hybrid procedure.

A common feature of all these approaches is the desire to capture some elements of the turbulence spectrum, i.e., to resolve in time and space parts—primarily at large scales—of the unsteady turbulent motion. In most methods the focus is on large, dominating eddy structure (beyond, e.g., vortex shedding that can be captured even with the conventional U-RANS) that preserves some coherence and determinism even if the flow is not separated and is steady in the mean. However, because such approaches require a considerable portion of the turbulence spectrum to be modeled (much larger than the conventional subgrid-scale motion in LES),

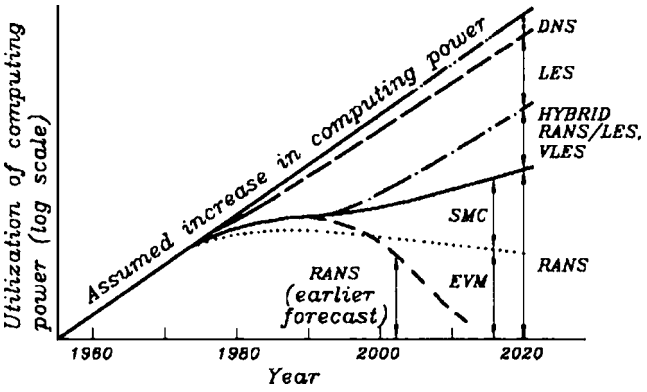

Fig. 1 A conjectured prospect on utilization of the available computing power by different computational approaches

the modeling remains an important issue, which draws to a larger or lesser extent to the RANS experience and makes use of elements of the RANS modeling. This in turn brings new demands and new constraints on RANS models, providing a new incentive for their research.

Putting aside these new developments where RANS models in their original or modified forms will take a new role as "subscale" models (in contrast to subgrid-scale in LES), the fact remains that despite disappointments, we have seen no decline in the use of the conventional RANS models among industry. It is conjectured that this trend will remain for a foreseeable future, more or less in line with the increase in the computing power, because of

- increasing market pressure to shorten the design and marketing time, putting higher demands on faster parametrization and design optimization
- increasing improvement and wider (and less expensive) availability of the commercial CFD codes, easier and user-friendly grid-generation, and postprocessing (visualization and animation) software
- expanding the number of CFD users among medium and small industries
- broadening of the applicability of CFD and the increasing needs to handle more and more complex industrial problems involving heat and mass transfer, combustion and other chemical reactions, multi phases, etc., where prohibitive demands on computer resources and uncertainties in modeling physical phenomena other than turbulence make little incentive to use sophisticated turbulence models and LES.

Pope [7] also argues that most of the increase in the computer power will in the near future be used for RANS, aimed at improving spatial resolution and better numerical accuracy by using larger and better designed numerical meshes and more accurate representation of geometry and its boundaries, as well as using more sophisticated models of turbulence and other phenomena. We can also expect more use of U-RANS for 3D computations of complete bluff bodies to capture better unsteady separation effects. Also, visualization and animation, which usually requires large computing power, will be more and more in use as a tool for identifying some global or local flow features that can help in improving design.

A conjecture on possible future utilization of the increased computing power is presented in Fig. 1. Of course, the proportion of LES (and DNS) will be much smaller among the industrial users, whereas the opposite can be expected in research communities.

LES Niches for Heat Transfer

For accurate predictions of wall bounded flows, especially if wall phenomena—friction, heat and mass transfer—are in focus,

LES is severely constrained by the near-wall resolution requirements. Proper resolution of the near-wall streaky structures requires grid density close to that for DNS with near-wall grid spacing not larger than $\Delta y^+ = O(1)$, $\Delta x^+ = O(50)$, and $\Delta z^+ = O(20)$, where y^+ denotes the wall-normal, x^+ streamwise, and z^+ spanwise direction in wall units. As Re and Ra numbers increase, the molecular sublayers becomes progressively thinner, imposing formidable demand on grid finesse. Handling complex wall topology is another problem with LES, because a rational boundary fitting requires an unstructured grid which is still not widely tested for LES.

Yet, there are many flows and heat transfer problems of practical relevance where the Re or Ra numbers are relatively low and where LES can be very suitable, reliable, and even the indispensable technique. Currently actual examples are electronics cooling, internal cooling of gas turbine blades, crystal growth, and others. While RANS models can also give useful results, the ever-increasing trends toward miniaturization and hence higher specific heat dissipation in electronics cooling, or higher heat fluxes in internal passages of high-load gas turbine blades, bring in focus the problem of hot spots and thermal fatigue, which require accurate prediction of temperature distribution and its time variation. This is illustrated in an example where LES in conjunction with an unstructured solver has been applied for conjugate flow and heat transfer over a multi-layered wall-mounted protrusion imitating an electronic component. Apart from the cubical shape, chosen on purpose to serve as a reference for investigating conjugate heat transfer, all other aspects correspond to real electronics element: a copper core of 13.5 mm cube heated electrically simulates the heat dissipation, whereas the low-conducting 1.5 mm thick epoxy layer on the cube surface mimics the real coating. Because of low conducting surface layer, the surface temperature is highly nonuniform and—depending on the local flow and turbulence structure—locally it may exceed the technological limits (local hot spots) and cause equipment malfunctioning. The time-averaged temperature distribution over the surface can easily be measured (liquid crystals, infrared camera, thermocouples, etc.) but capturing well-resolved instantaneous temperature field is almost impossible with the available techniques because of high frequencies of the fluctuations. Well-resolved LES or DNS appear to be the only route to predict accurately the time variation of the surface temperature distribution.

An example of such simulations can be found in Niceno et al. [8] where LES of flow and conduction in the epoxy layer have been solved simultaneously. Filtered momentum and energy equations (1) and (2) were closed by $\tau_{ij} = 2\nu_{sgs}\langle S_{ij}\rangle$ and $\tau_{\theta i} = (\nu_{sgs}/\mathrm{Pr})\langle \partial T/\partial x_i\rangle$ and solved on an unstructured grid. Because near the cube walls the grid is sufficiently fine to approach DNS, the choice of the subgrid scale model is not influential. Thus, the standard Smagorinski subgrid-scale model was used with $\nu_{sgs} = (C_s\Delta)^2(2\langle S_{ij}S_{ij}\rangle)^{1/2}$ where $\Delta = \min(d, \Delta V^{1/3})$, $C_s = 0.1$, and d is the distance from the nearest wall.

Comparison of various computed properties with experiments of Meinders and Hanjalic [9] are reported in detail in [8], showing generally very good agreement. It is noted that the time-averaged temperature shows a strong variation over the cube surface, dropping from maximum of 60°C at the rear surface to 40°C at the intensively cooled front edges (note that the copper core was at 75°C) [8]. This surface temperature nonuniformity was found to reflect a range of vortex structures, which are difficult to capture by any RANS model.

Especially useful results from the LES are the *instantaneous* temperature imprints on the cube surfaces, which cannot be obtained by any other technique, experimental or numerical, except by DNS. The simulations show high local temperature nonuniformities with a pattern changing continuously with a stochastic periodicity, as can be observed from the surface temperature animation. Figure 2 shows one realization of the instantaneous surface temperature viewed from the front and rear side. Local hot spots

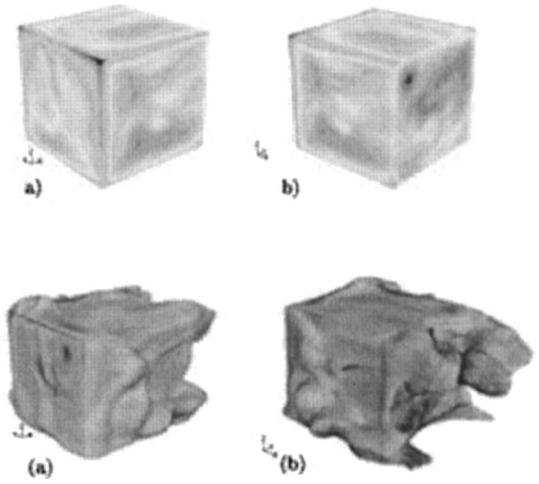

Fig. 2 Instantaneous temperature on the cube surface (above) and thermal plumes around the cube, defined by the isosurface of $T = 24.5$°C (below). (*a*) view from the front, (*b*) view from the back. The flow is in the *x* direction [8].

are discernible on the rear face. The instantaneous fluid temperature corresponding to the same realizations is also shown in the form of thermal plumes defined by the surface of constant temperature of 24.5°C and colored by fluid velocity magnitude.

Some Recent Developments in RANS

Limitations of linear eddy viscosity models (EVMs) have been recognized already in the early days of turbulence modeling and the attention has been turned to the second moment closure (SMC) that makes the most logical and physically most appropriate RANS modeling framework. This approach requires modeling and solution of the transport equations for the turbulent stress and scalar flux:

$$\frac{D\overline{u_iu_j}}{Dt} - D_{ij} = (\overline{f_iu_j} + \overline{f_ju_i}) - \left(\overline{u_iu_k}\frac{\partial U_j}{\partial x_k} + \overline{u_ju_k}\frac{\partial U_i}{\partial x_k}\right) + \phi_{ij} - \varepsilon_{ij} \tag{3}$$

$$\frac{D\overline{\theta u_i}}{Dt} - D_{\theta i} = -\overline{u_iu_j}\frac{\partial T}{\partial x_j} - \overline{\theta u_j}\frac{\partial U_i}{\partial x_j} - \overline{f_i\theta} - \varepsilon_{\theta i} + \phi_{\theta i} \tag{4}$$

which are closed by a scale-providing equation, usually energy dissipation rate ε or $\omega = \varepsilon/k$. This level of modeling enables the exact treatment of the turbulence production by the mean strain or body forces. Furthermore, the solution of transport equations for each stress component makes it possible—at least in principle—to reproduce accurately the stress field and its anisotropy, which reflects the structure and orientation of the stress-bearing turbulent eddies. This in turn makes it possible to reproduce effects of streamline curvature, rotation and swirl, secondary motion, and other effects encountered in complex flows, better than with an eddy-viscosity concept [10].

Despite obvious advantages, two issues emerged immediately as critical: modeling, especially of the pressure-strain terms φ_{ij} and $\varphi_{\theta i}$, and the numerical stiffness of the coupling of Eqs. (3) and (4) with the mean momentum and energy equations. While the modeling has been reasonably successful with some notable improvements over the past few years, the numerical stiffness and the reluctance of users to solve more differential equations remained long the major deterrent. Over the years it became clear that the numerical problem has been associated primarily with the tendency to use the available Navier-Stokes solver designed for equations with dominant diffusive second-order term pertinent to eddy viscosity approach. Providing turbulent stresses and fluxes

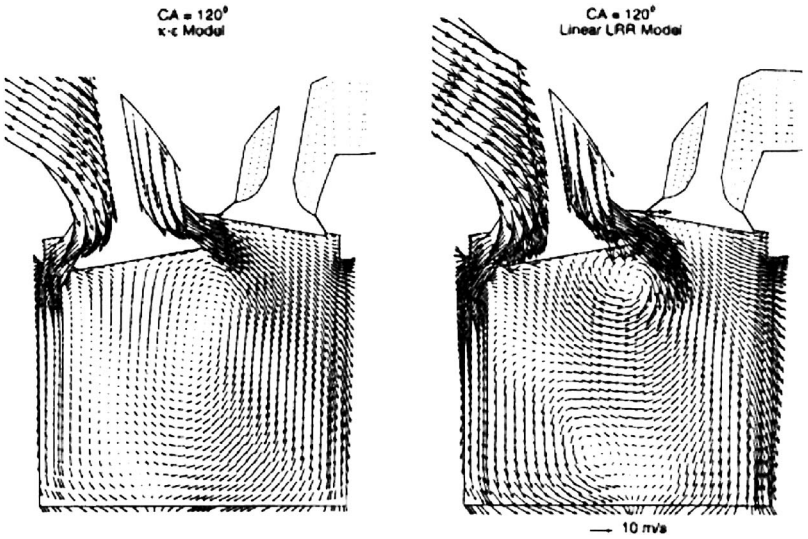

Fig. 3 Velocity vectors in the midplane of a DOHC IC engine at CA=120°, 3D RANS [18]. Left: k-ε; right: SMC.

from separate differential equations requires more care in coupling the equations. This was demonstrated recently by Gerolymos et al. [11], who, thanks to an efficient implicit implementation of the second-moment closure, succeeded in computing several complex turbomachinery flows with a near-wall second-moment closure with only 30% more computing time than required for the k-ε model. Over the past decade a number of groups, both in industry and academia (Craft and Launder at UMIST, e.g., [12], Leschziner et al. at Imperial College [13], Basara et al. AVL, Graz, Austria [14,15], Gerolymos et al. at Univ. Pieree-et-Marie Curie in Paris, [11,16], Yang et al. at Michigan Tech., Houghton, USA [17,18], to name only a few), succeeded in designing similar or other remedies that make the solution of the second-moment closure almost a routine procedure that requires only marginally larger effort and computing resources as compared with the EVMs. The improvements, however, in most cases appeared to be worth the effort. A number of examples illustrating the superiority of the second-moment closure can be found in the above cited and other references. A good selection of complex industrial flows, solved in parallel with the k-ε and the SMC models (all with wall functions) using KIVA code, can be found in Refs. [17,18]. These include a nonreacting multi-point lean direct injection (LDI) gas turbine combustor with discrete jet- and helical axial swirlers of different orientations, a simplified direct injection stratified charged (DISC) IC engine, a lean-premixed prevaporized (LPP) combustor, and a four-valve double-overhead camshaft (DOHC) IC engine. In all cases, the predictions with the SMC with the Speziale, Sarkar and Gatski (SSG) [19] pressure-strain model appeared in better agreement with experiments (where available) than the standard k-ε. In cases where no experimental data for field properties were available, the integral parameters were compared, showing again better agreement with the SMC. For example, for the DOHC engine the experimentally observed strong swirl generated by the canted valves and the piston motion at CA approaching 180° was much better reproduced by the SMC (Fig. 3). While there is still room for improvement, these and other examples serve as good illustrations of the current achievements in solving complex flows of industrial relevance with the second-moment closure.

Second-moment closures have also served as inspiration for a number of improvements of lower-order models. Algebraic stress and flux models based on their differential parent equations—in implicit or explicit forms—have been found to perform generally better than the nonlinear eddy viscosity models that were derived independently, e.g., Wallin and Johanson [20].

The elliptic relaxation EVM of Durbin [21] was also inspired and derived with resource to the model differential stress equation (3). A broad variety of nonlinear eddy-viscosity models, developed for the desire of industry with the hope to become a more user-friendly surrogate for second-moment closure, have generally not fulfilled their promises. Some of the rigorously derived models that were relatively free from arbitrary tuning of numerous coefficients, such as the TCL (two-component limit) cubic model of Craft et al. [22], were reported to perform well in several flows considered, though less satisfactory in some other flows, e.g., [23]. However, because of their complexity, the more successful (but, as a rule, more complex) nonlinear models have not yet appealed to industry.

In view of the above discussion, it is fair to say that the RANS models are witnessing their renaissance and that we shall see in the near future more extensive use of advanced RANS models applied to complex flows.

We consider briefly some recent advancements, aimed at robust application of advanced models to complex flows. Recently reported novelties are too numerous for this brief coverage and we will restrict the discussion to only a few developments originating from the author's group.

Robust Elliptic Relaxation EVMs. The v^2-f model of Durbin [20] appeared as an interesting novelty in engineering turbulence modeling. By introducing an additional ("wall-normal") velocity scale v^2 and an elliptic relaxation concept to sensitize v^2 to the inviscid wall blocking effect, the model dispenses with the conventional practice of introducing empirical damping functions. Because of its physical rationale and of its simplicity, it is gaining in popularity and appeal especially among industrial users. While in complex three-dimensional flows, with strong secondary circulation, rotation, and swirl, where the evolution of the complete stress field may be essential for proper reproduction of flow features, the model remains still inferior to the full second-moment and advanced nonlinear eddy viscosity models, it is certainly a much better option than the conventional near-wall k-ε, k-ω, and similar models.

However, the original v^2-f model possesses some features that

impair its computational efficiencies. The main problem is with the wall boundary condition $f_w \to -20\nu^2\nu^2/(\varepsilon y^4)$ when $y \to 0$, which makes the computations sensitive to the near-wall grid clustering and—contrary to most other near-wall models—does not tolerate too small y^+ for the first near-wall grid point. The problem can be obviated by solving simultaneously the v^2 and f equation, but most commercial as well as in-house codes use more convenient segregated solvers. Alternative formulations of the v^2 and f equations that permit $f_w=0$ usually perform less satisfactorily than the original model and require some retuning of the coefficients.

Recently a version of the eddy-viscosity model based on Durbin's elliptic relaxation concept has been proposed [24], which solves a transport equation for the velocity scale ratio $\zeta=v^2/k$ instead of the equation for v^2,

$$\frac{D\zeta}{Dt} = f - \frac{\zeta}{k}P + \frac{\partial}{\partial x_j}\left[\left(\nu + \frac{\nu_t}{\sigma_\zeta}\right)\frac{\partial \zeta}{\partial x_j}\right] \tag{5}$$

in combination with an elliptic relaxation function (here based on the SSG [19] quasi-linear pressure-strain model)

$$L^2\nabla^2 f - f = \frac{1}{\tau}\left(c_1 + C_2\frac{P}{\varepsilon}\right)\left(\zeta - \frac{2}{3}\right) \tag{6}$$

Here the eddy viscosity is defined as $\nu_t=c_\mu\zeta k\tau$, where c_μ is different from the conventional C_μ, and τ is the time scale, equal to k/ε away from a wall. Because of a more convenient formulation of the equation for ζ and especially of the wall boundary condition for the elliptic function $f_w=-2\nu\zeta/y^2$, this model is more robust and less sensitive to nonuniformities and clustering of the computational grid. Alternatively, one can solve Eq. (6) for a "homogeneous" function f' with zero wall boundary conditions $f'_w=0$, and then obtain $f=f'-2\nu(\partial\zeta^{1/2}/\partial x_n)^2$ (in analogy with Jones-Launder equation for homogeneous dissipation). The computations of flow and heat transfer in a plane channel, behind a backward-facing step and in a round impinging jet, show in all cases satisfactory agreement with experiments and direct numerical simulations [24].

Elliptic-Blending SMC. As an example of a robust second-moment closure suitable for complex near-wall flows, we discuss briefly the elliptic blending model (EBM) of Manceau and Hanjalic [25]. The model, based on Durbin's [26] SMC, solves Eq. (3) in conjunction with the ε equation, but instead of solving six elliptic relaxation equations for the functions corresponding to each stress component, a single scalar elliptic equation is solved:

$$\alpha - L^2\nabla^2\alpha = 1 \tag{7}$$

The pressure strain term and the stress dissipation are modeled by blending the "homogeneous" (away from the wall) and the near-wall models

$$\phi_{ij} = (1-\alpha^2)\phi_{ij}^w + \alpha^2\phi_{ij}^h \tag{8}$$

$$\varepsilon_{ij} = (1-\alpha^2)\frac{\overline{u_iu_j}}{k}\varepsilon + \frac{2}{3}\alpha^2\varepsilon\delta_{ij} \tag{9}$$

In Eq. (8), ϕ_{ij}^h can be chosen from any known model (we use SSG), whereas the wall model for the pressure strain, satisfying the exact wall limit and stress budget, is defined by

$$\phi_{ij}^w = -5\frac{\varepsilon}{k}\left(\overline{u_iu_k}n_jn_k + \overline{u_ju_k}n_in_k - \frac{1}{2}\overline{u_ku_l}n_kn_l(n_in_j+\delta_{ij})\right) \tag{10}$$

where the unit wall-normal vector is evaluated from

$$\mathbf{n} = \frac{\nabla\alpha}{\|\nabla\alpha\|} \tag{11}$$

Illustration of the EBM in Multiple-Impinging Jets. As an illustration of the performance of the EBM, we show some results of computations of flow and heat transfer in a multiple impinging jets configuration, shown in Fig. 4 [27,28]. Besides its relevance for cooling, heating, and drying in various applications, impinging jets have long served as a generic benchmark for turbulence and heat transfer modeling.

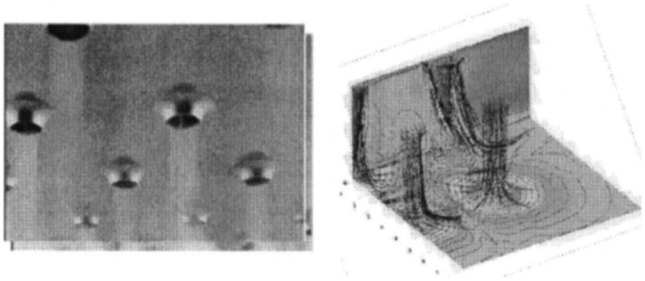

Fig. 4 Nozzle configuration and computational view of streamlines and surface temperature

In the wall layer in an impinging jet, the turbulent stress tensor shows high anisotropy which is reflected in the turbulent heat flux anisotropy and, in turn, in the local wall heat transfer. The wall-normal heat flux wall is governed primarily by the wall-normal velocity fluctuation. The change of flow direction from a normally impinging jet to a radial wall jet causes a strong redistribution between the stress component, as well as a change of the roles of different components of the mean velocity gradient from one region to another. This leads to a strong evolution of stress and heat flux anisotropy and to a change in the intensity and the role of the wall-normal stress component. Because most linear eddy-viscosity models cannot reproduce properly the stress anisotropy, they fail in reproducing heat transfer. That the stress field is closely related to heat transfer can be illustrated also indirectly: the models which reproduce well the turbulence stress field yield as a rule better predictions of wall heat transfer, even if a simple eddy-diffusivity concept is used for the turbulent heat flux.

Multiple-impinging jets are more complex. Possible jet interaction prior to impingement and the collision of wall jets on the target plate create complex 3D patterns with ejection fountain, recirculation, and embedded vortices in the space between the jets, as well as a cross flow towards escape openings. The arrangement and spacing of the jets have crucial roles in achieving optimum effects. Instantaneous PIV shows that closely spaced jets only intermittently reach the impinging surface with full strength [29]. Curious phenomena, such as symmetry breaking, have been observed in some arrangement affecting heat transfer uniformity. Reliable computational optimization is essential for reaching the optimum effects and, because of flow complexity, sophisticated models are required to trust the computations. Wall functions are unreliable and equations must be integrated up to the wall.

We present some results for a square arrangement of nine equal parallel jets issuing from the same orifices, with three models: the conventional k-ε+WF, the v^2-f, and the EBM, compared with experiments. The EBM has been used in conjunction with two different heat flux models, i.e., the isotropic and nonisotropic eddy diffusivity models (known also as simple and generalized gradient diffusion hypotheses, SGDH and GGDH, respectively):

$$\text{SGDH: } \overline{\theta u_i} = -\frac{\nu_t}{\sigma_T}\frac{\partial T}{\partial x_i}; \quad \text{GGDH: } \overline{\theta u_i} = -C_\theta\frac{k}{\varepsilon}\overline{u_iu_j}\frac{\partial T}{\partial x_j}$$

All models indicate that the jets do not interact much prior to the impingement and a void space appears in between where a trapped low-momentum vortex resides asymmetrically displaced above the 45° symmetry line, as shown in Figs. 5 and 6. This broken symmetry, despite fully symmetric stationary conditions imposed on both interior vertical and horizontal symmetry planes of the solution domain, is also confirmed by experiments [29] as shown in the figures.

The predictions of the flow pattern and Nusselt (Nu) number

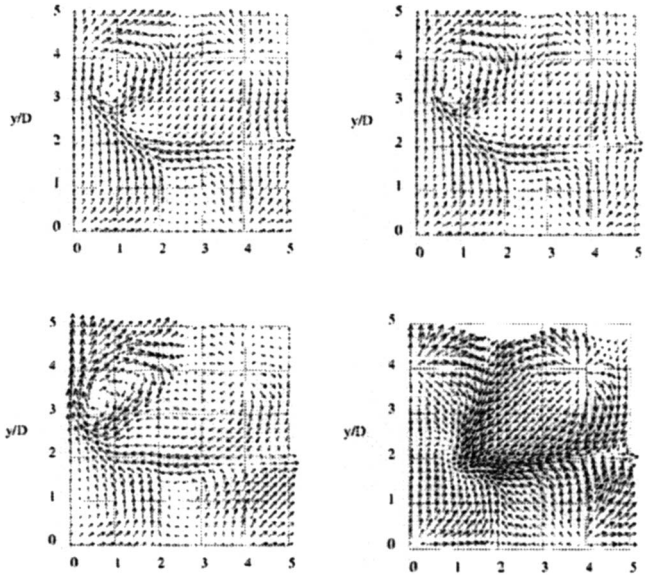

Fig. 5 Velocity vectors in a plane at $z/D=0.54$ above the impinging plane. Top: k-ε+WF (left), EBM (right); bottom: k-v2-f (left), PIV measurements (right) [28].

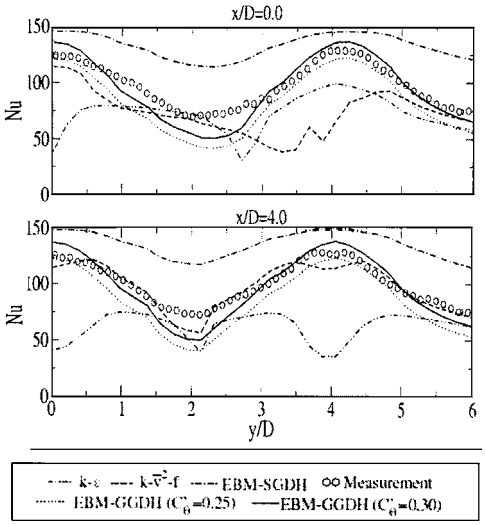

Fig. 7 Nusselt number distribution across the jets centerlines for two locations [28]

with different models differ significantly. Unlike in single jets, where the k-ε model predicts maximum Nu number in the stagnation region, here it shows notable underprediction. In contrast, the v^2-f returns higher Nu, somewhat in better agreement with experiments, but still unsatisfactory. The EBM second-moment closure shows surprisingly good reproduction of details of the flow pattern in the whole domain and excellent predictions of Nusselt number, as shown also in Fig. 7, where the effect of the heat flux model is also illustrated.

Multiple-Scale RANS. Another niche where we may see more activity in the near future are the two-scale or multi-scale RANS models in which additional scalar equations are solved to provide extra turbulence scales. The usage of a single turbulence time and length scale to characterize all processes and to model undefined terms in the governing equations has long been recognized as one of the major deficiencies of the conventional RANS. Early attempts based on a split spectrum method [30,31], where a set of model equations was derived and solved for each of the two (or more) spectrum slices, seemed promising but the development was discouraged by the lack of information on spectral splitting in complex flows and by the inevitable increase in the number of empirical coefficients (a separate set needed for each spectrum slice). Some developments following different rationale have been reported recently, aimed primarily at deriving an equation for an additional turbulence scale to distinguish the spectral energy transfer from the turbulence dissipation rate. Such a model, based on the weighted integration of the dynamic equation for the cova-

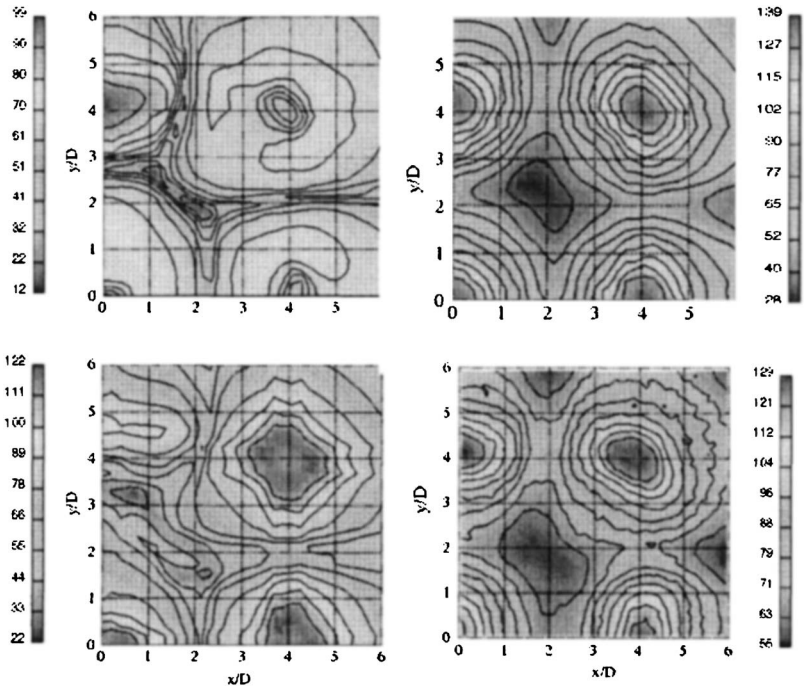

Fig. 6 Nusselt number predicted by different models. Top: k-ε+WF (left), EBM+GGDH (right); bottom: k-v2-f (left), LCT measurements (right) [28].

riance spectrum, with an assumed shape of the energy spectrum and spectral anisotropy function, has been considered by Cadiou et al. [32]. With some simplification, separate equations are derived for the spectral energy transfer function ε_p and the true dissipation rate ε, which in spectral equilibrium become equal. Tests in several nonequilibrium flows, which include a periodically perturbed flow over a backward-facing step and over a square-section rod, showed interesting dynamics of the two time scales, defined as k/ε_p and k/ε [32].

Hybrid RANS/LES

It is recalled that the proper resolution of dynamically important scales with LES requires the grid density to increase with $\mathrm{Re}^{0.4}$ in regions away from a solid wall, but this constraint becomes much more severe in near-wall regions where the grid density should follow $\mathrm{Re}^{1.8}$. In contrast, the RANS grid requires clustering only in the wall-normal direction, making the grid requirements proportional to ln(Re). For realistic engineering and environmental flows an attractive proposition is to combine the LES with RANS strategy. Most approaches currently under exploration can be grouped into two categories. The first is the zonal approach in which the conventional coarse-grid LES is applied in one flow region, usually away from a solid wall, and a RANS model is applied in the other, usually the near-wall region. The switching from one to another field is made at a suitably chosen interface. The key problem is to ensure proper matching conditions at the interface, which are usually based on the equality of the total (resolved+modeled) stress or total viscosity. Because the resolved motion on both sides of the interface should be the same, and RANS model yields a much larger modeled contribution than the LES subgrid-scale model, the RANS model needs to be damped. A way to accomplish matching is to damp the RANS eddy viscosity either by damping the eddy-viscosity coefficient C_μ [33] or by decreasing the RANS kinetic energy or by increasing the dissipation rate [34]. Other approaches have also been reported, e.g., a parabolic treatment of the near-wall boundary layer with imbedded solutions using a simple damped mixing length model in the near-wall RANS region, or the simultaneous solution of the parabolic momentum equation—again with mixing length, with LES in the outer region.

The second approach is based on continuous (nonzonal) simulations using the same model for the unresolved motion in the complete solution domain, which serves as a RANS model in the near-wall region and as a subgrid-scale model in the outer LES region. The switching between one and the other approach is accomplished by changing the length scale: in the near-wall RANS region the distance from the wall is used whereas in the LES region this is replaced by the representative grid size. The most known method in this category is Spalart's detached eddy simulation (DES) [35] in which the Spalart-Almaras (S-A) one-equation model for eddy viscosity is used in both regions. This approach, just like the zonal one, contains a dose of arbitrariness: the interface between the RANS and LES region is determined by the adopted mesh. The switching parameter can of course be adjusted by an empirical coefficient, but the desired criterion is difficult to know in advance in unknown complex flows. The problem is in the strong deterioration of the predictions when the switching occurs at larger distances from the wall ($y^+ > 30$). It is also noted that the S-A model was tuned for external aerodynamic flows and has been shown to perform badly in some other flow types.

The zonal approach seems more appealing because outside the wall boundary layers, the conventional LES method [with prescribed sub-grid-scale (sgs) or dynamic modeling] is used without any intervention in the subgrid modeling. However, the crucial issues and problems to address are the location and the definition of the interface, the nature of matching conditions, especially for flows in complex geometries, and the receptivity of the RANS region to the LES unsteadiness and the RANS feedback into the LES region. Even if the RANS model is adjusted to meet the constraint of continuity of eddy viscosity and other quantities across the interface, an insufficient level in small-scale activity that RANS feeds into LES across the interface produces in most circumstances nonphysical features (a bump) in the velocity profile around the interface. Several proposals have been published for introducing an extra small-scale forcing. Piomelli et al. [36] suggested a "stochastic backscatter" generated by random number with an envelope dependent on the wall distance. Davidson and Dahlström [37] proposed to add turbulent fluctuations, obtained from DNS of a generic boundary layer, to the momentum equation at the LES side of interface. Hanjalic et al. [6,33] found that by feeding the instantaneous instead of homogeneously averaged value of C_μ at the interface (that matches the RANS eddy viscosity with the subgrid-scale viscosity on the LES side) the anomaly diminishes. This suggests that the "noisy" instantaneous C_μ acts in a similar spirit as the additional random or stochastic forcing, but it is much simpler.

Defining the criteria for the positioning of the interface is another problem. The kink in the velocity profile seems most visible if the interface is placed in the region populated by coherent streaks (centered around $y^+ = 60-100$). Because of insufficient spanwise grid spacing, the computed streaks are much wider ("superstreaks") and their distance much larger than in reality. Moving the interface closer to the wall would lead to a greater proportion of the small-scale structure being captured, but reproducing faithfully the streak topology would require the grid to be substantially refined, especially in the spanwise direction, thus departing from the main motivation for the hybrid approach. On the other hand, moving the interface further away from the wall leads to the streaky pattern becoming progressively indistinct.

Paradoxically, with the interface placed at a distance sufficiently large to lose the fine near-wall structure, the anomaly in the velocity profile gradually disappears. This finding may sound discomforting on theoretical grounds, but has comforting implications in the simulation of complex flows at very high Re numbers, where the wall boundary layers are in any case so thin that they cannot be resolved in any event.

The above arguments call, however, for more advanced RANS models to be used in the near-wall RANS regions. An example of such an approach is the combination of an elliptic relaxation EVM (v^2-f or ζ-f) model for RANS with the dynamic sgs for LES [38]. The dissipation rate in the k equation is multiplied by a function in terms of the RANS and LES length scale ratio, i.e.,

$$\frac{Dk}{Dt} = \frac{\partial}{\partial x_j}\left((\nu + \nu_t)\frac{\partial k}{\partial x_j}\right) + P - \xi\varepsilon \tag{12}$$

where

$$\xi = \max\left(1, \frac{L_{RANS}}{L_{LES}}\right); \quad L_{RANS} = \frac{k_{tot}^{3/2}}{\varepsilon}; \quad L_{LES} = 0.8(\Delta x \Delta y \Delta z)^{1/3}$$

and $k_{tot.} = k_{\mathrm{res}} + k_{\mathrm{mod}.}$. Hence, for $L_{RANS} < L_{LES}$, the RANS model is in play, and for $\xi > 1$ we should have a dynamic LES. In order to avoid a discontinuity at the interface when $\xi = 1$, a "buffer" zone is introduced where RANS is still in play but with an automatic adjustment (through $\xi > 1$) in the RANS eddy viscosity to the LES sgs dynamic viscosity. In examples shown below the buffer zone extends up to $\xi \approx 1.5$, covering only a few cells for the typical RANS and coarse-LES grids used here.

Figure 8 shows velocity profiles in a plane channel obtained from hybrid computations with the above model for three Reynolds numbers using a RANS-type (coarse) mesh of $64 \times 64 \times 32$ cells (mesh 1) for $\mathrm{Re}_\tau = 590$ and 2000, and $64 \times 90 \times 32$ (mesh 2) for $\mathrm{Re}_\tau = 20{,}000$. Note that the grids for the two higher Re's are two orders of magnitude smaller than required for properly resolved LES. The results are very satisfactory, though the true test must await justification in more complex flows.

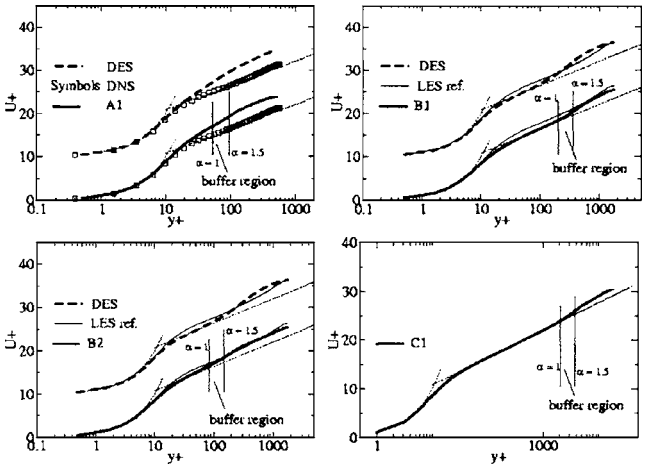

Fig. 8 Hybrid RANS (v^2-f)+LES (dynamic sgs) velocity in a plane channel [38]. A, B, and C indicate three different Re numbers, and 1 and 2 indicate two different grids.

T-RANS-Based VLES

Methods that combine RANS and LES strategy can generally be classified as very-large eddy simulations (VLESS). The name implies a form of LES (not necessarily based on grid-size filtering) with a cutoff filter at a much lower wave number, or simply solving ensemble averaged equations. The basic rationale behind VLES is resolve only very large, coherent, or deterministic structures and model the rest! Modeling a larger part of the spectrum requires a more sophisticated model than the standard sub-grid-scale model for LES, i.e., a form of RANS model that is not related to the size of the numerical mesh. As compared with the conventional RANS, the model is required only for the incoherent random fluctuations, while the large scales are resolved. The solution of the resolved part of the spectrum can follow the traditional LES practice using grid size as a basis for defining the filter (hence the name hybrid RANS/LES), or solve ensemble-or conditionally averaged Navier-Stokes equations.

We present here briefly some features and illustrations of the latter approach, named T-RANS (transient RANS) [39,40] and demonstrate its application to confined turbulent flows subjected to thermal buoyancy. It is recalled that an instantaneous flow can be decomposed into unsteady ensemble-averaged (organized) motion and random (incoherent) fluctuations, so that the instantaneous flow property $\hat{\Psi}(x_i,t)$ can be written as the sum of time-mean, deterministic, and random parts. The ensemble averaged (mean plus deterministic) quantities are fully resolved by solving in time and space equations (1) and (2)—just as in LES, whereas the unresolved contribution is modeled using RANS models for instantaneous stress and scalar flux. The total long-term averaged second moments consist of the resolved (deterministic) and incoherent (random) part which are assumed not to interact, i.e., $\overline{\hat{\Psi}\hat{Y}} = \bar{\Psi}\bar{Y} + \tilde{\Psi}\tilde{Y} + \overline{\varphi\gamma} = \overline{\langle\Psi\rangle\langle Y\rangle} + \overline{\varphi\gamma}$. Both parts are expected to be of the same order of magnitude, with the modeled contribution prevailing in the near-wall regions where the deterministic motion is weak. The dominance of the modeled contribution in the near-wall region emphasizes the importance of the RANS model which needs to be well tuned to capture near-wall behavior of turbulent stress and scalar flux.

We illustrate the potential of T-RANS in the example of Rayleigh-Bénard convection at extreme Rayleigh numbers, which are inaccessible to either conventional LES (or DNS) or to classic RANS. Here we use the algebraic subscale flux model and the corresponding algebraic stress model in which all variables are evaluated as time dependent [39,40]. Extensive testing of the RANS subscale model in a number of confined natural convection cases provides confidence in its performance close to walls. Outside the wall layers, the role of the model fades away because the dominant large-scale quasi-deterministic roll structures are fully resolved in time and space.

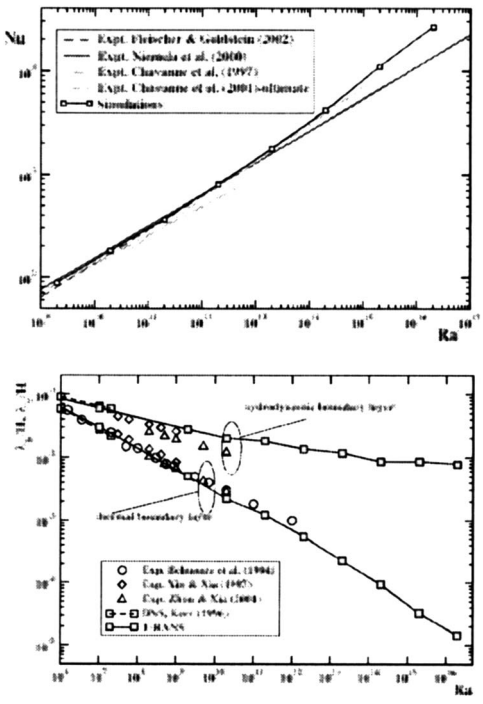

Fig. 9 T-RANS predictions of Nu number (above) and of hydrodynamic (λ_ν) and thermal (λ_θ) wall layer thickness (bellow) in R-B convection over ten decades of Ra number [40]

Figure 9 shows T-RANS computations of the Nusselt number and of the hydrodynamic (λ_ν) and thermal (λ_θ) wall layer thickness (defined by peak positions of the turbulent kinetic energy and temperature variance, respectively) as a function of Rayleigh number over ten decades, up to 10^{16} [40]. It is noted that the maximum Ra achievable by DNS is around 10^8 and by true LES about 10^9. The T-RANS computations agree very well with the available DNS for low Ra numbers as well with the experiments for low and moderate Ra (up to 10^{12}) in accord with the known correlations $\mathrm{Nu} \propto \mathrm{Ra}^{0.3}$; $\lambda_\nu/H \propto \mathrm{Ra}^{-1/7}$ and $\lambda_\theta/H \propto \mathrm{Ra}^{-1/3}$.

For higher Ra numbers the T-RANS shows clearly an increase in the exponent of Ra in accord with Kraichnan's asymptotic theory ($n \to 0.5$ for $\mathrm{Ra} \to \infty$) and recent experiments. This change in Nu-Ra slope is reflected in the change of the slopes of $\lambda_\nu(\mathrm{Ra})$ and $\lambda_\theta(\mathrm{Ra})$ curves. The capability of T-RANS for capturing the instantaneous structures is illustrated in Fig. 10, where instantaneous streaklines are presented for the central and a near-wall

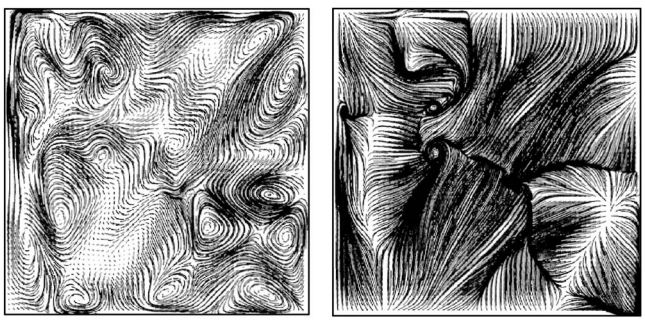

Fig. 10 T-RANS instantaneous trajectories in R-B convection for $\mathrm{Ra}=2\times10^{14}$ ($\mathrm{Pr}=0.71$). Left: at midplane ($z/H=0.5$); right: close to the top wall ($z/H=0.925$) [40].

plane for $Ra = 2 \times 10^{14}$. The T-RANS method proved subsequently to be very suitable for real engineering and environmental flows and transport phenomena at mezzo scales, e.g., for predicting diurnal change in air flow and pollutant dispersion [41].

Conclusions

Will RANS methods survive LES? This author believes that they will, at least in the next few decades. True, the anticipated further increase in computing power and wider accessibility of inexpensive high performance computers will certainly breed expanded efforts in the LES and further improvements in LES-specific numerics and subgrid-scale models can be foreseen. Already, we are witnessing LES on meshes with $O(10^8)$ cells and it is realistic to expect that within a decade such computations would be much more frequent. LES in knowledgeable hands will take an increasingly important role as a research tool in parallel with DNS. But we will probably witness also more LES abuse and false claims: LES is relatively easy to perform provided one has sufficient computing power at one's disposal. And, temptations are great. Conventional LES on a too-coarse grid of wall bounded flows, especially in attached flows regions, can be very erroneous and inferior to even simple conventional RANS.

However, in the view of this writer, it is difficult to imagine that LES will in the foreseeable future replace RANS as a daily design tool. The major impact of the impressive increase in the computing power over the past three decades has been in the shortening of the design cycle and marketing time for new products, but has had little influence on industrial preference for turbulence models. Despite the undisputable progress in the development of advanced models, the rudimentary k-ε (and, to a less extent, k-ω) model launched 35 years ago serves still as the most frequently used closure. It is realistic that this trend will continue, though hopefully we should expect to see more advanced RANS and U-RANS based on second-moment closure and their hybridization with LES.

Acknowledgment

The illustration used in this paper originated from the work of my colleagues and students: S. Kenjereš, B. Niceno, L. Tielen, and S. L. Yang.

References

[1] Hanjalic, K., and Kenjereš, S., 2001, "T-RANS Simulation of Deterministic Eddy Structure in Flows Driven by Thermal Buoyancy and Lorentz Force," Flow, Turbul. Combust., **66**, pp. 427–451.
[2] Ha Minh, H., and Kourta, A., 1993, "Semi-Deterministic Turbulence Modeling for Flows Dominated by Strong Organized Structures," *Proc. 9th Int. Symp. on Turb. Shear Flows*, Kyoto, Japan, pp. 10.5-1–10.5.6.
[3] Farge, M., Schneider, K., Pellegrino, G., Wray, A. A., and Rogallo, R. S., 2003, "Coherent Vortex Extraction in Three-Dimensional Homogeneous Turbulence: Comparison Between CVS-Wavelet and POD-Fourier Decompsition," Phys. Fluids, **15**(10), pp. 2886–2896.
[4] Girimaji, S. S., Srinivasan, R., and Jeong, E., 2003, "PANS Turbulence Model for Seamless Transition Between RANS and LES: Fixed-Point Analysis and Preliminary Results," Paper No FEDSM2003-45336, Proc. ASME FEDSM'03.
[5] Spalart, P., 2000, "Strategies for Turbulence Modelling and Simulations," Int. J. Heat Fluid Flow, **21**, pp. 252–263.
[6] Hanjalic, K., Hadziabdic, M., Temmerman, L., and Leschziner, M., 2004, "Merging LES and RANS Strategies: Zonal or Seamless Coupling?" in *Direct and Large Eddy Simulations V.*, R. Friedrich, B. Geurts, and O. Metais, eds., Kluwer Academic Publishers, Dordrecht, pp. 451–464.
[7] Pope, S. B., 1999, "A Perspective on Turbulence Modeling," in *Modeling Complex Flows*, M. D. Salas, J. N. Hefner, and L. Sakell (eds.), Kluwer Academic Publisher, Dordrecht, pp. 53–67.
[8] Niceno, B., Dronkers, A. D. T., and Hanjalic, K., 2002, "Turbulent Heat Transfer From a Multi-Layered Wall-Mounted Cube Matrix: an LES," Int. J. Heat Fluid Flow, **23**, pp. 173–185.
[9] Mainders, E., and Hanjalic, K., 1999, "Vortex Structure and Heat Transfer in Turbulent Flow Over a Wall-Mounted Natrix of Cubes," Int. J. Heat Fluid Flow, **20**, pp. 255–267.
[10] Hanjalic, K., and Jakirlic, S., 2002, "Second-Moment Turbulence Closure Modelling," in *Closure Strategies for Turbulent and Transitional Flows*, B. E. Launder and N. Sandham, eds., Cambridge University Press, Cambridge, pp. 47–101.
[11] Geroymos, G. A., Neubauer, J., Sharma, V. C., and Vallet, I., 2002, "Improved Prediction of Turbomachinery Flows Using Near-Wall Reynolds-Stress Model," ASME J. Turbomach., **124**, pp. 86–99.
[12] Craft, T. J., and Launder, B. E., 2002, "Closure Modelling Near the Two-Component Limit," in *Closure strategies for turbulent and transitional flows*, B. E. Launder and N. Sandham, eds., Cambridge University Press, Cambridge, pp. 102–126.
[13] Leschziner, M. A., and Lien, F.-S., 2002, "Numerical Aspects of Applying Second-Moment Closure to Complex Flows," In *Closure Strategies for Turbulent and Transitional Flows*, B. E. Launder and N. Sandham, eds., Cambridge University Press, Cambridge, pp. 153–187.
[14] Basara, B., 2004, "Employment of the Second-Moment Turbulence Closure on Arbitrary Unstructured Grid," Int. J. Numer. Methods Fluids, **44**(4), pp. 377–408.
[15] Basara, B., and Jakirlic, S., 2003, "A New Hybrid Modelling Strategy for Industrial CFD," Int. J. Numer. Methods Fluids, **42**, pp. 89–116.
[16] Chassaing, J., Gerolymos, G. A., and Vallet, I., 2003, "Reynolds-Stress Model Dual-Time-Stepping Computation of Unsteady Three-Dimensional Flows," AIAA J., **41**, pp. 1882–1894.
[17] Yang, S. L., Peschke, D. B., and Hanjalic, K., 2000, "Second-Moment Closure Model for IC Engine Flow Simulation Using KIVA Code," ASME J. Eng. Gas Turbines Power, **122**, pp. 355–363.
[18] Yang, S. L., Siow, Y. K., Teo, C. Y., and Hanjalic, K., 2005, "A KIVA Code With Reynolds-Stress Model for Engine Simulation," Energy Int. J., **30**, pp. 427–445.
[19] Speziale, C. G., Sarkar, S., and Gatski, T. B., 1991, "Modelling the Pressure Strain Correlation of Turbulence: An Invariant Dynamic System Approach," J. Fluid Mech., **227**, pp. 245–272.
[20] Wallin, S., and Johansson, A., 2002, "Modelling Streamline Curvature Effects in Explicit Algebraic Reynolds Stress Turbulence Models," Int. J. Heat Fluid Flow, **23**, pp. 721–730.
[21] Durbin, P., 1991, "Near-Wall Turbulence Closure Modeling Without 'Damping Functions,'" Theor. Comput. Fluid Dyn., **3**, pp. 1–13.
[22] Craft, T. J., Launder, B. E., and Suga, K., 1996, "Development and Application of a Cubic Eddy-Viscosity Model of Turbulence," Int. J. Heat Fluid Flow, **17**, pp. 108–115.
[23] Chen, W. L., Lien, F. S., and Leschziner, M. A., 1998, "Computational Prediction of Flow Around Highly Loaded Compressor-Cascade Blades With Non-Linear Eddy-Viscosity Models," Int. J. Heat Fluid Flow, **19**, pp. 307–319.
[24] Hanjalic, K., Popovac, M., and Hadziabdic, M., 2004, "A Robust Near-Wall Elliptic Relaxation Eddy-Viscosity Turbulence Model for CFD," Int. J. Heat Fluid Flow, **25**, pp. 1047–1051.
[25] Manceau, R., and Hanjalic, K., 2002, "Elliptic Blending Model: A New Near-Wall Reynolds-Stress Turbulence Closure," Phys. Fluids, **14**(2), pp. 744–754.
[26] Durbin, P. A., 1993, "Reynolds Stress Model for Near-Wall Turbulence," J. Fluid Mech., **249**, pp. 465–498.
[27] Thielen, L., Jonker, H. J., and Hanjalic, K., 2003, "Symmetry Breaking of Flow and Heat Transfer in Multiple Impinging Jets," Int. J. Heat Fluid Flow, **24**, pp. 444–453.
[28] Thielen, L., Hanjalic, K., Jonker, H., and Manceau, R., 2005, "Predictions of Flow and Heat Transfer in Multiple Impinging Jets With an Elliptic-Blending Second-Moment Closure," Int. J. Heat Mass Transfer, **48**, pp. 1583–1598.
[29] Geers, L. F. G., Tummers, M., and Hanjalic, K., 2004, "Experimental Investigation of Impinging Jet Arrays," Exp. Fluids, **36**, pp. 946–958.
[30] Hanjalic, K., Launder, B. E., and Schiestel, R., 1980, "Multiple-Scale Concepts in Turbulenct Transport Modelling," In *Turbulent Shear Flow 2*, F. Durst et al., eds., Springer, Berlin, pp. 36–49.
[31] Schiestel, R., 1987, "Multiple-Time Scale Modeling of Turbulent Flows in One Point Closures," Phys. Fluids, **30**(3), pp. 722–731.
[32] Cadiou, A., Hanjalic, K., and Stawiarski, K., 2004, "A Two-Scale Second-Moment Turbulence Closure Based on Weighted Spectrum Integration," Theor. Comput. Fluid Dyn., **18**, pp. 1–26.
[33] Temmerman, L., Leschziner, M. A., Hadziabdic, M., and Hanjalic, K., 2005, "A Hybrid Two-Layer URANS-LES Approach for Large-Eddy Simulation at Hight Reynolds Numbers," Int. J. Heat Fluid Flow, **26**, pp. 173–190.
[34] Schiestel, R., and Dejoan, A., 2005, "Towards a New Partially Integrated Transport Model for Coarse Grid and Unsteady Turbulent Flow Simulations," Theor. Comput. Fluid Dyn., **18**, pp. 443–468.
[35] Nikitin, N. V., Nocoud, F., Wasistho, B., Squires, K. D., and Spalart, P. R., 2000, "An Approach to Wall Modelling in Large-Eddy Simulations," Phys. Fluids, **12**(7), pp. 1629–1632.
[36] Piomelli, U., Balaras, E., Pasinato, H., Squires, H., and Spalart, P., 2003, "The Inner-Outer Layer Interface in Large-Eddy Simulations With Wall-Layer Models," Int. J. Heat Fluid Flow, **24**, pp. 538–550.
[37] Davidson, L., and Dahlström, S., 2004, "Hybrid LES-RANS: An Approach to Make LES Applicable at High Reynolds Number," *Proc. (CD) CHT-04, Int. Symp. on Advances in Computational Heat Transfer*, April 19–25, Norvey, ICHMT/Begell House.
[38] Hadziabdic, M., and Hanjalic, K. (to be published).
[39] Hanjalic, K., 2002, "One-Point Closure Models for Buoyancy-Driven Turbulent Flows," Annu. Rev. Fluid Mech., **34**, pp. 321–347.
[40] Kenjereš, S., and Hanjalic, K., 2002, "Numerical Insight Into Flow Structure in Ultraturbulent Thermal Convection," Phys. Rev. E, **66**, p. 036307.
[41] Kenjereš, S., and Hanjalic, K., 2002, "Combined Effects of Terrain Orography and Thermal Stratification on Pollutant Dispersion in a Town Valley: a T-RANS Simulation," J. Turbul., **3**, pp. 1–21.

Implication of Mismatch Between Stress and Strain-Rate in Turbulence Subjected to Rapid Straining and Destraining on Dynamic LES Models

Jun Chen
Department of Mechanical Engineering, Johns Hopkins University, 223 Latrobe Hall, 3400 North Charles Street, Baltimore, MD 21218
e-mail: junchen@jhu.edu
Phone: 1-410-516-5427

Joseph Katz
Department of Mechanical Engineering, Johns Hopkins University, 118 Latrobe Hall, 3400 North Charles Street, Baltimore, MD 21218
e-mail: katz@jhu.edu
Phone: 1-410-516-5470

Charles Meneveau
Department of Mechanical Engineering, Johns Hopkins University, 127 Latrobe Hall, 3400 North Charles Street, Baltimore, MD 21218
e-mail: meneveau@jhu.edu
Phone: 1-410-516-7802

Planar straining and destraining of turbulence is an idealized form of turbulence-meanflow interaction that is representative of many complex engineering applications. This paper studies experimentally the response of turbulence subjected to a process involving planar straining, a brief relaxation and destraining. Subsequent analysis quantifies the impact of the applied distortions on model coefficients of various eddy viscosity subgrid-scale models. The data are obtained using planar particle image velocimetry (PIV) in a water tank, in which high Reynolds number turbulence with very low mean velocity is generated by an array of spinning grids. Planar straining and destraining mean flows are produced by pushing and pulling a rectangular piston towards and away from the bottom wall of the tank. The velocity distributions are processed to yield the time evolution of mean subgrid dissipation rate, the Smagorinsky and dynamic model coefficients, as well as the mean subgrid-scale momentum flux during the entire process. It is found that the Smagorinsky coefficient is strongly scale dependent during periods of straining and destraining. The standard dynamic approach overpredicts the dissipation based Smagorinsky coefficient, with the model coefficient at scale Δ in the standard dynamic Smagorinsky model being close to the dissipation based Smagorinsky coefficient at scale 2Δ. The scale-dependent Smagorinsky model, which is designed to compensate for such discrepancies, yields unsatisfactory results due to subtle phase lags between the responses of the subgrid-scale stress and strain-rate tensors to the applied strains. Time lags are also observed for the SGS momentum flux at the larger filter scales considered. The dynamic and scale-dependent dynamic nonlinear mixed models do not show a significant improvement. These potential problems of SGS models suggest that more research is needed to further improve and validate SGS models in highly unsteady flows. [DOI: 10.1115/1.1989360]

1 Introduction

In most engineering applications, turbulent flows are regularly subjected to strong large-scale mean deformation. Examples include turbulent flows inside contracting or expanding channels, flows inside pumps, flows around propellers, etc. When the turbulence-to-mean-shear time scale ratio is large enough, namely $S\cdot k/\varepsilon \to \infty$ (S is the mean strain; $k \equiv 0.5\langle u_i' u_i' \rangle$ is the turbulence kinetic energy with $\langle\cdot\rangle$ denoting the averaging operation; and ε is the dissipation rate), the evolution of turbulence can be predicted by rapid-distortion theory (RDT), which neglects the nonlinear terms in the evolution equation of turbulence, thus the equation can be solved analytically (e.g., Ref. [1]). However, in many engineering flows, the turbulence-to-mean-shear time scale ratio is large, but not large enough to apply RDT.

The interactions between turbulence and strong mean straining flow have already been studied extensively. Townsend [2], Keffer [3], and Tucker and Reynolds [4] conducted hot-wire measurements of decaying grid turbulence inside a specially designed, distorting section of wind tunnel. Lee and Reynolds [5] performed direct numerical simulations (DNS) of turbulence response to several types of irrotational straining, including planar and axisymmetric straining. The simulations were performed at a Taylor microscale Reynolds number, $\mathrm{Re}_\lambda = u\lambda/\nu$, of less than 100, where u is the characteristic turbulent fluctuation and λ is the Taylor microscale.

Presently, large eddy simulation (LES) is the most rapidly developing turbulence prediction technique. Thus, it is of considerable interest to study the effects of straining on turbulence from the point of view of LES. Liu et al. [6] studied scale interactions and evolution of statistics of subgrid-scale (SGS) variables of interest in LES during axisymmetric distortion with $S\cdot k/\varepsilon \sim 7$ and $\mathrm{Re}_\lambda \sim 290$. They concluded that the simple Smagorinsky eddy-viscosity SGS model overpredicts the SGS dissipation, i.e., the flow of energy to scales smaller than the filter scale, during strong straining, and that mixed model formulations improve the model performance. The moderate Reynolds number and limited data of the Liu et al. study prevented detailed tests of the popular dynamic model [7]. Due to limitations of their experimental setup, Liu et al. only studied the effect of axisymmetric straining, and there was no possibility to study return-to-isotropy, relaxation, or destraining.

In the present study we experimentally investigate the evolution of flow variables in a cycle consisting of planar straining, relaxation, and destraining. Such a scenario is a simplification of many engineering flows, e.g., turbulence passing around a propeller blade. There, the turbulence is strained near the leading edge of the blade, and the deformation is partially reversed during the

Contributed by the Fluids Engineering Division for publication in the JOURNAL OF FLUIDS ENGINEERING. Manuscript received by the Fluids Engineering Division, August 5, 2004; Final revision: June 1, 2005. Associate Editor: Ismail Celik.

pressure recovery region, towards the trailing edge of the blade. If the flow is not massively separated, and the blade is long (almost 2D), 2-D irrotational straining (stagnation point flow) is a reasonable idealization. The main focus of this study is the response of the Smagorinsky model at various filter scales, and the performance of the dynamic and scale-dependent dynamic Smagorinsky models in reproducing the measured evolution of the Smagorinsky coefficient. A brief review of LES modeling issues, including the Smagorinsky and nonlinear mixed SGS models, is given in Sec. 2. Also discussed are the standard dynamic and scale-dependent dynamic approaches to determine the model coefficients. Details about the experimental facility and instrumentation are presented in Sec. 3. The characteristics of mean flow and turbulence before straining are documented in Sec. 4. The evolution of SGS dissipation, and a priori tests of the Smagorinksy and nonlinear mixed models are shown in Sec. 5. The performance of the Smagorinsky model for prediction of SGS momentum flux is quantified in Sec. 6. Conclusions are presented in Sec. 7.

2 Large Eddy Simulation and SGS Stress Models

Proposed in the 1960s, large eddy simulation provides a promising approach to numerically study engineering flows with complex geometry at high Reynolds number [8,9]. LES decomposes the flow variables into resolved and unresolved (subgrid scale) parts by applying a filtering operation given by

$$\widetilde{f}(\mathbf{x},t)=\int_D f(\mathbf{x}',t)G_\Delta(\mathbf{x},\mathbf{x}')d\mathbf{x}', \tag{1}$$

where D is the computational domain and G_Δ is a filtering kernel with a characteristic scale Δ. For incompressible flows, the filtered Navier-Stokes equations solved in LES are

$$\begin{aligned}\frac{\partial \widetilde{u}_i}{\partial x_i}&=0,\\ \frac{\partial \widetilde{u}_i}{\partial t}+\widetilde{u}_j\frac{\partial \widetilde{u}_i}{\partial x_j}&=-\frac{\partial}{\partial x_j}\left[\frac{\widetilde{p}}{\rho}\delta_{ij}+\tau_{ij}\right]+\nu\frac{\partial^2\widetilde{u}_i}{\partial x_j^2},\end{aligned} \tag{2}$$

where the subgrid-scale (SGS) stress, τ_{ij}, is defined as

$$\tau_{ij}=\widetilde{u_iu_j}-\widetilde{u}_i\widetilde{u}_j. \tag{3}$$

The SGS stress must be modeled properly in order to close the equation system (2).

Scale interactions, such as energy transfer between resolved and SGS scales, referring to scales larger and smaller than Δ, respectively, are fundamental physical phenomena in turbulent flows. Understanding the processes underlying the energy transfer in a turbulent field is important in successful application of LES. The influence of the SGS stresses on the resolved flow field is reflected in the transport equation of resolved and/or subgrid kinetic energy [10]. The so-called sub-grid scale energy dissipation,

$$\Pi_\Delta=-\langle\tau_{ij}\widetilde{S}_{ij}\rangle, \tag{4}$$

where

$$\widetilde{S}_{ij}=\frac{1}{2}\left(\frac{\partial\widetilde{u}_i}{\partial x_j}+\frac{\partial\widetilde{u}_j}{\partial x_i}\right) \tag{5}$$

is the resolved strain-rate tensor, plays a vital role in these equations. The SGS dissipation enters as a sink in the transport equation for mean resolved kinetic energy, and as a source term in the equation for unresolved kinetic energy [10]. It thus quantitatively describes the net energy transfer between resolved and subgrid scales. While the overall trend of energy transfer is typically from resolved to subgrid scales (forward scattering), there are locations in the flow field where the subgrid scales return energy to resolved scales (back scattering) [10,11]. In the inertial range, the mean SGS dissipation is dominant in the energy budget. Thus, its key features must be reproduced properly by SGS models.

Many different SGS models have been proposed (see reviews in Refs. [8,12]). The most popular are of the eddy-viscosity type

$$\tau_{ij}^{Smag}=-2\nu_T\widetilde{S}_{ij}, \tag{6}$$

where ν_T is the scalar eddy viscosity which relates the deviatoric part of the SGS stress to the resolved strain. The Smagorinsky model [13] is a representative of this class with

$$\nu_T=(C_S^\Delta\Delta)^2|\widetilde{S}|, \tag{7}$$

where C_S^Δ is the (Static) Smagorinsky coefficient and $|\widetilde{S}|=\sqrt{2\widetilde{S}_{ij}\widetilde{S}_{ij}}$. The so-called nonlinear mixed SGS model was proposed by applying a Taylor series expansion of $\widetilde{u}_i$ and adding the Smagorinsky model as a dissipative term [14–16]:

$$\tau_{ij}^{NL}=-2(C_{S,NL}^\Delta\Delta)^2|\widetilde{S}|\widetilde{S}_{ij}+\frac{1}{12}\Delta^2\frac{\partial\widetilde{u}_i}{\partial x_l}\frac{\partial\widetilde{u}_j}{\partial x_l} \tag{8}$$

with a model coefficient $C_{S,NL}^\Delta$ (the subscript "*NL*" denotes the nonlinear mixed model). Other widely used models are reviewed in Ref. [15].

The performance of SGS models can be evaluated by a priori tests, and by a posteriori tests [17]. In a priori tests, some selected features of the modeled stresses, $\tau_{ij}^{\mathrm{mod}}(\mathbf{x},t)$, are compared with the "real" SGS stresses, $\tau_{ij}(\mathbf{x},t)$, calculated using its definition, i.e., Eq. (3). Since a necessary condition for LES to be considered successful is that it yield correct energetics of the resolved flow, SGS models can be tested a priori by comparing the relevant effect of the SGS stresses upon the energetics, namely by comparing the measured mean SGS dissipation with the modeled mean SGS dissipation, $-\langle\tau_{ij}^{\mathrm{mod}}\widetilde{S}_{ij}\rangle$ [18].

Experiments have provided data for a priori tests of SGS models, typically in flow fields whose Reynolds numbers are higher than those provided by DNS. For example, Liu et al. [11] applied particle image velocimetry (PIV) in a turbulent jet at $\mathrm{Re}_\lambda\approx310$, and studied the performance of several SGS models. O'Neil and Meneveau [19] conducted hot-wire measurements in a turbulent plane wake at $\mathrm{Re}_\lambda\approx500$. Tao et al. [20] evaluated the statistical geometry of subgrid-scale stresses based on 3-D holographic PIV measurement in a duct flow at $\mathrm{Re}_\lambda\approx260$. Porte-Agel et al. [21] and Kleissl et al. [22] performed a priori tests using field experimental data of atmospheric boundary layer, collected by arrays of sonic anemometers. These investigations have provided considerable insight into the underlying physics of SGS dynamics, and quantified the effects of various flow parameters, such as stratification [22].

The static Smagorinsky model [13] is expressed by employing a scale-invariant constant for C_S, and its value is $C_S\approx0.16$ [23]. It is well known that a constant scale-invariant coefficient is not appropriate in complex engineering flows (e.g., Ref. [15]). Germano et al. [7,24] proposed a dynamic Smagorinsky model to determine the model coefficient locally from the resolved scales. A test filter at scale $\alpha\Delta$ (typically $\alpha=2$) is adopted and the model coefficient is determined using [24]

$$(C_S^{\Delta,DM})^2=\frac{\langle L_{ij}M_{ij}\rangle}{\langle M_{ij}M_{ij}\rangle}, \tag{9}$$

where $L_{ij}=\overline{\widetilde{u}_i\widetilde{u}_j}-\overline{\widetilde{u}}_i\cdot\overline{\widetilde{u}}_j$ and $M_{ij}=-2\Delta^2(\alpha^2|\overline{\widetilde{S}}|\overline{\widetilde{S}}_{ij}-\overline{|\widetilde{S}|\widetilde{S}_{ij}})$, and $\bar{(\ )}$ indicates filtering at $\alpha\Delta$. The averaging is done over spatial domains of statistical homogeneity or by following a fluid element in time, as in the Lagrangian dynamic model [25]. A central assumption of the traditional dynamic model is scale invariance, i.e., $C_S^\Delta=C_S^{\alpha\Delta}$ [15]. For complex flows, where this assumption is not valid (as will be seen to occur during straining of turbulence in the present analysis), a new scale-dependent dynamic model was proposed by Porte-Agel et al. [26]. In this approach, the ratio of the coefficient at two scales

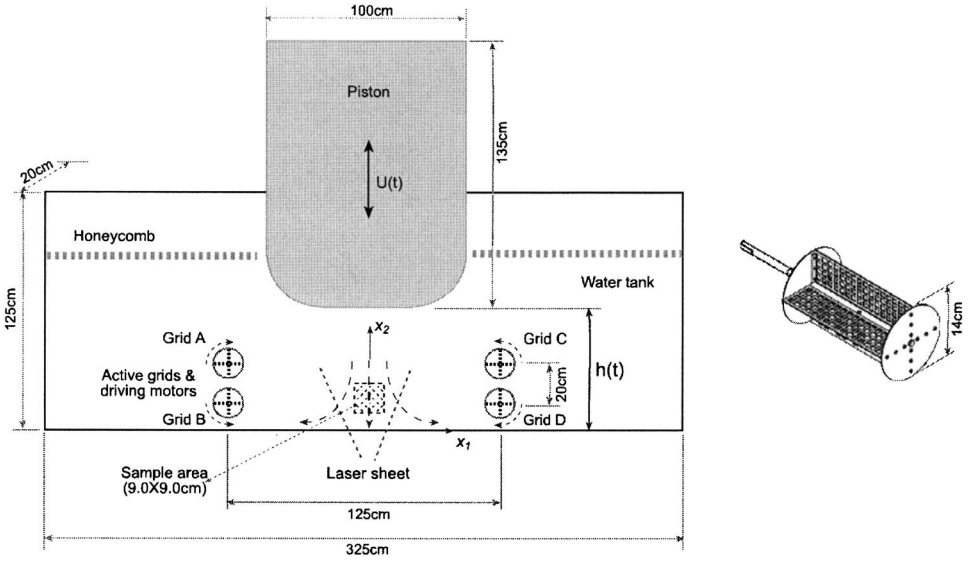

Fig. 1 Schematic description of (*a*) the experimental facility and (*b*) the activity grid

$$\beta = \frac{(C_S^{\alpha\Delta,DM})^2}{(C_S^{\Delta,DM})^2} \tag{10}$$

is introduced as another variable (a scale-dependence correction factor), to be determined dynamically. Implementation of this model involves a second test-filtering at a larger scale, $\alpha^2\Delta$, and an assumption that the scale-dependence correction factor is in itself scale-invariant, i.e.,

$$\beta = \frac{(C_S^{\alpha\Delta,DM})^2}{(C_S^{\Delta,DM})^2} = \frac{(C_S^{\alpha^2\Delta,DM})^2}{(C_S^{\alpha\Delta,DM})^2}. \tag{11}$$

As shown in Porte-Agel et al. [26], substituting in a pair of Germano identities [7] at both test-filter scales provides a solution for β from a polynomial equation, which is constructed from the first test filtering at a scale $\alpha\Delta$, and the second test filtering at scale $\alpha^2\Delta$ (denoted by $\hat{(\,)}$). Then, the tensor $M_{ij} = -2\Delta^2(\beta\alpha^2|\bar{\tilde{S}}|\bar{\tilde{S}}_{ij} - \widehat{|\tilde{S}|\tilde{S}_{ij}})$ is evaluated with the actual value of β. Solution of the polynomial equation can be quite cumbersome, especially in conjunction with the Lagrangian dynamic model. To simplify the formulation, Bou-Zeid et al. [27] proposed to utilize the observation [28,26] that the standard dynamic model yields the model coefficient appropriate to the test-filter scale, and not to that of the basic grid filter scale, i.e.,

$$(C_S^{\alpha\Delta})^2 \approx (C_S^{\Delta,DM})^2 = \frac{\langle L_{ij}M_{ij}\rangle}{\langle M_{ij}M_{ij}\rangle}, \tag{12}$$

where M_{ij} is evaluated assuming that $\beta=1$. This observation was made in the scale-dependent cases, when the filter scale tends to the Kolmogorov scale [28], or to the integral scale near a solid wall [28]. One of the objectives of the present work is to test whether this observation holds also in the case of strained turbulence. Since in LES we require the coefficient at scale Δ and not at $\alpha\Delta$, by using a second test-filter, we can write

$$(C_S^{\alpha^2\Delta})^2 \approx (C_S^{\alpha\Delta,DM})^2 = \frac{\langle Q_{ij}N_{ij}\rangle}{\langle N_{ij}N_{ij}\rangle}, \tag{13}$$

where $Q_{ij} = \widehat{\tilde{u}_i\tilde{u}_j} - \hat{\tilde{u}}_i\hat{\tilde{u}}_j$ and $N_{ij} = -2\Delta^2(\alpha^2|\hat{\tilde{S}}|\hat{\tilde{S}}_{ij} - \widehat{|\tilde{S}|\tilde{S}_{ij}})$. Then, β is computed as the ratio of Eqs. (12) and (13), and assuming that β is scale invariant, the scale-dependent dynamic model coefficient at scale Δ ($C_S^{\Delta,SDDM}$) can be expressed as a geometric extrapolation

$$(C_S^{\Delta,SDDM})^2 = \frac{(C_S^{\Delta,DM})^4}{(C_S^{\alpha\Delta,DM})^2}. \tag{14}$$

The aforementioned dynamic approaches can also be used to determine the eddy-viscosity coefficient in the nonlinear mixed model, Eq. (8), and one obtains

$$(C_{S,NL}^{\Delta,DM})^2 = \frac{\langle L_{ij}M_{ij}\rangle - \langle Y_{ij}M_{ij}\rangle}{\langle M_{ij}M_{ij}\rangle}, \tag{15}$$

where

$$Y_{ij} = \frac{1}{12}\Delta^2\left(\alpha^2\frac{\partial\bar{\tilde{u}}_i}{\partial x_l}\frac{\partial\bar{\tilde{u}}_j}{\partial x_l} - \overline{\frac{\partial\tilde{u}_i}{\partial x_l}\frac{\partial\tilde{u}_j}{\partial x_l}}\right).$$

Moreover, if the scale-dependent dynamic approach is applied, the nonlinear mixed model coefficient can be determined by

$$(C_{S,NL}^{\Delta,SDDM})^2 = \frac{(C_{S,NL}^{\Delta,DM})^4}{(C_{S,NL}^{\alpha\Delta,DM})^2} \tag{16}$$

with

$$(C_{S,NL}^{\alpha\Delta,DM})^2 = \frac{\langle Q_{ij}N_{ij}\rangle - \langle Z_{ij}N_{ij}\rangle}{\langle N_{ij}N_{ij}\rangle},$$

where

$$Z_{ij} = \frac{1}{12}\Delta^2\left(\alpha^2\frac{\partial\hat{\tilde{u}}_i}{\partial x_l}\frac{\partial\hat{\tilde{u}}_j}{\partial x_l} - \widehat{\frac{\partial\tilde{u}_i}{\partial x_l}\frac{\partial\tilde{u}_j}{\partial x_l}}\right).$$

Later in this paper we use PIV data to evaluate the evolution of measured and modeled SGS dissipation at various scales, and the resulting impact on the modeled coefficients introduced in this section.

3 Experimental Setup

3.1 Facility. A schematic description of the test facility is shown in Fig. 1. The experimental setup is composed of two subsystems. The first one generates homogeneous, isotropic turbulence (initial equilibrium turbulence) at moderately high Reynolds numbers. The turbulence is generated using symmetrically located four active grids driven by four synchronized motors whose operating parameters are adjusted to obtain near zero mean velocity prior to straining. The second subsystem applies uniform straining-relaxation-destraining on the turbulence by translating a piston vertically at prescribed velocities. The piston occupies almost the entire width of the tank. The dimensions of the water tank are 325 cm (L) $\times$ 125 cm (H) $\times$ 20 cm (W). The sample area (10×10 cm^2) is located near the center-bottom of the tank, as indicated by dashed lines in Fig. 1. Windows below and on both sides of the sample area provide optical access for PIV measurement.

Active grids have been proven to be an effective method to generate high Reynolds number isotropic turbulence. For example, Makita [29] utilized an agitator wing array driven by stepping motors in a wind tunnel. Mydlarski and Warhaft [30] employed the same idea to study the characteristics of turbulence with Re_λ varying from 50 to 473. Liu et al. [6] introduced the four rotating grids inside a small water tank to generate high-intensity turbulence with very little mean flow. The present rotating grid is shown in Fig. 1(*b*). It has four blades made of perforated metal plates with a solidity of 40%. Each grid is independently driven by a $\frac{1}{2}$ horsepower ac motor, with variable frequency inverter providing speed control. The grids can be maintained at a stable speed up to 500 rpm. The speed of each grid is adjusted separately to optimize the homogeneity of turbulence in the test section, as determined from repeated measurements. For all the data discussed in this paper, the bottom two grids are operated at a constant speed of 450 rpm and the top two at 375 rpm. The differences in speed are needed to achieve acceptable spatial uniformity of the turbulence.

When the piston moves vertically, the flow pattern under it becomes a 2-D stagnation-point flow with spatially uniform strain rate. The resulting strain rate tensor is

$$\mathbf{S}(t) = S(t)\begin{bmatrix} 1 & 0 & 0 \\ 0 & -1 & 0 \\ 0 & 0 & 0 \end{bmatrix}, \tag{17}$$

where $S(t)$ is the strain rate magnitude. Moreover, if the piston elevation, $h(t)$, is exponential in time, i.e.,

$$h(t) = He^{-S(t-t_0)} \tag{18}$$

the strain rate is also time independent.

The bottom surface of the piston has rounded corners to prevent possible flow separation which is critical when the flow is destrained. The piston is driven by a motion control system through a lever with a magnification ratio of 3. The motion control system consists of an Exlar GS60-1010 linear electric actuator, an Emerson MX-1600 brushless drive, and an Emerson AXIMA 2000 programmable motion control module, as illustrated in Fig. 2. The dynamic load rating of the actuator is 21,200 N, and its maximum velocity is 1.018 m/s. The stroke of the actuator is 25.4 cm, i.e., the maximum displacement of the piston is 76.2 cm. The trajectory of the piston is programmed through the motion control module, enabling us to adjust the relevant parameters and to obtain different trajectories. Two honeycombs (8.0 cm thick, 1.0 cm cell diameter) are placed near the top part of the water tank to alleviate the influence of surface waves.

The trajectory of the piston designed for this study is shown in Fig. 3. In each cycle, the piston moves downward to generate straining, rests for some time (relaxation), and then moves upward to generate destraining. Details of the actual piston's trajectory and its effect on the flow will be analyzed in the next section. The trajectory of the piston is monitored by a high-speed video camera (Kodak Ektapro EM) operating at 250 frames per second, as shown in Fig. 2. Results confirm that the motion control system is repeatable. The rms value of variance between piston trajectories in different runs at any given time is about 2 mm.

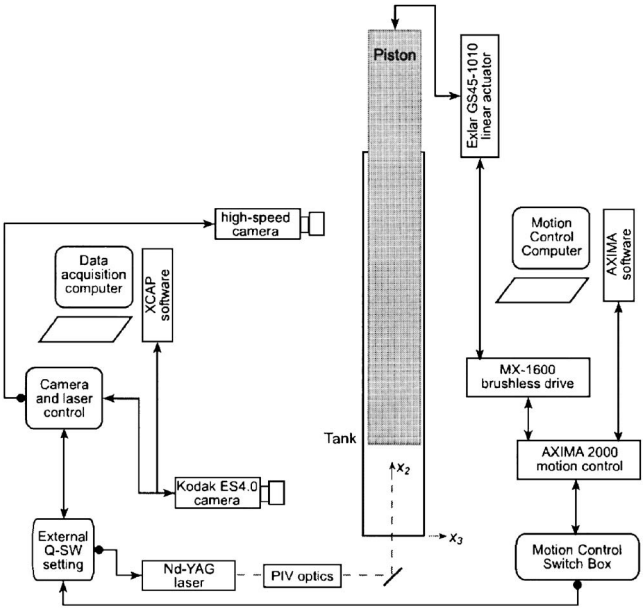

Fig. 2 Schematics of the instrumentation and control system

3.2 Instrumentation. Particle image velocimetry (PIV) is used to measure the velocity field. The flow field is seeded with hollow glass beads (median diameter 10 μm, specific gravity 1.1). The light source is a dual-head Nd-YAG laser (532 nm, 120 mJ) whose beam is expanded to a sheet and illuminates the x_1-x_2 plane along the centerline of the tank. A Kodak ES-4.0 digital camera, with 2048 pixel $\times$ 2048 pixel resolution, operating at 5 Hz under double-exposure mode, is used to record images. The sample area is 9.0×9.0 cm^2 of which the upper 9.0×7.5 cm^2 is used during the analysis. The lower 1.5 cm part shows some bottom effects and thus is discarded. The analysis consists of image enhancement, followed by cross correlation to determine the velocity [31,32]. The size of interrogation windows is 32×32 pixel. With 50% overlap, the vector spacing is 0.7 mm. A total of 120×100 vectors are obtained from each image pair.

As shown in Fig. 2, the motion control system and the PIV measurement are synchronized in order to obtain repeated mea-

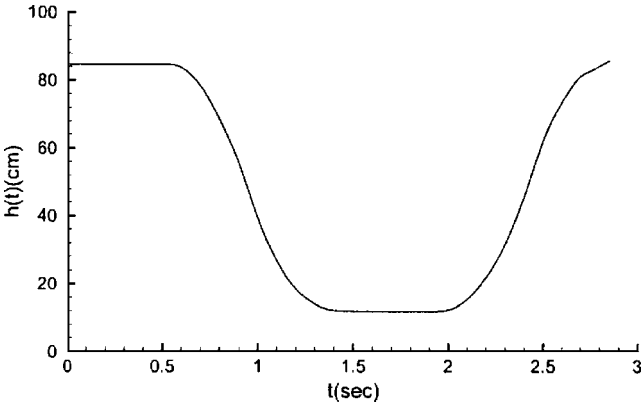

Fig. 3 Piston motion trajectory

surements at exactly the same time in every cycle. Repeated measurements enable us to calculate the ensemble statistics as a function of phase in the piston cycle. Since the present camera operates up to 5 Hz under the double-exposure mode, the temporal resolution of the measurements is 0.2 s. To increase the temporal resolution of the statistics, we record sequences at varying initial delay. The data are obtained at a total of 48 phases during the trajectory cycle providing a temporal resolution of 0.05 s. Since no frequency spectra or time derivative are needed, this resolution is appropriate for this study. At every time step, the measurement is repeated 1000 times, which provides a good ensemble set for statistical analysis and statistical convergence. The minimum interval between adjacent repeated measurements is set to 3 min, so that the background turbulence in later runs is not influenced by the history of previous runs.

The typical conservative uncertainty of the instantaneous data is 0.2 pixels, and the relative uncertainty is about 2% (for a characteristic displacement of 10.0 pixels). Consequently, the uncertainty in the mean velocity (ensemble set of 1000) is 0.06%, and the rms value is 0.4%. The uncertainty in terms involving mean velocity gradient is about 0.5%. Further details on errors and uncertainties in the present analysis procedure are presented in Roth et al. [31] and Roth and Katz [32]. Extended discussion on uncertainties in PIV data analysis can be found in Refs. [33–35], etc.

4 Flow Characterization

4.1 Mean Flow. Prior to straining, the flow consists of the grid generated turbulence, whereas during the straining one can identify the stagnation point flow along with the turbulence. The characteristics of the mean flow are evaluated by calculating an ensemble mean of velocity components, $U_1(\mathbf{x},t)$ and $U_2(\mathbf{x},t)$, at every point. Figure 4 shows some streamlines of the mean flow at $t=1.160$ s and $t=2.160$ s, corresponding to the times with strong straining and destraining, respectively. The mean flow is of stagnation-point-type in both cases.

The strain rate of mean flow is then evaluated from the data using central finite differencing:

$$\begin{cases} S_{11}(\mathbf{x},t) = \partial U_1(\mathbf{x},t)/\partial x_1, \\ S_{22}(\mathbf{x},t) = \partial U_2(\mathbf{x},t)/\partial x_2, \end{cases} \qquad S = (S_{11} - S_{22})/2. \tag{19}$$

The evolution of the spatially averaged strain rate of mean flow is presented in Fig. 5. The error bars represent the standard deviation of the local values from the spatially averaged strain, i.e., the applied straining and destraining are nearly uniform across the field of view. According to the sign of mean straining, the cycle can be divided into four regimes: initial equilibrium, plane straining, relaxation, and plane destraining. The magnitudes of peak straining and destraining are both about 3.5 s^{-1}.

4.2 Initial Equilibrium Turbulence. The fluctuating velocity components are calculated from the measured velocity, $u_i(\mathbf{x},t)$, using Reynolds decomposition:

$$u_i'(\mathbf{x},t) \equiv u_i(\mathbf{x},t) - U_i(\mathbf{x},t). \tag{20}$$

The mean and rms values of the initial equilibrium turbulence, U_i and $u_i^{rms}=\langle u_i' u_i' \rangle^{1/2}$ (no summation over i), are analyzed based on the data ensemble at $t=0.210$ s. The mean values of the two velocity components, $U_1 \approx 0.003$ m/s and $U_2 \approx 0.029$ m/s, are much weaker than the mean velocity applied by straining and destraining. The initial spatial mean of the rms velocity fluctuations are $u_1^{rms} \approx 0.084$ m/s and $u_2^{rms} \approx 0.076$ m/s. Their spatial distributions, shown in Fig. 6, display good spatial homogeneity for both components. The homogeneity at different scales is also verified by comparing energy spectra at different locations in the field (not shown). Figure 7 shows the one-dimensional kinetic energy spectra of the initial equilibrium turbulence. The spectra are calculated using data along four lines near the image center, horizontal lines for κ_1 and vertical lines for κ_2. The ensemble mean velocity of every point is subtracted, and the data are linearly detrended, i.e., the mean linear trend of the finite instantaneous data (determined through least-square fit) is subtracted from the original values. This procedure maintains only the fluctuating components with nearly periodic boundary conditions for spectral analysis. There is no additional windowing assuring minimal impact on the variance, as discussed in Ref. [36]. The spectra are calculated using fast Fourier transforms (FFTs), and then averaged over the four lines, and over the 1000 realizations in the ensemble set. Two longitudinal, $E_{11}(\kappa_1)$ and $E_{22}(\kappa_2)$, and two transverse, $\frac{3}{4}E_{11}(\kappa_2)$ and $\frac{3}{4}E_{22}(\kappa_1)$, spectra in both directions, are presented. The four curves show fairly good agreement except at the high wave number range, which verifies that the initial equilibrium turbulence is nearly isotropic [37]. In the inertial range of homogeneous isotropic turbulence

$$E_{11}(\kappa_1) = \tfrac{18}{55} C_\kappa \varepsilon^{2/3} \kappa_1^{-5/3} \tag{21}$$

where C_κ is the Kolmogorov constant, taken as $C_\kappa=1.7$ in the present study. With the available 1-D spectra, one may estimate

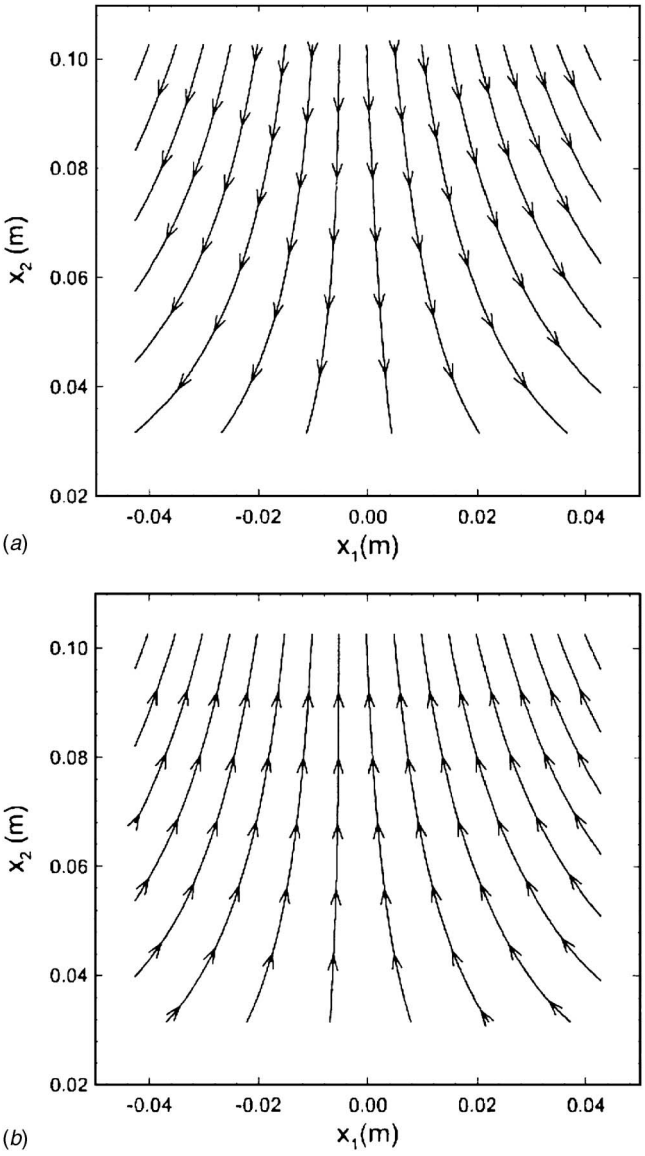

Fig. 4 Mean flow streamline patterns at (*a*) $t=1.160$ s and (*b*) $t=2.160$ s

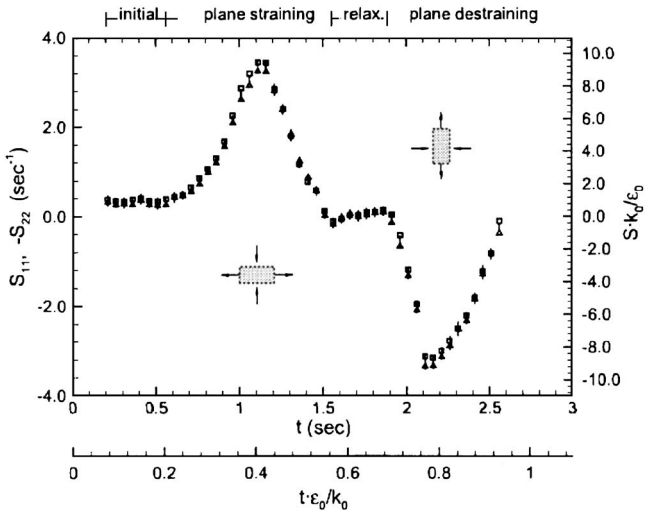

Fig. 5 Evolution of mean strain, spatially averaged rate S_{11} (squares) and $-S_{22}$ (triangles). The error bars represent the standard deviation of spatial distribution of $S(t)$.

the dissipation rate by curve-fitting a $-\frac{5}{3}$ slope line to the data. The estimated initial dissipation rate for the present result is $\varepsilon_0 \sim 0.0035\ \mathrm{m}^2/\mathrm{s}^3$.

Other turbulence parameters of the initial equilibrium turbulence may be estimated based on ε_0 and characteristic turbulence rms velocity $u \equiv (u_1^{rms}+u_2^{rms})/2 \sim 0.08$ m/s. The results are: integral scale, $l_0 \sim u^3/\varepsilon_0 = 0.13$ m; turbulent kinetic energy, $k_0 = 3/2 \cdot u^2 = 0.0096\ \mathrm{m}^2/\mathrm{s}^2$; Taylor's microscale, $\lambda_0 \sim u\sqrt{15\nu/\varepsilon_0} = 0.0052$ m; Kolmogorov length scale, $\eta_0 \sim (\nu^3/\varepsilon_0)^{1/4} \sim 130\ \mu$m; and the microscale Reynolds number, $\mathrm{Re}_\lambda \sim 400$. The turbulence-to-mean-strain time scale ratio is evaluated as $S_{\max} \cdot k_0/\varepsilon_0 \sim 9.5$.

5 Evolution of Mean SGS Statistics

As in Liu et al. [6], we use a two-dimensional top-hat filter with scale Δ, defined as

$$G_\Delta(x_1,x_2) = \begin{cases} \dfrac{1}{\Delta^2} & \text{if } |x_1| < \dfrac{\Delta}{2} \,\&\, |x_2| < \dfrac{\Delta}{2}, \\ 0 & \text{otherwise.} \end{cases} \tag{22}$$

The filtered velocities and SGS stresses are then calculated according to Eqs. (1) and (3). Convolutions are evaluated in the physical space.

5.1 Mean SGS Dissipation. The evolution of mean SGS dissipation is given in Fig. 8. In the present study, which is based on 2D PIV, a 2D surrogate is evaluated using only the available two-dimensional terms:

$$\Pi_\Delta = -(\langle \tau_{11}\widetilde{S}_{11}\rangle + \langle \tau_{22}\widetilde{S}_{22}\rangle + 2\langle \tau_{12}\widetilde{S}_{12}\rangle) \tag{23}$$

The analysis is repeated at three filter scales: $\Delta = 25\eta_0$, $\Delta = 50\eta_0$, and $\Delta = 100\eta_0$. One can see that for these scales, the mean SGS dissipation is positive at all times, i.e., there is no global backscatter. During the initial stage, the SGS dissipation is nearly scale independent, as expected in the inertial range. However, during the straining and destraining periods, the SGS dissipation is strongly scale-dependent. During the relaxation regime, $1.6s \leqslant t \leqslant 1.9s$, all three curves collapse, suggesting a scale-independent behavior during unforced relaxation conditions. One striking trend is that the dissipation peak in the destraining period is significantly lower than the peak in the straining period, although the amplitudes of the straining and destraining are about the same. The ratio of peak SGS dissipation during straining and destraining is about 2:1, well beyond the range that can be caused by measurement uncertainties. The cause of this trend is related to the fact that the initial condition for the destraining differs from isotropic turbulence since the relaxation to isotropy has not fully ended. This phenomenon is studied in more detail in a separate publication [35].

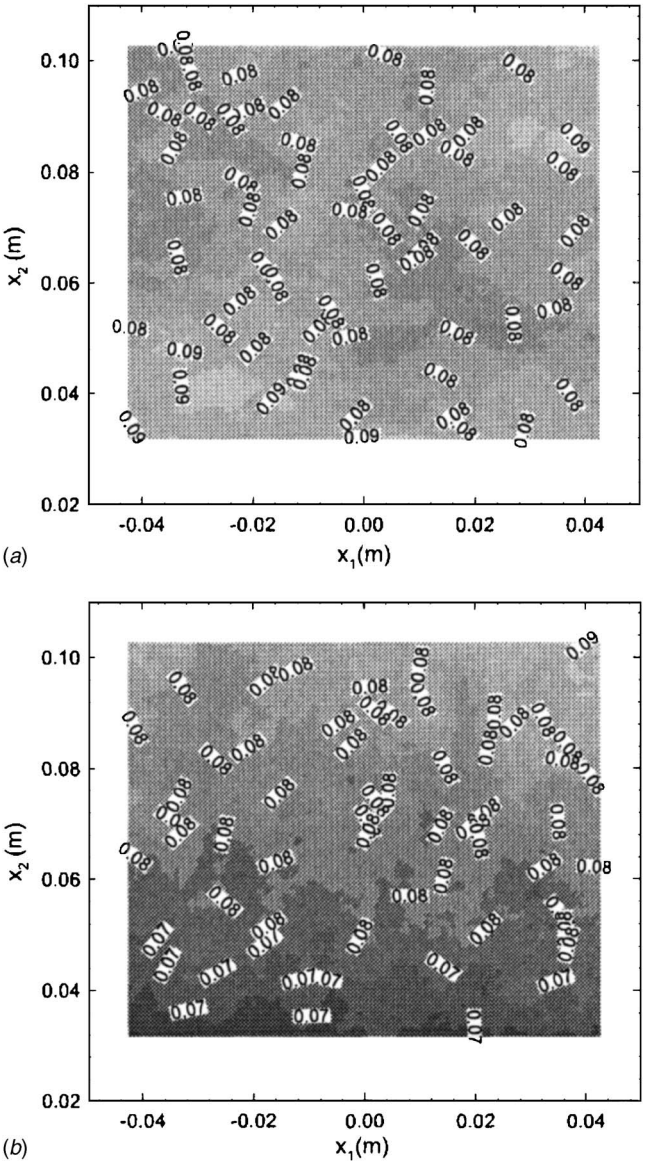

Fig. 6 Spatial distribution of rms velocity fluctuations of the initial turbulence (t=0.210 s) (*a*) u_1 and (*b*) u_2

5.2 Dissipation Based Smagorinsky Model Coefficient. The dissipation based Smagorinsky model coefficient at different times during the motion cycle can be computed by balancing the mean SGS dissipation and the modeled one using the Smagorinsky model, i.e.,

$$-\langle \tau_{ij}\widetilde{S}_{ij}\rangle = 2(C_S^\Delta \Delta)^2 \langle |\widetilde{S}|\widetilde{S}_{ij}\widetilde{S}_{ij}\rangle \tag{24}$$

The coefficients obtained in this way guarantee the correct reproduction of mean energetics, and thus can be used to evaluate the model coefficients determined using other approaches. The evolution of the term $2\Delta^2\langle |\widetilde{S}|\widetilde{S}_{ij}\widetilde{S}_{ij}\rangle$ at three different filter scales is presented in Fig. 9, again using a 2D surrogate evaluation based on the PIV data, which involves three terms, as in Eq. (23). The dissipation based Smagorinsky model coefficient

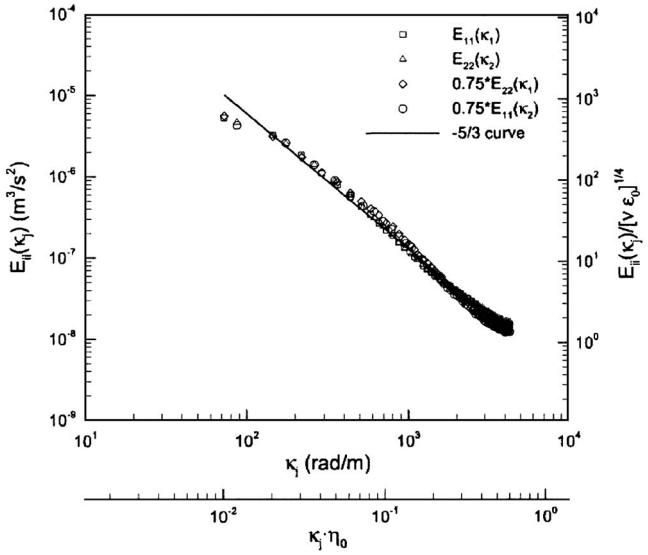

Fig. 7 Kinetic energy spectra of the initial equilibrium turbulence (t=0.210 s)

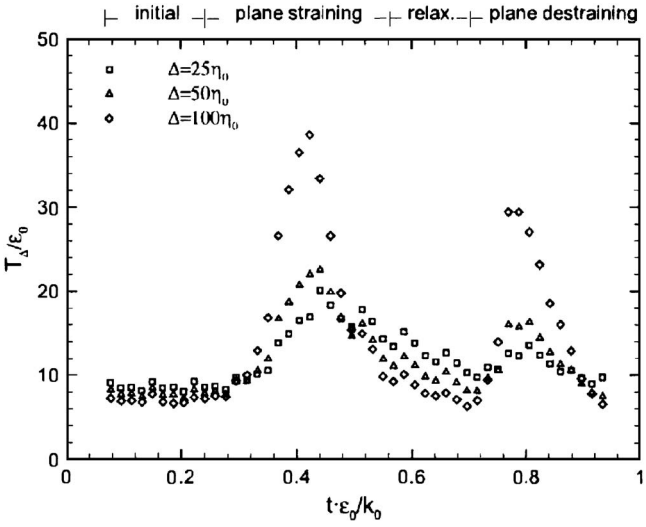

Fig. 9 Evolution of the term $T_\Delta=2\Delta^2\langle|\tilde{S}|\tilde{S}_{ij}\tilde{S}_{ij}\rangle$ at different scales

$$(C_S^\Delta)^2=\frac{-\langle\tau_{ij}\tilde{S}_{ij}\rangle}{2\Delta^2\langle|\tilde{S}|\tilde{S}_{ij}\tilde{S}_{ij}\rangle} \tag{25}$$

is plotted in Fig. 10 for three different filter scales. The lines in this figure (and subsequently in Figs. 11–17) represent running averages using a five-point filter with the following weights: [0:075; 0:175; 0:5; 0:175; 0:075], centered around each point. This process reduces the fluctuations in the original data, which is shown as symbols. Another line representing the static Smagorinsky model coefficient, C_S=0.16, is also shown. The main trends of the dissipation based coefficient during the flow evolution are as follows: after an approximately scale-invariant behavior before straining, in which $(C_S^\Delta)^2$ is in a range between 0.026 and 0.032, there is a sudden drop of $(C_S^\Delta)^2$ when the straining starts. The cause is that $2\Delta^2\langle|\tilde{S}|\tilde{S}_{ij}\tilde{S}_{ij}\rangle$ responds slightly more quickly to the applied strain than the SGS dissipation, which contains the SGS stress. After the initial decrease, the coefficients increase above the equilibrium value, with the deviation increasing with Δ. The destraining period is similar, with a decrease in coefficient followed by an increase. The relaxation period is also characterized by a scale-dependent coefficient. The denominator decreases faster than the real dissipation since the former depends significantly on the applied strain, especially at large scales.

5.3 Dynamic Smagorinsky Model Coefficient. The Smagorinsky model coefficients determined by the standard dynamic model [Eq. (9), α=2] at two different scales are shown in Fig. 11. For the purpose of comparison, the corresponding dissipation based Smagorinsky model coefficients at the same scale are also plotted. For $\Delta=25\eta_0$, the dynamic Smagorinsky model significantly overpredicts the coefficient during straining. Overprediction during straining is also observed at $\Delta=50\eta_0$. These results imply that the dynamic Smagorinsky model overpredicts the SGS dissipation. In fact, for $\Delta=25\eta_0$, using the static coefficient would yield more accurate results than the dynamic Smagorinsky model. For $\Delta=50\eta_0$, the dynamic Smagorinsky model overestimates the coefficient during straining by as much as the static Smagorinsky model underpredicts it.

As summarized in Sec. 1, prior work has shown that when the

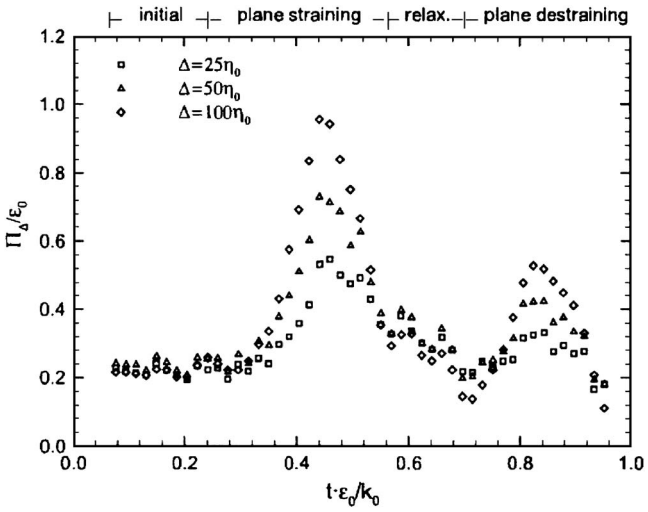

Fig. 8 Evolution of mean SGS dissipation

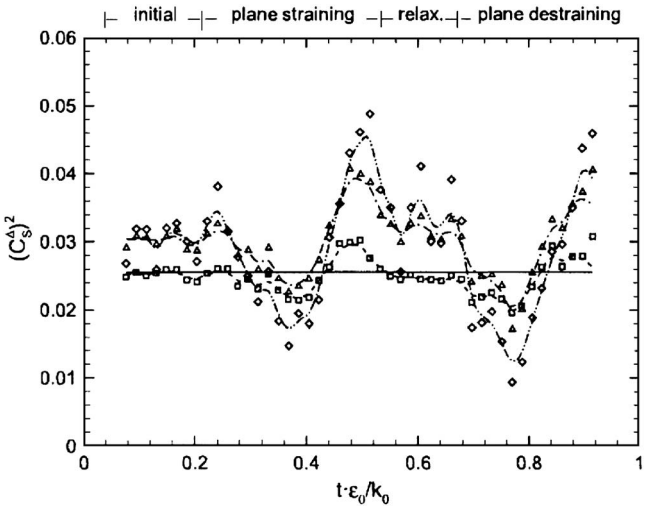

Fig. 10 Evolution of the dissipation based Smagorinsky model coefficients $(C_S^\Delta)^2$ at three different filter scales. Squares+dash line: $\Delta=25\eta_0$, triangles+dashdot line: $\Delta=50\eta_0$, diamonds+dashdotdot line: $\Delta=100\eta_0$, and solid line: C_S^Δ=0.16.

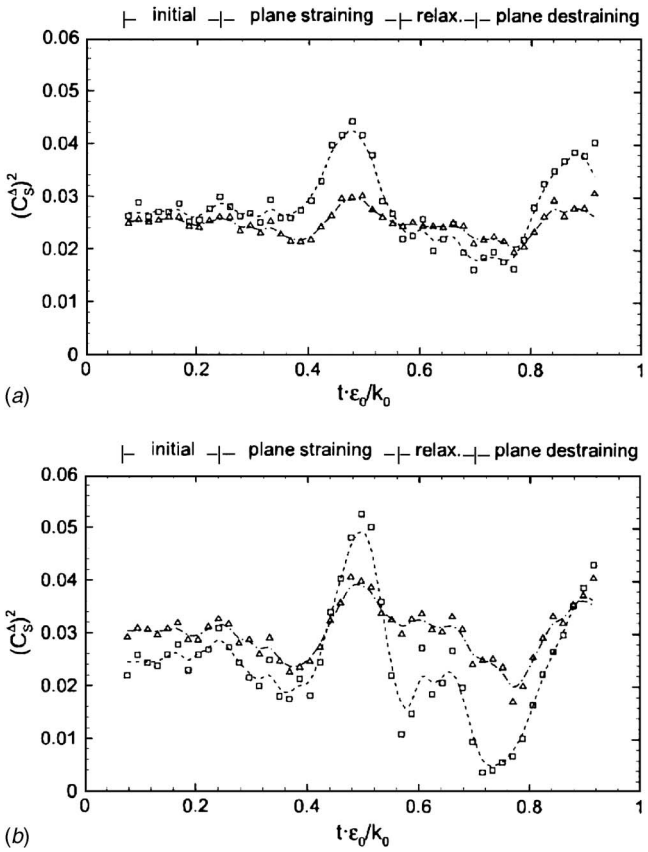

Fig. 11 Evolution of standard dynamic model coefficients (squares and dash lines) and comparison with the dissipation based Smagorinsky model coefficients (triangles and dashdot lines, given in Fig. 12). (*a*) $\Delta = 25\eta_0$ and (*b*) $\Delta = 50\eta_0$.

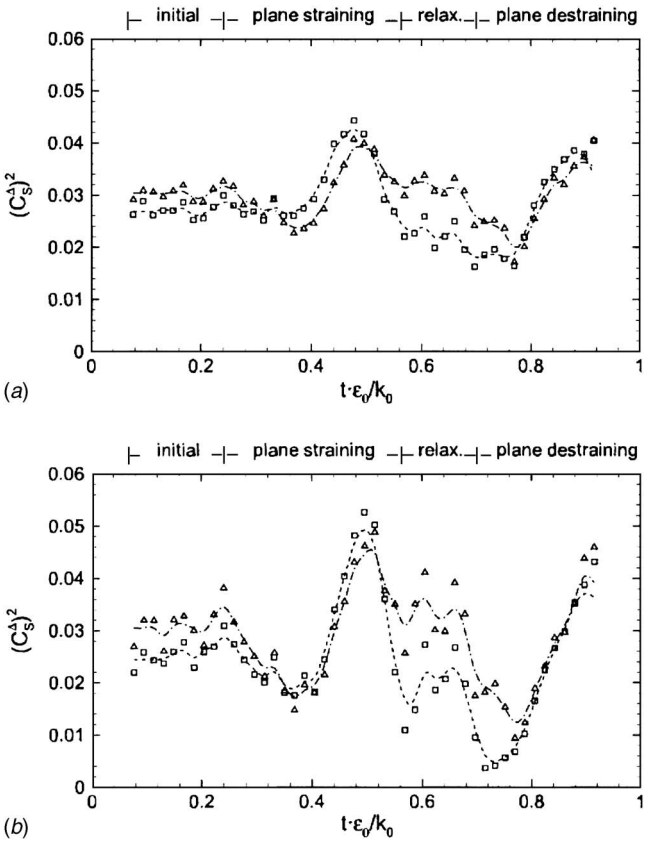

Fig. 12 Evolution of standard dynamic model coefficient at scale Δ (squares and dash lines) compared to the evolution of the dissipation-based Smagorinsky model coefficient at scale 2Δ (triangles and dashdot lines). (*a*) $\Delta = 25\eta_0$ and (*b*) $\Delta = 50\eta_0$.

Smagorinsky model coefficient is scale dependent, the standard dynamic Smagorinsky model yields the coefficient appropriate for the test-filter scale ($\alpha\Delta$). To test this trend in the present data, Fig. 12 compares the Smagorinsky coefficient determined by the dynamic approach at scale Δ with the dissipation based Smagorinsky coefficient at scale 2Δ. As is evident, the two curves agree with each other very well during straining and destraining periods. However, the agreement does not persisit for the entire time. In particular, there are differences during the relaxation period, for both $\Delta = 25\eta_0$ and $\Delta = 50\eta_0$.

5.4 Scale-Dependent Dynamic Smagorinsky Model Coefficient. The scale-dependent dynamic Smagorinsky model requires filtering at scale 4Δ, and since $100\eta_0$ is the largest filter size that we can apply to our data due to its finite extent, only the $\Delta = 25\eta_0$ case is amenable to analysis. Figure 13 presents the evolution of model coefficient for the scale-dependent dynamic Smagorinsky model computed according to Eq. (14). The evolutions of the dynamic and dissipation based Smagorinsky coefficients are also plotted for comparison. Right after the peak straining, i.e., between $t = 1.2$ s and $t = 1.4$ s the scale-dependent dynamic Smagorinsky model does give a slightly better estimation of the model coefficient than the standard (scale-invariant) dynamic Smagorinsky model, in the sense that coefficient obtained by the scale-dependent dynamic approach is lower (i.e., closer to the dissipation based coefficient) than the value obtained by the standard dynamic approach. Nevertheless, during the initial stages of straining up to the peak value, during the relaxation period, and during destraining, the prediction is worse than that of the standard dynamic Smagorinsky model. To understand the origin of this unexpected behavior, note that according to Eq. (14), the scale-dependent dynamic Smagorinsky coefficients involves the ratio of two dynamic Smagorinsky model coefficients, which are very sensitive to small phase shifts in their time response to the applied straining. To examine the phase difference, Fig. 14 compares the evolution of the two dynamic Smagorinsky coefficients, $C_S^{\Delta,DM}$ and $C_S^{2\Delta,DM}$. As is evident, during the rise of straining and destraining there is a small temporal phase mismatch between the

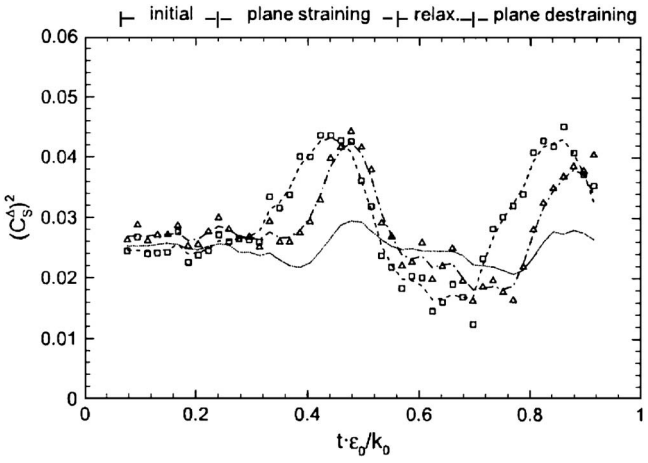

Fig. 13 Evolution of scale-dependent dynamic model coefficient $C_S^{\Delta,SDDM}$ (squares+dash line) in comparison to the dissipation-based Smagorinsky model coefficient C_S^{Δ} (dotted line), and the standard dynamic model coefficient $C_S^{\Delta,DM}$ (triangles+dashdot line). $\Delta = 25\eta_0$ for all three curves.

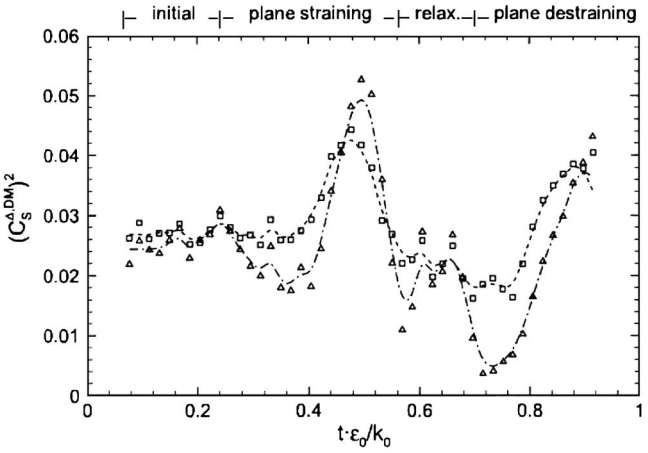

Fig. 14 Evolution of the coefficient $C_S^{\Delta,DM}$ (squares+dash line) and $C_S^{2\Delta,DM}$ (triangles+dashdot line) for $\Delta=25\eta_0$, which are used in the scale-dependent dynamic approach, Eq. (13)

two curves. The coefficient at the larger scale rises slightly later, and as a result it is actually smaller than the coefficient at the smaller scale, even though the coefficient at the larger scale reaches larger values later on. Such a small mismatch causes the significant overprediction of model coefficient in Fig. 13.

In summary, for $\Delta=25\eta_0$ and for this particular flow, the dynamic and scale-dependent dynamic Smagorinsky models overreact to the applied distortion, and predict coefficients that would perform worse than the static Smagorinsky model.

5.5 Model Coefficients in Nonlinear Mixed Model. Figure 15 shows the dissipation based model coefficient of the nonlinear mixed model, $C_{S,NL}^{\Delta}$, determined by balancing the modeled and real SGS dissipation, and by the standard dynamic approach at two scales. They show limited improvement compared to the standard dynamic Smagorinsky model results (Fig. 11). The coefficients of scale-dependent dynamic mixed model are given in Fig. 16. The scale-dependent dynamic approach again has a worse performance, which can again be attributed to a response time mismatch of the SGS stresses calculated at different filter scales.

5.6 Uncertainty Estimates of the Measured Model Coefficients. The uncertainty associated with the aforementioned model coefficients is difficult to evaluate formally using error propagation concepts due to the very complicated processes involving filtering, high-order moments, and differentiation, e.g., Eqs. (25), (9), and (14). Instead, we adopt a Monte Carlo approach to estimate the uncertainty and error propagation. Every vector of instantaneous measurement is contaminated by a synthetically generated noise, which follows a Gaussian distribution with zero mean and a standard deviation simulating the 0.2 pixel uncertainty of the PIV measurement. In other words, we add noise with deviation 0.0044 m/s to each velocity component. Using ten realizations of such randomly contaminated data, we observe relative differences of at most 0.3% in the computed Smagorinsky coefficients. For the standard and scale-dependent dynamic Smagorinsky models of the same test cases, the differences in the coefficients were even lower, about 0.08%.

6 SGS Momentum Flux

In the previous section, the effectiveness of three typical SGS models is evaluated by analyzing their ability to reproduce the correct SGS dissipation. Besides SGS dissipation, other turbulence statistics related to SGS physics are also of interest. The mean SGS stress $\langle \tau_{ij} \rangle$, or SGS momentum flux, plays a significant role in the mean momentum transport, as reflected in the ensemble average of the filtered momentum equation [Eq. (2)], when the

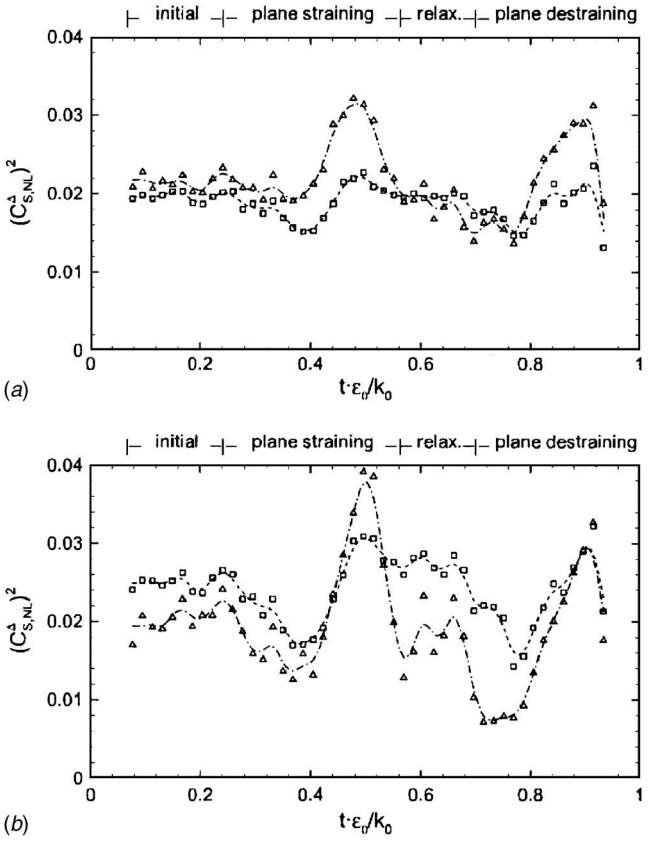

Fig. 15 Evolution of standard dynamic coefficient $(C_{S,NL}^{\Delta,DM})^2$ of Eq. (15) (triangles and dashdot lines) in the mixed model in comparison with the dissipation-based model coefficient obtained by balancing SGS dissipation (squares and dash lines). (a) $\Delta=25\eta_0$ and (b) $\Delta=50\eta_0$.

filter scale is not negligibly small compared to the size of the large-scale eddies. It has often been stated that the Smagorinsky models cannot reproduce both SGS dissipation and the SGS stress magnitudes simultaneously (see Refs. [1,15]). However, recently Li and Meneveau [38] have shown theoretically, from a model spectrum for strained turbulence, that as far as the mean SGS

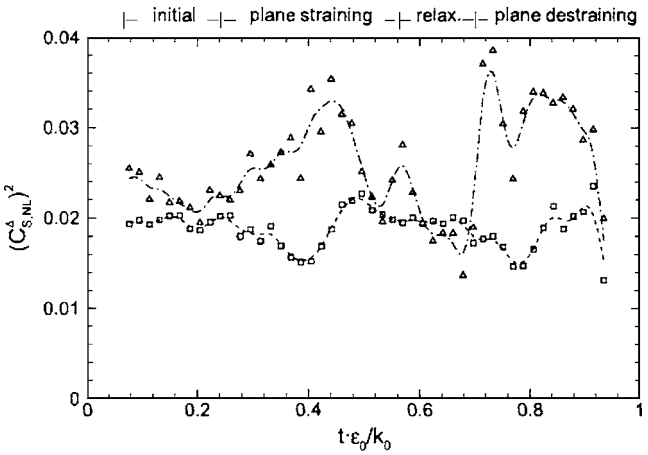

Fig. 16 Evolution of scale-dependent dynamic nonlinear model coefficient $(C_{S,NL}^{\Delta,SDDM})^2$ of Eq. (16) (triangles and dashdot lines) in comparison with the dissipation-based nonlinear model coefficients (squares and dash lines).

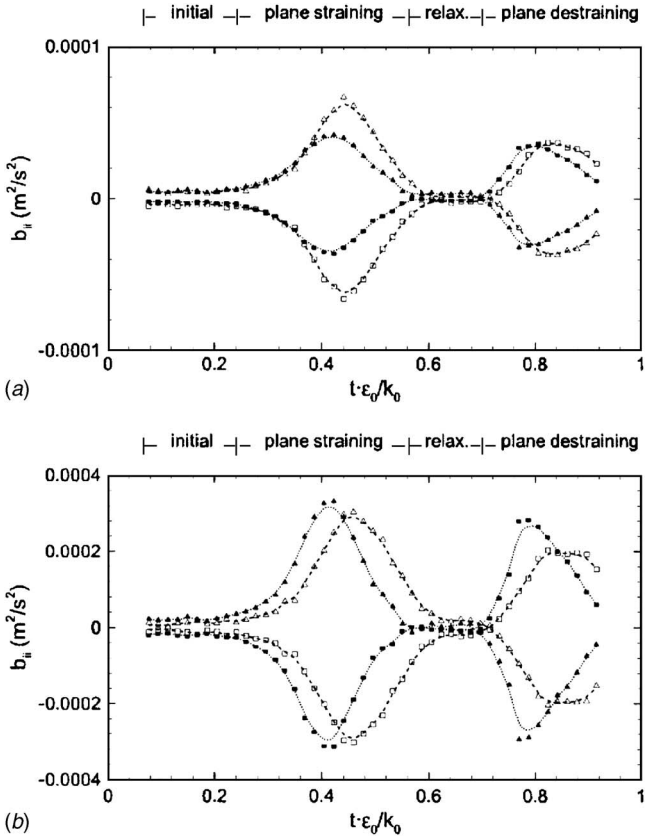

Fig. 17 Evolution of the modeled and dissipation-based mean SGS stress anisotropy tensor terms (b_{11} and b_{22}). (*a*) $\Delta = 25\eta_0$ and (*b*) $\Delta = 100\eta_0$. Open squares+dash lines: b_{11}, solid squares+dotted lines: b_{11}^{mod}, open triangles+dash lines: b_{22}, and solid triangles+dotted lines: b_{22}^{mod}.

stress, or mean momentum flux, is concerned, the predictions from the Smagorinsky model should be fairly accurate.

We evaluate the mean SGS stress from the data. To focus upon the anisotropy, we compute a 2-D surrogate of the anisotropy tensor,

$$b_{ij} = \langle \tau_{ij} \rangle - \tfrac{1}{2} \langle \tau_{kk} \rangle \delta_{ij}. \tag{26}$$

The same quantity is computed using the static Smagorinsky model with $C_S^{\Delta} = 0.16$. The results are presented at two filter scales in Figs. 17(*a*) and 17(*b*). It is evident that the anisotropy tensor increases with Δ during straining and destraining. At both scales, during straining and destraining, the Smagorinsky model predictions are of the same order of magnitude as the real measured values, in rough agreement with the analysis of Li and Meneveau [38], which states that in the presence of weak straining $\langle \tau_{ij} \rangle \approx \langle \tau_{ij}^{\mathrm{mod}} \rangle$. In more detail, however, the Smagorinsky model underpredicts the real SGS mean stress by about 30% for $\Delta = 25\eta_0$. The result at $\Delta = 100\eta_0$ shows a different behavior. The peak is predicted well during straining and overpredicted during destraining, and the mean stress predicted by the Smagorinsky model shows a premature response compared with the real SGS momentum flux. This behavior is also consistent with the general observation that the SGS stress response is delayed with respect to the applied straining.

7 Conclusions

An experimental a priori study of various eddy viscosity SGS models is performed on turbulence subjected to a sequence of straining and destraining. The experiments subject initially homogeneous isotropic turbulence to 2D irrotational straining, followed by relaxation, and then by destraining. The turbulence is generated using four active grids and a computer controlled piston creating a stagnation point flow generates the straining. Planar PIV is used for measuring the velocity. The data base, consisting of 1000 vector maps at every phase of the cycle, is used for statistical analysis.

A priori tests are performed on three SGS models: Smagorinsky, standard dynamic, and scale-dependent Smagorinsky models, as well as on the nonlinear mixed models. The dissipation based Smagorinsky model coefficient is obtained by matching predicted SGS dissipation with the real one. It shows strong scale dependence during the straining-relaxation-destraining, while the turbulence is in a strong anisotropic state. The model coefficients obtained from both the standard and the scale-dependent dynamic approaches overpredict the dissipation based Smagorinsky coefficient. The model coefficient at scale Δ in the standard dynamic model is close to the dissipation based Smagorinsky coefficient at scale 2Δ. Still, the scale-dependent dynamic model does not yield improvements, and in some cases even worsens the predictions, due to subtle phase lags between the responses at different scales. The dynamic and scale-dependent dynamic nonlinear mixed models do not show an improvement, at least as far as evolution of the coefficients is concerned. We conclude that the mismatch between stress and strain-rate tensor responses to the applied straining causes, in the present experiment, difficulties for turbulence modeling based on a purely algebraic SGS closure.

It should be pointed out that the present measurements of coefficients and comparisons are performed by neglecting the effects of the third velocity component. Three-dimensional measurements are needed to quantify the effects of this approximation, although it appears unlikely that it could affect the observed mismatch between scales significantly.

The prediction of mean SGS momentum flux from the Smagorinsky model is correct in terms of order of magnitude, which is surprising, but in agreement with a recent theoretical result of Li and Meneveau [24]. However, the delayed response of the SGS stress compared to the strain rate also affects the agreement of mean stresses. The present results provide support for an approach of involving a solution to additional transport equation for the SGS kinetic energy, although such an approach requires specification of three model parameters (see Ref. [39]).

Acknowledgments

The authors would like to thank research engineers Y. Ronzhes for his close involvement in facility design, and S. King for his assistance in system integration. This research is sponsored by the Office of Naval Research, under Grant No. N0014-03-0361, monitored by program officer Dr. Ronald Joslin.

References

[1] Pope, S., 2000, *Turbulent Flows*, Cambridge University Press, Cambridge.
[2] Townsend, A., 1954, "The Uniform Distortion of Homogeneous Turbulence," Q. J. Mech. Appl. Math., **7**(1), pp. 104–127.
[3] Keffer, J., 1965, "The Uniform Distortion of a Turbulent Wake," J. Fluid Mech., **22**, pp. 135–160.
[4] Tucker, H., and Reynolds, A., 1968, "The Distortion of Turbulence by Irrotational Plane Strain," J. Fluid Mech., **32**, pp. 657–673.
[5] Lee, M., and Reynolds, W., 1985, *Numerical Experiments on the Structure of Homogenous Turbulence*, Stanford University Report, TF-24
[6] Liu, S., Katz, J., and Meneveau, C., 1999, "Evolution and Modeling of Subgrid Scales During Rapid Straining of Turbulence," J. Fluid Mech., **387**, pp. 281–320.
[7] Germano, M., Piomeeli, U., et al., 1991, "A Dynamic Subgrid-Scale Eddy Viscosity Model," Physica A, **3**, pp. 1760–1765.
[8] Rogallo, R., and Moin, P., 1984, "Numerical Simulation of Turbulent Flows," Annu. Rev. Fluid Mech., **16**, p. 99.
[9] Reynolds, W., 1990, "The Potential and Limitation of Direct and Large Eddy Simulations," in *Whither Turbulence? Or Turbulence at Crossroads*, edited by J. L. Lumley, Springer, New York.
[10] Piomelli, U., Cabot, W. H., Moin, P., and Lee, S., 1991, "Subgrid-Scale Backscatter in Turbulent and Transitional Flows," Phys. Fluids A, **3**(7), pp. 1766–1771.

[11] Liu, S., Meneveau, C., and Katz, J., 1994, "On the Properties of Similarity Subgrid-Scale Models as Deduced From Measurement in Turbulent Jet," J. Fluid Mech., **275**, pp. 83–119.
[12] Lesieur, M., and Metais, O., 1996, "New Trends in Large-Eddy Simulations of Turbulence," Annu. Rev. Fluid Mech., **28**, pp. 45–82.
[13] Smagorinsky, J., 1963, "General Circulation Experiments With the Primitive Equations, Part 1: The Basic Experiment," Mon. Weather Rev., **91**, pp. 99–164.
[14] Leonard, A., 1997, "Large-Eddy Simulation of Chaotic Convection and Beyound," AIAA Pap. 97-0204.
[15] Meneveau, C., and Katz, J., 2000, "Scale-Invariance and Turbulence Models for Large-Eddy Simulation," Annu. Rev. Fluid Mech., **32**, pp. 1–32.
[16] Borue, V., and Orszag, S. A., 1998, "Local Energy Flux and Subgrid-Scale Statistics in Three Dimensional Turbulence," J. Fluid Mech., **366**, pp. 1–31.
[17] Piomelli, U., Moin, P., and Ferziger, J., 1988, "Model Consistency in Large Eddy Simulation of Turbulent Channel Flows," Phys. Fluids, **31**(7), pp. 1884–1891.
[18] Meneveau, C., 1994, "Statistics of Turbulence Subgrid-Scale Stresses: Necessary Conditions and Experimental Tests," Phys. Fluids, **6**(2), pp. 815–833.
[19] O'Neil, J., and Meneveau, C., 1997, "Subgrid-Scale Stresses and Their Modelling in a Turbulent Plane Wake," J. Fluid Mech., **349**, pp. 253–293.
[20] Tao, B., Katz, J., and Meneveau, C., 2002, "Statistical Geometry of Subgrid-Scale Stresses Determined From Holographic Particle Image Velocimetry Measurements," J. Fluid Mech., **467**, pp. 35–78.
[21] Porte-Agel, F., Parlange, M. B., Meneveau, C., and Eichinger, W. E., 2001, "A Priori Field Study of the Subgrid-Scale Heat Fluxes and Dissipation in the Atmospheric Surface Layer," J. Atmos. Sci., **58**, pp. 2673–2698.
[22] Kleissl, J., Meneveau, C., and Parlange, M., 2003, "On the Magnitude and Variability of Subgrid-Scale Eddy-Diffusion Coefficients in the Atmospheric Surface Layer," J. Atmos. Sci., **60**, pp. 2372–2388.
[23] Lilly, D. K., 1967, "The Representation of Small-Scale Turbulence in Numerical Simulation Experiments," in Proc. IBM Scientific Computing Symp. Environ. Sci., p. 195.
[24] Lilly, D. K., 1992, "A Proposed Modification of the Germano Subgrid-Scale Closure Method," Phys. Fluids A, **4**, pp. 633–635.
[25] Meneveau, C., and Lund, T. S., 1997, "The Dynamic Model and Scale-Dependent Coefficient in the Viscous Range of Turbulence," Phys. Fluids, **9**, pp. 3932–3934.
[26] Porte-Agel, F., Meneveau, C., and Parlange, M., 2000, "A Scale-Dependent Dynamic Model for Large-Eddy Simulation: Application to a Neutral Atmospheric Boundary Layer," J. Fluid Mech., **415**, pp. 261–284.
[27] Bou-Zeid, E., Meneveau, C., and Parlange, M., 2005, "A Scale-Dependent Lagrangian Dynamic Model for Large Eddy Simulation of Complex Turbulent Flow," Phys. Fluids, **17**, p. 025105.
[28] Meneveau, C., Lund, T., and Cabot, W., 1996, "A Lagrangian Dynamic Subgrid-Scale Model of Turbulence," J. Fluid Mech., **319**, pp. 353–385.
[29] Makita, H., 1991, "Realization of a Large-Scale Turbulence Field in a Small Wind Tunnel," Fluid Dyn. Res., **8**, pp. 53–64.
[30] Mydlarsky, L., and Warhaft, Z., 1996, "On the Onset of High-Reynolds-Number Grid-Generated Wind Tunnel Turbulence," J. Fluid Mech., **320**, pp. 331–368.
[31] Roth, G., Mascenik, D., and Katz, J., 1999, "Measurement of the Flow Structure and Turbulence Within a Ship Bow Wave," Phys. Fluids, **11**, pp. 3512–3523.
[32] Roth, G., and Katz, J., 2001, "Five Techniques for Increasing the Speed and Accuracy of PIV Interrogation," Meas. Sci. Technol., **12**, pp. 238–245.
[33] Keane, R., and Adrian, R., 1990, "Optimization of Particle Image Velocimeters, Part I, Double Pulsed Systems," Meas. Sci. Technol., **1**, pp. 1202–1215.
[34] Huang, H., Dabiri, D., and Gharib, M., 1997, "On Errors of Digital Particle Image Velocimetry," Meas. Sci. Technol., **8**, pp. 1427–1440.
[35] Chen, J., Meneveau, C., and Katz, J., 2005, "Scale Interactions of Turbulence Subjected to a Straining-Relaxation-Destraining Cycle," J. Fluid Mech., submitted.
[36] Nimmo-Smith, W., Katz, J., and Osborn, T., 2005, "Flow Structure in the Bottom Boundary Layer of the Coastal Ocean," J. Phys. Oceanogr., **35**(1), pp. 72–93.
[37] Monin, A., and Yaglom, A., 1971, *Statistical Fluid Mechanics*, MIT Press, Cambridge.
[38] Li, Y., and Meneveau, C., 2004, "Analysis of Mean Momentum Flux in Subgrid Models of Turbulence," Phys. Fluids, **16**, pp. 3483–3486.
[39] Wong, V. C., 1992, "A Proposed Statistical-Dynamic Closure Method for the Linear or Nonlinear Subgrid-Scale Stresses," Phys. Fluids, pp. 1080–1082.

Nonboundary Conforming Methods for Large-Eddy Simulations of Biological Flows

Elias Balaras[1]
e-mail: balaras@eng.umd.edu

Jianming Yang

Department of Mechanical Engineering,
University of Maryland, College Park, MD 20742

In the present paper a computational algorithm suitable for large-eddy simulations of fluid/structure problems that are commonly encountered in biological flows is presented. It is based on a mixed Eurelian-Lagrangian formulation, where the governing equations are solved on a fixed grid, which is not aligned with the body surface, and the nonslip conditions are enforced via local reconstructions of the solution near the solid interface. With this strategy we can compute the flow around complex stationary/moving boundaries and at the same time maintain the efficiency and optimal conservation properties of the underlying Cartesian solver. A variety of examples, that establish the accuracy and range of applicability of the method are included. [DOI: 10.1115/1.1988346]

Introduction

Today, due to the impressive advancements in high performance parallel computing the large-eddy simulation (LES) approach has emerged as a valuable tool for turbulence research and has contributed invaluable information on the structure and dynamics of a variety of flows which are of engineering interest. There are, however, applications from biology and physiology where the use of LES has received considerably less attention as a result of exceedingly complex fluid/structure interactions that dominate the dynamics of these flows. Characteristic examples include the flow of blood in the heart or around medical implants, insect locomotion and bird flight. Massive computations using LES can contribute to a new fundamental understanding of the dynamics of such flows and help bring to fruition novel devices.

From scaling considerations of the required spatial and temporal resolution, LES of such flows are well within reach of today's supercomputers. On the other hand, these class of problems introduce new challenges to high-fidelity numerical methods since the flow is highly unsteady and involves moving and/or deforming boundaries composed of anisotropic nonlinear materials. Boundary conforming methods that are traditionally employed in complex geometrical configurations have been successfully extended to problems involving moving boundaries. While such methods have been demonstrated to be very effective in creeping and low Reynolds number problems (see for example [1,2]), little work has been completed for moderate/high Reynolds number flows because of the associated computational cost and resolution constraints [3,4]. Considering work that has been completed for turbulent flows, most of the developments have been done in the framework of the Reynolds Averaged Navier-Stokes (RANS) approach (i.e. [5,6]). These schemes typically employ stable, dissipative discretizations, making their use in LES problematic.

An attractive alternative, which can be a cost/effective strategy in a variety of biological flows, are nonboundary conforming methods. In such a case the equations governing the fluid flow are solved on a fixed Cartesian grid. The effect of a stationary or moving boundary, which in this case does not coincide with the grid, is introduced through proper treatment of the solution variables at the cells in the vicinity of the boundary. An advantage of this type of method is that the need for grid regeneration or deformation is eliminated, and highly efficient solvers can be used with minimal changes. In terms of the imposition of boundary conditions there are two broad categories of methods that are usually adopted: *Cartesian* or *cut-cell* methods and *immersed boundary* methods.

In *Cartesian* methods a solid boundary is tracked as a sharp interface and the grid cells at the body interface are modified according to their intersections with the underlying Cartesian grid. Using proper interpolation strategies the flow variables on the modified cells can be computed according to the boundary conditions on the body. *Cartesian* methods allow for a clear distinction between the solid and the fluid by practically generating a boundary-fitted grid around the body. Successful applications of such methods for a variety of flow problems can be found in [7,8]. However, due the variety of possible intersections between the grid and the boundary a large number of "interface-cells" is generated leading to an equally large number of "special treatments." Also in complex configurations the unavoidable generation of irregularly shaped cells with very small size can have an adverse impact of the conservation and stability properties of the solver. Recently Ye et al. [9] suggested a cell merging scheme to address this problem. This formulation was also extended to treat moving boundaries with good results for a variety of two-dimensional problems [10]. The extention of the methodology in complex three-dimensional configurations remains to be investigated.

In *immersed boundary* formulations the governing equations are discretized on a fixed Cartesian grid, but in this case the effect of a stationary or moving boundary is introduced through an external force field. The method has been introduced by Peskin [11] in the beginning of the 1970s to study blood flow in the heart [12,13]. In these computations the motion of the boundary was determined by the fluid itself, and vice verca. The vascular boundary was modeled as a set of elements linked by springs, and a Lagrangian coordinate system was attached to track their location in space. The tracking information was then used to compute the proper structure of the external force field that was introduced to the underlying Eulerian grid on which the governing equation for the fluid flow are solved. A disadvantage of the above formulation is the need to distribute the forcing over 3–4 grid nodes (usually through a discrete delta function), which unavoidably introduces some blurring between the fluid and the solid. This feature increases substantially the resolution requirements, and appears to be a major obstacle in the extention of the method to LES, where the proper representation of the thin shear layers near a solid body is crucial for the accuracy of the computations.

To overcome this limitation Mohd-Yusof [14] and Fadlun et al. [15] proposed a methodology where the forcing function is considered in the framework of the discretized equations of motion.

[1]Corresponding author.

Contributed by the Fluids Engineering Division for the publication in the JOURNAL OF FLUIDS ENGINEERING. Manuscript received by the Fluids Engineering Division, July 22, 2004; Final revision: April 19, 2005. Associate Editor: Ismail B. Celik

This formulation introduces a set of discrete body-forces at the grid nodes nearest to the boundary, which is practically equivalent to a local reconstruction of the solution based on the target boundary values. In this respect the method can be viewed as a hybrid Cartesian/immersed boundary formulation since it shares features with both approaches. The method has been successfully applied to a variety of problems including large-eddy simulation (LES) of turbulent flow inside a motored IC piston/cylinder assembly [15].

Central to the accuracy of the above formulation is the way the solution is reconstructed near the boundary. Fadlun et al. [15] suggested a simple one-dimensional scheme, where the solution is reconstructed along an arbitrary grid line. The method is straightforward, second order accurate and works well for bodies that are largely aligned with the grid lines. In cases of complex bodies the choice of the reconstruction direction at several points in the flow field can be arbitrary. Multidimensional schemes can remove this limitation. Kim et al. [16] suggested a hybrid scheme, which uses a bilinear reconstruction procedure that is however, reduced to a one-dimensional linear one, when there are no available points in the vicinity of the boundary to support the 2D stencil. Balaras [17] introduced a more general scheme which is applicable to complex boundaries without special treatments, since the reconstruction is always performed at the well defined line normal to the interface. The scheme was tested in a variety of laminar and turbulent flows with very good results. In the present paper an extention of the work in [17] to moving boundaries is presented. Examples of laminar and turbulent flows are included to establish the accuracy and range of applicability of the method.

Numerical Method

Basic Solver. In LES, the resolved, large-scale, velocity and pressure fields can be obtained from direct solution of the filtered Navier-Stokes equations, where scales smaller than the grid size are modeled. In the present, finite-difference implementation, a top-hat filter in physical space that is implicitly applied by the finite-difference operators separates the resolved from unresolved scales. The resulting subgrid scale (SGS) stresses are modeled using the Lagrangian dynamic eddy-viscosity model [18]. Details on the present implementation of the model together with an evaluation of its accuracy in equilibrium and nonequilibrium flows, is given in [19].

The equations governing the evolution of the large scales are solved on an underlying grid (in Cartesian or cylindrical coordinates) that covers the entire computational domain without the bodies. Integration is done using a fractional-step method, with an implicit Crank-Nicolson scheme for the viscous terms and a third-order Runge-Kutta (RK3) explicit scheme for all other terms. All spatial derivatives are approximated with second-order central differences on a staggered grid. The large-band matrix associated to the solution of the Poisson equation is inverted using direct methods. The above procedure can be summarized into the following steps:

$$\frac{\hat{u}_i^k - u_i^{k-1}}{\Delta t} = -\left[\gamma_k A(u_i^{k-1}) + \rho_k A(u_i^{k-2})\right] + \frac{1}{2}\alpha_k\left[B(\hat{u}_i^k) + B(u_i^{k-1})\right] - \alpha_k \frac{\partial p^{k-1}}{\partial x_i} + f_i^k, \tag{1}$$

$$\nabla^2 \phi^k = \frac{1}{\alpha_k \Delta t}\frac{\partial \hat{u}_i^k}{\partial x_i}, \tag{2}$$

$$u_i^k = \hat{u}_i^k - \alpha_k \Delta t \frac{\partial \phi^k}{\partial x_i}, \tag{3}$$

$$p^k = p^{k-1} + \phi^k - \frac{\alpha_k \Delta t}{2\,\mathrm{Re}}\frac{\partial^2 \phi^k}{\partial x_i^2}, \tag{4}$$

where $\hat{u}_i^k$ is the intermediate velocity and ϕ is the scalar used to project $\hat{u}_i^k$ into a divergence-free space. p^k is the actual pressure. Operator A represents the terms treated explicitly, and B the ones treated implicitly. f_i^k is the momentum forcing adopted to enforce proper boundary conditions on immersed boundaries and will be discussed in the next section. Δt is the time step and k is the substep index ($k=1-3$). The RK3 coefficients are $\alpha_1=8/15$, $\gamma_1=8/15$, $\rho_1=0$; $\alpha_2=2/15$; $\gamma_2=5/12$, $\rho_2=-17/60$; $\alpha_3=1/3$, $\gamma_3=3/4$, $\rho_3=-5/12$.

Treatment of Immersed Boundaries. To compute the flow around complex objects which are not aligned with the grid, we have developed a methodology that practically reconstructs the solution in the vicinity of the body according to the target boundary values [17]. The approach allows for a precise imposition of the boundary conditions without compromising the accuracy and efficiency of the solver. In particular, the application of velocity boundary conditions on a body immersed in the Cartesian grid involves the following steps: (a) Identification of the interface between the body and the fluid; (b) Establishment of the grid/interface relation and identification of the points in the solution variable grid where boundary conditions will be enforced; (c) Reconstruction of the solution on the above points. For steps (a) and (b), which are usually referred to as "interface tracking," a scheme based on algorithms devised for solidification problems and multiphase flow dynamics [20,21] is used. With this approach, an immersed boundary of arbitrary shape is identified by a series of material-fixed interfacial markers whose location is defined in the reference configuration of the solid. This information is then used to identify the Eulerian grid nodes involved in the reconstruction of the solution near the boundary in a way that the desired boundary conditions for the fluid are satisfied to the desired order of accuracy. The reconstruction is performed "around" the points in the fluid phase closest to the solid boundary (all points that have least one neighbor in the solid phase). In the framework of the present fractional step method the imposition of boundary conditions on an immersed boundary is equivalent to the addition to Eq. (1) of a forcing term of the form,

$$f_i^k = \frac{\hat{V}_i^k - u_i^{k-1}}{\Delta t} + \left[\gamma_k A(u_i^{k-1}) + \rho_k A(u_i^{k-2})\right] - \frac{1}{2}\alpha_k\left[B(\hat{u}_i^k) + B(u_i^{k-1})\right] + \alpha_k \frac{\partial p^{k-1}}{\partial x_i} \tag{5}$$

where $\hat{V}_i^k$ is the reconstructed intermediate velocity, such that the desired boundary conditions are satisfied on the immersed boundary. Note that in the above algorithm, boundary conditions for the pressure near the interface are not imposed directly, but they are essentially implicit into the RHS of the Poisson equation. A more detailed discussion on this issue can be found in [15,17].

When the immersed boundary moves, the role of several computational nodes in the vicinity of the boundary changes with time. This is illustrated in Fig. 1, where the boundary moves from its position at time step t^{k-1} (grey shadow region) to a new position at time step t^k (black shadow region). Some velocity nodes (hereinafter referred as "boundary" points), which were central to the reconstruction of the solution, become interior "fluid," points. In addition, other nodes inside the body (hereinafter referred as "body" points) at time step t^{k-1} emerge into the fluid and become "boundary" points at t^k. The latter family of points does not require any special treatment because the solution at t^k would be reconstructed based on known values. On the other hand, the former family of points introduces problems when computing the RHS of Eq. (1) at t^k: all the grid nodes that were "boundary" points at t^{k-1} would have the correct value of u_i^{k-1} (this is the

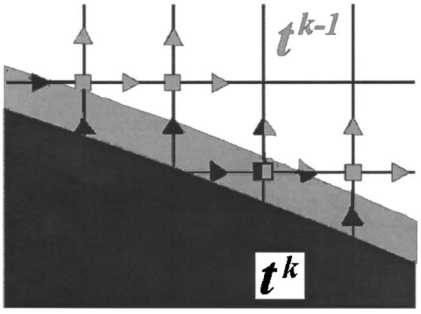

Fig. 1 Staggered grid arrangement near the body for the 2D problem. Grey area denotes the location of the body at t^{k-1} and black at t^k; □ p; △ u_i.

boundary condition that was enforced at t^{k-1}), but most derivatives of u_i^{k-1} would be incorrect since they involve points previously in the interior of the body. To alleviate this problem the velocity and pressure at these points is "extended" to the interior of the body at time t^{k-1}, using second-order multidimensional reconstructions [22].

Results

Numerical Examples of Laminar Flows. To verify the accuracy of the proposed methodology, initially a series of computations of laminar flows, for which detailed numerical and experimental data are available in the literature, is conducted. Two cases are presented in this section that involve both stationary and moving immersed boundaries: the three-dimensional flow around a sphere, and two-dimensional flow around a cylinder oscillating in a cross flow.

A schematic of the computational domain for the flow around the sphere is shown in Fig. 2. Cylindrical coordinates are used for a more efficient distribution of the grid points. Computations have been conducted for Reynolds numbers ($\mathrm{Re}=UD/\nu$, where U is the freestream velocity, D the diameter of the sphere) ranging from 50 to 300. The flow is steady and axisymmetric for Reynolds numbers up to 200, while for the highest Reynolds number ($\mathrm{Re}=300$) the flow is unsteady and is dominated by vortex shedding. The size of the computational box in the streamwise direction is

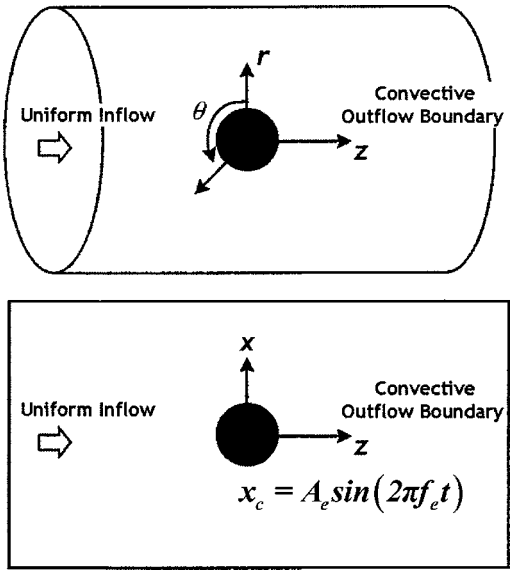

Fig. 2 Sketch of computational domain for the case of the sphere (top) and oscillating cylinder (bottom)

Table 1 Prediction of C_D for the case of the sphere

Re	50	100	150	200
Grid 1	1.707	1.229	1.045	0.945
Grid 2	1.609	1.118	0.919	0.807
Grid 3	1.586	1.095	0.894	0.776
Experiment [24]	1.574	1.087	0.889	0.776
Ref. simulation [25]	1.575	1.100	0.900	0.775

$30D$ with the sphere located in the middle, and $15D$ in the radial direction. To investigate the influence of grid resolution on the results three different grids have been considered for the low Reynolds number cases ($\mathrm{Re}=50-200$). Grid 1 involves $100\times40\times40$ computational points in the streamwise, radial and azimuthal directions respectively. In the other two cases the grid is refined in the streamwise and radial directions (Grid 2: $200\times40\times80$ and Grid 3: $400\times40\times160$ respectively). All three grids are stretched in the streamwise and radial directions to cluster points near the surface of the sphere. The resulting average grid spacing near the sphere for the three different resolutions is approximately $0.1D$, $0.05D$, and $0.025D$ respectively. The computations for $\mathrm{Re}=300$ case are performed on single refined grid involving $420\times64\times112$ nodes. With this resolution approximately 10 grid points are located in the boundary layers near the stagnation point. In the grid refinement study the same time step, $\Delta t=0.001$, was used on all different grids. For all other computations reported in this study the timesep implied by the stability limit of the present RK3 scheme (approximately 1.2) was used. In all cases a uniform velocity field is specified at the inflow plane. A convective boundary condition is used at the outflow boundary [23], and radiative boundary conditions are applied at the freestream boundary.

Table 1 shows the present results in comparison with the experimental results in [24], and the well resolved simulations by Johnson and Patel [25] where body-fitted grids are used. For all Reynolds numbers and grid resolutions the main features of the flow are properly captured. The drag coefficient on the coarsest grid, is a little higher (approximately 8%) in comparison with the reference experimental and numerical data. As the grid is refined, however, the agreement is very good. The error in drag coefficient, which is computed using the experimental results in [24] as the reference values, as a function of grid spacing near the sphere is shown in Fig. 3. It can be seen that the error reduces with a second-order slope, which is consistent with the order of accuracy of the method.

A more challenging test for the present methodology is the case at $\mathrm{Re}=300$, where the flow becomes unsteady and the wake is dominated by periodic vortex shedding. The vortical structures in the wake are shown in Fig. 4, where isosurfaces of the second invariant of the velocity gradient tensor (or Q criterion [26]) are used for their visualization. Hairpin-like vortices originating from the surface of the sphere can be observed, with new vortical structures developing around their legs as they are convected downstream. This behavior is nearly the same as the one shown in [25] indicating that the present method properly captures the three-dimensional vorticity field. The values of the drag and lift coefficient are also in excellent agreement with the reference data. In particular, the predicted drag and lift coefficients are $C_D=0.655$ and $C_L=0.064$, respectively, which are within 1% to the values reported in [24,25].

To evaluate the accuracy of the method for the case of moving boundaries the flow around a cylinder oscillating transversally in a

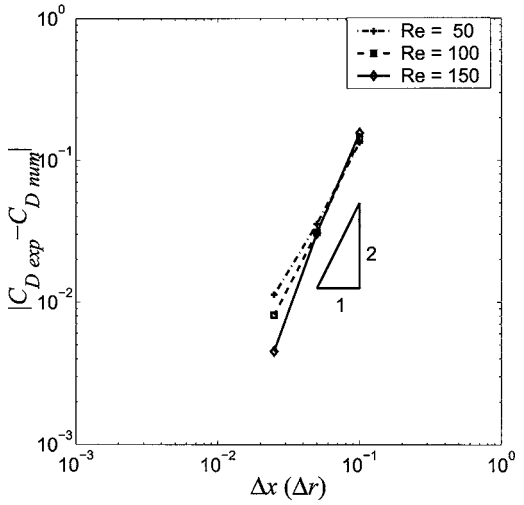

Fig. 3 Error in the drag coefficient for the flow around the sphere as a function of grid resolution

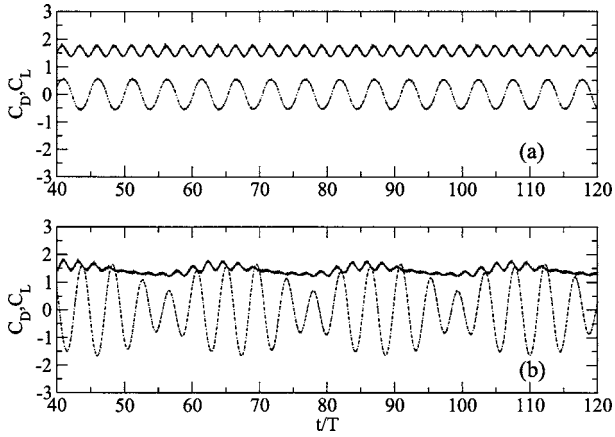

Fig. 5 Temporal evolution of the lift and drag coefficients for the case of the cylinder oscillating in a cross flow. (*a*) $f_e/f_o=1.0$; (*b*) $f_e/f_o=1.2$. —, C_D; – – –, C_L.

free-stream is computed. All flow parameters are chosen to replicate the conditions in the simulations reported in [27], where very fine body-fitted grids are used. The Reynolds number ($\mathrm{Re}=UD/\nu$, where U is the freestream velocity and D the cylinder diameter) is 185. Other important parameters are the oscillation frequency f_e and amplitude A_e. In all computations the motion of the cylinder is given by a simple harmonic function $x_c=A_e\sin(2\pi f_e t)$, with $A_e=0.2$. A variety of frequencies is considered ranging from $f_e/f_o=0.8$ to $f_e/f_o=1.2$, where f_o is the natural shedding frequency of the stationary cylinder at the same Reynolds number. The size of the computational box is $50D\times 30D$ in the streamwise and crossstream directions, respectively, with the cylinder located $20D$ from the inflow plane (Fig. 2). As for the case of the sphere a uniform velocity field is specified at the inflow plane, and convective and radiative boundary conditions are used at the outflow and freestream boundaries, respectively. All computations are performed on a nonuniform grid involving 300×300 points. The average grid spacing near the cylinder surface is of the order of $0.01D$.

The temporal variation of the lift and drag coefficients changes substantially when the excitation frequency is varied near the natural shedding frequency f_o. An example is shown in Fig. 5 for $f_e/f_o=1.0$ and $f_e/f_o=1.2$. In the former case a fairly regular behavior of the lift and drag coefficients can be observed once vortex shedding is established. In the latter the appearance of a higher harmonic is apparent. This behavior has also been observed in previous experimental and numerical studies and can be attributed to the change in sign of the energy transfer between the fluid and the cylinder. In Fig. 6 the mean value of the drag coefficient, $\bar{C}_D$, the root mean square of the drag coefficient, $C_D$rms, and the root mean square of the lift coefficient, $C_L$rms, are shown as a function of the excitation frequency f_e/f_o. The mean value of C_D has a peak at $f_e/f_o=1.0$, as expected, and then decreases are f_e/f_o increases. $C_L$rms, on the other hand, peaks at $f_e/f_o=1.1$ where the vortex switching occurs. These results are also in very good quantitative agreement with the corresponding values reported in [27]. In Fig. 7 instantaneous spanwise vorticity isolines in four different phase during the harmonic oscillation are shown for $f_e/f_o=1.0$. During the upward motion of the cylinder vorticity is formed at the base, whose sign is opposite to the one in the upper shear layer. Their interaction results in a decrease of the vorticity available for roll-up in the wake.

Pulsatile Flow in a Model of Arterial Stenosis. A more challenging test for the accuracy and efficiency of the present method is the computation of transitional flow in a model of arterial stenosis. Initially a planar model is considered. The constriction is generated by placing two approximately semicircular sections on the top and bottom walls of a plane channel, resulting in area reduction of 50% (see Fig. 8). This choice reduces substantially the cost compared to the axisymmetric case and facilitates a timely examination of all different parameters that affect the dynamics of the flow. Nevertheless, the fundamental dynamics of the flow are similar to the ones observed in axisymmetric experiments reported in the literature.

A schematic of the computational domain is given in Fig. 8. The throat of the stenosis and the outflow plane are located $10H$ and $30H$ from inflow plane respectively (H is the channel height). The spanwise domain size is $3H$, which was found sufficient for the two-point correlations to go to zero. The average Reynolds number during the pulsatile cycle is $\mathrm{Re}_b=1200$ ($\mathrm{Re}_b=U_bH/\nu$, where U_b is the average bulk velocity during the cycle, H is the channel hight, and ν is the kinematic viscosity). During one cycle Re_b varies almost sinusoidally with a minimum value of 270 and

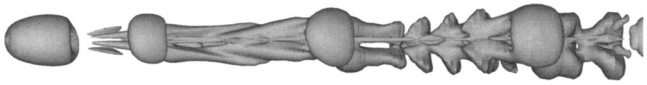

Fig. 4 Vortical structures in the wake of the sphere for Re =300. Isosurfaces of $Q=0.001$ are shown.

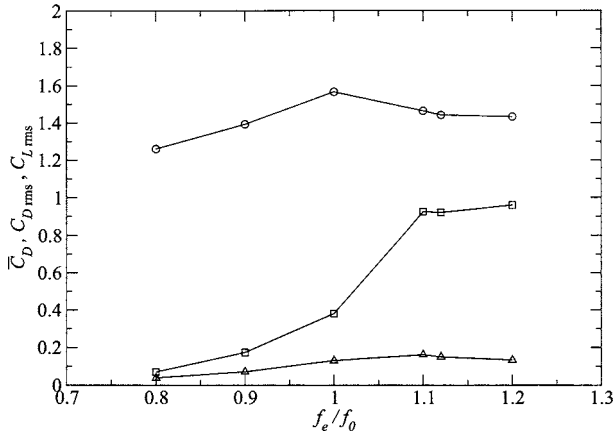

Fig. 6 Variation of: ○, $\bar{C}_D$; △, $C_D$rms; □, $C_L$rms for the case of the cylinder oscillating in a cross flow as a function of f_e/f_o

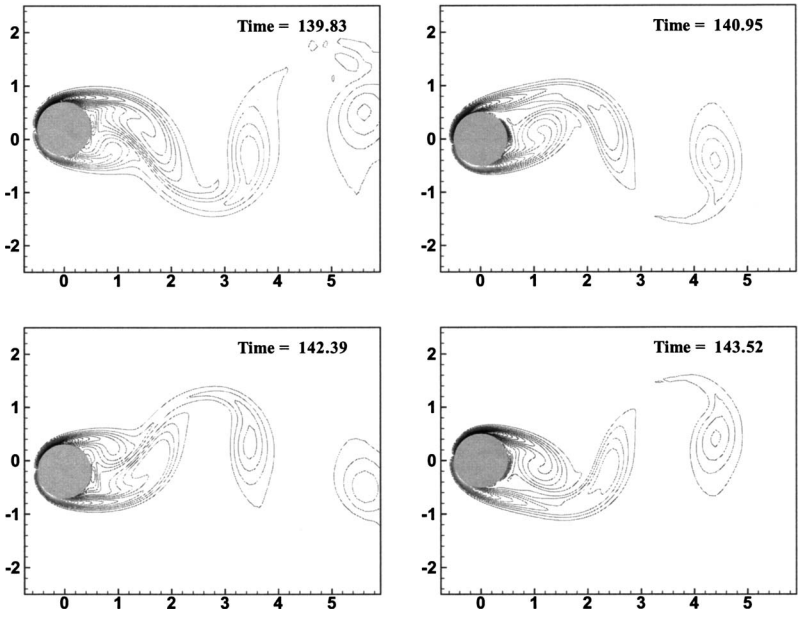

Fig. 7 Spanwise vorticity isolines for $f_e/f_o=1.0$

a maximum of 1500. The corresponding frequency parameter is $\alpha\sim 8$. [$\alpha=h(\omega/\nu)^{1/2}$, where $h=H/2$, and ω is the fundamental pulsatile frequency.] The choice of the geometry and parametric space above, mimics closely the conditions in Particle Image Velocimetry (PIV) experiments that were conducted in parallel to the present computations for the purpose of validation of the present method [28]. The establish the grid independency of the solution, computations with different grid resolution in all three coordinate directions were conducted. It was found that approximately 1.0 million nodes ($360\times 32\times 82$ in the streamwise, spanwise and wall-normal directions, respectively) were sufficient for that purpose. Periodic boundary conditions are used in the spanwise, homogeneous direction and a convective boundary condition at the outflow plane.

The specification of the inflow boundary conditions was guided by the measurements. In the experiment organized disturbances were observed upstream of the constriction, and most likely were the result of an instability that never grow into a turbulent state [29]. In the simulations, accurate reproduction of this "disturbed-laminar-flow" environment is a challenging task, since it cannot be directly reproduced from the measured velocity statistics. For this reason, the velocity at the inflow plane was specified as the sum of two parts: a laminar component, which was obtained from the experimental results, and a random component that was introduced to trigger instabilities when inflection points were present in the velocity profiles. The random component consisted of fluctuations that were isotropic, satisfied the continuity equation and had a von Karman energy spectrum. The fluctuations were also scaled to have the magnitude of the background noise in the experiments. Details on the noise generation algorithm can be found in [30]. The quality of the inflow conditions produced by the above method was monitored by direct comparison of the disturbance statistics with the corresponding experimental ones (not shown here) and was found to be very satisfactory.

To visualize the basic dynamics of the flow in the vicinity of the stenosis, spatially and phase-averaged spanwise vorticity isolines are shown in Fig. 9 at three characteristic times during the pulsatile cycle. Note that the phase-averaged statistics in all computations are extracted over 10 pulsatile cycles. Prior to sampling, 5 cycles were completed for the flow to became independent of the initial conditions. During the initial stages of the accelerating part of the cycle a jet is formed as the flow goes through the constriction [see Fig. 9(*a*)]. The flow at this stage is fairly symmetric. At a letter stage of the same part of the cycle the jet becomes unstable and the shear layers in the proximal poststenotic area break down generating large spanwise coherent structures

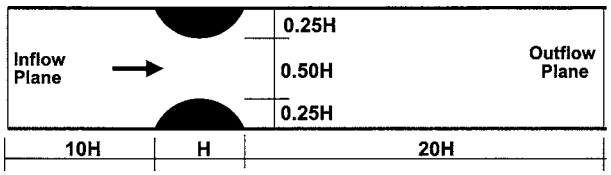

Fig. 8 Schematic of the computational domain for the case of flow in a model of arterial stenosis

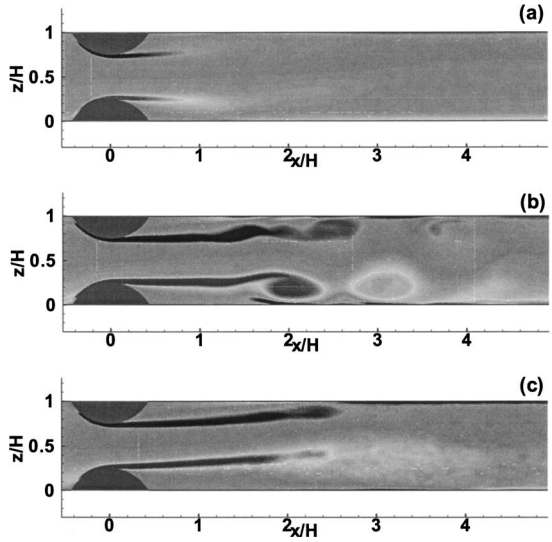

Fig. 9 Phase-averaged spanwise vorticity distribution. (*a*) $T=250$ deg; (*b*) $T=320$ deg; (*c*) $T=100$ deg. The accelerating part of the cycle is from $T=180$ deg to $T=360$ deg and the decelerating part is from $T=0$ deg to $T=180$ deg.

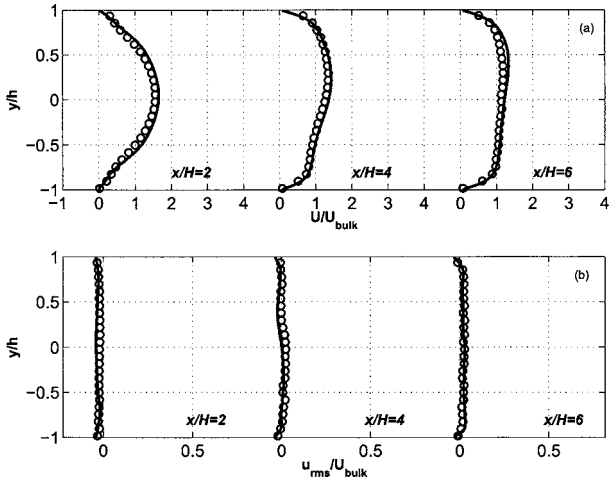

Fig. 10 Phase-averaged streamwise velocity statistics at $T=270$ deg. —, simulation; ○, experiment [28]. (*a*) $\langle u \rangle$; (*b*) u_{rms}.

[see Fig. 9(*b*)]. These structures are convected downstream interacting with the boundary layers at the walls triggering transition to turbulence. During the decelerating part of the cycle, turbulence is enhanced and turbulent boundary layers appear just downstream of the reattachment point. At the same time, very close to the throat of the stenosis the shear layer attaches to one side of the channel [see Fig. 9(*c*)]. This behavior has also been observed in the experiments. In Figs. 10 and 11 phase-average profiles of the mean streamwise velocity and velocity fluctuations are shown for $T=270°$ and $T=350°$, respectively. Both time instances are during the acceleration phase with the latter corresponding to a time just after the breakdown of the shear layer. Three stations in the proximal downstream area are shown: $x/H=2$, $x/H=4$, and $x/H=6$ from the throat of the stenosis. The agreement with the corresponding experimental data is very good.

Conclusions

In the present paper a methodology to perform LES around complex moving boundaries on fixed grids is presented. The method is based on earlier work reported in [17], and introduces a "field extention" approach to address problems encountered during the motion of immersed boundaries. Validation is performed for the cases of the flow around a sphere, a cylinder oscillating in a cross-flow and pulsatile flow in a model of arterial stenosis. In all cases the agreement with reference experimental and numerical results is very good indicating that embedded-boundary formulations can be cost-efficient strategies especially for moving boundary problems without sacrificing accuracy. The main limitation of these methods comes from the inflexibility in distributing grid points near a complex body. Although the use of cylindrical coordinates increases the range of applicability of the method alternative local grid refinement strategies could be promising. Their cost/efficiency, however, remains to be investigated.

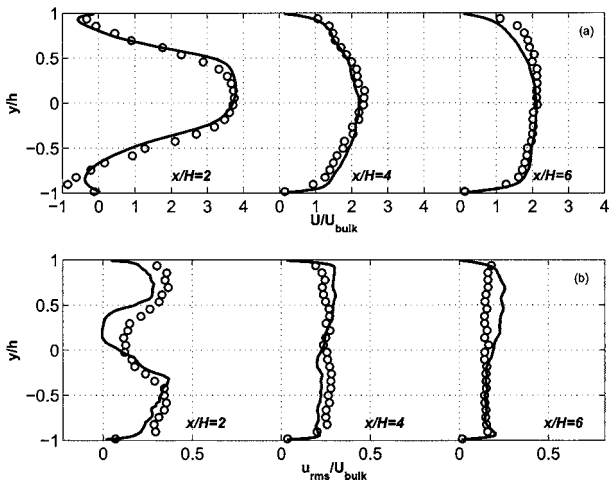

Fig. 11 Phase-averaged streamwise velocity statistics at $T=350$ deg. —, simulation; ○, experiment [28]. (*a*) $\langle u \rangle$; (*b*) u_{rms}.

Acknowledgments

This work is supported by NIH Grant No. R01-HL-07262 and NSF Grant No. CTS-0347011. The authors are grateful to Professor K. Kiger for making the experimental data for the pulsatile stenotic flow available, and to Mr. N. Beratlis for preparing some of the plots in the paper.

References

[1] Johnston, A. A., and Tezduyar, D. E., 1997, "3D Simulation of Fluid-Particle Interactions With the Number of Particles Reaching 100," Comput. Methods Appl. Mech. Eng., **145**, pp. 301–321.
[2] Hu, H. H., Patankar, N. A., and Zhu, M.-Y., 2001, "Numerical Simulations of Fluid-Solid Systems Using Arbitrary-Lagrangian-Eulerian Technique," J. Comput. Phys., **169**, pp. 427–462.
[3] Newman, D. J., and Karniadakis, G. E., 1997, "Simulations of Flow Past a Freely Vibrating Cable," J. Fluid Mech., **344**, p. 95.
[4] Evangelinos, C., and Karniadakis, G. E., 1999, "Dynamics and Flow Structures in the Turbulent Wake of Rigid and Flexible Cylinders Subject to Vortex-Induced Vibrations," J. Fluid Mech., **400**, pp. 91–124.
[5] Ramamurti, R., and Sandberg, W. C., 2001, "Computational Study of 3D Flapping Foil Flows," AIAA paper No. 2001-0605.
[6] Jouette, C., Laget, O., Gouez, J.-M., and Viviand, H., 2002, "A Dual Time Stepping Method for Fluid-Structure Interaction Problems," Comput. Fluids, **31**, pp. 509–537.
[7] De Zeeuw, D., and Powell, K. G., 1991, "An Adaptively Refined Cartesian Mesh Solver for the Euler Equations," AIAA Paper No. 91-1542-CP.
[8] Quirk, J. J., 1994, "An Alternative to Unstructured Grids for Computing Gas Dynamic Flows Around Arbitrary Two-Dimensional Bodies," Comput. Fluids, **23**, p. 125.
[9] Ye, T., Mittal, R., Udaykumar, H. S., and Shyy, W., 1999, "An Accurate Cartesian Grid Method for Viscous Incompressible Flows With Complex Immersed Boundaries," J. Comput. Phys., **156**, pp. 209–240.
[10] Udaykumar, H. S., Mittal, R., Rampunggoon, P., and Khanna, A., 2001, "A Sharp Interface Cartesian Grid Method for Simulating Flows With Complex Moving Boundaries," J. Comput. Phys., **174**, pp. 345–380.
[11] Peskin, C. S., 1972, "Flow Patterns Around Heart Valves: A Numerical Method," J. Comput. Phys., **10**, pp. 252–271.
[12] Peskin, C. S., and McQueen, D. M., 1992, "Cardiac Fluid Dynamics," Crit. Rev. Biomed. Eng., **20**, pp. 451–459.
[13] Peskin, C. S., and McQueen, D. M., 1997, "Shared-Memory Parallel Vector Implementation of the Immersed Boundary Method for the Computation of Blood Flow in the Beating Mammalian Heart," J. Supercomput., **11**, pp. 213–236.
[14] Mohd-Yusof, J., 1997, "Combined Immersed Boundaries/B-Splines Methods for Simulations of Flows in Complex Geometries," *CTR Annual Research Briefs*, NASA Ames/Stanford University.
[15] Fadlun, E. A., Verzicco, R., Orlandi, P., and Mohd-Yusof, J., 2000, "Combined Immersed-Boundary Finite-Difference Methods for Three-Dimensional Complex Flow Simulations," J. Comput. Phys., **161**, pp. 35–60.
[16] Kim, J., Kim, D., and Choi, H., 2001, "An Immersed-Boundary Finite-Volume Method for Simulations of Flow in Complex Geometries," J. Comput. Phys., **171**, pp. 132–150.
[17] Balaras, E., 2004, "Modeling Complex Boundaries Using an External Force Field on Fixed Cartesian Grids in Large-Eddy Simulations," Comput. Fluids, **33**, pp. 375–404.
[18] Meneveau, C., Lund, T. S., and Cabot, W. H., 1996, "A Lagrangian Dynamic Subgrid-Scale Model of Turbulence," J. Fluid Mech., **319**, p. 353.
[19] Sarghini, F., Piomelli, U., and Balaras, E., 1999, "Scale-Similar Models for Large-Eddy Simulations," Phys. Fluids, **11**, pp. 1596–1607.
[20] Udaykumar, H. S., Kan, H.-C., Shyy, W., and Tran-Son-Tay, R., 1997, "Multiphase Dynamics in Arbitrary Geometries on Fixed Cartesian Grids," J. Comput. Phys., **137**, pp. 366–405.
[21] Udaykumar, H. S., Mittal, R., and Shyy, W., 1999, "Computation od Solid Liquid Phase Fronts in the Sharp Interface Limit on Fixed Grids," J. Comput. Phys., **153**, pp. 535–574.

[22] Tseng, Y. H., and Ferziger, J. H., 2003, "A Ghost-Cell Immersed Boundary Method for Flow in Complex Geometry," J. Comput. Phys., **192**, pp. 593–623.
[23] Orlansky, I., 1976, "A Simple Boundary Condition for Unbounded Hyperbolic Flows," J. Comput. Phys., **21**, p. 251.
[24] Clift, R., Grace, J. R., and Weber, M. E.,1978, *Bubbles, Drops and Particles*, Academic, San Diego, CA.
[25] Johnson, T., and Patel, V. C., 1999, "Flow Past a Sphere up to a Reynolds Number of 300," J. Fluid Mech., **378**, p. 10.
[26] Hunt, J. C. R., Wray, A. A., and Moin, P., 1988, "Eddies, Streams and Convergence Zones in Turbulent Flows. Center for Turbulence Research," in Proceedings of the Summer Program 1988, p. 193.
[27] Guilmineau, E., and Queutey, P., 2002, "A Numerical Simulation of Vortex Shedding From an Oscillating Circular Cylinder," J. Fluids Struct., **16**, pp. 773–794.
[28] Kiger, K., 2004 (private communication).
[29] Hino, M., Sawamoto, M., and Takasu, S., 1976, "Experiments on Transition to Turbulence in an Oscillating Pipe Flow," J. Fluid Mech., **75**, pp. 193–207.
[30] Ovchinnikov, V., Piomelli, U., and Choudhari, M. M., 2004, "Inflow Conditions for Numerical Simulations of Bypass Transition," AIAA 2004-0591.

Coherent Structures In Open-Channel Flows Over a Fixed Dune

Wusi Yue
Department of Geography and Environmental Engineering,
The Johns Hopkins University,
Baltimore, Maryland 21218
e-mail: yue@jhu.edu

Ching-Long Lin

Virendra C. Patel

Department of Mechanical and Industrial Engineering, and IIHR-Hydroscience and Engineering,
The University of Iowa,
Iowa City, Iowa 52242

Turbulent open-channel flow over a two-dimensional laboratory-scale dune is studied using large eddy simulation. Free surface motion is simulated using level set method. Two subgrid scale models, namely, dynamic Smagorinsky model and dynamic two-parameter model, are employed for assessing model effects on the free surface flow. The present numerical predictions of mean flow field and turbulence statistics are in good agreement with experimental data. The mean flow can be divided into two zones, an inner zone where turbulence strongly depends on the dune bed geometry and an outer layer free from the direct influence of the bed geometry. Streaky structures are observed in the wall layer after flow reattachment. Quadrant two events are found to prevail in near-wall and near-surface motions, indicating the predominance of turbulence ejections in open-channel flows. Large-scale coherent structures are produced behind the dune crest by a strong shear layer riding over the recirculation zone. These quasistreamwise tubelike vortical structures are transported downstream with the mean flow and most are destructed before arriving at the next crest. Free surface deformation is visualized, demonstrating complex patterns of upwelling and downdraft. [DOI: 10.1115/1.1988345]

Introduction

Turbulent flows over dunes, the general bed-forms arising in natural alluvial channels, have been extensively studied by laboratory experiments and numerical simulations in the past five decades, owing to the importance in determining sediment transport. Dunes are developed due to interactions of channel bed with near-wall turbulence structures and free surface motion. They are nearly triangular in shape, with a straight steep lee face and a slightly curved stoss face. A shear layer develops from the dune crest and extends to the flow reattachment point at the stoss face, delimiting a recirculation zone with main stream. Instability of the shear layer induces large-scale coherent structures carrying significant momentum and sediment. Large-scale coherent structures have been experimentally observed, e.g., Nezu and Nakagawa [1], Müller and Gyr [2], Bennett and Best [3], Kadota and Nezu [4], but rarely investigated in numerical simulations.

Most previous numerical simulations on this practical flow were based on two-dimensional Reynolds-Averaged Navier-Stokes (RANS) methods, with the free surface treated as a flat shear-free plane, e.g., Mendoza and Shen [5], Jones et al. [6], and Yoon and Patel [7]. The RANS simulations do not predict the turbulent coherent structures that characterize the flow and determine sediment transport. Moreover, very few attempts have been made to simulate the physical deformable free surface, particularly in turbulent open-channel flow over a bed of complex geometry, such as dunes. In this paper, a numerical model coupling level set method to describe a deformable free surface with the filtered incompressible Navier-Stokes equations for large-eddy simulation (LES) is presented for a more comprehensive representation of the real flow situation. In particular, calculations are made for the dune geometry and flow conditions used in the experiments of Balachandar et al. [8]. In this two-phase flow representation, free surface is an interface between air and water, described by evolution of level set function which represents the kinematic condition of the free surface. The free surface is instantaneously captured by the contour of zero level set. The dynamic condition of the free surface is implicitly embedded in the numerical model.

The major objective of the present study is to examine the coherent structures induced by the dune and their interactions with the free surface. The predicted mean flow and turbulence statistics will be compared with the experimental measurements as validation of the present numerical model. Two subgrid-scale (SGS) models, namely, dynamic Smagorinsky model and dynamic two-parameter model, are compared to assess model effects on the free-surface flow.

Mathematical Model

Large eddy simulation (LES) resolves large scales of motion that carry most of turbulent kinetic energy and models smaller scales that are more isotropic and less affected by flow geometry and boundary conditions. The separation of the large scales from the small scales is based on a filtering process. A flow variable f is decomposed into a resolved component (large scale), $\bar{f}$, and a SGS component (small scale), f', i.e., $f=\bar{f}+f'$ where $\bar{f}=\int f(x'')G(x,x'')dx''$, and G is a filter function. A level set function, ϕ, is employed to describe properties of the free surface, which is a mathematical scalar defined as a signed distance function from the free surface. The free surface is identified as the zero level set at any time. The air-water two-phase flow can be described by one set of governing equations with fluid density and viscosity expressed as functions of ϕ. To accurately resolve the dune bed form, a curvilinear coordinate system is used in mathematical descriptions. The filtered incompressible Navier-Stokes equations in a curvilinear coordinate are then written as

$$\frac{\partial \bar{U}_m}{\partial \xi_m} = 0 \tag{1}$$

Contributed by the Fluids Engineering Division for the publication in the JOURNAL OF FLUIDS ENGINEERING. Manuscript received by the Fluids Engineering Division, July 22, 2004; Final revision February 27, 2005. Associate Editor: Ismail B. Celik.

$$\frac{\partial(J^{-1}\bar{u}_i)}{\partial t}+\frac{\partial \bar{U}_m\bar{u}_i}{\partial \xi_m}=-\frac{1}{\rho(\phi)}\frac{\partial}{\partial \xi_m}\left(J^{-1}\frac{\partial \xi_m}{\partial x_i}\bar{p}\right)-J^{-1}g_i$$
$$-\frac{\sigma\kappa(\phi)\delta(\phi)}{\rho(\phi)}\frac{\partial}{\partial \xi_m}\left(J^{-1}\frac{\partial \xi_m}{\partial x_i}\phi\right)$$
$$+\frac{1}{\rho(\phi)}\frac{\partial}{\partial \xi_m}\left(\mu(\phi)G^{mn}\frac{\partial \bar{u}_i}{\partial \xi_n}\right)$$
$$+\frac{1}{\rho(\phi)}\frac{\partial}{\partial \xi_m}\left(J^{-1}\frac{\partial \xi_m}{\partial x_j}\frac{\partial \xi_n}{\partial x_i}\mu(\phi)\frac{\partial \bar{u}_j}{\partial \xi_n}\right)$$
$$-\frac{\partial}{\partial \xi_m}\left(J^{-1}\frac{\partial \xi_m}{\partial x_j}\tau_{ij}\right) \tag{2}$$

where u_i is the velocity component in Cartesian space, J^{-1} is the inverse of the Jacobian, defined as $\det(\partial x_i/\partial \xi_m)$, where x_i and ξ_m are Cartesian and curvilinear coordinate components, respectively, and det represents determinant. U_m is the volume flux normal to the surface of constant ξ_m, defined as $J^{-1}(\partial \xi_m/\partial x_j)u_j$. G^{mn} is mesh skewness tensor, defined as $J^{-1}(\partial \xi_m/\partial x_j)(\partial \xi_n/\partial x_j)$. g_i is the gravitational acceleration component in the i-direction. μ is the dynamic viscosity of the fluid. $\tau_{ij}=\overline{u_iu_j}-\bar{u}_i\bar{u}_j$, resulting from the nonlinear convection term, is called SGS stress, which has to be modeled with a so-called SGS model. δ is a delta function centered at free surface. κ is curvature of free surface. ϕ is solved with the evolution equation as follows:

$$\frac{\partial(J^{-1}\phi)}{\partial t}+\frac{\partial(\bar{U}_m\phi)}{\partial \xi_m}=0 \tag{3}$$

Equation (3) implies the kinematic condition of free surface since the zero level set, $\phi(x_i,t)=0$, represents the free surface position. Equations (2) imply that a transition (or mixing) zone across the free surface is required by the spatial filtering at the free surface where there exist jumps in the fluid density and viscosity. The density and viscosity are assumed smooth between water to air over this narrow transition zone,

$$\rho(\phi)=\rho_a+(\rho_w-\rho_a)H(\phi)$$
$$\mu(\phi)=\mu_a+(\mu_w-\mu_a)H(\phi) \tag{4}$$

where ρ_w and ρ_a are densities of water and air, respectively. $H(\phi)$ is a smoothed Heaviside function,

$$H(\phi)=\begin{cases}0 & \text{if } \phi<-\varepsilon\\ \frac{1}{2}\left[1+\frac{\phi}{\varepsilon}+\frac{1}{\pi}\sin\left(\frac{\pi\phi}{\varepsilon}\right)\right] & \text{if } |\phi|\leqslant\varepsilon\\ 1 & \text{if } \phi>\varepsilon\end{cases} \tag{5}$$

where ε is the thickness of the transition zone, equal to two grid-cell width here, i.e., the transition zone covers four grid cells in the normal direction. In Eqs. (2), the term containing the delta function, $\delta(\phi)=\nabla_\phi H(\phi)$, represents the surface tension spread over the transition zone, i.e., the surface tension is now changed into a volume force. The level set function, ϕ, is initialized and maintained as a signed distance function from the free surface [9].

In this study, two SGS models, namely, dynamic Smagorinsky model (DSM) [10,11] and dynamic two-parameter model (DTM) [12], are employed to compute the SGS stress tensor τ_{ij}. In DSM, τ_{ij} is assumed to be proportional to the resolved strain rate, $\bar{S}_{ij}$,

$$\tau_{ij}-\frac{\delta_{ij}}{3}\tau_{kk}=-2C_s\bar{\Delta}^2|\bar{S}|\bar{S}_{ij} \tag{6}$$

where $\bar{S}_{ij}=(\partial\bar{u}_i/\partial x_j+\partial\bar{u}_j/\partial x_i)/2$, $|\bar{S}|=\sqrt{2\bar{S}_{ij}\bar{S}_{ij}}$, $\bar{\Delta}=\sqrt[3]{\Delta x_1\Delta x_2\Delta x_3}$. A dynamic procedure based on the Germano identity [10], employing a test filter (denoted as $\sim$) wider than the grid filter scale, is used to compute C_s which is assumed invariant between these two scales. By using a least square procedure [11], C_s reads

$$C_s=-\frac{\mathrm{L}_{ij}M_{ij}}{2\bar{\Delta}^2M_{ij}M_{ij}} \tag{7}$$

where $M_{ij}=\alpha^2|\tilde{\bar{S}}|\tilde{\bar{S}}_{ij}-\widetilde{|\bar{S}|\bar{S}_{ij}}$, $\mathrm{L}_{ij}=\widetilde{\bar{u}_i\bar{u}_j}-\tilde{\bar{u}}_i\tilde{\bar{u}}_j$, $\alpha=\tilde{\bar{\Delta}}/\bar{\Delta}$. Typically, $\tilde{\bar{\Delta}}$ is twice as large as $\bar{\Delta}$, thus $\alpha=2$. In DTM, τ_{ij} is split into three terms, namely, modified Leonard term L_{ij}^m computed directly from the resolved velocity, the modified cross term C_{ij}^m assumed to be proportional to L_{ij}^m, and the modified SGS Reynolds term R_{ij}^m assumed to be proportional to $\bar{S}_{ij}$. Therefore, the SGS stress tensor is calculated as follows:

$$\tau_{ij}-\frac{\delta_{ij}}{3}\tau_{kk}=-2C_t\bar{\Delta}^2|\bar{S}|\bar{S}_{ij}+D_t\left(L_{ij}^m-\frac{\delta_{ij}}{3}L_{kk}^m\right) \tag{8}$$

DTM originated from the dynamic mixed model [13], except that C_{ij}^m is assumed to be proportional to R_{ij}^m in the dynamic mixed model (i.e., $D_t\equiv 1$). Both DTM and the dynamic mixed model avoid the assumption of alignment of the principal axes of the SGS stress tensor with those of the resolved strain rate, which is inherited in DSM and not supported by experimental data. There are two model parameters, C_t and D_t, to be determined in DTM, therefore, DTM is more computational costly than DSM and the dynamic mixed model. Employing a dynamic procedure similar to that in DSM results in

$$D_t=\frac{PB-AE}{QB-E^2},\quad C_t=\frac{D_tE-A}{2\bar{\Delta}^2B} \tag{9}$$

where $L_{ij}^m=\widetilde{\bar{u}_i\bar{u}_j}-\tilde{\bar{u}}_i\tilde{\bar{u}}_j$, $H_{ij}=\widetilde{\bar{u}_i\bar{u}_j}-\tilde{\bar{u}}_i\tilde{\bar{u}}_j$, $A=\mathrm{L}_{ij}M_{ij}$, $B=M_{ij}M_{ij}$, $E=H_{ij}M_{ij}$, $P=\mathrm{L}_{ij}H_{ij}-\mathrm{L}_{kk}H_{ll}/3$; $Q=H_{ij}H_{ij}-H_{kk}^2/3$. In both Eqs. (6) and (8), the model coefficients, C_s, C_t, and D_t, are averaged along the spanwise direction to avoid numerical instability.

A finite volume method is used to discretize the governing equations based on a nonstaggered grid [14]. The Crank-Nicolson scheme advances the diagonal part of the viscous and SGS stress terms. The convective terms, off-diagonal viscous and SGS stress terms, and all other terms are advanced with the second-order Adams-Bashforth schemes. A four-step fractional step method is used to solve the momentum equations. The convective terms are discretized with the third order quadratic upwind interpolation for convective kinematics (QUICK) schemes, and diffusion terms are discretized with the second order central scheme. A third-order essentially nonoscillatory scheme (ENO) is used to solve the evolution equation of the level set function, Eq. (3) [9]. The numerical model was extensively validated and verified for laminar free surface problems, such as a solitary wave, breaking dams, and open-channel flow [15]. The good agreement of the predicted solutions by the present numerical model with the available experimental data, analytical solutions, and benchmark data demonstrates the accuracy and stability of the numerical methods used in this study.

Computational Results

Description of Flow. Figure 1 shows a schematic of the geometry of the two-dimensional dune simulated in this study, following the LDV and PIV experiments of Balachandar et al. [8]. The experimental measurements were carried out on the 17th dune of a train of 22 identical dunes mounted in a hydraulic flume such that the turbulent flow can be considered to be fully developed. The flow is driven by the gravity force, $g\sin\theta$. The origin of the coordinate system is set at the dune crest. The dune height h is 20 mm. Dune wavelength is $\lambda=20h$. The width of the computational box (in spanwise direction), L_y, is $7h$ (note that the width of the experimental flume is $30h$). The mean water depth, L, is $6.6h$, (which is $6h$ in the experiment). It is difficult to adjust the simulated water depth to the exact same value as in the experiment

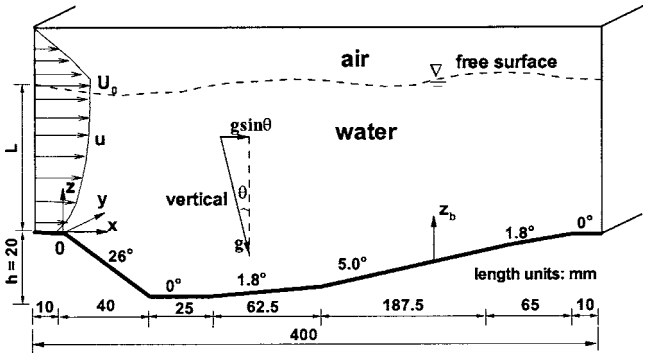

Fig. 1 Schematic of geometry of open-channel flow over a two-dimensional dune (not to scale)

considering that the free surface deforms instantaneously and no accurate initial flow field is available (the computation is initialized with a zero velocity field in this paper). This difference in depth is assumed not to cause appreciable changes in mean flow quantities and turbulence statistics. The Reynolds number, based on L and the free-surface velocity (U_0) at the flow inlet, is 5.8×10^4, the same as in the experiment. Since the free surface is treated as the interface of the air-water two-phase flow, the computational domain covers both water and air. The vertical extent of the computational domain is $8h$. A nonuniform grid of $80 \times 48 \times 84$ in the respective x, y, and z directions is used, as shown in Fig. 2. The grid points nearest to the bed are set within the viscous sublayer. The present grid was chosen based on some preliminary tests, taking into account grid sensitivity and available computer resources. The computations took about three weeks for the DSM simulation and five weeks for the DTM simulation on a Dell® Dimension 8200 desktop with a 1.8G Pentium® IV processor.

The top boundary for air is set as a no-slip wall for computational convenience. In reality, this does not affect the motion of the free surface because the momentum of the air is negligible compared to that of water. Periodic boundary conditions are imposed at both the streamwise and spanwise boundaries. The flow reaches a statistically steady state when the total (sum of pressure and viscous components) resistance on the dune bed is in balance with the streamwise component of gravity force of the water. The solution is continued for about 15 large-eddy turnover times

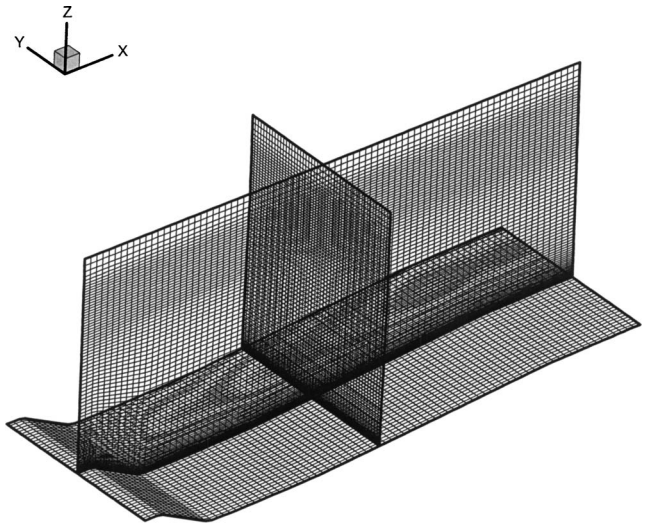

Fig. 2 Grid used in numerical simulations

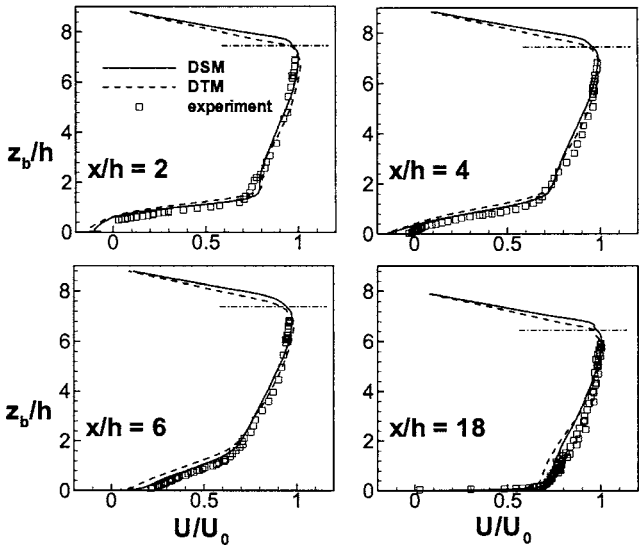

Fig. 3 Comparison of mean streamwise velocity profiles at selected longitudinal stations. Dashed-dotted lines represent predicted free surface positions.

(L/u_τ, where u_τ is mean friction velocity) to record 1000 data sets for calculation of mean flow quantities and turbulence statistics at the middle plane of the channel ($y=L_y/2$).

Mean Flow and Turbulence Statistics. Figure 3 shows the comparison of the mean streamwise velocity (U) predicted by DSM and DTM with the experimental data at four typical longitudinal stations, $x/h=2$, 4, 6, and 18. The uncertainty in the experimental measurement of the mean velocity is ±1.5%. Other flow features are also explored at these four stations in the subsequent discussions. The location of the free surface is shown in the figure, which is identified by the contour of $\phi=0$ at the central plane of the channel. DSM and DTM predict very similar results and are in very good agreement with the experimental measurements. The negative values of the near-wall velocity at $x/h=2$ and 4 indicate that these two stations are located within the mean separation zone. The streamwise velocity profiles are linear in the air region, implying that the motion of the air is basically driven by the free surface velocity, as a Couette flow.

Figure 4 shows the comparison of the mean vertical velocity (W) profiles. Again, DSM and DTM predict close results. At $x/h=18$, $\partial W/\partial z$ is negative away from the wall while positive at $x/h=2$, 4, and 6, implying the flow acceleration at $x/h=18$ and declaration at the other three stations in terms of the continuity constraint (note that the mean spanwise velocity vanishes in this flow). This is due to the fact that the channel contracts at $x/h=18$, and the flow over the recirculation zone forms an expansion section.

Figure 5 shows the streamwise component of root-mean-square (rms) turbulence intensities at the four longitudinal stations. Prominent peaks (labeled A, B, and C in water) are observed in these profiles. The uncertainty in the experimental measurement of the velocity rms is ±1.5%. The peaks are found in the LES predictions as well as in the experiment at all the stations. The primary peak A occurs at almost the same vertical distance from the bed at the first three stations, but is slightly raised by the newly produced near-wall peak C at $x/h=18$. Farther from the bed, the secondary peak B is observed in the experiment and the numerical predictions at the first three stations, which may result from the free-surface deformation. The predicted secondary peaks B are farther from the bed than those of the experiment. A noticeable feature in the figure is the enhancement of u' below the free surface at all the stations. The same enhancement is also observed

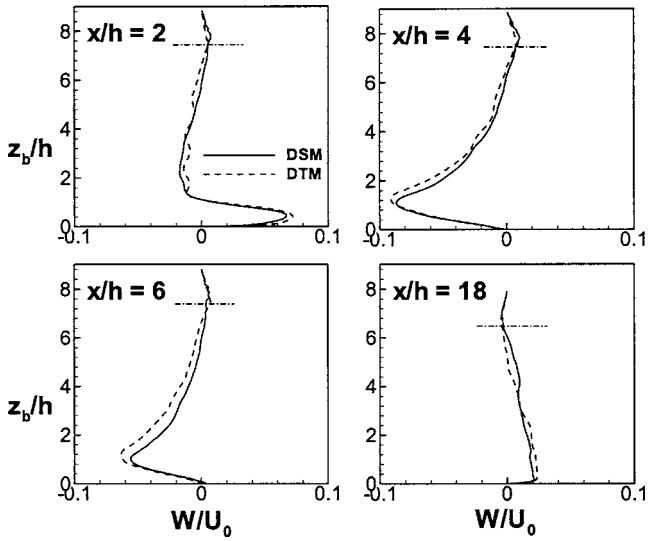

Fig. 4 Comparison of mean vertical velocity profiles at selected longitudinal stations. Dashed-dotted lines represent predicted free surface positions.

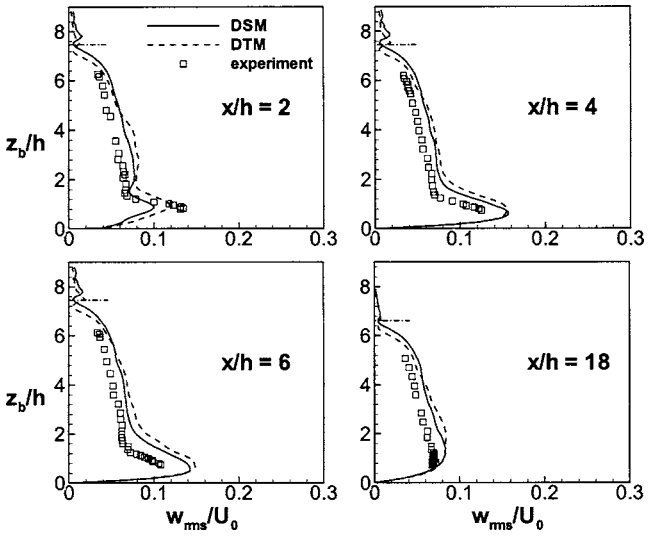

Fig. 6 Comparison of vertical component of turbulence intensities at selected longitudinal stations. Dashed-dotted lines represent predicted free surface positions.

in the profiles of v' (as shown in Fig. 7), while w' approaches to zero at the free surface (as shown in Fig. 6). This is a redistribution of turbulence kinetic energy among its three components near the free surface. In other words, the structure of turbulence shows quasi-two-dimensional character near the free surface. This is observed in experiments [16] in turbulent open-channel flows with a flat bottom wall, and also in DNS [17] in which the free surface is treated as a slip-wall. The major discrepancy between DSM and DTM lies in the air region where DSM predicts prominent peaks (labeled D) which are very weak in the DTM prediction. Due to the low momentum of air, this discrepancy, however, does not significantly affect the structure of turbulence at the free surface.

Figure 6 shows the vertical component of rms turbulence intensities. Near-wall peaks are observed in the numerical predictions as well as in the experiment at the first three stations. The predicted values show an overall 10% increase over the experimental data. The vertical component of turbulence intensities approaches zero at the free surface, indicating the damping effect of the free surface for the vertical motion. Figure 7 shows the spanwise component of rms turbulence intensities. No experimental data is available for this component. The enhancement of v' below the surface transition zone is observed, similar to u'. There are strong near-wall peaks in the v' profiles at $x/h=4$ and 6, around the mean flow reattachment, demonstrating the strong flow three-dimensionality around the mean flow reattachment ($x/h=5$). The magnitudes of the near-bed peaks in the v' profiles are smaller than those of u' but larger than those of w'.

Figure 8 shows the contours of time-averaged turbulent kinetic energy, $(u'^2+v'^2+w'^2)/2$. DSM and DTM predict similar patterns and magnitudes. Large values are centered at the core of the separation vortex. Turbulence energy remains almost constant at constant depths in the upper part of the channel but varies significantly near the bed. Figure 9 shows the contours of time-averaged Reynolds stress, $-\overline{u'w'}$. The similar pattern to Fig. 8 is observed. The shear stress is strong around the core of the separation vortex, and nearly constant horizontally far away from the dune. There-

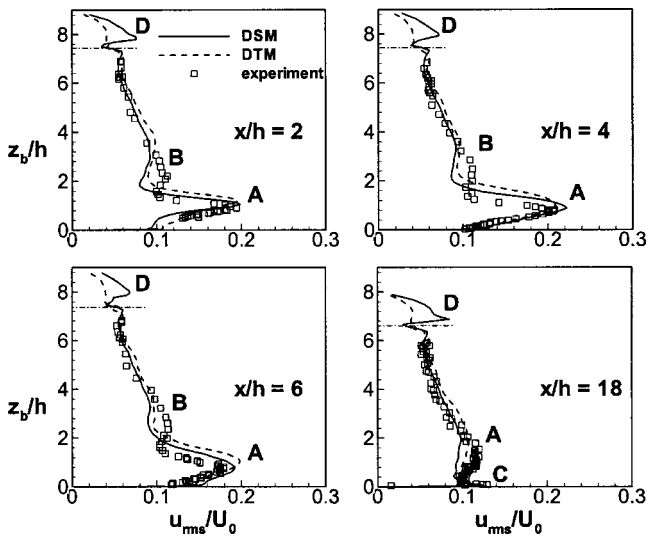

Fig. 5 Comparison of streamwise component of turbulence intensities at selected longitudinal stations. Dashed-dotted lines represent predicted free surface positions.

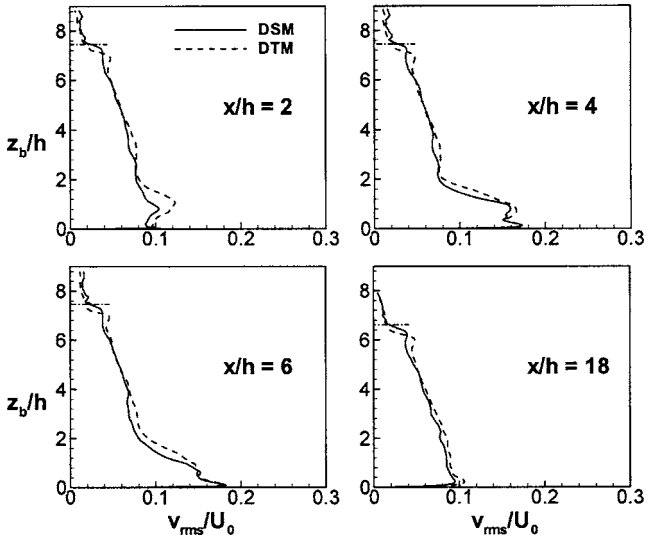

Fig. 7 Comparison of spanwise component of turbulence intensities at selected longitudinal stations. Dashed-dotted lines represent predicted free surface positions.

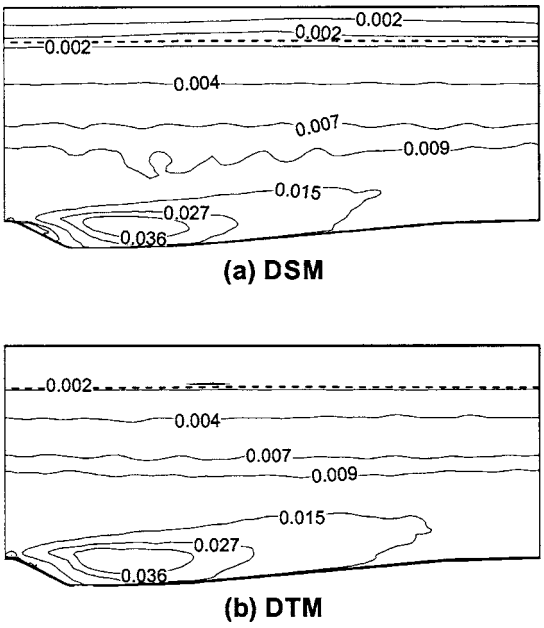

Fig. 8 Contours of time-averaged turbulent kinetic energy at the middle plane of the channel. The dashed lines represent time-averaged free surface positions.

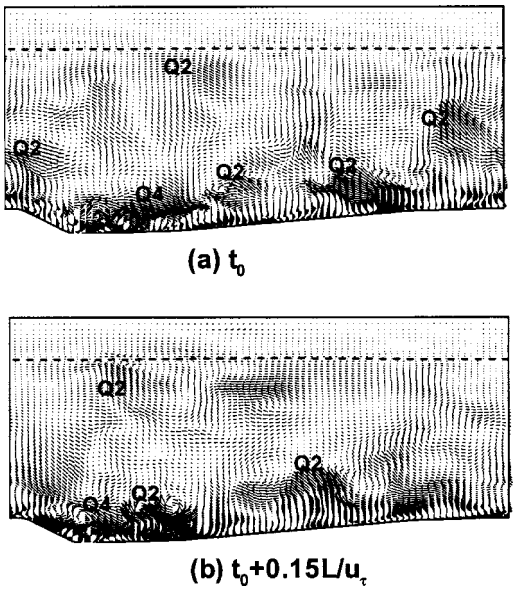

Fig. 10 Instantaneous velocity fluctuation fields of u' and w' in the middle plane of the channel. Dashed lines represent the instantaneous free-surface positions. Q2 and Q4 stand for quadrant two and four events, respectively.

fore, the flow is divided into two zones, an inner zone where turbulence strongly depends on the dune bed geometry and an outer layer free from the direct influence of the bed geometry. Since DSM and DTM predict very close results, only DSM results will be used in the following discussions of instantaneous flow field.

Instantaneous Flow Field. Figure 10 shows instantaneous velocity fluctuation fields (u',w'). Second quadrant (Q2) events $(u'<0,w'>0)$ appear to dominate the near-wall flow. Strong Q4 (fourth quadrant) events $(u'>0,w'<0)$ occur in the recirculation zone, paired with Q2 events. Q2 events also appear close to the free surface. Near-wall Q2 and Q4 events are usually used to detect turbulence ejections and sweeps, respectively. Therefore, strong near-bed dune-induced turbulence ejection- and sweeplike motions are suggested by Fig. 10. The impingement of Q2 events on the free surface results in turbulence disturbance of the air motion that may be responsible for the turbulence peaks in the air region shown in Figs. 5–7. Figure 10 clearly shows that the vertical motion is suppressed at the free surface, as indicated in Fig. 6.

Figure 11 shows snapshots of the isosurfaces $\lambda_2=-200$, where λ_2 is the second largest eigenvalue of the tensor $S_{ik}S_{kj}+\Omega_{ik}\Omega_{kj}$,

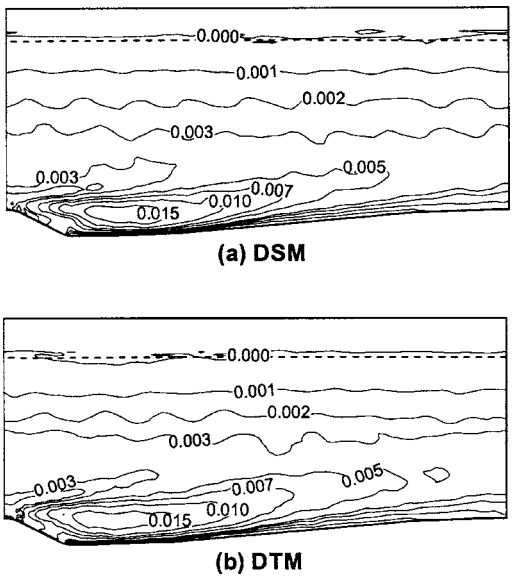

Fig. 9 Contours of time-averaged Reynolds shear stress at the middle plane of the channel. The dashed lines represent time-averaged free surface positions.

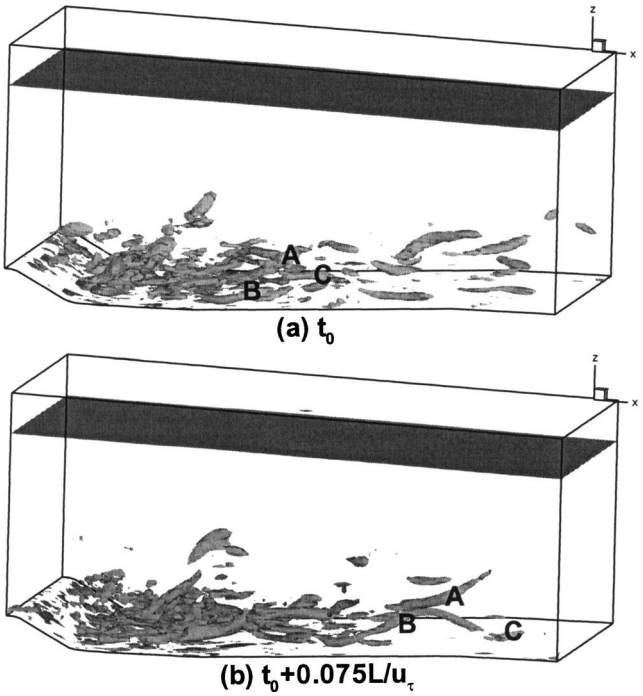

Fig. 11 Instantaneous isosurface of $\lambda_2=-200$. Shadow areas represent instantaneous free surface positions. Labels A, B, and C mark different large-scale structures.

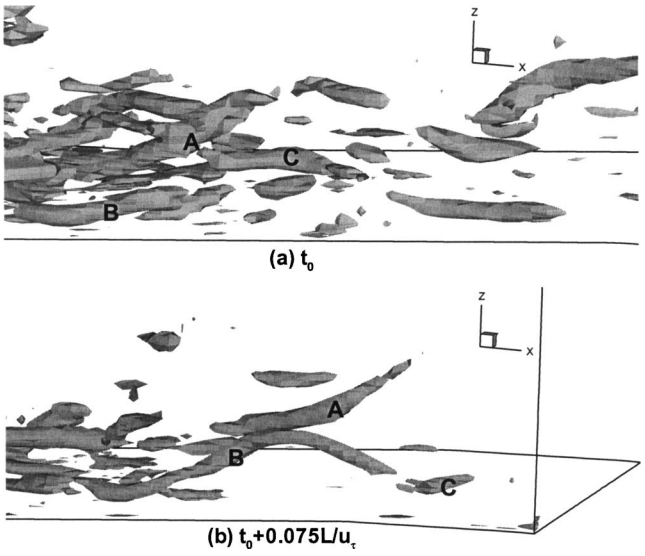

Fig. 12 Close-up view of structures A, B, and C in Fig. 11

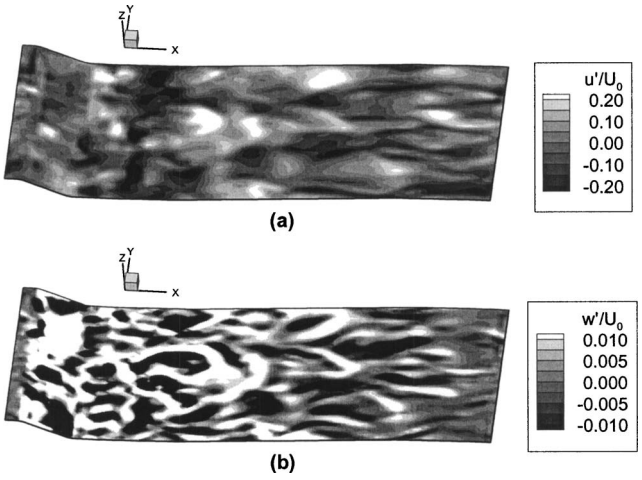

Fig. 13 Contours of three components of velocity fluctuations at the wall layer $z_b^+=9$. (a) u'; (b) w'.

where S_{ij} and Ω_{ij} are the symmetric and antisymmetric parts of the deformation rate tensor $\partial\bar{u}_i/\partial x_j$, respectively. Isosurface of λ_2 is used to identify vortex cores [18]. Tubelike vortical structures are produced in the separation zone and transported downstream along with the mean flow. These structures tilt at different angles to the bed but in general quasistreamwise, either attached to the bed or suspended in the main stream. Three typical structures, marked A, B, and C, are chosen to show the evolution and destruction of these coherent structures. A close-up view of these structures is shown in Fig. 12. The structure A attaching on the bed at time t_0 moves downstream and detaches from the bed at time $t_0+0.075\ L/u_\tau$ with a shortened and thinner body, thus more susceptible to viscous dissipation. The structure B elongates and develops into an arch structure after time $0.075L/u_\tau$. The structure C parallel to the bed at time t_0 is almost dissipated in the boundary layer during the transport. Similar tubelike structures are continuously produced in the separation zone by the strong shear layer developed from the dune crest. These large-scale structures are far from reaching the free surface because of the large flow depth and relatively low Reynolds number, therefore do not interact directly with the free surface. However, these structures may significantly affect sediment movement at the bed, thus determine bed-form generation and movement in alluvial channels.

Streaky structures are observed in wall-layers of turbulent wall-bounded channel flows in many experiments and numerical simulations. It is of interest to investigate whether such structures are present in this complex flow. Figure 13 shows the contours of u' and w' at $z_b^+=9$ where $z_b^+=\nu z_b/u_\tau$. Low-speed streaks ($u'<0$, dark zones) are observed in Fig. 13(*a*), alternating with high-speed fluid ($u'>0$, light zones) on the stoss face of the bed downstream of reattachment. These spatially organized streaks are the signatures of the near-wall coherent structures. Unlike u', stripes of w' emerge over the entire dune bed [Fig. 13(*b*)], suggesting that the vertical motion is more spatially organized in the recirculation zone.

Figure 14 shows snapshots of the free surface captured by the contour of the zero level set, magnified in the vertical direction. Surface upwelling (labeled as *U*) and downdraft (labeled as *D*) are clearly observed. Similar flow patterns were also observed in experiment [19]. They result from interactions of the free surface and the flow structures of scales smaller than those in Fig. 13. If the interactions are sufficiently strong, e.g., with lower water depth and larger Reynolds number, the surface upwelling and downdraft may develop into "boil," a protruding oval patch on water surface, which brings sediments to water surface and disperses them into water to develop and reshape bed-forms in alluvial channels [20].

Concluding Remarks

Turbulent open-channel flow over a two-dimensional dune is simulated by large eddy simulation and the free surface is simulated by the level set method. The kinematic condition of the free surface is substituted with the evolution of the zero level set, and the dynamic condition is embedded in the momentum equations by smearing the surface tension into a volume force within a narrow transition zone. Two SGS models, namely, dynamic Smagorinsky and dynamic two-parameter models, were employed to access the model effects on the free surface turbulence. They basically have similar performance in predicting the mean flow field and turbulence statistics. The numerical predictions are in agreement with the experimental data.

A noticeable feature of the free surface is that the vertical component of turbulence intensities is suppressed while the horizontal ones are enhanced, suggesting the quasi-two-dimensionality of the

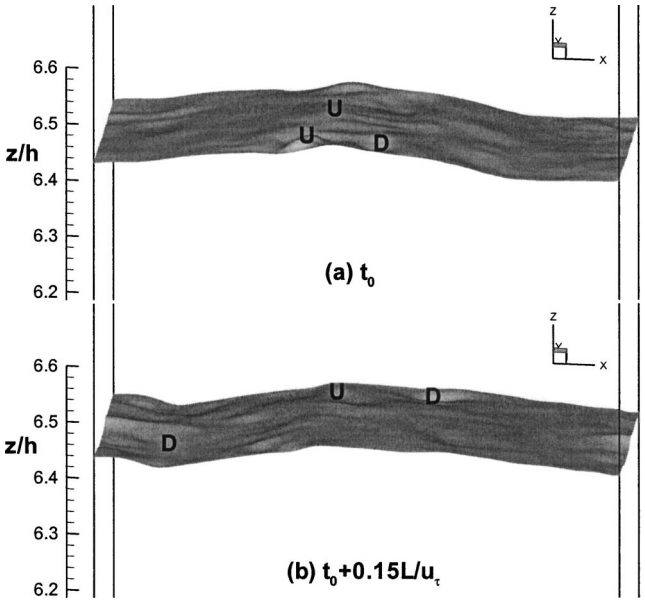

Fig. 14 Instantaneous free-surface patterns. *U* and *D* stand for upwelling and downdraft, respectively.

free surface turbulence. The mean flow is divided into two layers, an inner layer under the influence of dune bed geometry and an outer layer horizontally homogeneous. Q2 events are found to prevail in the near-wall and near-surface motions, indicating the predominance of turbulence ejections in open-channel flows. Vortical structures are continuously produced by the shear layer riding over the separation zone, and transported downstream with the mean flow. Most of these large-scale coherent structures are destructed in the downstream of reattachment before arriving at the next dune crest.

Streaky structures are observed in the wall layer after the flow reattachment, as signatures of the near-wall coherent structures. Free surface deformations, such as upwellings and downdrafts, are visualized, suggesting that they are general patterns of free surface turbulence.

Acknowledgments

This work is partially supported by ONR under Contract No. N00014-01-0262. The authors are indebted to R. L. Street and Y. Zang for providing the base LES code. R. Balachandar is gratefully thanked for experimental data. W.Y. thanks Marc B. Parlange and Charles Meneveau for their support in completing the manuscript.

References

[1] Nezu, I., and Nakagawa, H., 1989, "Turbulent Structure of Backward-Facing Step Flow and Coherent Vortex Shedding from Reattachment in Open Channel Flows," *Turbulent Shear Flows 6*, F. Durst, et al., eds., Springer-Verlag, Berlin, pp. 313–337.

[2] Müller, A., and Gyr, A., 1986, "On the Vortex Formation in the Mixing Layer Behind Dunes," J. Hydraul. Res., **24**, pp. 359–375.

[3] Bennett, S. J., and Best, J. L., 1995, "Mean Flow and Turbulence Structure Over Fixed Two-Dimensional Dunes: Implications for Sediment Transport and Bedform Stability," Sedimentology, **42**, pp. 491–514.

[4] Kadota, A., and Nezu, I., 1999, "Three-Dimensional Structure of Space-Time Correlation on Coherent Vortices Generated Behind Dune Crest," J. Hydraul. Res., **37**, pp. 59–79.

[5] Mendoza, C., and Shen, H. W., 1990, "Investigation of Turbulent Flow Over Dunes," J. Hydraul. Eng., **116**, pp. 459–477.

[6] Johns, B., Soulsby, R. L., and Xing, J., 1993, "A Comparison of Numerical Model Experiments of Free Surface Flow Over Topography With Flume and Field Observations," J. Hydraul. Res., **31**, pp. 215–228.

[7] Yoon, J. Y., and Patel, V. C., 1996, "Numerical Model of Turbulent Flow Over Sand Dune," J. Hydraul. Eng., **122**, pp. 10–18.

[8] Balachandar, R., Polatel, C., Hyun, B.-S., Yu, K., Lin, C.-L., Yue, W., and Patel, V. C., 2002, "LDV, PIV and LES Investigation of Flow Over a Fixed Dune," *Proceedings of the Symposium held in Monte Vertà: Sedimentation and Sediment Transport*, Kluwer Academic, Dordrecht, pp. 171–178.

[9] Yue, W., Lin, C.-L., and Patel, V. C., 2003, "Numerical Simulation of Unsteady Multidimensional Free Surface Motions by Level Set Method," Int. J. Numer. Methods Fluids, **42**, pp. 853–884.

[10] Germano, M., Piomelli, U., Moin, P., and Cabot, W. H.,1991, "A Dynamic Subgrid-Scale Eddy Viscosity Model," Phys. Fluids A, **3**, pp. 1760–1765.

[11] Lilly, D. K., 1992, "A Proposed Modification of the Germano Subgrid Scale Closure Method," Phys. Fluids A, **4**, pp. 633–635.

[12] Salvetti, M. V., and Banerjee, S., 1994, "A Priori Tests of a New Dynamic Subgrid-Scale Model for Finite-Difference Large-Eddy Simulation," Phys. Fluids, **7**, pp. 2831–2847.

[13] Zang, Y., Street, R. L., and Koseff, J. R., 1993, "A Dynamic Mixed Subgrid-Scale Model and its Application to Turbulent Recirculating Flows," Phys. Fluids A, **5**, pp. 3186–3196.

[14] Zang, Y., Street, R. L., and Koseff, J. R., 1994, "A Nonstaggered Grid, Fractional Step Method for Time-Dependent Incompressible Navier-Stokes Equations in Curvilinear Coordinates," J. Comput. Phys., **114**, pp. 18–33.

[15] Yue, W., Lin, C.-L., and Patel, V. C., 2003, "Numerical Investigations of Turbulent Free Surface Flows Using Level Set Method and Large Eddy Simulation," IIHR Technical Report No. 435, The University of Iowa, Iowa City, Iowa.

[16] Kumar, S., Gupta, R., and Banerjee, S., 1996, "Attached Vortices in Free-Surface Turbulence," in *Proceedings of the 20th Symposium on Naval Hydrodynamics*, Santa Barbara, California.

[17] Pan, Y., and Banerjee, S., 1995, "A Numerical Study of Free Surface Turbulence in Channel Flow," Phys. Fluids, **7**, pp. 1649–1664.

[18] Jeong, J., and Hussain, F., 1995, "On the Identification of a Vortex," J. Fluid Mech., **285**, pp. 69–94.

[19] Banerjee, S., 1994, "Upwellings, Downdrafts, and Whirlpools: Dominant Structures in Free Surface Turbulence," Appl. Mech. Rev., **47**(6), pp. S166–172.

[20] Nezu, I., and Nakagawa, H., 1993, *Turbulence in Open-Channel Flows*, A. A. Balkema, Rotterdam, The Netherlands, Chap. 9.

LES of Turbulent Separated Flow and Heat Transfer in a Symmetric Expansion Plane Channel

Kazuaki Sugawara

Hiroyuki Yoshikawa

Terukazu Ota
e-mail: ota@cc.mech.tohoku.ac.jp

Department of Mechanical Systems and Design,
Tohoku University, 6-6-01 Aoba, Aramaki,
Aoba-ku, Sendai 980-8579, Japan

The LES method was applied to analyze numerically an unsteady turbulent separated and reattached flow and heat transfer in a symmetric expansion plane channel of expansion ratio 2.0. The Smagorinsky model was used in the analysis and fundamental equations were discretized by means of the finite difference method, and their resulting finite difference equations were solved using the SMAC method. The calculations were conducted for Re=15,000. *It is found that the present numerical results, in general, agree well with the previous experimental ones. The complicated vortical flow structures in the channel and their correlations with heat transfer characteristics are visualized through various fields of flow quantities.* [DOI: 10.1115/1.1988344]

1 Introduction

Prediction of the separated and reattached flow of incompressible viscous fluid and the heat transfer therein has been recognized to be very important in relation to many types of fluid machinery and heat exchangers, and there have been numerous experimental and numerical works. It has been noticed that the flow structure in the separated and reattached regions is extremely complicated and details of the turbulent heat transfer mechanism are not fully understood up to the present.

A symmetric expansion plane channel is a basic geometrical configuration in which the separation and reattachment of flow occur. Accordingly, there have been a plenty of experimental and numerical studies on the flow in such the channel since a pioneering work by Abbott and Kline [1–14]. It has been clarified in these studies that the flow in the channel deflects to one wall even at relatively low Reynolds number. The cause of becoming such a steady asymmetric flow may be discussed as follows. It has been well established that a thin shear layer of incompressible viscous fluid is very sensitive to small disturbances. An instability of the separated shear layer brings about some difference of the velocity between two separated shear layers bounding the main flow, resulting in some pressure difference in the channel downstream of the step. The main flow is deflected to the lower pressure side and an asymmetry of the flow is steadily maintained because of its large momentum. Several investigations [15–17] have been conducted in order to clarify the critical Reynolds number beginning the asymmetric flow, and the critical Reynolds number was found to decrease with increasing the channel expansion ratio and also the step aspect ratio [17].

On the other hand, there have been only some investigations of the laminar and turbulent heat transfer in such the channel [18–20]. Ota and his colleagues have made the experimental and numerical studies on the flow and heat transfer in the separated and reattached regions in a symmetric expansion plane channel [21–25]. These previous works are extensively reviewed by Ota [26]. In engineering applications, however, studies on the turbulent heat transfer have been noticed to be very important. A numerical simulation methodology is useful to investigate details of the flow and heat transfer characteristics in such the complicated flow. However, most of the previous numerical studies cited above have concerned about the low Reynolds number cases. Just recently, a few numerical studies at high Reynolds number have been made by the large eddy simulation methodology [27,28].

The purpose of the present numerical study is to clarify the three-dimensional structure of an unsteady turbulent separated flow and heat transfer in a symmetric expansion plane channel of expansion ratio 2.0 by the large eddy simulation methodology.

2 Numerical Procedures

Figure 1 presents the flow configuration, coordinate system and important physical parameters in the analysis. The channel height is W_1 at the inlet and W_2 at the outlet, and the step height is H. The spanwise computational region is W_3, as illustrated in the figure. Fundamental equations in the LES methodology are obtained by filtering the continuity, Navier-Stokes and energy equations for an incompressible viscous fluid with constant physical properties, along with the Smagorinsky model, as follows:

$$\frac{\partial \hat{u}_i}{\partial x_i} = 0 \tag{1}$$

$$\frac{\partial \hat{u}_i}{\partial t} + \frac{\partial}{\partial x_j}(\hat{u}_j \hat{u}_i) = -\frac{1}{\rho}\frac{\partial \hat{p}}{\partial x_i} + \frac{\partial}{\partial x_j}\left[(\upsilon + \upsilon_{\mathrm{SGS}})\left(\frac{\partial \hat{u}_i}{\partial x_j} + \frac{\partial \hat{u}_j}{\partial x_i}\right)\right] \tag{2}$$

$$\frac{\partial \hat{\theta}}{\partial t} + \frac{\partial}{\partial x_j}(\hat{u}_j \hat{\theta}) = \frac{\partial}{\partial x_j}\left[\left(\frac{\lambda}{\rho \tilde{c}} + \frac{\upsilon_{\mathrm{SGS}}}{\mathrm{Pr}_{\mathrm{SGS}}}\right)\frac{\partial \hat{\theta}}{\partial x_j}\right] \tag{3}$$

where

$$\upsilon_{\mathrm{SGS}} = (C_S \Delta)^2 (2\hat{S}_{ij}\hat{S}_{ij})^{1/2}$$

$$\Delta = (\Delta_1 \Delta_2 \Delta_3)^{1/3}$$

$$\hat{S}_{ij} = \frac{1}{2}\left(\frac{\partial \hat{u}_i}{\partial x_j} + \frac{\partial \hat{u}_j}{\partial x_i}\right)$$

Superscript $\hat{}$ denotes a grid filtering operation on the grid width Δ_i, C_S the Smagorinsky constant, and $\mathrm{Pr}_{\mathrm{SGS}}$ the SGS turbulent Prandtl number. In the following calculations, the space coordinates x_i, velocity u_i, pressure p, and time t are nondimensionalized by $x_i^* = x_i/H$, $u_i^* = u_i/U_m$, $p^* = p/\rho U_m^2$, $t^* = T = tU_m/H$, and $\theta^* = \lambda(\theta - \theta_0)/q_w H$, respectively. In previous studies with the LES methodology, several values were recommended to C_S. A value of 0.10 was selected in the main body of the present calculations, but 0.09 and 0.11 were also used in some preliminary studies, since the calculated values with $C_S = 0.10$ for the fully developed turbulent channel flow were detected to estimate very well the measured

Contributed by the Fluids Engineering Division for the publication in the JOURNAL OF FLUIDS ENGINEERING. Manuscript received by the Fluids Engineering Division, July 22, 2004; revision received, May 23, 2005. Associate Editor: Ismail Celik.

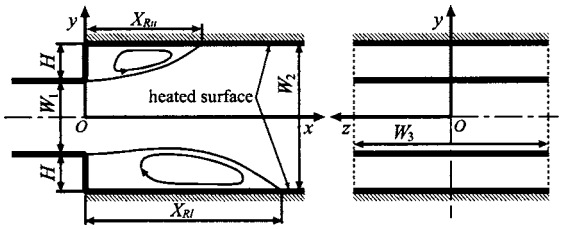

Fig. 1 Flow configuration and coordinate system

ones. A selected value of Pr_{SGS} was 0.7 in the present study after searching its optimum value. It was detected there that as Pr_{SGS} decreases, $\overline{Nu}$ increases but its peak location moves downstream and, on the contrary, as Pr_{SGS} increases, the maximum of $\overline{Nu}$ in the reattachment region is very underestimated. The results with $Pr_{SGS}=0.7$ shown in the following were found to generally well estimate the measured ones. Further, in the calculations, the wall damping effect was included by the well-known Van Driest function [29].

Equations (1)–(3) are discretized on the nonuniform orthogonal grid by means of the finite difference method. In the time marching of Eq. (2), the Crank-Nicholson method for the convective and viscous terms, and the Euler backward first order difference for the pressure terms are employed, respectively. As for the space derivatives, the QUICK method is used for the convection terms, and the second-order central difference for other terms, respectively. In some preliminary calculations, the higher order scheme for the pressure terms was tried, but it resulted in an unstable scheme. In order to improve the time variation, the time step of calculations was set to a small value. Resulting finite difference equations were solved using the SMAC method [30].

The boundary conditions are as follows: The 1/7th power velocity law is presumed at the inlet. The no-slip condition on the wall, and the convection condition at the outlet are employed, respectively. The periodicity of flow and temperature on the spanwise boundaries is assumed. As for the temperature, it is assumed to be uniform at the inlet, and the lower and upper wall surfaces downstream of the step are heated under the condition of uniform heat flux, and other walls are adiabatic. The second derivative is assumed to be zero at the outlet.

A sudden expansion plane channel treated in the present study is an expansion ratio of 2.0 and the Prandtl number of fluid is 0.7. The computational region extends from $-20H$ to $40H$ in the x-direction and from $-2H$ to $2H$ in the y-direction. As for the spanwise region, $10H$ is selected in consideration of previous experimental results [21]. The computational grid with non-uniform orthogonal spacings mainly used is $301\times129\times101$. However, in order to investigate the grid dependency of the present numerical scheme, two other grids of $281\times101\times101$ and $291\times121\times101$ are also used in some preliminary computations. It was found that the grid of $281\times101\times101$ is not enough to simulate reasonably well the real flow. The finest grid of $301\times129\times101$ is used in the present calculations, since the high reliability of results are expected. The thermal boundary layer is naturally very thin in the reattachment flow region. Accordingly, the grid points are needed to be closer to the wall for the better estimation of Nusselt number. Some attempts were made using the present grid of $301\times129\times101$ in which the grid points near the wall, however, were moved closer to the wall compared with the present ones. However, an improvement of $\overline{Nu}$ estimation was very small. In consideration of these results, the present grid system was employed in the calculations.

The Reynolds number based on the maximum velocity in the upstream channel and the step height ($Re=U_mH/\nu$) is 15,000. This value of Reynolds number is selected for comparing the present numerical results with our previous experimental ones [21]. The interval of time advancement is $0.001H/U_m$. In calculating the time averaged and turbulent statistical values, the sampling time is $6500H/U_m$ and the sampling size 6.5×10^6. This sampling time is estimated to be longer than that in the experiments [21].

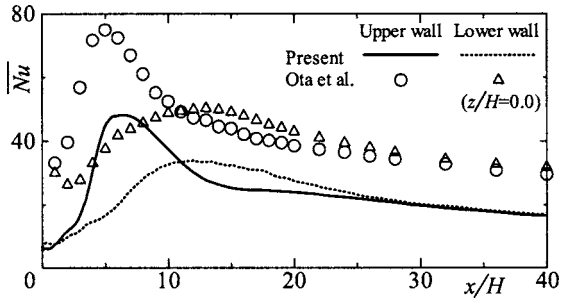

Fig. 2 Time averaged Nusselt number ($z/H=0.0$)

There has been very few work on the unsteady turbulent separated flow and heat transfer in a symmetric expansion plane channel, as described above. In such the present stage of our understanding, first it is important to estimate details of the unsteady flow and temperature fields. Accordingly, in the present study, the free stream velocity of 1/7th power law is employed as the inlet boundary condition without including the turbulence. The unsteady inlet conditions in the LES were discussed recently by Smirnov et al. [31].

3 Numerical Results and Discussion

Present numerical results for Re=15,000 are compared with our previous experimental data at the same Reynolds number [21]. Their experimental conditions are almost the same as the present ones except the free stream turbulence. That is, ER=2.0, AR=10.0, Pr=0.7, and Re=15,000 though the closed test section provides two side walls in the experiments. In the present numerical study, however, the periodic condition is employed on the two spanwise boundaries. In the experimental work by Escudier et al. [6], the time averaged flow in the channel central region was found to be essentially two-dimensional in the case of the step aspect ratio greater than 10. Further, in our previous experiments for AR=10 [21], the spanwise variations of the flow and temperature fields were measured and they were detected to be relatively small in the channel central region.

Figure 2 compares the local Nusselt number distribution on the two walls. Present numerical results are qualitatively in good agreement with the experimental ones, but underestimate in the whole field, though the streamwise location of the maximum Nusselt number almost agrees with each other on both the upper and lower walls.

Figure 3 shows the reverse flow rate near the two walls. The present results agree well with the experimental ones in the downstream region of the separation bubble especially on the lower wall where the long separation bubble is formed. On the upper

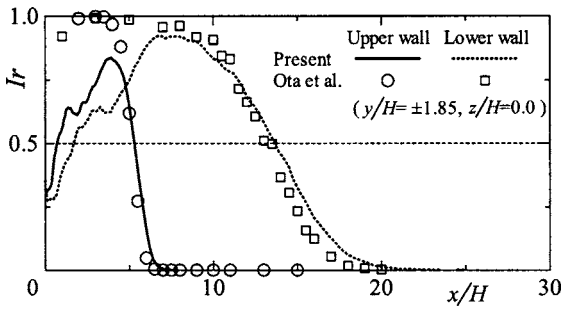

Fig. 3 Reverse flow rate ($y/H=\pm1.85, z/H=0.0$)

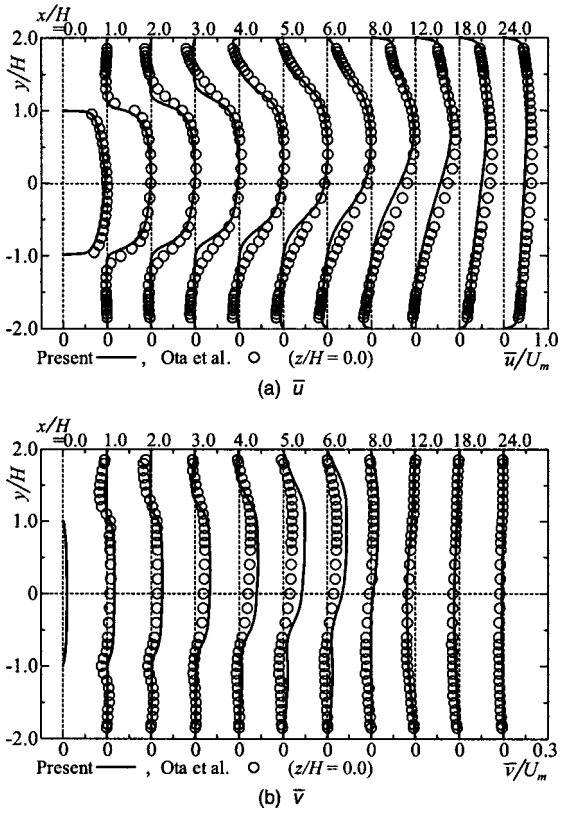

Fig. 4 Time averaged velocity ($z/H=0.0$). (*a*) $\bar{u}$; (*b*) $\bar{v}$.

wall where the short separation bubble is formed, on the other hand, the present numerical scheme underestimates the reverse flow rate in the upstream region of the separation bubble.

Figure 4 presents comparisons of two components of the mean velocity $\bar{u}$ and $\bar{v}$. Further, Fig. 5 shows two turbulence intensities u'_{rms} and v'_{rms}, the Reynolds shear stress $-\overline{u'v'}$ and the turbulent kinetic energy. It is clearly illustrated that the present numerical results are generally in good agreement with the experimental ones almost in the whole flow field, though some difference is detected locally. The upward deflection of the main flow and the diffusion of the separated shear layer are also clearly exhibited in the figures.

These comparisons clarify that the present numerical scheme estimates reasonably well the time averaged flow field observed in the experimental study, though there are several important problems to be solved in a future work.

First, the mean Nusselt number is underestimated in the whole flow region. One of the most important factor for such a difference is supposed to be the free stream turbulence. In the experiment, the free stream turbulence intensity was about 2% in the channel center and increased to nearly 5% in the boundary layer on the channel wall upstream of the step. Such a highly turbulent free stream is inferred to promote strongly the heat transfer.

Secondly, the present turbulence intensity in the separated shear layer is also underestimated compared to the measured one. It brings about smaller values of the entrainment rate of the fluid into the shear layer and the reverse flow velocity, especially in the upstream region of the separated shear layer.

Thirdly, the present stage of the LES methodology is not easy to predict quantitatively the turbulent flow and heat transfer characteristics including the thin separated shear layer in which the flow quickly transits to the turbulent one [32].

Figure 6 shows the time averaged SGS eddy viscosity $\overline{\nu_{\mathrm{SGS}}}$, which presents the energy of the SGS small eddy and turbulence.

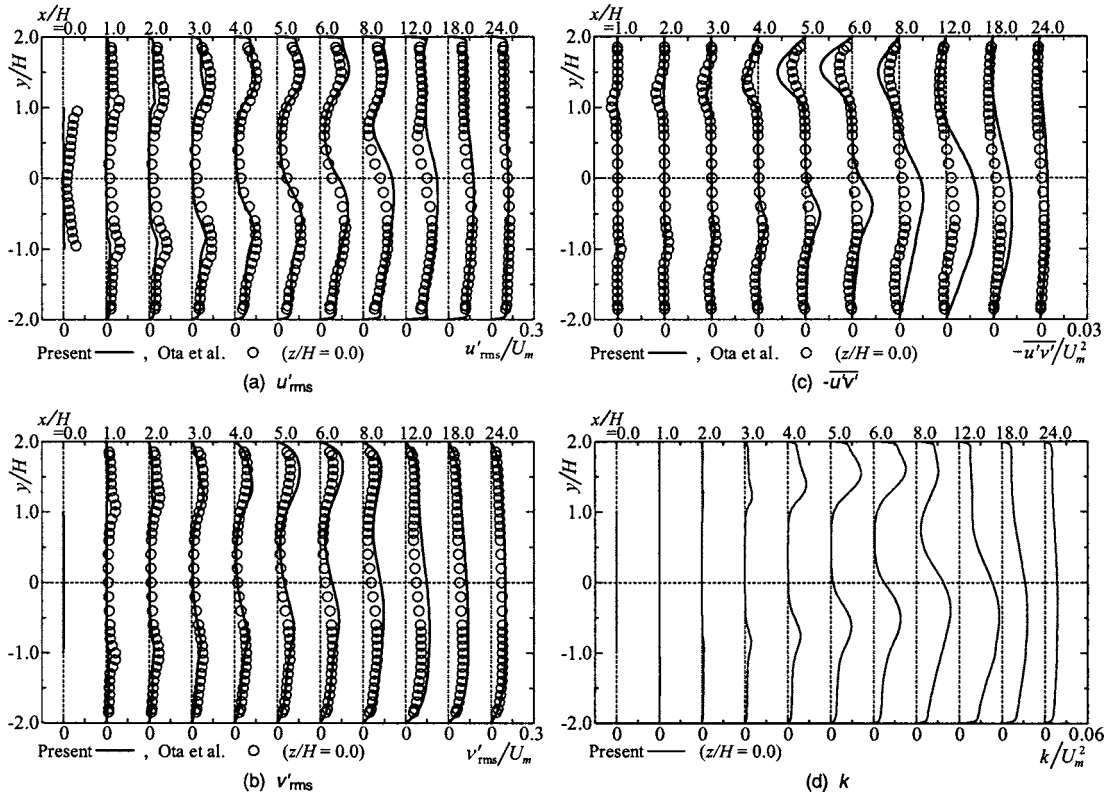

Fig. 5 Turbulence intensities, Reynolds shear stress and turbulent kinetic energy ($z/H=0.0$). (*a*) u'_{rms}; (*b*) v'_{rms}; (*c*) $-\overline{u'v'}$; (*d*) k.

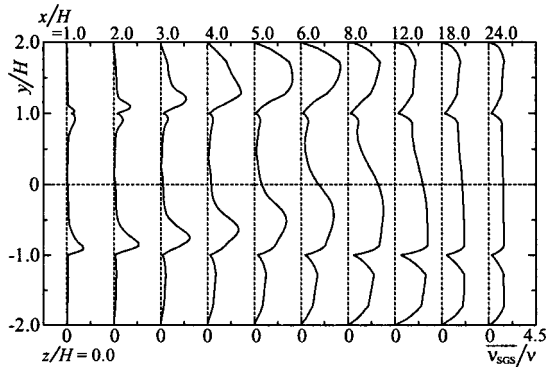

Fig. 6 Time averaged SGS eddy viscosity (z/H=0.0)

It is found that $\overline{v_{SGS}}$ is large in the separated shear layer just downstream of the channel expansion and becomes larger in the reattachment regions on both the upper and lower walls. In the redeveloping flow region downstream of the reattachment point, $\overline{v_{SGS}}$ weakens gradually.

Power spectra of the velocity fluctuation v' and also the temperature fluctuation θ' at $y/H=1.0, z/H=0.0$ are illustrated in Figs. 7 and 8, respectively. It is found in Fig. 7 that the dominant energy exists at a high frequency around $fH/U_m=0.5$ just downstream of the separation point, as suggesting a formation of small vortices along the separated shear layer. The peak frequency decreases in the downstream direction, as exhibiting the formation of large scale vortices. In the far downstream, there is no clear peak frequency, which suggests the relatively quick diffusion of large scale vortices. The results of θ' represent almost the same characteristics as v', as suggesting large effects of the vortices upon the heat transfer features.

Figure 9 shows the surface pressure along the channel center. In the short separation bubble on the upper wall, $\overline{C_p}$ is much lower than that on the lower wall. It is originated from the strong entrainment of stagnant fluid in the separation bubble into the very thin separated shear layer, which locates nearer to the wall. Small hump found around $x/H=7.0$ is produced by the reattachment of the separated shear layer, though its position locates somewhat downstream of the reattachment point.

Figure 10 presents the streamwise surface skin friction coefficient on the channel center. The time averaged reattachment point is reasonably defined as a point of $\overline{C_{fx}}=0$. The present results show that $X_{Ru}=6.03H$ and $X_{Rl}=15.5H$, which agree very well with the experimental ones [21]. On the upper wall, $\overline{C_{fx}}$ attains the

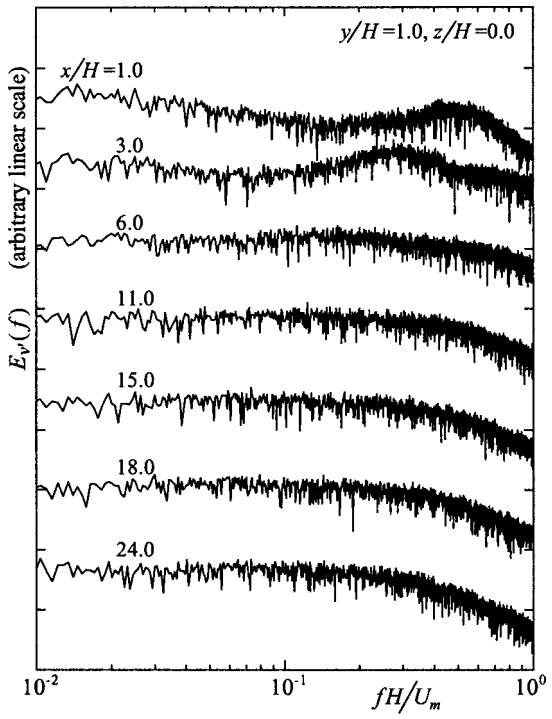

Fig. 7 Power spectrum of v' (y/H=1.0, z/H=0.0)

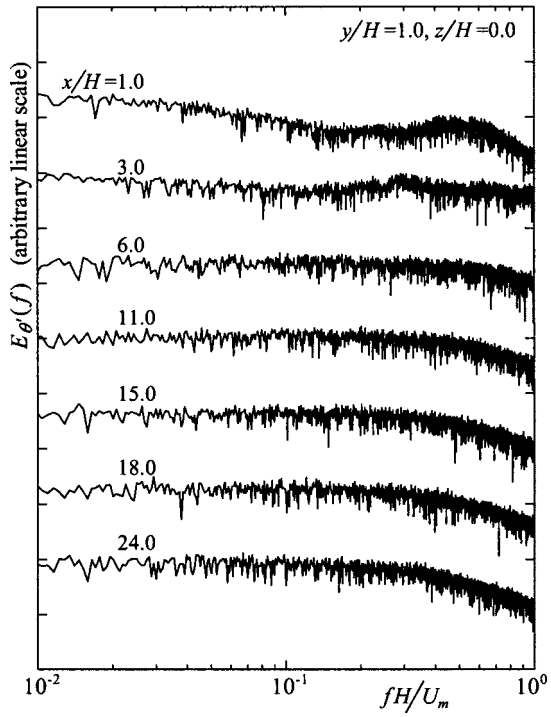

Fig. 8 Power spectrum of θ' (y/H=1.0, z/H=0.0)

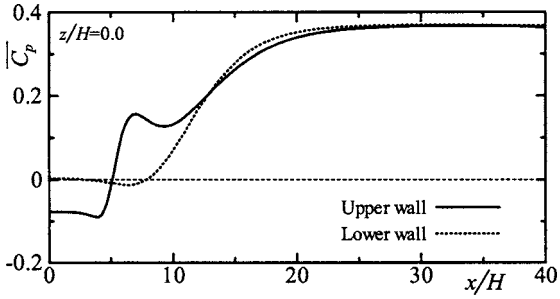

Fig. 9 Time averaged surface pressure coefficient (z/H=0.0)

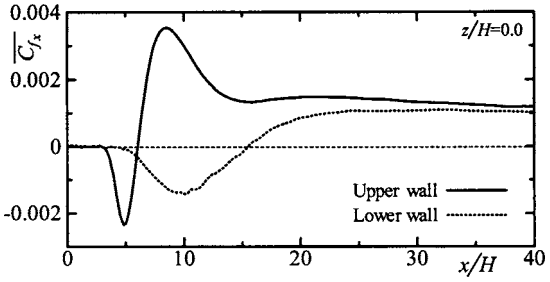

Fig. 10 Time averaged skin friction coefficient (z/H=0.0)

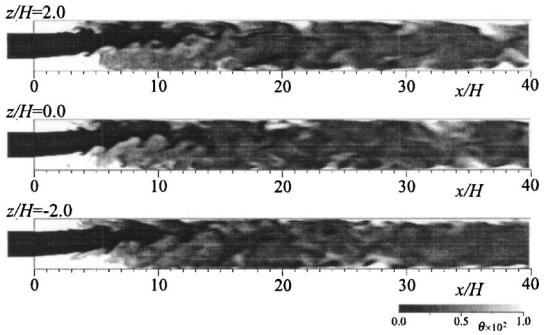

Fig. 11 Instantaneous temperature ($T=0$)

large maximum at about $x/H=8$, where the main flow just outside the separated shear layer reattaches onto the surface.

In the following, the instantaneous flow and temperature fields are investigated by visualizing several useful physical quantities.

Figures 11 and 12 exhibit the instantaneous temperature and enstrophy fields in three x-y cross sections. Further, Figs. 13 and 14 present also the instantaneous temperature and enstrophy fields in six y-z cross sections. These results clarify the development of the separated shear layer, formation of large scale vortices, their shedding from the reattachment flow region, mutual interaction of the two separated shear layers on the upper and lower walls and the turbulent mixing process. It can be detected that the two-dimensionality of the flow and temperature fields is maintained in the upstream region of the separation bubble, say to $x=(5-6)H$, and also their three-dimensionality becomes noticeable in the reattachment flow regions on the two walls.

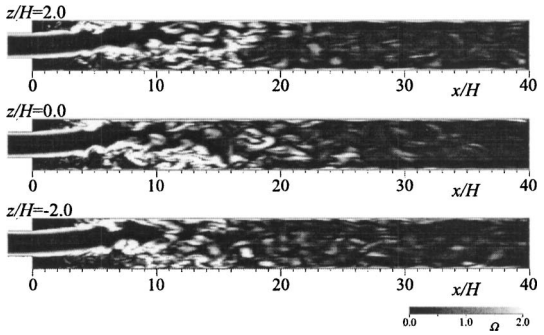

Fig. 12 Instantaneous enstrophy ($T=0$)

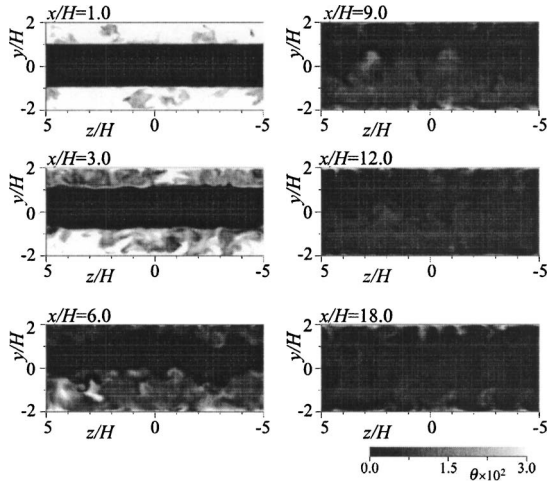

Fig. 13 Instantaneous temperature ($T=0$)

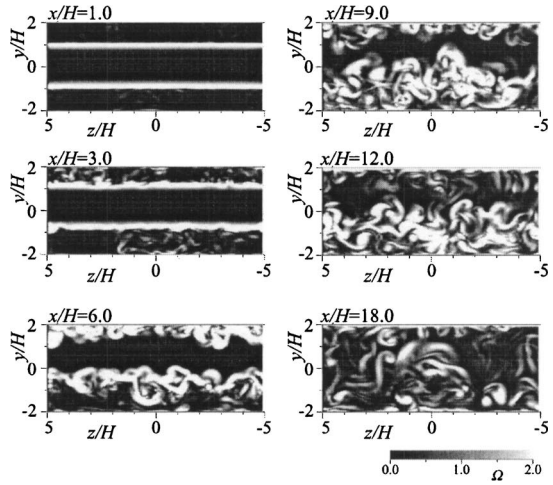

Fig. 14 Instantaneous enstrophy ($T=0$)

Figure 15 illustrates the instantaneous enstrophy distribution in five x-z planes. In the central region from $y=-H$ to H, the two-dimensionality of the flow field is maintained. However, the strong three-dimensional flow is formed in the outer region, and the streak structure is clearly demonstrated in the downstream of the reattachment region.

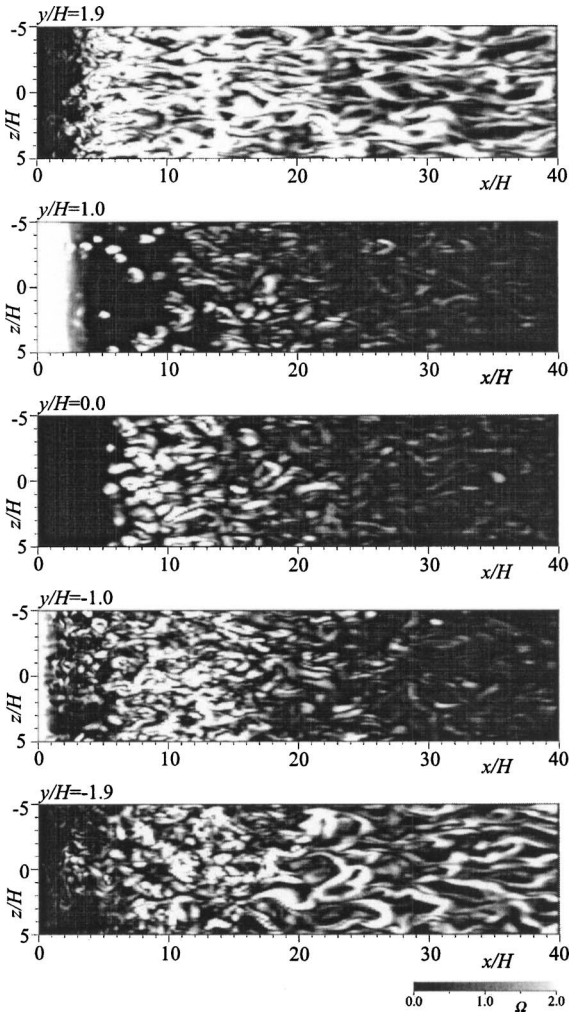

Fig. 15 Instantaneous enstrophy ($T=0$)

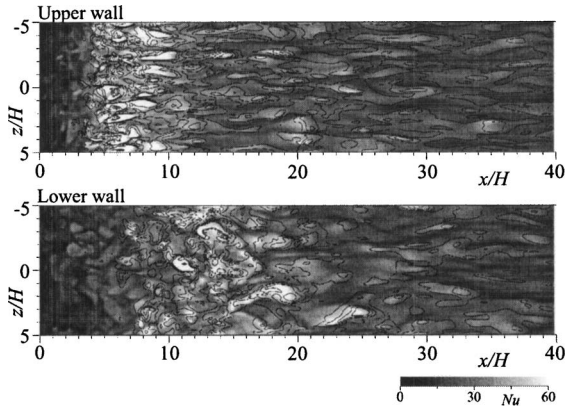

Fig. 16 Instantaneous Nusselt number and skin friction coefficient ($\Delta C_f=1.0\times10^{-3}, T=0$)

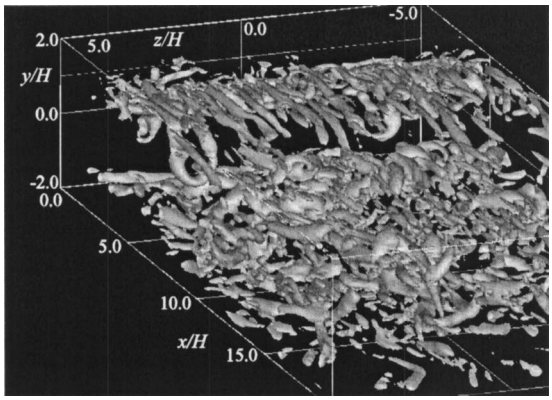

Fig. 17 Isosurface of Q ($Q=0.8, T=0$)

Figure 16 shows an instantaneous isocontour of the surface skin friction coefficient along with the instantaneous Nusselt number. High Nusselt number concentrates in the large skin friction regions, and it is found that the streak structure is formed in the downstream of the reattachment region on the upper wall.

Figure 17 represents an isosurface of the second invariant of velocity gradient tensor Q. The region of positive value of Q is considered to indicate the small vortex tube included in the large scale vortex. Three-dimensional vortical structure is clearly represented in the figure and the viscous dissipation of the turbulent energy is active around the vortex tubes, though the corresponding figure is omitted in the present paper.

4 Concluding Remarks

The turbulent separated and reattached flow and heat transfer in a symmetric expansion plane channel was numerically studied with the LES method. The Smagorinsky model along with the finite difference method was employed in the calculations. The channel expansion ratio is 2.0, and the Prandtl number of fluid 0.7, respectively. The Reynolds number treated is 15,000, and the spanwise computational region extends to $10H$. The main results obtained are as follows.

The present numerical results agree reasonably well with our experimental ones including the time averaged velocities and the turbulence intensities and turbulent shear stress, though some quantitative difference is found for the Nusselt number distribution. The time averaged reattachment length is well simulated.

The three-dimensional vortical structure of the instantaneous flow and temperature fields is clearly represented through evaluations of the flow quantities such as the enstrophy and the second invariant of the velocity gradient tensor.

The correlation of the turbulent heat transfer in the separated and reattached flow with the three-dimensional vortical flow structure is minutely investigated, suggesting the importancy of the streak structure of vortices.

Acknowledgments

The present calculations were conducted using a supercomputer SX-4/128H4 and SX-7 at the Information Synergy Center, Tohoku University.

Nomenclature

AR = step aspect ratio $=W_3/H$
C_f = skin friction coefficient $=\tau_w/(\rho U_m^2/2)$
C_p = pressure coefficient $=(p-p_0)/(\rho U_m^2/2)$
C_S = Smagorinsky constant
$\tilde{c}$ = specific heat at constant pressure
ER = expansion ratio $=W_2/W_1$
$E_x(f)$ = power spectrum of x
f = frequency
H = step height
h = heat transfer coefficient $=q_w/(\theta_w-\theta_0)$
Ir = reverse flow rate
k = turbulent kinetic energy
Nu = Nusselt number $=hH/\lambda$
Pr = Prandtl number
$\mathrm{Pr_{SGS}}$ = SGS turbulent Prandtl number
p = pressure
Q = second invariant of velocity gradient tensor
q_w = heat flux
Re = Reynolds number $=U_mH/v$
T = nondimensional time $=tU_m/H$
t = time
U_m = maximum velocity at inlet
u_i = velocity components $(u_1,u_2,u_3)=(u,v,w)$
W_1 = channel height at inlet
W_2 = channel height at outlet
W_3 = spanwise length of computation
X_R = time-averaged reattachment length
x_i = coordinates $(x_1,x_2,x_3)=(x,y,z)$
θ = temperature
λ = thermal conductivity
v = kinematic viscosity
v_{SGS} = SGS eddy viscosity
ρ = density
τ_w = skin friction stress
Ω = enstrophy $=|\omega|^2/2$
ω = vorticity vector

Subscripts

l = lower wall
rms = root mean square
u = upper wall
w = wall
x = x-direction
0 = inlet

Superscripts

$\overline{}$ = time averaged
$'$ = fluctuating
$\hat{}$ = filtering on grid width
$*$ = nondimensional quantity

References

[1] Abbott, D. E., and Kline, S. J., 1962, "Experimental Investigation of Subsonic

Turbulent Flow Over Single and Double Backward Facing Steps," ASME J. Basic Eng., **84**, pp. 317–325.
[2] Durst, F., Melling, A., and Whitelaw, J. H., 1974, "Low Reynolds Number Flow Over a Plane Symmetric Sudden Expansion," J. Fluid Mech., **64**, pp. 111–128.
[3] Smyth, R., 1979, "Turbulent Flow Over a Plane Symmetric Sudden Expansion," ASME J. Fluids Eng., **101**, pp. 348–353.
[4] Durst, F., Pereira, J. C. F., and Tropea, C., 1993, "The Plane Symmetric Sudden Expansion Flow at Low Reynolds Numbers," J. Fluid Mech., **248**, pp. 567–581.
[5] De Zilwa, S. R. N., Khezzar, L., and Whitelaw, J. H., 1997, "Flows Through Plane Sudden-Expansions," Int. J. Numer. Methods Fluids, **32**, pp. 313–329.
[6] Escudier, M. P., Oliveira, P. J., and Poole, R. J., 2002, "Turbulent Flow Through a Plane Sudden Expansion of Modest Aspect Ratio," Phys. Fluids, **14**, pp. 3641–3654.
[7] Macagno, E. O., and Hung, T.-K., 1967, "Pressure, Bernoulli sum, and Momentum and Energy Relations in a Laminar Zone of Separation," Phys. Fluids, **10**, pp. 78–82.
[8] Mitsunaga, S., and Hirose, T., 1976, "A Contribution to the Coanda Effect," Trans. Jpn. Soc. Mech. Eng., **42**, pp. 3899–3905.
[9] Lewis, J. P., and Pletcher, R. H., 1986, "Limitations of the Boundary-Layer Equations for Predicting Laminar Symmetric Sudden Expansion Flows," ASME J. Fluids Eng., **108**, pp. 208–213.
[10] Sobey, I. J., and Drazin, P. G., 1986, "Bifurcations of Two-Dimensional Channel Flows," J. Fluid Mech., **171**, pp. 263–287.
[11] Fearn, R. M., Mullin, T., and Cliffe, K. A., 1990, "Nonlinear Flow Phenomena in a Symmetric Sudden Expansion," J. Fluid Mech., **211**, pp. 595–608.
[12] Nakanishi, S., Sakurai, M., and Osaka, H., 1995, "Numerical Study on Two-Dimensional Symmetric Sudden Expansion Channel Flow (Dynamic Characteristics)," Trans. Jpn. Soc. Mech. Eng., Ser. B, **61**, pp. 84–91.
[13] Alleborn, N., Nandakumar, K., Raszillier, H., and Durst, F., 1997, "Further Contributions on the Two-Dimensional Flow in a Sudden Expansion," J. Fluid Mech., **330**, pp. 169–188.
[14] Drikakis, D., 1997, "Bifurcation Phenomena in Incompressible Sudden Expansion Flows," Phys. Fluids, **9**, pp. 76–87.
[15] Cherdron, W., Durst, F., and Whitelaw, J. H., 1978, "Asymmetric Flows and Instabilities in Symmetric Ducts with Sudden Expansions," J. Fluid Mech., **84**, pp. 13–31.
[16] Schreck, E., and Schäfer, M., 2000, "Numerical Study of Bifurcation in Three-Dimensional Sudden Channel Expansions," Comput. Fluids, **29**, pp. 283–293.
[17] Yoshikawa, H., Yoshikawa, M., Yanaoka, H., and Ota, T., 2004, "Three-Dimensional Simulation of Separated Flow and Heat Transfer in a Rectangular Channel With Sudden Expansion," in Proceedings of the International Symposium Advances in Computational Heat Transfer, CHT-04-162.
[18] Filetti, E. G., and Kays, W. M., 1967, "Heat Transfer in Separated, Reattached, and Redevelopment Regions Behind a Double Step at Entrance to a Flat Duct," ASME J. Heat Transfer, **89**, pp. 163–168.
[19] Seki, N., Fukusako, S., and Hirata, T., 1976, "Turbulent Fluctuations and Heat Transfer for Separated Flow Associated With a Double Step at Entrance to an Enlarged Flat Duct," ASME J. Heat Transfer, **98**, pp. 588–593.
[20] Seki, N., Fukusako, S., and Hirata, T., 1978, "Laminar Heat Transfer Downstream of a Sudden Enlargement of a Duct," Bull. JSME, **21**, pp. 254–257.
[21] Ota, T., Okagawa, Y., Suzuki, T., and Park, S.-K., 2003, "Turbulent Heat Transfer in a Symmetric Expansion Plane Channel," in Proceedings of the 6th ASME-JSME Thermal Engineering Jt. Conference, TED-AJ03-187.
[22] Ota, T., and Toda, Y., 1990, "Prediction of Laminar Heat Transfer and Flow in a Plane Enlarged Channels," Heat Transfer, **6**, pp. 305–311.
[23] Ota, T., and Hata, T., 1992, "Numerical Analysis of Laminar Heat Transfer and Flow in a Plane Enlarged Channel," in Proceedings of the 2nd JSME-KSME Thermal Engineering Jt. Conference, 1, pp. 63–68.
[24] Ota, T., Yanaoka, H., Shibuya, K., Nakajima, M., and Yoshikawa, H., 2000, "Numerical Simulation of Separated Flow and Heat Transfer in a Rectangular Channel with Sudden Expansion," in Proceedings of the ASME FEDSM 2000, FEDSM00-11004.
[25] Ota, T., Yanaoka, H., and Hata, T., 1994, "Numerical Analysis of Laminar Flow and Heat Transfer in a Two-Dimensional Symmetrically Enlarged Channel," Trans. Jpn. Soc. Mech. Eng., Ser. B, **60**, pp. 3930–3936.
[26] Ota, T., 2000, "A Survey of Heat Transfer in Separated and Reattached Flows," Appl. Mech. Rev., **53**, pp. 219–235.
[27] Okamoto, R., and Ota, T., 1996, "Large Eddy Simulation of a Separated and Reattached Flow and Heat Transfer Over a Blunt Flat Plate," in Proceedings of the 3rd KSME-JSME Thermal Engineering Conference, Vol. 1, pp. 43–48.
[28] Labbë, O., Sagaut, P., and Montreuil, E., 2002, "Large-Eddy Simulation of Heat Transfer Over a Backward-Facing Step," Numer. Heat Transfer, Part A, **42**, pp. 73–90.
[29] Van Driest, E. R., 1956, "On Turbulent Flow Near a Wall," J. Aeronaut. Sci., **23**, pp. 1007–1011.
[30] Amsden, A. A., and Harlow, F. H., 1970, "A Simplified MAC Technique for Incompressible Fluid Flow Calculations," J. Comput. Phys., **6**, pp. 322–325.
[31] Smirnov, A., Shi, S., and Celik, I., 2001, "Random Flow Generation Technique for Large Eddy Simulations and Particle Dynamics Modeling," ASME J. Fluids Eng., **123**, pp. 359–371.
[32] Rodi, W., Ferziger, J. H., Breuer, M., and Pourquie, M., 1997, "Status of Large Eddy Simulation: Results of a Workshop," ASME J. Fluids Eng., **119**, pp. 248–262.

Comparative LES and Unsteady RANS Computations for a Periodically-Perturbed Separated Flow Over a Backward-Facing Step

A. Dejoan
e-mail: a.dejoan@imperial.ac.uk

Y.-J. Jang

M. A. Leschziner
e-mail: mike.leschziner@imperial.ac.uk

Department of Aeronautics,
Imperial College London,
London SW7 2AZ, UK.

Large eddy simulation and statistical turbulence closures are used to investigate and contrast the ability of both strategies to represent the effects arising from the unsteady perturbation of a separated backward-facing-step flow caused by a slot jet injected periodically at zero net mass-flow rate into the flow at the step edge, at an angle of 45 deg relative to the flow direction. Experimental data show the effects to depend nonlinearly on the perturbation frequency, the strongest response arising at a Strouhal number of 0.2, which is the condition investigated herein. The principal response is a shortening of the separation bubble by almost 30%, a result that is highly pertinent to active flow control. As the injection frequency lies within the low-frequency range of the large scales of the turbulence spectrum, an issue of particular interest that is addressed herein is the ability of the statistical models, operating within a phase-averaged URANS framework, to reproduce the experimental observations and the response derived from the simulation. [DOI: 10.1115/1.2033012]

1 Introduction

There is general uncertainty about the appropriateness of using RANS methods, as an alternative to LES, for predicting unsteady flows that contain vigorous organized, periodic components. Such flows occur in numerous technological applications: vortex shedding in bluff-body aerodynamics, wake-blade interaction in turbomachinery, Bénard convection in high-Rayleigh-number flows and pulsed jets in active flow control are just a few examples. In flows in which the organized unsteadiness is the result of an inherent instability, experience suggests that the instability mechanism has to be strong and the turbulence model of high fidelity to ensure that the instability is not damped out altogether. For example, vortex shedding in the wake of a cylinder reflects such a strong instability mechanism, and this can be resolved, albeit not well, with RANS methods, if these incorporate either advanced anisotropy-resolving turbulence models or realizable versions of simpler eddy-viscosity models, both of which tend to return significantly lower levels of turbulent transport than standard linear eddy-viscosity models. Flows in which the unsteadiness is introduced by external forcing are less challenging for RANS schemes, at least in the sense that they generally capture the first-order response of the flow to the forcing. However, even then, much uncertainty arises from the potential for interference between turbulence-related unsteadiness and the perturbing component. The strength of such interference is likely to be governed by the proximity of the time scales of the organized perturbation and the large-scale turbulent motion. Thus, the interaction is likely to be significant if the perturbation time scale is of the order of that associated with turbulence-generation mechanisms, as is so in the present case, or of the time scale of any influential process within other parts of the spectrum of turbulent motion. In such circumstance, in which scale-separation is lost, the use of RANS models is suspect, at best, quite apart from the fact that it is incompatible with the basic principles of Reynolds-averaging. This is the case, for example, in active aerodynamic-flow control with high-frequency "zero-mass-flux" pulsed jets.

The above issues are at the center of the present study, in which an external unsteady perturbation is introduced to control the characteristics of a separated flow. The flow under consideration is shown in Fig. 1. Separation is provoked by a backward-facing step in a plane channel, at an expansion ratio of 1.5. The flow is perturbed by a slot jet at the step edge, extending over the entire spanwise width of the channel. Fluid is injected and extracted in a continuous sinusoidal cycle, such that the time-integrated injection flow rate is zero. The most explicit response of the flow to the perturbation has been observed experimentally by Chun and Sung [1] and Yoshioka et al. [2] to be a significant reduction in the time-averaged length of the recirculation zone. This reduction was found to depend sensitively on the injection frequency, however, with a distinct peak reduction of 30% arising at a Strouhal number, based on step height, of 0.2. This observation of a strong frequency dependence suggests that the reduction in separation is not simply due to a direct enhancement of momentum exchange by periodic "flapping" in the flow, but is also linked to a coupling mechanism between the injection and structural features in the separated shear layer above the recirculation zone. Two pertinent interaction mechanisms have been identified as the "shear-layer instability" and the "shedding-type instability," and these have been discussed by Sigurdson [3], Kiya et al. [4], and Hasan [5]. The former, related to formation of vortices in early parts of the shear layer, is close to the present injection frequency, while the latter, associated with large-scale structures evolving further downstream, is lower by a factor of almost 3.

The present paper reports LES as well as RANS computations for the configuration examined experimentally with PIV by Yoshioka et al. [6]. The Reynolds number, based on maximum inlet-channel velocity, U_c, and step height h, is $R_e = U_c h/\nu = 3700$. The jet is injected at 45 deg through a 1 mm slot with a velocity $V_j = 0.3U_c \sin(2\pi f_e t)$, where U_c is the maximum velocity of the fully-developed flow in the channel upstream of the step.

Contributed by the Fluids Engineering Division for publication in the JOURNAL OF FLUIDS ENGINEERING. Manuscript received by the Fluids Engineering Division, July 22, 2004; Final revision: March 16, 2005. Associate Editor: Ismail B. Celik.

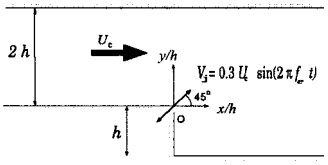

Fig. 1 The flow configuration

Simulations were performed for the unperturbed and perturbed flow, the latter at the Strouhal number $St=f_e h/U_c=0.2$ and the former in order to establish the reference state against which to contrast the effects of the perturbation. The purpose of undertaking the LES computations, against the background of the experimental data, was twofold. First, as the RANS computations presume statistical two-dimensionality, it was necessary to obtain the best possible computational representation of the real flow, but subject to freedom from 3D contamination that is inevitable even at an upstream channel aspect ratio of 12 used in the experiment. Such a contamination was avoided in the LES computations by imposing spanwise periodicity. Second, the LES provided much more detailed data than the experiments, allowing a wider range of fundamental issues to be more readily examined. In what follows, equal weight is given to the physical insight derived from the LES and to the level of predictive realism derived from the RANS computations, relative to the experiments and the LES solution.

2 The Simulations

The computational domain extended from 4 step heights upstream of the step to 12 step heights downstream. The spanwise direction was treated as statistically homogeneous, with periodic conditions prescribed at the spanwise boundaries of the computational box having a depth of $4\pi h/3$. Figure 2 shows, for the unperturbed simulation, distributions of the autocorrelation coefficient R_{uu} along several spanwise lines at different streamwise locations within the separated shear layer. As can be seen, the spanwise box is sufficient to ensure spanwise decorrelation. The inlet conditions were generated by a precursor simulation for a fully-developed channel flow in a periodic domain of length 4 times the channel height. The conditions were then prescribed at the upstream-channel inlet, 4 step heights upstream of the step, by feeding in realizations of the cross-sectional conditions from a data file, subject to the Taylor hypothesis. The profiles of the normal Reynolds stresses, obtained at the step location, $x/h=0$, with two grids differing in resolution by half an order of magnitude in terms of the number of cells, are given in Fig. 6 and commented upon below within a discussion on grid sensitivity. At the outlet, the convective condition

$$\frac{\partial U_i}{\partial t} + \bar{U}\frac{\partial U_i}{\partial x} = 0 \tag{1}$$

was imposed, where $\bar{U}$ is the average outlet velocity.

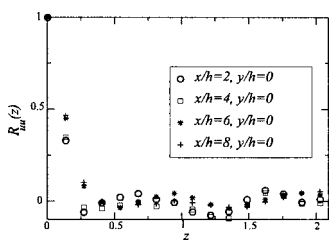

Fig. 2 Autocorrelation coefficient of the streamwise velocity fluctuations in the spanwise direction at different locations *x/h*, from the LES of the unperturbed flow

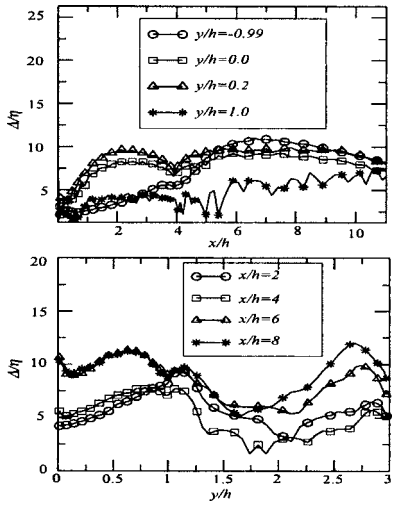

Fig. 3 Ratio of the Kolmogorov length scale to the grid length scale, from the LES of the unperturbed flow

The computational method used is a general multiblock finite-volume scheme with nonorthogonal-mesh capabilities (Lardat and Leschziner [7]). In the present case, a two-block rectilinear-mesh system was used, with one block covering the upstream channel and the other the downstream channel. The finite-volume scheme is second-order accurate in space, based on central differencing for advection and diffusion. Time-marching is effected by a fractional-step method, with the time derivative being discretized by a second-order backward-biased approximation. The flux terms are advanced explicitly with the Adams-Bashforth method. The pressure is computed as a solution to the pressure-Poisson problem by means of a partial-diagonalization technique in the spanwise direction and a V-cycle multigrid algorithm operating in conjunction with a successive-line over-relaxation scheme. The code is fully parallelized and was run on a multi-processor Cray T3E computer.

The results presented herein were obtained with a mesh of $96\times80\times32$ cells covering the domain downstream of the step, while the inlet channel was covered by a separate mesh having $96\times40\times32$ cells. The total number of cells was thus around 4×10^5. An especially fine grid was used in the step and injection region. The *maximum* distance $y^+=yu_\tau/\nu$ (where u_τ is the friction velocity) of the wall-nearest computational nodes was 1.5, at both the lower and upper walls, and the cell-aspect ratios were, typically, $\Delta y^+/\Delta x^+/\Delta z^+=1.5/28/20$ at the wall and 4.5/28/20 in the shear layer. The expansion ratio of the grid did not exceed 1.05. This grid was the outcome of extensive precursor testing. The maximum value of the CFL number was limited to 0.2. Among a number of aspects considered as parts of the grid-density study was the level of the Kolmogorov length, $\eta=(\nu^3/\varepsilon)^{1/4}$, relative to $\Delta=(\Delta x\Delta y\Delta z)^{1/3}$. To determine this ratio, plotted in Fig. 3 for the unperturbed case along several streamwise and cross-flow lines, the dissipation rate was obtained from the turbulence-energy budget. As seen, the ratio is lower than 10 everywhere. Hence, the cut-off lies close to the dissipative part of the wave-number range. As demonstrated by Fig. 4, showing frequency spectra for the streamwise normal Reynolds stress at two locations downstream of the step for the unperturbed flow, the simulation resolved scales which span 2.5 decades. The spectrum at $x/h=3$ shows, furthermore, that the jet-injection frequency, St=0.2, is well within the part of the spectrum associated with turbulence generation via large-scale structures in the shear layer. Thus, scale separation is not satisfied in this flow. The peaks identified in the spectra at St=0.2 and 0.077 are those associated, respectively, with the instability mode of the shear layer and with a more global flapping

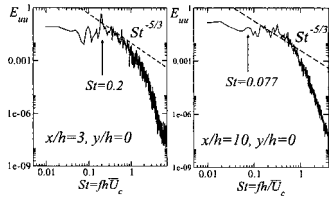

Fig. 4 Energy spectra of the streamwise velocity fluctuation, from the LES of the unperturbed flow

mode, referred to as "shedding-type instability." As the spectra are for the unperturbed flow, the former peak is obviously *not* caused by the periodic jet, but is associated with the natural initial roll-up process of the shear layer giving rise to vortical structures that emerge from the step, develop and convect downstream. The lower-frequency peak at St=0.077 is directly related to the large-scale structures of the shear layer, which impinge on the wall, reflecting an interaction between the entire shear layer and the wall.

In the case of the unperturbed flow, a finer grid, comprising of 2×10^6 nodes, was also used as part of the grid-dependence studies. Profiles of the streamwise velocity and of the streamwise normal stress, at a location roughly midway along the recirculation zone are given in Fig. 5. Respective profiles are seen to differ only slightly, an observation supporting earlier statements. Moreover, both simulations of the unperturbed flow gave virtually identical time-averaged reattachment points, $x_r/h=7.$, suggesting that the slight under-prediction of the turbulence intensity at the step location, caused by the coarser grid and shown in Fig. 6, is not influential.

Subgrid-scale processes were represented by means of either the Smagorinsky model (with van-Driest damping) or the WALE model (Ducros et al. [8]). Much as expected, in view of the above considerations on the choice of grid, there were insignificant differences between the statistical properties of the solutions, including second-moment distributions. The perturbed-flow simulation was started with a full 3D realization of the unperturbed case used

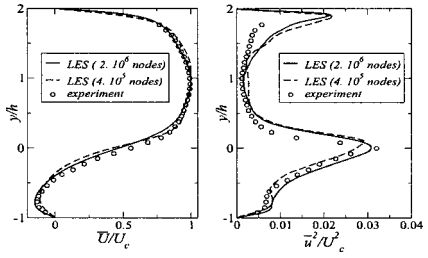

Fig. 5 Velocity and streamwise normal-stress profiles, from the LES of the unperturbed flow performed with two grid resolutions

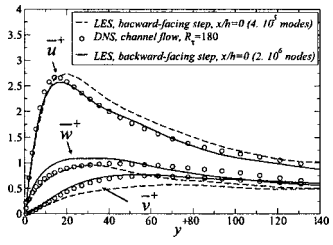

Fig. 6 Profiles of normal-stress components above the step corner, from the LES of the unperturbed flow performed with two grid resolutions. Comparison with Moser et al.'s DNS data [16] (R_τ=180, i.e., R_e=3250).

as the initial state. Following injection, the flow was then allowed to evolve towards a "periodic" state within 15 injection periods, corresponding to $TU_c/h=79$.

3 The RANS Computations

Computations are included herein for two models: the linear eddy-viscosity model of Launder and Sharma [9] and the quadratic eddy-viscosity model of Abe et al. [10] (strictly, an explicit algebraic Reynolds-stress model), both being low-Reynolds-number models permitting integration to the wall. These are two of several models examined, and they have been selected here as representatives of their respective categories. The Launder-Sharma model is widely used and needs no further elaboration. The quadratic low-*Re* model of Abe et al. (AJL-ε), although sharing some basic features with other nonlinear eddy-viscosity models, differs from them in its ability to return the correct rate of decay of the Reynolds stresses towards the state of two-component turbulence at the wall that is observed in DNS. This decay cannot be represented solely by the use of terms combining the strain and vorticity, and there is a need to introduce a tensorially consistent term that takes into account the wall orientation. In the model variant used here, the wall-direction indicator is $d_i=N_i/\sqrt{N_kN_k}$, where $N_i=\partial l_d/\partial x_i$, $l_d=y_n$(=wall distance), which is then used in the wall-anisotropy correction,

$$^{w}a_{ij}=-f_w\left(d_id_j-\frac{\delta_{ij}}{3}d_kd_k\right)\times f(S_{ik}S_{kj},S_{ik}\Omega_{kj},S_{kj}\Omega_{ik},S^2,\Omega^2), \tag{2}$$

where f_w is a viscosity-related damping function, $S_{ij}=(\partial\bar{U}_i/\partial x_j+\partial\bar{U}_j/\partial x_i)/2$, is the strain-rate tensor and $\Omega_{ij}=(\partial\bar{U}_i/\partial x_j-\partial\bar{U}_j/\partial x_i)/2$, is the vorticity tensor. Alternative wall-orientation indicators that are independent of wall distance may readily be adopted. In the above damping function, a composite time scale is used, which combines the macroscale k/ε with the Kolmogorov scale $\sqrt{\nu/\varepsilon}$. The damping function f_w then provides a smooth transition between the two scales across the near-wall layer. There are two versions of the model, one using an equation for the specific dissipation, ω, and the other for the conventional dissipation rate, ε. Here, the latter form has been adopted. This model has been found by Jang et al. [11] to perform especially well in a study directed towards predicting separation from the curved surface of a hill-shaped constriction in a channel. The RANS computations were performed with a nonorthogonal, collocated, cell-centered finite-volume approach implemented in the code STREAM (Lien and Leschziner [12], Apsley and Leschziner [13]). Convection of both mean-flow and turbulence quantities is approximated by the UMIST scheme (Lien and Leschziner [14])—a second-order TVD approximation of the QUICK scheme. Mass conservation is enforced indirectly by way of a pressure-correction algorithm. Within this scheme, the transport and the pressure-correction equations are solved sequentially and iterated to convergence. As in the case of the simulation, a two-block mesh was also used in the RANS computations, one covering the upstream channel to a distance of 4 step heights upstream of the step and the other the downstream channel of length 28 step heights. The meshes covering the two subdomains contained 80 $\times$64 and 121$\times$128 nodes, respectively, with 13 nodes covering the injection slot ahead of the step. The maximum CFL number dictating the time step was limited to 0.5. This choice was based on extensive grid- and time-step-dependence tests performed in a precursor study with linear eddy-viscosity models. Inlet conditions, at 4 step heights upstream of the step, were taken from the precursor channel-flow simulation, also used to prescribe the inlet conditions for the LES computation.

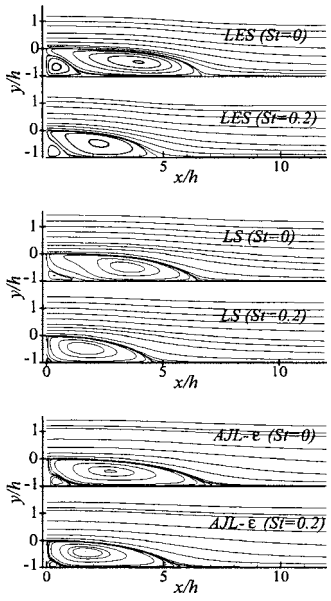

Fig. 7 Time-averaged streamfunction contours; unperturbed and perturbed flows

4 Results

4.1 Time-Mean Behavior. The effects of the perturbations on the mean flow are conveyed in Fig. 7–9 and Table 1. In line with the experimental observation, the reattachment length derived from the LES has been found to be substantially reduced by the perturbation. The predicted value is $x_r/h=5.2$, relative to 7.0 for the unperturbed case. Thus, the predicted reduction is 26%, a level that agrees well with the experimental finding of 30%. Both reattachment lengths are larger than those measured, however, most probably reflecting 3D contamination in the experiment due to spanwise confinement. Figure 7 shows that the global response returned by the RANS models is similar to that produced by the simulation. While the computed solutions differ from each other and from the simulation in detail, both models predict a reduction of order 20%–30% in the size of the recirculation zone. The linear Launder-Sharma (LS) model underestimates the reattachment distance and virtually fails to resolve the secondary corner recirculation bubble, especially in the perturbed flow. In contrast, the nonlinear Abe et al. (AJL-ε) model gives an excessive reattachment length, largely as a result of an especially low rate of recovery as reattachment is approached (note the acute angle of the zero streamfunction contour at the lower wall). However, this model returns a better representation of the secondary corner eddy. Figure 8, comparing the mean skin-friction distributions for the perturbed and unperturbed flows, reinforces the significant reduction in separation brought about by the perturbation, as already noted by reference to Fig. 7. However, the maximum and minimum levels of skin friction are unaffected by the perturbation. The two

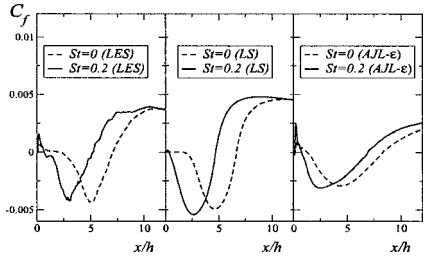

Fig. 8 Skin-friction coefficient at the bottom wall downstream of the step; unperturbed and perturbed flows

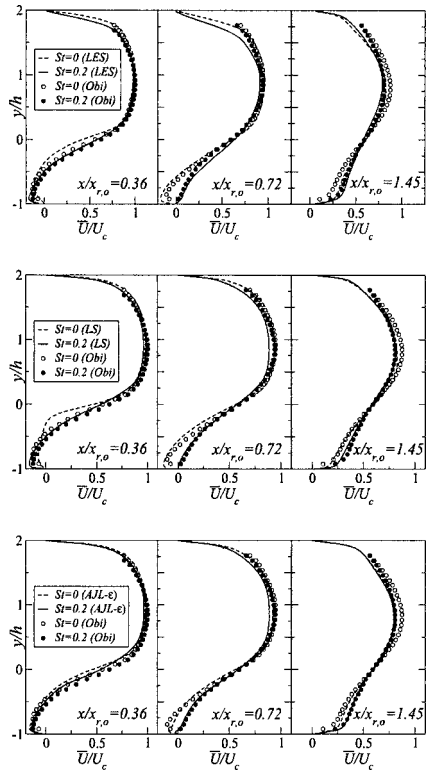

Fig. 9 Time-averaged streamwise-velocity profiles; unperturbed and perturbed flows

models predict friction-factor distributions which lie on either side of those produced by the LES, the AJL-ε model giving substantially lower levels, which are indicative of correspondingly lower turbulence activity in the near-wall region. Figure 9 compares computed velocity profiles to experimental data at three specific locations normalized by the reattachment distance of the unperturbed flow, $x/x_{r,o}$. The objective of this normalization is to bring out more clearly the consequences of the perturbation relative to the unperturbed state. Agreement between the LES solution and the experiment is close, and the same applies to the AJL-ε model. The profiles of the LS model reveal a defect which becomes even clearer upon reference to the shear-stress distributions considered later. Thus, at $x/x_{r,o}=0.36$, the shear strain of the unperturbed flow is seen to be much too high, suggesting a grossly insufficient level of turbulent mixing. The perturbation produces a substantial increase in mixing due to the combination of dispersion by the unsteadiness itself and the elevation of turbulence generation it causes, with the effect being disproportionately high in the case of the LS model. Consistent with the above changes to the mean flow, Fig. 10 shows the perturbation to result in a significant increase in the shear stress, especially within the separated shear layer and the recirculation zone below it. It is this elevation and its effect on entrainment into the shear layer that are the causes of the shortening in the recirculation length. The simulation is seen to reproduce the measured shear stress very well. Both RANS models perform less well, but nevertheless give a credible representa-

Table 1 Reattachment length for the unperturbed flow, $x_{r,o}$ and the perturbed flow, x_r

St	Obi *et al.*	LES	LS	AJL
0.0	$x_{r,o}=5.2h$	$x_{r,o}=7h$	$x_{r,o}=6.5h$	$x_{r,o}=8h$
0.2	$x_{r,o}=3.8h$	$x_r=5.5h$	$x_r=4.6h$	$x_r=6.5h$

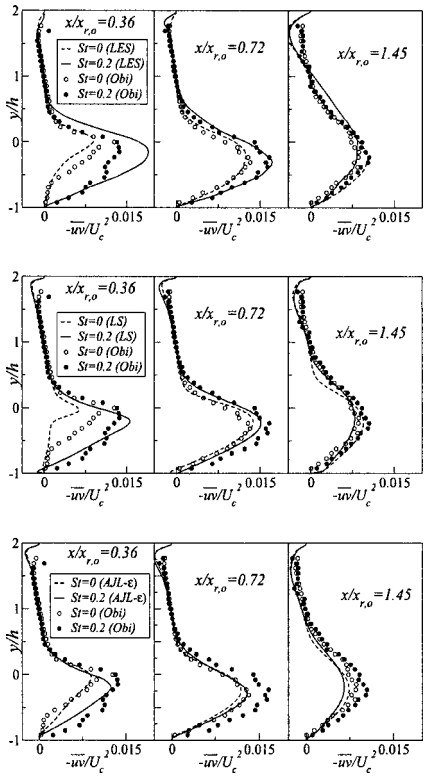

Fig. 10 Time-averaged profiles of the Reynolds shear stress; unperturbed and perturbed flows

tion. However, both models substantially underestimate the sensitivity of the stress to the perturbations beyond the initial upstream portion of the separated shear layer and recirculation zone, indicating that the models do not resolve faithfully the dynamics in the shear layer induced by the perturbation. In relation to the LS model, it is noted that the shear stress at $x/x_{r,o}=0.36$ is much too low in the unperturbed flow, and this is the cause for the excessive shear strain seen in Fig. 9. Downstream of the reattachment point, at the location $x/x_{r,o}=1.45$, the LES as well as the turbulence models exhibit lower shear stress in the perturbed flow than the unperturbed flow, a behavior that is contrary to the experiment. However, reference to Fig. 9 shows that, for both the computations and the experiment, the shear strain in the near-wall region of the perturbed flow at $x/x_{r,o}=1.45$ is significantly lower than that of the unperturbed one. Hence, the expectation is that the shear stress should also be lower. This is indeed so for the simulation, but not the experiment. In terms of turbulence field, the recovery of the perturbed flow is predicted to progress at a higher rate than that measured. It is relevant to add here that Chun and Sung [1] observed in their experiments a faster postreattachment recovery in the forced flow, relative to the equivalent unforced configuration, a behavior in accord with the present predictions.

In the case of an unsteady RANS computation, it is trivial to determine the relative contributions of the modeled and resolved stresses to the total level. In the present case of a periodic flow, the modeled stress is the phase-averaged component, while the resolved contribution is that associated with the unsteady motion captured by the computation. The relative importance of the components is indicated in Fig. 11, which contains profiles of the modeled and resolved shear stresses for the AJL-ε model at $x/x_{r,o}=0.36$. At this location, the resolved contribution is observed to be substantially larger than at other locations for which results are not included. Yet, even close to the injection point, the contribution is relatively small, and the conclusion is thus that the elevation of the shear stress shown in Fig. 10 is primarily a result of the additional unsteady strain enhancing stress production, rather

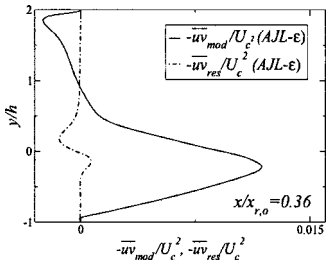

Fig. 11 Time-averaged modeled and resolved Reynolds shear stress at the location $x/h=0.36$; perturbed flow, (AJL-ε) model

than due to the direct contribution arising from time-averaging the unsteady (phase-averaged) motion resolved by the URANS method.

4.2 Phase-Averaged Behavior. A view of the dynamic effects of the perturbation is given by Fig. 12, which shows the evolution of phase-averaged structures within the recirculation zone in terms of stream function contours. Corresponding plots for the turbulence energy and its rate of generation are entirely consistent with the streamfunction plots and are not included because of space constraints. For each computation, four plots are included, each separated by a quarter of a jet-injection period from its neighbor plots. All computations indicate the presence of

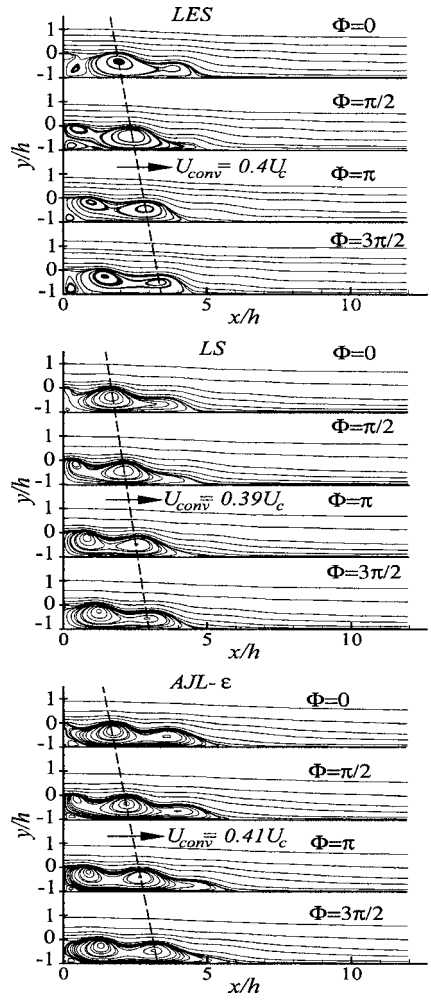

Fig. 12 Phase-averaged streamlines contours at the phase angles $\Phi=0$, $\pi/2$, π, $3\pi/2$; perturbed flow

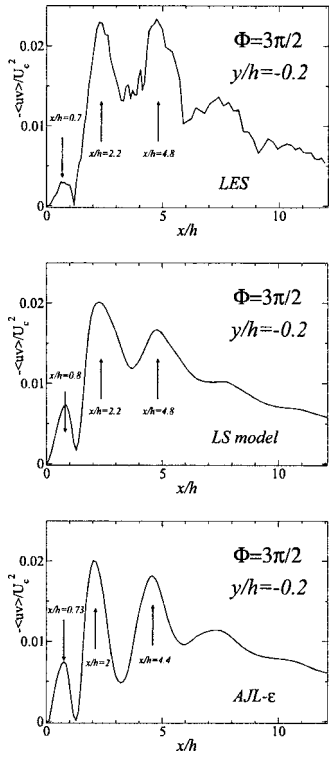

Fig. 13 Phase-averaged Reynolds shear stress along the streamwise direction at the locations $y/h=-0.2$, perturbed flow

large-scale vortical features induced by the periodic perturbations. These may be loosely described as reflecting a "flapping motion." Although, in reality, the perturbation is likely to modify the structural features in the shear layer—for example, through an enhancement of the shear-layer instability and the rate of growth of structures that are associated with the shedding-type instability—it seems that the primary response of the flow to the perturbation is not linked to this type of structural modification. Rather, the large-scale vortical structures are formed at the perturbation frequency. These propagate below the shear layer towards the reattachment point, beyond which they manifest themselves as wavy undulations. The dashed lines in Fig. 12 indicate the speed with which the structures propagate downstream, and it is evident that all computations give a result close to $0.4U_c$. Figure 13 gives the variation of the phase-averaged Reynolds shear stress along the streamwise direction in the shear layer at the distance $y/h=-0.2$ and at the phase $\Phi=3\pi/2$, obtained from both the LES and the two turbulence closures. When compared to the phase-averaged streamlines at the same phase angle (Fig. 12), the distribution of the Reynolds shear stress is observed to be strongly correlated with the large vortical structures forming in the recirculation zone. The maxima of shear stress coincide with regions lying between vortices, while minima are in line with vortex centers. The peaks of shear stress are a consequence of the high strain between vortices and are directly related to the increase in the time-mean shear stress induced by the perturbation and shown earlier in Fig. 10. The variations of the shear stress at $\Phi=0, \pi/2$ and π are similar to that at $\Phi=3\pi/2$ and are not presented here. The strain-induced enhancement described above has also been observed in the experiment. The results thus suggest that the primary cause for the reduction in the size of the separation zone is the same in both the simulation and the RANS computations, and is largely divorced from the instability modes discussed earlier. What is not clear at this stage, however, is whether the RANS models return correctly the degree of sensitivity of the flow to the perturbation frequency. Reproducing the nonlinearity of this sensitivity may well depend on the ability of the calculation to resolve the interaction between the perturbation and the instability modes inherent in the unperturbed flow.

5 Conclusions

The results presented here show that, for the perturbation frequency considered, the turbulence models reproduce well the gross effects of the perturbation, as observed in the experiment and derived from the simulation. This is somewhat surprising in view of the absence of a clear separation between the time scales of the perturbation and the low-frequency portion of the turbulence spectrum. The broadly favorable performance of the RANS models is due to the fact that the principal effect of the periodic disturbance is to cause unsteady variations in the strain field, which then give rise to an increase in the turbulence-production levels. An analysis of the LES results (Dejoan and Leschziner [15]) suggests that one effect of the perturbation is to alter the structure of the vortex evolution in the separated shear layer. This mechanism cannot be reproduced by the RANS models, but it seems that it is of subordinate importance in terms of the primary effect of the instability. More important is the generation of the large-scale vortical structures under the separated shear layer, associated with "flapping," these are reproduced well by the RANS calculations.

Of the two models examined, the nonlinear model of Abe et al. performs substantially better in the unperturbed case, in so far as it gives a superior representation of the separated shear layer and the recirculation zone. Both models underestimate the significant elevation of the shear stress beyond about one half of the axial extent of the recirculation zone, suggesting a deficiency in the detailed representation of the dynamic mechanisms induced by the perturbation.

Acknowledgments

The authors are grateful for the financial support provided by the UK Engineering and Physical Sciences Research Council (EPSRC) and by BAE Systems. The simulations were performed on the Cray T3E computer of the national CSAR service at the University of Manchester with an allocation provided to the authors by EPSRC.

References

[1] Chun, K. B., and Sung, H. J., 1996, "Control of Turbulent Separated Flow Over a Backward-Facing Step by Local Forcing," Exp. Fluids, **21**, pp. 417–426.
[2] Yoshioka, S., Obi, S., and Masuda, S., 2001, "Turbulence Statistics of Periodically Perturbed Separated Flow Over a Backward-Facing Step," Int. J. Heat Fluid Flow, **22**, pp. 393–401.
[3] Sigurdson, L. W., 1995, "The Structure and Control of a Turbulent Reattaching Flow," J. Fluid Mech., **298**, pp. 139–165.
[4] Kiya M., Shimizu, M., and Mochizuki, O., 1997, "Sinusoidal Forcing of a Turbulent Separation Bubble," J. Fluid Mech., **342**, pp. 119–139.
[5] Hasan, M. A. Z., 1992, "The Flow Over a Backward-Facing Step Under Controlled Perturbation: Laminar Separation," J. Fluid Mech., **238**, pp. 73–96.
[6] Yoshioka, S., Obi, S. and Masuda, S., 2001, "Organized Vortex Motion in Periodically Perturbed Turbulent Separated Flow Over a Backward-Facing Step," Int. J. Heat Fluid Flow, **22**, pp. 301–307.
[7] Lardat, R., and Leschziner, M. A., 1998, "A Navier-Stokes Solver for LES on Parallel Computers," Technical Report, Department Mechanical Engineering, UMIST.
[8] Ducros, F., Nicoud, F., and Poinsot, T., 1998, "Wall-Adapting Local Eddy-Viscosity Models for Simulation in Complex Geometries," *6th ICFD Conference on Numerical Methods for Fluid Dynamics*, pp. 293–299.
[9] Launder, B. E. and Sharma, B. I., 1974, "Application of the Energy-Dissipation Model of Turbulence to the Calculation of Flow Near a Spinning Disc," Lett. Heat Mass Transfer, **1**, pp. 131–138.
[10] Abe, K., Jang, Y. J., and Leschziner, M. A., 2003, "An Investigation of Wall-

Anisotropy Expressions and Length-Scale Equations for Non-Linear Eddy-Viscosity Models," Int. J. Heat Fluid Flow, **24**, pp. 181–198.
[11] Jang, Y. J., Leschziner, M. A., Abe, K., and Temmerman, L., 2002, "Investigation of Anisotropy-Resolving Turbulence Models by Reference to Highly-Resolved les Data for Separated Flow," Flow, Turbul. Combust., **69**, pp. 161–203.
[12] Lien, F. S., and Leschziner, M. A., 1994, "A General Non-Orthogonal Collocated Finite Volume Algorithm for Turbulent Flow at all Speeds Incorporating Second-Moment Turbulence-Transport Closure, Part I: Computational Implementation," Comput. Methods Appl. Mech. Eng., **114**, pp. 123–148.
[13] Apsley, D. D., and Leschziner, M. A., 2000, "Advanced Turbulence Modelling of Separated Flow in a Diffuser," Flow, Turbul. Combust., **63**, pp. 81–112.
[14] Lien, F. S., and Leschziner, M. A., 1994, "Upstream Monotonic Interpolation for Scalar Transport With Application to Complex Turbulent Flows", Int. J. Numer. Methods Fluids, **19**, pp. 527–548.
[15] Dejoan, A., and Leschziner, M. A., 2004, "Large Eddy Simulation of Periodically Perturbed Separated Flow Over a Backward-Facing Step," Int. J. Heat Fluid Flow, **25**, pp. 581–592.
[16] Moser, R. D., Kim, J., and Mansour, N. N., 1999, "Direct Simulation of Turbulent Channel Flow up to R_e=590," Phys. Fluids, **11**, pp. 943–945.

A Periodically Perturbed Backward-Facing Step Flow by Means of LES, DES and T-RANS: An Example of Flow Separation Control

S. Šarić

S. Jakirlić

C. Tropea

Chair of Fluid Mechanics and Aerodynamics,
Darmstadt University of Technology,
Petersenstrasse 30, D-64287 Darmstadt,
Germany

*Turbulent flow over a backward-facing step, perturbed periodically by alternative blowing/suction through a thin slit (*0.05 H *width) situated at the step edge, was studied computationally using (LES) large eddy simulation, (DES) detached eddy simulation, and (T-RANS) transient Reynolds-averaged Navier–Stokes techniques. The flow configuration considered* ($Re_H = U_c H/\nu = 3700$) *has been investigated experimentally by Yoshioka et al. [1,2]. The periodic blowing/suction with zero net mass flux is governed by a sinusoidal law:* $v_e = 0.3 U_c \sin(2\pi f_e t)$, U_c *being the centerline velocity in the inlet channel. Perturbation frequencies* f_e *corresponding to the Strouhal numbers* $St = 0.08$, *0.19, and 0.30 were investigated* ($St = f_e H/U_c$). *The experimental observation that the perturbation frequency* $St = 0.19$ *represents the most effective case, that is the case with the minimum reattachment length, was confirmed by all computational methods. However, the closest agreement with experiment (the reattachment length reduction of 28.3% compared to the unperturbed case) was obtained with LES (24.5%) and DES (35%), whereas the T-RANS computations showed a weaker sensitivity to the perturbation: 5.9% when using the Spalart–Allmaras model and 12.9% using the* $k-\omega$ *SST model.*
[DOI: 10.1115/1.2012502]

Introduction

Active flow separation control is of great concern in numerous engineering applications. The phenomena of flow separation and reattachment are accompanied by large energy losses, influencing the performance of fluid machinery and imposing severe limitations on the operation and the design of many fluid flow devices. Recent studies have shown that periodic perturbation can delay separation (e.g., Seifert and Pack, [3,4] studied flow configurations at high Reynolds numbers relevant to aircraft aerodynamics: flow over an airfoil and flow over an upper-airfoil-surface-mounted hump) and provide reattachment control (flow over a backward-facing step: Chun and Sung [5]; Jin et al. [6]; Yoshioka et al. [1,2]) more effectively then steady blowing or suction.

The backward-facing step flow is a well-known test case for studying the influence of local streamline curvature. The flow separates at the step edge, forming a curved shear layer which bifurcates at the reattachment region; one branch flowing back creates a separation bubble behind the step, another branch creates a new boundary layer downstream. The level of turbulence in the separated shear layer aligned with the mean dividing streamline bordering the separation bubble is of decisive importance when controlling the reattachment length. A higher level of the shear stress implies an enhancement of the fluid entrainment into the shear layer—higher momentum transport—and consequently a shortening of the recirculation bubble (see, e.g., Fig. 13 for illustration). In addition to the strong mean flow gradient in the vertical direction, representing the main source of turbulence production, and a curvature-generated turbulence production, the turbulence can be further generated by introducing a high-velocity jet into the shear layer. The flow perturbation created in such a way causes an intensive flow stretching (mean flow deformation enhancement, especially with respect to the axial velocity component) leading consequently to an enhanced turbulence level (see, e.g., Yoshioka et al. [1,2], for experimental evidence). The backward-facing step flow configuration considered here (Fig. 1; $\mathrm{Re}_H = U_c H/\nu = 3700$) has been investigated experimentally by Yoshioka et al. [1,2]. The injection velocity is parameterized by a sinusoidal law: $v_e = V_e \sin\phi$, V_e being the velocity amplitude ($V_e = 0.3 U_c$) and ϕ the phase angle. Perturbation frequencies, f_e ($\phi = 2\pi f_e t$), corresponding to the Strouhal numbers $St = 0.08$, 0.19, and 0.30 were investigated ($St = f_e H/U_c$, U_c being the centerline velocity in the inlet channel). It was found experimentally that the perturbation frequency $St = 0.19$ yields the minimum mean reattachment length.

The purpose of the present work was the computational study of the effects of local perturbation on the mean flow and turbulence using various methods for unsteady flow computations: large eddy simulation (LES), detached eddy simulation (DES), and transient Reynolds-averaged Navier–Stokes (T-RANS) aiming also at mutual comparison of their features and performance in such a complex flow situation.

Numerical Method

All computations were performed with an in-house computer code FASTEST based on a finite volume numerical method for solving both three-dimensional filtered and Reynolds-averaged Navier–Stokes equations on block structured, body fitted, nonorthogonal meshes. Block interfaces are treated in a conservative manner, consistent with the treatment of inner cell faces. A cell centered (collocated) variable arrangement and Cartesian vector and tensor components are used. The well-known SIMPLE algorithm was applied for coupling the velocity and pressure fields.

Contributed by the Fluids Engineering Division for publication in the JOURNAL OF FLUIDS ENGINEERING. Manuscript received by the Fluids Engineering Division July 23, 2004; final revision: July 7, 2005. Associate Editor: Ismail B. Celik.

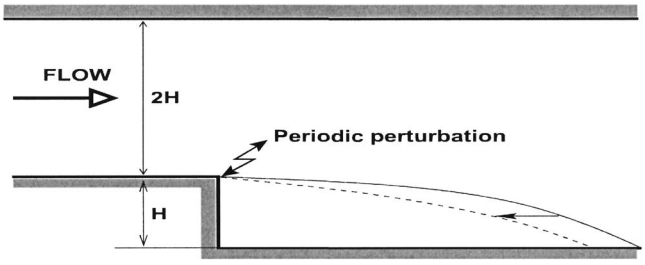

Fig. 1 Schematic of the flow configuration considered

The convective transport of all variables was discretized by a second-order central differencing scheme, whose stability was enhanced through the so-called deferred correction approach (see e.g., Khosla and Rubin [7]). Time discretization was accomplished by applying the second order (implicit) Crank–Nicolson method.

T-RANS. T-RANS computations were performed using the one-equation model by Spalart and Allmaras (SA, [8]) and the $k-\omega$ SST model (Menter, [9]), the two most popular statistical turbulence models in aerodynamics. Additional results were available from the Ninth ERCOFTAC workshop on refined turbulence modeling (Jakirlic et al., [10]), where this experimental configuration served as one of the test cases. These additional results were obtained by employing several algebraic and differential Reynolds-stress models including also a two-scale Reynolds-stress model due to Stawiarski and Hanjalic [11]. The workshop results exhibited a certain scatter and are probably not suitable for very detailed comparison. But generally speaking, all turbulence models have exhibited a weaker sensitivity to the perturbation compared to the experimental results. The reduction of the reattachment length was predicted in all T-RANS computations; however, compared to the reference case without perturbation, the magnitude of the reduction was far below that observed in the experiment. Hence, it was challenging to compute the flow considered by LES and DES, the CFD techniques which are expected to reproduce unsteady flows better than statistical turbulence models. In particular, it was interesting to see how the same model (SA) performed in two different computational frameworks: RANS and DES.

LES. The three-dimensional, incompressible unsteady Navier–Stokes equations, upon filtering read:

$$\frac{\partial \bar{U}_i}{\partial x_i} = 0, \tag{1}$$

$$\frac{\partial \bar{U}_i}{\partial t} + \frac{\partial (\bar{U}_i \bar{U}_j)}{\partial x_j} = -\frac{1}{\rho}\frac{\partial \bar{P}}{\partial x_i} + \frac{\partial}{\partial x_j}\left(\nu \frac{\partial \bar{U}_i}{\partial x_j} - \tau_{ij}\right), \tag{2}$$

where the filter width is determined implicitly by a mesh size: $\Delta = (\Delta x \Delta y \Delta z)^{1/3}$. The subgrid scale tensor τ_{ij} was approximated by employing the Boussinesq's formulation based on the SGS turbulent viscosity, which was modeled using the Smagorinsky formulation:

$$\nu_t = (C_s \Delta)^2 |\bar{S}_{ij}|. \tag{3}$$

The majority of the computations were performed with the Smagorinsky constant C_s set to 0.065, without damping in the near-wall region. Some additional simulations of the channel flow using different settings ($C_s = 0.1$ with and without inclusion of the standard Van Driest damping of the Smagorinsky coefficient) have shown a small influence of both the C_s value and the damping. This might be due to a very low flow Reynolds number corresponding to $\mathrm{Re}_\tau \approx 190$.

DES. A one-equation turbulence model by Spalart and Allmaras (SA, [8]), based on the transport equation for turbulence viscosity, was employed to model the influence of the smallest, unresolved scales on the resolved ones in the framework of the DES computational scheme (e.g., Spalart et al., [12]; Travin et al., [13]). The SA-RANS model determines the modified turbulent viscosity ($\tilde{\nu}$) from the corresponding transport equation, whose destruction term is modeled in terms of the distance to the nearest wall d:

$$\frac{D\tilde{\nu}}{Dt} = C_{b1}\tilde{S}\tilde{\nu} + \frac{1}{\sigma_{\tilde{\nu}}}\left[\frac{\partial}{\partial x_j}\left((\nu + \tilde{\nu})\frac{\partial \tilde{\nu}}{\partial x_j}\right)\right] + \frac{C_{b2}}{\sigma_{\tilde{\nu}}}\left(\frac{\partial \tilde{\nu}}{\partial x_j}\right)^2 - C_{w1} f_w \frac{\tilde{\nu}}{d^2}. \tag{4}$$

The DES formulation is obtained by replacing the wall distance by $\tilde{d}$, where $\tilde{d}$ is defined as

$$\tilde{d} = \min(d, C_{\mathrm{DES}} \Delta_{\mathrm{DES}}), \tag{5}$$

where a somewhat modified length scale ("a DES filter") valid in the "LES part" of the flow field is introduced as $\Delta_{\mathrm{DES}} = \max(\Delta x, \Delta y, \Delta z)$. This modification of the destruction term in Eq. (4) tunes the model to function in the RANS mode in the near-wall regions ('attached' boundary layers), whereas away from the walls, in the detached regions of the flow, the closure reduces to a (one-equation) Smagorinsky-like model for the SGS eddy viscosity. The original value of the corresponding model constant $C_{\mathrm{DES}} = 0.65$ was used in this work.

Table 1 Plane channel flow computations

Run	$\frac{L_x}{H}$	$\frac{L_z}{H}$	Re_τ	$\frac{\Delta t U_c}{H}$	Δx^+	Δy^+ $\frac{min}{max}$	Δz^+
$LES - 64x32x32$	2π	π	188	0.047	18.5	$\frac{0.14}{37.7}$	18.5
$LES - 100x60x32$	2π	4	188	0.019	11.8	$\frac{0.56}{14.2}$	23.5
$LES - 48x96x48$	2π	π	196	0.047	19.2	$\frac{0.05}{13.3}$	12.8
$DES - 100x60x32$	2π	4	181	0.019	11.4	$\frac{0.54}{13.6}$	22.7

Computational Details

The size of solution domain adopted behind the step was $L_x \times L_y \times L_z = 30\,\mathrm{H} \times 3\,\mathrm{H} \times \pi\,\mathrm{H}$. Different grids were employed comprising between 190 000 ($142 \times 82 \times 16$) and 590 000 ($220 \times 82 \times 32$) grid cells, but preserving the number ($N_y = 82$) and distribution of the cells in the wall-normal direction. The two grids specified were finally adopted for the reference DES and LES simulations, respectively. In the course of the grid sensitivity study different grid resolutions and spanwise dimensions were also tested (see Tables 1 and 2 and corresponding discussions for more details). The grid resolution in the near-wall region has been chosen to ensure between 6 and 8 grid cells within the viscous sublayer for all the cases computed. One of the main difficulties in tackling this flow with LES or DES is imposing the proper inflow boundary conditions. The inlet data corresponding to a fully developed channel flow were generated computationally by using both LES and DES. It should be noted that the majority of the LES and DES simulations were performed with the LES inlet profiles, having the same wall-normal and spanwise grid spacing as well as the time step, avoiding any interpolation at the inlet plane. However, the additional DES of the backward-facing step flow with the inlet profiles generated by DES of the channel flow (with spanwise domain size extended to 4H and finer grid in the

Table 2 Backward-facing step computations

Run	$\frac{L_z}{H}$	St	$\frac{\Delta t U_c}{H}$	Δx^+ $\frac{min}{max}$	Δy^+ $\frac{min}{max}$	Δz^+
$LES-220x82x32$	π	*all*	0.047	$\frac{14}{107}$	$\frac{0.14}{37.7}$	18.5
$DES-220x82x32$	π	0.0	0.047	$\frac{14}{107}$	$\frac{0.14}{37.7}$	18.5
$DES-142x82x16$	π	*all*	0.047	$\frac{25}{115}$	$\frac{0.14}{37.7}$	37
$DES-142x110x32$	4	0.0	0.019	$\frac{25}{115}$	$\frac{0.54}{13.6}$	22.7

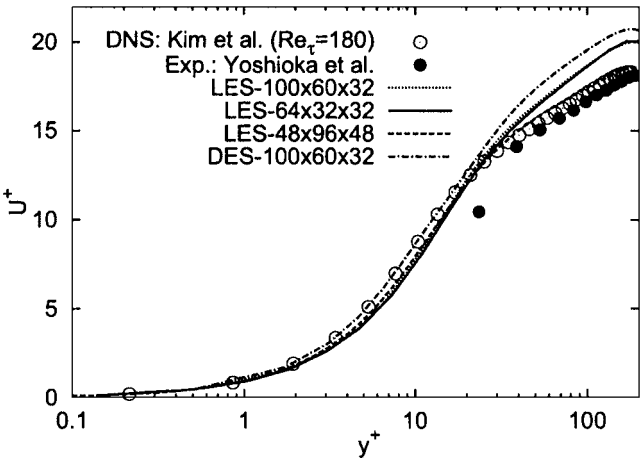

Fig. 3 Semilog profiles of the mean velocity

wall-normal direction), indicate that the results are not expected to differ significantly, whatever inlet data are taken (LES or DES). Once, a developed turbulence was generated, the instantaneous inlet velocities from presimulations were prescribed at the inlet. The channel length before expansion was taken to be $H/2$. The periodic boundary conditions were employed in the spanwise direction, whereas the convective boundary condition:

$$\frac{\partial \bar{U}_i}{\partial t} + U_{\text{con}} \frac{\partial \bar{U}_i}{\partial x} = 0, \tag{6}$$

was imposed at the outflow plane, the convective velocity being set to the mean streamwise velocity integrated across the exit plane.

The computational grid typically consisted of four blocks, two upstream (one comprising the region of the narrow opening and one upstream of it) and two downstream of the step edge (one situated behind the step covering one third of the corresponding channel height and one above it). The grid detail of the inlet region and the part of the domain around and just downstream of the step edge is shown in Fig. 2. A simple, periodically oscillating jet discharging with a uniform velocity profile $[v_e = V_e \sin(2\pi f_e t)]$ was assumed at the slit (0.05 H=1 mm width), which was covered by five control volumes.

Tables 1 and 2 give the basic data about the computations, providing also the notation used throughout when presenting the results. The dimensions of the computational boxes in both streamwise (only for channel flow) and spanwise directions were in line with the conclusions drawn from the works of Moin and Kim [14] and Akselvoll and Moin [15]. The simulations were started with the flow field obtained by RANS, which was initially perturbed, or with the previous LES or DES flow field in subsequent computations. Depending on the initial conditions, the flow was computed for a period of 2–6 flowthrough times before taking the statistics. The statistics were sampled over a period of 6–8 flowthrough times. The CFL number, representing the time step chosen, was less than unity over the majority of the solution domain. The exceptions are the narrow region around the thin slit (1 mm) at the step edge, and the long region with refined grid at $y=H$, Fig. 2. Here, due to the high grid resolution in the vertical direction and the large normal velocity component caused by the perturbations, the CFL number reaches its maximum value between 1.5 (fine grid, unperturbed case), 5.3 (fine grid, perturbed case), and 13.3 (coarse grid, perturbed case).

Results and Discussion

The results of the plane channel flow are presented first; afterwards the discussion of the backward-facing step simulations will be addressed. In both cases the time-averaged results have been extracted.

Channel Flow. The results of the precursor simulations of a plane channel flow, used to generate the inflow data, are given in Figs. 3–5. Besides the experimental data upstream of the step ($x/H=-0.6$), the direct numerical simulations of a fully developed turbulent channel flow at $\text{Re}_\tau=180$ (Kim et al., [16]) are used for comparison. One should keep in mind that the computed Re_τ values differ slightly when compared to the DNS and the experimental value (estimated as $\text{Re}_\tau=200$), as shown in Table 1. The mean velocity profiles obtained from the simulations with 32 or 60

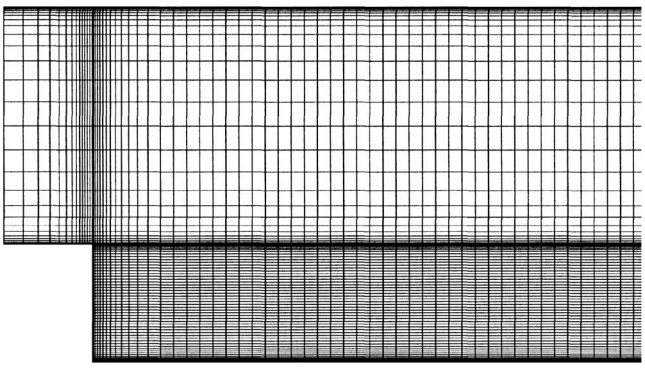

Fig. 2 Grid detail in the region around step

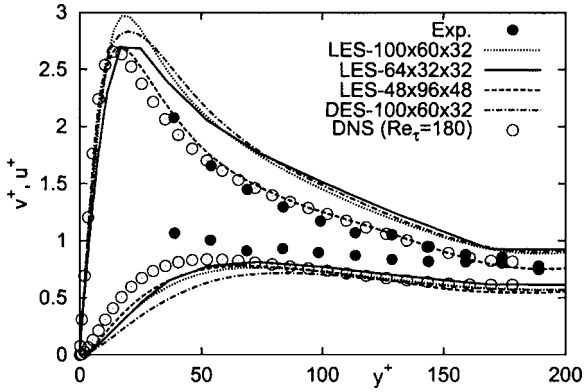

Fig. 4 Streamwise and normal-to-wall stresses

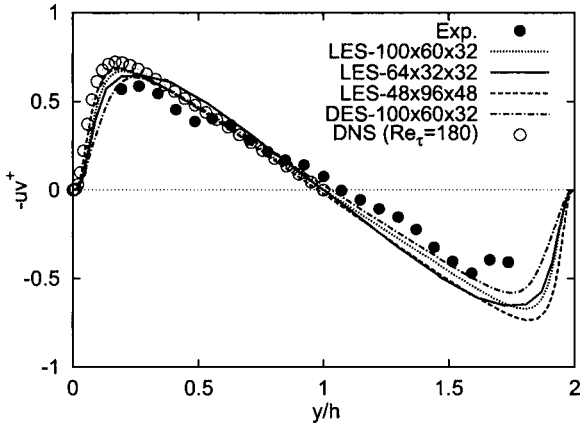

Fig. 5 Reynolds shear stress profiles

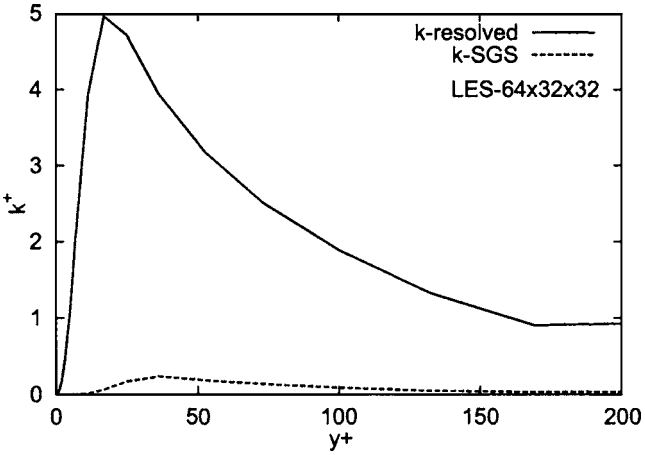

Fig. 6 Computed and modelled SGS kinetic energy

points in the wall-normal direction are overpredicted in the log-law region when compared to the DNS and experimental data (Fig. 3). It is regarded as an expected outcome with respect to the relatively coarse resolution. Also, a certain underprediction of the velocity in the viscous sublayer is clearly noticable. In general, the streamwise velocity fluctuations are overpredicted, while the wall-normal fluctuations are underpredicted (Fig. 4), which can again be attributed to the coarser grid resolution. The Reynolds shear stress profiles, given in Fig. 5, show the same tendency. The only exception is the run DES-$100\times60\times32$. Obviously, it is due to the fact that in this region the DES operates as a RANS.

Important information here is the position of the "interface" between the LES and RANS flow domain parts in the DES framework, which is dictated by the grid applied. They matched at $y^+=14.8$ ($y/H=0.082$), which could be regarded as an upper limit. By placing the interface further from the wall, the results return to those obtained by using the SA RANS model, exhibiting a severe underprediction of near-wall maximum of streamwise stress component (Leschziner, [17]), typical of all linear eddy-viscosity model schemes. On the other hand, the interface penetrating into the viscous sublayer should also be avoided. If the LES region in this hybrid approach resides too close to the wall due to insufficient resolution (one would have actually a resolution typical for RANS in the LES region), too low viscosity and turbulence levels could be obtained, possibly causing poor flow predictions. This explains the reasons for adopting somewhat larger spanwise dimensions ($4H$ instead of πH), providing the proper interface location for the given grid size (the companion LES simulation—LES-$100\times60\times32$—was performed just in order to validate the DES results). It results in a somewhat larger representative mesh size $\Delta_{\mathrm{DES}}=\max(\Delta x,\Delta y,\Delta z)$ leading consequently to a wider RANS-operating flow domain in accordance with Eq. (5).

The SGS contribution to turbulence kinetic energy was estimated from the LES simulation using the grid $64\times32\times32$. This analysis shows a minor contribution to the total k value. The absolute amount of the modeled SGS kinetic energy (estimated as $k_{sgs}=\Delta^2S^2/0.3$) reaches its maximum in the near-wall region (Fig. 6) but it is still only about 8% of the resolved kinetic energy. Finally, the frequency spectra of the streamwise velocity fluctuations, calculated in the symmetry plane of the channel at $y/H=1$, is plotted in Fig. 7. The time scales of the fluctuations may also be interpreted as spatial scales of turbulent fluctuations (the Taylor hypothesis). One can observe the trend towards a $f^{-5/3}$ range. The following conclusion may be drawn: the results obtained in this preliminary simulation with the given grid configurations agree fairly well with the available experimental data.

In order to overcome the overprediction of the streamwise stress component and the underprediction of the shear stress, a higher grid resolution in the wall-normal direction was necessary. In order to demonstrate it, an additional simulation was performed (these results were not used in the backward-step simulations). The grid refinement in both the wall-normal and spanwise direction, even with the coarser streamwise resolution (LES-48-96-48), significantly improves the results. However, the underprediction of the velocity in the viscous sublayer is still present even with the finest grid. A still finer grid resolution in both the wall-normal and spanwise direction would be needed to duplicate the DNS results. However, it should be pointed out that the channel flow computations were performed as a prelude to simulating the backward-facing step flow. Accordingly, our interest was not "a perfect LES." We were not intending to generate a highly resolved data field, but considered the LES and DES computational schemes as engineering CFD tools used for analysis in parallel with the results of RANS calculations. The goal was to employ a reasonable grid size being limited to 590 000 $C-V$'s, which could be easily handled using a single PC.

Backward-Facing Step, Unperturbed Case. The backward-facing step computations followed the channel flow simulations. They were conducted with the time dependent, velocity inlet profiles obtained initially with the run LES-$64\times32\times32$. The results of the reference case (without perturbation) are considered first. All the results pertain (if not explicitely stated) to the runs LES-$220\times82\times32$ (finer grid) and DES-$142\times82\times32$ (coarser grid), which are denoted simply by LES and DES in the remaining text. The position of the interface dividing the solution domain into a RANS region and a LES region resulting from the coarser grid used is at $y/H=0.128$ at the reattachment ($x/H=5$), $y/H=0.171$ ($y^+=32$) in the recovery region ($x/H=15$) and $y/H=0.361$ (y^+

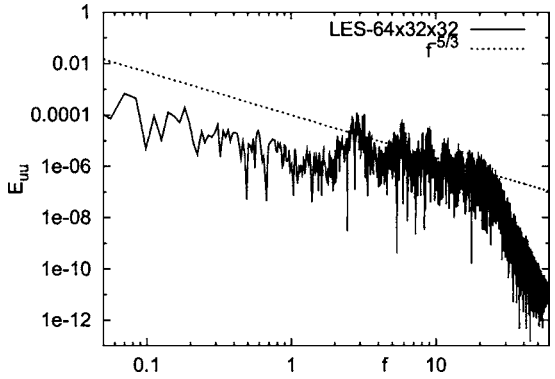

Fig. 7 Frequency-spectra of the streamwise velocity fluctuations at the symmetry plane $-y^+=188$

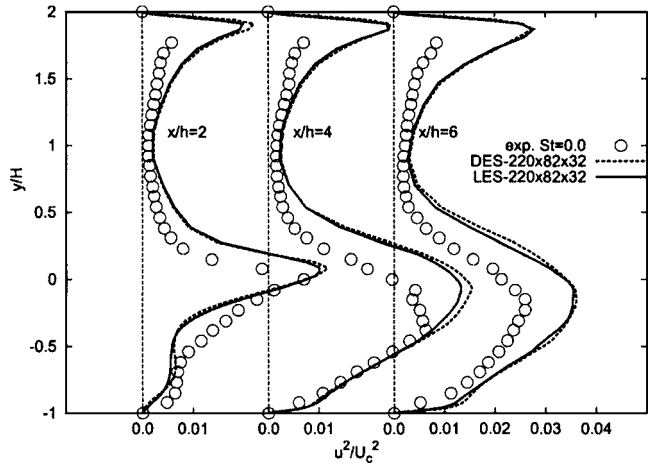

Fig. 8 LES vs DES: streamwise turbulence intensities, *St* =0.0

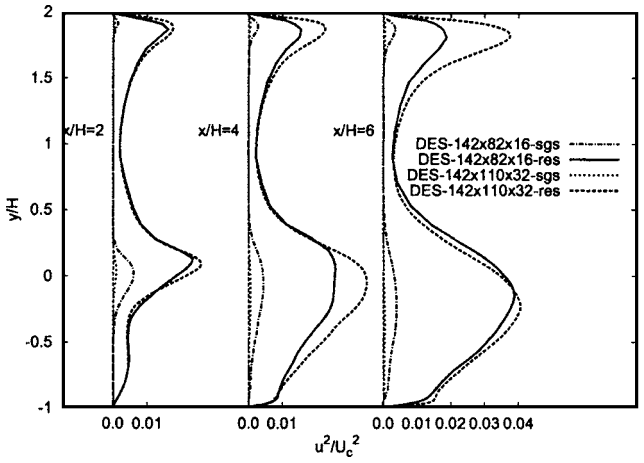

Fig. 10 Resolved vs modelled: streamwise turbulence intensities, *St*=0.0

=68) within the new boundary layer ($x/H=25$) throughout the flow domain. The DES simulation on a grid with a significantly finer grid resolution in the normal-to-the-wall direction ($N_y=110$) was additionally performed (Table 2). Similar as in the DES of the channel flow, the proper interface location was achieved by slightly extending the spanwise dimension from πH to $4H$ by preserved number of the grid points $N_z=32$.

Figures 8–10 display some selected results obtained with both LES and DES using considerably different grid resolutions. As already mentioned, the unperturbed case was computed by DES employing the same grid as used by LES. The results obtained are almost identical, as illustrated in Fig. 8 by displaying the profiles of streamwise turbulence intensities. Almost overlapping profiles indicate that the choice of SGS model was not that significant in the computations. However, the goal was to investigate the DES performance on coarser grids. It is believed, that a more advanced SGS model, here the grid-dependent SA model (certainly constrained by its calibration in the RANS mode), will cope better with lower grid resolution and an increasingly anisotropic grid than a simple Smagorinsky model. The hope expressed was certainly not fulfilled if the results obtained for unperturbed case are compared, Figs. 11 and 12. The largest deviation was documented in the far region, coinciding with the lowest streamwise grid resolution in the entire flow domain. The deviations are substantially less for perturbed cases, Figs. 15 and 16. In order to estimate the numerical error in the DES simulations, three different grids were employed for the unperturbed case. Figure 9 shows computed streamwise turbulence stresses. At the streamwise location $x=6H$, one can clearly see the improvement of results with the grid refinement. However, the reattachment length is still significantly overpredicted due to generally lower grid resolutions, in which case the SGS model plays a more significant role. Presumably, one may expect a larger numerical error in the region just before

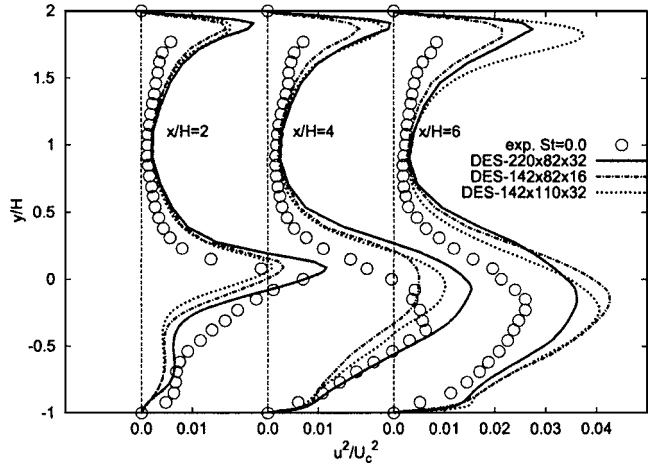

Fig. 9 Streamwise turbulence intensities, *St*=0.0

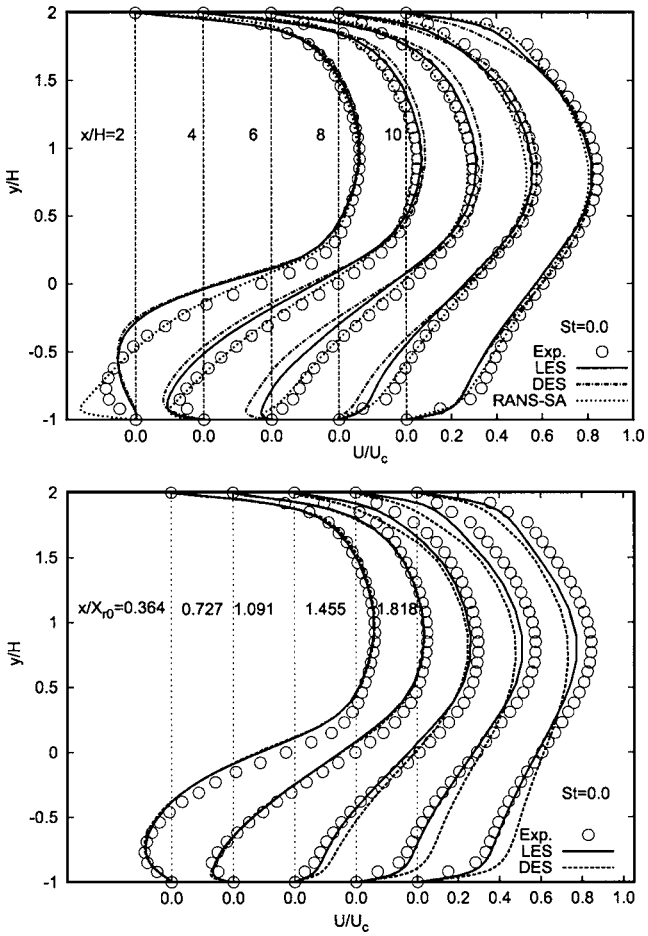

Fig. 11 Mean streamwise velocity profiles for the unperturbed case (*St*=0.0) at selected streamwise locations normalized by *H* (upper) and corresponding reattachment length X_R (lower)

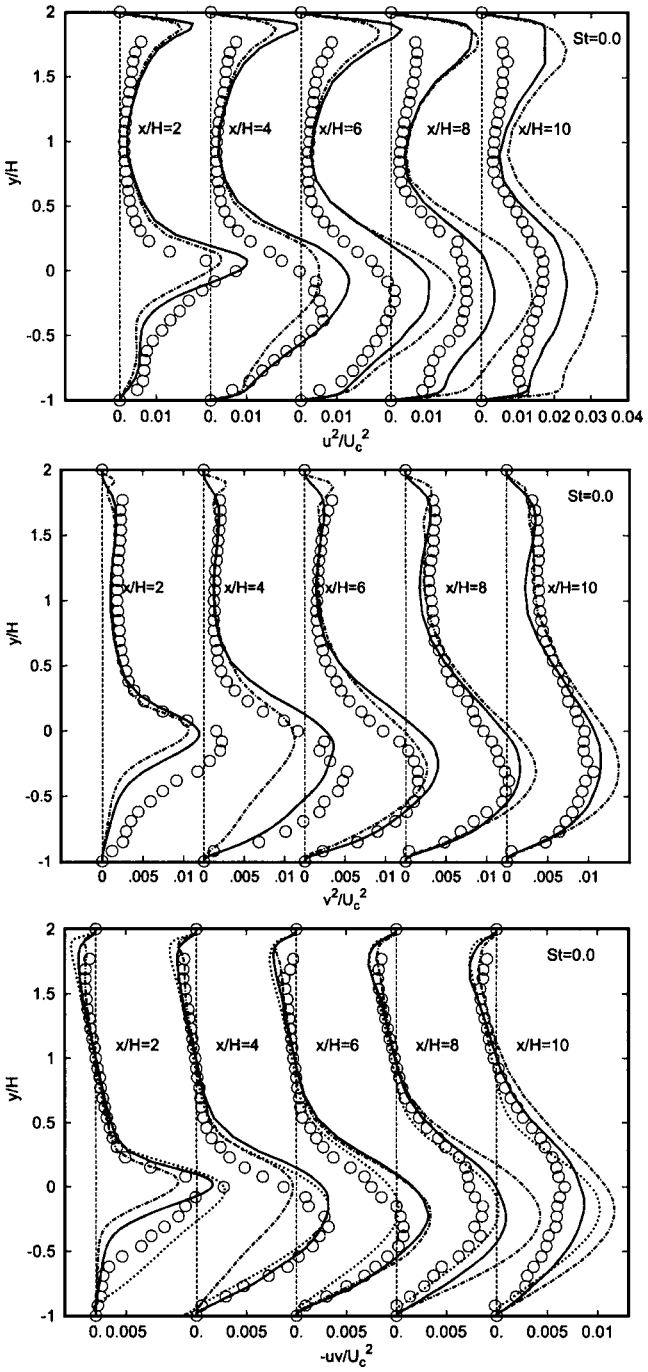

Fig. 12 Profiles of streamwise, normal-to-wall and shear stress components, *St*=0.0

and just after the reattachment point. This is confirmed by comparing the resolved and modeled streamwise turbulence stresses, as shown in Fig. 10.

Figures 11 and 12 show the mean velocity profiles and Reynolds stress components obtained by all three computational schemes (RANS, LES, and DES). All the computations significantly overpredict the measured reattachment length $X_R/H=6.0$ (this value represents a corrected value, Obi [18]); the originally reported value corresponds to $X_R/H=5.5$, Yoshioka et al. [1,2]): $X_R/H(\text{LES})=7.18$ (DES using the same grid as LES returned the same reattachment length, see also Fig. 8 for further comparison), $X_R/H(\text{DES})=8.36$, $X_R/H(\text{RANS}-\text{KWSST})=7.38$ and $X_R/H(\text{RANS}-\text{SA})=6.81$ (see also Fig. 14). One can observe that the RANS-SA outperforms the LES and DES at all the stations except $x=2h$. A fact that the reattachment length obtained by RANS-SA is the shortest one and consequently closest to the experimental result is not surprising for this steady case in which the 2D RANS computation used substantially higher wall-normal resolution $N_y=110$, whereas the LES and DES use lower grid resolutions (Table 2). It is well-known that the eddy-viscosity-based RANS models return traditionally a shorter corner bubble (secondary recirculation zone; it represents an outcome of the action of the normal stress components, which are not reproducible by an eddy-viscosity model scheme) as well as the backflow of a lower intensity, especially in the reattachment region (see, e.g., velocity profile at $x/H=6$ in Fig. 11 upper). However, the conditions under which the experimental results were obtained should also be pointed out. Particularly important is the aspect ratio based on the channel height after expansion ($3H$) and its spanwise dimension, which was only 1:4. This is regarded as too short for providing a 2D flow in the midspan plane. The possibility, that the side walls contaminated the results is very high. For example, Kasagi and Matsunaga [19] performed an experiment at a comparable Reynolds number ($\text{Re}_H=5540$) for the same expansion ratio. However, the above mentioned aspect ratio was 1: 6.7. Accordingly the reattachment length is substantially larger $X_R/H=6.51$. In favor of the computational results obtained here is the LES of the Yoshioka et al. case performed by Dejoan et al. [20]), where a reattachment length of $X_R/H=7.0$ was obtained. Finally, the comparison of the velocity profiles at selected streamwise locations normalized by corresponding reattachment length (instead of step height) shows very good agreement between LES, DES, and experiment in the region of flow reversal, Fig. 11 lower. Figure 12 shows that the mean turbulence stresses obtained by LES and DES agree reasonably well with experimental results in the near field immediately downstream of the step $x=2H$ and $x=4H$. The RANS-SA model generally fails to catch the peak in the separated shear layer. At the last three streamwise locations the streamwise turbulence intensities are overpredicted, which is characteristic for the somewhat lower grid resolution in this flow region.

The performance of LES and DES may be explained by the following facts: the inflow data, grid resolution, and spanwise dimension may have a great impact on the results. The possible underprediction of computed turbulence intensities in the precursor channel flow simulations could lead to such an overestimate of the reattachment ($7.18H$), compared to the measured value ($6.0H$; Obi, [18]). Furthermore, the grid resolution, especially in the spanwise direction, might be insufficient. At the same time, the spanwise domain size of πH could be responsible for the overprediction of the reattachment length. Arnal and Friedrich [21] indicated that the choice of the spanwise dimension was of decisive importance. They concluded that an overprediction of the reattachment length up to 30% could occur if the size of the flow domain in the spanwise direction was of the order of $<4H$. They found that $L_z \geqslant 8H$ was necessary to eliminate the influence of the periodic inlet/outlet through the side planes of the computational box. In order to check the latter, two additional simulations with substantially refined grid (LES-$354\times110\times32$) and a doubled spanwise domain dimension (LES-$220\times82\times64$, $L_z=2\pi H$) were performed. The results obtained (not shown here) show no important differences in comparison with the reference LES (LES-$220\times82\times32$, $L_z=\pi H$). Accordingly, the grid sizes adopted for the reference simulations can be regarded as optimal ones. The main goal was, however, to study the effects of perturbations on flow characteristics compared to the reference, unperturbed case. The results of simulations with perturbations are presented in the following section.

Backward-Facing Step, Perturbed Cases. Computational investigations were performed focussing on the influence of the oscillatory blowing/suction on the reattachment pattern for all perturbation frequencies treated experimentally: $St=0.08$, 0.19, and

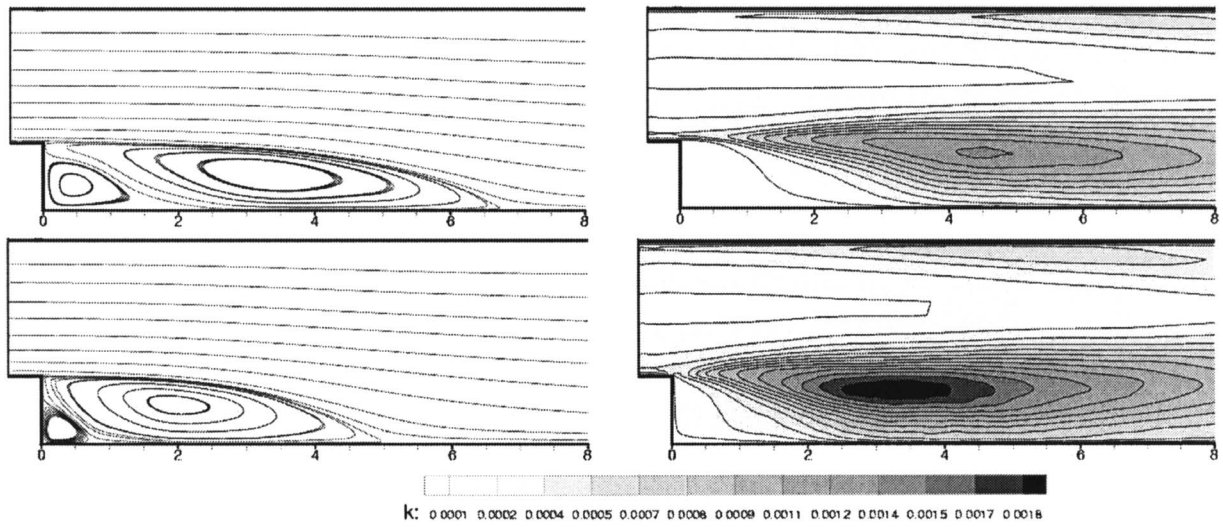

Fig. 13 Time-averaged streamlines and kinetic energy contours for unperturbed (upper) and perturbed (St=0.19; lower) cases

0.30. Due to lack of space we will preferably present the results obtained for the optimum frequency St=0.19. The main effect of the oscillatory blowing on a separated shear layer is that it reattachs earlier due to momentum transfer enhancement caused by an increase in turbulence production. Figure 13 displays the time-averaged streamlines and contours of the kinetic energy of turbulence behind the step obtained by using the LES method for both perturbed and unperturbed (St=0.19) flow cases. The increase in turbulence intensity in the shear layer (denoted by a dark area) and consequent shortening of the mean recirculation zone are clearly recognizable.

Figure 14 displays the evolution of the reattachment length (normalized by the reattachment length obtained for the unperturbed case X_{R0}) in terms of imposed perturbation frequencies. Although the quantitative agreement between experimental and computational results is rather poor, it is encouraging to see that also the T-RANS computations using SA and $k-\omega$ SST statistical models reproduced a reduction of the reattachment length with respect to the steady case (St=0.0), and that the reattachment length minimum is reached at the position St=0.19, comparing well with experiment. However, the relative decrease is too small. The T-RANS method employing SA (only 5.9% compared to the unperturbed case) and $k-\omega$ SST (12.9%) models results in a very weak sensitivity to the perturbation. Contrary, very close agreement with experiment was obtained with the DES (24.5%) and LES (35%) methods.

Figures 15 and 16 display the profiles of mean axial velocity and all three Reynolds stresses ($\overline{u^2}$, $\overline{v^2}$, and $\overline{uv}$) in all characteristics regions behind the step: within the recirculation zone (x/H=2 and 4), close to reattachment (x/H=6), and in the recovery region (x/H=8 and 10). It can be seen that both the LES and DES predictions are generally in better agreement with the experimental data, when compared to the unperturbed case. Similar behavior is obtained for the other two perturbation frequencies, St=0.08 and St=0.30. Exceptions are observed for the stations x=4H and 6H. These discrepancies in the lower near-wall region as well as the underprediction of the streamwise velocity in the upper near-wall region in the post-reattachment zone can be attributed to insufficient grid resolution. A difference can only be seen in the wall-normal turbulence intensity profiles, which are consistently underpredicted at the position immediatelly downstream of the step (x=2H) for all frequencies investigated. This may be related to the inlet profiles (note underprediction of the $\overline{v^2}$ stress component in Fig. 4).

The influence of the perturbation frequency on the intensity of the backflow in the mean recirculation zone, as well as on the size

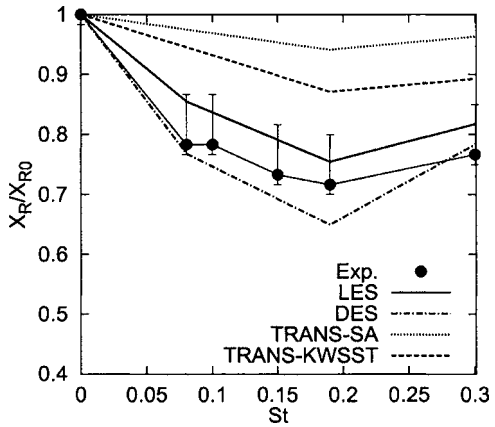

Fig. 14 Evolution of the relative reattachment lengths in terms of *St*. Exp.: Obi (2002)

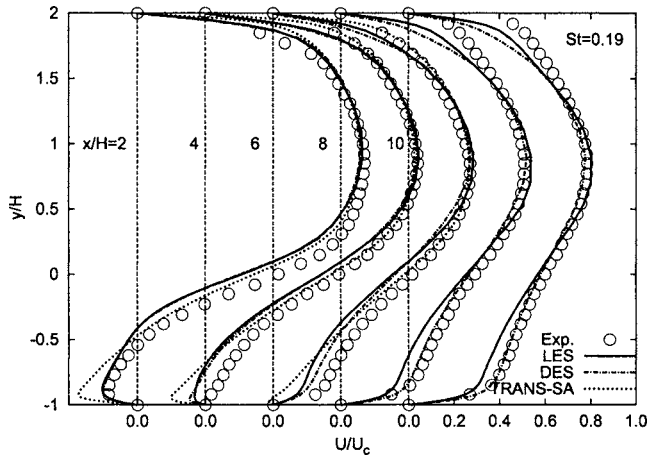

Fig. 15 Mean streamwise velocity profiles, *St*=0.19

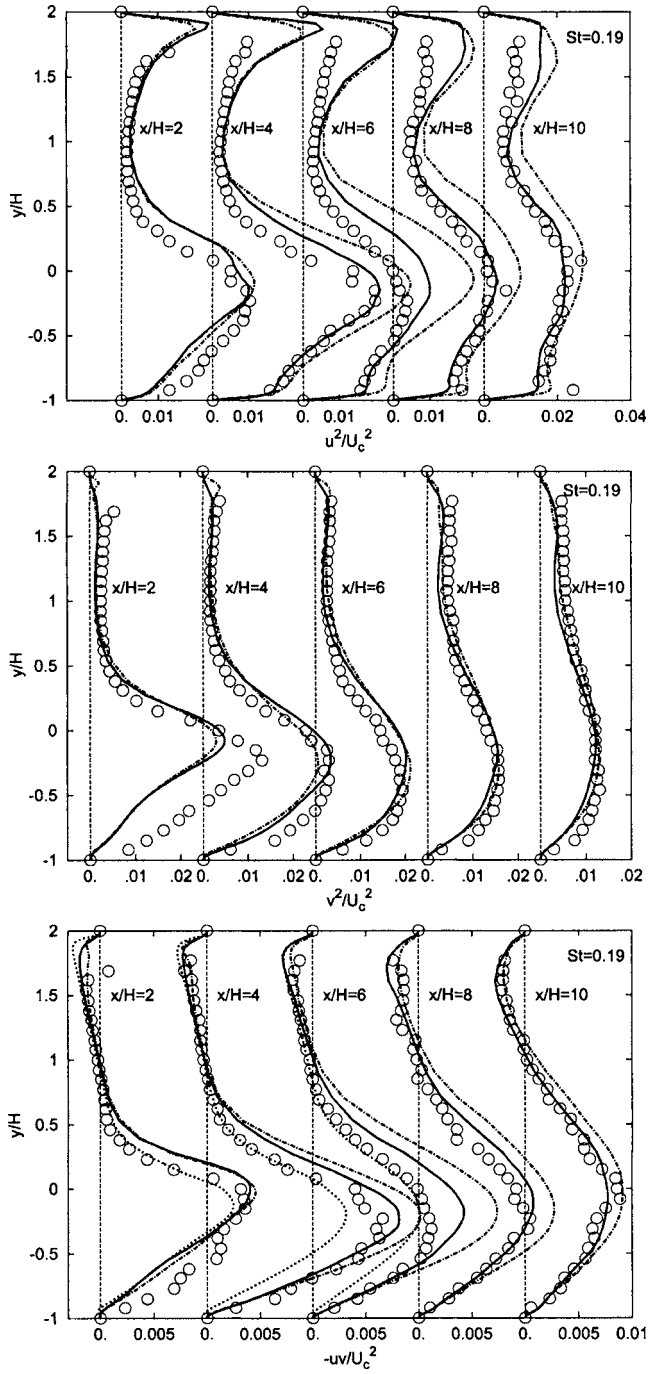

Fig. 16 Profiles of streamwise, normal-to-wall and shear stress components, *St*=0.19

(length and height) of the separation bubble itself, is documented in Fig. 17 (left). The obvious shortening of the reattachment length can also be deduced from the position of the zero value of the mean velocity, being closest to the wall in the case of the optimal frequency $St=0.19$. Figure 18 (right) shows the profiles of the streamwise stress component for all perturbation frequencies considered, closely following the experimentally obtained results.

Fig. 19 documents the very well-known weaknesses of RANS models, namely very low turbulence intensities (here the shear stress component is shown) in the shear layer. As already discussed, the proper level of turbulence in this region is of crucial importance for the correct prediction of the reattachment length. The reason for such a result lies in the unsteady nature of the

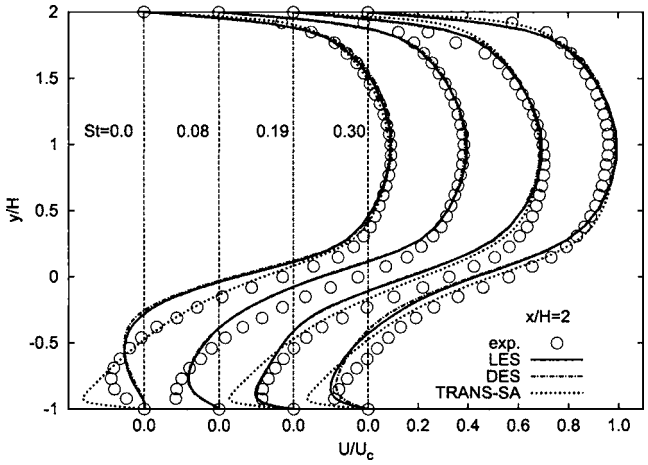

Fig. 17 Mean velocity profiles in terms of *St*

flapping motion of the separated shear layer (Fig. 20) and oscillation of the instantaneous reattachment point (Fig. 20 upper), which cannot be fully reproduced by RANS models.

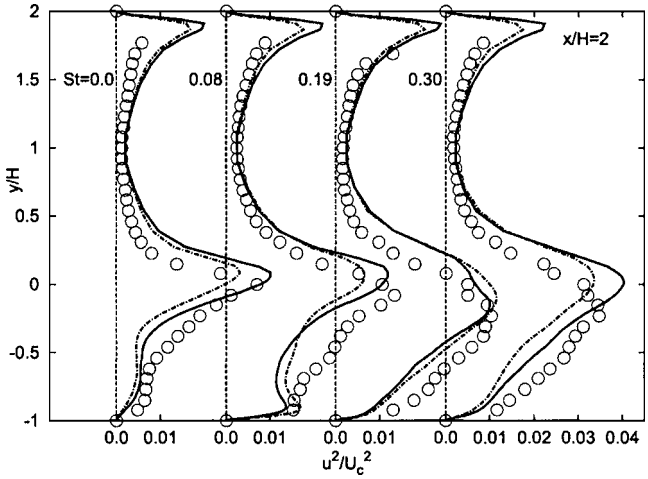

Fig. 18 Streamwise stress profiles in terms of *St*

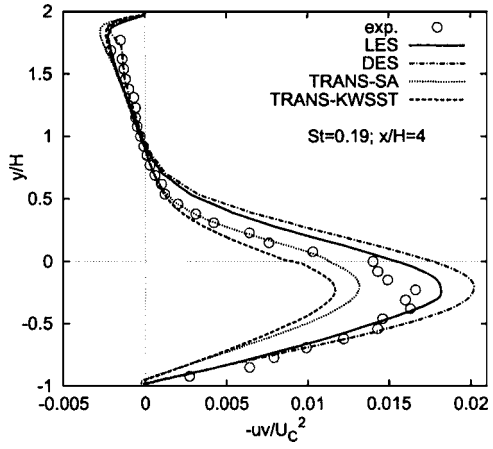

Fig. 19 Shear stress profiles: comparison of LES, DES, and T-RANS results with experiments

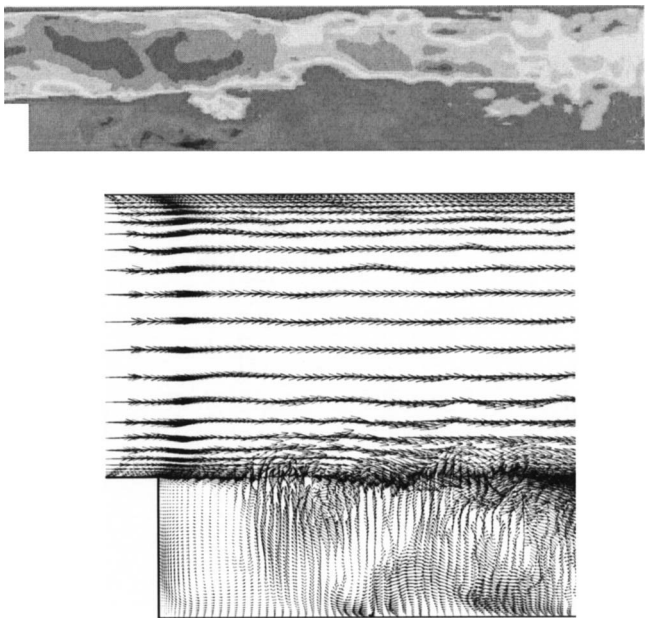

Fig. 20 Instantaneous velocity contours and vectors, $St=0.19$

Conclusions

The potential of the methods for unsteady flow computations: LES, DES, and T-RANS was investigated by predicting the flow and turbulence in a backward-facing step flow configuration perturbed by periodic blowing/suction with zero net mass flux from a thin slit situated at the step edge. In general, both the LES and DES computations have reproduced all important effects observed in the experiment. The imposed perturbation frequency corresponding to $St=0.19$ was found to be the optimum one, leading to the maximum reduction of the reattachment length. Compared to the measured value of 28.3%, LES and DES exhibit the closest agreement, predicting the reduction of 24.5% and 35%, respectively. The T-RANS method underpredicts substantially the intensity of the reduction with 5.9% (SA model) and 12.9% ($k-\omega$ SST model), showing a very weak sensitivity to the perturbations. The computations with the physically more plausible turbulence models, such as differential Reynolds stress models, are in progress. The grid resolution and spanwise size of the computational domain and their relation to an overprediction of the absolute reattachment length for both LES and DES were discussed. However, a further grid refinement, as well as a doubling of the spanwise dimension did not result in any significant change. The normal-to-the-wall and shear stress components, including also the wall shear stress at the step edge obtained from the preliminary channel simulation were underpredicted compared to the experiment. A more detailed computational analysis of the influence originating from the inflow boundary conditions is necessary.

Acknowledgments

The authors (S.Š.) gratefully acknowledge financial support of the Deutsche Forschungsgemeinschaft through the grants GK "Modelling and Numerical Description of Technical Flows" and the research group on "LES of Complex Flows" (FOR 507/1, JA 941/7-1). Our special thanks go to Prof. S. Obi, Keio University, for making his experimental data available. We are grateful for the numerous specific comments and suggestions from the reviewers.

References

[1] Yoshioka, S., Obi, S., and Masuda, S., 2001, "Organized Vortex Motion in Periodically Perturbed Separated Flow Over a Backward-Facing Step," Int. J. Heat Fluid Flow, **22**, pp. 301–307.
[2] Yoshioka, S., Obi, S., and Masuda, S., 2001, "Turbulence Statistics of Periodically Perturbed Separated Flow Over Backward-Facing Step," Int. J. Heat Fluid Flow, **22**, pp. 393–401.
[3] Seifert, A., and Pack, L. G., 1999, "Oscillatory Control of Separation at High Reynolds Numbers," AIAA J., **37**, pp. 1062–1071.
[4] Seifert, A., and Pack, L. G., 2002, "Active Flow Separation Control on Wall-Mounted Hump at High Reynolds Numbers," AIAA J., **40**, pp. 1363–1372.
[5] Chun, K. B., and Sung, H. J., 1996, "Control of Turbulent Separated Flow Over a Backward-Facing Step," Exp. Fluids, **21**, pp. 417–426.
[6] Jin, S., Choi, H., Kim, S., Yul, Y.-J., and Kim, S.-R., 2001, "An Experimental Study of Turbulent Backward-Facing Step Flow Under Two-Frequency Forcing," Exp. Heat Transfer, *Fluid Mechanics and Thermodynamics*, Celata et al., eds., Edizioni ETS, Pisa, pp. 1933–1938.
[7] Khosla, P. K., and Rubin, S. G., 1974, "A Diagonally Dominant Second-Order Accurate Implicit Scheme," Comput. Fluids, **2**, pp. 207–209.
[8] Spalart, P. R., and Allmaras, S. R., 1994, "A One-Equation Turbulence Model for Aerodynamic Flows," La Rech. A'erospatiale, **1**, pp. 5–21.
[9] Menter, F. R., 1994, "Zonal Two-Equation $k-\omega$ Turbulence Model for Aerodynamic Flows," AIAA P 1993–2906.
[10] Jakirlić, S., Jester-Zürker, R., and Tropea, C., 2002, "9th ERCOFTAC/IAHR/COST Workshop on Refined Turbulence Modelling," ERCOFTAC Bulletin, December, **55**, pp. 36–43.
[11] Stawiarski, K., and Hanjalic, K., 2002, "A Two-Scale Second-Moment One-Pont Turbulence Closure," *Engineering Turbulence Modelling and Experiment*, 5, W. Rodi and N. Fueyo, eds., Elsevier Science, pp. 97–106.
[12] Spalart, P. R., Jou, W.-H., Strelets, M., and Allmaras, S. R., 1997, "Comments on the Feasibility of LES for Wings and on Hybrid RANS/LES Approach," *Proc. First AFOSR International Conference on DNS and LES*, Ruston, LA, USA.
[13] Travin, A., Shur, M., Strelets, M., and Spalart, P. R., 2002, "Physical and Numerical Upgrades in the Detached-Eddy Simulation of Complex Turbulence Flows," In *Fluid Mechanics and Its Application: Advances in LES of Complex Flows*, R. Friedrich and W. Rodi, eds., 65, Kluwer Academic Publisher, pp. 239–254.
[14] Moin, P., and Kim, J., 1982, "Numerical Investigation of Turbulent Channel Flow," J. Fluid Mech., **118**, pp. 341–377.
[15] Akselvoll, K., and Moin, P., 1993, "Large Eddy Simulation of a Backward Facing Step Flow," *Engineering Turbulence Modeling and Experiment*, 2, W. Rodi and F. Martelli, eds., Elsevier Science Ltd., pp. 303–313.
[16] Kim, J., Moin, P., and Moser, R., 1987, "Turbulence Statistics in Fully Developed Channel Flow at the Low Reynolds Number," J. Fluid Mech., **177**, pp. 133–166.
[17] Leschziner, M. A., 2001, "At the Crossroads of Turbulence Modelling and Simulation: Opportunities and Challenges," *Proc. Eighth IAHR International Symposium on Flow Modelling and Turbulence Measurements*, Tokyo, Japan, December 4–6.
[18] Obi, S., 2002 (private communication).
[19] Kasagi, N., and Matsunaga, A., 1995, "Three-Dimensional Particle-Tracking Velocity Measurements of Turbulence Statistics and Energy Budget in a Backward-Facing Step Flow," Int. J. Heat Fluid Flow, **16**, pp. 477–485.
[20] Dejoan, A., Jang, Y.-J., and Leschziner, M., 2004, "LES and Unsteady RANS Computations for a Periodically-Perturbed Separated Flow Over a Backward-Facing Step," *Proc. ASME Heat Transfer/Fluids Engineering Summer Conference*, Charlotte, NC, USA, July 11–15.
[21] Arnal, M., and Friedrich, R., 1993, "Large-Eddy Simulation of a Turbulent Flow With Separation," *Turbulent Shear Flows*, 8, F. Durst et al., eds., Springer Verlag, pp. 169–187.

Detached Eddy Simulation of Turbulent Flow and Heat Transfer in a Ribbed Duct

Aroon K. Viswanathan

Danesh K. Tafti
Phone: +1 540 231 9975
Fax: +1 540 231 9100
e-mail: dtafti@vt.edu

Mechanical Engineering Department, Virginia Polytechnic Institute and State University, Blacksburg, VA 24060

Detached Eddy Simulation (DES) of a hydrodynamic and thermally developed turbulent flow is presented for a stationary duct with square ribs aligned normal to the main flow direction. The rib height to channel hydraulic diameter (e/D_h) is 0.1, the rib pitch to rib height (P/e) is 10 and the calculations have been carried out for a bulk Reynolds number of 20,000. DES calculations are carried out on a 96^3 grid, a 64^3 grid, and a 48^3 grid to study the effect of grid resolution. Based on the agreement with earlier LES computations, the 64^3 grid is observed to be suitable for the DES computation. DES and RANS calculations carried out on the 64^3 grid are compared to LES calculations on $96^3/128^3$ grids and experimental measurements. The flow and heat transfer characteristics for the DES cases compare well with the LES results and the experiments. The average friction and the augmentation ratios are consistent with experimental results, predicting values within 10% of the measured quantities, at a cost lower than the LES calculations. RANS fails to capture some key features of the flow. [DOI: 10.1115/1.2033010]

Introduction

Motivation. The efficient design of the internal cooling ducts in gas turbine blades and nozzle vanes requires a detailed knowledge of the flow and heat phenomena occurring inside these passages. Modern computational techniques have the potential of providing detailed physical understanding as well as tools for design. Numerical techniques range from the solution of the full flow field without any empiricism, such as in Direct Numerical Simulations (DNS), to the modeling of the turbulence using Reynolds Averaged Navier-Stokes Equations (RANS), which are based on semi-empirical relations to obtain closure. The inability of the eddy-viscosity RANS models to predict secondary flows which influence heat transfer in the ribbed ducts [1] make linear eddy-viscosity RANS models a poor choice. Numerical predictions using Large Eddy Simulations (LES) are accurate [2], but they are expensive in terms of computational resources. Spalart [3] proposed a hybrid RANS-LES model or Detached Eddy Simulations (DES), which is a modification of the RANS equation, such that the equation can take a subgrid scale form in regions with richer turbulent physics. This scheme is less expensive than LES but has the potential of maintaining the accuracy of the LES model in regions with rich eddy content.

In this paper the ability of the DES modes of the k-ω equations and Menter's Shear Stress Transport (M-SST) model are investigated. The accuracy of the solution has been evaluated by comparing the results with experimental data of Rau et al. [4] and with LES results from Tafti [2].

Experimental Studies. Over the past couple of decades several experimental studies have been carried out to study the heat transfer characteristics of ribbed ducts. Han et al. [5–9] have carried out studies on ribbed ducts which give a comprehensive knowledge of the effect of the different rib angles, rib sections, blockage ratios, pitch/height ratios, different channel aspect ratios, and Reynolds numbers of the flow on the heat transfer characteristics. Similar LDV studies have also been reported by Liou et al. [10,11]. Sato et al. [12] carried out LDV measurements on a repeated ribbed channel for symmetric, staggered and asymmetrical rib arrangements. The primary objective of the study was to characterize the turbulent flow in the channels with repeated ribbed roughness. Yokosawa et al. [13] measured the flow resistance in a ribbed square duct using hot wire anemometry and reported the presence of secondary flow in the ribbed ducts.

These studies have shown that the ribs enhance heat transfer by a factor of around 2–4 on the ribbed walls and between 1.5 and 2 on the smooth walls compared to a smooth duct flow.

Computational Studies. Most of the reported computational predictions are focused on the solution of the RANS equations. Different closure models have been used, and it has been observed that while eddy-viscosity models which assume isotropy of turbulence (Prakesh and Zerkle [14]) fail to capture the flow accurately, more complicated models perform reasonably well (Jia et al. [15]).

Liou et al. [10,11] used a k-ε algebraic stress model to predict flow in a stationary 2D ribbed duct with ribs on one wall. Their studies showed that the k-ε model fails to predict the flow accurately while the k-ε-A model, which accounts for the anisotropy of turbulence, gives reasonable results. Saidi et al. [16] also used k-ε models in a periodic channel with inline orthogonal ribs, and the computations showed mixed results. Iacovides [17] carried out computations using k-ε and low-Re zonal differential stress models (DSM) in a periodic ribbed duct for stationary and rotating cases. Though a reasonable flow behavior was predicted by the k-ε model, the thermal behavior was not predicted accurately. The low-Re DSM model gave better predictions than the k-ε. Iacovides et al. [18] introduced a modified version of the Yap correction to the low-Re DSM models and obtained reasonable heat transfer results in a 180 deg bend channel. Ooi et al. [1] present predictions using a v^2-f model on orthogonal in-line ribs and found that the model performs better than the k-ε and S-A RANS models.

Large Eddy Simulations (LES) have been used in the past to study the heat transfer in ribbed channels. Murata and Mochizuki [19] studied the effect of Coriolis force and the duct cross section on the heat transfer in smooth and ribbed channels. Watanabe and Takahashi [20] carried out LES computations and experimental studies on a rectangular channel with traverse ribs which are heated from one side and got good agreement with the experiments. The studies also revealed the unsteady mechanism that enhanced the heat transfer in the ribbed channel. Tafti [2] used 96^3 and 128^3 grids to predict the heat transfer in a channel with or-

Contributed by the Fluids Engineering Division for publication in the JOURNAL OF FLUIDS ENGINEERING. Manuscript received: July 29, 2004. Final revision: July 13, 2005. Associate Editor: Ismail Celik.

thogonal ribs with a pitch to rib height ratio (P/e) of 10 and a rib height to hydraulic diameter (e/D_h) of 0.1. The computations also gave a comprehensive knowledge of the major flow structures in the flow field and compared very well with experiments. Additional LES computations have also been carried out by Tafti et al. [21–24] for several cases, such as the developing regions of the cooling channel (stationary and rotating cases), rotating periodic ribbed channels with ribs orthogonal to the flow direction and computations on 45 deg ribs, which show excellent agreement with the earlier experimental studies.

While accurate results have been obtained with the LES computations, the grid requirements are very demanding. The resolution in the boundary layer has to be fine and increases with Reynolds number. This calls for a special treatment of the boundary layer to limit the number of grid points. One of the several techniques available for wall modeling is Detached Eddy Simulation (DES), which was proposed by Spalart et al. [3]. This technique, initially proposed based on the Spalart-Allmaras turbulence model, treats the boundary layer in a RANS mode and by modifying the length scale in the destruction term the model switches to a sub-grid type formulation. Later this technique was generalized by Strelets [25] who defined a DES scheme for the Menter's Shear Stress Transport model.

Objective of the Study. The objective of the current study is to implement DES on a periodic ribbed duct, at a cost cheaper than the analogous LES computation, but attain reasonable accuracy than what is attained with a traditional RANS computation. All previous published work has applied DES to external aerodynamic flows. In this paper, DES is applied to an internal duct flow with heat transfer, which poses its own challenges. Computations are carried out for a ribbed channel with a rib pitch to rib height of 10 and rib height to hydraulic diameter of 0.1 for a bulk Reynolds number of 20,000. Results are initially compared for three grid resolutions 96^3, 64^3, and 48^3 and the optimal grid for computations derived upon. This grid has been used further in a comprehensive study of the flow field and the heat transfer predictions.

The solution has been evaluated by comparing the solution with the experimental results by Rau et al. [4] and LES computations by Tafti [2]. The experiments were conducted for a bulk Reynolds number of 30,000 in a ribbed duct with varying P/e and $e/D_h = 0.1$. The LES computations, using the dynamic Smagorinsky model, have been carried out for a fully developed flow in a ribbed duct with $P/e = 10$ and $e/D_h = 0.1$ on 96^3 and 128^3 grids for $\mathrm{Re} = 20,000$.

Detached Eddy Simulations. DES is a modification of a RANS model in which the model switches to a subgrid scale formulation in regions fine enough for LES calculations. Regions near solid boundaries and where the turbulent length scale is less than the maximum grid dimension are assigned the RANS mode of solution. As the turbulent length scale exceeds the grid dimension, the regions are solved using the LES mode. Therefore the grid resolution is not as demanding as pure LES, thereby considerably cutting down the cost of the computation. The RANS length scale, $l_{k\text{-}\omega}$, which is defined as $l_{k\text{-}\omega} = \sqrt{k}/\beta^*\omega$ for the k-ω model is replaced by a DES length scale δ, where $\delta = \min(l_{k\text{-}\omega}, C_{\mathrm{DES}}\Delta)$ and $\Delta = \min(\Delta_x, \Delta_y, \Delta_z)$ and the resulting subgrid model reduces into a Smagorinsky-type model. Based on this, the dissipation term in the k-transport equation is reduced to $D^k = \rho k^{3/2}/\delta$. For the Wilcox's k-ω models the DES constant C_{DES} can be used directly. When Menter's BSL or SST models are used the blending function F_1 is used to determine the value of the DES constant,

$$C_{\mathrm{DES}} = (1 - F_1)C^{k\text{-}\varepsilon}_{\mathrm{DES}} + F_1 C^{k\text{-}\omega}_{\mathrm{DES}}, \quad C^{k\text{-}\omega}_{\mathrm{DES}} = 0.78, \quad C^{k\text{-}\varepsilon}_{\mathrm{DES}} = 0.61.$$

However the k-ε value of the C_{DES} value is encountered more often when the RANS-LES switch takes place.

Numerical Method. The governing equations for momentum and energy are discretized with a conservative finite-volume formulation using a nonstaggered grid topology. The Cartesian velocities, pressure, and temperature are calculated and stored at the cell center, whereas contravariant fluxes are stored and calculated at the cell faces. For the time integration of the discretized continuity and momentum equations, a projection method is used. The temporal advancement is performed in two steps, a predictor step, which calculates an intermediate velocity field, and a corrector step, which calculates the updated velocity at the new time step by satisfying discrete continuity. The energy equation is advanced in time by the predictor step. A second order central difference scheme is used in the momentum and energy equations. The equations for the turbulent kinetic energy and the dissipation rate are solved using a second order central difference scheme with a TVD limiter.

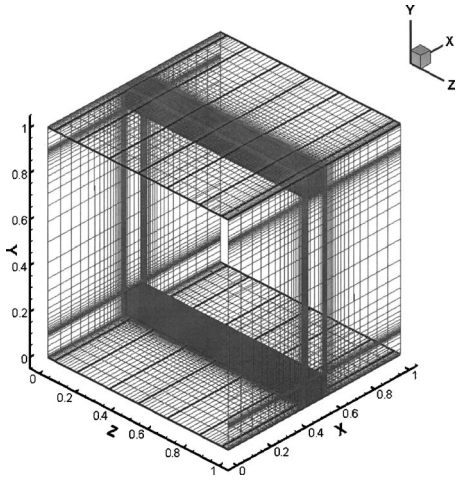

Fig. 1 The computational model. A pair of ribs placed at the center of the duct. Flow in the duct is periodic in streamwise direction. A 64^3 mesh (baseline grid) is used to grid the domain. The dark lines represent the 8 blocks into which the domain is divided.

Computational Details. The model assumes fully-developed flow and heat transfer and simulates a streamwise periodic spatial unit consisting of two ribs (one on either side of the duct). The walls (ribbed and side walls) and the ribs are heated by a constant heat flux (q'') and a stationary case is considered. The governing flow and energy equations are nondimensionalized by a characteristic length scale which is chosen to be the hydraulic diameter of the channel (D_h), a characteristic velocity scale given by the friction velocity (u_τ), and a characteristic temperature scale given by $q''D_h/k$. The form drag is computed by integrating the pressure forces on the ribs. The contribution of shear to friction losses on each of the walls and the ribs are computed by integrating the shear stresses on the surface. The augmentation ratios for both heat transfer and friction are calculated with reference to a smooth channel

The computational domain consists of a ribbed channel, with two ribs placed at the center of the channel, at the top and the bottom. The grid and the coordinate system used are shown in Fig. 1. A 96^3 grid used for earlier LES studies was considered as the fine grid used in the study. A coarser grid (64^3) was formed by maintaining the same grid resolution near the walls and coarsening the grid in the inter-rib spacing and in regions away from the channel walls. A coarser grid (48^3 cells), was obtained by coarsening the 64^3 grid in regions away from the walls. Henceforth, the 96^3, 64^3 and the 48^3 grids are referred to as fine grid, baseline grid, and the coarse grid, respectively. A nondimensional time step of 5×10^{-5} was used in all of the cases. Calculations are initiated by assuming an initial bulk velocity and integrating in time until a

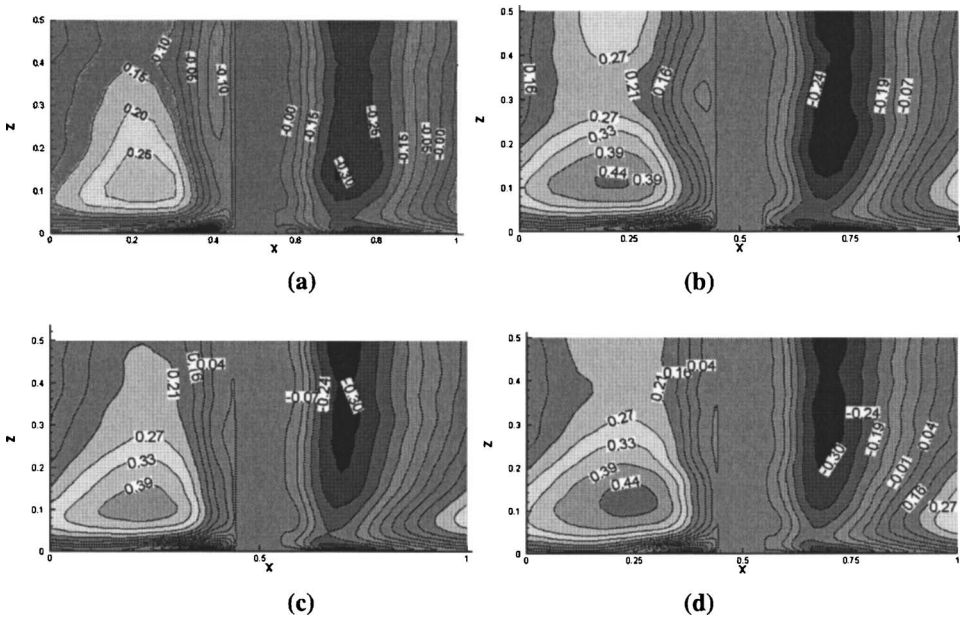

Fig. 2 Comparison of the streamwise velocities in a plane through the ribs ($Y/e=0.25$) for the (*a*) 48^3 grid, (*b*) 64^3 grid, (*c*) 96^3 grid, and (*d*) LES 128^3 case. 64^3 and the 96^3 case show the best agreement. 48^3 grid underpredits the velocities.

balance between the internal losses and the specified pressure gradient was obtained. Although the whole domain is considered for the calculation, owing to the symmetry along the y and z directions, the average solution for a quadrant is presented.

Results

Grid Sensitivity Comparisons. DES is sensitive to grid resolution as shown by earlier DES calculations. The grid dependency is not similar to LES, where an increase in resolution of the grid improves the solution. In DES, a grid which is fine might trigger an LES solution in the boundary layer, which might be detrimental if the resolution is not fine enough for LES. On the other hand, a coarse grid may eliminate the LES regions in the grid altogether, and in the limit the calculation would default to a URANS calculation. In the three resolutions tested, the near wall grid resolution was maintained and only the regions away from the wall were modified to generate coarser meshes. The intent is to maintain the quality of the mesh near the walls, however because of the presence of walls in two directions (unlike most external flows), changes in the grid made in one direction (say y-direction) does affect the quality of the grid in the near wall region in the z-direction. Obviously, as the grid is coarsened, more and more of the turbulence is treated in a RANS mode.

DES k-ω computations were carried out on the three grids and a comparison of the average streamwise velocities (Fig. 2) shows that while the baseline grid and the dense grid compare well with the LES results, the coarse grid fails to accurately predict the velocity levels. A comparison of the baseline grid and the denser grid shows that both grids predict the streamwise velocity contours to good accuracy (Fig. 2) and capture the secondary recirculation behind the rib. The denser grid did not show any added value, and so the baseline grid was considered to be sufficiently accurate for further study. The k-ω RANS calculations are also carried out on the baseline grid.

DES Regions. The fraction of time during the whole computation when the turbulence is resolved in the LES mode is shown in Fig. 3. The near wall region is always resolved in the RANS mode which transitions to the LES mode as the distance from the wall increases. The flow in the vicinity of the ribs is mostly resolved in LES mode all the way to the channel center. This includes the unsteady large-scale dynamics of the separated shear layer as shown in the figure. In the inter-rib spacing, LES is only active near the ribbed wall and transitions to a full RANS mode at the center of the channel. The spatial distribution of the two methods (LES and RANS) of resolving turbulence are consistent with the underlying principles of DES and to a large degree is facilitated by some a priori knowledge of the flow and judicious grid selection.

Flow Field Predictions. The mean flow pattern observed in the symmetry plane of the span is shown in Fig. 4. Flow patterns produced by the LES cases [2], the RANS models [1], and the experiments [4], show a similar pattern. The flow is characterized by a recirculating eddy in front of the rib, followed by shear layer

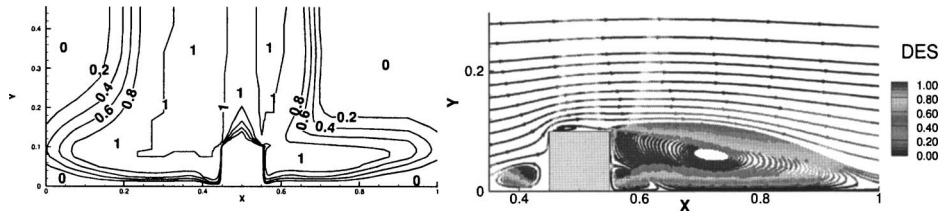

Fig. 3 Plot of the LES and RANS region in the DES computation for the 64^3 grid in a Z plane. A value of 1 represents a complete LES region and a value of 0 a complete RANS region.

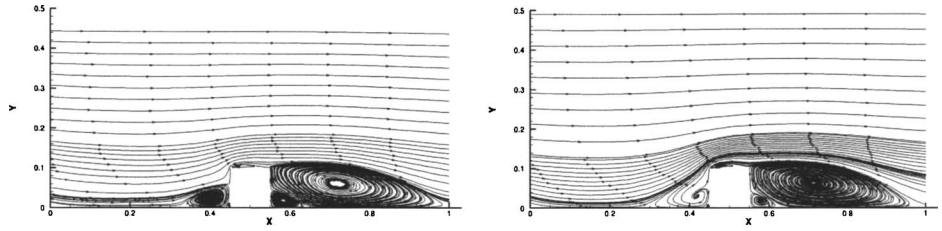

Fig. 4 Streamline plots at the center of the duct for the (*a*) *k*-ω and (*b*) Menter's SST DES calculations showing flow separation and reattachment

separation on the rib and the presence of a recirculation region on top of the rib and behind it. Between the main recirculation region and the rib there is an additional counter-rotating eddy. The reattachment length is calculated as $4.3e$ (for k-ω) and $4.1e$ (for SST) from the rib, as compared to the LES predictions of $4.1e$ and experimentally observed value of $4.0e$–$4.25e$. The prediction of the reattachment length is sensitive to the level of turbulence in the separated shear layer, so the turbulence level may be slightly underpredicted in the k-ω case, due to which the reattachment length is overpredicted.

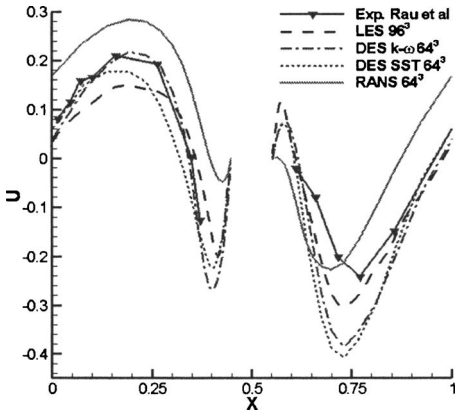

Fig. 5 Streamwise velocity distributions at the center of the duct at $Y/e=0.1$

A plot of the normalized streamwise velocities (Fig. 5) at a plane close to the floor ($Y/e=0.1$) indicates the acceleration and deceleration of the flow in the inter-rib region. The separated region behind the rib experiences a reverse flow, which is evident from the negative velocities behind the rib up to the reattachment region. The flow accelerates after reattachment and separates in front of the next rib, owing to the rise in pressure. The separation in front of the rib and the secondary reverse flow behind the rib are predicted by both DES calculations, and the velocity magnitudes are consistent with the LES calculations and the measurements. The k-ω RANS fails to predict the flow correctly in these regions.

A contour plot (Fig. 6) of the streamwise velocities in a plane passing through the rib (at $Y/e=0.25$) shows that the maximum velocities do not occur in the center of the channel but closer to the wall. The flow separation behind the ribs causes this shift. While DES successfully reproduces the trend observed by the experiments, the k-ω RANS case fails to capture the variation. Similar results were reported by Ooi et al. [1] for their RANS calculations. The DES distributions match well with the LES cases [2].

Figure 7 shows the lateral W velocities above the rib along a line close to the smooth side wall ($Y/e=1.5, Z/D_h=0.45$), as an indication of the strength of the localized secondary flow in the vicinity of the rib. The DES and the k-ω RANS calculations are compared with the measured values and LES. While RANS completely fails at resolving this feature of the flow, DES does a good

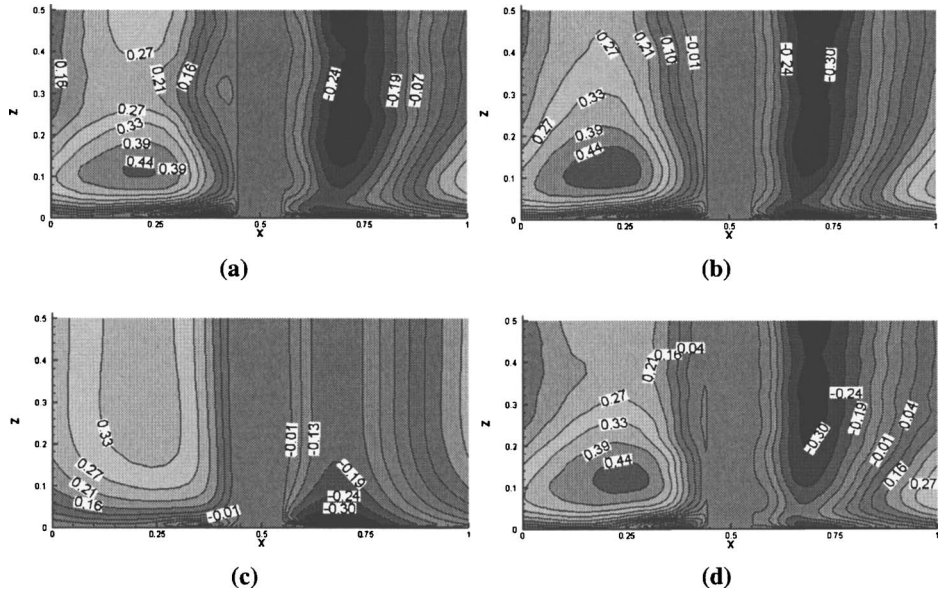

Fig. 6 Comparison of streamwise velocity distributions at $Y/e=0.25$ for the (*a*) *k*-ω DES case, (*b*) SST DES case, (*c*) *k*-ω RANS case, and (d) LES case

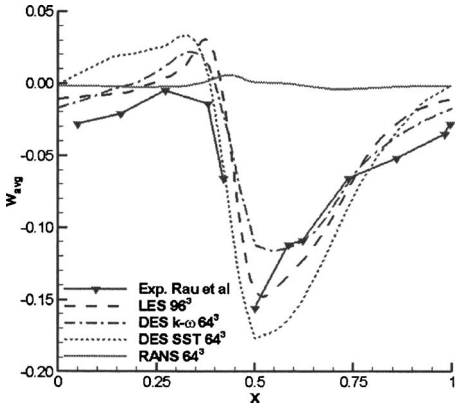

Fig. 7 Comparison of the secondary flow distribution at $Y/e=1.5$ and $Z/D_h=0.45$

job at resolving the correct distribution.

Mean secondary flow patterns in the cross-section were studied experimentally by Liou et al. [11] using LDV techniques. These secondary flow structures are strongest in the vicinity of the ribs and are generated by turbulence. The flow causes core fluid in the center of the duct to be drawn towards the side walls. The impinging secondary flow has a large effect on enhancing heat transfer. Ooi et al. [1] reported a large inconsistency between the k-ω RANS calculations and the experimental observations, resulting in large disagreement between the experimentally measured and the calculated side wall heat transfer. A similar discrepancy in the prediction of the secondary flow was observed in the k-ω RANS calculation. But the DES versions of the k-ω and the SST models predicted the secondary structures accurately (Fig. 8). Near the center of the channel there is a flow towards the ribbed walls. The flow turns near the corners and moves along the smooth walls towards the center of the channel.

Table 1 shows the percentage of form losses and friction losses (due to shear) which contribute to the overall friction factor. Rib form drag contributes substantially to overall frictional losses, as is evident from Table 1. The predicted values agree well with the form losses measured by Rau [4] at around 85% and the LES predictions of 91% by Tafti [2]. The SST-DES predicts a higher percentage at 95%. The ribbed walls and the ribs contribute negative shear losses because of the recirculating zones which act in the opposite direction, whereas the smooth walls contribute about 8%–10% of the total losses. The DES calculations resolve the small recirculation on the rib while the k-ω RANS calculation does not. However, overall all methods perform reasonably well in predicting the form and shear loss contribution to total friction losses.

The average friction factor augmentation ratios summarized in Table 2 give an estimate of the additional pressure loss incurred due to the introduction of the ribs in the duct. The average friction factor predicted by the DES schemes is very close to the experimentally measured values, and is within an accuracy of 2.5%. The k-ω RANS calculation predicts a value which is within acceptable

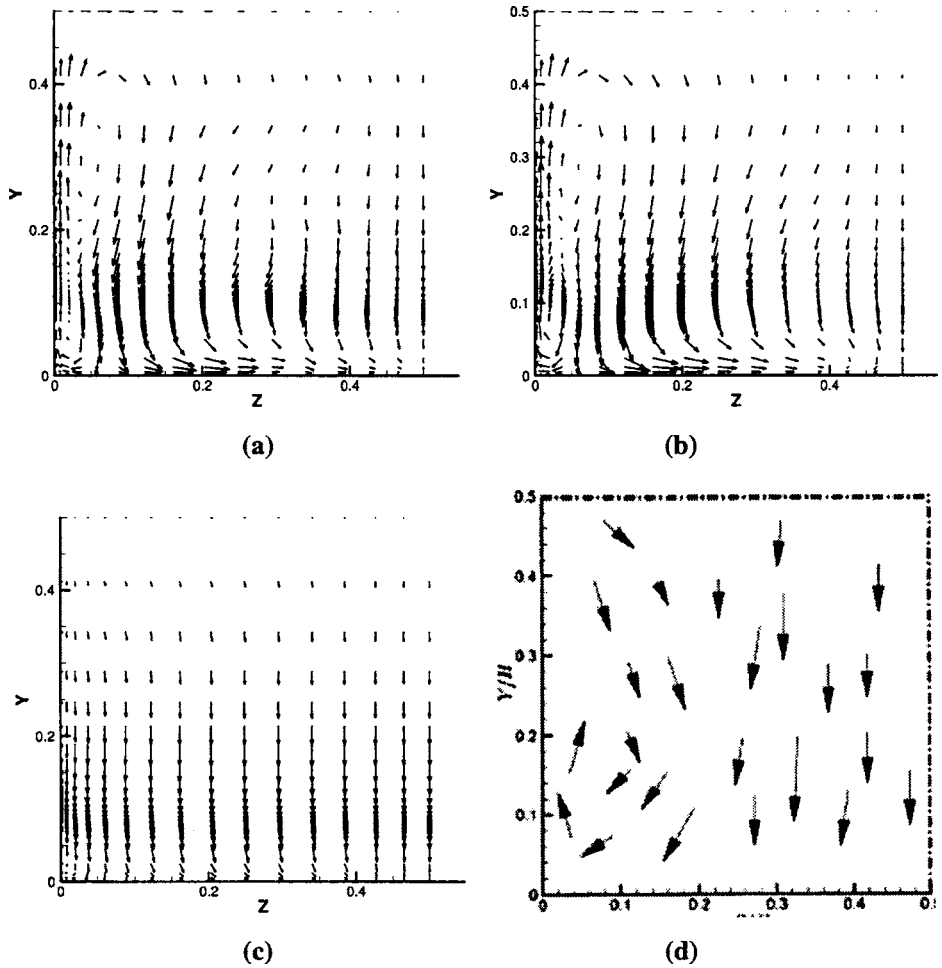

Fig. 8 Comparison of the secondary flow (*a*) predicted by DES k-ω model, (*b*) DES SST model, (*c*) k-ω RANS model, (*d*) experiment [10,11]

Table 1 Percentage form and friction losses in the ribbed duct [1]

	DES k-ω	DES SST	RANS k-ω	LES 128^3
Form Loss	91.9%	95.0%	88.0%	91.0%
Ribbed Wall friction	-2.5%	-2.5%	-1.4%	-1.7%
Smooth wall friction	7.9%	6.1%	11.8%	7.8%
Rib friction	-0.5%	-0.5%	0.3%	-0.8%

limits, even though the localized predictions are not accurate. This is due to the over-predictions in some regions compensating for other localized underpredicted values.

Heat Transfer Enhancement. Figure 9 shows the distribution of heat transfer augmentation at the ribbed wall and the smooth walls of the duct. The augmentation ratio is high in front of the rib as a result of the unsteady vortices in this region. These secondary vortices continuously transport cooler fluid from the mainstream to the ribbed wall increasing the heat transfer coefficient. Immediately behind the rib, a secondary recirculation is trapped between the wall and the primary recirculation zone. Although the action of the secondary eddy causes some localized augmentation in this region, the overall augmentation is low and similar to that in a smooth duct. Further downstream, the heat transfer coefficient increases steadily as the vortices from the separated shear layer impinge on the wall. The heat transfer reaches a maximum value at about 3.5*e* downstream of the rib, which is upstream of the mean reattachment line and coincides with the region of maximum shear. In the spanwise direction, the heat transfer does not show much variation. However, on moving closer to the smooth walls the heat transfer augmentation drops and the minimum heat transfer is observed at the corners formed by the ribbed and the smooth walls. Heat transfer augmentation on the smooth walls is dominated by secondary flow impingement at the top upstream corners of the rib, and decreases towards the center of the channel.

Table 2 Comparison of the overall heat transfer augmentation and the friction factor

	LES 128^3	DES k-ω	DES SST	RANS k-ω	Rau *et al.*
Nu/Nu_0 Ribbed Wall	2.4	2.17	2.35	2.14	2.4
Error	*0.0%*	*9.4%*	*2.1%*	*10.6%*	
Nu/Nu_0 Side Wall	1.89	1.89	1.86	1.83	2.05
Error	*7.7%*	*7.7%*	*9.2%*	*10.8%*	
Nu/Nu_0 Ribs	2.89	2.40	2.41	2.38	
f/f_0	8.60	9.30	9.56	8.76	9.50
Error	*9.4%*	*2.1%*	*-0.5%*	*7.8%*	

The distribution of augmentation ratios on the ribbed wall is plotted in Figs. 10 and 11(*a*) along the centerline. Both DES calculations are consistent with LES and experiments in reproducing the spatial distribution of augmentation ratios, whereas the distribution predicted by RANS is quite different. RANS fails to resolve the secondary eddy behind the rib and its associated effect on augmentation. It also fails to resolve the high augmentation at the front of the rib. These shortcomings can be clearly identified in Fig. 11(*a*) at the center of the channel, in which the augmentation predicted by RANS immediately before and after the rib is much lower than the other methods. Ooi et al. [1] observed a similar trend. Both DES calculations resolve these features. However, the DES calculations fail to sustain the high augmentation after reattachment at the centerline. While the SST model does reach a maximum augmentation of 3 at the centerline, the *k-ω* model only reaches a value of 2.6 compared to 3 in the experiments and LES. This could be a consequence of the predominance of the RANS mode of computation in the inter-rib spacing (Fig. 3). On the other hand, the RANS calculation, in spite of severe shortcomings in predicting the salient features, predicts the augmentation in the inter-rib spacing quite well.

While the heat transfer on the ribbed wall is enhanced due to the streamwise flow, the secondary flow impingement plays a major role in the heat transfer on the side walls. Predictions on the smooth side walls also show the inefficiency of linear eddy-viscosity RANS in Figs. 11(*b*) and 12. The *k-ω* RANS calculation fails to capture the augmentation at the upstream corner of the rib

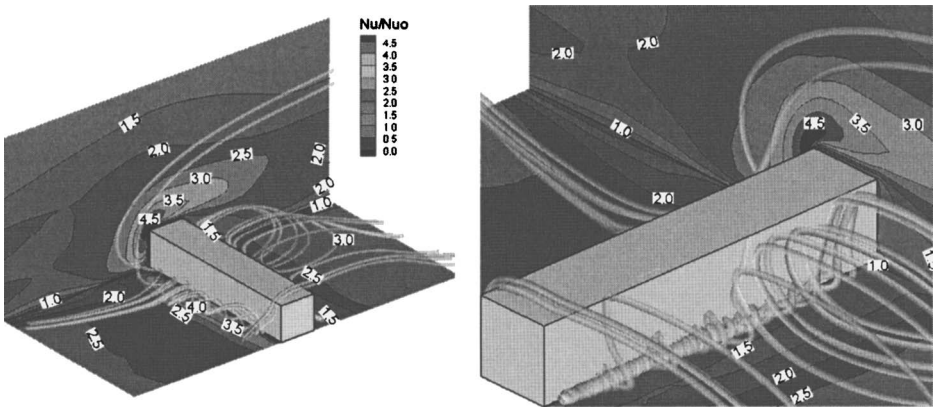

Fig. 9 Streamlines showing the recirculation region in front of the rib and primary and secondary circulations behind the rib and their effect on heat transfer on the walls. Red regions represent high heat transfer, while blue regions represent low heat transfer.

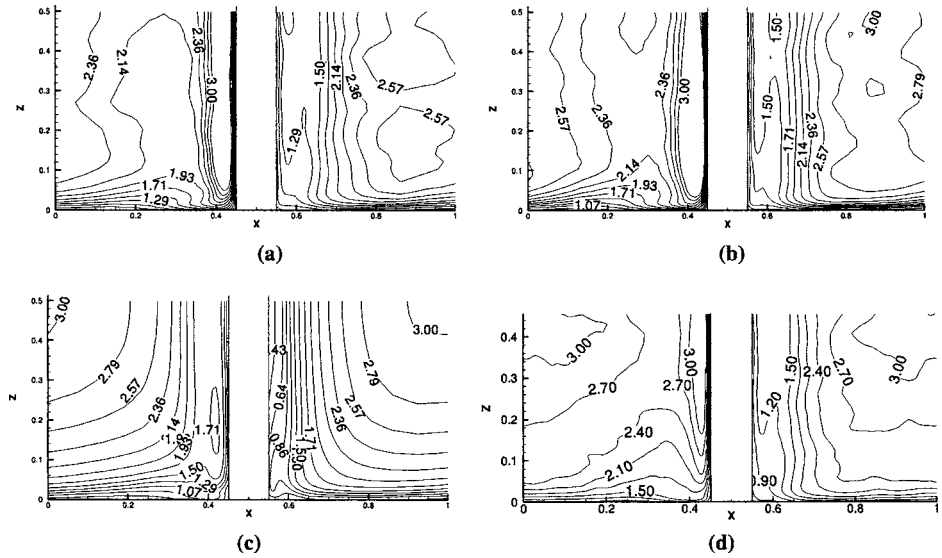

Fig. 10 Comparison of augmentation ratios on the ribbed floor for the (*a*) *k-ω* DES case, (*b*) Menter's SST DES case, (*c*) *k-ω* RANS case, and (*d*) LES case

which is caused by the secondary flow impingement. On moving away from the ribbed walls the enhancement ratio is almost constant in *k-ω* RANS, in contrast to the experimental observations, in which the heat transfer decreases on moving towards the center of the channel. The DES predictions capture the high heat transfer near the rib and also show the decreasing trend in heat transfer.

Table 2 shows the surface averaged augmentation ratios at the ribbed wall, smooth wall and the ribs in comparison to experimental values. All prediction techniques are within 10% of the experiments. However, it is noted that the good agreement of the *k-ω* RANS model is fortuitous and is brought about by a cancellation of errors.

Conclusions

DES and RANS computations are presented in a square duct with normal ribs. The domain is discretized using a 64^3 grid and the computations are compared to the experimental mean and turbulent flow calculations and heat transfer results obtained by Rau et al. [4] and LES computations by Tafti [2].

From the computations performed, the following conclusions can be derived:

(1) The average flow characteristics are predicted with good accuracy by the DES computations. DES accurately captures the recirculation regions in front of the rib, behind the rib, and on top of the rib. Owing to the accurate prediction of the main flow characteristics, the heat transfer on the ribbed wall, which is triggered mostly by the main flow, is also predicted with reasonable accuracy.

(2) The secondary flow is also accurately captured by the DES computations, while *k-ω* RANS fails to capture the secondary flow. Consequently, the heat transfer augmentation on the side walls is predicted with good accuracy by DES, whereas the *k-ω* RANS calculation fails to accurately capture the side wall heat transfer.

(3) The overall flow characteristics and heat transfer predicted by DES agree well with the LES computations and the experimental results, at approximately one-tenth the computational cost of LES.

(4) RANS models with known limitations perform better in the DES framework than they would normally in the RANS or URANS framework.

(5) By directly resolving more of the turbulent energy, DES, as

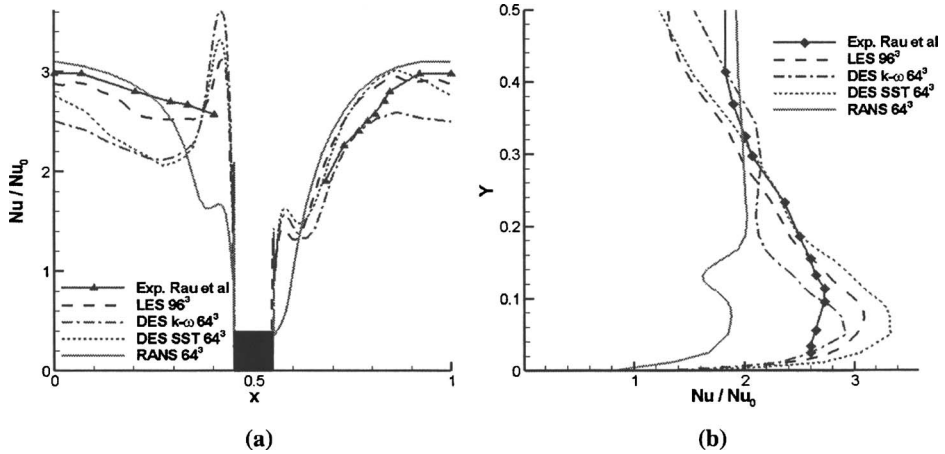

Fig. 11 Comparison of the augmentation ratios (*a*) at the center of the ribbed floor and (*b*) side walls upstream of the rib

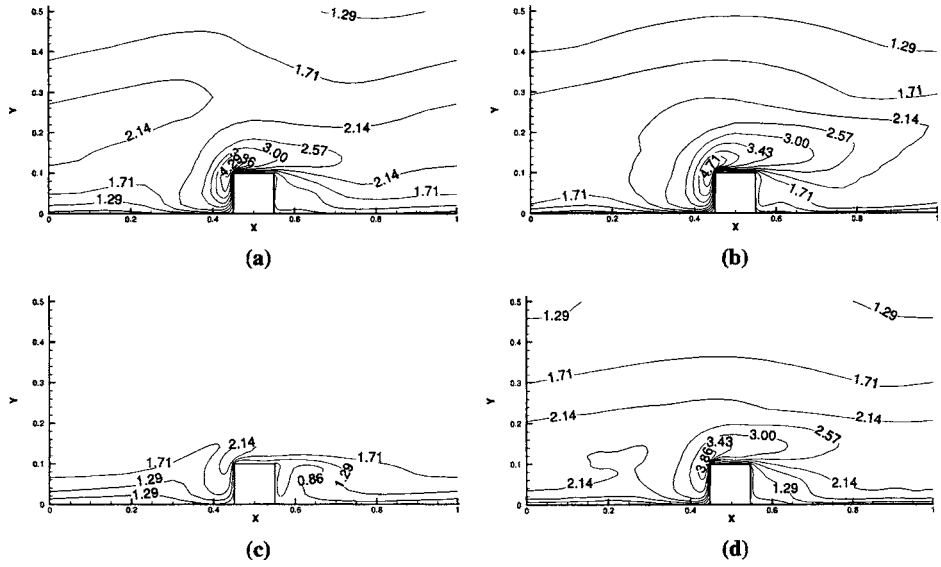

Fig. 12 Comparison of the heat transfer augmentation ratios on the side walls (*a*) *k-ω* DES, (*b*) Menter's SST DES, (*c*) *k-ω* RANS, and (*d*) LES

with LES, is less dependent on the base RANS modeling capability.

Acknowledgments

This research was supported by the U.S. DOE, Office of Fossil Energy, and National Energy Technology Laboratory. Any opinions, findings, conclusions, or recommendations expressed herein are those of the authors and do not necessarily reflect the views of the DOE. The authors would like to acknowledge Dr. Patrick Hu who was responsible for the initial implementation of DES.

Nomenclature

D_h = hydraulic diameter (characteristic length)
e = rib height
f = fanning friction factor, $f=1/2\cdot\bar{u}_b^2$
f_0 = friction factor in a smooth channel, $f_0=0.046\cdot \mathrm{Re}_b^{-0.2}$
k = thermal conductivity
Nu = local Nusselt number $\mathrm{Nu}=1/(\theta_s-\theta_{\mathrm{ref}})$
$\langle \mathrm{Nu}\rangle$ = spatially averaged Nusselt number $\langle \mathrm{Nu}\rangle=(\iint_A 1/(\theta_s-\theta_{\mathrm{ref}})dA)/(\iint_A dA)$
Nu_0 = Nusslet number in a smooth channel, $\mathrm{Nu}_0=0.023\cdot \mathrm{Re}_b^{0.8}\cdot \mathrm{Pr}^{0.4}$
P = rib pitch
q'' = nondimensional heat flux on duct walls and rib
Q_x = Calculated nondimensional flow rate in streamwise direction
Re = Reynolds number based on bulk velocity
Re_τ = Reynolds number based on friction velocity
$\mathbf{u}$ = Cartesian velocity vector
$\bar{u}_b$ = mean bulk flow velocity (characteristic velocity)
u_τ = friction velocity
$\mathbf{x}$ = physical coordinates
β = mean nondimensional pressure gradient
γ = mean nondimensional temperature gradient
θ = fluctuating, modified or homogenized nondimensional temperature
Ω = heat transfer surface area
$\vec{\xi}$ = computational coordinates

Subscripts

s = surface
b = bulk
o = smooth duct
t = turbulent parameters

References

[1] Ooi, A., laccarino, G., Durbin, P. A., and Behnia, M., 2002, "Reynolds Averaged Simulation of Flow and Heat Transfer in Ribbed Ducts," Int. J. Heat Fluid Flow, **23**, pp. 750–757.
[2] Tafti, D. K., 2005, "Evaluating the Role of Subgrid Stress Modeling in a Ribbed Duct for the Internal Cooling of Turbine Blades," Int. J. Heat Fluid Flow, **26**(1), pp. 92–104.
[3] Spalart, P. R., Jou, W. H., Streletes. M., and Allmaras. S. R., 1997, "Comments on the Feasibility of LES for Wings and a Hybrid RANS/LES Approach," *First AFSOR Int. Conf. on DNS/LES, August 4–8, 1997, in Advances in DNS/LES*, C. Liu and Z. Liu, eds., Greyden, Columbus, OH.
[4] Rau, G., Cakan, M., Moeller, D., and Arts, T., 1998, "The Effect of Periodic Ribs on Local Aerodynamic and Heat Transfer Performance of a Straight Cooling Channel," ASME J. Turbomach., **120**, pp. 368–375.
[5] Han, J. C., Park, J. S., and Lei. C. K., 1985 "Heat Transfer Enhancement in Channels With Turbulence Promoters," J. Eng. Gas Turbines Power, **107**, pp. 628–635.
[6] Han, J. C. and Lei, C. K., "Heat Transfer and Friction in Square Ducts With Two Opposite Rib-roughened Walls," ASME Paper No. 83-HT-26.
[7] Han, J. C., 1984, "Heat Transfer and Friction in Channels With Two Opposite Rib-roughened Walls," J. Heat Transfer, **106**, No. 4, pp. 774–782.
[8] Han, J. C., 1988, "Heat Transfer and Friction in Rectangular Channels With Rib Turbulators," ASME J. Heat Transfer, **110**, pp. 321–328.
[9] Han, J. C., Dutta, S., and Ekkad, S. V., 2000, *Gas Turbine Heat Transfer and Cooling Technology*, Taylor and Francis, NY.
[10] Liou, T. M., Hwang, J. J., and Chen, S. H., 1992, "Turbulent Transport Phenomena in a Channel With Periodic Rib Turbulators," J. Thermophys. Heat Transfer, **6** (3), pp. 513–521.
[11] Liou, T. M., Wu, Y. Y., and Chang, Y., 1993, "LDV Measurements of Periodic Fully Developed Main and Secondary Flows in a Channel With Rib-disturbed Walls," ASME J. Fluids Eng., **115**, pp. 109–114.
[12] Sato, H., Hishida, K., and Maeda, M., 1989, "Turbulent Flow Characteristics in a Rectangular Channel With Repeated Rib Roughness," Heat Transfer in Convective Flows, **107**, pp. 191–196.
[13] Yokosawa, H., Fujita, H., and Iwata, S., "1989, Measurement of Turbulent Flow in a Square Duct With Roughened Walls on Two Opposite Sides," Int. J. Heat Fluid Flow, **10**(2), pp. 125–135.
[14] Prakash, C., and Zerkle, R., 1995, "Prediction of Turbulent Flow and Heat Transfer in a Ribbed Rectangular Duct With and Without Rotation," ASME J. Turbomach., **117**, pp. 255–264.
[15] Jia, R., Saidi, A., and Sunden, B., "Heat Transfer Enhancements in Square Ducts With V-Shaped Ribs of Various Angles," in *Proceedings of the ASME Turbo Expo*, GT 2002-30209.

[16] Saidi, A., and Sunden, B., 2001, "On Prediction of Thermal-Hydraulic Characteristics of Square-Sectioned Ribbed Cooling Ducts," ASME J. Turbomach., **123**, pp. 614–620.
[17] Iacovides, H., 1998, "Computation of Flow and Heat Transfer through Rotating Ribbed Passages," Int. J. Heat Fluid Flow, **19**, pp. 393–400.
[18] Iacovides, H., and Raisee, M., 1999, "Recent Progress in the Computation of Flow and Heat Transfer in Internal Cooling Passages of Turbine Blades," Int. J. Heat Fluid Flow, **20**, pp. 320–328.
[19] Murata, A., and Mochizuki, S., 2001, "Comparison Between Laminar and Turbulent Heat Transfer in Stationary Square Ducts With Transverse or Angled Rib Turbulators," Int. J. Heat Mass Transfer, **44**, pp. 1127–1141.
[20] Watanabe, K., and Takahashi, T., 2002, "LES Simulation and Experimental Measurement of Fully Developed Ribbed Channel Flow and Heat Transfer," *Proceedings of the ASME Turbo Expo*, Amsterdam, The Netherlands.
[21] Abdel-Wahab, S., and Tafti, D. K., 2004, "Large Eddy Simulation of Flow and Heat Transfer in a 90° Ribbed Duct With Rotation: Effect of Corolis and Centrifugal Buoyancy Forces," J. Turbomach., **126**(4), pp. 627–636.
[22] Abdel-Wahab, S., and Tafti, D. K., "Large Eddy Simulation of Flow and Heat Transfer in a Staggered 45° Ribbed Duct," *ASME Turbo Expo: 2004*, Vienna, Austria, GT2004-53800.
[23] Sewall, E. A., and Tafti, D. K., 2004, "Large Eddy Simulation of the Developing Region of a Stationary Ribbed Internal Turbine Blade Cooling Channel," *ASME Turbo Expo*, Vienna, Austria. GT2004-53832.
[24] Sewall, E. A., Tafti, D. K., 2004, "Large Eddy Simulations of the Developing Region of a Rotating Ribbed Internal Turbine Blade Cooling Channel," *ASME Turbo Expo*, Vienna, Austria. GT2004-53833.
[25] Strelets, M., "Detached Eddy Simulation of Massively Separated Flows," AIAA 2001-0879.

Detached-Eddy Simulation of High-Reynolds-Number Beveled-Trailing-Edge Boundary Layers and Wakes

Eric G. Paterson
e-mail: eric-paterson@psu.edu

Leonard J. Peltier
e-mail: peltierlj@psu.edu

Computational Mechanics Division, Applied Research Laboratory and Department of Mechanical and Nuclear Engineering, The Pennsylvania State University, State College, P.O. Box 30, PA 16804, USA

Flow over three different trailing-edge geometries is studied using incompressible detached-eddy simulation and unsteady Reynolds-averaged Navier Stokes CFD methods. Of interest is the ability of DES, coupled, with localized overset-grid refinement, to resolve the proper physics of separated flows from trailing edges—trailing-edge turbulence and vortex shedding, in particular. The DES model is shown to provide a good qualitative description of the trailing-edge flow. However, the modeled separations are overly energetic due to premature separation related to artificially low turbulence levels from upstream. The transition from RANS to DES is isolated as an issue. The simulated physics of the wake are shown to be in agreement with other LES studies: the model produces the "rib/roller" structures representing the first instability modes, horseshoe vortices are observed, and in regions of high resolution, small scales are formed, as expected. The turbulence statistics are qualitatively similar to benchmark data near the trailing edge and in the near wake, however, quantitative comparisons of u_{rms} show an over prediction in magnitude of 50%–100%. Despite this, the results are promising, and future modeling efforts have been motivated and identified. [DOI: 10.1115/1.2012501]

Introduction

Prediction of hydroacoustics and vibration associated with lifting surfaces, rotating machines, and turbulent nozzle flows is of critical importance for design of quiet machinery. Since direct numerical simulation of this coupled problem does not appear possible in the foreseeable future, engineering tools have been developed which separately model flow-induced sources due to turbulence ingestion [17], turbulent boundary-layer forcing [24], and trailing-edge vortex shedding [22]. These models currently rely upon Reynolds-averaged Navier-Stokes (RANS) computational fluid dynamics (CFD) to set mean flow field properties such as turbulence intensity, inflow distortions, and mean surface pressure and represent a range of empirical and first-principle methods. The goal of the work presented here is to bring higher-fidelity CFD methods to the problem of trailing-edge hydroacoustics.

Trailing-edge hydroacoustics is a phenomenon which contributes to the overall acoustic signature. Having been studied for nearly 50 years [6], the historical approach is to decompose the problem into two separate sources; a broadband component due to turbulent boundary layer being scattered by the trailing edge, and a tonal component due to vortex shedding, the latter of which can lead to a hydroacoustic structural resonance known as singing.

Previous CFD studies of trailing-edge flow includes the use of URANS [15] and LES methods [34,33], both of which showed limitations in solving the overall problem. URANS simulations accurately resolved the organized shedding frequency for some trailing-edge shapes, but separation details were sensitive to the turbulence model. Full LES [34] was applied to one of the trailing edges studied herein. A small domain (38% of the foil and 1/2 strut thickness in the spanwise direction) was used and inflow conditions were diagnosed from RANS with turbulence scales in the boundary layer extracted from flat-plate LES. Mean-field and low-order turbulence statistics compared reasonably well with existing experimental data [5], though some discrepancies were found. The limited domain size, inadequate inflow conditions, and experimental error were identified as possible explanations. The computational resource requirements for the simulation were fairly high. A wall-resolved calculation required nearly 10^7 grid points and about 42 CPU-days of integration time. An overall 90% reduction in CPU time can be achieved with 80% reduction in grid resolution using a RANS-type, near-wall, approximate boundary condition, without loss of solution fidelity [33].

Clearly, the primary challenge to practical use of LES remains computational resources. To capture the fluctuating lift from vortex shedding, a LES grid would need to resolve the entire foil geometry. Furthermore, the spanwise extent of the computational domain ideally would be increased to ensure no spurious correlations of the spanwise flow. Based on grid and CPU usage for LES [33], the resource cost of a full calculation would be large, even with the benefits of the approximate near-wall conditions. Simulations for more complicated geometries would be even more demanding. More efficient solution strategies are required for LES-type solutions to become part of an industrial/applied research tool kit in the near term.

Recently, hybrid RANS/LES models have been advanced that seek to benefit from the computational economy of RANS but give the higher-fidelity of LES in regions of interest. Hydroacoustics, which motivates our work, is one field where turbulence data are required, but which are not directly provided by RANS.

Speziale's [30] RANS/VLES and Spalart's [29] detached-Eddy simulation (DES) are the original prescriptions for the hybrid RANS/LES solution strategies that underlie most recent work. Both techniques interpret the filter scale of the governing equations in terms of the local grid scale. LES is allowed locally when the grid resolution is fine enough to support turbulence fluctuations. Elsewhere the solution is RANS. Speziale did not fully specify the transfer function relating the RANS turbulence diffusivity to a local value. His work, though, has motivated several variants such as flow simulation methodology [14], limited numerical scales model [2], and hybrid RANS/LES [26]. DES has

Contributed by the Fluids Engineering Division for publication in the JOURNAL OF FLUIDS ENGINEERING. Manuscript received by the Fluids Engineering Division July 27, 2004; Final revision: May 10, 2005. Associate Editor: Ismail Celik.

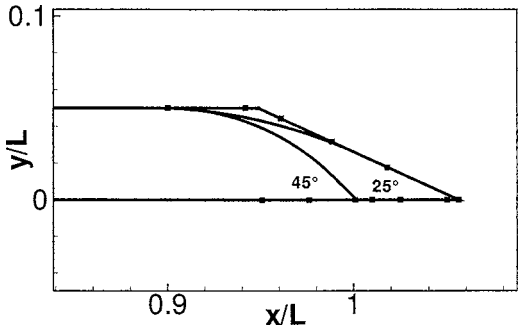

Fig. 1 Geometry of trailing-edge variants

been extended for two-equation $k-\omega/k-\varepsilon$ models [31], grid-resolution-independent length scales [19], and zonal formulation [27].

Recent literature is rich with successes of hybrid RANS/LES for massively separated flows, see [9,10,13,20] as examples. Experience with hybrid RANS/LES methods for boundary layers is not as successful. An implementation of DES has been successfully used as a subgrid model for turbulent channel flow [21]; however, another implementation [19] failed to support turbulence. Implementation specific choices, then, influence a DES model as do grid generation decisions.

Spalart [28] in his guideline for generation of DES grids, speaks of "gray areas" in computations where the model's response to the underlying grid does not yield either a fully LES or a fully RANS solution. The principle concern in these regions is lost physics. For example, in the transition from a RANS region near a wall to a LES region in a flow, the modeled Reynolds stresses are intended to be replaced by resolved stresses. The resolved stresses though do not evolve instantly, so a region will exist lacking appropriate LES content that may seriously degrade the fidelity of the numerical solution. Menter [19] has described one aspect of this dysfunction in the modeling of the RANS to LES transition as "grid-induced separation."

The objectives of the current investigation are to apply a recently developed DES model to the problem of a lifting-surface trailing-edge flow and wake, and compare solutions to benchmark data. The goal is to demonstrate the ability of DES, coupled with localized overset-grid refinement, to capture energy-containing turbulent eddies for complete geometries at high Reynolds numbers, undertake detailed analysis to understand strengths and weaknesses of the approach, and identify/motivate future model development.

Model Problem

The model problem studied here corresponds to the experiments conducted by Blake [5], wherein a flat strut with a family of trailing-edge shapes was tested in an anechoic wind tunnel. While modern validation experiments have recently been conducted [8,7], this work remains a valuable comprehensive validation database due to its simple geometry and family of trailing-edge shapes which produce both random and periodic wakes, and due to the fact that a number of associated CFD studies have previously been undertaken [11,15,33,34].

The geometry is a flat strut with a circular leading edge and a nominal length and thickness of 36 and 2 in., respectively. Three trailing edges, which are shown in Fig. 1, are studied in this paper: 25° bevel, 25° knuckle, and 45° bevel. The edges add 6.25 and 4 in. to nominal length of 36 in. to give an overall length of 42.25 in. for the 25° bevel/25° knuckle and 40.0 in. for the 45° bevel.

Simulation flow conditions are set to the experimental conditions where $U_0=100$ ft/s (30.48 m/s) and viscosity $\nu=1.6\times10^{-4}$ ft^2/s (1.5×10^{-5} m^2/s). Using a common length scale $L=40$ in. (1.016 m) for all cases, the Reynolds number is set to $\mathrm{Re}=U_0L/\nu=2.04\times10^6$. It is assumed that freestream turbulence is negligible.

Detailed data include boundary layer profiles, chordwise distributions of pressure, Strouhal number as a function of Reynolds number, and cross-spectral densities and cross correlations of surface pressure. To compare with CFD, data are extracted from the original report by scanning individual figures and using the g3data data-extraction program [12].

Flow Code

CFDSHIP. [23] serves as the core flow solver for the RANS and DES computations. The core algorithm and recent DES model development is described in the following sections.

Unsteady RANS. CFDSHIP is a general-purpose parallel unsteady incompressible Reynolds-averaged Navier–Stokes (RANS) CFD code. The computational approach is based upon fully implicit, structured overset grid, higher-order finite-difference, and pressure-implicit split-operator (PISO) numerical methods. The production turbulence model uses a linear closure and the blended $k-\omega/k-\varepsilon$ SST 2-equation model [18]. Efficient parallel computing is achieved using coarse-grain parallelism via MPI distributed computing. For time-accurate unsteady simulations, global solution of the pressure-Poisson equation is achieved using preconditioned GMRES and the PETSc libraries [1].

Detached-Eddy Simulation. DES [31] is a three-dimensional unsteady numerical method using a single turbulence model, which functions as a subgrid-scale model in regions where the grid density is fine enough for a LES, and as a RANS model in all other regions. Implementation of DES was accomplished by modifying the turbulence model and convective-term discretization. The turbulence model is modified by introducing a DES length scale

$$\tilde{\ell} = \min(\ell_{k\omega}, C_{\mathrm{DES}}\Delta), \tag{1}$$

which compares the turbulence length scale from RANS, $\ell_{k\omega}$, to the local grid size, Δ, where Δ is based on the largest dimension of the local grid cell:

$$\ell_{k\omega} = \frac{k^{1/2}}{\beta^*\omega}, \quad \Delta = \max(\delta_x, \delta_y, \delta_z). \tag{2}$$

C_{DES} is a model constant with a value between 0.78 and 0.61 weighted by the Menter $k-\omega/k-\epsilon$ blending function [18]. The new length scale $\tilde{\ell}$ replaces $\ell_{k\omega}$ in the dissipative term of the k transport equation

$$D^k_{\mathrm{RANS}} = \rho\beta^* k\omega = \frac{\rho k^{3/2}}{\ell_{k\omega}} \Rightarrow D^k_{\mathrm{DES}} = \frac{\rho k^{3/2}}{\tilde{\ell}}. \tag{3}$$

The effect of this modification is to increase dissipation in LES regions such that the turbulence budget shifts energy from subgrid, or modeled, scales, to resolvable scales as defined by the filter width $C_{\mathrm{DES}}\Delta$.

The second modification aims to reduce numerical dissipation inherent in the upwind convective–term discretization scheme. The implemented approach is based upon a hybrid central/upwind approximation of the convective terms:

$$F_{inv} = (1-\sigma)F_{ctr} + \sigma F_{upw} \tag{4}$$

where σ is defined as

$$\sigma = \max\left[\tanh\left(\frac{C_{\mathrm{DES}}\Delta}{l_{k\omega}}\right)^n, \tanh\left(\frac{|U|\Delta t}{\Delta}\right)^m\right]. \tag{5}$$

The result is that σ smoothly transitions between 1.0 in the RANS regions, resulting in a local upwind scheme, and near 0.0 in the LES regions, where a centered scheme is desired. In addition, a

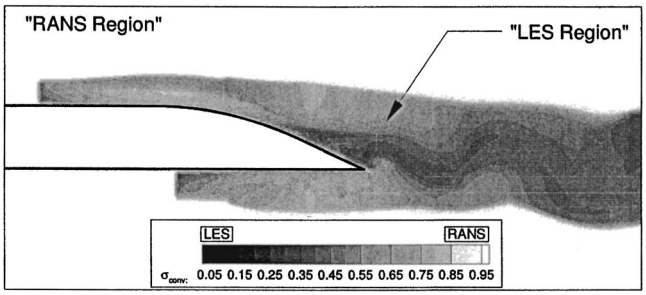

Fig. 2 Typical σ contours

Courant-number constraint of 1.0 has been imposed which requires that the time step be sufficiently small to support turbulent eddies. The coefficients n,m permit the interface between RANS and LES regions to be arbitrarily "sharpened," however, currently we use $n=m=1$ due to the fact that higher-order coefficients have resulted in unstable simulations.

Figure 2 shows contours of σ for our 25° bevel case. The "white" region is interpreted by the code to be URANS. DES is active in the "gray/black" region. Note the abrupt transition from RANS to DES upstream of the bevel on the pressure and suction sides in response to an abrupt increase in local grid resolution. A thin-band of white is observed near the foil surface, indicating that the near-wall boundary-layer is modeled by URANS, as desired.

The convective terms are discretized with the following higher-order upwind formula

$$U^k\frac{\partial\phi}{\partial\xi_k}=\frac{1}{2}(U^k+|U^k|)\delta^-_{\xi_k}\phi+\frac{1}{2}(U^k-|U^k|)\delta^+_{\xi_k}\phi. \tag{6}$$

The discrete upwinding operators $\delta^-_{\xi_k}$ and $\delta^+_{\xi_k}$ are calculated using a 5 point stencil

$$\delta^-_{\xi_i}\phi=W_{mm}\phi_{i-2}+W_m\phi_{i-1}+W_n\phi_i+W_p\phi_{i+2}+W_{pp}\phi_{i+2} \tag{7}$$

$$\delta^+_{\xi_i}\phi=-W_{pp}\phi_{i-2}-W_p\phi_{i-1}-W_n\phi_i-W_m\phi_{i+2}-W_{mm}\phi_{i+2},$$

with the coefficients W_i defined as a weighted sum of the coefficients w_i for the fourth-order central and the second-order upwind schemes, $W_i=(1-\sigma)w_i^{4c}+\sigma w_i^{2u}$.

Finally, as discussed in the following section, it is noted that CFDSHIP is an overset-grid capable CFD code with an interface to PEGASUS 5.1 [32]. This capability will be exploited to perform local grid refinement and flow adaptation in the wake and LES regions.

Grid Generation, Computational Parameters, and Boundary Conditions

The computational domain extends from $-1.0\leqslant x/L\leqslant 2.0$, $-1.5\leqslant y/L\leqslant 1.5$, and $0.0\leqslant z/L\leqslant 0.2$, the latter of which is 4 times the strut thickness. Strelets [31] reports that the minimum domain width for a NACA0012 airfoil at high angle of attack must be comparable to the chord. For that case the separated zone scaled with the chord length. In the current study, the separated zone, and thus the domain width, is expected to scale with the trailing-edge-bevel length, not the strut chord length. We believe that our domain width of 4 times the strut thickness is likely close to the minimum one required for a transverse correlation length to be resolved.

Near-wall spacing was set to $y/L=1.0\times10^{-5}$, which is an estimate based upon a turbulent flat plate boundary layer, $\mathrm{Re}=2.04\times10^6$, and a target $y^+=1$. The expected dimensionless boundary-layer thickness approaching the trailing edge, based on a flat-plate estimate, is $\delta\approx0.02$ (see Fig. 11(*a*)). The wake refinement grid was designed to have nearly isotropic cells with $\Delta=0.0025$. We note that our grid generation choices were made to ensure sufficient resolution of turbulence scales in the separated zone while retaining a RANS-like resolution of the boundary layer. The practical result that $\delta>\Delta$ hints at a potential Menter-type [19] grid-induced separation problem.

Grids were generated using hyperbolic and translational extrusion capabilities of the Gridgen software from Pointwise, Inc. This process produces high-quality nearly-orthogonal cells.

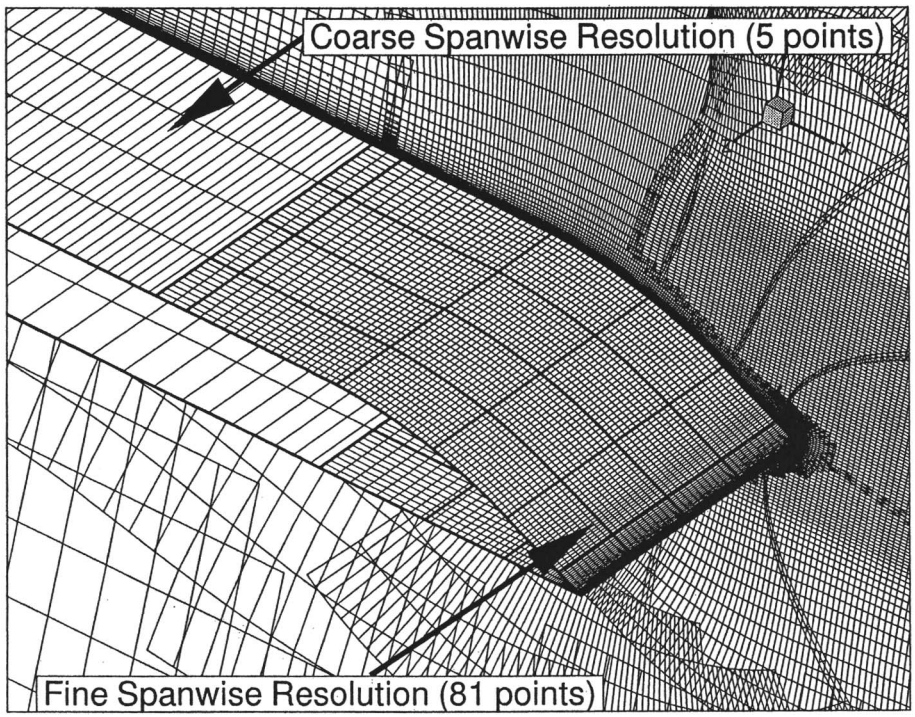

Fig. 3 Surface grid illustrating spanwise resolution in RANS and DES regions

Table 1 Typical CPU times for 10 000 time-step DES simulation

	Mins/time-step	Wall-clock (h)	Total cpu (h)
SCI origin 3800	1.4	235	18 369
IBM NH-2 SMP P3	1.1	178	13 845
IBM P3	1.8	295	23 067

As shown in Fig. 3, our use of an overset grid method allows us to use very different spanwise resolutions to resolve the RANS and LES domains. On the fore- and midbody and in the farfield, only five points are used to span the z direction of the domain. In contrast, in the LES region, 81 uniformly spaced points are used. Spalart [28] noted the advantage in terms of computational resource savings of this approach.

Another benefit of using overset grids is that for the three trailing-edge variants, only the blocks on the trailing edge have to be modified. For the 25° edges, the overall grid consists of 78 blocks with a total of 3 382 215 points and a maximum block size of 52 521 points. Since the 45° edge is physically smaller, its grid system contains 66 blocks with 2 905 935 points and a maximum block size of 52 521 points.

Algorithm-related parameters to control the simulation include: second-order upwind convective scheme for the RANS regions; second-order in time; PETSc GMRES solver; 50 subiterations maximum for momentum and turbulence equations; 3 PISO steps; 250 subiterations maximum for pressure-Poisson equation; and convergence criteria of 10^{-4} for momentum (residual based upon change between iterations) and 10^{-3} for pressure (normalized residual based upon error of the discrete equation). Flow-related parameters include $\mathrm{Re}=2.04\times10^{6}$; and dimensionless time steps $\Delta t^{\star}=U_0\Delta t/L=0.0025$, 0.001 25, 0.000 612 5. Note that a time-step study was performed only for the 25° bevel and that all other simulations were performed only with the coarse time step $\Delta t=0.0025$.

All grid systems contain a mixture of overset and pointwise-continuous multiblock boundary interfaces. For the overset boundaries, PEGASUS 5.1 [32] is used to compute double-fringe interpolation coefficients for all outer- and hole-boundary fringe points. Level-2 interpolation is used to minimize overlap and improve interpolation quality.

Remaining boundaries are prescribed to be either no-slip, inlet, far-field, or exit conditions. Details of these conditions are provided in the CFDSHIP users manual [23]. It is noted that all boundary conditions, including the overset-grid trilinear-interpolation formula, are built directly into the global coefficient matrix for the pressure-Poisson equation which results in significant acceleration of the iterative convergence.

Results

In this section, computing resources used to obtain the results are first described. Then, the results are discussed using flow-field visualizations, and statistical and Fourier analysis as a means to explain the simulated flow physics.

Computing Resources. Simulations were performed on three machines: SGI Origin 3800 with 512 R12000 (400 MHz) processors and total memory of 384 GB at ARL-MSRC; IBM NH-2 SMP P3 with 1024 Power3 (375 MHz) processors and total memory of 1024 GB at ARL-MSRC; and IBM P3 with 528 RS/6000 (375 MHz) processors and total memory of 528 GB at ASC-MSRC. Typical CPU times for DES are shown in Table 1. Total CPU time used for this study was ~100 000 h.

Instantaneous Flow Field. The instantaneous flow fields for URANS simulations are shown in Fig. 4, which plots contours of the axial-component of velocity. It is shown that the 45° bevel and 25° knuckle are unsteady and shed vortices, whereas the 25° bevel converges to a steady solution, the latter of which is consistent with the original experiment. Although not shown, all three cases display two-dimensional flow fields.

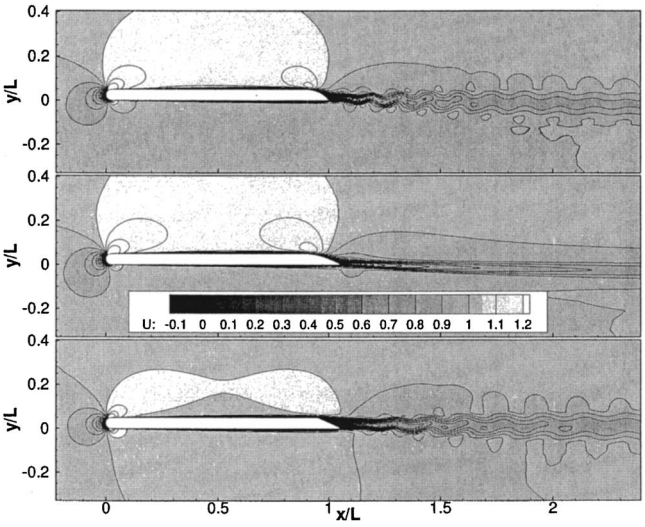

Fig. 4 Instantaneous URANS axial-velocity contours for 45° bevel, 25° bevel, and 25° knuckle

Figures 5 and 6 are visualizations of the DES flow fields using isosurfaces of the intrinsic swirl parameter [4] shaded by normalized helicity. The intrinsic swirl parameter is based upon a ratio of the local rotational to convective time scales for a fluid parcel and effectively extracts vortical structures. Normalized helicity ranges from −1.0 (light gray) to 1.0 (black) and indicates direction of rotation and eddy alignment with flow vector.

Together, these figures show that, for all three edges, the first two instability modes have been resolved, i.e., spanwise rollers and longitudinal ribs. Also apparent are horse-shoe structures and small scales very near the trailing-edge surface, both of which scale in size (from 25° bevel to 45° bevel to 25° knuckle) with overall size of separated region.

Statistical Analysis. Mean and root-mean-square (rms) statistics are computed for each dependent flow variable (U,V,W,k,ω,p) at every point in the grid. For the results presented here, statistics were calculated over 2000 time steps. This corresponds to a nondimensional integration period of 5.0 and 1.25 for $\Delta t=0.0025$ and 0.000 612 5, respectively. Since statistics were both relatively constant in the spanwise direction and insensitive to time step, it is assumed that the uncertainty due to sample size is small.

Mean Velocity Field. Figure 7 shows a comparison of the mean axial velocity for URANS and DES. Each frame also in-

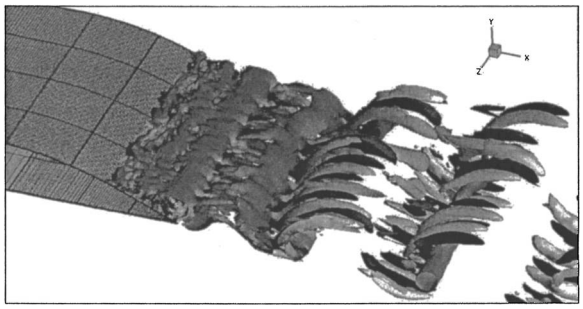

Fig. 5 Instantaneous DES flow field: perspective view of isosurface of intrinsic swirl (isolevel=3) shaded by normalized helicity for 25° bevel

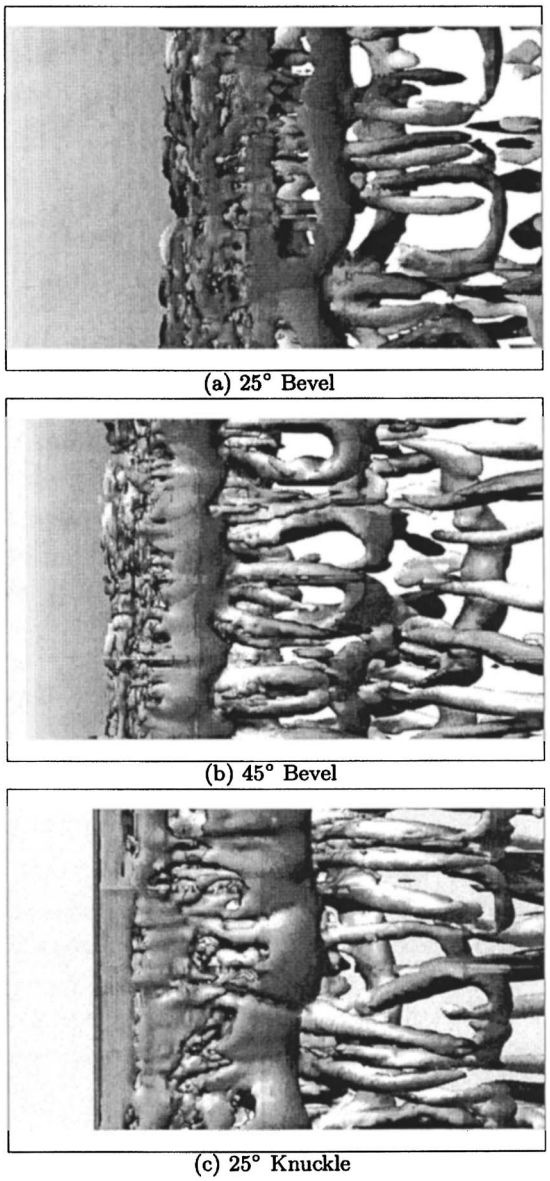

Fig. 6 Instantaneous DES flow field: top view of isosurface of intrinsic swirl (isolevel=3) shaded by normalized helicity

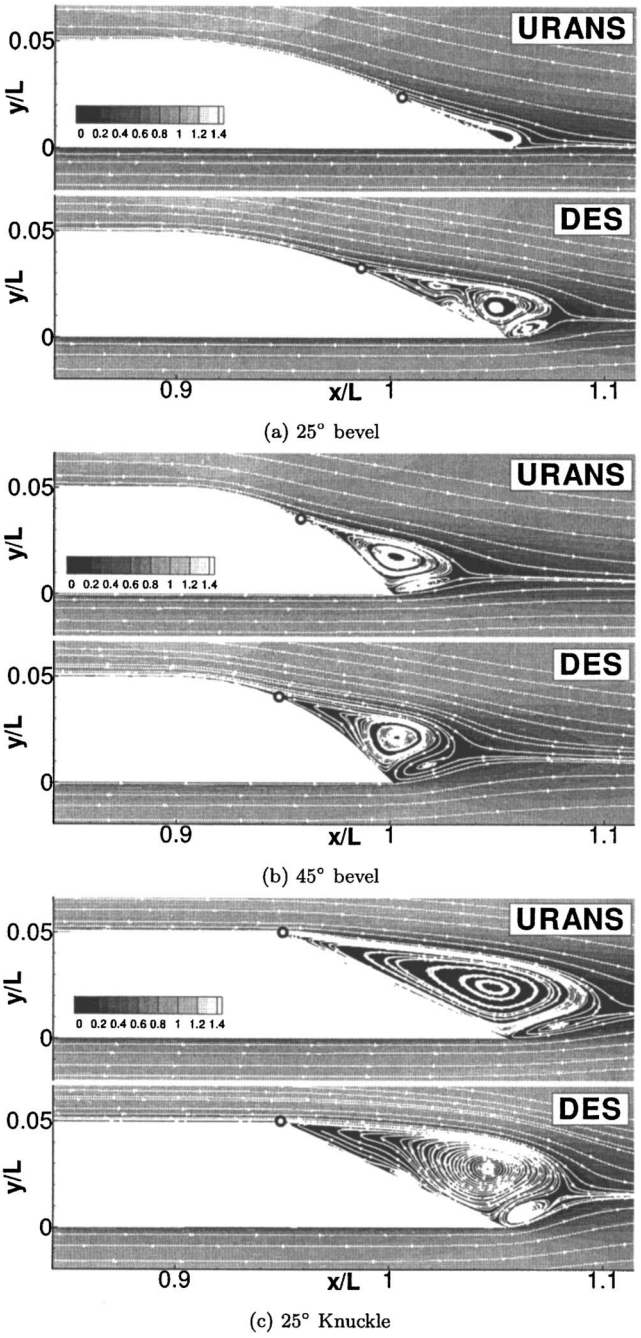

Fig. 7 Mean velocity field: contours of axial velocity and streamlines

cludes a symbol indicating the location of flow separation in the mean field. In general, URANS and DES are similar, however, as shown in Fig. 7(*a*), the largest discrepancy between URANS and DES is for the 25° bevel where DES predicts a significantly larger separated region and secondary vortices. The 45° bevel case shows much closer agreement between URANS and DES with only slight differences in the predicted separation location and shape of the separation vortices. For the 25° knuckle, the separation point is fixed by the geometry, which is confirmed by Fig. 7(*c*), and the DES contains a small secondary vortex not shown in the URANS results.

Turbulent Kinetic Energy. Figures 8–10 present an analysis of the turbulent kinetic energy (TKE) for each trailing edge. Contributions to the TKE are from the resolved turbulence field, $\overline{u_i^r u_i^r}$, and from the unresolved subgrid interactions, $\overline{u_i^s u_i^s}$ and $\overline{u_i^r u_i^s}$,

$$k^{\mathrm{tot}} = \frac{1}{2}\overline{u_i u_i} = \frac{1}{2}(\overline{u_i^r u_i^r} + 2\overline{u_i^r u_i^s} + \overline{u_i^s u_i^s}) = \frac{1}{2}\overline{u_i^r u_i^r} + k^{\mathrm{SGS}}; \qquad (8)$$

where $\overline{u_i^r u_i^r}$ is the variance of the velocity field, k^{SGS} is the modeled subgrid turbulence directly computed from the $k-\omega$ model [Eq. (3)], and the overbar denotes time averaging. For URANS, $\overline{u_i^r u_i^r}$ represents the fluctuating energy contained in the time-dependent, deterministic motions, i.e., the organized vortex shedding from the trailing edge. For DES $\overline{u_i^r u_i^r}$ includes both the deterministic motions and the resolved turbulence fluctuations.

For the results shown in Figs. 8–10, analysis showed that the URANS computations contained negligible resolvable-scale contribution to the TKE field; therefore, only the total TKE contours are presented for the URANS results. In contrast, the TKE field for the DES calculations displays contributions from both the resolved and subgrid scales and is therefore presented in the figures as the total TKE and its resolved and subgrid components.

All three trailing-edge variants show similar trends. DES k^{tot} is smaller in the separation region and larger in the wake in com-

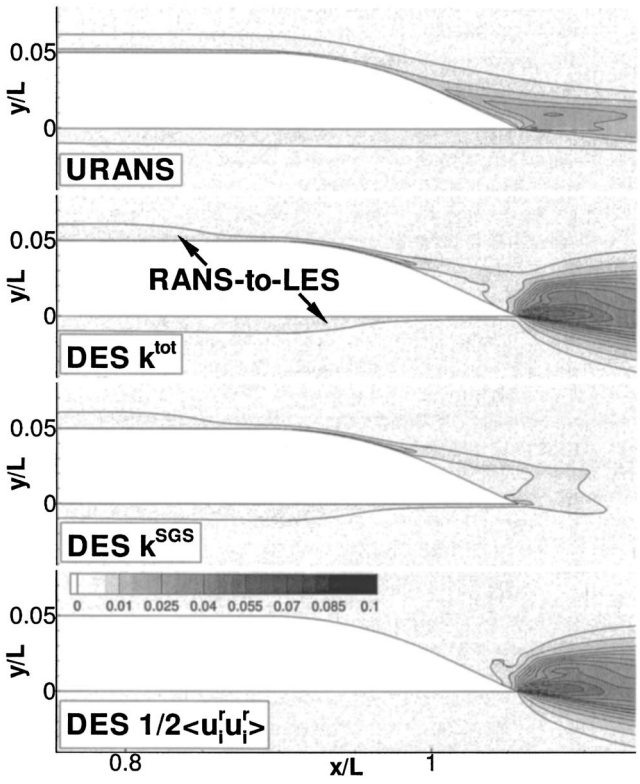

Fig. 8 Turbulent kinetic energy 25° bevel: URANS and total, subgrid, and resolvable DES components

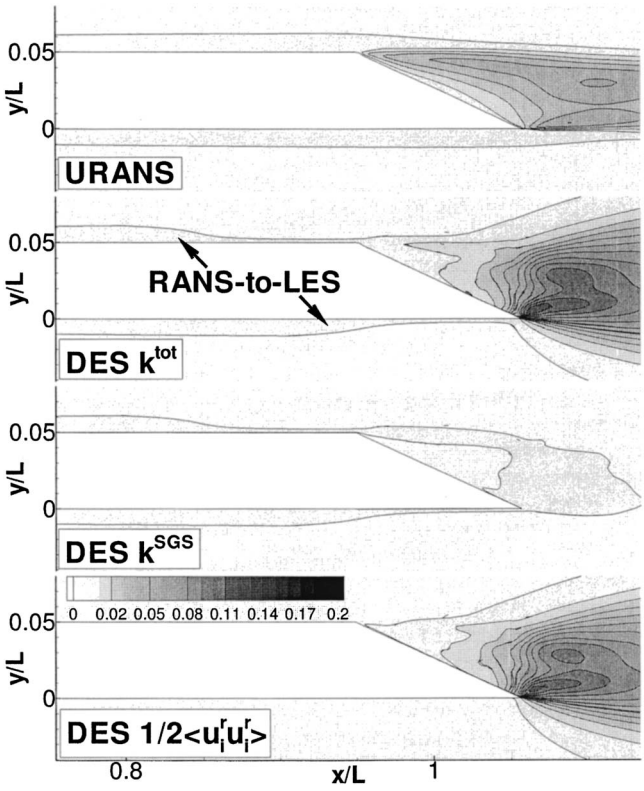

Fig. 10 Turbulent kinetic energy 25° knuckle: URANS and total, subgrid, and resolvable DES components

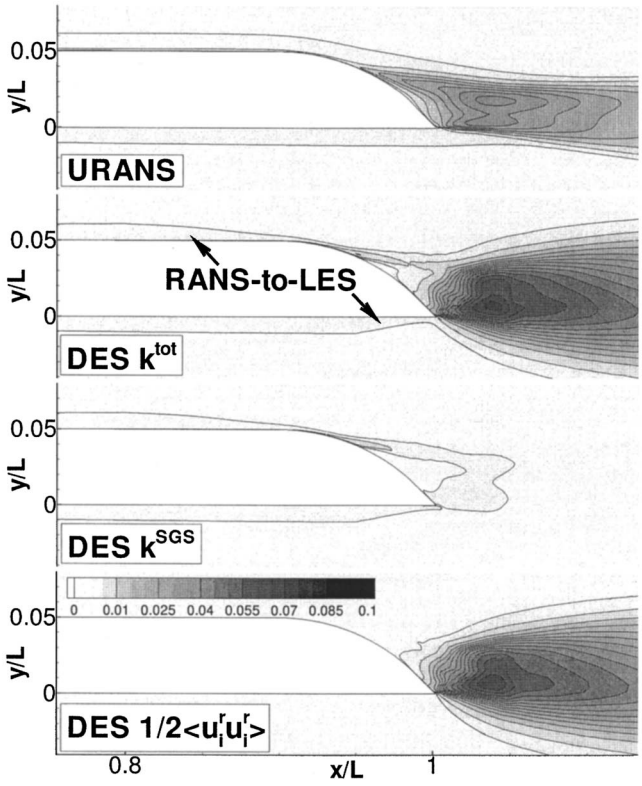

Fig. 9 Turbulent kinetic energy 45° bevel: URANS and total, subgrid, and resolvable DES components

parison to URANS. DES k^{SGS} shows a reduction at the locations where the simulation switches from RANS to LES, as labeled in the figures. There, the algorithm determines (correctly) that the local grid is able to support some of the turbulent fluctuations, which results in a reduction of the turbulence diffusivity. However, the governing equations cannot respond abruptly, so the lost statistical Reynolds stress is not replaced by corresponding resolvable-scale interactions yielding a region of unphysical flow. The downstream result is a grid-induced premature separation at the trailing edge, similar to the discussion of Menter [19].

Documenting this result was one of the goals of this work. It identifies a limitation of baseline DES for application-level modeling of trailing-edge-type flow fields. The adverse impact in the separated zone of the abrupt change in grid resolution underscores the need to develop improved modeling techniques. It is our opinion that approaches to mitigate this problem and the subsequent impact on the evolving boundary layer and wake may include introduction of realistic LES content to increase locally the resolved stresses (e.g., synthetic turbulence [16,3]) with enhanced modeling of turbulence production at the RANS/LES interface to support turbulence scales in the outer flow (e.g., stochastic forcing [25]), or grid-independent control of the transition between the RANS and LES regions (e.g., the scale-adaptive simulation model [19] and zonal DES [27]).

Mean and rms Velocity Profiles. To further support observations in the previous section, a comparison of mean and rms axial velocity profiles is made at several locations for the 25° bevel (in general, similar conclusions can be made from the other geometries). Figure 11 shows that at $x/L=0.875$, which is close to the RANS-LES transition, the DES and URANS results are the same and are in good agreement with the data, especially in the outer part of the boundary layer. The simulation data shows a monotonically increasing profile for u_{rms} to a location much closer to the wall than indicated by the experimental data. One expects u_{rms}

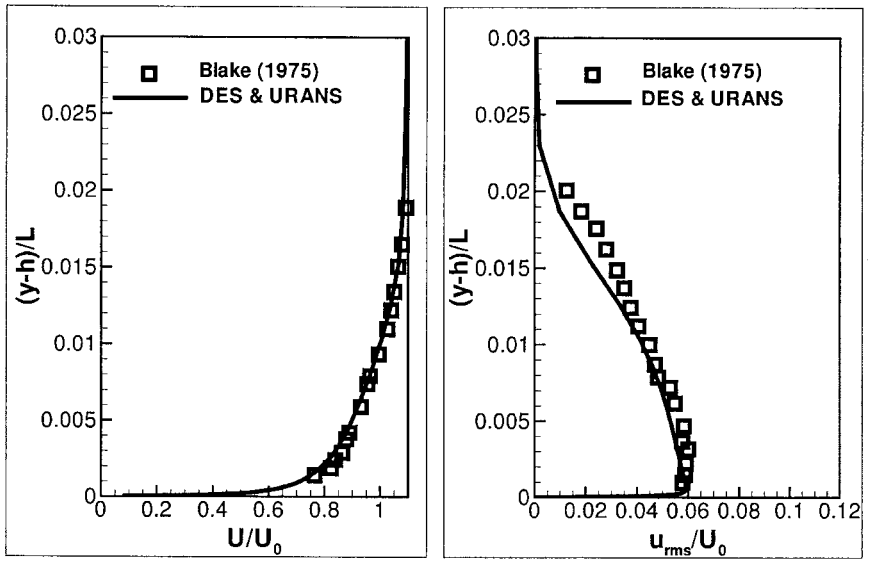

Fig. 11 Velocity profiles at $x/L=0.875$ for 25° bevel

to grow monotonically until very near the surface. The change in behavior of the data may indicate probe volume filtering thus may demark where meaningful comparisons are possible.

The mean velocity in the near wake is shown in Fig. 12. In comparison to the URANS result, DES displays a broader profile with the wake centerline moving from $y/L=0.04$ to 0.13. The wake deficit is similar between simulation and data, however, the data profile shows a larger magnitude at the wake edges.

Figure 13 shows a comparison of predicted rms profiles of the streamwise velocity to data at locations downstream of separation and in the near wake. For the numerical results, we show rms profiles for the total streamwise energy (u_{rms}), which is comprised of resolvable-scale (u^r_{rms}) and subgrid-scale contributions (u^s_{rms}). We diagnose u^s_{rms} from the modeled subgrid kinetic energy, k^{SGS}, assuming isotropy, $u^s_{\mathrm{rms}} \approx \left(\frac{2}{3}k^{\mathrm{SGS}}\right)^{1/2}$. At $x/L=1.025$, which is upstream of the trailing edge, it is shown that DES under resolves the intensity in comparison to URANS and data, the latter of which are in close agreement. At the locations in the wake, neither URANS nor DES fully capture the data profiles. DES displays a profile shape which is similar to the data, particularly at $x/L=1.106$, however, a "transition overshoot" is shown wherein the intensity goes from being underpredicted on the strut surface to overpredicted by 50%–100% in the wake.

Surface Pressure. Comparison of mean surface pressure is shown in Fig. 14. URANS results are remarkably close to the data where the mean pressure shows a decrease due to the flow acceleration around the bevel, followed by an adverse gradient, and then a constant amplitude region which correlates to flow separation. The DES results are similar, but are affected by the premature separation, i.e., the lift envelope is decreased, and the length of the separated region is increased, particularly for the beveled

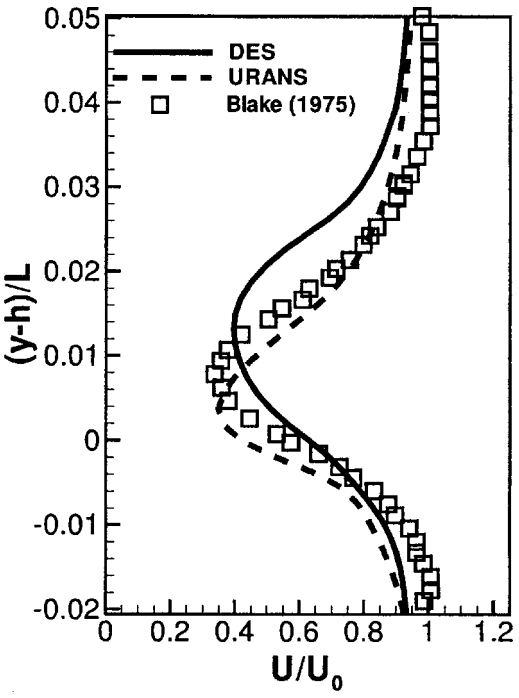

Fig. 12 Mean-velocity profile at $x/L=1.106$ for 25° bevel

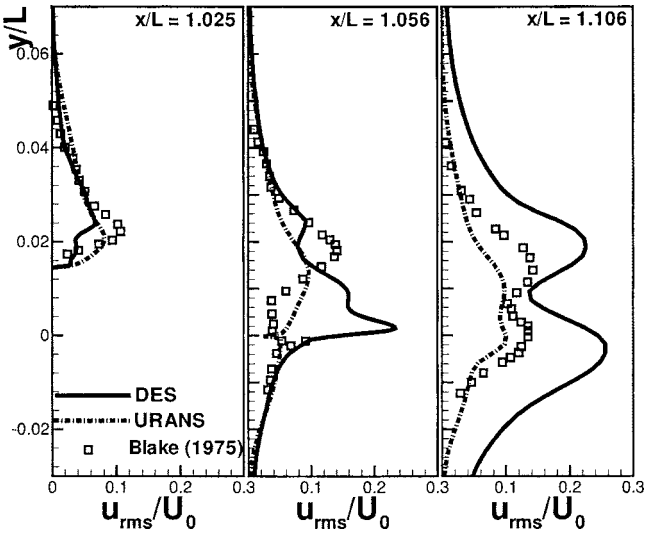

Fig. 13 rms velocity profiles for 25° bevel

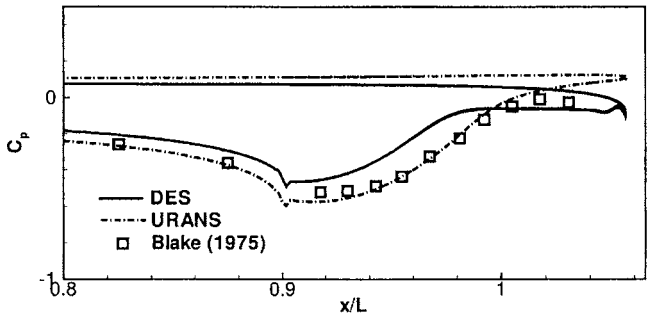

(a) 25° bevel

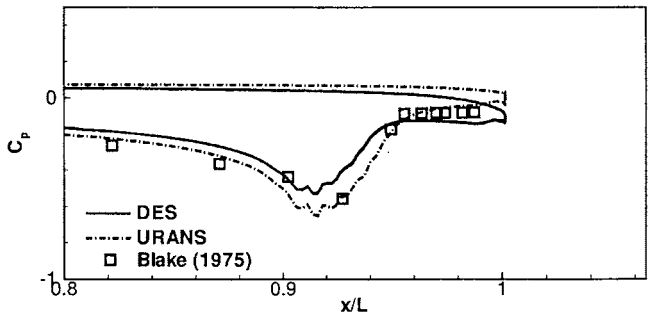

(b) 45° Bevel

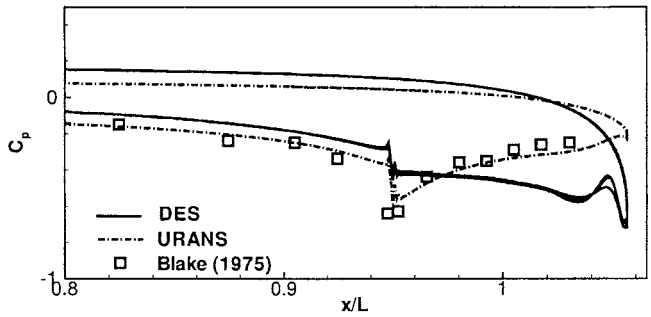

(c) 25° Knuckle

Fig. 14 Mean surface-pressure distribution

edges, consistent with the mean velocity contours.

Figure 15 shows the pressure variance on a semilog plot with the horizontal axis being distance from the trailing edge. Magnitude shows a rapid decrease from the trailing edge, followed by an increase up to the point of separation, followed by a decay to a finite value at the leading edge (although not shown). The magnitudes and relative locations of these peaks and troughs are consistent with the differences thus far shown between the different edge geometries. Also it is noted that the nonzero leading-edge rms

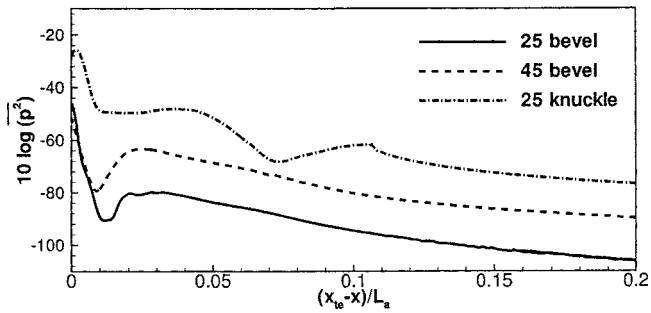

Fig. 15 $\overline{p^2}$ surface distribution from DES

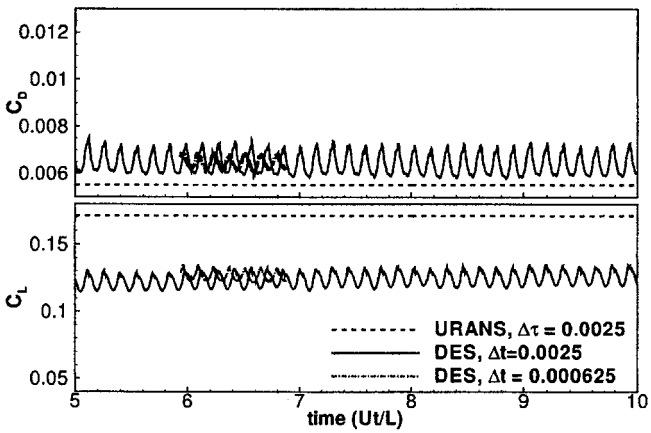

(a) 25° Bevel

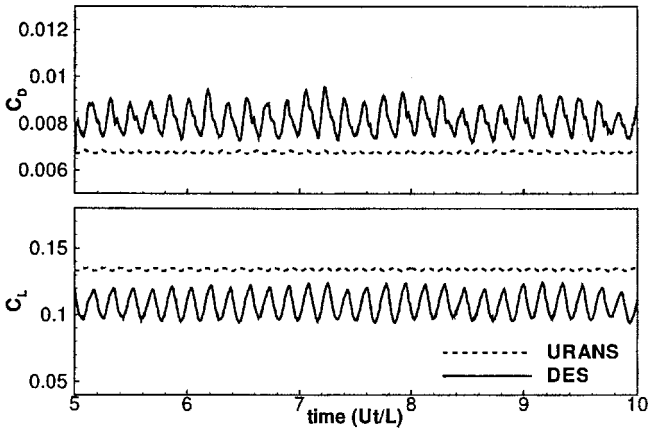

(b) 45° Bevel

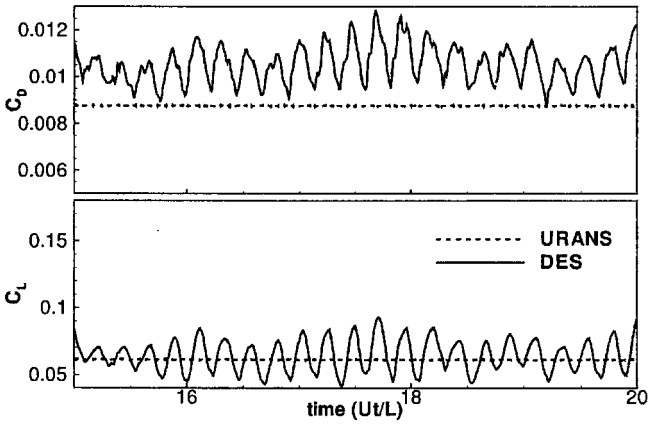

(c) 25° Knuckle

Fig. 16 Unsteady lift and drag

pressure indicates that the entire blade must be simulated to resolve unsteady lift generated by the vortex shedding process. This obviously cannot be resolved with small-domain LES formulations.

Fourier Analysis

Lift and Drag. The time histories of the lift and drag coefficients are shown in Fig. 16 and the mean values and shedding frequencies, obtained via fast-Fourier transform of the time histories, are summarized in Table 2. The differences between DES and URANS are fairly significant. For the 25° bevel, URANS is

Table 2 Strouhal number and mean forces

	f^*			$\overline{C_D}\times 10^3$			$\overline{C_L}\times 10^1$		
	25b	45b	25k	25b	45b	25k	25b	45b	25k
URANS	0	6.5	5.1	5.5	6.8	8.8	1.7	1.3	6.1
DES	6.8	5.8	4.5	6.4	8.2	10.8	1.2	1.1	6.9

steady whereas DES shows increased mean drag $\overline{C_D}$ and decreased mean lift $\overline{C_L}$ with a Strouhal number of $f^*=fL/U_0=6.8$. Also, the finest time step is shown to slightly decrease the amplitude of oscillation. Similar trends in $\overline{C_D}$ and $\overline{C_L}$ are shown for the other edges, which is consistent with the change in flow separation already discussed. DES also shows a decreased shedding frequency which is also directly correlated with an increase in the size of the separated region.

Trailing-Edge Pressure. Temporal surface-pressure data was collected at the axial locations indicated as black symbols shown in Fig. 1. Pressure autospectra and the correlation phase angle at two points ($x/L=1.025$) across the trailing edge are shown in Fig. 17 for the 25° bevel and 25° knuckle. Both solutions demonstrate tonals. Moreover, 25° bevel case displays well-defined superharmonics, all of which are most likely nonphysical due to premature separation; a conclusion based upon the data (and URANS result) which showed only a broadband response for this trailing edge. The response for the 25° knuckle case is at least 10 dB higher than the bevel case. At the tonal frequency, both cases show a phase angle response where the pressure and suction sides are almost 180° out of phase, which if correct, has important implications for propensity to generate vibration and lock-in phenomenon. The importance of this observation demands further study and validation of DES methods.

Conclusions and Future Work

This study comprises an evaluation of baseline DES as implemented in a Navy hydrodynamics code and applied to separated flow in the trailing-edge region of a hydrofoil. Three trailing-edge geometries were considered, a 25° rounded bevel, a 25° knuckled bevel, and a 45° rounded bevel. These cases were chosen because they represent simple geometries that produce both random and periodic wakes, because experimental data is available for solution validation, and because they were the subject of previous CFD analysis.

The results showed that the DES model, coupled with localized overset-grid refinement, is able to capture the separated flow and to resolve the "rib/roller" instability modes. In regions of high grid resolution, the spawning of small scales is observed. Flow statistics indicate that the separated flow is overenergized relative to the experimental results. We argue that this characteristic is an outcome of premature separation due to the loss of statistical upstream turbulence in the transition from RANS to LES. The separated zone is artificially large and therefore more energetic. Our observations agree with the discussion by Menter [19] describing "grid-induced separation." Despite these modeling issues, the DES approach has allowed the entire geometry to be simulated, thus permitting resolution of the fluctuating circulation and resultant unsteady lift and drag associated with vortex shedding.

Future work will focus on model implementation and/or development that mitigates the grid-induced separation problem. Candidates include the use of stochastic forcing of the buffer-layer [25], use of synthetic turbulence with mean-flow correlation [16,3], or alternatively, not allowing transition to LES in the boundary layer through the use of scale-adaptive simulation [19] or zonal DES [27] models.

In addition, it is recognized that grid-resolution studies are necessary, however, because the DES model and the grid are not independent, the results could be ambiguous. A possible solution to this problem includes the scale-adaptive simulation model [19] which separates the filter scale from the grid, and, as such, is a model of interest for future evaluation. Finally, it is noted that grid-resolution studies via grid-doubling presents an eightfold increase in grid number such that simulation size approaches 25–30 million grid points and ~100 000 CPU hours per simulation.

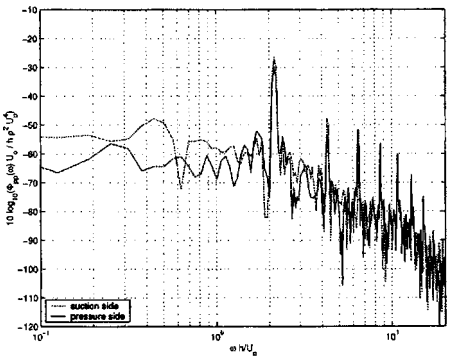

(a) pressure autospectra 25° bevel

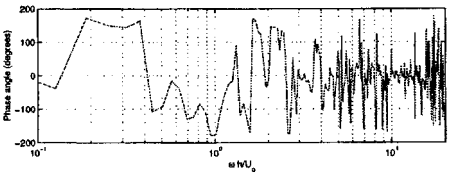

(b) phase angle across trailing edge 25° bevel

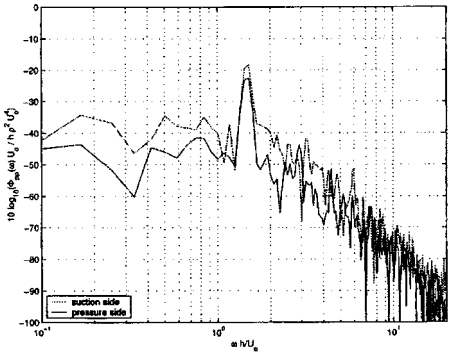

(c) pressure autospectra 25° knuckle

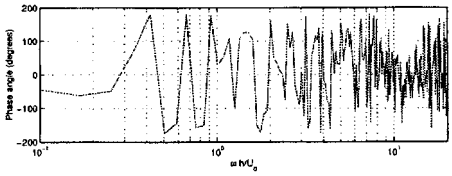

(d) phase angle across trailing edge 25° knuckle

Fig. 17 Spectral analysis of surface pressure at $x/L=1.025$

Since this is prohibitive with current resources, grid refinement should be limited to $\sqrt{2}$ in each coordinate direction from current grid levels.

Acknowledgments

This work was supported by ARL Penn State Internal Research and Development funds and by the Office of Naval Research Grant No. N00014-03-1-0122, monitored by Dr. Ron Joslin. The DoD High Performance Computing Modernization Office (HPCMO) and Army Research Laboratory-Major Shared Resource Center are acknowledged for providing computing resources through a DoD HPCMO Challenge Project.

References

[1] Balay, S., Buschelman, K., Gropp, W. D., Kaushik, D., Knepley, M., Curfman McInnes, L., Smith, B. F., and Zhang, H., 2001, PETSc home page. http://www.mcs.anl.gov/petsc

[2] Batten, P., Goldberg, U., and Chakravarthy, S., 2002, "LNS—An Approach Towards Embedded LES," AIAA Paper 2002–0427, Reno, NV.

[3] Batten, P., Goldberg, U., and Chakravarthy, S., 2004, "Interfacing Statistical Turbulence Closures With Large Eddy Simulation," AIAA J., 42.

[4] Berdahl, C. H., and Thompson, D. S., 1993, "Eduction of Swirling Structure Using the Velocity Gradient Tensor," AIAA J., 31.

[5] Blake, W. K., 1975, "A Statistical Description of Pressure and Velocity Fields at the Trailing-Edges of a Flat Strut," Report 4241, David W. Taylor Naval Ship Research and Development Center, Bethesda, MD.

[6] Blake, W. K., and Gershfeld, J. L., 1989, *Lecture Notes in Engineering*, volume 46 of *Frontiers in Experimental Fluid Mechanics*, Chap. The Aeroacoustics of Trailing Edges. Springer, Berlin.

[7] Bourgoyne, D. A., Ceccio, S. L., and Dowling, D. R., 2005, "Vortex Shedding From a Hydrofoil at High Reynolds Number," J. Fluid Mech., **531**, pp. 293–324.

[8] Bourgoyne, D. A., Hamel, J. M., Ceccio, S. L., and Dowling, D. R., 2003, "Time-Averaged Flow Over a Hydrofoil at High Reynolds Number," J. Fluid Mech., **496**, pp. 365–404.

[9] Constantinescu, G. S., Pacheco, R., and Squires, K. D., 2002, "Detached-Eddy Simulation of Flow Over a Sphere," AIAA Paper 2002–0425, Reno, NV.

[10] Constantinescu, G. S., Pasinato, H., Wang, Y.-Q., and Squires, K. D., 2002, "Numerical Investigation of Flow Past a Prolate Spheroid," AIAA Paper 2002–0588, Reno, NV.

[11] Deng, G. B., Guilmineau, E., Queutey, P., and Visonneau, M., 2001, "High Reynolds Number Simulations Over the Hifoil Project Body," Technical Report UMR 6598, Division Modelisation Numerique, Laboratoire de Mecanique des Fluides, Ecole Centrale Nantes.

[12] Frantz, J., 2004, g3data home page. http://freshmeat.net/projects/g3data/

[13] Hedges, L. S., Travin, A. K., and Spalart, P. R., 2002, "Detached-Eddy Simulations Over a Simplified Landing Gear," J. Fluids Eng., **124**, pp. 413–423.

[14] Israel, D. M., and Fasel, H. F., 2002, "Numerical Investigation of Turbulent Separation Control Using Periodic Disturbances," AIAA Paper 2002–0409, Reno, NV.

[15] Knight, C. J., and Peltier, L. J., 1997, "Unsteady Viscous Simulation for Beveled Trailing Edge Flow Fields," AIAA Paper 1997-0662, Reno, NV. In 35th AIAA Aerospace Sciences Meeting and Exhibit Proceedings.

[16] Lund, T. S., Wu, X., and Squires, K. D., 1998, "Generation of Turbulent Inflow Data for Spatially-Developing Boundary Layer Simulations," J. Comput. Phys., **140**, pp. 233–258.

[17] Lysak, P. D., and Brungart, T. A., 2003, "Velocity, Spectrum Model for Turbulence Ingestion Noise From Computational Fluid Dynamics Calculations," AIAA J., **41**, 1827–1829.

[18] Menter, F. R., 1994, "Two-Equation Eddy Viscosity Turbulence Models for Engineering Applications," AIAA J., 32.

[19] Menter, F. R., Kuntz, M., and Bender, R., 2003, "A Scale-Adaptive Simulation Model for Turbulent Flow Predictions," AIAA Paper 2003-0767, Reno, NV.

[20] Morton, S. A., and Steenman, M. B., 2003, "DES Grid Resolution Issues for Vortical Flows on a Delta Wing and an F-18C," AIAA Paper 2003-1103, Reno, NV.

[21] Nikitin, N. V., Nicoud, F., Wassistho, B., Squires, K. D., and Spalart, P. R., 2000, "An Approach to Wall Modeling in Large-Eddy Simulations," Phys. Fluids, **12**, pp. 1629–1632.

[22] Paterson, E. G., Poremba, J. E., Peltier, L. J., and Hambric, S. A., 2004, "A Physics-Based Simulation Methodology for Predicting Hydrofoil Singing," In *25th Symposium on Naval Hydrodynamics*, St. Johns, Newfoundland and Labrador, Canada.

[23] Paterson, E. G., Wilson, R. V., and Stern, F., 2003, "General-Purpose Parallel Unsteady RANS Ship Hydrodynamics Code: CFDSHIP-IOWA," Technical Report 432, IIHR Hydroscience and Engineering, The University of Iowa, Iowa City, IA.

[24] Peltier, L. J., and Hambric, S. A., 2005, "Estimating Turbulent Boundary Layer Wall Pressure Spectra From CFD RANS Solutions," J. Fluids Struct., In Press.

[25] Peltier, L. J., and Zajaczkowski, F. J., 2001, "Maintenance of the Near-Wall Cycle of Turbulence for Hybrid RANS/LES of Fully-Developed Channel Flow," In C. Liu and Z. Liu, editors, *DNS/LES Progress and Challenges: Third AFOSR International Conference*, Arlington, TX, Greyden Press.

[26] Peltier, L. J., Zajaczkowski, F. J., and Wyngaard, J. C., 2000, "A Hybrid RANS/LES Approach to Large-Eddy Simulation of High-Reynolds-Number Wall-Bounded Turbulence," FEDSM Paper 2000-11177, Boston, MA.

[27] Slimon, S., 2003, "Computation of Internal Separated Flows Using a Zonal Detached Eddy Simulation Approach," In *Proceedings of the 2003 ASME International Mechanical Engineering Congress*, Washington, DC.

[28] Spalart, P., 2001, "Young-Person's Guide to Detached-Eddy Simulation Grids," Technical Report CR-2001-211032, NASS.

[29] Spalart, P. R., Jou, W.-H., and Allmaras, S. R., 1997, "Comments on the Feasibility of LES for Wings, and on a Hybrid RANS/LES Approach," In C. Liu and Z. Liu, editors, *Advances in DNS/LES: First AFOSR Int. Conf. on DNS/LES*, Greyden Press, Columbus, OH.

[30] Speziale, C. G., 1998, "Turbulence Modeling for Time-Dependent RANS and VLES: A Review," AIAA J., **36**, pp. 173–184.

[31] Strelets, M., 2001, "Detached-Eddy Simulation of Massively Separated Flows," AIAA Paper 2001-0879, Reno, NV. In 39th AIAA Aerospace Sciences Meeting and Exhibit Proceedings.

[32] Suhs, N. E., Dietz, W. E., Rogers, S. E., Nash, S. M., and Onufer, T., 2000, J. Pegasus user's guide, version 5.1e. Technical report, NASA.

[33] Wang, M., 2000, "Dynamic Wall Modeling for LES of Complex Turbulent Flows," Annual research briefs 2000, Center for Turbulence Research, Stanford University.

[34] Wang, M., and Moin, P., 2000, "Computation of Trailing-Edge Flow and Noise Using Large-Eddy Simulation," AIAA J., **38**, pp. 2201–2209.

Flow Around a Simplified Car, Part 1: Large Eddy Simulation

Siniša Krajnović
e-mail: sinisa@chalmers.se

Lars Davidson

Division of Fluid Dynamics,
Department of Applied Mechanics,
Chalmers University of Technology,
SE-412 96 Gothenburg, Sweden

Large eddy simulations (LES) were made of flows around a generic ground vehicle with sharp edges at the rear end (an Ahmed body with a 25° angle of the rear slanted surface). Separation of the flow at the rear results in large regions with recirculating flow. As the separation is determined by the geometry, the Reynolds number effects are minimized. Resolution requirements of this recirculating flow are smaller than those in LES of wall attached flows. These two consequences of the geometry of the body are used to predict the experimental flow at relatively high Reynolds number. Recommendations are presented for the preparation and realization of LES for vehicle flows. Comparison of the LES results with the experimental data shows good agreement.
[DOI: 10.1115/1.1989371]

Keywords: Large Eddy Simulation, LES, Generic Car Body, Vehicle Aerodynamics, Ground Vehicle

1 Introduction

It has long been known that the shape of ground vehicles determines their aerodynamic properties. A modification of the shape that produces better aerodynamic properties requires a thorough understanding of turbulent flows around vehicles. Unfortunately, after several decades of experimental and numerical studies, our understanding of the flow around ground vehicles is still often limited to a qualitative picture of the time-averaged large flow structures. Experimental techniques were first adopted in studies of flows around ground vehicles and are still more commonly used than numerical methods in the design. Although numerical simulations have been conducted in automobile companies, they were unable until some 10 years ago to predict the flow with the same level of accuracy as wind tunnel tests. Only recently have numerical simulations taken over the role of some experimental studies and become a design tool in some of the automobile companies (such as Volvo Cars). Experimental and numerical methods both have their advantages and disadvantages. Measuring techniques are limited to a part of the domain and are often used to measure time-averaged flow rather than the temporal development of the instantaneous flow. It should be mentioned, however, that it is now possible to study instantaneous flows in a single plane using the particle image velocimetry (PIV) technique. Computational fluid dynamics (CFD) can easily provide spatial information about the flow in the entire domain (virtual wind tunnel). Before we discuss the ability of CFD to predict the development of the flow in time (i.e., temporal information), it is appropriate to make some remarks about the CFD results.

Turbulent scales in the flow around a ground vehicle range from those of the size of the vehicle to microscopic ones. Unfortunately most turbulent scales in this flow are small owing to high Reynolds number, making resolution requirements very high. This makes the solution of time-dependent Navier-Stokes equations for the flows around ground vehicles at operating velocities infeasible. As a result of the limitations in computer resources, simulations of time-averaged Reynolds Averaged Navier-Stokes (RANS) equations have chiefly been used in the literature.

Instead of using real vehicles, very simplified (generic) vehicle models are used in research to study how flow changes with geometry. Using such an approach we can isolate a few geometric properties and study their influence on the flow.

The objective of the pioneer work of Ahmed et al. [1] was to study the influence of the angle between the roof and the rear end slanted surface of a car with a typical fastback geometry (such as the Volkswagen Golf I or Volkswagen Polo I) on the flow. Their investigation showed a clear influence of the rear slant angle to the time-averaged flow structures. As they varied this angle they found that the flow changes character at an angle of about 30°, which prompted researchers to make further experimental and numerical studies of this flow. Some of the experimental studies are described in [2,3]. Numerical studies such as those in [4,5] are used to validate the CFD technique (often a RANS simulation). A large number of RANS simulations (using different turbulence models) and one large eddy simulation (LES) of the flow around the body defined by Ahmed et al. [1] are presented in [5]. Only two angles of the rear slanted surface, 25° and 35°, were considered in these simulations. The results of the simulations were compared with the experimental data produced by Lienhart and Becker [3]. The main conclusion drawn from these simulations was that, while the simulations were relatively successful in their prediction of the 35° case, they were unsuccessful in the 25° case.

The aim of this paper is to demonstrate that, if carefully applied, the LES can give an accurate representation of the flow around this generic car body characterized by the sharp edges at the rear and the rear slant angle of 25°.

2 Generic Ground Vehicle Body

The generic vehicle body was chosen to be the same as in the experiments of Ahmed et al. [1] and Lienhart and Becker [3]. The geometry of the body and the computational domain are given in Fig. 1. All the geometric quantities are normalized with the body height, H, equal to 0.288 m. The values of the geometric quantities are $l_r/H=2.928$, $G/H=0.697$, and $W/H=1.35$. The front part is rounded with a radius of $R/H=0.347$ in the planes, $y=0$ and $z=0$. The geometry of the rounded corners was made from the data (in the form of distinct points) measured at the body used in Ahmed et al. [1] and Lienhart and Becker [3]. This body is placed in the channel with a cross section of $B\times F=6.493H\times 4.861H$ (width $\times$ height). The cross section of this channel is identical to the open test section of the wind tunnel used in the experiments of Lienhart and Becker [3]. The front face of the body is located at a distance of $x_1=7.3H$ from the channel inlet and the downstream length between the rear face of the body, and the channel outlet is $x_2=21H$. The body is lifted from the floor, producing a ground clearance of $c/H=0.174$, as in the experiments. The Reynolds number, based on the incoming velocity, U_∞, and the car height,

Contributed by the Fluids Engineering Division for publication in the JOURNAL OF FLUIDS ENGINEERING. Manuscript received by the Fluids Engineering Division, July 26, 2004; final revision: May 12, 2005. Associate Editor: Ismail B. Celik.

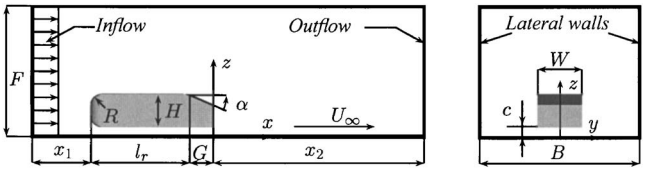

Fig. 1 Schematic representation of the computational domain with vehicle body. Left: view from the side; right: view from behind the body.

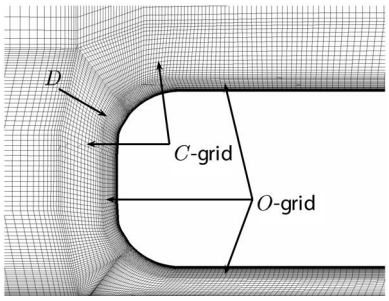

Fig. 2 The computational grid in symmetry plane $y=0$. *D* indicates the position of the dummy surface. View from the side of the front part of the body.

H, of $\mathrm{Re}=7.68\times10^5$ used in the experiments [3] was reduced to $\mathrm{Re}=2\times10^5$. Krajnović and Davidson [6] have already demonstrated successful LES of this lower Reynolds number case with no rear body slant angle, i.e., $\alpha=0°$ (generic bus body). We expect that the slanted rear end will produce a wide spectrum of turbulent scales that must be resolved in LES.

3 Making Large Eddy Simulation

Resolution requirements of the near-wall regions in attached flows such as channel flow or a flat plate flow are similar to those in direct numerical simulations. This is because the coherent structures (so called low- and high-speed streaks) near the walls are responsible for most of the turbulence production in the boundary layer. Thus an accurate representation of these structures is crucial to the results of the LES of the flat plate flow, for example.

Flows around bluff bodies such as those around ground vehicles are different from channel or flat plate flows. They contain a number of separating regions with large coherent structures that contain much more turbulent energy than the near-wall structures. Let us consider the following question. What is the size of the smallest turbulent structures that must be resolved in a LES of the flow around ground vehicles?

In the regions of separated flow (such as the wake behind the vehicle) the transport of momentum is dominated by large recirculating motions of the flow and there is limited influence of the small near-wall structures. Thus the structures that must be resolved in this region are the smallest "large" (recirculating) structures. What is the case for the attached regions in the flow around the vehicle? Prediction of drag is often the main objective of CFD studies in vehicle aerodynamics. As the pressure drag is much larger than the friction drag and is dominated by the low pressure in the wake, prediction of the wake flow is crucial. Does this mean that it is sufficient to predict the wake flow and ignore the resolution requirements for the regions located upstream from the wake? The wake flow is influenced by the upstream flow (and vice versa), but the question is how strong this influence is. The boundary layer developed on the roof surface of the body separates at the location where the roof goes over to the rear face of the body. We can distinguish between two main situations. First, the changeover from the roof to the rear face can be continuous, such as that in a circular cylinder. In that case the position of the separation and the nature of the downstream flow are determined by the upstream history of the flow. The second situation is that in which the geometry defines the separation of the flow, such as in the generic car body studied in this paper. How great is the influence of the upstream flow on the wake in this case? Is the resolution of the upstream boundary layer equally important here as in the case of the continuous changeover in the surface geometry? We believe that in this case the influence of the geometry (i.e., separation defined by the sharp edges) is much greater than that of the upstream history of the flow.

3.1 Our Approach. Although we assume that the upstream boundary layer has limited influence on the flow in the wake, in the flow around our generic car body, we cannot neglect it. Thus we should try to predict the flow in the near-wall region as well as possible. The near-wall coherent structures unfortunately decrease in size with the Reynolds number and the task of resolving these structures is overwhelming for the Reynolds number of 7.68×10^5 used in the experiments by Lienhart and Becker [3] (see [7] for the estimate of the computational cost for the resolution of the near-wall structures in the flow around a ground vehicle body).

We have already assumed that the geometry rather than the upstream flow defines the flow in the wake, which means that we can reduce the Reynolds number in our LES and obtain a flow similar to that in the experiment characterized by the higher Reynolds number. We emphasize that this is only an assumption.

If our hypothesis of Reynolds number independence of the wake flow is correct, how much can we reduce the Reynolds number and still obtain this independence? This is not clear, but the simulated flow on the roof should be as similar as possible to that in the experiment at high Reynolds number. Thus if the high Reynolds number roof flow does not separate at the leading edge, our simulated low Reynolds number flow should not separate or should have as small separated regions as possible. Our knowledge of the dependence of the Reynolds number and the shape of the front of the ground vehicle (i.e., roundedness of the leading edges) is poor and is limited to the dependence of the drag coefficient on the Reynolds number and the roundedness of the leading edges of prismatic bodies [8]. The issue of leading flow separation is discussed in the present paper when the results are reported.

The spatial resolution in the y direction on the top and the roof, and in the z direction on the lateral sides required for LES, could not be obtained for the Reynolds number of 7.68×10^5 used in the experiments [3]. We assume that this Reynolds number can be decreased because of the sharp edges on the rear of the body. Krajnović and Davidson [6] showed that LES can predict the flow around the ground vehicle body that is characterized by a Reynolds number of about 2×10^5 (based on the height of the body and the velocity at the inlet). Thus we choose for our LES the Reynolds number of 2×10^5 instead of the experimental 7.68×10^5.

3.2 Preparation and Realization of LES. Most LES of the flow around bluff bodies use structured hexahedral grids, which give better accuracy than, for example, tetrahedral grids. Making a structured hexahedral grid such that the computational cells are concentrated where they are needed is far from trivial, even around a relatively simple bluff body such as the ground vehicle body studied in this paper. Providing the optimal structured grid for the detailed passenger car is quite a challenge.

Here we shall demonstrate one of the approaches that can be used to concentrate most of the cells in the region around the body. Instead of using only H grid topology, which spreads the fine resolution in the boundary layer of the body all the way to the boundaries of the wind tunnel, we use a combination of O and C grid topologies (see Fig. 2) which enables local refinement of the grid. The topology of the grid consists of an O grid with a thick-

ness of $0.1H$ and a C grid around the O grid (see Fig. 2). An additional "dummy" car surface was made around the surface of the car, and the O grid was projected on these two surfaces. The rest of the blocking structure was made using H grids. This strategy resulted in the following distribution of the computational cells. The O grid (i.e., the region in a belt of thickness $0.1H$ around the body) contained 4.4 and 7.5 million cells with a total of 9.6 and 16.5 million cells in the medium and the fine grids, respectively. The regions containing the O and the C grids together (i.e., the region in a belt of a thickness of $0.28H$ around a car) hold 6.3 and 10.8 million cells in the medium and the fine grids, respectively.

Unlike the results of steady RANS simulations, the results of time-dependent LES are dependent on the time at which we start to monitor our results (i.e., when the fully developed flow is obtained). Unfortunately, in LES of the flow around ground vehicles, the fully developed flow is unknown and must be estimated. The initial fully developed flow is often computed from the fluid at rest (as in this paper) or from a previous solution of a RANS simulation. How do we know that the flow has become fully developed? The only way to be sure that the flow has developed is probably the a posteriori one (i.e., after the entire simulation). Such a test could prove that the mean, rms values, and the spectral picture of the solution are not dependent on the position in time at which we started the sampling of the solution. As we need to start the time averaging before we can perform the a posteriori test, some approximate method must be used to ensure that the characteristics of the flow are not changing. We monitored the time required for the fluid particle to travel from the front to the rear face of the car body. We then computed the mean and the rms values of the global quantities (aerodynamic forces) and local variables (velocity components and pressure in several points in and around the wake behind the body) for this time interval. The time averaging was started when no significant differences were found between two consequent time sequences. The computational cost of obtaining the fully developed flow is significant and, for the simulations presented in this paper, the computational times for obtaining fully developed conditions were roughly one-fourth of the total time of the simulations.

When the flow has evolved to become fully developed, monitoring of the instantaneous results and their averaging can begin. Numerical time steps in LES are short to retain accuracy. The short time steps lead to large number of time steps for resolving the low-frequency events and the time averaging. Our experience is that the number of time steps required for resolving the low-frequency events is larger than that needed for obtaining the time-averaged results [6]. The symmetry of the flow around the symmetry plane ($y=0$ plane) was used in this paper as proof of a sufficiently long averaging time.

4 Governing Equations and Subgrid-Scale Modeling

The governing LES equations are the incompressible Navier-Stokes and the continuity equations filtered with the implicit spatial filter of characteristic width Δ (Δ is the grid resolution in this work):

$$\frac{\partial \bar{u}_i}{\partial t} + \frac{\partial}{\partial x_j}(\bar{u}_i \bar{u}_j) = -\frac{1}{\rho}\frac{\partial \bar{p}}{\partial x_i} + \nu \frac{\partial^2 \bar{u}_i}{\partial x_j \partial x_j} - \frac{\partial \tau_{ij}}{\partial x_j} \tag{1}$$

and

$$\frac{\partial \bar{u}_i}{\partial x_i} = 0. \tag{2}$$

Here, $\bar{u}_i$ and $\bar{p}_i$ are the resolved velocity and pressure, respectively, and the bar over the variable denotes filtering.

These equations are derived applying a filtering operation

$$\bar{f}(x_i) = \int_\Omega f(x_i')G(x_i, x_i')dx_i' \tag{3}$$

on the Navier-Stokes and the continuity equations. Here G is a top hat filter function and Ω represents the entire flow domain. The filtered variables in the governing Eqs. (1) and (2) are obtained implicitly through the spatial discretization.

The goal of the filtering is to decompose the fluid motion into a large-scale component that is resolved and the small subgrid scale (SGS) where the latter is modeled. The influence of the small scales of the turbulence on the large energy carrying scales in Eq. (1) appears in the SGS stress tensor, $\tau_{ij} = \overline{u_i u_j} - \bar{u}_i \bar{u}_j$. The algebraic eddy viscosity model originally proposed by Smagorinsky [9] is used in this paper for its simplicity and low computational cost. The Smagorinsky model represents the anisotropic part of the SGS stress tensor, τ_{ij}, as

$$\tau_{ij} - \tfrac{1}{3}\delta_{ij}\tau_{kk} = -2\nu_{sgs}\bar{S}_{ij} \tag{4}$$

where $\nu_{sgs} = (C_s f \Delta)^2 |\bar{S}|$ is the SGS viscosity,

$$\bar{S}_{ij} = \frac{1}{2}\left(\frac{\partial \bar{u}_i}{\partial x_j} + \frac{\partial \bar{u}_j}{\partial x_i}\right) \tag{5}$$

is the resolved rate-of-strain tensor, and $|\bar{S}| = (2\bar{S}_{ij}\bar{S}_{ij})^{1/2}$. f in the expression for the SGS viscosity is the van Driest damping function

$$f = 1 - \exp\left(\frac{n^+}{25}\right), \tag{6}$$

where n is the wall normal distance. Using this damping function, wall effects are partially taken into account by "damping" length scale $l = C_s\Delta$ near the walls. The value of $C_s = 0.1$ previously used for bluff-body flows [10] and flow around a simplified bus [7,6] is used in this work. The filter width, Δ, is defined in this work as $\Delta = (\Delta_1\Delta_2\Delta_3)^{1/3}$, where Δ_i are the computational cell sizes in three coordinate directions.

5 Boundary Conditions and Numerical Details

The average turbulent intensity at the inlet of the wind tunnel used in the experiments of Lienhart and Becker [3] was low (0.25%). A uniform velocity profile, U_∞, constant in time was thus used as the inlet boundary condition in our LES. The convective boundary condition $\partial \bar{u}_i/\partial t + U_\infty(\partial \bar{u}_i/\partial x) = 0$ was used at the downstream boundary. The lateral surfaces and the ceiling were treated as slip surfaces using symmetry conditions ($\partial \bar{u}/\partial y = \partial \bar{w}/\partial y = \bar{v} = 0$ for the lateral sides and $\partial \bar{u}/\partial z = \partial \bar{v}/\partial z = \bar{w} = 0$ for the ceiling). This boundary condition is different from the experimental one, where the test section had a floor but no lateral sides or ceiling. The consequence of this boundary condition is that the flow across the lateral sides and the ceiling is permitted in the experiment but not in the simulation, resulting in different "effective" blocking of the cross section. This will probably have some influence on the aerodynamic forces. No-slip boundary conditions were used on the surface of the body and the instantaneous wall functions based on the log-law (see [6] for details) were applied on the channel floor.

The experimental setup included a turbulent trip wire that was glued around the entire circumference close to the front end of the model and that makes the flow relatively Reynolds number independent. Unfortunately the exact position of this trip wire is not known, and it is not clear how to model this trip wire in our simulation. The trip wire was neither modeled nor included in the present study.

Numerical accuracy was established by making three LES on different computational grids containing 3.5, 9.6, and 16.5 million nodes. The fine computational grid (containing 16.5 million nodes) has a wall normal resolution of $n^+ < 0.33, 13 < \Delta s^+ < 250$ in the streamwise direction and $23 < \Delta l^+ < 70$ in the direction par-

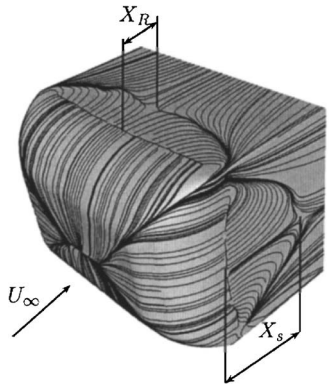

Fig. 3 Time-averaged trace lines on the surface of the front part of the body showing the extensions of the roof vortex, X_R, and the lateral vortex, X_s

allel with the surface of the body and normal to the streamwise direction (the mean Δl^+ is around 30). Here $\Delta n^+ = \Delta n \langle u_\tau \rangle_t / \nu$, $\Delta s^+ = \Delta s \langle u_\tau \rangle_t / \nu$, $\Delta l^+ = \Delta l \langle u_\tau \rangle_t / \nu$ and $\langle u_\tau \rangle_t$ is the time-averaged friction velocity. The time step was 1×10^{-4}, giving a maximum CFL number of approximately 0.9. The averaging time, tU_∞ / H, in the simulations was 38.2 (110,000 time steps).

6 Numerical Method

Equations (1) and (2) are discretized using a 3D finite volume method for solving the incompressible Navier-Stokes equations using a collocated grid arrangement [11]. Both convective and viscous plus subgrid fluxes are approximated by central differences of second-order accuracy. The time integration is done using the second-order Crank-Nicolson scheme. Although no explicit dissipation is added to prevent odd-even decoupling, an implicit dissipation is present. This is done by adding the difference between the pressure gradient at the face and the node. It can be shown that this term is proportional to the third derivative of pressure, i.e., $\partial^3 p / \partial x_i^3$. This term corresponds to Rhie-Chow dissipation [12]. The SIMPLEC algorithm is used for the pressure-velocity coupling. The code is parallelized using block decomposition and the MPI message passing system [13].

7 Results

Our LES resulted in a large amount of instantaneous and time-averaged data. Presenting all these results in a systematic way requires dividing the results among two papers. In this paper we concentrate on presenting the comparison of the LES and the experimental data. The three LES on different grids will be compared among themselves and the influence of the grid refinement will be studied. In the second paper [14] we use our results to describe both the instantaneous and the time-averaged flows in details.

7.1 Global Quantities. This section presents the lengths of the recirculating regions and the aerodynamic forces. Both the time-averaged and the rms values of the forces are reported. Results of our three LES are compared with the experimental data (when available).

As will be demonstrated in the second paper [14], the flow separates at the front end of the body (see Fig. 3). The length of the separation region on the roof, X_R, is equal to $0.23H$, $0.15H$, and $0.08H$ in the LES using coarse, medium, and fine grids, respectively. The separation region, R, on the roof is very thin, with a thickness of $0.0052H$, $0.0024H$, and $0.0024H$ in the LES using coarse, medium, and fine grids, respectively. On the lateral sides we have measured X_s to be equal to $0.52H$, $0.295H$, and $0.128H$, in the coarse, medium, and fine grid LES, respectively. This separation region is thicker than the separation region on the roof. Its

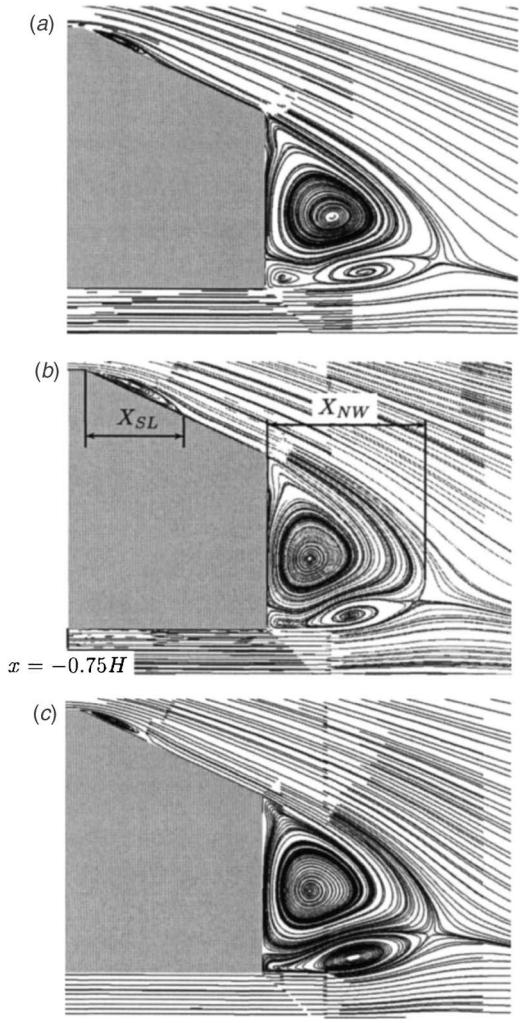

Fig. 4 Time-averaged streamlines projected onto symmetry plane $y=0$ of the car body from LES using (*a*) coarse grid, (*b*) medium grid, and (*c*) fine grid. View is from the lateral side of the body.

thickness is $0.0086H$, $0.0038H$, and $0.0038H$ in the coarse, medium, and fine grid LES, respectively. Finally, we found that the flow separates at the lower rounded edge in the LES using the fine grid. This resulted in the separation region on the underbody that has a maximal extension in the streamwise direction equal to $0.049H$ and a thickness of $0.00035H$ (at $y=-0.347H$). Thus this separation region is about one order of magnitude thinner and shorter than those on the roof and the lateral sides of the body. Both LES using coarse and medium grids produced an attached flow in this region.

The only experimental data on the separation lengths on the front end of the body come from the oil-film visualization of the flow characterized by a Reynolds number of 1.71×10^5 [15]. They measured the length of the recirculating region equal to $0.2175H$ (it is not clear from their paper whether this is the length of the region on the roof or the lateral sides.).

Let us now consider the predicted near-wake flow from our simulations. Figure 4 shows a comparison of the time-averaged streamlines projected onto the symmetry plane, $y=0$, from our LES using different grids. We found that the length from the separation on the upper edge of the rear slant surface to the reattachment, X_{SL}, was approximately equal to $0.28H$, $0.3H$, and $0.35H$ in the coarse, medium, and fine grid LES, respectively. The extension of the near-wake separation bubble (X_{NW} in Fig. 4) obtained

Table 1 Time-averaged pressure drag ($\langle C_D\rangle_t$), and lift ($\langle C_L\rangle_t$) coefficients, and pressure coefficients integrated on the front ($\langle C_K\rangle_t$), rear slanted ($\langle C_S\rangle_t$), and rear vertical surface ($\langle C_B\rangle_t$). The rms values are denoted with the subscript *RMS* (such as $C_{SF_{RMS}}$ in the rms value of the side force coefficient.)

Case	$\langle C_D\rangle_t$	$C_{D_{RMS}}$	$\langle C_K\rangle_t$	$C_{K_{RMS}}$	$\langle C_S\rangle_t$	$C_{S_{RMS}}$	$\langle C_B\rangle_t$	$C_{B_{RMS}}$	$C_{SF_{RMS}}$	$\langle C_L\rangle_t$	$C_{L_{RMS}}$
coarse	0.288	0.004	0.001	0.001	0.582	0.006	0.234	0.004	0.005	0.334	0.011
medium	0.305	0.007	0.001	0.001	0.648	0.002	0.286	0.009	0.005	0.348	0.018
fine	0.292	0.005	0.001	0.001	0.618	0.009	0.265	0.006	0.005	0.344	0.014

in the coarse, medium, and fine grid simulations was $0.6H$, $0.65H$, and $0.65H$, respectively. The center plane projection of the near wake in Fig. 4(*a*) shows three vortices in the coarse grid simulation. The lower vortex close to the rear face loses its form in the medium grid LES and disappears in the fine grid LES [see Figs. 4(*b*) and 4(*c*)]. Thus this false structure is a result of an inadequate resolution in the coarse and medium grid LES.

7.2 Aerodynamic Forces. We have already mentioned that the boundary conditions for the lateral channel walls are different in the experimental investigations and our LES. This disagreement implies differences in the blockage of the experimental and the numerical wind tunnels, resulting in differences in aerodynamic forces. Thus the comparison of the results between experiments and simulations would require some kind of blockage correction for the forces. An additional difficulty in comparing the numerical and the experimental forces is that Ahmed et al. [1] measured pressure drag only at three angles of the rear slant surface, 5°, 12.5°, and 30°. These values were then used to interpolate pressure drag for all angles between 0° and 30°. Lienhart and Becker [3] did not measure the drag but only the distribution of the pressure coefficient on the rear part of the body. Furthermore, the body used in both experiments had stilts that were omitted in our numerical model. These stilts are responsible for some contribution to the drag measured in the experiment.

In the absence of reliable drag corrections, we present results of the three simulations and discuss their agreement with the experimental values, keeping in mind the differences in the geometry and the blocking of the cross section.

The time history of the aerodynamic force coefficients in all three directions, i.e., the drag, the lift, and the side forces coefficients, were computed as $C_D=D/0.5\rho U_\infty^2 A$, $C_L=L/0.5\rho U_\infty^2 A$, and $C_{SF}=SF/0.5\rho U_\infty^2 A$, respectively. Here ρ is density; D, L, and SF are drag, lift and side force due to the pressure, respectively; and A is the frontal area (note that the reference area for all three coefficients is the same projected frontal area in the streamwise direction). These force coefficients were later used to compute the mean and the rms values presented in Table 1. As expected (owing to higher blockage), all three values of the time-averaged drag coefficients from our LES are higher than the value of $\langle C_D\rangle_t = 0.24$ that can be interpolated from the results of Ahmed et al. [1]. The deviation (rms values) from the mean drag coefficient was found to be around 2% of the mean value in all three simulations (see Table 1). The side force coefficient, C_{SF}, was found to vary by approximately 0.005 in all three simulations. The time-averaged lift force coefficient $\langle C_L\rangle_t$ was relatively independent of the grid refinement, having a value between 0.334 and 0.348. Its rms value was between 3% and 5% of the time-averaged lift force coefficients.

Table 1 shows that the aerodynamic forces from three LES from different grids are not consistent with the grid refinement (i.e., they do not only increase or only decrease with the grid refinement). This inconsistency is a result of a very poor resolution in the coarse grid simulation. Too little turbulent kinetic energy is resolved and too much is left to the subgrid-scale model.

Similar to that which Ahmed et al. [1] did, we integrated the streamwise component of the pressure forces for the front, the rear slanted, and the rear vertical surfaces (see Fig. 5 and Table 1). These were then used to break down the total pressure drag into the contributions from the front, the slanted, and the vertical rear surfaces. The three forces are of course dependent on the positions of the reference pressure, which should be the same in the experimental and the numerical studies. Unfortunately, the position of the reference pressure from the experiment of Ahmed et al. [1] is not known, and the differences in its location may influence our comparison. Table 1 gives the time-averaged forces and their rms values. The force on the rear slanted surface, C_S, was found to dominate the total pressure, followed by the force on the vertical rear surface, C_B. Their rms values were between 3% and 10% and 2% and 3% of the time-averaged values for C_S and C_B, respectively. Breaking down the total pressure drag with the help of C_S and C_B gives the relative contributions presented in Table 2. The contributions of the vertical rear surface, $\langle C_B\rangle_t/\langle C_D\rangle_t$, from the three LES are close to the experimental value of 0.07, but there are large differences between $\langle C_K\rangle_t/\langle C_D\rangle_t=0.018$ and $\langle C_S\rangle_t/\langle C_D\rangle_t=0.146$ measured in [1] and our LES results that are given in Table 2. The contribution of the front part coefficient, C_K, to the total pressure drag is very small (see Tables 1 and 2). The low values of C_K are caused by the separated regions on the leading part that reduce the pressure. It is appropriate to mention that the C_K can even become negative (depending on the roundedness of the front and the choice of the reference pressure), such as in [6].

Again there are many uncertainties in this comparison of the experimental data and our LES results for the aerodynamic forces, and these results should be used only as an indication of the magnitude of the contributions of the integrated pressure on the front, the slanted, and the vertical rear surfaces to the total pressure drag.

The time histories of the integrated pressure coefficients were Fourier transformed and the dominating frequencies were identified. Here we present results of the fine grid simulation. Two dominating frequencies were found in the Fourier transform of the drag coefficient signal. These correspond to Strouhal numbers St $=0.15$ and St$=0.26$. The same two frequencies were found in the

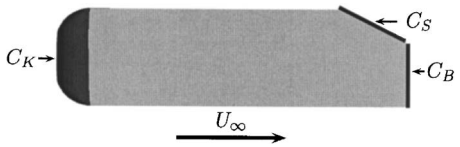

Fig. 5 Schematic representation of the pressure drag breakdown. C_K, C_S, and C_B are integrated pressure force coefficients from the front, the rear slanted, and the rear vertical surfaces, respectively.

Table 2 Relative contributions of the front, rear slanted, and rear vertical surfaces to the total pressure drag (see Fig. 5)

Case	$\langle C_K\rangle_t/\langle C_D\rangle_t$	$\langle C_S\rangle_t/\langle C_D\rangle_t$	$\langle C_B\rangle_t/\langle C_D\rangle_t$
coarse	0.0004	0.205	0.079
medium	0.0004	0.211	0.093
fine	0.0004	0.204	0.088

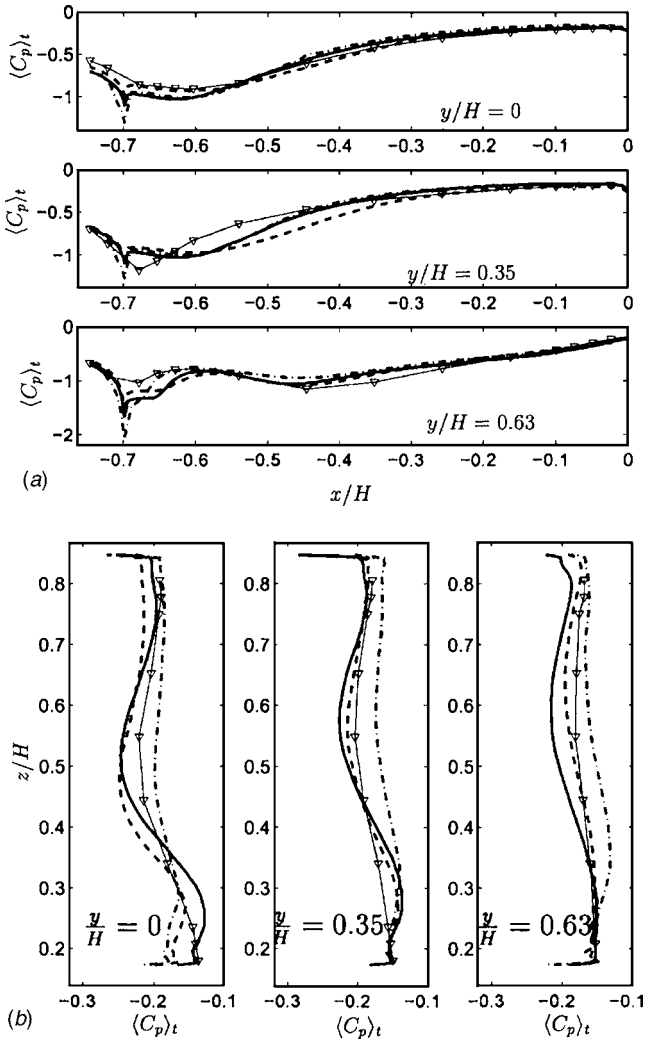

Fig. 6 Distribution of the time-averaged surface pressure coefficients in three planes: $y=0$, $y=0.35H$, and $y=0.63H$. These are plotted along (*a*) the slanted surface and (*b*) the rear vertical surface. Fine grid (solid curve); medium grid (dashed curve); coarse grid (dashed-dotted curve); experiment (symbols).

signal of the pressure coefficient integrated over the rear slanted surface, C_S. This was expected since we found that the pressure drag coefficient is dominated by the surface pressure on the slanted surface (see Table 2). The strongest peak in the Fourier transform of the lift coefficient was found to be at Strouhal number St=0.23 but there were also three other peaks at St=0.1, 0.38, and 0.5 of similar magnitude. The side force signal is very irregular and lacks any dominating frequency in its Fourier transform.

Instead of comparing the results for integrated pressure coefficients C_S and C_B described above, it is probably better to make a comparison of the shapes of the pressure coefficient on the rear slanted and the vertical surfaces. For this comparison we use the data of Lienhart and Becker [3]. As reference pressure they took the static pressure in the undisturbed flow upstream of the model close to the exit of the contraction [16] (the exact position is not reported). The reference pressure in our simulations was taken at the inlet close to the left lateral wall of the channel at $z=2F/3$ (see Fig. 1). However, as can be seen in Fig. 6(*a*), the predicted and experimental C_p at the trailing edge of the slanted surface ($x/H=0$) agree well.

Profiles of the $\langle C_p \rangle_t$ for three planes ($y=0$, $y=0.35H$, and $y=0.63H$) are shown in Fig. 6. The distribution of the surface pressure coefficients along the rear slanted surface is shown in Fig. 6(*a*). The flow must change direction when it separates on the sharp spanwise edge between the roof and the slanted surface forming the shear layer. This change in the flow direction results in the pressure gradient, and a dip in a surface pressure is formed at the position of the sharp edge ($x/H=-0.698$). This rapid decrease in the surface pressure coefficient $\langle C_p \rangle_t$ was observed in all three simulations in Fig. 6(*a*). The mesh of the pressure taps used in the experiment was too coarse to capture this dip [see Fig. 6(*a*)]. All three LES are in good agreement with the experimental $\langle C_p \rangle_t$ between approximately $x/H=-0.55$ and $x/H=0$ (the position of the rear vertical surface) in the center plane ($y/H=0$). For $x/H<-0.55$ we found that the profiles from LES using coarse and fine grids are lower, while the medium grid LES produced a $\langle C_p \rangle_t$ in good agreement with the experiment. This advantage of the medium grid simulation disappears in plane $y=0.35H$, where the profiles from the fine grid simulation are in better agreement with the experiment. Although the magnitude and the shapes of the fine grid LES are the same as in the experiments for $-0.45 \leqslant x/H \leqslant 0$, they are different for $x/H<-0.45$. Agreement between the simulated and experimental profiles in plane $y=0.63H$ is good, with some differences around the dip in the surface pressure coefficient [see Fig. 6(*a*)].

Surface pressure coefficients on the rear vertical surface are presented in Fig. 6(*b*). Although it appears that the coarse grid LES gives a $\langle C_p \rangle_t$ coefficient in good agreement with the experiment in the center plane ($y=0$), the profile is too flat and the $\langle C_p \rangle_t$ values close to the lower edge of the body are too low as compared with the experimental ones. The curvature of the experimental profile is captured much better in the medium and the fine grid LES. The profiles in plane $y/H=0.35$ from the medium and the fine grid simulations have the same amplitude as the experimental, with slightly lower and higher $\langle C_p \rangle_t$ in the medium and lower parts of the profiles, respectively. The coarse grid simulation predicted too high a surface pressure along the entire length of the surface in this plane. Surprisingly, the medium grid LES gave a prediction of the $\langle C_p \rangle_t$ for $y/H=0.63$ that was in best agreement with the measurements. This "better agreement" of the medium grid profile compared with fine grid profile at this position is probably a matter of coincidence. Although the pressure coefficients from the fine grid LES have lower values than the experimental in this plane, the shapes with only one valley between the lower and upper edges are similar. However, the shape of the coarse grid LES profile is different, showing a hill followed by a valley (from the lower to the upper edges of the surface) compared to the experimental profile.

8 Comparison of the Velocities and Reynolds Stresses

Although we have compared all the profiles for the velocities and the Reynolds stresses available in the data files provided from the experimental work [3], space limitations prevent us from reporting all the results in this paper. We thus choose to present the parts of the results that give a fair representation of the comparison of LES and experiments.

Velocity and Reynolds stresses were measured in [3] using a two-component laser-Doppler anemometer (LDA). In this paper we have chosen to present comparisons of the profiles in three planes, $y=0$, $y=0.35H$ and $y=0.63H$. As we compare LES and experimental profiles, we should keep in mind that the experimental data come from several different experimental runs. As we will show later, we have found some discrepancies between our LES profiles and the experimental data for some positions that came from one data set and no discrepancies for other positions that were almost identical to the former ones but whose experimental data came from another set of experiments. These differences will be discussed in the following text.

Comparisons of the velocity profiles and the Reynolds stresses in plane $y=0$ are presented in Figs. 7 and 8. Figure 7(*a*) shows

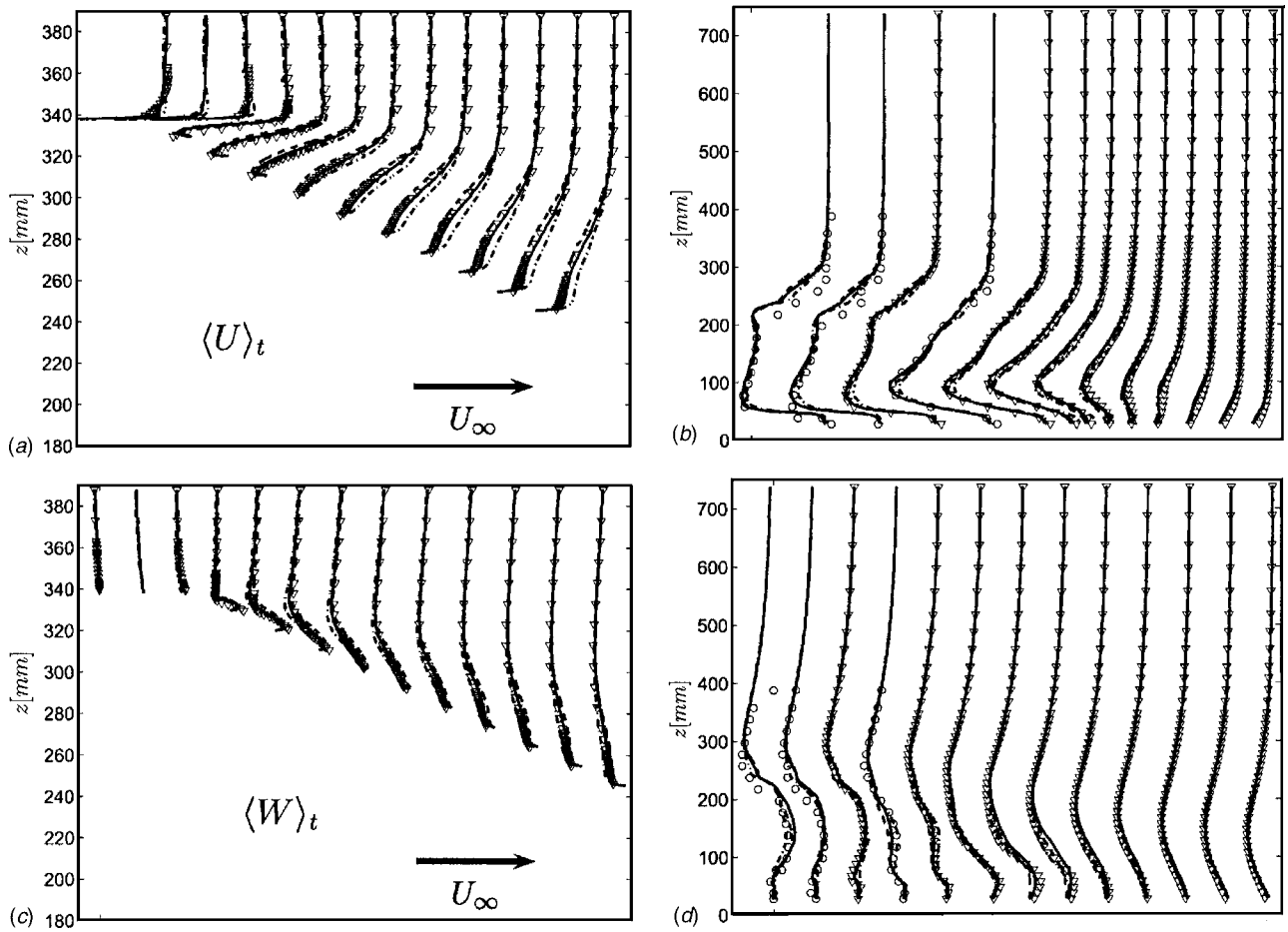

Fig. 7 Time-averaged $\langle U\rangle_t$ [(*a*) and (*b*)] and $\langle W\rangle_t$ [(*c*) and (*d*)] velocity profiles in the symmetry plane ($y=0$). Left: slanted surface; right: wake region. Fine grid (solid curve); medium grid (dashed curve); coarse grid (dashed-dotted curve); experiment (symbols).

streamwise velocity profiles $\langle U\rangle_t$ on the roof and the slanted surface for positions between $x=-0.844H$ and $x=-0.01H$ (from left to right), where the space difference between two profiles is $\Delta x=0.07H$. The experimental profiles for position $x=-0.774H$ are not available, and the LES profiles are presented here only to show the development of the predicted boundary layer at this position. The fine grid LES (denoted with a solid line) overlaps the experimental profiles at all positions except perhaps at the positions on the roof of the body (i.e., $x=-0.844H$ and $-0.705H$). The discrepancies on the roof probably stem from different Reynolds numbers in the experiments and our simulations. Although the flow separates on the leading edge of the front end of the body in our simulation, the separation region is very thin in both the streamwise and wall normal directions. There are no experimental observations of the flow around the front part of the body at the high Reynolds number, but it is reasonable to expect that the separation region becomes thinner as the Reynolds number is increased. Thus the flow on the roof is principally that of a turbulent boundary layer and is therefore defined by the viscosity. The Reynolds number in our LES is about four times lower than in the experiments, resulting in differences in boundary layer thicknesses. The influence of the Reynolds number is already reduced at the position directly after the upstream sharp edge of the slanted surface [i.e., the fourth profile from the left ($x=-0.635H$) in Fig. 7(*a*)] and the geometry starts to dictate the downstream flow. The coarse grid simulation (dashed-dotted curve in the figure) predicts very unrealistic flow far above the boundary layer with oscillations [see the third profile from the left in Fig. 7(*a*)]. It is interesting to observe how the change from attached to separated flow downstream of the fourth profile position ($x=-0.635H$) smooths these oscillations. Differences between profiles from our LES on the coarse and the medium grids and the experimental data are smaller in the region of the separation bubble than in the region after the reattachment on the slanted surface [see Fig. 7(*a*)]. The coarse grid simulation predicts too high a momentum above the slanted surface in the region after the reattachment (the first to the sixth profile from the right).

The $\langle W\rangle_t$ velocities along the slanted surface are in very good agreement with the experimental profiles for all three LES [see Fig. 7(*c*)]. Also here are some differences between simulations but they appear to be smaller than for the $\langle U\rangle_t$ velocities.

Figures 7(*b*) and 7(*d*) present $\langle U\rangle_t$ and $\langle W\rangle_t$ velocity profiles in the wake region behind the body for positions x equal to $0.059H$, $0.128H$, $0.132H$, $0.302H$, $0.306H$, $0.479H$, $0.653H$, $0.826H$, H, $1.174H$, $1.521H$, $1.868H$, and $2.215H$ from left to right. Let us first consider all profiles at all positions except $x=0.059H$, $0.128H$, and $0.302H$. Although the LES using the fine grid gives an almost exact representation of the experimental profiles, all three LES have predicted velocity profiles in very good agreement with the experimental data. Coarse LES have some difficulty giving an accurate representation of the lower recirculating region [see profiles at $x=0.132H$ and $x=0.306H$ in Fig. 7(*b*)] (i.e., the third and fifth profiles from the left, respectively) but the medium simulation manages to capture these regions very well. Let us now return to the remaining three positions (the first, second, and fourth profiles from the left, i.e., $x=0.059H$, $0.128H$, and $0.302H$). The experimental data for these profiles are denoted here with

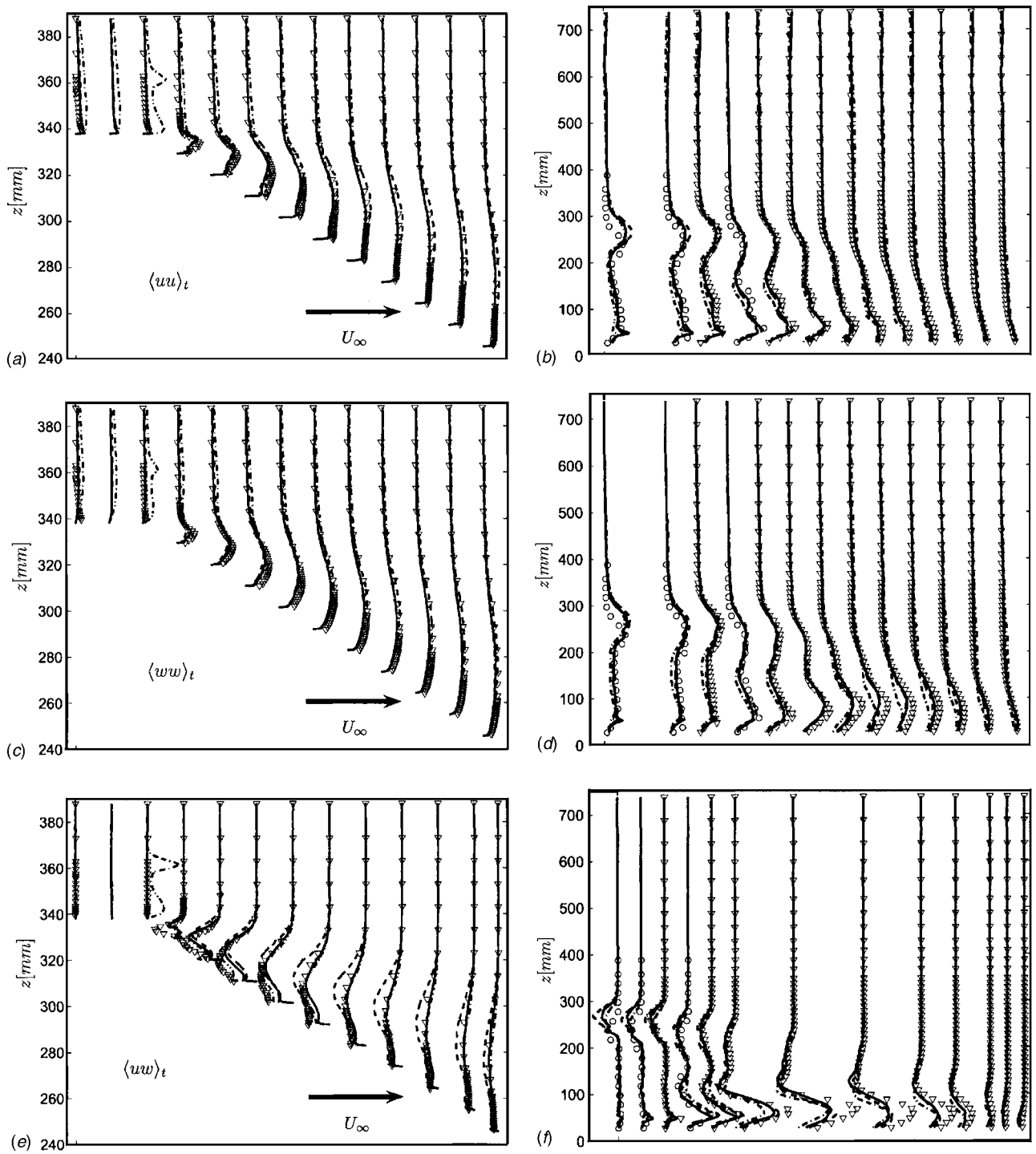

Fig. 8 Time-averaged Reynolds stresses in the symmetry plane ($y=0$). $\langle uu\rangle_t$ [(*a*) and (*b*)]; $\langle ww\rangle_t$ [(*c*) and (*d*)]; $\langle uw\rangle_t$ [(*e*) and (*f*)]. Left: slanted surface; right: wake region. Fine grid (solid curve); medium grid (dashed curve); coarse grid (dashed-dotted curve); experiment (symbols).

circles and come from a different data set than the one that contains all the other profiles in the wake. The experimental profiles for these positions are provided only up to $z=388$ mm compared to other profiles that go up to $z=738$ mm. All LES simulations are in relatively poor agreement with experiment in the upper part (between $z=200$ mm and $z=388$ mm) of the velocity profiles at these positions [see Figs. 7(*b*) and 7(*d*)]. Profiles $x=0.128H$ (the second profile from the left) and $x=0.302H$ (the fourth profile from the left) are located at positions only 1 mm from profiles in the first data set, $x=0.132H$ (the third profile) and $x=0.306H$ (the fifth profile), respectively. Yet the flow in the experimental data changes to a relative great extent between these almost identical positions. Furthermore, our LES using a fine grid gives exact representations of the experimental profiles from the first data set. We thus believe that something is wrong with the experimental data in the second data set (i.e., at positions $x=0.059H$, $0.128H$, and $0.302H$ in plane $y=0$).

Figure 8 presents a comparison between experimental and LES time-averaged Reynolds stresses $\langle uu\rangle_t$, $\langle ww\rangle_t$, and $\langle uw\rangle_t$ in the

center plane, $y=0$. We concentrate first on the flow above the slanted surface in Figs. 8(*a*), 8(*c*), and 8(*e*). The oscillations in the coarse LES of the flow above the roof (the first, second, and third profiles from the left) found in the velocity field are amplified here [see the third profile from the left in Figs. 8(*a*), 8(*c*), and 8(*e*)]. In addition, the normal Reynolds stresses are overpredicted in the flow above the roof in this coarse grid simulation [see $\langle uu\rangle_t$ and $\langle ww\rangle_t$ in the first three profiles from the left in Figs. 8(*a*) and 8(*c*)]. As we move downstream and pass the separation edge (profiles number four, five, etc.), the oscillations in the coarse LES disappear. All three LES produce slightly lower normal Reynolds stresses in the region of recirculating flow [see Figs. 8(*a*) and 8(*c*)], indicating that the experimental flow is slightly more unsteady than the simulated one. The part of the predicted profiles in the coarse grid LES that is located above the recirculating region displays slightly higher normal stresses [see the fourth, fifth, and sixth profiles from the left in Fig. 8(*a*) for $z>340$ mm], similar to what is seen in the upstream flow above the roof. The magnitude of the shear stress profiles $\langle uw\rangle_t$ in the separating region [see Fig. 8(*e*)] is somewhat underpredicted in our LES, but our LES still give much better prediction of these profiles than any of the simulations described in [5]. Profiles $\langle uw\rangle_t$ downstream of the reattachment on the slanted surface are very well captured with both the coarse and fine grid LES. Surprisingly, the medium grid simulation appears to give the worst prediction of the stresses at these positions.

The stresses in the wake flow in our LES are in good agreement with the experimental profiles [see Figs. 8(*b*), 8(*d*), and 8(*f*)]. Some differences between the fine grid LES and the experimental normal stresses are again visible for positions $x=0.059H$, $0.128H$, and $0.302H$ (the first, second, and fourth profiles coming from the different data set as compared to the other profiles). The coarse grid LES predicts a lower magnitude of the normal stresses in the lower part of the profiles at almost all positions (this is particularly visible in the region around the end of the near-wake separation bubble, i.e., the third to the seventh $\langle ww\rangle_t$ profiles from the right). The shear stresses $\langle uw\rangle_t$ are underpredicted in the region close to the rear point of the wake bubble [see Fig. 8(*f*)]. Some small differences between the LES and experimental $\langle uu\rangle_t$ and $\langle ww\rangle_t$ profiles are also visible at these positions [see Figs. 8(*b*) and 8(*d*)].

Let us now consider the results for two other planes, $y=0.35H$ and $y=0.63H$. Figures 9(*a*), 9(*c*), and 9(*e*) show comparisons of the velocity profiles above the slanted surface in plane $y=0.35H$. Unfortunately, measurements are not available close to the wall. Profiles in these figures are for the same x positions as in the center plane.

As in the profiles in the center plane, we find the unphysical oscillations in the flow above the boundary layer on the roof in the LES using the coarse grid [see Fig. 9(*a*)]. These oscillations are not damped directly after the separation on the sharp edge between the roof and the slanted surface as they are in the center plane [see profiles at the fourth to the eighth positions from the left in Fig. 9(*a*)]. Although we lack experimental data in the boundary layer, we find that the lower part of the streamwise velocities from our LES has a lower magnitude after the separation than the experimental profiles (if we extrapolate these down to the wall of the body).

The spanwise velocity components above the slanted surface are shown in Fig. 9(*c*). The magnitudes of these velocities are lower than the magnitudes of the streamwise components, and the LES profiles give an accurate representation of the experimental profiles (again it is not possible to judge the capability of our LES to predict the near-wall region due to the lack of the experimental data in this region).

The $\langle W\rangle_t$ velocities on the slanted surface in our LES are compared with the experimental data in Fig. 9(*e*). They are in very good agreement except very close to the separation edge [see $x=-0.635H$ and $x=-0.566H$ (i.e., the fourth and fifth profiles)].

Compared to the large number of x positions available in the center plane, only three profiles ($x=0.059H$, $0.128H$, and $0.302H$) are provided in plane $y=0.35H$ in the experiments of Lienhart and Becker [3]. Our LES give an accurate representation of all three velocity components [see Figs. 9(*b*), 9(*d*), and 9(*e*)]. The magnitudes of the $\langle U\rangle_t$ and $\langle W\rangle_t$ LES velocities are slightly lower in the medium part of the profiles at position $x=0.302H$ (the third profiles from the left), indicating a smaller recirculation of the near wake bubble. We have also found that the turbulent kinetic energy at this position is slightly lower in the LES compared to that measured in the experiment (not shown here) that indicates a more steady flow. The lower parts of the $\langle V\rangle_t$ profiles for positions $x=0.059H$ and $x=0.128H$ (i.e., the first and second profiles from the left) are better predicted using the fine and the medium grids than the coarse grid [see Fig. 9(*d*)]. Surprisingly, the $\langle W\rangle_t$ velocity at position $x=0.059H$ [the first profile from the left in Fig. 9(*f*)] in the case of the coarse grid has the best agreement with the experimental data. Again, this "better" agreement of one or two profiles from the coarser grid with the experimental data is only coincidental.

Comparisons of the velocity profiles in plane $y=0.63H$ are shown in Fig. 10. Both the $\langle U\rangle_t$ and the $\langle V\rangle_t$ velocities from the fine grid LES are in very good agreement with the experimental data at all positions in the flow above the slanted surface [see Figs. 10(*a*) and 10(*c*)]. Some differences are visible between the LES and the experimental $\langle W\rangle_t$ velocities at the positions between $x=-0.434H$ and $x=-0.08H$ [the seventh to eleventh profiles from the left in Fig. 10(*e*)]. The lower magnitude of the LES profiles at these positions indicates thinner, cone-like vortices that form at the rear slanted edges. The coarse grid simulation suffers from the poor resolution in the lower part of the slanted surface. This is particularly visible in the $\langle W\rangle_t$ profiles, where the profiles from the coarse grid LES are not able to follow the curved experimental profiles.

Figures 10(*b*), 10(*d*), and 10(*f*) present comparisons of the velocity profiles in the near wake at positions $x=0.059H$, $x=0.128H$, and $x=0.302H$, for which experimental data are available. The chief differences between our LES and the experimental profiles were found in the streamwise velocities, $\langle U\rangle_t$, for $z<50$ mm (thus in the wake flow below the body). The differences between these profiles can be explained by the differences in the geometries of the bodies used in the experiment and our numerical studies. The model used in the experiments was placed on four stilts with a diameter of 30 mm at positions $y=\pm 163.5$ mm. Thus the extension of the stilts was up to $y=\pm 178.5$ mm, which is very close to the position ($y=180$ mm) of the profiles in Fig. 10. Although the rear pair of stilts is located relatively far from the near wake (at $x=-1.292H$), the resulting wake behind the stilts decreases the streamwise velocity in the experiment.

Another influence of the stilts is the unsteadiness of their wakes. The profiles of the turbulent kinetic energy (Fig. 11) show that, while the flow in our LES is almost steady ($\langle k\rangle_t \sim 0$) below the body, the flow measured in the experiments has relatively high turbulent kinetic energy in this region (particularly for the first profile from the left, i.e., $x=0.059H$). The turbulent kinetic energy in the experimental flow may be the consequence of the unsteadiness in the wake behind the stilts.

9 Conclusions

The large eddy simulation technique has yet not matured sufficiently to be used to obtain design quantities in the external aerodynamics of the ground vehicles, such as drag or lift. Its use is prohibited by the requirement on resolution in the near-wall region. Several promising approaches that reduce resolution requirements by their modeling of the near-wall region are under devel-

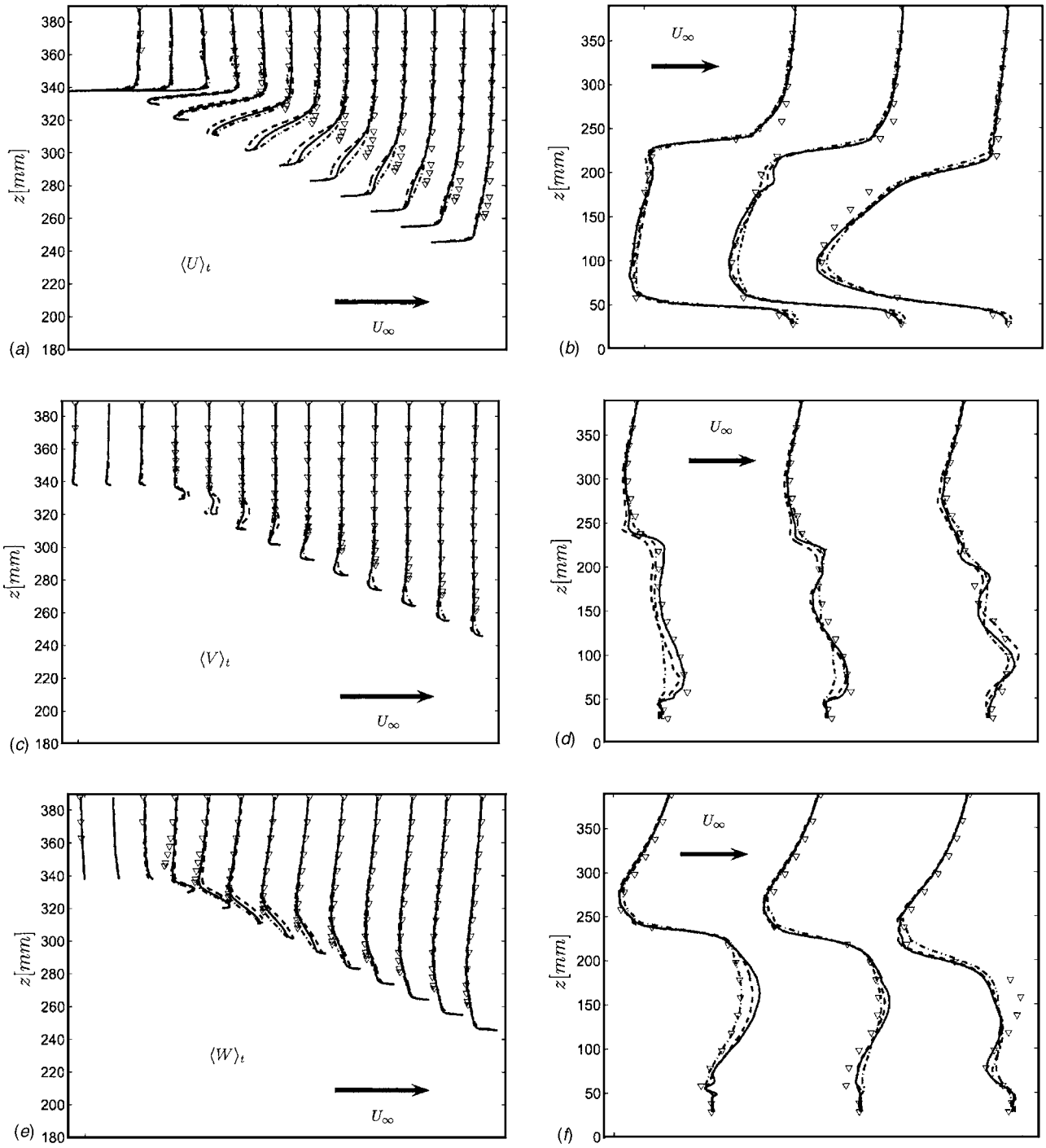

Fig. 9 Time-averaged $\langle U\rangle_t$ [(*a*) and (*b*)], $\langle V\rangle_t$ [(*c*) and (*d*)], and $\langle W\rangle_t$ [(*e*) and (*f*)] velocity profiles in plane $y=0.35H$. Left: slanted surface; right: wake region. Fine grid (solid curve); medium grid (dashed curve); coarse grid (dashed-dotted curve); experiment (symbols).

opment. Among these are the hybrid methods, so-called hybrid LES-RANS or detached eddy simulations (DES), that use RANS solution in the near-wall region and the LES in the rest of the domain. Unfortunately these are still not fully developed and several problems remain to be solved (such as choice of turbulence model, where to put the matching line between the RANS and the LES regions, how to provide the correct boundary conditions for the LES region from the RANS region, etc.) before they can be used in vehicle aerodynamics.

Some alternative approaches in using LES in vehicle aerodynamics are thus needed. This paper has suggested one approach that uses the constraints that are put on the flow by the geometry, such as separation defined by the sharp edge. It has been assumed that the Reynolds number and the resolution requirements could be decreased if the positions of the recirculating regions in the flow are defined by the geometry rather than by the viscosity and the upstream conditions (such as turbulence at the inlet and the boundary layer thickness).

Our approach was tested on the flow around a generic car (a so-called Ahmed body) with the angle of the rear slanted surface of 25%. Earlier RANS and LES applications in this flow have been unsuccessful [5]. The Reynolds number was decreased about

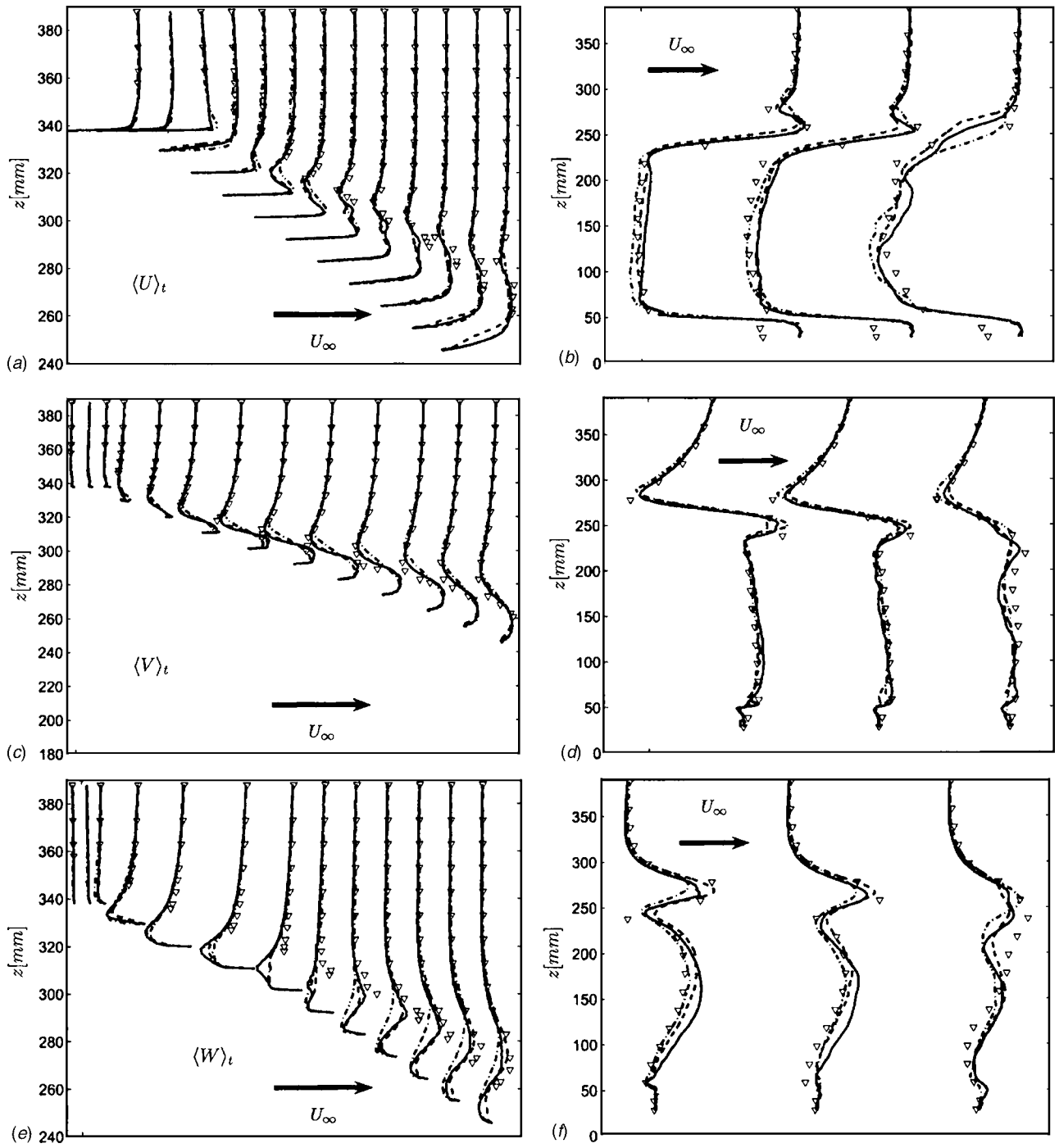

Fig. 10 Time-averaged $\langle U\rangle_t$ [(*a*) and (*b*)], $\langle V\rangle_t$ [(*c*) and (*d*)], and $\langle W\rangle_t$ [(*e*) and (*f*)] velocity profiles in plane $y=0.63H$. Left: slanted surface; right: wake region. Fine grid (solid curve); medium grid (dashed curve); coarse grid (dashed-dotted curve); experiment (symbols).

four times in our LES as compared with the experimental one [3]. Although the experimental setup included a turbulent trip wire that was glued to the front end of the model, making the flow relatively Reynolds number independent, there are still differences in the experimental and simulated boundary layers on the body. However, our results show that the dependence on the results in the wake, after the separations at the sharp edges, of the Reynolds number is very small.

An extensive comparison has been given of our LES results and the experimental data. This comparison confirmed our assumptions and the usefulness of the new LES approach that we suggest. Only small discrepancies were found between our LES and experimental results, and some of these are believed to be problems in the experiments.

This paper showed that the flow around an Ahmed body (and especially the flow after its sharp edge separations) at high Reynolds number can be simulated using LES at lower Reynolds number. We believe that the main reason for this relative Reynolds number independence of the flow around and behind the rear of the body are the sharp edge separations in combination with the tripping of the turbulent boundary layer at the front of the body in the experiments. We must stress that there is nothing in this paper

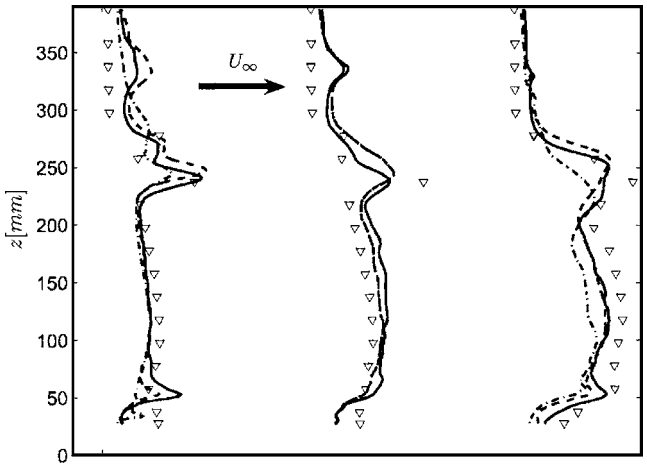

Fig. 11 Time-averaged turbulent kinetic energy $\langle \bar{k} \rangle_t$ in plane $y=0.63H$. Fine grid (solid curve); medium grid (dashed curve); coarse grid (dashed-dotted curve); experiment (symbols).

that shows that this method is general and will work for flow around vehicles with smooth surface separations. The present paper shows only that the method is useful in the such flows as are studied in this paper, i.e., the flow around bodies where the separations are defined by the geometry.

Now that we have proved the accuracy of our LES in adequately representing the flow around the generic car body, we shall in [14] use the LES results to explore this flow in detail.

Acknowledgments

This work was supported by the FLOMANIA project. The FLOMANIA (Flow Physics Modeling—An Integrated Approach) is a collaboration between Alenia, AEA, Bombardier, Dassault, EADS-CASA, EADS-Military Aircraft, EDF, NUMECA, DLR, FOI, IMFT, ONERA, Chalmers University, Imperial College, TU Berlin, UMIST, and St. Petersburg State University. The project is funded by the European Union and administrated by the CEC, Research Directorate-General, Growth Programme, under Contract No. G4RD-CT2001-00613. Computer time on the Linux cluster, provided by the NSC (National Supercomputer Center in Sweden), is gratefully acknowledged.

References

[1] Ahmed, S. R., Ramm, G., and Faltin, G., 1984, "Some Salient Features of the Time Averaged Ground Vehicle Wake," SAE paper no. 840300.
[2] Spohn, A., and Gillieron, P., 2002, "Flow Separations Generated by a Simplified Geometry of an Automotive Vehicle," in *IUTAM Symposium: Unsteady Separated Flows*, April 8–12, Toulouse, France.
[3] Lienhart, H., and Becker, S., 2003, "Flow and Turbulent Structure in the Wake of a Simplified Car Model," SAE paper no. 2003-01-0656.
[4] Han, T., 1989, "Computational Analysis of Three-Dimensional Turbulent Flow Around a Bluff Body in Ground Proximity," AIAA J., **27**(9), pp. 1213–1219.
[5] Manceau, R., and Bonnet, J.-P., 2000, 10th Joint ERCOFTAC (SIG-15)/IAHR/QNET-CFD Workshop on Refined Turbulence Modelling, Poitiers.
[6] Krajnović, S., and Davidson, L., 2003, "Numerical Study of the Flow Around the Bus-Shaped Body," ASME J. Fluids Eng., **125**, pp. 500–509.
[7] Krajnović, S., 2002, "Large Eddy Simulations for Computing the Flow Around Vehicles," Ph.D. thesis, Chalmers University of Technology, Gothenburg.
[8] Cooper, K. R., 1985, "The Effect of Front-Edge Rounding and Rear Edge Shaping on the Aerodynamic Drag of Bluff Vehicles in Ground Proximity," SAE paper no. 850288.
[9] Smagorinsky, J., 1963, "General Circulation Experiments with the Primitive Equations," Mon. Weather Rev., **91**(3), pp. 99–165.
[10] Krajnović, S., and Davidson, L., 2002, "Large Eddy Simulation of the Flow Around a Bluff Body," AIAA J., **40**(5), pp. 927–936.
[11] Davidson, L., and Farhanieh, B., 1995, "CALC-BFC: A Finite-Volume Code Employing Collocated Variable Arrangement and Cartesian Velocity Components for Computation of Fluid Flow and Heat Transfer in Complex Three-Dimensional Geometries," Report 95/11, Department of Thermo and Fluid Dynamics, Chalmers University of Technology, Gothenburg.
[12] Rhie, C. M., and Chow, W. L., 1983, "Numerical Study of the Turbulent Flow Past an Airfoil with Trailing Edge Separation," AIAA J., **21**(11), pp. 1525–1532.
[13] Nilsson, H., and Davidson, L., 1998, "CALC-PVM: A Parallel SIMPLEC Multiblock Solver for Turbulent Flow in Complex Domains," Internal report 98/12, Department of Thermo and Fluid Dynamics, Chalmers University of Technology, Gothenburg.
[14] Krajnović, S., and Davidson, L., 2005, "Flow Around a Simplified Car, Part 2: Understanding the Flow," ASME J. Fluids Eng., **127**, pp. 919–928.
[15] Sims-Williams, D. B., and Dominy, R. G., 1998, "Experimental Investigation into Unsteadiness and Instability in Passanger Car Aerodynamics," SAE paper no. 980391.
[16] Lienhart, H., 2004, private communication, Universität Erlangen-Nürnberg.

Flow Around a Simplified Car, Part 2: Understanding the Flow

Siniša Krajnović
e-mail: sinisa@chalmers.se

Lars Davidson

Division of Fluid Dynamics,
Department of Applied Mechanics,
Chalmers University of Technology,
SE-41296 Gothenburg, Sweden

Results of a large eddy simulation (LES) are used to explore the flow around a generic car model. A new, refined picture of this flow is established. Many parts and aspects of this flow are studied and explained. The development of the instantaneous flow and its resulting time-averaged flow are depicted. Large differences are found between the instantaneous and the time-averaged flows. Special attention is given to the flow above the rear slanted surface. The origin, the development, and the interactions of the instantaneous vortices in this part of the flow are presented for the first time. This instantaneous flow is shown to be very unsteady and to contain a large number of different vortices that range in size from those of the size of the body over the intermediate hairpin-like vortices to very small coherent structures. Besides the variety in the length scales, the flow covers a wide spectrum of the time scales from the relatively steady motion of the cone-like trailing vortices on the slanted edges to highly frequent collisions of the hairpin-like vortices in the region of the attachment on the rear slanted surface.
[DOI: 10.1115/1.1989372]

Keywords: Large Eddy Simulation, LES, Generic Car, Vehicle Aerodynamics, Ground Vehicle

1 Introduction

Descriptions of flow features and their interactions are important for understanding the aerodynamic properties of a vehicle body. Probably the first picture of the flow around the ground vehicle body studied here (i.e., a body with a rear slant angle of 25°) was given by Ahmed et al. [1]. This included only a representation of the time-averaged flow around the rear part of the body. They observed two vortices trailing around the slanted side edges of the body. In addition to observing these vortices they found that the separation bubble in the near wake contains a pair of horseshoe vortices, situated one above the other. Ahmed et al. [1] also gave an explanation of the interactions of these structures on the basis of their measurements and visualizations and a rough description of the surface flow features on the rear slanted and vertical surfaces. The picture of the flow around the rear part of the body found in [1] was confirmed in the experimental work of Lienhart and Becker [2], who used more accurate measurements (laser-Doppler anemometry) than the measuring technique used in [1]. Another visualization study of the flow around this body is that of Spohn and Gillieron [3], who in addition to the wake flow also studied the flow along the body. The focus of their study was the instantaneous flow structures. The Reynolds number in their study was very low (8.3×10^3, based on the incoming velocity and the height of the body). To our knowledge the only description of the flow around the front part of the body of the Ahmed body at a Reynolds number comparable with that used in our large eddy simulation (LES) is that by Sims-Williams and Dominy [4]. They used oil-film visualization and registered three imprints of spanwise vortices (one on the top and one on each of the lateral sides of the body), similar to those found in Krajnović and Davidson [5] around the front of a similar body.

The present paper gives a thorough presentation of the flow structures and their interactions. The suggested vortical structures from [1,2,4] are compared with those found in our large eddy simulations. Their existence as well as the suggested explanation of their interactions are explored. The main objective of the present paper is to use the large amount of results from our LES calculations [6] together with state of the art visualization techniques to give an accurate representation of the flow. Both instantaneous and time-dependent structures are presented and the mechanisms of their origins are explained. The flow contains flow structures with a wide spectrum of time and length scales. These are studied with various visualization tools.

The paper is organized as follows: after the short review of visualization tools in Sec. 2, a brief summary of our LES calculation from [6] is given in Sec. 3.1. The flow around the front of the body is discussed in Sec. 3.2. This is followed by a description of the flow along the lateral edges of the body in Sec. 3.3. The most complex parts of the flow are those on the rear slanted surface and in the near wake, and these are described in Secs. 3.4 and 3.5, respectively. Finally, concluding remarks are given and the relevance and use of the results obtained are discussed in Sec. 4.

2 Visualization Tools

Several different visualization techniques were used to analyze the data from our LES calculations in [6]. Our experience is that different techniques are needed in different parts of the flow. The visualization software used in this paper is EnSight. The isosurfaces of the instantaneous second invariant of velocity gradient $Q=-1/2\partial u_i/\partial x_j \partial u_j/\partial x_i$ (see [7]) were used to study the temporal evolution of the coherent structures around the body. The time-averaged streamlines, velocity vectors, and isosurfaces of low static pressure were used to visualize time-averaged flow features. Vortex cores were calculated using EnSight postprocessing software which uses algorithms based on techniques outlined by Sujudi and Haimes [8]. Two of these algorithms are implemented in EnSight, the eigenvalue analysis algorithm and the vorticity-based algorithm. Both are linear and nodal, i.e., "*They are based on decomposing finite elements into tetrahedron and then solving closed-form equations to determine the velocity gradient tensor value at the nodes. Also, any variables with values at element centers are first averaged to element nodes before processing*" [9]. We have found in our previous work that the eigenvalue analysis algorithm is more suitable for the flows around ground vehicle bodies. "*This algorithm uses classification of eigenvalues and vectors to determine whether the vortex core intersects any faces of the decomposed tetrahedron*" [9]. Unfortunately, the eigenvalue analysis algorithm may produce false cores if the flow contains

Contributed by the Fluids Engineering Division for publication in the JOURNAL OF FLUIDS ENGINEERING. Manuscript received by the Fluids Engineering Division, July 26, 2004. Final revision: May 16, 2005. Associate Editor: Ismail B. Celik.

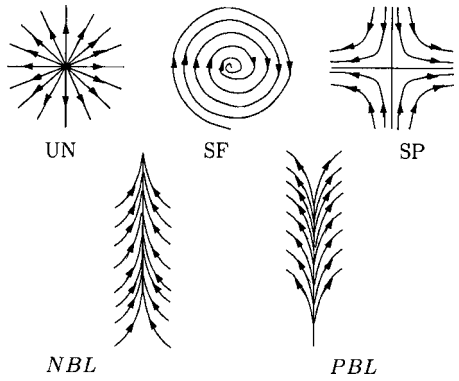

Fig. 1 Schematic representation of an unstable node (UN), stable focus (SF), and saddle point (SP). *NBL* and *PBL* are negative and positive bifurcation lines, respectively.

several vortices located close to each other [9]. In addition, both algorithms have difficulty finding the cores of curved vortices owing to the linear implementation of algorithms in EnSight [9]. As we will see later in the paper, this may cause problems in identifying the correct shape of the vortices in the near wake.

Time-averaged trace lines and streamlines are used to reveal critical points (i.e., points at which all the spatial derivatives of the velocity are zero) and bifurcation lines in the flow. Critical points can be classified into three main groups—nodes, foci, and saddles—of which nodes and foci can be stable and unstable (see Fig. 1). "*Bifurcation lines are lines drawn in the flow toward which the trajectories are asymptòtic*" [10]. They are denoted negative bifurcation lines (*NBL*) or positive bifurcation lines (*PBL*) depending on whether the trajectories on the wall are converging to or diverging from the bifurcation line (see Fig. 1). These lines are associated with flow attachment (*PBL*) or separation (*NBL*). For a complete description of critical points and bifurcation lines, we refer to [10].

3 Description of the Flow

3.1 Description of the LES Calculations. Large eddy simulations of the flow around the Ahmed body with the rear slanted surface at an angle of 25° (see Fig. 2) at a Reynolds number of about 2×10^5 (based on the height of the body and the velocity at the inlet) were reported in [6]. Three different computational grids were used and the present paper considers the results of the finest grid only. This computational grid contains around 16.5 million nodes which, in combination with a clever block arrangement, made possible a spatial resolution that has a resolution of $n^+<0.33$ in the wall normal direction, $13<\Delta s^+<250$ in the streamwise direction and $23<\Delta l^+<70$ in the direction parallel with the surface of the body and normal to the streamwise direction (the mean Δl^+ is around 30). Here $\Delta n^+=\Delta n\langle u_\tau\rangle_t/\nu$, $\Delta s^+=\Delta s\langle u_\tau\rangle_t/\nu$, $\Delta l^+=\Delta l\langle u_\tau\rangle_t/\nu$, and $\langle u_\tau\rangle_t$ is the time-averaged friction velocity. The time step was 1×10^4, giving a maximum CFL number of approximately 0.9 during the entire simulation. The averaging time, tU_∞/H, in the simulation was 38.2 (110,000 time steps). The time-averaged streamlines projected onto the several z planes downstream of the body were found to be approximately symmetric with respect to plane $y=0$, which indicates that the number of averaging samples and the averaging time were approximately sufficient. It should be mentioned that, in more careful investigation in the present paper, we found some asymmetry of the time-averaged flow with respect to plane $y=0$. This indicates that the flow contains some low-frequency events that require even longer averaging times. The computational time was already very long, however, and it was not possible to increase it considerably. The influence of the longer averaging time was tested (not shown here) on the medium grid simulation without finding any significant change in the flow features. As the flow structures are approximately the same on the medium and the fine grids in [6] we conclude that the averaging time of $tU_\infty/H=38.2$ is sufficient to produce an authentic picture of the mean flow. The subgrid-scale model used in the simulation was the standard Smagorinsky model with the constant $C_s=0.1$. A complete description of the numerical details in our LES calculations can be found in [6].

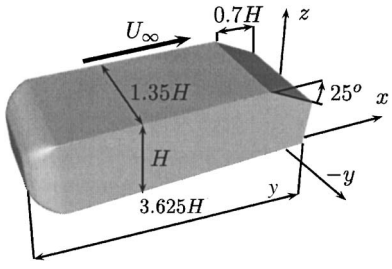

Fig. 2 Geometry of the Ahmed body. View from the side of the body. Note that *z*=0 is the ground plane and *x*=0 and *y*=0 are at the position of the rear vertical surface and the symmetry plane of the body, respectively.

This section describes the flow structures and their origins. Both the "real," i.e., the instantaneous flow, and the resulting time-averaged representation of that flow are considered. Observed flow features are compared with the findings of previous experimental studies. Some hypotheses presented in the past about the flow are closely examined and either confirmed or rejected on the basis of our findings. The presentation of the flow starts with the front part of the body, to continue with the flow along the body and its rear part. Finally the structures in the wake of the body are described.

3.2 Front Part of the Body. The flow around the front part of the Ahmed body is seldom studied, partly because of Ahmed et al.'s [1] stating that "*The interference between the rear end and the fore body flow is weak; this could be a consequence of the relatively long midsection.*" Two descriptions of the front part of the flow are given by Sims-Williams and Dominy [4] and Spohn and Gillieron [3]. The former discusses the flow at a Reynolds number of 1.71×10^5, based on the incoming velocity and the height of the body, which is close to that in the present paper. Sims-Williams and Dominy [4] used oil-film visualization to visualize the regions of the recirculating flows on the lateral sides and the roof of the body. Spohn and Gillieron [3] studied the instantaneous flow at a Reynolds number of 8.3×10^3 and found that the flow separates at the leading edge, forming vortical structures similar to Kelvin-Helmholtz vortices with their axes parallel to the separation line on the leading edge of the front of the body. Results of our LES calculations show that the instantaneous vortices are more of the hairpin-like type, similar to those found in [5], than of the Kelvin-Helmholtz type. They do not extend between the two foci found in the time-averaged flow (see Figs. 3 and 4) as assumed in the study by Spohn and Gillieron [3]. The identification of the Kelvin-Helmholtz vortices in [3] was based on two-dimensional photography from the lateral side of the body, which does not give sufficient information on the character of the vortical structures (i.e., two-dimensional, such as Kelvin-Helmholtz vortices, or three-dimensional, such as hairpin vortices). Thus the observation of the Kelvin-Helmholtz vortices in [3] probably has to do with the shortcomings of the visualization technique.

The oncoming time-averaged flow is divided on the front of the body into four regions, of which two end on the lateral sides, one on the top and one on the bottom side of the body (see Fig. 3). These regions are separated by positive bifurcation lines (such as PBL_f in Fig. 3) starting in the stagnation point and ending in the corners of the front surface. The flow separates as it reaches the

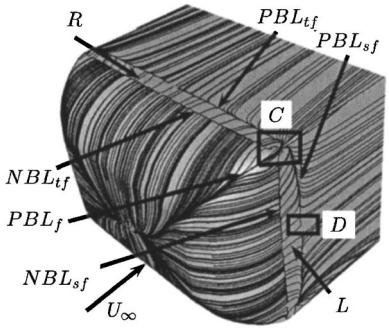

Fig. 3 Time-averaged trace lines on the surface of the body showing the roof and the lateral vortices. View of the front of the body from above and the lateral side.

top, the lateral, and the bottom sides of the body, forming negative bifurcation lines (NBL_{tf}, NBL_{sf}, and NBL_{lf}, respectively) as shown in Figs. 3 and 5. Figure 5 shows the underbody of the front of the vehicle. Downstream of these lines, we observe regions of recirculating flow (see *R* and *L* in Fig. 3 and *B* in Fig. 5). The imprints of vortices *R* and *L* in Fig. 3 are similar to those observed in [4]. The reattachments of the flows in regions *R*, *L*, and *B* are denoted by the positive bifurcation lines, PBL_{tf} and PBL_{sf} in Fig. 3, and PBL_{lf} in Fig. 5.

The flow following the positive bifurcation line, PBL_f (Fig. 3), splits into two parts (Fig. 4) that diverge and form two positive bifurcation lines (PBL_{tf} and PBL_{sf}), indicating the end of the separated flow (see Figs. 3 and 4). As this happens, the surface flow closest to the lateral edges moves in spiral motions ending in two stable foci, F_{ful} and F_{fsl} (see Fig. 4). These foci indicate the positions where vortices *R* and *L* are attached to the surface of the

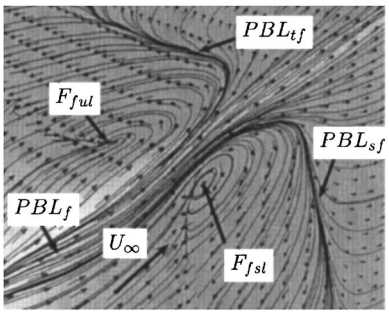

Fig. 4 Time-averaged trace lines on the surface of the body. Zoom of region *C* in Fig. 3 showing two foci, F_{ful} and F_{fsl}.

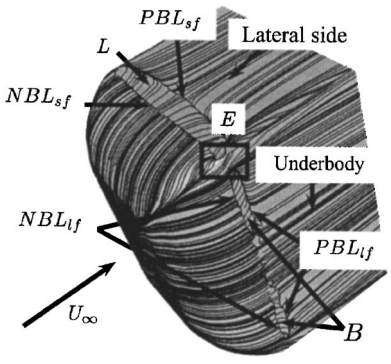

Fig. 5 Time-averaged trace lines on the surface of the body showing the vortices on the lateral side and underneath the body. View of the front of the body from below and the lateral side.

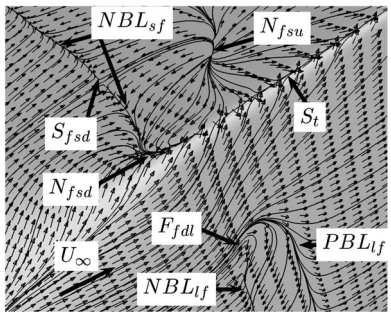

Fig. 6 Time-averaged trace lines on the surface of the body. Zoom of region *E* in Fig. 5 showing one stable N_{fsd} and one unstable node N_{fsu}, saddle point S_{fsd} and focus F_{fdl}.

body. The core of the time-averaged roof vortex, *R*, starts in focus F_{ful} and ends in the corresponding foci on the roof surface on the mirror side of the body (not shown here). Spohn and Gillieron [3] also identified two foci similar to F_{ful} and its mirror image.

The direction of the main part of the core of vortex *R* is parallel with the separation line, NBL_{tf} in Fig. 3. In the same way, the lateral vortex, *L*, in Fig. 3 is parallel with its separation line. The vortex core starts in focus F_{fsl} (in Fig. 4) and stretches parallel with the line of separation indicated by the NBL_{sf} (see Fig. 3). The lower corner of the front of the body is shown in Fig. 6. The instantaneous vortices downstream of this corner and along the edge S_t are presented in Fig. 7. Two different kinds of instantaneous vortices are shown in this figure, λ and T_i vortices. The λ vortex shown in Fig. 7 is a so-called hairpin vortex and is formed in the following way: as the instantaneous flow separates at the lateral rounded edge of the body approximately at the position of the NBL_{sf} in Fig. 3, vortices are formed parallel with the instantaneous separation line (which is approximately at the position of time-averaged separation line NBL_{sf}). On their way downstream, their middle parts are lifted from the surface of the body, forming hairpin vortices, λ. When averaged, the λ vortices form the time-averaged lateral vortex *L* (we can see the imprint of *L* on the body in Fig. 3). Similar hairpin vortices are formed in the instantaneous flow on the roof of the body, approximately downstream of the NBL_{tf}. These structures average into the time-averaged vortex *R* in Fig. 3. The merging of the instantaneous structures λ and T_i in region *M* is visualized in Fig. 7.

At approximately half the body height, positive bifurcation line PBL_{sf} is divided by saddle point S_{fsl} (see Fig. 8). At approximately the same height, there is a saddle point on NBL_{sf} (not shown here). In a similar way, the flow coming from the opposite sides of lines PBL_{tf} and NBL_{tf} (see Fig. 3) on the roof of the body

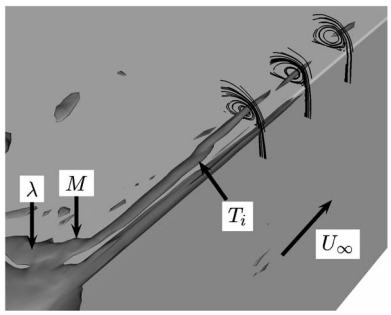

Fig. 7 The isosurface of the instantaneous second invariant of the velocity gradient, $Q=4000$, around the lower lateral edge. T_i are the instantaneous structures that average to become the time-averaged vortex in Fig. 9. *M* indicates the approximate position of merging of λ vortices on the lateral side with the T_i structures. View of the body from below and the lateral side.

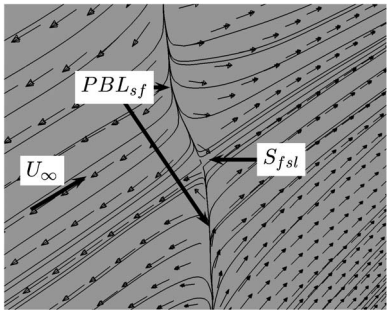

Fig. 8 Time-averaged trace lines on the surface of the body. Zoom of region *D* in Fig. 3 showing saddle point S_{fsl}.

collides in saddle points (not shown here).

The lower side of the body displays the separated region *B* which is divided into three parts (see Fig. 5). We have found that both the negative bifurcation line, NBL_{lf} (separation), and the positive bifurcation line, PBL_{lf} (reattachment), stretch only one-third of the width from each lateral edge (see Fig. 5). It was difficult to identify the bifurcation lines in the middle one-third of the width of the body. As seen in [6], separation region *B* is much thinner than regions *R* and *L* on the roof and the lateral sides, respectively.

We shall now consider the flow around one of the lower front corners (*E* in Fig. 5) shown in Fig. 6. The time-averaged separation region on the lateral side extends from the upper to the lower corners of the lateral side in Fig. 3. (all the way from focus F_{fsl} in Fig. 4 to the stable node N_{fsd} in Fig. 6). One saddle point, S_{fsd} (Fig. 6), was found on the NBL_{sf} close to node N_{fsd}. The unstable node, N_{fsu}, appears as we move downstream on the lateral side of the body. Figure 6 indicates that the surface flow is redistributed in N_{fsu} in all four directions in a spiral shape.

Let us now return to the flow close to the leading edge of the bottom side of the body (see Figs. 5 and 6). As mentioned earlier the flow separates on the bottom edge. The upstream flow that reaches the bottom side of the body closest to the lateral edge is deflected toward that edge and feeds the longitudinal trailing vortex stretching along edge S_t (see Fig. 6). The rest of the surface flow is attached on the surface for approximately one-tenth of the width and separates close to stable focus F_{fdl} (see Fig. 6). This point indicates the singular point between the negative and positive bifurcation lines, NBL_{lf} and PBL_{lf}. We have found that the origin of the vortex core of time-averaged vortex *B* is located in this point (not shown here). The vortex core of *B* was difficult to identify in the middle one-third of the width of the body.

Krajnović and Davidson [5,11] studied the flow around a similar body and observed no separation at the leading lower edge. A possible explanation of the change from attached flow in [5,11] to separated flow in the present study is that the ground clearance, $c/H=0.17$, in the present flow is larger than $c/H=0.08$ in [5,11]. The larger ground clearance allows the flow to separate and then reattach, forming coherent structures. Another possible explanation is related to the spatial resolution used in [5,11]. We found that the separating bubble *B* is very thin and was observed only in the fine mesh LES [6]. Thus it is possible that a similar bubble exists in the flow in [5,11] but was not detected owing to relatively insufficient resolution.

3.3 Longitudinal Vortices Along the Body. Boundary layers are formed both on the stationary floor and the underbody of the car model. These decelerate the fluid and, to satisfy continuity, the fluid, instead of accelerating in the center region between the floor and the underbody, spreads outward to the lateral sides and forms the coherent structures, T_i, in Fig. 7 that average into the longitudinal vortex in Fig. 9.

This time-averaged longitudinal vortex initially grows in diameter along the lateral edge, S_t, in the downstream direction. Then, downstream of approximately $x=-1.5H$, it has a constant diameter for the main part of the body length (see Fig. 9). The core of the vortex in Fig. 9 keeps the initial position in the *x-y* plane along and behind the body. Some longitudinal structures (*LS*) were observed above the floor [see Fig. 9(*b*)]. It is not clear whether these were caused by the stationary floor or whether they are a result of insufficient averaging time.

3.4 Rear Slanted Surface of the Body. This section describes the part of the flow that has the greatest influence on the aerodynamics of the body, i.e., the flow on the slanted surface. The instantaneous flow structures are described first. This is followed by a presentation of the picture of the resulting time-averaged flow.

3.4.1 Instantaneous Flow on the Rear Slanted Surface. The fluid separates at the sharp edge [S_s in Fig. 10(*a*)] between the roof surface and the slanted rear surface. Elongated coherent structures that extend in the spanwise direction are formed as a result of this separation. The axes of these structures are parallel with the edge along the middle part of the edge. The vortices that

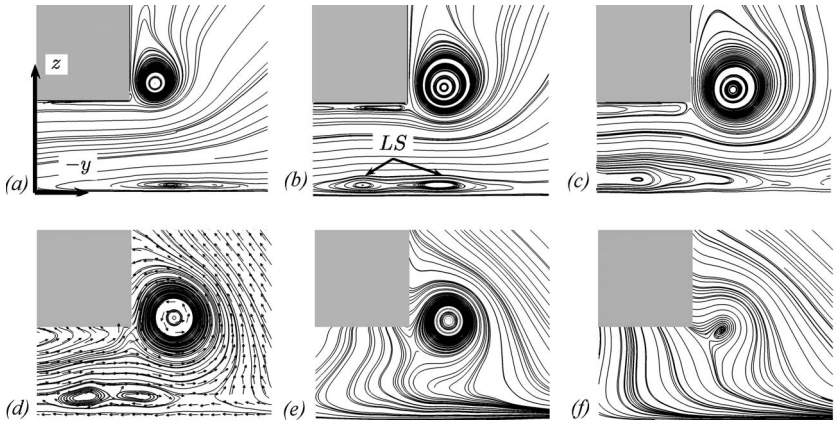

Fig. 9 Time-averaged streamline projected onto planes: (*a*) $x=-2.08H$, (*b*) $x=-1.39H$, (*c*) $x=-0.69H$, (*d*) $x=0$ (the plane of the rear vertical surface), (*e*) $x=0.21H$, and (*f*) $x=0.38H$. View from the front of the lower left edge of the body. Note that *z* and *y* axes in the figure do not indicate the origin of the coordinate system. The real $y=0$ is at the position of the symmetry plane of the body. Flow is from the observer into the plane.

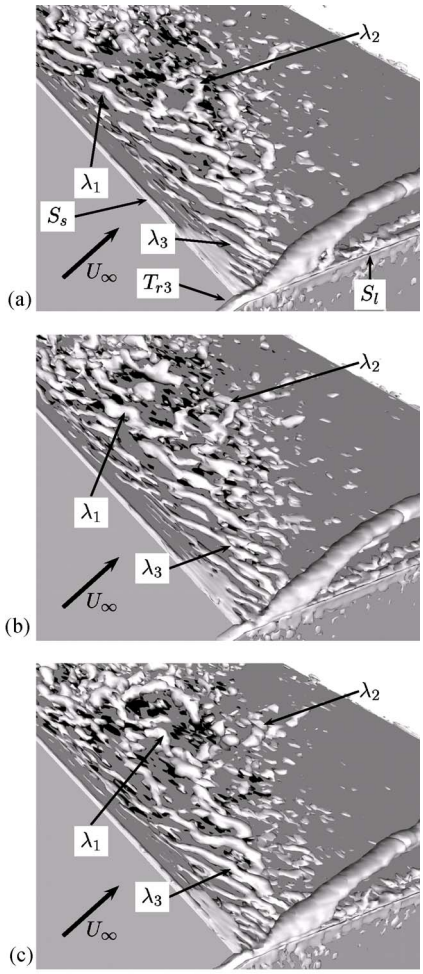

Fig. 10 The isosurface of the instantaneous second invariant of the velocity gradient, $Q=6500$. The time difference between two pictures is $tU_\infty/H=0.055$. Flow is from left to right and the view is from the lateral side and above the body. The sharp edge between the roof and the slanted surface is denoted by S_s and the slanted lateral edge is denoted by S_l. Vortices are colored by the streamwise velocity. The white vortices are traveling downstream and the black vortices are traveling upstream.

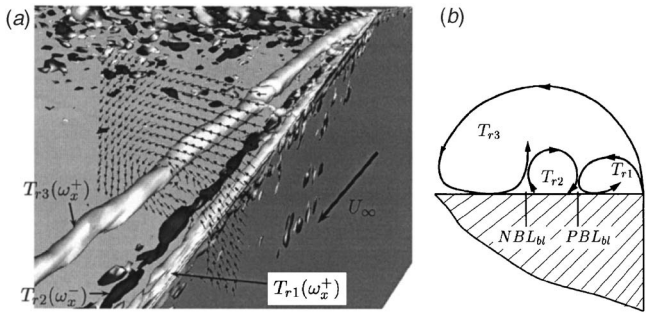

Fig. 11 (*a*) The isosurface of the instantaneous second invariant of the velocity gradient, $Q=6500$. View is from behind and the lateral side of the right slanted edge. Note that only core parts of the cone vortices are shown. The cone vortices are colored by the vorticity component in the streamwise direction ω_x. Vortices colored with black and white have clockwise and counter-clockwise directions of rotation, respectively. (*b*) Schematic representation of the mantles of vortices T_{r1}, T_{r2}, and T_{r3} seen from behind the body. The positions of NBL_{bl} and PBL_{bl} near the opposite lateral side are also shown in Fig. 16(*b*).

are born close to the end of the edge are tilted so that they travel toward the center of the slanted surface. When the spanwise vortices are convected downstream, they merge with each other to form slightly larger vortices such as λ_1 in Fig. 10(*a*). The next step in their development is further merging and becoming larger, such as λ_1 in Fig. 10(*b*), before their tip is lifted from the surface and forms hairpin-like vortices [see λ_1 in Fig. 10(*c*)]. Their life as hairpin vortices with both legs attached on the slanted surface [such as λ_2 in Fig. 10(*a*)] is short. One of their legs separates from the surface or is simply broken, such as in λ_2 in Fig. 10(*b*). Finally, close to the reattachment around the half length of the slanted surface, the other leg of the vortex is destroyed [see λ_2 in Fig. 10(*c*)] and only a small part continues downstream and possibly enters the wake region. Vortices traveling downstream are colored white and those traveling upstream are colored black. As we can see, the recirculation region contains chiefly vortices that travel downstream (see Fig. 10). They are much stronger than the black-colored vortices close to the surface, which are traveling upstream.

The flow coming from the lateral side up over the slanted lateral edge [S_l in Fig. 10(*a*)] at high velocity separates, which results in a pressure suction peak along the edge. This takes place on two levels. One thin cone-like vortex, T_{r1}, is formed close to the slanted edge with a larger vortex, T_{r3}, around it (see Fig. 11). These vortices are reminiscent of a gearwheel mechanism although they do not actually drive each other. The rotational movement of the mantle of vortex T_{r3} (gearwheel number three) starts as the shear layer on the slanted edge, S_l, follows the conical path, and ends on the slanted surface [see Fig. 11(*b*)]. When the mantle again leaves the surface to continue counter-clockwise rotation, it draws the neighboring fluid particles in the upward direction [see the sketch in Fig. 11(*b*)]. On the other side of vortex T_{r2}, vortex T_{r1} (gearwheel number one) reattaches on the slanted surface, drawing its neighboring fluid particles down toward the surface. These two mechanisms produce the third cone-like vortex, T_{r2} (gearwheel number two), with a clockwise direction of rotation (see Fig. 11). Only two of these vortices (i.e., T_{r2} and T_{r3}) were observed in previous studies by Ahmed et al. [1] and Spohn and Gilleron [3].

The motion of the fluid from the lateral side to the slanted surface that is involved in the formation of "gearwheel" vortices can be observed upstream of the separation edge, S_s (see vortex T_{r3} in Fig. 10). One of these time-averaged vortices is shown in Fig. 12. We found that these vortices stretch upstream to approximately $x=-1.56H$. A similar motion of fluid from the lateral side to the roof (over the upper lateral edge) was observed in the instantaneous flow in [3] at position $x=-0.768H$. Note that $x=0$ and $z=0$ are the positions of the rear vertical surface of the body and

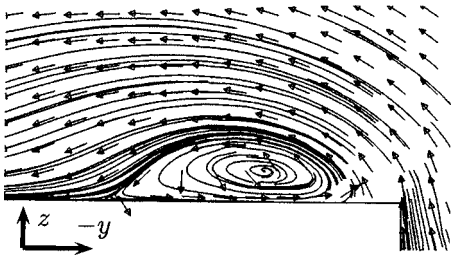

Fig. 12 Time-averaged streamlines and velocity vectors projected onto plane $x=-0.8H$. View from the front of the upper left lateral edge. Flow is from the observer into the plane. Note that $z=0$ is the ground plane and that the z and y axes in the figure do not indicate the origin of the coordinate system. The real $x=0$ and $y=0$ are at the position of the rear vertical surface and the symmetry plane of the body, respectively.

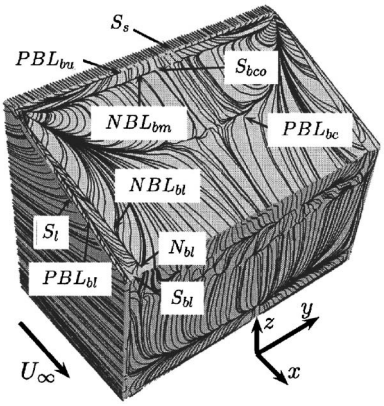

Fig. 13 Time-averaged trace lines on the rear slanted surface of the body. View of the lateral, slanted, and rear vertical faces of the body.

the ground of the wind tunnel, respectively.

Let us now return to the spanwise vortices close to the upper corners of the slanted surface (such as λ_3 in Fig. 10). As already mentioned, their axes are tilted with respect to edge S_s. This behavior is caused by the cone-like shape of vortex T_{r3}. As it propagates downstream, it grows in diameter, pushing the λ vortices away from the slanted edge, S_l. The resulting orientation of the λ vortices closest to the T_{r3} is toward the center of the slanted surface.

3.4.2 Time-Averaged Flow on the Rear Slanted Surface. Engineers' interest is often limited to time-averaged quantities such as mean lift and drag forces, which consist mainly of the pressure contributions from the rear of the body. Besides the indication of the low pressure regions on the surface of the body, the time-averaged structure tell us about the vortex-induced mean aerodynamic forces. One good example is cone-like vortices on the rear window of some cars that cause vortex-induced drag and lift. (As we will see later in the text such vortices are formed on the slanted surface of the vehicle studied in this paper.) Other issues, such as regions of accumulation of dirt and water, can also be addressed studying the time-averaged picture of the flow. These are only some examples of where knowledge of the time-averaged flow is helpful in the vehicle design process.

In the following sections we present the time-averaged flow around the rear of the body, keeping in mind that the real flow is very time dependent and that the time-averaged picture only gives *a measure* of the flow that is interesting in terms of design.

When the instantaneous structures on the slanted surface described above are averaged, they form the flow structures that are indicated by surface patterns shown in Fig. 13. We describe these structures in the following text and explain their meaning.

The largest imprint on the slanted surface stretches from edge S_s and the positive bifurcation line, PBL_{bc} (see Fig. 13). A more detailed picture of the fluid motion on the surface in the region between edge S_s and PBL_{bc} can be seen in Fig. 14. The fluid separates along NBL_{bm} and reattach at the position of PBL_{bu} [see Figs. 14(*a*) and 14(*b*)]. From PBL_{bu} the fluid particles move downstream toward the NBL_{bm} and upstream toward edge S_s [see Figs. 14(*a*) and 14(*b*)]. On both sides of PBL_{bu}, the flow direction is parallel with the x axes close to the center plane, $y=0$ [see Figs. 14(*a*) and 14(*b*)], and changes its direction to a more spanwise one [i.e., in the y direction] away from the center plane [see the left side of Fig. 14(*a*)]. The mirror symmetry of the flow around plane $y=0$ on the NBL_{bm} results in one critical point in the saddle point, S_{bco}, in Fig. 14(*b*). Downstream of the NBL_{bm} the flow moves from the PBL_{bc} in Figs. 13 and 14(*c*). The two parts of the PBL_{bc} meet in the very unsteady flow region in Fig. 14(*c*). We expected

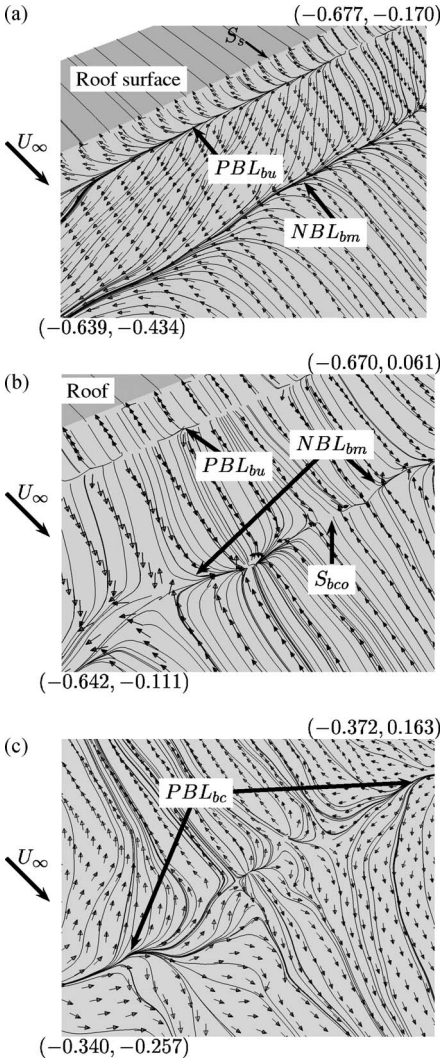

Fig. 14 Time-averaged trace lines on the surface of the body. (*a*) Zoom of the patterns in Fig. 13 showing NBL_{bu} and NBL_{bm}. (*b*) Zoom of the patterns in Fig. 13 showing saddle point S_{bco}. (*c*) Zoom of the unsteady reattachment in Fig. 13. Coordinates ($x/H, y/H$) are given for lower left and upper right corners in all three figures. The lateral sides are located at $y=\pm 0.675H$.

a saddle point here similar to those on the front part of the body (for example S_{fsl} in Fig. 8). No critical point was found here because the flow has not fully converged owing to very unsteady flow around the reattachment [see Fig. 14(*c*)], although we averaged over a very long time period (110,000 time steps corresponding to time $tU_\infty/H=38.2$). This highly unsteady separation can also be observed in the oil-film visualization in [2] and in the visualization of the instantaneous flow in [3]. Spohn and Gillieron [3] suggested that the unsteadiness in this flow region is caused by oscillations of the trailing vortices themselves and their interactions with vortices shed from the front. We found the trailing vortices to be relatively steady, with their cores remaining at approximately the same position for a long period of time. It is more likely that the interaction between λ vortices is the reason for the high levels of unsteadiness at the lower part of the slanted surface. As the λ vortices traveling in the streamwise direction (such as λ_1 and λ_2 in Fig. 10) approach the region of the reattachment, they break up (as described above) and meet the λ vortices coming from the upstream corners (such as λ_3 in Fig. 10). These meetings result in a large number of collisions which together with the break-up of vortices such as λ_1 and λ_2 make this region of the

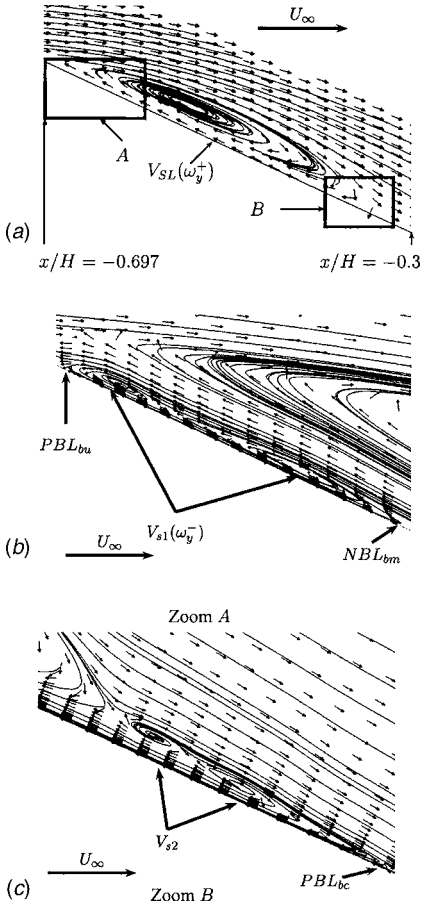

Fig. 15 (*a*) Time-averaged streamlines and velocity vectors projected onto symmetry plane $y=0$ showing the flow above the slanted surface. The velocity vectors are extrapolated and plotted on coarser grid than that used in the simulation to make the direction of the flow visible. (*b*) Zoom *A* from (*a*). (*c*) Zoom *B* from (*a*). The direction of rotation of vortices is indicated by the vorticity component in the *y* direction (i.e., ω_y^+ and ω_y^- are positive and negative vorticity components, respectively).

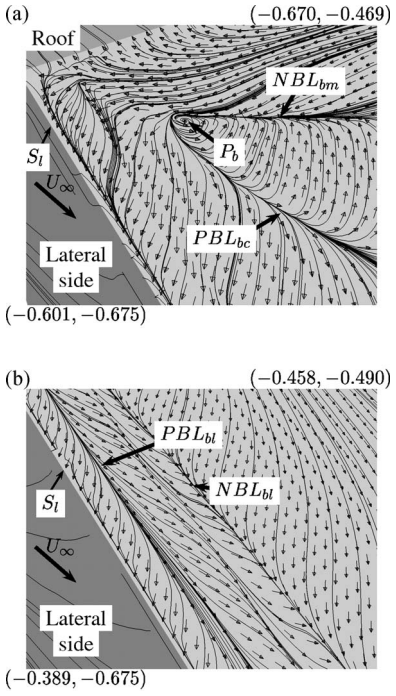

Fig. 16 Time-averaged trace lines on the surface of the body. (*a*) Zoom of the patterns in Fig. 13 showing the stable focus, P_b. (*b*) Zoom of the patterns in Fig. 13 showing the negative and positive bifurcation lines, NBL_{bl} and PBL_{bl}, respectively. Coordinates ($x/H, y/H$) are given for lower left and upper right corners in both figures. NBL_{bl} and PBL_{bl} are also shown in Fig. 11(*b*).

flow very unsteady. Thus we believe that the unsteady character of the flow in the lower part of the slant is not a direct consequence of the trailing vortices. It is rather the result of their indirect influence on the λ_3 vortices, making them change their paths (as previously mentioned) and interacting with the λ_1 and λ_2 vortices.

The information from Fig. 14 is not sufficient to allow conclusions to be drawn about the time-averaged structures above the slanted surface. The imprints of the vortices in Fig. 14 could for example be interpreted as the traces of one vortex between edge S_s and the PBL_{bu} (rotating with positive vorticity ω_y^+), one vortex between the NBL_{bm} and the PBL_{bu} (rotating with negative vorticity ω_y^-) and one vortex between the NBL_{bm} and the unsteady region of PBL_{bc} in Fig. 14(*c*) (rotating with positive vorticity ω_y^+). Let us now consider the flow picture in the symmetry plane, $y=0$, in Fig. 15. We see that the main part of this region is dominated by the large vortex V_{SL} in Fig. 15(*a*), which has a positive direction of rotation ω_y^+ and stretches between spanwise edge S_s and some position upstream of the unsteady region in the middle of PBL_{bc} [see Fig. 15(*a*)]. In the upper part of the slant [see Fig. 15(*b*)], we find vortex V_{s1}, which rotates in the negative direction (ω_y^-) and is located below vortex V_{SL} and between PBL_{bu} and NBL_{bm}. It was found that this vortex extends at least out to $y=\pm 0.625H$ in the spanwise direction. It is worth mentioning that the flow is very unsteady at the position of V_{s1} and a very long time is required to average it. The unsteady flow just above the unsteady reattachment in PBL_{bc} appears to form the vortex structure V_{s2} [see Fig. 15(*c*)]. This is not a real vortex but a result of highly unsteady flow in this region and disappears as we move from the symmetry plane toward lateral edge S_l. Similar unsteady reattachment was observed in the experiments by Lienhart and Becker [2].

The positive and negative bifurcation lines, PBL_{bc} and NBL_{bm}, meet close to the slanted edge, S_l [see Fig. 16(*a*)]. The direction of the fluid around these lines results in a critical point in the form of a stable focus, P_b. Such a focus was also found in the experiments of Spohn and Gillieron [3]. This focus is the origin of the vortex core of vortex V_{SL} [see Fig. 15(*a*)] that stretches to the mirror focus on the other side of plane $y=0$.

3.4.3 Time-Averaged Cone-like Trailing Vortices. Figure 16(*b*) shows the existence of the negative bifurcation line, NBL_{bl}, and the positive bifurcation line, PBL_{bl}, close to the slanted edge, S_l. Instantaneous vortices T_{r1}, T_{r2}, and T_{r3} (see Fig. 11) average to three time-averaged vortices that are located around these bifurcation lines. Figure 17 shows these vortices above the imprints in Fig. 16 (thus the mirror side of that shown in Fig. 11). The mechanism of feeding the chief trailing vortex, T_{3l}, with the upstream flow is illustrated in Fig. 17(*a*). The streamlines, STR_l, that come parallel with the streamwise direction of the flow are first deflected upward toward the lateral slanted edge, S_l, and then sucked in above the slanted surface. Further downstream they continue to roll around the vortex core of vortex T_{3l} [see Fig. 17(*a*)]. The upward deflection of the lateral flow toward the lateral slanted edge can also be observed in Fig. 13 (here in the pattern of the trace lines on the surface of the lateral side of the body that are deflected toward the slanted edge, S_l). Similar to the instantaneous vortices, the time-averaged ones have direction of rotation similar to three gearwheels placed in tandem [see Fig. 17(*b*)].

The process of formation of vortex V_{SL} can be followed in Fig.

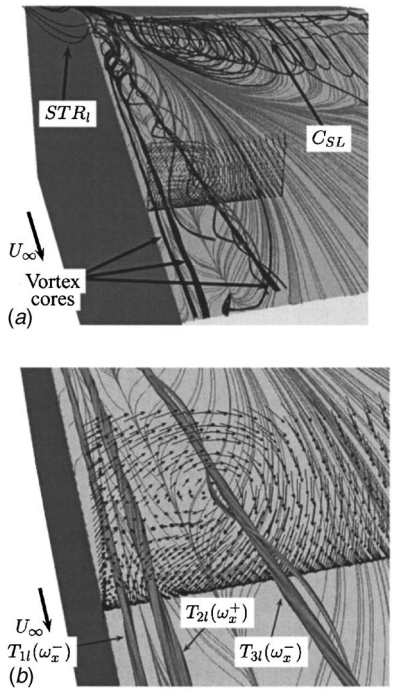

Fig. 17 (*a*) Vortex cores of the time-averaged vortices wrapped in the streamlines that are generated using vortex cores as a source. Time-averaged trace lines are shown on the surface. View from behind the body. (*b*) Zoom of (*a*). (Note that streamlines STR_l are removed in this zoom for clarity.)

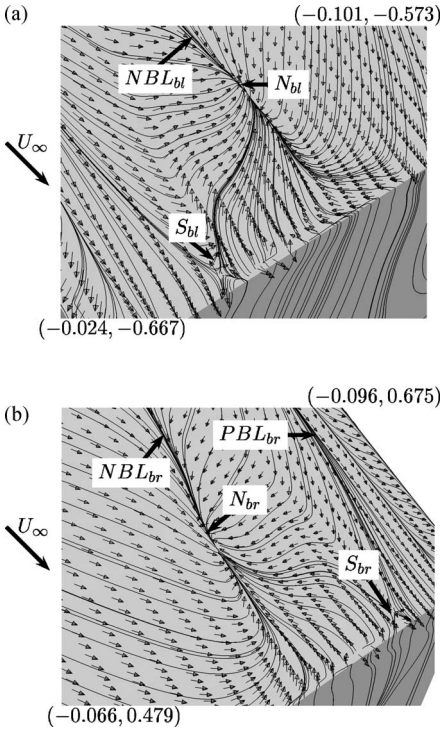

Fig. 18 Time-averaged trace lines on the surface of the body. Zoom of the flow structures from Fig. 13 showing (*a*) the lower left corner of the slanted surface and (*b*) the lower right corner of the slanted surface. Coordinates ($x/H, y/H$) are given for lower left and upper right corners in both figures.

17(*a*). The streamlines coming from above the roof of the body are pulled in toward the low pressure recirculating region rolling in spiral motion around vortex core C_{SL} [see Fig. 17(*a*)].

Let us now consider the flow close to the downstream corners of the slanted surface shown in Fig. 18. Two stable nodes, N_{bl} and N_{br}, are formed close to the lower corners of the slanted surface (see Fig. 18). Located on the negative bifurcation lines, NBL_{bl} and NBL_{br}, these nodes attract most of the surface flow that is located under vortices T_{2l}, T_{2r} and T_{3l}, T_{3r} (see Fig. 17). The flow between vortices T_{1l}, T_{1r} and T_{2l}, T_{2r} splits in saddle points S_{bl} and S_{br}. Although the instantaneous flow in the region between S_{bl} (S_{br}) and N_{bl} (N_{br}) changes direction between downstream and upstream, the upstream motion prevails (see the time-averaged flow in Fig. 18).

3.5 Near-Wake Flow. The previous work of Ahmed et al. [1] suggested that the near-wake flow contains two horseshoe vortices situated one above the other with their legs stretching in the streamwise direction. This section presents the survey of this flow region from our LES results. The assumptions of Ahmed et al. [1] about the flow structures in the near wake will be investigated and a new, revised picture of this flow will be established.

We have used two visualization techniques to investigate this part of the flow. The first technique uses vortex cores and projections of the streamlines on planes across the wake in all three directions. Five such planes are shown in Fig. 19(*a*). Planes $y=0$ and $y=0.521H$ in this figure show the existence of two vortices, U_h and U_l, one above the other. As we move toward the lateral side (from $y=0$ to $y=0.521H$), the core of the upper vortex, U_h, moves in the positive z direction [see vortex core in Fig. 19(*a*)]. The legs of U_h are bent in the streamwise direction at approximately $y=\pm 0.53H$ and stretch in the streamwise direction [see planes $x=0.347H$, $x=0.868H$ and $x=1.389H$ in Fig. 19(*a*)]. The core of the lower vortex, U_l, keeps approximately the same height with respect to the floor (approximately $z=0.07H$). It bends at $y=\pm 0.6H$ and two legs are formed that extend in the positive z-direction. Figure 19(*a*) shows that cone-like vortex T_{3l} and the upper vortex, U_h, both move downstream in the near wake but that the lower vortex, U_l, does not (see planes $x=0.347H$, $0.868H$, and $x=1.389H$). However, we have found that this vortex moves in the positive z direction (not shown in this figure). Moving in the positive z direction, the focus of vortex U_l moves toward the body.

The technique of low pressure isosurfaces and the vortex cores is used in Fig. 19(*b*) to visualize the time-averaged vortices around the rear part of the body. From the description of horseshoe vortices U_h and U_l found above, it is clear that they are very curved between their tips and legs. As mentioned in Sec. 2, the algorithm used for the calculation of vortex cores has a linear implementation and thus has difficulty finding the cores of curved vortices. This is probably the reason why both cores of the curvatures between the tip and legs of vortex U_h and one (the left one) of vortex U_l are missing in Fig. 19(*b*). We also mentioned in Sec. 2 that the eigenvalue analysis algorithm may produce incorrect results when the flow contains several vortices close to each other. Here we have two vortices of approximately the same strength, and their cores appear to merge into one ring-like vortex core in Fig. 19(*b*). Although these two vortices interact with each other, as we have seen above, they exist as two separate vortices. Another explanation of the discontinuous vortex cores and slightly false picture of the vortex cores in Fig. 19(*b*) can be that the flow has not completely converged in time.

Ahmed et al. [1] studied these structures and concluded, in agreement with our observations, that the vortex tips of U_h and U_l are approximately parallel with the base surface of the body. They found the streamwise extension of the legs of vortex U_h and concluded that these merge with the trailing cone-like vortices T_{3l} and T_{3r}. Our results confirm their findings [see Fig. 19(*a*)]. As vortex T_{3l} weakens in strength and appears to vanish downstream of position $x=0.57H$, the U_h vortex continues its extension after that

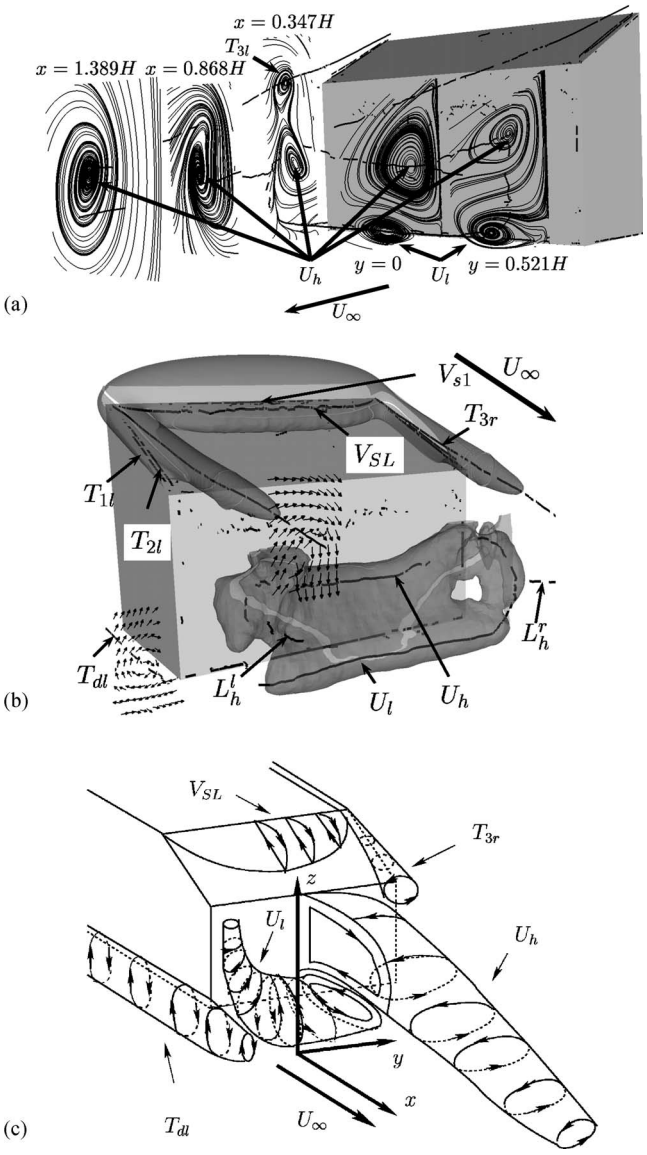

Fig. 19 Time-averaged near-wake flow. (*a*) Time-averaged streamlines projected onto planes (from left to right in the figure): $x=1.389H$ ($-0.675H \leq y \leq 0$, $0.174H \leq z \leq 0.833H$), $x=0.868H$ ($-0.675H \leq y \leq -0.278H$, $0.174H \leq z \leq 0.833H$), $x=0.347H$ ($-0.675H \leq y \leq -0.382H$, $0.174H \leq y \leq 1.042H$), $y=0$ ($-0.59H \leq x \leq 0$, $0.174H \leq z \leq 0.833H$) and $y=0.521H$ ($-0.59H \leq x \leq 0$, $0.174H \leq z \leq 0.833H$). (*b*) Isosurfaces of the static pressure, $p=-0.16$ and $p=-0.19$. L_h^l and L_h^r are cores of the legs of vortex U_h. (*b*) Schematic representation of the time-averaged wake flow. Note that only half of the horseshoe vortices U_l and U_h for $y \leq 0$ and $y \geq 0$, respectively, are shown.

position and grows in diameter. Cone-like vortices T_{3l} and T_{3r} probably enter the horseshoe vortex, U_h, somewhere downstream of $x=0.57H$.

A schematic representation of the time-averaged flow structures shown in Fig. 19(*c*) summarizes the vortices around the rear of the body. Only half of the U_h and U_l vortices in the positive and negative y directions, respectively, are shown in this figure for the sake of clarity. As shown in this sketch, the downstream extension of the U_l vortex assumed in the work of Ahmed et al. [1] is probably incorrect and it is here revised with a somewhat odd extension of this vortex in the positive z-direction. It is possible that vortex U_l interacts with the longitudinal vortices T_{dl} and T_{dr}. However, already along the body the vortices T_{dl} and T_{dr} are weak compared to the cone-like vortices T_{3l} and T_{3r}. Their strength downstream the body is even smaller (see Fig. 9) and their influence on the vortex U_l is probably negligible (note that the size of the vortices and in particular of T_{dl} in Fig. 19 are not drawn to scale).

4 Conclusions and Relevance of the Results

Results of large eddy simulations in conjunction with visualization tools are used to establish complete pictures of both the instantaneous and the time-averaged flows around an Ahmed body with a rear slant angle of 25°. The flow contains a large variety of time and length scales that interact with each other, making the flow extremely complex. Among the instantaneous coherent structures found in the flow, two structures distinguish themselves, cone-like vortices along the rear slanted edges and hairpin-like vortices in the regions of separated flows on the front and the rear slanted surface of the body. Both the time and the length scales of these two structures differ. While the cone-like vortices are of the size of the body and are relatively steady, the hairpin-like vortices are very small structures that change in shape over a short period of time.

Our detailed study has not only presented the unknown instantaneous flow around the Ahmed body but also enriched our knowledge of the time-averaged flow. For example, it has been found that the flow on the rear slanted surface contains three pairs of cone-like vortices as compared to only two pairs known from previous experimental studies. The inaccurate position of the horseshoe vortices, assumed in the experiments of Ahmed et al. [1] to be located one above the other in the wake with their legs stretching in the streamwise direction, was corrected here. Flow around the front of the body is presented for the first time, showing rich flow patterns on all four sides of the body.

Although a very detailed picture of the flow is presented in this paper, it is important to reflect on the relevance of the information provided here. Information on flows around ground vehicle bodies has previously been limited to the time-averaged flow (such as in [1]). We have tried in this paper to provide both the instantaneous and time-averaged representation of the flow. It has been difficult to find some sense and structure in some parts of the instantaneous flow, and more results from the time-averaged flow are reported in the present paper. The time-averaged flow structures are more smooth than the instantaneous ones and are easier to analyze. We are used to seeing time-averaged structures in textbooks and can relatively easily identify them. Previous knowledge about instantaneous flow structures around the body studied in the present work was very poor and was gathered from only a few experimental studies that chiefly present flow visualizations at low Reynolds numbers. The present paper gives a description of a large part of this instantaneous flow.

Much of the influences on the aerodynamics of the vehicle, such as directional stability and wind noise, can only be understood if the instantaneous flow can be accurately represented. If the real flow is very time dependent and is never coincident with the time-averaged flow, what is the meaning of the time-averaged flow? The time-averaged vortices on the surface of the body tell us about the parts of the body that are affected by large pressure forces that cause aerodynamic forces and moments. The time-averaged streamlines on the surface expose the regions where water and dirt accumulate over a long period of time. The time-averaged coherent structures around the body give an explanation of the vortex-induced mean drag and lift forces. However, if we want to study the processes of vortex interaction that cause the change in aerodynamic forces, for example, we must study the instantaneous flow.

Some parts of the time-averaged flow studied in the present paper, such as flow above the slanted surface (apart from the cone-like vortices), are completely different from their instantaneous counterparts. Another example is the time-averaged wake flow containing horseshoe vortices U_h and U_l, where the corre-

sponding instantaneous flow contains only smaller irregular structures that change over time. The relevance of the time-averaged flow in such regions for the aerodynamic properties of the vehicle is probably very small.

Acknowledgments

This work was supported by the FLOMANIA project. The FLOMANIA (Flow Physics Modelling-An Integrated Approach) is a collaboration between Alenia, AEA, Bombardier, Dassault, EADS-CASA, EADS-Military Aircraft, EDF, NUMECA, DLR, FOI, IMFT, ONERA, Chalmers University, Imperial College, TU Berlin, UMIST, and St. Petersburg State University. The project is funded by the European Union and administrated by the CEC, Research Directorate-General, Growth Programme, under Contract No. G4RD-CT2001-00613. Computer time on the Linux cluster, provided by the NSC (National Supercomputer Center in Sweden), is gratefully acknowledged.

References

[1] Ahmed, S. R., Ramm, G., and Faltin, G., 1984, "Some Salient Features of the Time Averaged Ground Vehicle Wake," SAE paper no. 840300.

[2] Lienhart, H., and Becker, S., 2003, "Flow and Turbulent Structure in the Wake of a Simplified Car Model," SAE paper no. 2003-01-0656.

[3] Spohn, A., and Gillieron, P., 2002, "Flow Separations Generated by a Simplified Geometry of an Automotive Vehicle," in *IUTAM Symposium: Unsteady Separated Flows*, April 8–12, Toulouse, France.

[4] Sims-Williams, D. B., and Dominy, R. G., 1998, "Experimental Investigation Into Unsteadiniess and Instability in Passanger Car Aerodynamics," SAE paper no. 980391.

[5] Krajnović, S., and Davidson, L., 2003, "Numerical Study of the Flow Around the Bus-Shaped Body," ASME J. Fluids Eng., **125**, pp. 500–509.

[6] Krajnović, S., and Davidson, L., 2005, "Flow Around a Simplified Car, Part 1: Large Eddy Simulation," ASME J. Fluids Eng., **127**, pp. 907–918.

[7] Jeong, J., and Hussain, F., 1995, "On the Identification of a Vortex," J. Fluid Mech., **285**, pp. 69–94.

[8] Sujudi, D., and Haimes, R., 1995, "Identification of Swirling Flow in 3-D Vector Fields," AIAA Pap., paper no. AIAA 95-1715.

[9] Computational Engineering International, Ins., Apex, USA, 2003, *EnSight User Manual for Version 7.6*.

[10] Perry, A. E., and Chong, M. S., 1987, "A Description of Eddying Motions and Flow Patterns Using Critical-Point Concepts," Annu. Rev. Fluid Mech., **19**, pp. 125–155.

[11] Krajnović, S., and Davidson, L., 2002, "Exploring the Flow Around a Simplified Bus with Large Eddy Simulation and Topological Tools," in *The Aerodynamics of Heavy Vehicles: Trucks, Busses and Trains* (Spinger, Monterey, CA).

DNS of Drag-Reducing Turbulent Channel Flow With Coexisting Newtonian and Non-Newtonian Fluid

Bo Yu
Department of Oil and Gas Storage and Transportation Engineering,
China University of Petroleum,
Beijing, 102249, People's Republic of China

Yasuo Kawaguchi
Institute for Energy Utilization,
National Institute of Advanced Industrial Science and Technology,
Ibaraki 305-8564, Japan

In the present study, we numerically investigated drag-reducing turbulent channel flows by surfactant additives. Surfactant additives were assumed to be uniformly distributed in the entire flow region by turbulent convection and diffusion, etc., but it was assumed that the shear-induced structure (SIS) (network of rod-like micelles) could form either in the region next to the walls or in the center region of the channel, making the fluid viscoelastic. In other regions surfactant additives were assumed to be incapable of building a network structure, and to exist in the form of molecules or micelles that do not affect the Newtonian properties of the fluid. With these assumptions, we studied the drag-reducing phenomenon with coexisting Newtonian and non-Newtonian fluids. From the study we identified the effectiveness of the network structures at different flow regions, and showed that the phenomenon of drag-reduction (DR) by surfactant additives is not only closely associated with the reduction of Reynolds shear stress but also related to the induced viscoelastic shear stress. [DOI: 10.1115/1.2012500]

Introduction

It is well known that surfactant additives are good drag reducers with long-term action, and can be applied to district heating and cooling systems. The mechanism of drag reduction by surfactant additives is still not well understood, but it is generally accepted that drag-reduction is associated with the network structures in the surfactant solution [1]. These network structures show elasticity, prevent the generation of turbulence, and thus reduce frictional drag. Recently we carried out a direct numerical simulation (DNS) study to quantitatively study the mechanism of drag reduction. By using viscoelastic Giesekus constitutive equations to model the interaction between the network structures and solvent (water), we successfully reproduced many features observed in the experiments such as a wider buffer layer and decrease of Reynolds shear stress [2]. However, our previous DNS study had certain limitations: (1) the network structures were assumed to exist in the entire flow region and the fluid was non-Newtonian in the whole computational domain. However, experiments show that the network structures are sensitive to shear stress and temperature; for example, high temperature and a high shear rate can destroy the network structures. The recent experiment of our research group [3] shows the profile of the Reynolds shear stress displays a two-layer structure, which can be explained by the different states of surfactant additives due to the local shear stress and supports that the network structure region and non-network structure region may coexist. (2) Since we assumed the fluid was non-Newtonian in the whole computational domain, the effectiveness of the network structures in reducing frictional drag at different layers was not isolated.

In the present study, we investigated turbulent channel flow with coexisting Newtonian and non-Newtonian fluids in order to identify the effectiveness of the network structures at different flow layers. The prediction of the limiting condition of the network structure is extremely important in practice, such as designing a flow system using the DR additives. Once the function of the network structures is clearly understood, some methods can be proposed to control the turbulence by controlling the network structures through adjusting the concentration, temperature, and shear rate distribution in the surfactant solution. Another purpose of this study was to better reproduce some phenomena observed in practical problems that were not found in our previous DNS study.

Modeling of Flow

A bilayer model for flow with Newtonian and non-Newtonian fluid coexistence is proposed. The flow to be studied was a fully developed channel flow. Two types of fluid motion, flow A and flow B shown in Fig. 1, were studied, where Newtonian and non-Newtonian fluids separately flow at different layers with the interface between them being parallel to the walls. In flow A, the network structures exist at the center region of the channel, whereas in flow B they exist at the near-wall region. By moving the interface position, it is possible to study how the network structures reduce frictional drag at different flow layers. For flow A, we did four calculations with non-Newtonian fluid thicknesses of $2\times0h$, $2\times0.4h$, $2\times0.6h$, and $2\times0.9h$. For flow B, we carried out three computations with non-Newtonian fluid thicknesses of $2\times0.2h$, $2\times0.4h$, and $2\times h$. The first case of flow A is Newtonian fluid and the last case of flow B is non-Newtonian fluid. For all the other cases, Newtonian and non-Newtonian fluids coexist.

It should be pointed out that the shear-stress and temperature-dependent network structures evolve in time, and the interface shape in Fig. 1 should be irregular and dynamic. For simplicity we proposed the bilayer structures to model the complicated inhomogeneous distributions of additives in the flow. This model can be used to predict the behavior of the DR rate versus the Reynolds number, as shown later. The model is also usable to analyze the additive inject cases, for example, we can evaluate the DR performance by injecting surfactant additives surround a ship hull.

Governing Equations

The dimensionless governing equations for fully developed turbulent channel flow with a Giesekus model can be written as:

Contributed by the Fluids Engineering Division for publication in the JOURNAL OF FLUIDS ENGINEERING. Manuscript received by the Fluids Engineering Division August 17, 2004. Final revision: June 16, 2005. Associate Editor: Ismail Celik.

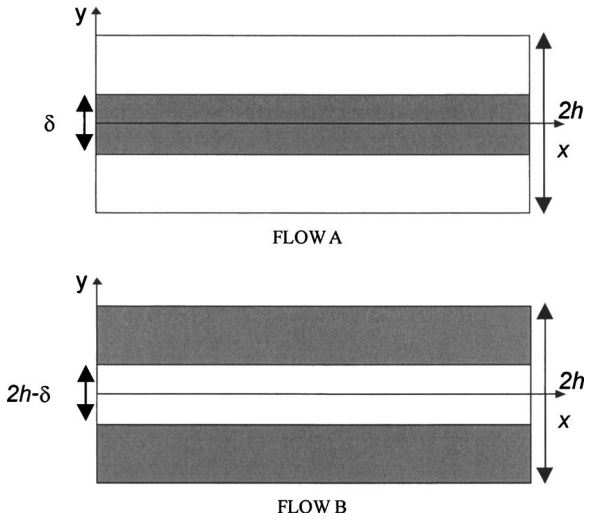

Fig. 1 Bilayer model of flows with Newtonian and non-Newtonian fluid coexistence. The gray color represents non-Newtonian fluid and the white color represents Newtonian fluid. The thickness of the non-Newtonian region is δ for flow A in the center region, and $\delta/2$ in the near-wall region for flow B.

$$\frac{\partial u_i^+}{\partial x_i^*} = 0 \tag{1}$$

$$\frac{\partial u_i^+}{\partial t^*} + u_j^+ \frac{\partial u_i^+}{\partial x_j^*} = -\frac{\partial p^+}{\partial x_i^*} + \frac{1}{\mathrm{Re}_\tau}\frac{\partial}{\partial x_j^*}\left(\frac{\partial u_i^+}{\partial x_j^*}\right) + \frac{\beta}{\mathrm{We}_\tau}\frac{\partial c_{ij}^+}{\partial x_j^*} + \delta_{1i} \tag{2}$$

$$\frac{\partial c_{ij}^+}{\partial t^*} + \frac{\partial u_m^+ c_{ij}^+}{\partial x_m^*} - \frac{\partial u_i^+}{\partial x_m^*} c_{mj}^+ - \frac{\partial u_j^+}{\partial x_m^*} c_{mi}^+ + \frac{\mathrm{Re}_\tau}{\mathrm{We}_\tau}[c_{ij}^+ - \delta_{ij} + \alpha(c_{im}^+ - \delta_{im})(c_{mj}^+ - \delta_{mj})] = 0 \tag{3}$$

It is seen compared to Newtonian fluid in the momentum equation [Eq. (2)], there is an extra term associated with the interaction of the network structure with the solvent. Equation (3) is the Giesekus constitutive equation to calculate the conformation tensor of the network structure.

Calculations were performed with parameters $\mathrm{Re}_\tau = 125$, $\mathrm{We}_\tau = 25$, $\alpha = 0.001$, and $\beta = 0.1$ in the non-Newtonian fluid region and $\mathrm{Re}_\tau = 125$ in the Newtonian fluid region. A computational box $3h \times 2h \times 2h$ in the x, y, and z directions was chosen for simulation and the computational domain in wall units was $375 \times 250 \times 250$ ($x \times y \times z$). A grid system of $64 \times 78 \times 64$ (in x, y, and z) meshes was adopted. Nonuniform grids in the wall-normal direction were used with grids clustered in the near-wall region and at the interface region. Grid-spacing Δy^+ ranged from around 0.3 next to the wall to 6 in the center. Uniform grids were used in the x and z directions and the corresponding grid spacings were $\Delta x^+ = 5.86$ and $\Delta z^+ = 3.9$, respectively. The periodic boundary conditions were imposed in both the streamwise (x) and spanwise (z) directions, while the nonslip condition was adopted for the top and bottom walls. The numerical method used here was a fractional-step method. A dimensionless time step 2×10^{-4} was used. The Adams-Bashforth scheme was used for time advancement and a second-order faithful finite difference scheme of Yu et al. [4] was used to enhance the numerical stability. The grid and time-step resolution used in the present study was shown to be adequate in Yu et al. [4]. At the interface of the Newtonian and non-Newtonian fluid regions, the following shear stress and normal stress balance equations were satisfied:

$$(\partial u^+/\partial y^*)_N = (\partial u^+/\partial y^*)_{NN} + \beta\,\mathrm{Re}_\tau\, c_{xy}^+/\mathrm{We}_\tau \tag{4}$$

Table 1 Reynolds number, friction factor and DR rate

	δ	Re_b	f	f^D	DR %
Flow A(1)	$2 \times 0h$	3653	0.009 36	0.009 39	0%
Flow A(2)	$2 \times 0.4h$	3651	0.009 37	0.009 39	0%
Flow A(3)	$2 \times 0.6h$	3726	0.009 00	0.009 34	3.63%
Flow A(4)	$2 \times 0.9h$	4071	0.007 54	0.009 14	17.5%
Flow B(1)	$2 \times 0.2h$	3848	0.008 44	0.009 27	8.94%
Flow B(2)	$2 \times 0.4h$	4175	0.007 17	0.009 08	21.0%
Flow B(3)	$2 \times h$	4263	0.006 88	0.009 03	23.9%

$$(\partial w^+/\partial y^*)_N = (\partial w^+/\partial y^*)_{NN} + \beta\,\mathrm{Re}_\tau\, c_{yz}^+/\mathrm{We}_\tau \tag{5}$$

$$(\partial v^+/\partial y^*)_N = (\partial v^+/\partial y^*)_{NN} + \beta\,\mathrm{Re}_\tau (c_{yy}^+ - 1)/\mathrm{We}_\tau \tag{6}$$

Results and Discussions

The drag-reduction rate was defined as the reduction of the friction factor with respect to Newtonian fluid at equal mean Reynolds number Re_b,

$$DR\,\% = \frac{f^D - f}{f^D} \times 100\,\% . \tag{7}$$

f^D was evaluated by Dean's equation [5]. Table 1 shows the calculated frictional factor f, evaluated frictional factor f^D, and drag-reduction rate. It is seen that for Newtonian fluid, the calculated frictional factor agrees quite well with Dean's correlation. It is also seen that there is no drag reduction for flow A(2) and a largest drag-reduction rate for flow B(3). For flow A(3), a small drag-reduction rate of around 4% is obtained. Flow A(2) and flow A(3) show that the network structures are not effective in reducing frictional drag in the bulk flow region, especially in the center of the channel. In flow B(1), the non-Newtonian fluid region is 20% of the entire flow region, and a drag-reduction rate of about 9% is obtained. In flow B(2) the non-Newtonian fluid region is 40% of the entire flow region and the drag-reduction rate approaches that in flow B(3). Flow B(1) and flow B(2) indicate that the network structures are most effective at the region near the wall. By comparing flow A(4) and flow B(3), it is seen in flow A(4) that the network structures cover most of the fluid region except the viscous sublayer ($0 \leqslant y^+ \leqslant 5$) and a small part of the buffer layer ($5 < y^+ \leqslant 12.5$), but its drag-reduction ability is 25% less than that of flow B(3). In addition, the non-Newtonian fluid region of A(4) is 2.25 times as large as that of flow B(2), but it has a smaller drag-reduction rate. All these findings support the hypothesis of Lumley [6,7] that the primary action of additives takes place in the buffer layer. The local fractional contribution to DR in Fig. 2 shows more clearly that additives are important in the near-wall region. There are some discrepancies in the contributions in flow A and flow B, which must come from the nonlinear characteristics of the governing equations. This indicates that fluid dynamics with Newtonian and non-Newtonian fluid is complex and the contribution cannot be simply superposed.

Figure 3 shows the mean velocity profiles. For both flow A and flow B, as the drag-reduction rate increases, the velocity profile upshifts in the logarithmic region and the buffer layer becomes larger, which agrees with the experimental result (Reischman and Tiederman [8] and Yu et al. [2]). The velocity profile of flow A(2) almost collapses to that of flow A(1) in the viscous sublayer and buffer layer, but differs from flow A(1) in the center region of the channel. This indicates that though the network structures in the bulk flow region are not effective in reducing frictional drag, they

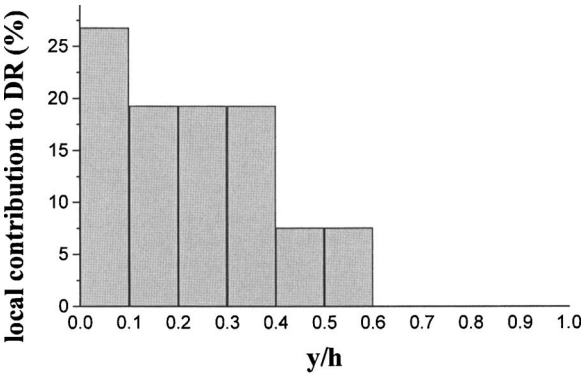

Fig. 2 Local fractional contribution to the drag-reduction rate

do interact with the solvent. The velocity profile of flow B(2) is almost the same as that of flow B(3) up to $y^+=40$. The network structures in flow B(2) exist up to $y^+=50$, but in the region next to the interface from $y^+=40$ to $y^+=50$, the velocity values are smaller than those of flow B(3). This means the effect of Newtonian fluid penetrates to the non-Newtonian region.

The root-mean-square velocity fluctuations are compared in Figs. 4–6. Generally, the peak value positions of u_{rms} shift to the bulk flow region for drag-reduction cases. For drag-reduction cases, u_{rms} is larger than that of the solvent except flow B(1). For flows A(2) and A(3), v_{rms} and w_{rms} decrease in the center region. For flows B(1) and B(2), v_{rms} and w_{rms} decrease in the near-wall region. Flows B(1) and B(2) have a larger drag-reduction rate, which means that larger drag reduction is associated with the suppression of cross-flow in the near-wall region. In general, the

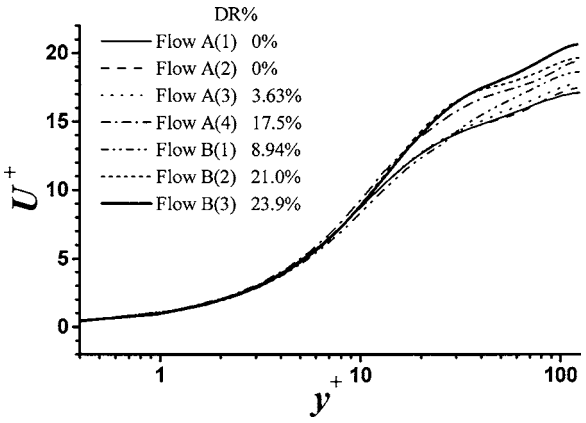

Fig. 3 Mean velocity profiles

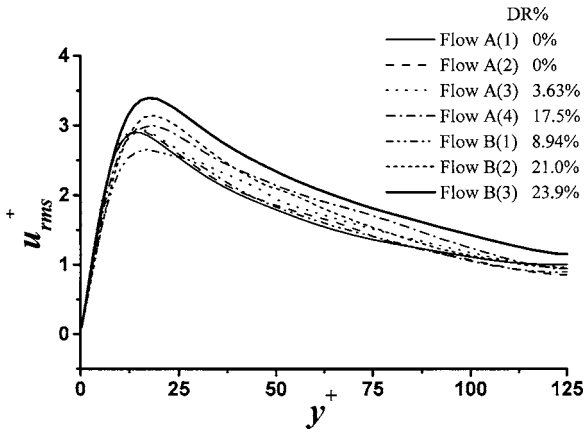

Fig. 4 The rms of streamwise velocity fluctuations

smaller v_{rms} and w_{rms} in the near-wall region, the larger the drag-reduction rate. In flow B(3), v_{rms} and w_{rms} are appreciably suppressed in both the near-wall region and the center region and the largest drag-reduction rate was obtained.

The total shear stress can be used as an indicator of whether the calculation has reached a statistically steady state. When a steady state is reached, the following balance equation is satisfied:

$$\tau_{\mathrm{total}} = 1 - \frac{y^+}{\mathrm{Re}_\tau} = -\overline{u'^+ v'^+} + \frac{\partial U^+}{\partial y^+} + \beta \frac{C^+_{xy}}{\mathrm{We}_\tau}. \tag{8}$$

The last term on the right-hand side of Eq. (8) is the mean viscoelastic stress due to the elasticity of the network structures. Statistically steady states have been confirmed for all the calcula-

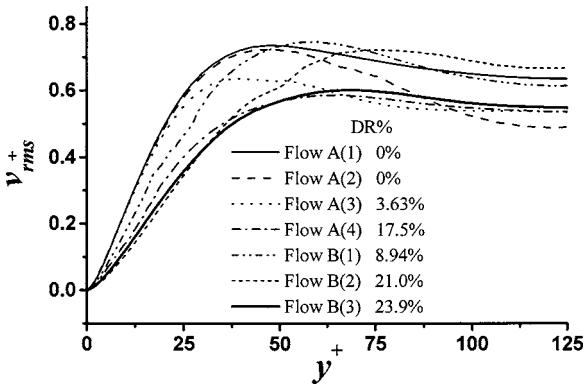

Fig. 5 The rms of wall-normal velocity fluctuations

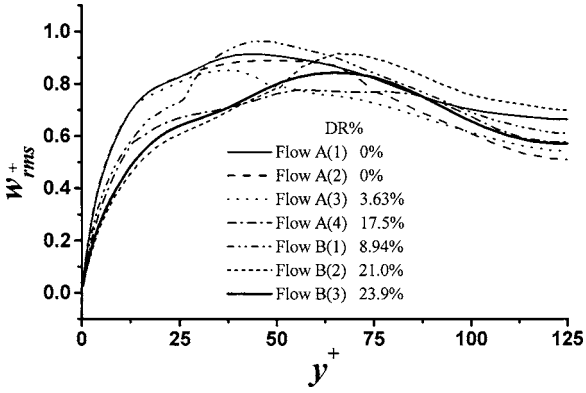

Fig. 6 The rms of spanwise velocity fluctuations

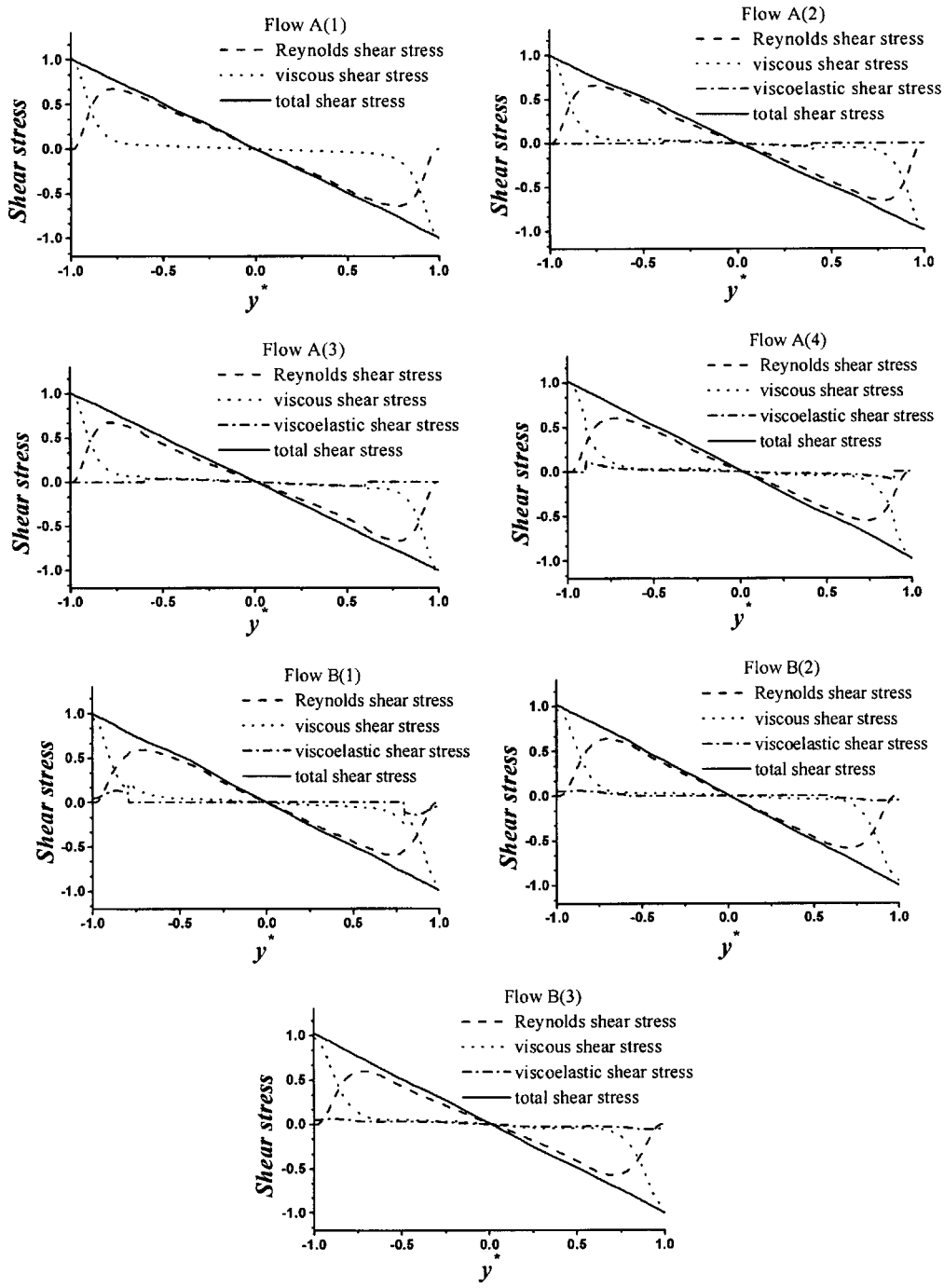

Fig. 7 Budget of shear stress

tions, as seen in Fig. 7. The jump of viscous shear stress at the interface of the Newtonian fluid and non-Newtonian fluid regions is clearly seen especially in flow A(4) and flow B(1), which is due to the induced viscoelastic shear stress in the non-Newtonian fluid region. The abrupt change of viscous shear stress, which is not seen in the experiments, is due to the crude assumption that the interface between the Newtonian and non-Newtonian fluid region is fixed and parallel to the wall. Actually, shear-stress-dependent network structure evolves with time, and the interface shape should be irregular and dynamic.

The Reynolds shear stresses are compared in Fig. 8. Drag reduction is often explained by the decrease of Reynolds shear stress. It is seen that in our calculations, the Reynolds shear stress decreases for all the DR cases. However, flow A(4) has a larger Reynolds shear stress than flow B(1), but it also has a larger DR rate. This is because in flow B(1), though the Reynolds shear stress is smaller, the viscoelastic shear stress is large in the near-wall region, which increases frictional drag. The comparison of Reynolds shear stress indicates that the DR rate is associated with, but not proportional to, the decrease of Reynolds shear stress. The decrease of Reynolds shear stress is only one important factor for achieving a large DR rate. Equation (8) shows that frictional drag is derived from three components: viscous shear stress, Reynolds shear stress, and viscoelastic shear stress. An integration equation for the friction factor can be obtained by applying two-fold integration $\int_0^1 \int_0^y dy^* \, dy^*$ to Eq. (8), transforming multiple integration to single integration as follows:

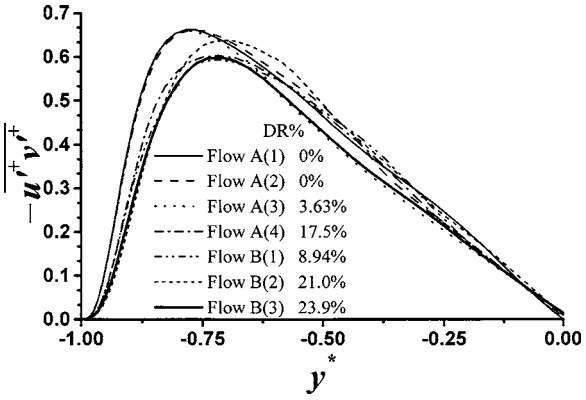

Fig. 8 A comparison of Reynolds shear stresses

$$C_f = 12/\mathrm{Re}_b + 6\int_0^1 \frac{(-\overline{u'^+v'^+})(1-y^*)}{U_b^{+2}}dy^* + 6\int_0^1 \beta\frac{C_{xy}^+}{\mathrm{We}_\tau U_b^{+2}}(1-y^*)dy^* \quad (9)$$

viscous contribution; turbulence contribution; viscoelastic contribution

This integration was first proposed by Fukagata et al. [9] (FIK integration) to evaluate active turbulent control and we extend it to drag-reducing flow by additives. The above equation shows that the friction factor is decomposed into a viscous contribution, which is identical to the laminar solution, the turbulence contribution, and the viscoelastic contribution. The turbulence contribution and viscoelastic contribution are linear weighted integrations with the weighted factor larger at the near-wall region. This indicates that the decrease of Reynolds shear stress and the increase of viscoelastic shear stress at the near-wall region have the largest effect on the frictional factor. The smaller Reynolds shear stress and smaller viscoelastic shear stress at the near-wall region can result in a smaller friction factor. The network structures give rise to viscoelastic shear stress that increases frictional drag, whereas a decrease in Reynolds shear stress reduces frictional drag. When the decrease effect is larger than the increase effect, DR occurs. Table 2 shows the relative contributions of the three components in Eq. (9) to frictional drag. In flow A(2), the viscoelastic contribution is negligible, which is due to the small values of viscoelastic shear stress and the small weighted factor, and the viscous and turbulence contributions are almost the same as those of Newtonian fluids. It is seen clearly that with the increase of the DR rate, the viscous contribution becomes larger, indicating that the flow is further laminarized. For all the DR cases, the turbulence contribution becomes smaller as compared to the Newtonian fluid case and flow B(3) has the smallest turbulence contribution, but the drag-reduction rate is not proportional to the decrease of turbulence contribution. The turbulence contributions of flow A(4), flow B(1), and flow B(2) are almost the same, but their DR rates differ from each other. This is due to different viscoelastic contributions, for example, flow B(1) has the largest viscoelastic contribution to increase frictional drag; thus its drag-reducing ability is smallest. The comparisons show that a large DR rate depends on not only the decrease of Reynolds shear stress but also the viscoelastic shear stress.

Table 2 Fractional contributions

	DR %	V^c	T^c	E^c
Flow A(1)	0%	34.5%	65.5%	0%
Flow A(2)	0%	34.7%	64.8%	0.453%
Flow A(3)	3.63%	35.2%	63.2%	1.56%
Flow A(4)	17.5%	37.7%	57.2%	5.14%
Flow B(1)	8.94%	36.6%	57.8%	5.62%
Flow B(2)	21.0%	38.4%	57.2%	4.39%
Flow B(3)	23.9%	39.9%	54.1%	5.97%

Table 3 Elastic dissipation

	DR %	Elastic dissipation
Flow A(1)	0%	0
Flow A(2)	0%	0.00544
Flow A(3)	3.63%	0.0110
Flow A(4)	17.5%	0.0180
Flow B(1)	8.94%	0.0210
Flow B(2)	21.0%	0.0203
Flow B(3)	23.9%	0.0285

The integrated balance equations of mean kinetic energy, turbulent kinetic energy, and elastic energy can be derived next:

$$\int_{-1}^{1}\frac{U^+}{\mathrm{Re}_\tau}dy^* = \int_{-1}^{1}-\overline{u'^+v'^+}\frac{\partial U^+}{\partial y^+}dy^* + \int_{-1}^{1}\left(\frac{dU^+}{dy^+}\right)^2 dy^* + \int_{-1}^{1}\frac{\beta}{\mathrm{We}_\tau}C_{xy}^+\frac{dU^+}{dy^+}dy^* \quad (10)$$

energy provided by mean pressure gradient; work by Reynolds shear stress; viscous dissipation; work by mean viscoelastic shear stress

$$\int_{-1}^{1}-\overline{u'^+v'^+}\frac{\partial U^+}{\partial y^+}dy^* = \int_{-1}^{1}\overline{\left(\frac{\partial u_i'^+}{\partial x_k^+}\right)\left(\frac{\partial u_i'^+}{\partial x_k^+}\right)}dy^* + \int_{-1}^{1}\frac{\beta}{\mathrm{We}_\tau}\overline{\left(c_{ik}'^+\frac{\partial u_i'^+}{\partial x_k^+}\right)}dy^* \quad (11)$$

turbulent dissipation; work by fluctuating viscoelastic shear stress

$$\int_{-1}^{1}\frac{\beta}{\mathrm{We}_\tau}\frac{\partial U^+}{\partial y^+}C_{xy}^+\,dy^* + \int_{-1}^{1}\frac{\beta}{\mathrm{We}_\tau}\overline{\left(c_{ik}'^+\frac{\partial u_i'^+}{\partial x_k^+}\right)}dy^* + \int_{-1}^{1}\frac{\beta}{2\mathrm{We}_\tau^2}[(3-C_{ii}^+)-\alpha(C_{im}^+-\delta_{im})^2]dy^* = 0 \quad (12)$$

elastic dissipation

It is seen that the interaction of network structures with solvent alters the energy transportation process. In the budget equations of mean kinetic energy and turbulent kinetic energy, there are additional terms due to the interaction of the network structures and solvent. The elastic energy equation shows that the stretching of the network structures absorbs energy from the mean kinetic energy and turbulent kinetic energy, and then the relaxation of the network structures releases the energy to elastic dissipation.

Table 3 lists elastic dissipations. It is seen that generally the larger the elastic dissipation, the larger the drag-reduction rate. But flow B(1) is an exception; it has a larger elastic dissipation than flow A(4) and flow B(2), but a smaller drag-reduction rate. This is because in flow B(1), most of the energy of the elastic dissipation comes from mean kinetic energy and only a small amount of energy comes from turbulent kinetic energy. Thus the turbulence has not been effectively suppressed.

Finally, we use our present DNS results to explain the drag-reduction and post drag-reduction phenomena. Figure 9 is a typical diagram of the DR rate versus Reynolds number. The figure is

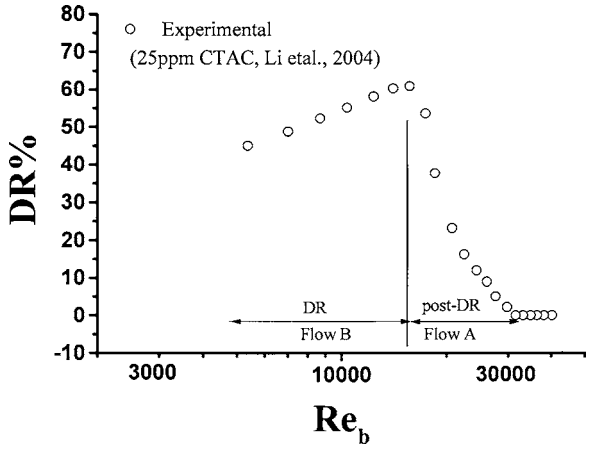

Fig. 9 Drag-reduction rate versus Reynolds number

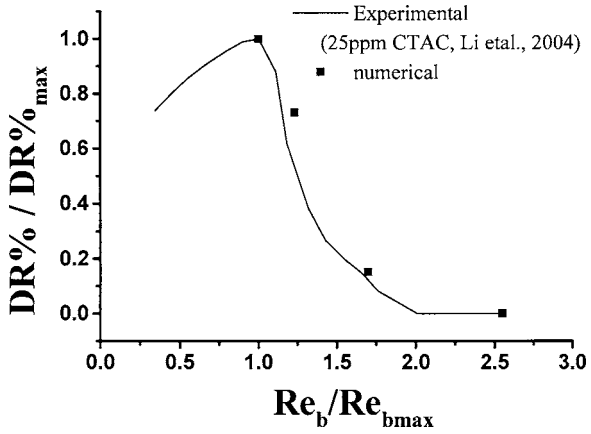

Fig. 10 Relationships between $DR\%/DR\%_{max}$ and $Re_b/Re_{b_{max}}$

characterized by two regions, the DR region and the post-DR region. In the DR region, the DR rate increases with the increase of Reynolds number, whereas in the post-DR region, the drag-reduction rate decreases. This phenomenon is well known for additive-type flow. Berman and George [10] showed breaking of the polymer molecules by flow occurs at sufficiently high strain rates, with a consequence loss of the drag-reduction ability. For surfactant additives the increase and then decrease of the DR rate can be explained as follows. It is generally accepted that the network structures are shear stress dependent. Above a critical shear stress, some rod-like micelles in the surfactant solution begin to connect to form network structures. With the increase of shear stress, more rod-like micelles connect to form network structures. At the DR region, the local effective shear stress at the wall region (viscous shear stress plus Reynolds shear stress) is above the critical shear stress and at the center region is below the critical value, so the network structures can form in the near-wall region; this flow motion is similar to flow B. However, as the shear stress increases larger than a second critical value, the network structures begin to be destroyed. In the post-DR region, the effective shear stress at the near-wall region becomes relatively large, and the network structures there begin to be destroyed. This flow motion can be modeled as flow A. By modeling the flow in the DR region as flow B and flow in the post-DR region as flow A, the increase and decrease tendency of the DR rate were qualitatively reproduced, as shown in Table 1. In addition, we have some turbulence statistics to support the drag-reducing flow at lower mean velocity, and the network structures exist in the near-wall region such as flow B(1). Experiments show that at low Reynols number, there is a lower velocity profile at the buffer layer, as compared to Newtonian fluid [11]. As shown in Fig. 3, the velocity profile of flow B(1) is lower than that of Newtonian fluid, in agreement with the experiments. Experiments also show that at a low Reynolds number, u_{rms} decreases as compared to Newtonian fluid (Schmidt [12] and Yu et al. [2]). The u_{rms} of flow B(1) decreases, which also agrees with the experiments, as shown in Fig. 4.

In the previous paragraph, we have explained that the viscous shear stress and Reynolds shear stress (effective shear stress) can help to form or destroy network structures dependent on their magnitude. When the effective shear stress is larger than the second critical value, which is equal to the viscous shear stress at the wall of the maximum DR rate flow [flow B(3)], the network structures begin to be destroyed. However, in the present DNS′, the interface of Newtonian and non-Newtonian fluids was assumed changeable at a fixed frictional Reynolds number. The effective shear stresses (dimensional) at the interface in flows A(2), A(3), and A(4) are less than the wall shear stress of flow B(3) with flow A(2) smallest, but the network structures between the wall and the interface were assumed to be destroyed. Therefore we can assume there are three flows, flow A′(2), flow A′(3), and flow A′(4), which have the same DR rate and shear stress budget as flows A(2), A(3), and A(4), respectively, but the sum of the dimensional viscous shear stress and Reynolds shear stress at the interface of the three flows are the same as that of the dimensional viscous wall shear stress of flow B(3). Based on this assumption we convert the interface positions to corresponding higher Reynolds numbers of flow A′(2), flow A′(3), flow A′(4), which are 1.23, 1.70, and 2.55 times as large as flow B(3). The relationships between $DR\%/DR\%_{\max}$ and $\mathrm{Re}_b/\mathrm{Re}_{b\,\max}$ ($\mathrm{Re}_{b\,\max}$ is the Reynolds number of the maximum DR rate) of the numerical prediction and experiment [3] are compared in Fig. 10. It is seen that the agreement is quantitatively good. The estimation based on the simple criterion ($\tau_{\mathrm{eff}} > \tau_{\mathrm{critical}}$) is surprisingly good. This fact suggests that the fracture of the micellar network structure is strikingly related to the local effective shear stress instead of the shear rate estimated by the mean velocity gradient. Further, an investigation on this point may be interesting in the scope of searching the fracture limit in the micellar destruction purpose [13].

Conclusion

We studied drag-reducing flow with coexisting Newtonian and non-Newtonian fluids. Numerical results show network structures are most effective in reducing frictional drag in the buffer layer. The drag-reduction rate is not only closely associated with the reduction of Reynolds shear stress but also the induced viscoelastic shear stress. The phenomena of DR and post-DR regions of surfactant solutions are qualitatively explained.

Acknowledgments

The authors thank Dr. Wei and Dr. Li at the National Institute of Advanced Industrial Science and Technology and Dr. Fukagata at Tokyo University for valuable discussions. This study was supported by the Ministry of Education, Culture, Sports, Science, and Technology, through the project "Smart Control of Turbulence: A Millennium Challenge for Innovative Thermal and Fluids Systems, Japan."

Nomenclature

c = conformation tensor
C = mean conformation tensor
f = friction factor $= 2\tau_w/\rho U_b^2$
h = half-height of the channel
Re_b = Reynolds number $= 2\rho U_b h/\eta_s$
Re_τ = Reynolds number $= \rho U_\tau h/\eta_s$
u = velocity
U = mean velocity
U_b = mean bulk velocity

U_τ = friction velocity $= \sqrt{\tau_w/\rho}$
We_τ = Weissenberg number $= \rho\lambda U_\tau^2/\eta_s$

Greek Symbols

α = mobility factor
β = ratio $= \eta_a/\eta_s$
δ = thickness of the non-Newtonian region
η_a = dynamic shear viscosity of surfactant contribution
η_s = dynamic shear viscosity of solvent contribution
η_0 = viscosity of the surfactant solution at zero-shear rate
λ = relaxation time

Subscripts

N = Newtonian fluid
NN = Non-Newtonian fluid

References

[1] Lu, B., Li, X., Zakin, J. L., and Talmon, Y., 1997, "A Non-Viscoelastic Drag-Reducing Cationic Surfactant System," J. Non-Newtonian Fluid Mech., **71**, pp. 59–72.

[2] Yu, B., Li, F. C., and Kawaguchi, Y., 2003, "Numerical and Experimental Investigation of Turbulent Characteristics in a Drag-Reducing Flow With Surfactant Additives," 3rd International Symposium on Turbulence and Shear Flow Phenomena, Sendai, 3, pp. 971–976.

[3] Li, F. C., Kawaguchi, Y., Segawa, T., and Hishida, K., 2005, "Reynolds Number Dependence of Turbulence Structures in a Drag-Reducing Surfactant Channel Flow Investigated by PIV," published in J. Phys. Fluids.

[4] Yu, B., and Kawaguchi, Y., 2004, "Direct Numerical Simulation of Viscoelastic Drag-Reducing Flow: A Faithful Finite Difference Method," J. Non-Newtonian Fluid Mech., **116**, pp. 431–466.

[5] Dean, R. B., 1978, "Reynolds Number Dependence of Skin Friction," ASME Trans. J. Fluids Eng., **100**, pp. 215–223.

[6] Lumley, J. L., 1969, "Drag Reduction by Additives," Annu. Rev. Fluid Mech., **1**, pp. 367–384.

[7] Lumley, J. L., 1973, "Drag Reduction in Turbulent Flow by Polymer Additives," J. Polym. Sci., Part A-1, **7**, pp. 263–290.

[8] Reischman, M. M., and Tiederman, W. G., 1975, "Laser-Doppler Anemometer Measurements in Drag-Reducing Channel Flow," J. Fluid Mech., **70**, pp. 369–392.

[9] Fukagata, K., Iwamoto, K., and Kasagi, N., 2002, "Contribution of Reynolds Stress Distribution to the Skin Friction in Wall-Bounded Flows," Phys. Fluids, **14**, pp. L73–L76.

[10] Berman, N. S., and George, W. K., 1974, "Time Scale and Molecular Weight Distribution to Dilute Polymer Solution Fluid Mechanics," in *Proc. Heat Trans. Fluid Mech. Inst.*, Stanford University Press, Stanford, CA, pp. 348–364.

[11] Eschenbacher, J. F., 2002, "Drag Reduction and Heat Transfer Characteristics of Surfactant-Added Flows With Large-Scale Longitudinal Vortices," Ph. D thesis, Kyoto University.

[12] Schmidt, G., 1997, "Surfactant Induced Drag-Reduction in a Channel Flow Facility," B.S. thesis, University of Illinois, Urbana-Champaign.

[13] Li, P. W., Kawaguchi, Y., Daisaka, H., Yabe, A., Hishida, K., and Maeda, M., 2001, "Heat Transfer Enhancement to the Drag-Reducing Flow of Surfactant Solution in Two-Dimensional Channel With Mesh-Screen Inserts at the Inlet," Trans. ASME, Ser. C: J. Heat Transfer, **123**, pp. 779–789.

[14] Kawaguchi, Y., Segawa, T., Feng, Z. P., and Li, P. W., 2002, "Experimental Study on Drag-Reducing Channel Flow With Surfactant Additives—Spatial Structure of Turbulence Investigated by PIV System," Int. J. Heat Fluid Flow, **23**, pp. 700–709.

The Use of Solution Adaptive Grid for Modeling Small Scale Turbulent Structures

G. de With[1]
e-mail: g.de.with@lafarge-roofing.com
Lafarge Roofing Technical Centers,
Sussex Manor Business Park,
Gatwick Road,
Crawley RH12 4LN, UK

A. E. Holdø
CFD Research Group,
University of Hertfordshire,
Dept. Aerospace Automotive and Design Eng.,
Hatfield Campus, College Lane,
Hatfield AL10 9AB, UK

The use of large eddy simulation (LES) is computationally intensive and various studies demonstrated the considerable range of vortex scales to be resolved in an LES type of simulation. The purpose of this study is to investigate the use of a dynamic grid adaptation (DGA) algorithm. Despite many developments related to adaptive methods and adaptive grid strategies, the use of DGA in the context of turbulence modeling is still not well understood, and various profound problems with DGA in relation to turbulence modeling are still present. The work presented in this paper focuses on the numerical modeling of flow around a circular cylinder in the sub-critical flow regime at a Reynolds number of $3.9 \cdot 10^3$. *LES simulations with conventional mesh and DGA have been performed with various mesh sizes, refinement criteria and re-meshing frequency, to investigate the effects of re-meshing on the flow field prediction. The results indicate that the turbulent flow field is sensitive to modifications in the mesh and re-meshing frequency, and it is suggested that the re-meshing in the unsteady flow region is affecting the onset of small scale flow motions in the free shear layer.* [DOI: 10.1115/1.1989359]

1 Introduction

The present study deals with the simulation of flow around a circular cylinder at a Reynolds number of $3.9 \cdot 10^3$. The subcritical flow has a laminar upstream boundary layer and transition to turbulence takes place after separation. Several studies have been previously reported for this type of flow [1] and it is gradually accepted that it is a difficult test case for computational fluid dynamics (CFD) [2,3]. Tutar and Holdø's results [1] suggest that the large eddy simulation (LES) method gives improved results compared to those of Reynolds averaged Navier-Stokes (RANS) based turbulence models. Studies by de With et al. [4] have indicated that the LES models yield good results when the mesh resolution is such that a sufficient part of the inertial range of the turbulent spectrum is resolved. In other words when a large part of the total kinetic energy is contained in the resolved scales. The nearly universal approach to accomplish this high mesh resolution is the use of automatic mesh generators. These type of meshes are characterized by high resolution in regions where gradients are not necessarily significant, consequently, these meshes have a large number of redundant cells.

An alternative and more appealing technique to reduce redundant cells is the use of dynamic grid adaptation (DGA). However, the use of DGA requires at present significant fine-tuning to accomplish a suitable DGA configuration [4]. A suitable configuration of the DGA algorithm is accomplished if the important flow features are captured by the mesh. This means that the turbulent scales unsuitable for LES subgrid modeling are captured in the mesh. To identify the range of flow scales that should be resolved is a difficult task. While DGA can be very useful in resolving turbulent scales, there are two main issues which at present need further consideration.

1. The effect of re-meshing on the resolved turbulent scales.
2. To separate the resolved scales from the unresolved subgrid scales.

One of the aims of the present paper is to give an insight into the above issues.

The use of a DGA algorithm and the inherent continuous modifications to the mesh will affect local flow structures. A suitable time increment for mesh modification is, therefore, based on the life span of local flow structures resolved in the computation. However, to anticipate the development of flow structures in areas where the mesh is coarse requires a rather small time increment. Previous work of de With et al. [5] investigated the effect of DGA in relation to the onset of vortex shedding at low Reynolds numbers, and concluded that DGA enforced small scale instabilities in the flow field. In turbulent flows where there is a transition from laminar to turbulent initial turbulence depends on the existence of these small scale flow motions. To ensure these small scale flow motions are part of a realistic flow field, moderate mesh modifications and variations in mesh resolution are preferred. De With et al. [6] suggested to remedy this problem using a reduced time increment of the CFD computation, however, the use of a reduced time increment comes with computational costs.

The second aspect of consideration is the scale separation or filtering operation to remove small scale motions from the flow and accomplish commutation with the governing equations. Commutation is generally satisfied if the filter has a constant width. However, in inhomogeneous turbulent flows, the minimum size of eddies that needs to be resolved varies throughout the flow. Thus, the filter width should also vary accordingly. Due to the lack of a straightforward and robust filtering procedure for inhomogeneous flows, most large eddy simulations performed to date have not made use of explicit filtering. In this study filtering is achieved by making use of the low-pass characteristics of the discretization elements. In such a case, additional length scales are added each time the mesh is refined, and thus the process converges to a direct numerical (DNS). In the context of DGA this is an important feature which is necessary to make use of increased mesh refinement. Nevertheless, the interference of DGA on small scale flow structures should be comprised with potential reductions in mesh size to enable a realistic representation of the smallest resolved scales.

The simulations that are performed as part of this study are aimed to address the various implications on LES turbulence modeling and to investigate in particular the effects of re-meshing on the unsteady, turbulent flow field. As part of this study high

[1]Correspondence to: Govert de With, Lafarge Roofing Technical Centers. Telephone: +44(0)1293 596039; Fax: +44(0)1293 596427.

Contributed by the Fluids Engineering Division for publication in the JOURNAL OF FLUIDS ENGINEERING. Manuscript received by the Fluids Engineering Division, July 23, 2004. Final revision: May 12, 2005. Associate Editor: Ismail B. Celik.

mesh resolution simulations are carried out to give an insight in the effects of DGA configuration on a large scale LES simulation. For analysis of the computational data, detailed plots of the mesh are presented and time integrated results are compared with experimental data from Norberg [7] and Lourenco and Shih [8].

2 Solution Method

In this study the CFD code FLUENT 6.1 [9] is used. The CFD code calculates the solution to the incompressible Navier-Stokes equations. The spatial discretization of the equations is based on an unstructured hexahedral mesh. The primitive variables are all discretized in a cell-centered fashion, with one value for each variable in each element. To avoid checker-boarding of pressure, the CFD code uses a procedure similar to that outlined by Rhie and Chow [10], the scheme interpolates the pressure values at the faces using momentum equation coefficients. Pressure-velocity coupling is achieved by using a semi-implicit method for pressure linked equations (SIMPLE) algorithm.

A second-order implicit discretization scheme is used in the temporal dimension while spatial discretization of the filtered equations is achieved using central differencing (CD). To satisfy the numerical requirements for LES the spatial discretization scheme provides at least second-order spatial accuracy. The scheme provides comparatively low levels of numerical dissipation and is a preferred discretisation scheme for LES and DES calculations [11]. The implicit equation are solved iteratively and the convergence criteria for U, V, W, and continuity are set to $1\cdot10^{-3}$.

2.1 Large Eddy Simulation. The SGS model used for LES turbulence modeling is the model proposed by Smagorinsky [12]. In here, the small scales are taken into account via an extra dissipation term, which accounts for the energy dissipation which occurs in the small scales.

For the turbulent flow computations the space averaged Navier-Stokes equations of an incompressible fluid are written as:

$$\frac{\partial \bar{u}_i}{\partial t} = \bar{u}_j \frac{\partial \bar{u}_i}{\partial x_j} = -\frac{1}{\rho}\frac{\partial \bar{p}}{\partial x_i} + \frac{(\mu_{lam}+\mu_t)}{\rho}\frac{\partial^2 \bar{u}_i}{\partial x_j \partial x_j} \tag{1}$$

Here the over bar represents the filtered variable which is obtained from the standard velocity decomposition $u=\bar{u}+u'$. The term μ_t for the space averaged equation is called the subgrid scale viscosity or turbulent viscosity, which is space and time dependent. Smagorinsky [12] proposed a method of calculating the subgrid scale viscosity as shown;

$$\mu_t = \rho l_s^2 |\bar{S}| \tag{2}$$

where l_s is the mixing length and $|\bar{S}| \equiv \sqrt{2\bar{S}_{ij}\bar{S}_{ij}}$. l_s is calculated as

$$l_s = \min(\kappa d, C_s \Delta) \tag{3}$$

where κ is the von Karman constant and d the distance to the nearest wall. The definition $l_s=\kappa d$ is applied in the vicinity of the wall to account for near wall flow structures. C_s is the Smagorinsky constant, which normally has a value in the range of 0.10–0.25. In this study the C_s constant is set to 0.1 corresponding to the models default value. Δ is the subgrid length scale or filter width associated with the grid size and is calculated as $\sqrt[3]{\Omega}$. The quantity $\bar{S}_{ij}$ is the resolvable strain rate;

$$\bar{S}_{ij} = \frac{1}{2}\left(\frac{\partial \bar{u}_i}{\partial x_j} + \frac{\partial \bar{u}_j}{\partial x_i}\right) \tag{4}$$

In the next step the locally calculated turbulent viscosity, which for each element varies in magnitude, is added to the laminar viscosity. In the new time step, the governing equations will be resolved, including the turbulent viscosity to account for the subgrid scales.

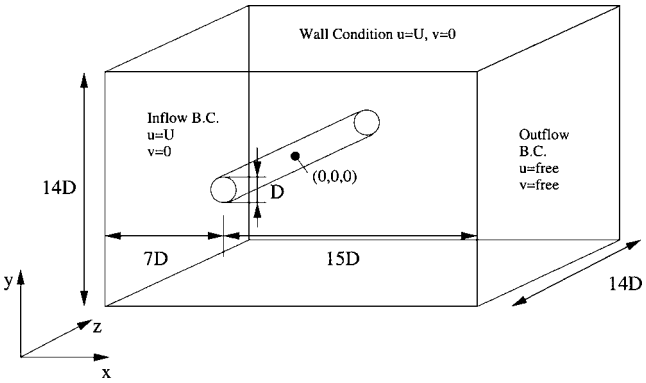

Fig. 1 Dimensions of the numerical domain

2.2 Dynamic Grid Adaptation. The grid adaptation strategy used in this study is the so-called H-refinement [13]. In this approach a variable number of grid points is used. Points are added to, or removed from, the grid according to the local requirements, without changing the positions of the other grid points. Error levels in the element are calculated based on the gradient approach. Work by Zienkiewicz and Wu [14] has shown that gradient-based refinement can give better refinement characteristics and is cheaper than that of curvature-based refinement. Furthermore, they showed that the mesh converges faster with fewer cycles of refinement than those of curvature. In this gradient approach the undivided Euclidean norm of the gradient of the selected refinement variable is multiplied by the element length scale.

$$|e_i| = \Omega^{1/3} |\nabla q| \tag{5}$$

In the above definition e_i is the error indicator, Ω is the element volume, and $|\nabla q|$ is the undivided Euclidean norm of the gradient of the refinement variable. No normalization is used for the error thresholds, to ensure that the refinement algorithm does not start drifting due to changing gradient levels. The error estimator used to guide the re-meshing is based on the gradient error obtained from the velocity magnitude $|U|$. The cube root of the velocity magnitude $|U|^{1/3}$ is used as a second refinement variable. This mathematical relation is selected to obtain a smooth mesh refinement in the wake. A smooth mesh throughout the wake region enables a continuation of the flow computation without grid adaptation, to study the specific effects of mesh modifications onto the flow computation.

3 Simulation Results and Discussions

3.1 Computational Domain and Simulations. The computational domain and boundary conditions used for the simulations are shown in Fig. 1. At the inlet boundary a uniform velocity profile is imposed, while on the outlet boundary pressure is imposed and velocity is set free. No-slip boundary conditions are applied on the cylinder wall and all velocity components are set to zero. On all four side boundaries the velocity in the y and z direction is set to $v=0$ and $w=0$ to ensure no flow can be entrained via these boundaries. To ensure no mesh refinement will take place along the horizontal boundaries, the x component of the velocity is set equal to the velocity imposed at the inlet in order not to generate any velocity gradient along these boundaries. Work performed by Valles [15] has shown that turbulent flow structures in the wake behind a bluff body may exceed more than five times the integral scale L in spanwise direction. To ensure these structures are accurately represented in the flow field the spanwise dimension of the model is set to $14D$. Due to sufficient spanwise dimensions of the model no periodic boundary conditions are applied to the side boundaries. All simulations use an initial flow field obtained from a transient auxiliary flow

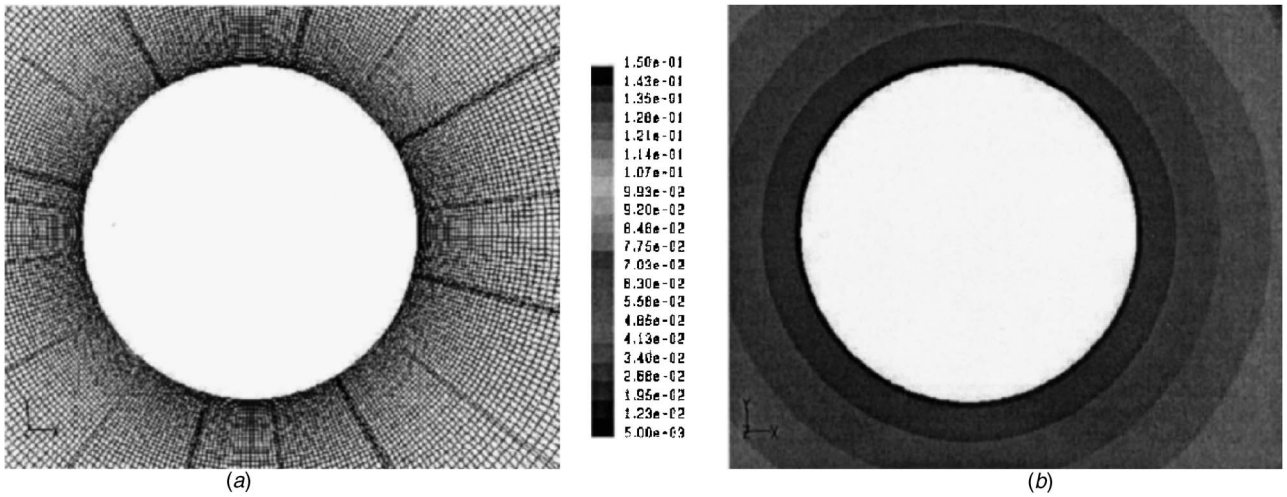

Fig. 2 A plot of the (*a*) mesh and (*b*) filter width for NO DGA $|2.4\cdot10^6$

simulation.

The work presented here is compared with experimental data from Lourenco and Shih [8]. Data for drag coefficient $\bar{C}_D$, fluctuating lift coefficient $\tilde{C}_L$ and Strouhal number *St* is obtained from work published by Norberg [7]. A further comparison in the downstream wake flow is made with experimental data from Ong and Wallace [16] and LES data previously obtained by Mittal and Moin [17].

In this work a total of six simulations are presented. The first three simulations are carried out with conventional mesh using $1.0\cdot10^6$, $2.4\cdot10^6$, and $3.0\cdot10^6$ nodes, a plot of the conventional mesh is seen in Fig. 2. The final three simulations are performed with DGA. The configuration of the DGA algorithm requires specification of a refinement variable, threshold values for mesh refinement and coarsening, as well as a minimum mesh size to restrict excessive mesh refinement and a time increment for mesh modification. Details of the DGA configuration are presented in Table 1. To investigate the effects of mesh modification on the flow prediction a simulation is performed with conventional mesh containing $3.0\cdot10^6$ nodes. This mesh was generated in the third simulation with DGA ($\nabla U^{1/3}|20|3.0\cdot10^6$). Plots of the mesh are shown in Figs. 3 and 4. To maintain sufficient isotropy in the mesh elements, mesh refinement is applied in all directions as seen in Fig. 5.

All simulations are carried out with a fix normalized time increment Δt_{norm}[2] of $5\cdot10^{-2}$. The normalized time increment is about three times the Kolmogorov time scale, which is $\text{Re}^{-1/2}=1.6\cdot10^{-2}$. The total number of time steps is set to 4000 which will capture approximately 40 vortex cycles.

Velocity profiles for the streamwise velocity component in both streamwise and transverse direction are presented, as well as the turbulent shear stress along the transverse axis. In addition, drag coefficient $\bar{C}_D$[3], Strouhal number S_t[4] and fluctuating lift $\tilde{C}_L$ are calculated from the time integrated flow field and presented in Table 2. Additionally the recirculation length L_r is presented in this table. The recirculation length is obtained from the time integrated velocity profile and is defined in diameters of the cylinder as the region with negative downstream velocity, starting from the back of the cylinder.

3.2 Basic Flow Features. If supplied with sufficient mesh the flow field is predicted well and confirms the experimental data from Lourenco and Shih [8]. In the DGA simulations the mesh resembles the flow features and mesh refinement has taken place in the regions dominated by a high rate of strain. The velocity decay in the downstream region shows some deviation from experimental data, as shown in Fig. 6. However, the general flow features in the downstream flow field are predicted well in the simulations with a mesh size of $1.8\cdot10^6$ nodes and above. The drag coefficient $\bar{C}_D$ varies between 1.0 and 1.49 and the fluctuating lift coefficient $\tilde{C}_L$ ranges from 0.04 to 0.73. The simulations performed with DGA show a drag coefficient in the order of 1.2–1.3. Best agreement is obtained with a mesh using $2.4\cdot10^6$ nodes, in this simulation $\bar{C}_D$, $\tilde{C}_L$, and Strouhal number *St* are in close agreement with the experimental data. It is important to remark that the increased mesh size in the final simulation is insufficient to maintain increased mesh resolution throughout in comparison

[2] Δt_{norm} is normalized with cylinder diameter and inlet velocity $\Delta t_{\text{norm}}=\Delta t u_\infty/D$.

[3] The drag coefficient is the sum of the streamwise pressure forces acting on the cylinder relative to the density and inlet velocity $\bar{C}_D=2\bar{F}_D/\rho u_\infty^2$.

[4] Strouhal number is the frequency of the periodic wave relative to cylinder diameter and inlet velocity $S_t=fD/u_\infty$.

Table 1 Threshold values for mesh refinement and coarsening as well as the minimum mesh resolution in terms of a micro scale and re-meshing frequency

	Refinement e_i	Coarsening e_i	Micro scale $[\Delta_{\min}/D]$	Re-meshing [*Time steps*]	Frequency-$[\Delta t_{\text{norm}}]$
NO DGA$\|1.0\cdot10^6$	—	—	$2.62\cdot10^{-2}$	—	—
NO DGA$\|2.4\cdot10^6$	—	—	$1.34\cdot10^{-2}$	—	—
NO DGA$\|3.0\cdot10^6$	—	—	$6.69\cdot10^{-3}$	—	—
$\nabla U\|20\|1.8\cdot10^6$	0.01	0.05	$6.71\cdot10^{-3}$	20	$1\cdot10^0$
$\nabla U\|10\|1.9\cdot10^6$	0.01	0.05	$6.67\cdot10^{-3}$	10	$5\cdot10^{-1}$
$\nabla U^{1/3}\|20\|3.0\cdot10^6$	0.08	0.13	$6.69\cdot10^{-3}$	20	$1\cdot10^0$

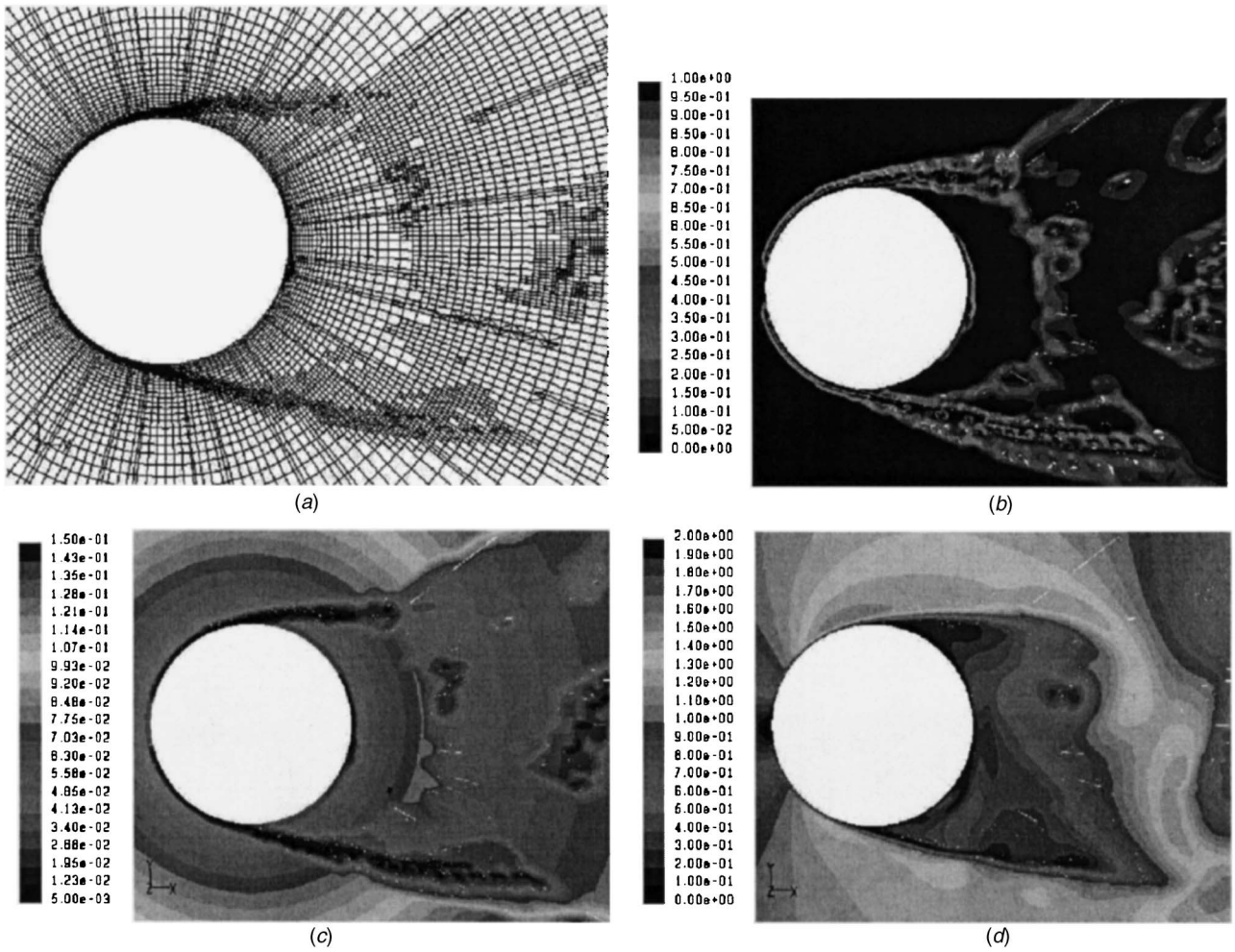

Fig. 3 A plot of the (*a*) mesh, (*b*) cell squish, (*c*) filter width, and (*d*) velocity magnitude for $\nabla U|20|1.8\cdot10^6$

with the intermediate mesh. Therefore, the final mesh does not provide a priori improved results. The flow features in the near wall region are demonstrated by the pressure coefficient C_p around the cylinder, presented in Fig. 7. Among the DGA simulations the deviation with experimental data is most profound directly behind the cylinder, hence the deviation in drag coefficient. On the contrary, the location of the separation region at $\theta \simeq 70°$ is predicted accurately in all simulations. Variations in the flow prediction are most dominant in the formation region due to the presence of a large spectrum of turbulent scales and the transition to turbulence (Figs. 6–12). Further downstream where the wake is fully developed turbulent quantities are predicted with less variation and the mesh refinement is more smooth and uniform.

Two simulations using a mesh with roughly $3.0\cdot10^6$ nodes are performed. The latter simulation is carried out using the DGA algorithm, while the former simulation is using a conventional mesh obtained from the simulation with DGA. Significant differences in the flow prediction are present between both simulations. The geometry of the wake region behind the cylinder, as well as the drag coefficient $\bar{C}_D$, Strouhal number S_t and fluctuating lift $\tilde{C}_L$ are predicted differently.

3.3 Discussion. A mesh containing $3.5\cdot10^5$ nodes is used as an initial mesh in the simulations with DGA and initial flow conditions are provided by an auxiliary simulation. Excessive mesh refinement takes place in the first stage of the simulation. In the simulations with DGA the mesh size doubled during the first mesh modification, and a semisteady mesh was established after roughly 5–10 mesh modifications. The mesh resolution that is maintained in the simulations with DGA is much higher in the boundary and free-shear layer compared to the simulation with conventional mesh ($2.4\cdot10^6$ nodes). Furthermore, no turbulent activity is observed in the boundary layer providing the bases for a steady mesh refinement with minimum variation.

To overcome excessive mesh refinement all simulations with DGA have a resolution limit. Elements with a length scale smaller then $1.55\cdot10^{-2}$ will not be considered for further refinement, as indicated by the micro scale[5] in Table 1. Despite a well defined mesh limitation, stable and efficient mesh refinement in the formation region is difficult to accomplish, as seen in Figs. 3(*a*), 3(*c*), 4(*a*), and 4(*c*). As a result the LES scale separation is less distinct and high resolution vortex scales are only present in some confined mesh structures [Figs. 3(*c*) and 4(*c*)]. Figures 3(*c*) and 4(*c*) indicate that there is distinct variation in mesh resolution among both simulations and a filter width of approximately $5\cdot10^{-2}$ and $2\cdot10^{-2}$ is maintained in the formation region which is substantial compared to the theoretical Kolmogorov scale presented in Table 3. A diffused mesh refinement is preferred to ensure the smaller turbulent scales can sustain in the mesh. Nevertheless, variations in mesh resolution are an inherent feature of DGA and, therefore, careful evaluation of the flow field and sufficient re-meshing must be invoked to optimize the grid adaptation.

[5]The micro scale is the normalized filter width based on the smallest element in the mesh and calculated as $\sqrt[3]{\Omega_{\min}}/D$.

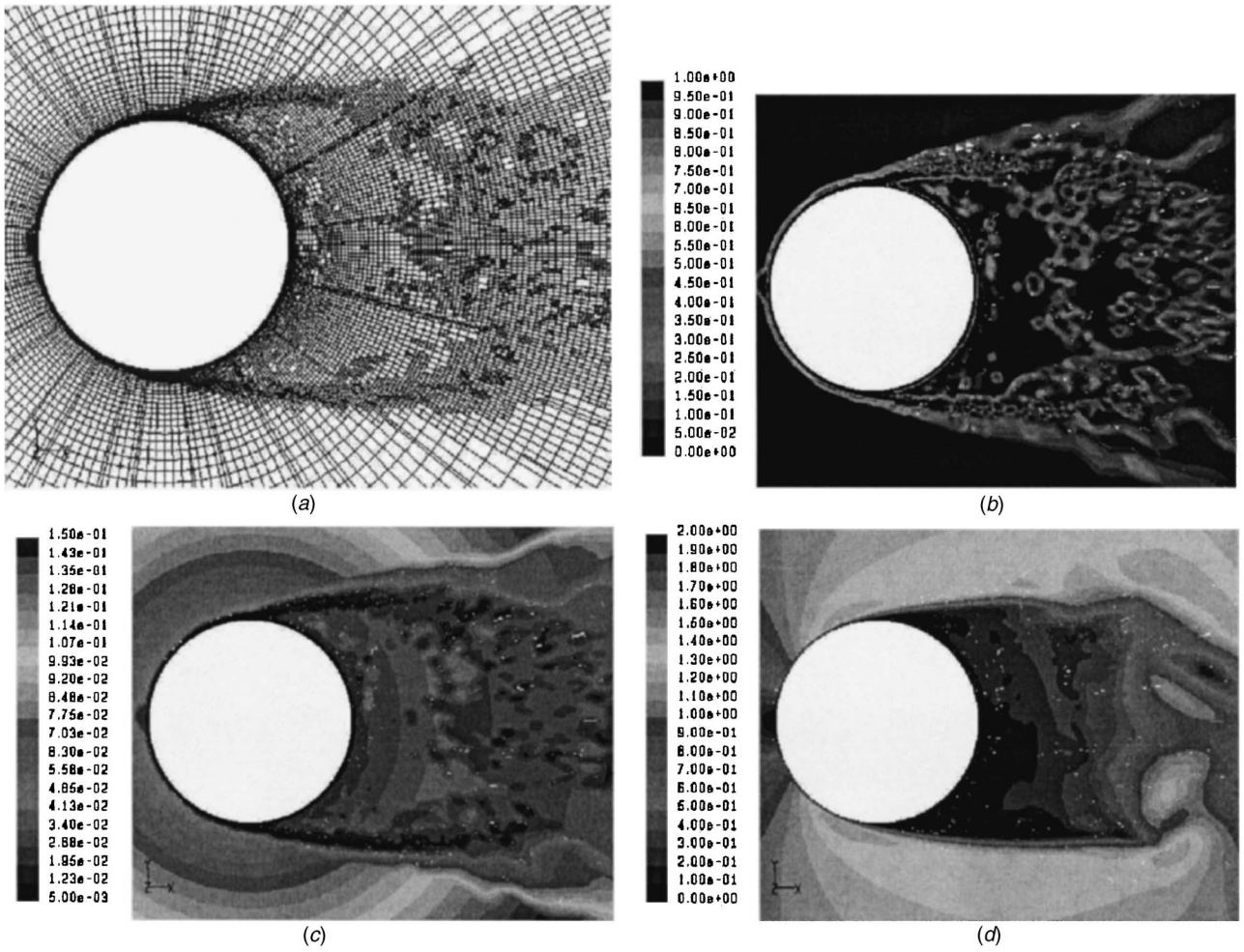

Fig. 4 A plot of the (*a*) mesh, (*b*) cell squish, (*c*) filter width, and (*d*) velocity magnitude for $\nabla U^{1/3}|20|3.0\cdot10^6$

The two final simulations using a mesh with $3.0\cdot10^6$ nodes were performed to study the effect of mesh modifications on the small scale turbulent structures. The mesh was obtained from the final DGA simulation and sufficient mesh resolution in the boundary layer and the wake was provided to enable conventional LES modeling. The variation in flow prediction is partly present due to reduced mesh resolution when the flow moves away from the refined regions. As a consequence there is a reduced mesh resolution in the free shear layer. Nevertheless, the distinct differences between both simulations, supported by the results obtained with a mesh size of $1.8\cdot10^6$ and $1.9\cdot10^6$ nodes suggest that re-meshing has an impact on the flow prediction. A plausible conjecture is the interference of the DGA algorithm on the small scale flow structures directly after separation. To visualize the turbulent structures a one-dimensional power spectrum for the y velocity component at three different locations is shown in Fig. 13. Comparison with Kolmogorovs similarity hypothesis indicates the presence of a similarity zone in the formation region, while further downstream $(x/D=7)$ the similarity is subject to meshing conditions. The spectrum suggests increased energy levels in the resolved frequency range for the LES simulations that are performed with DGA. The variation is seen particularly well in Figs. 13(*a*) and

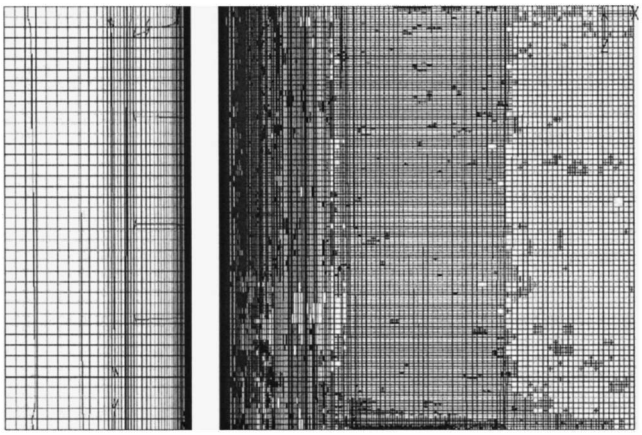

Fig. 5 Mesh resolution in the spanwise direction with DGA and a mesh size of $3.0\cdot10^6$

Table 2 Time integrated flow parameters for simulation using conventional mesh and DGA at $Re=3.9\cdot10^3$

Norberg [7] Lourenco and Shih [8]	$\bar{C}_D$ 0.98±0.05	S_t 0.20–0.22	$\tilde{C}_L$ 0.08+/−0.01	L_r 1.17
$NO\ DGA\,|1.0\cdot10^6$	1.49	0.225	0.73	0.50
$NO\ DGA\,|2.4\cdot10^6$	1.03	0.205	0.07	1.55
$NO\ DGA\,|3.0\cdot10^6$	1.11	0.222	0.04	1.41
$\nabla U|20|1.8\cdot10^6$	1.24	0.219	0.20	0.89
$\nabla U|10|1.9\cdot10^6$	1.27	0.210	0.13	0.81
$\nabla U^{1/3}|20|3.0\cdot10^6$	1.21	0.216	0.07	0.99

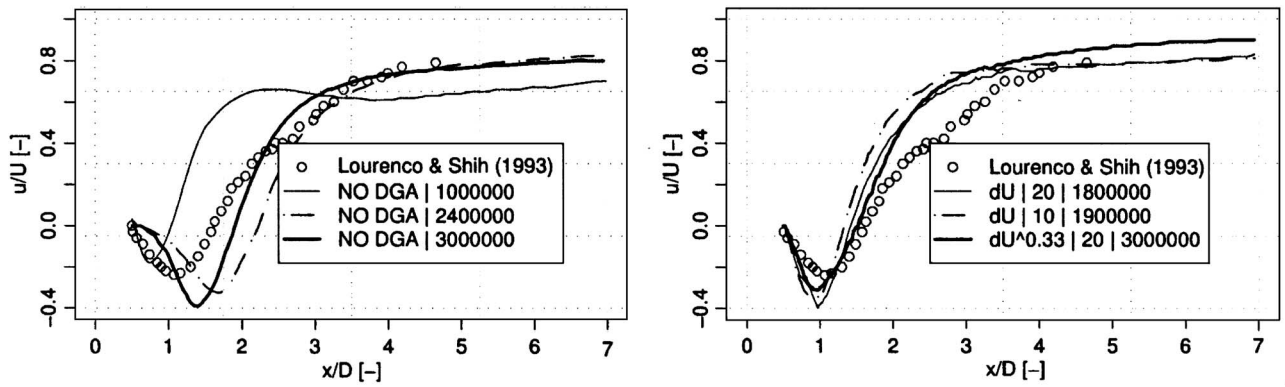

Fig. 6 Time integrated normalized velocity along streamwise axis at $y/D=0$, for simulations using conventional mesh and DGA

13(*d*) for frequencies in the range of 0.1–1. It is suggested that this phenomenon is due to small scale motions as a result of mesh modifications. At higher Reynolds numbers as studied in this work the onset of turbulence in the free shear layer is subject to small scale instabilities. In this region the mesh is very dynamic due to the unsteady nature of the free shear layer. As a consequence this region is subject to significant mesh modifications which accelerates the onset of turbulent structures.

The effect caused by re-meshing is due to the interpolation which is required to assign flow conditions to the new mesh points. Sampaio et al. [18] demonstrated the deleterious effect of a simple linear interpolation and suggested an interpolation scheme which is compatible with the CFD solver. Although a compatible interpolation scheme is used here, the effects of re-meshing are still very distinct. The transient nature of the vortex shedding and the transition from laminar to turbulent simply provide a physical process which is very sensitive to variations in the initial turbulence, hence small flow perturbations have a significant effect on the complete flow field. These results confirm previous work of De With et al. [5] who showed that the onset of vortex shedding at Reynolds numbers in the range of 50–100 is significantly accelerated in the case where a DGA algorithm is applied.

4 Conclusions

The aim of this study is to investigate the use of a DGA algorithm for LES turbulence modeling. This study has shown that a reduction in mesh size in comparison with the conventional mesh can be achieved. Nevertheless, a suitable configuration of the DGA algorithm is required to achieve effective mesh refinement. The following conclusions can be derived from the work presented in here:

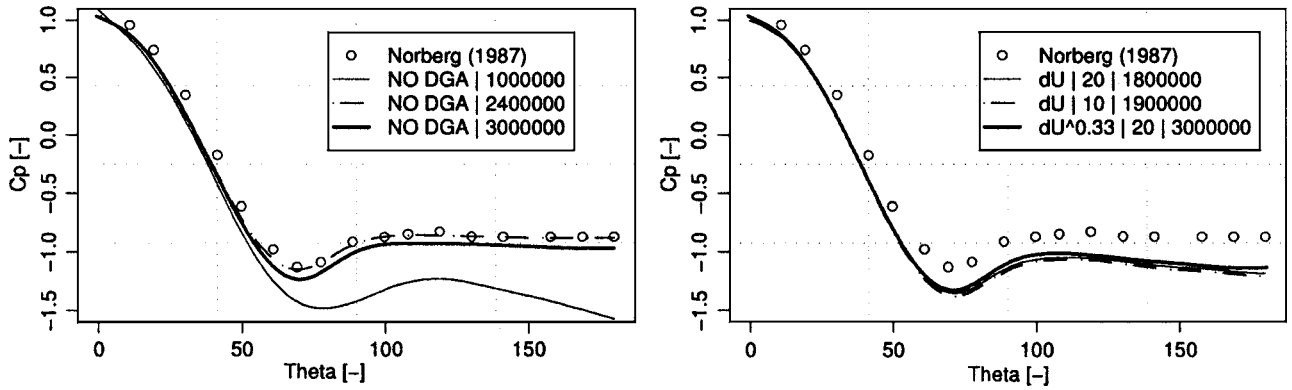

Fig. 7 Time integrated normalized pressure coefficient C_p on the surface of the cylinder

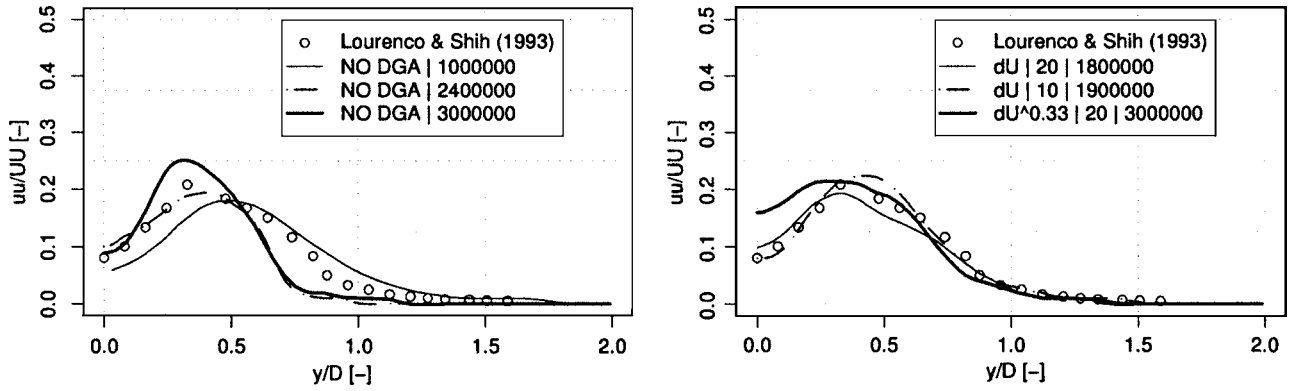

Fig. 8 Time integrated normalized Reynolds stress *uu* axis at $x/D=1.54$, for simulations using conventional mesh and DGA

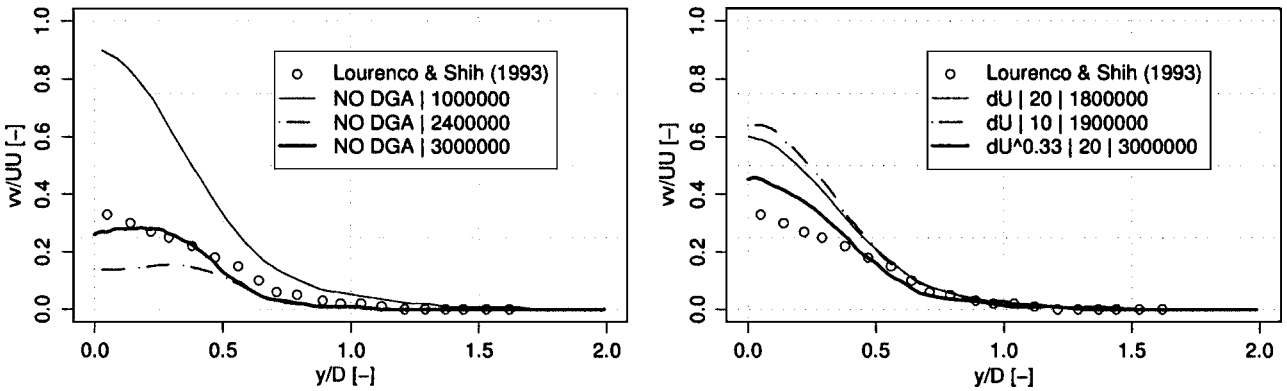

Fig. 9 Time integrated normalized Reynolds stress *vv* axis at *x*/*D*=1.54, for simulations using conventional mesh and DGA

- The mesh modifications in the free shear layer lead to distinct differences in the flow prediction. Variations in flow prediction are seen between the simulations containing $3.0 \cdot 10^6$ nodes, as well both simulations with DGA using a different re-meshing frequency. It is suggested that re-meshing introduces small scale perturbations which accelerate the onset of turbulent structures in the free shear layer.
- The main concern with DGA in the context for LES turbulence modeling is to minimize the interference of DGA on small scale flow structures while maintaining regular re-meshing to anticipate for potential turbulent structures.
- During the simulations, mesh modifications were less than $1 \cdot 10^5$ nodes, which corresponds with roughly 5% of the mesh. The normalized time scale associated with the re-meshing used in this study is $5 \cdot 10^{-1}$ and $1 \cdot 10^0$, this corresponds with 10 and 5 mesh adaptations respectively per vortex shedding.
- The refinement variables used in this study are the velocity magnitude and the cube root of the velocity magnitude. The use of a cube root velocity has advantages, as it provides smoother meshing. Nevertheless, it comes with an increase in the total mesh size.

Nomenclature

$\bar{C}_D$ = Drag coefficient
C_s = Smagorinsky constant
D = Cylinder diameter
e_i = Estimated error
f = Frequency of the periodic wave
L = Integral length scale
L_r = Recirculation length
l_s = Subgrid length scale
p = Pressure
$\bar{p}$ = Integrated pressure
q = Refinement variable
Re = Reynolds number

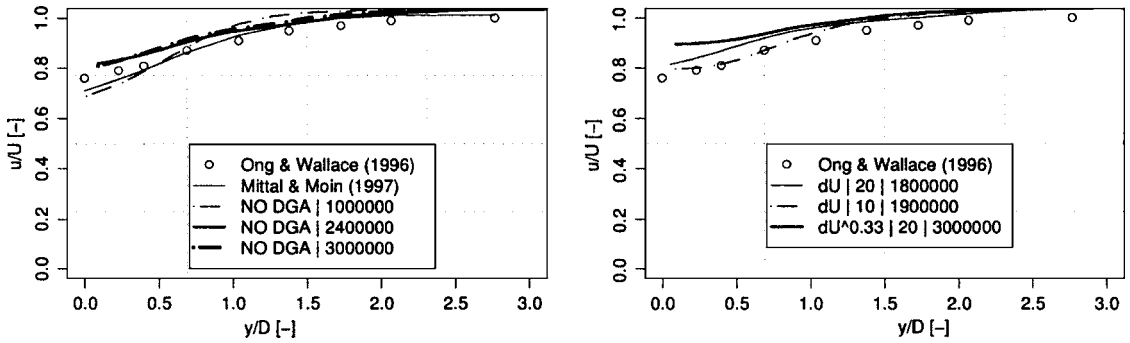

Fig. 10 Time integrated normalized velocity along streamwise axis at *x*/*D*=7, for simulations using conventional mesh and DGA

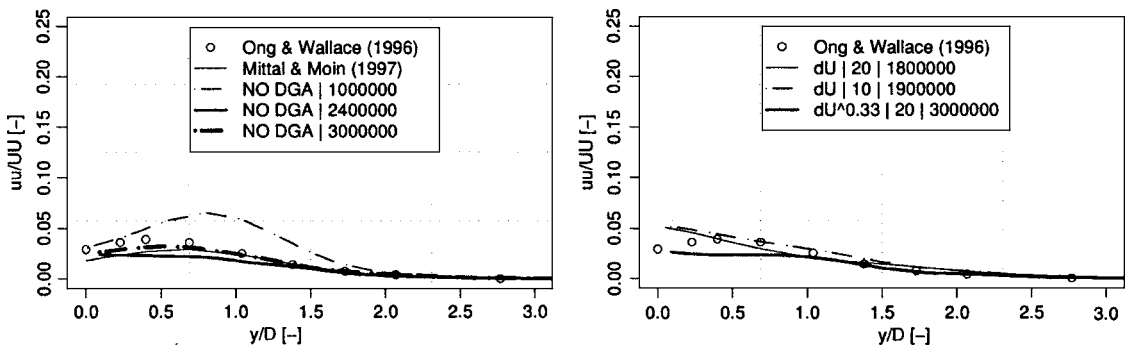

Fig. 11 Time integrated normalized Reynolds stress *uu* axis at *x*/*D*=7, for simulations using conventional mesh and DGA

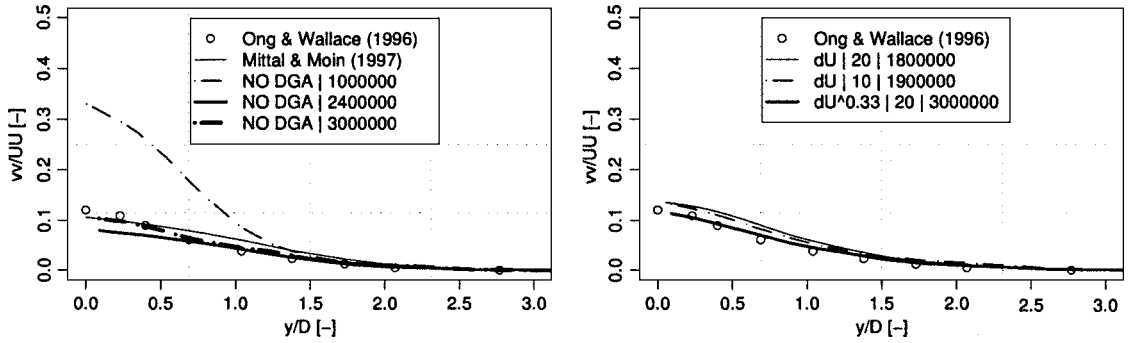

Fig. 12 Time integrated normalized Reynolds stress *vv* axis at *x*/*D*=7, for simulations using conventional mesh and DGA

$|\bar{S}|$ = Magnitude of strain
S_{ij} = Strain tensor
S_t = Strouhal number

t = Time
u = Streamwise velocity component
u_i = u,v,w, for $i=1,2,3$
$\bar{u}$ = Integrated velocity
u_i' = u,v,w fluc. velocity component for $i=1,2,3$
u_∞ = Main streamwise velocity
x = Space in streamwise direction
x_i = x,y,z for $i=1,2,3$, respectively
y = Space in lateral direction
Δ = Length scale

Table 3 Normalized Kolmogorov length scale and Kolmogorov time scale

Flow scales	$\eta/D[-]\mathrm{Re}^{-3/4}$	$\tau/T[-]\mathrm{Re}^{-1/2}$
	$2.02\cdot10^{-3}$	$1.6\cdot10^{-2}$

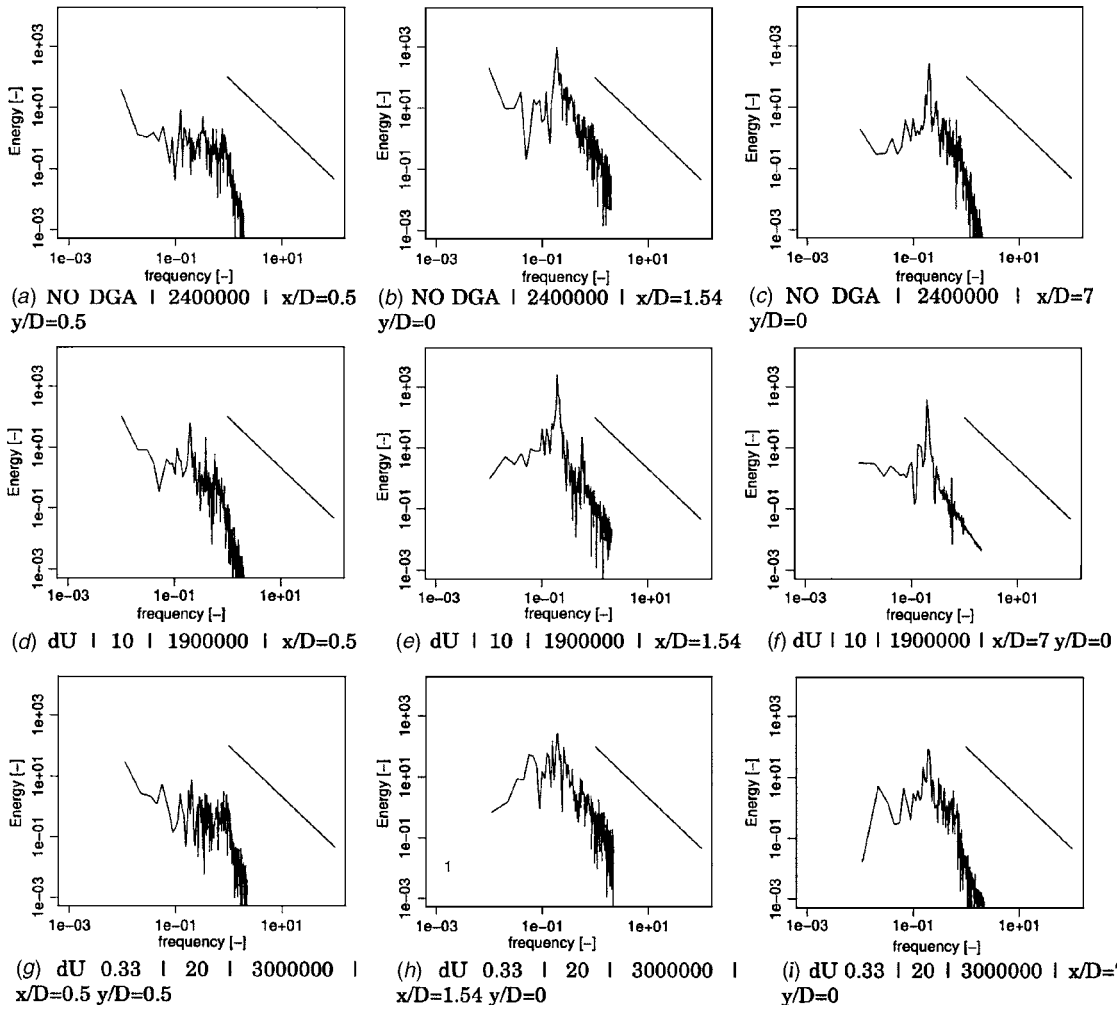

Fig. 13 One-dimensional power spectrum of the *y* velocity component compared with the Kolmogorov similarity hypothesis at (*a*) *x*/*D*=0.5, *y*/*D*=0.5, (*b*) *x*/*D*=1.54, *y*/*D*=0, and (*c*) *x*/*D*=7, *y*/*D*=0

η = Kolmogorov length scale
μ_{lam} = Dynamic viscosity
μ_t = Turbulent viscosity
ρ = Density
τ = Kolmogorov time scale

References

[1] Tutar, M., and Holdø, A. E., 2001, "Computational Modeling of Flow Around a Circular Cylinder in Sub-Critical Flow Regime With Various Turbulence Models," Int. J. Numer. Methods Fluids, **35**, pp. 763–784.

[2] Breuer, M., 2000, "A Challenging Test Case for Large Eddy Simulation: High Reynolds Number Circular Cylinder Flow," Int. J. Heat Fluid Flow, **21**(5), pp. 648–654.

[3] Travin, A., Shur, M., Strelets, M., and Spalart, P., 1999, "Detached-Eddy Simulations Past a Circular Cylinder," Flow, Turbul. Combust., **63**, pp. 293–313.

[4] de With, G., Holdø, A. E., and Huld, T. A., 2003, "The Use of Dynamic Grid Adaptation Algorithms for the Modeling of Flow Around a Circular Cylinder in Sub-Critical Flow Regime," Int. J. Numer. Methods Fluids, **41**, pp. 789–808.

[5] de With, G., Holdø, A. E., and Huld, T. A., 2003, "Solution Adaptive Grids Applied to Low Reynolds Number Flow," Int. J. Numer. Methods Fluids, **42**, pp. 1135–1154.

[6] de With, G., Holdø, A. E., and Huld, T. A., 2002, "Modeling of Flow Around a Circular Cylinder in the Sub-Critical Flow Regime With the Use of Dynamic Grid Adaptation," in Structures Proceedings of the A.S.M.E. PVP Conference on Emerging Technologies for Fluids and Fluid-Structure Interaction, edited by A. E. Holdø and M. Fischer, Vol. 446-2.

[7] Norberg, C., 2003, "Fluctuating Lift on a Circular Cylinder: Review and New Measurements," J. Fluids Struct., **17**(1), pp. 57–96.

[8] Lourenco, L. M., and Shih, C., 1998, "Characteristics of the Plane Turbulent Near Wake of a Circular Cylinder, a Particle Image Velocimetry Study," *Private Communication*, 1993. Data taken from Breuer.

[9] Fluent Inc., Lebanon NH03766 USA. FLUENT 6.1 *User's Guide*.

[10] Rhie, C. M., and Chow, W. L., 1983, "Numerical Study of the Turbulent Flow Past an Airfoil With Trailing Edge Separation," AIAA J., **21**(11), pp. 1525–1532.

[11] Davidson, L., Cokljat, D., Fröhlich, J., Leschziner, M. A., Mellen, C., and Rodi, W., 2003, *LESFOIL: Large Eddy Simulation of Flow Around a High Lift Airfoil*, Volume 83 of *Notes on Numerical Fluid Mechanics and Multidisciplinary Design (NNFM)*, Springer Verlag.

[12] Smagorinsky, J., 1963, "General Circulation Experiments With the Primitive Equations, Part 1: The Basic Experiment," Mon. Weather Rev., **91**, p. 99.

[13] de With, G., 2001, "*Dynamic Grid Adaptation Applied to Large Eddy Simulation Turbulence Modelling*," PhD thesis, University of Hertfordshire.

[14] Zienkiewicz, O. C., and Wu, J., 1994, "Automatic Directional Refinement in Adaptive Analysis of Compressible Flows," Int. J. Numer. Methods Eng., **37**, pp. 2189–2210.

[15] Vallès, B., 2001, "Computational Study of Vortex Shedding Behind Bluff Bodies," PhD thesis, NTNU Trondheim ISBN 82-471-5335-1.

[16] Ong, L., and Wallace, J., 1996, "The Velocity Field of the Turbulent Very Near Wake of a Circular Cylinder," Exp. Fluids, **20**(6), pp. 387–411.

[17] Mittal, R., and Moin, P., 1997, "Suitability of Upwind-Biased Finite Difference Schemes for Large-Eddy Simulation of Turbulent Flows," AIAA J., **35**(8), pp. 1415–1417.

[18] De Sampaio, P. A. B., Lyra, P. R. M., Morgan, K., and Weatheril, N. P., 1993, "Petrov-Galerkin Solutions of the Incompressible Navier-Stokes Equations in Primitive Variables With Adaptive Remeshing," Comput. Methods Appl. Mech. Eng., **106**, pp. 143–178.

Journal of Fluids Engineering

Technical Brief

Numerical Investigations of Turbulent Inflow Condition Generation for LES

Ph. Druault
Laboratoire de Mécanique Physique—Université Pierre et Marie Curie, FRE CNRS 2867—78210 Saint Cyr l'Ecole, France

J. F. Largeau

F. Coiffet

J. Delville

J. P. Bonnet

Laboratoire d'Etudes Aérodynamiques—Université de Poitiers, UMR CNRS 6609—86962 Futuroscope Chasseneuil, France

S. Lardeau
Department of Aeronautics, Imperial College, Prince Consort, South Kensington, London SW7 2BY, United Kingdom

[DOI: 10.1115/1.2012499]

Introduction

Imposing realistic inlet conditions for Direct and Large-Eddy Simulation of spatially developing flow is extremely challenging, and requires careful considerations, especially for fully turbulent conditions [1–8], and references therein. Indeed, the development of turbulent flow is highly dependent on the properties of the upstream conditions. A new strategy for specifying realistic turbulent inflow condition has been recently developed [9]. This method consists in using an experimental, time-dependent, highly turbulent velocity field as the inflow condition for spatially developing LES. Such methodology is based on the implementation of an interface between an experimental measurement section and the computational inlet section. Experimental time history data are obtained at few selected reference locations with hot-wire probes. From these measurements, the instantaneous velocity field is reconstructed at each grid point of the inlet mesh and is then used as an inflow condition for the simulation. On top of generating realistic turbulent inflow condition for LES, the interest of this association is to propose a new structure education method for representing and analyzing the three-dimensional (3D) dynamical evolution of the large-scale structures of the flow [10]. In this work, the experiment/simulation association has been tested for a specific test case flow configuration: the incompressible plane mixing layer.

Due to the limited number of probes that can be used simultaneously, previous studies have been performed to determine optimal probes locations and optimal reconstruction procedures preserving the coherent character of the flow [9,11]. As far as the mean shear transverse direction is concerned, numerical studies have been performed to validate this inflow condition generation methodology in a two-dimensional (2D) case. Thus, Druault et al. [11] showed that Linear Stochastic Estimation (LSE) is well suited to reconstruct an instantaneous velocity field on any transverse mesh from the knowledge of the velocity at only three reference probes located at the mixing layer center and at $\pm\delta_{\omega_0}/2$, where δ_{ω_0} is the local vorticity thickness. Indeed, such a reconstruction procedure has the advantage in preserving the large-scale structure of the flow. Moreover, based on experimental analysis [10,12], it has been shown that Proper Orthogonal Decomposition (POD) can be used to reconstruct the velocity field along the spanwise mesh domain providing velocity field periodic boundary conditions and energetic large-scale structure restitution. A specific experiment was then conducted with a *brush* of 66 hot wires measuring the three velocity components at 33 locations in a self-similar streamwise section of the flow [10]. The *brush* is composed of 11 separated transverse rakes of 3 X-wire probes located at $y=0$ and $y=\pm\delta_{\omega_0}/2$. These rakes are equally spaced ($0.33\delta_{\omega_0}$) in the spanwise direction. Based on these available velocity measurements, LSE and POD are used to reconstruct the velocity field at the inlet of the computational domain [8–10]. Preliminary simulations [9] using these reconstructed experimental data as an inflow condition have shown the advantage of this approach compared to other methodologies. But further investigations are necessary in order to analyze the real experiment/simulation interface possibilities.

Our purpose in this work is to validate this whole methodology by using a purely numerical approach, based on 3D Direct Numerical Simulations (DNS). Indeed, due to the preliminary knowledge of the complete flow field, it is then possible to accurately analyze this methodology. Notice that this new inflow condition generation methodology was only tested and validated on a specific flow test case. Some new test flow investigation validations have to be performed due to the high dependence of inlet flow conditions revealed in each particular flow.

Methodology

We consider the 3D spatially developing plane mixing layer between two streams ($U_1 > U_2$). The flow parameters are made

Contributed by the Fluids Engineering Division for publication in the JOURNAL OF FLUIDS ENGINEERING. Manuscript received by the Fluids Engineering Division July 22, 2004. Final revision July 7, 2005. Associate Editor: Ismail B. Celik.

similar to experimental ones [8,10]. The computational domain size is $(L_x, L_y, L_z) = (293\delta_{\omega_i}, 100\delta_{\omega_i}, 36\delta_{\omega_i})$ and $(n_x, n_y, n_z) = (587, 401, 144)$, where δ_{ω_i} is the initial vorticity thickness at $x = 0$. The Reynolds number based on δ_{ω_i} and $\Delta U = U_1 - U_2$ is 200. The computer memory requirement is 7Go.

The numerical code solves the 3D Navier-Stokes equations on a regular grid and a nonstaggered arrangement. Sixth-order compact centered difference schemes are used to evaluate all spatial derivatives and equations are integrated in time using a third-order Runge-Kutta method. A free slip boundary condition is imposed in the transverse direction at $y = \pm L_y/2$ and a periodic boundary condition is used in the spanwise direction. The outflow boundary condition at $x = L_x$ is deduced by solving a simplified convection equation.

The first step consists in performing a reference DNS on the full computational domain. For this simulation, correlated velocity perturbations of small amplitude are superimposed at the inflow section on a tangent hyperbolic velocity profile. Once the initial conditions are entirely evacuated and the flow has reached a fully developed state, a virtual simulation/simulation interface is defined in a streamwise section located at $x_1 = 75\delta_{\omega_i}$. In this section, instantaneous velocity field is stored at 33 reference positions corresponding exactly to the 33 experimental ones detailed above. The second step consists in reconstructing the instantaneous velocity field at each grid point of the x_1 plane [8,9]. Finally, a second DNS is performed on a truncated computational domain (in its upstream part, $L_x' = L_x - x_1$) using the reconstructed velocity field at the inlet.

Analysis of the Temporal Reconstruction

Based on the knowledge of the velocity field at only 11 locations, POD is first used to reconstruct the field on the spanwise domain. This spanwise reconstruction is performed for the three transverse reference positions. An illustration of the reconstruction is given in Fig. 1 for the instantaneous streamwise velocity component u located at the mixing layer y center. On these plots, the crosses indicate the reference spanwise locations. The reconstructed velocity profile is very similar to the reference one, especially for the large-scale structures, which are globally well restored. Similar results are obtained for the other velocity components. Note that some discrepancies may appear near the spanwise boundaries. These observations are an indirect consequence of the POD procedure that induces a filtering of the high-spanwise wave numbers. This behavior can be observed on the log-log representation of the spanwise wave number spectra at the center of the mixing layer (Fig. 1). It has also been shown that reconstructed temporal spectra are in good agreement with the original ones (Fig. 1). The POD procedure not only gives a good representation of the velocity field, but also preserves the spectral content of the flow.

Second, LSE is used to reconstruct the instantaneous velocity field along the transverse direction. In Fig. 2, the streamwise Reynolds stress component deduced from the preliminary calculation is superimposed on the reconstructed one. These components are computed using both spanwise and time averaging. The coincident property of the LSE procedure is satisfied at the three reference locations, where the same Reynolds stress values are obtained. Similar profiles are obtained for the other stresses [8].

Dynamical Analysis

A DNS on a truncated streamwise domain is then performed using the reconstructed data as an inflow condition. Figure 3 presents a comparative analysis of the instantaneous vorticity field in the (Oxy) plane. In this figure, a transient phase is observed due to the *nonperfect* character of this inlet condition. After this phase, the simulation acts as a dynamic reconstruction of the deteriorated inflow condition, which leads to the formation of *realistic* structures farther downstream [8]. Indeed, in this figure, large-scale

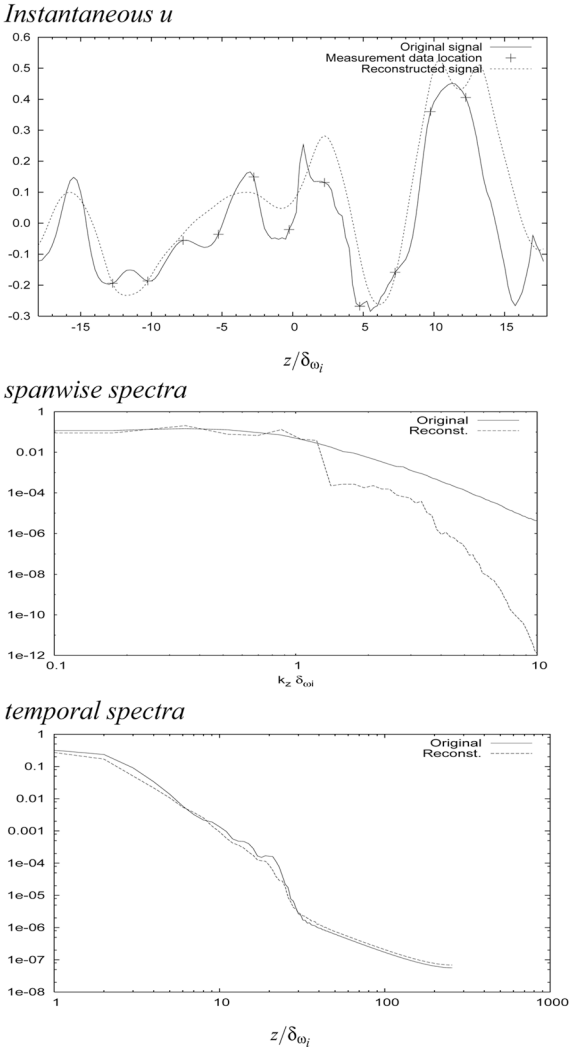

Fig. 1 Top to bottom: Reference streamwise velocity component superimposed on POD reconstructed one at the mixing layer center. Log-log representation of the spanwise wave number spectra at the center of the mixing layer. Temporal spectra at a position located between two consecutive reference spanwise points.

spanwise structures are well restored during the downstream development of the flow and compared quite well to those deduced from the original numerical simulation.

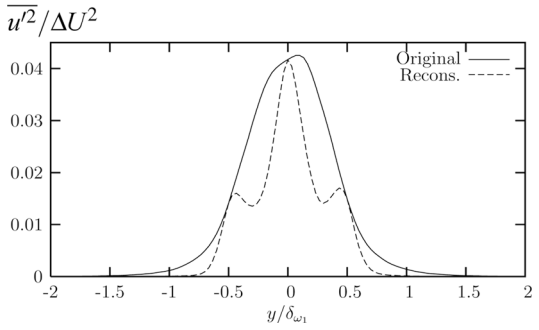

Fig. 2 Comparative analysis of the exact (original) streamwise Reynolds stress and the one calculated from the reconstructed velocity field (dotted line)

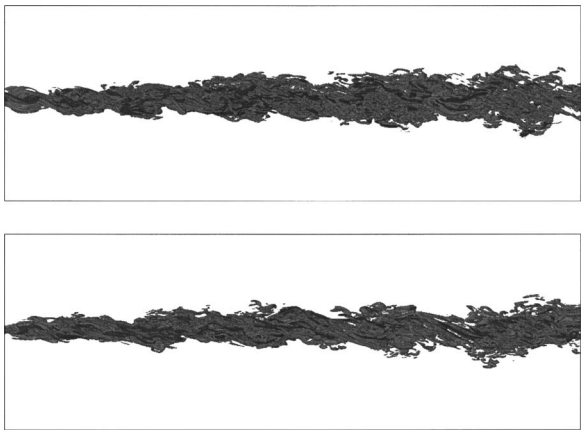

Fig. 3 Vorticity modulus isosurface in the (*Oxy*) plane: Reference DNS (top) truncated DNS (bottom)

A statistical analysis is now performed. The streamwise evolution of the vorticity thickness δ_ω for both simulations is given in Fig. 4. Globally, we observe that the vorticity thickness is well estimated, even near the inflow condition. The evolution of δ_ω arising from DNS using reconstructed inflow condition shows a slope close to the reference one. The slight differences are a consequence of a lack of statistical convergence. A comparative analysis of the downstream development of the mean flow field and the Reynolds stresses is also performed. The computations of these statistics are performed by using an average in the spanwise and temporal directions. The following error computations e_m, e_k, and e_{uv} (relative to mean flow fields, turbulent kinetic energy $0.5u_iu_i$, and Reynolds shear stress, respectively) are then investigated: $e_m(i)=\Sigma_{k=1}^{3}\Sigma_{j=1}^{n_y}(\overline{U_k^*(i,j)}-\overline{U_k(i,j)})/n_y\times\Delta U^2$

$$e_k(i)=\frac{\sum_{j=1}^{n_y}(k^*(i,j)-k(i,j))}{\sum_{j=1}^{ny}(k^*(i,j))};$$

$$e_{uv}(i)=\frac{\sum_{j=1}^{n_y}(uv^*(i,j)-uv(i,j))}{n_y\times\max(|uv^*(i)|)} \tag{1}$$

where $*$ indicates the target variable and the other corresponding variable is the one arising from the truncated simulation using reconstructed inflow data. Figure 5 represents the downstream development of these errors. We observe a very slight and quasiconstant mean error e_m because of the fact that only the fluctuating velocity field is reconstructed in the inlet section. On the other hand, near the inlet, the energy profiles and especially the Reynolds shear stress present noticeable differences. The important error observed for e_{uv} is a consequence of the normalization procedure used to preserve the normal Reynolds stresses along the spanwise direction [8], leading to an underestimation (of 50%) of the inlet Reynolds shear stress. A new normalization procedure that takes into account this stress component is under consideration. Nevertheless, farther downstream, it is observed that both errors decrease along the x direction. Hence, the energy profiles are quickly restored by the numerical simulation.

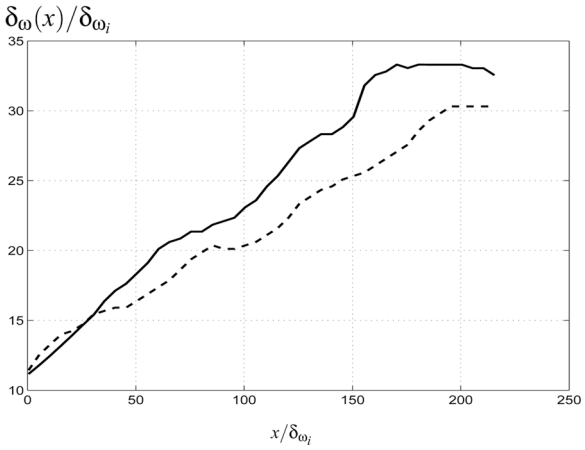

Fig. 4 Streamwise evolution of the vorticity thickness for the reference simulation (line) and for the simulation using the reconstructed data at an inflow condition (dotted line)

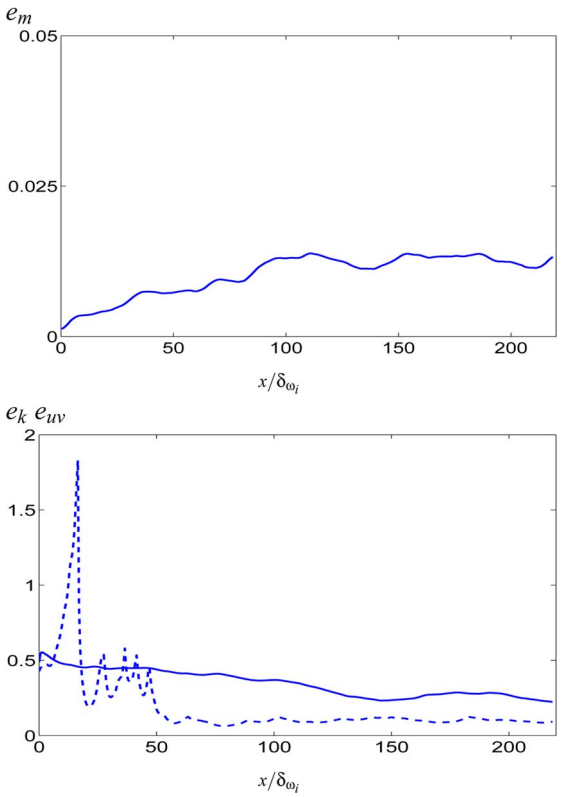

Fig. 5 Top: Downstream development of the mean flow field error; Bottom: Downstream development of the turbulent kinetic error (line) and the shear stress error (dotted line)

Conclusion

This purely numerical approach shows that this new inflow condition generation method provides satisfactory results for the statistics as well as for the instantaneous flow structure. More precisely, after a short transient region, which is a consequence of the deterioration of the inlet structure, the simulated flow field using the reconstructed inflow condition is very similar to the reference (complete) one. Indeed, due to the *real* space-time inflow information contained in the reference data (corresponding to the limited number of probes), the numerical resolution of the Navier Stokes equations allows a quick recovery of realistic energy profiles and, more important, a realistic 3D flow structure. A validation of this methodology of inlet turbulent flow field reconstruction is then achieved from the specific flow test case of a plane mixing layer. Nevertheless, note that the validity of this methodology may be highly dependent on the degrees of sensitivity to inlet conditions revealed in each particular flow configuration.

Acknowledgments

This study has been performed with the support of the French Agency for Defense (DGA). Computations were carried out at the Institut du Développement et des Ressources en Informatique Scientifique (IDRIS). We are also grateful to Professor Lamballais for helpful discussions.

References

[1] Lee, S., Lele, S. K., and Moin, P., 1992, "Simulation of Spatially Evolving Turbulence and the Applicability of Taylor's Hypothesis in Compressible Flow," Phys. Fluids A, **4**, pp. 1521–1530.

[2] Lund, T. S., Wu, X., and Squires, K. D., 1998, "Generation of Turbulent Inflow Data for Spatially-Developing Boundary Layer Simulations," J. Comput. Phys., **140**, pp. 233–258.

[3] Adrian, R. J., Meneveau, C., Moser, R. D., and Riley, J. J., 2000, "Final Report on Turbulence Measurements for Les," Technical Report UILU-ENG-2000-6012, TAM Report No. 937.

[4] Smirnov, A., Shi, S., and Celik, I., 2001, "Randow Flow Generation Technique for Large Eddy Simulations and Particle-Dynamics Modeling," J. Fluids Eng., **123**, pp. 359–371.

[5] Sagaut, P., 2002, *Large Eddy Simulation for Incompressible Flows—An Introduction*, Scientific Computation Series, Springer-Verlag, Berlin, 2nd ed.

[6] Keating, A., Piomelli, U., Balaras, E., and Kaltenbach, H. J., 2004, "*A Priori* and *A Posteriori* Tests of Inflow Conditions for Large Eddy Simulation," Phys. Fluids, **16**, pp. 4696–4712.

[7] "AIAA Journal: Special Issue on Boundary Conditions for Large Eddy Simulations," (2004), AIAA J., **42**, pp. 438–492.

[8] Druault, Ph., Largeau, J. F., Coiffet, F., Lardeau, S., and Bonnet, J. P., 2004, "Numerical Validation of a New Methodology for the Generation of Realistic Turbulent Inflow Conditions for LES," *Proc. of the ASME Heat Transfer/Fluids Eng. Summer Conf*.

[9] Druault, P., Lardeau, S., Bonnet, J.-P., Coiffet, F., Delville, J., Lamballais, E., Largeau, J.-F., and Perret, L., 2004, "Generation of Three-Dimensional Turbulent Inlet Conditions for Large-Eddy Simulation," AIAA J., **42**, pp. 447–456.

[10] Druault, P., Delville, J., and Bonnet, J.-P., 2005, "Experimental 3D Analysis of the Large Scale Behaviour of a Plane Turbulent Mixing Layer," Flow, Turbul. Combust., **74**(2), pp. 207–233.

[11] Druault, Ph., Lamballais, E., Delville, J., and Bonnet, J.-P., 1999, "Development of Experiment/Simulation Interfaces for Hybrid Turbulent Results Analysis *Via the Use of DNS/LES*," *Proc. 1st Int. Symp. TSFP*, Santa Barbara.

[12] Coiffet, F., Delville, J., and Lamballais, E., 2002, "DNS/LES of a Turbulent Mixing Layer Using Instantaneous Experimental Data as Inflow Conditions," *Proc. of the 9th European Turbulence Conference*, Southampton, UK.

Index of Resolution Quality for Large Eddy Simulations

I. B. Celik
e-mail: ismail.celik@mail.wvu.edu

Z. N. Cehreli

I. Yavuz

Mechanical and Aerospace Engineering,
West Virginia University, P.O. Box 6106,
Morgantown, WV, 25506-6106

In the light of rapidly increasing applications of large-eddy simulations (LES), it is deemed necessary to impose some quality assessment measures for such studies. The verification of LES calculations is difficult because of the fact that both the subgrid scale (SGS) model contribution and numerical discretization errors are functions of the grid resolution. In this study, various indexes of quality measures, hereafter referred to as LES_IQ, are proposed. The recommended LES_IQ is based on the Richardson extrapolation concept. This method has been applied to various cases and the calculated LES_IQ results are compared with the relative total experimental and direct numerical simulation (DNS) error, defined as IQ_EX and IQ_DNS, respectively. It is postulated that in practical applications of LES, numerical dissipation will always be a significant part of the overall dissipation, and it must be accounted for in any assessment of the quality of LES. It is further suggested that LES_IQ of 75% to 85% can be considered adequate for most engineering applications that typically occur at high Reynolds numbers; the proposed index is an indicator of good resolution (i.e., verification), but not necessarily a good or accurate model (i.e., validation). [DOI: 10.1115/1.1990201]

Keywords: Numerical Uncertainty, Large Eddy Simulation (LES), Quality Index, Computational Fluid Dynamics (CFD)

1 Introduction

It is anticipated that the use of LES (large-eddy simulation) in engineering applications will increase significantly in the coming years. It is already becoming a user option in commercial CFD (computational fluid dynamics) packages such as FLUENT. It is then imperative that there should be some quality control on the simulations claimed to be LES. Uncertainty/quality assessment in RANS (Reynolds-averaged Navier–Stokes) simulations has been investigated at length [1–4] and there are even some guidelines [5–7] for assessment and reporting of numerical uncertainty in such simulations. The assessment of uncertainty in LES is not so trivial, as both the numerical discretization error and the subgrid scale contributions are proportional to grid size. As it was rightly pointed out by Speziale [8], a good LES is that which tends to DNS (direct numerical simulations) as the grid resolution tends to the smallest scales, i.e., the Kolmogorov scales. Therefore, there is no such thing as grid-independent LES in theory, because a grid-independent LES is essentially DNS, and the philosophy of LES loses its meaning if it is grid independent; the advantage of LES over DNS being that LES is much more economical while it only requires the resolution of the most energetic eddies that determine the essential flow quantities and their consequences. If the main purpose of an LES is to capture only the mean flow dynamics, the above argument may not hold, but that would be a very limited and costly purpose for LES. It is well known that physical phenomena such as mixing and combustion are strongly dependent on intensity of turbulent fluctuations and the convection by these fluctuations that eventually exhibit themselves as turbulent diffusion. Hence, in most applications of LES the prediction of turbulence statistics is at least as important as the prediction of mean flow quantities. With such a premise, it is necessary that some quality assessment measures be formulated for LES geared towards engineering applications. This is the subject of the present study.

According to Vreman et al. [9,10], there are two approaches for testing the performance of SGS (subgrid scale) models: (i) a priori tests whereby model predictions are compared to the SGS stresses obtained from DNS (or experiments) by filtering; (ii) a posteriori testing whereby actual LES results are compared with results from DNS or experiments. Vreman et al. [9] dismiss the a priori testing procedure, arguing that they usually are too pessimistic, since low correlations between stresses and predictions do not necessarily lead to poor LES results. Pope [11] also mentions that models that perform poorly on a priori tests may perform well on a posteriori tests. The second approach has the well-known difficulty of discriminating between the numerical or discretization errors and the modeling errors [12] in order to determine the magnitude of turbulent energy dissipation rate introduced by the SGS model, i.e., $\varepsilon_{\mathrm{SGS}}$.

The total error (hence the uncertainty) in LES, $\varepsilon_{\mathrm{LES}}$, consists of two major components, namely numerical discretization error, $\varepsilon_{\mathrm{num}}$, and modeling (i.e., subgrid scale, model) error, $\varepsilon_{\mathrm{SGS}}$. Although these components are usually correlated, for brevity one can write

$$\varepsilon_{\mathrm{LES}} = \varepsilon_{\mathrm{num}} + \varepsilon_{\mathrm{SGS}}, \tag{1a}$$

$$\varepsilon_{\mathrm{LES}} = \tau_{ij}^{h}\bar{S}_{ij} + \tau_{ij}^{r}\bar{S}_{ij} \tag{1b}$$

where τ_{ij}^{h} is the numerical stress and τ_{ij}^{r} is the residual (or subgrid) stress. In a good LES study, for a given filter width Δ, the grid size h should be chosen such that $\tau_{ij}^{h} \ll \tau_{ij}^{r}$. It is important to note that in some cases $\varepsilon_{\mathrm{num}}$ and $\varepsilon_{\mathrm{SGS}}$ may have different signs, thus canceling each other, which would result in a small total error.

In Eq. (1*a*) $\varepsilon_{\mathrm{num}}$ must be minimized, which inevitably will require fine-grid LES. This is problematic not only because of the computational cost and time, but also it has the disadvantage that in most practical applications of LES as $\varepsilon_{\mathrm{num}}$ decreases so does $\varepsilon_{\mathrm{SGS}}$. Such calculations seem to constitute the bulk of LES studies [13,14]. Only in rare cases where $\varepsilon_{\mathrm{num}}$ goes to zero much more rapidly than $\varepsilon_{\mathrm{SGS}}$ would grid independent solutions be feasible. Consider for example the most widely used Smagorinsky model, where the subgrid eddy viscosity v_{SGS} is proportional to $\Delta^{4/3}$ (Ref. [11], p. 588), Δ being the filter length which is usually taken proportional to the grid size, h. If the numerical scheme is second order and the order of accuracy degenerates slightly for various reasons such as maintaining stability, then the above procedure

Contributed by the Fluids Engineering Division for publication in the JOURNAL OF FLUIDS ENGINEERING.

will not work. It should be pointed out that LES using second-order schemes has many advantages [15], and they are becoming more and more popular. Even with higher order schemes, Ref. [9] observed that ε_{num} and ε_{SGS} are of comparable order and may partially cancel each other. Thus, grid refinement may not necessarily lead to smaller ε_{LES}.

A further concern is that the two approaches mentioned above that use DNS or experiments as a benchmark will be limited in most cases to simple flow problems, since DNS will either be too costly, and/or impossible for many problems of engineering interest. Moreover, for every application of LES, if DNS or experiments are required for validation and uncertainty assessment, then the predictive purpose of these studies will be diminished and they will not be viewed as tools for engineering analysis.

Therefore, a quality assessment procedure is necessary that can be applied independent of experimental or DNS data, such that it does not require LES simulations at grid resolutions that are prohibitively costly.

The present study is undertaken to formulate such an assessment procedure, which we call "LES Index of Resolution Quality, in short, LES_IQ." The procedure is based on the concept of Richardson extrapolation [16,17,3].

The methods proposed in this paper are aimed at LES studies where the filter length, Δ, is implicitly related to the grid cell size h, and those with at least second-order accuracy in time and space, but we have made an attempt to generalize them to include other cases.

The errors in LES are primarily dependent on the filter length, Δ, and the grid size, h. Geurts and Froehlich [18] have developed error estimates for LES the philosophy of which are substantially different than the current paper. Geurts and Froehlich [19] present their results in terms of a grid activity parameter [Eq. (2)] and subgrid activity, s, and SGS resolution parameter, $r=h/\Delta$. The implications of using these parameters are elucidated in the next section. The rest of the paper deals with testing and assessment of the newly proposed LES_IQ, with examples to demonstrate the feasibility of such an approach.

It must be mentioned that it is not the objective of this paper to assess the performance or accuracy of SGS models; this falls in the realm of validation. Our aim is more of a verification rather than validation (see Ref. [3], for appropriate definitions of verification and validation).

2 Subgrid Activity Parameter

Geurts and Froehlich [19] suggested a subgrid activity parameter, s, to be used as an independent parameter in assessment of errors in LES. It is stated that by definition $s=1$ corresponds to LES, whereas $s=0$ corresponds DNS at infinite Reynolds number, Re. This parameter is defined as

$$s = \frac{\langle \varepsilon_t \rangle}{\langle \varepsilon_t \rangle + \langle \varepsilon_\mu \rangle} \tag{2}$$

Here, $\langle\ \rangle$ denotes an averaged (or filtered) quantity, ε_t is the turbulent dissipation, and ε_μ is the molecular dissipation; ε_t can be expressed in terms of the turbulent viscosity. For example, for Smagorinsky-type models we have

$$\langle \varepsilon_t \rangle = (C_s\Delta)^2(\bar{S}^3) \cong (C_s\Delta)^2(\bar{S}^2)^{3/2} \tag{3a}$$

$$\langle v_t \rangle = (C_s\Delta)^2(\bar{S}) \tag{3b}$$

$$\langle \varepsilon_t \rangle = \frac{\langle v_t \rangle^3}{(C_s\Delta)^4} \tag{3c}$$

where $\bar{S}=(2\bar{S}_{ij}S_{ij})^{1/2}$. The approximation $\langle \bar{S}^3 \rangle \cong \langle \bar{S}^2 \rangle^{3/2}$ is adopted from Pope (Ref. [11], p. 588) and it is due originally to Lilly [20].

The molecular dissipation can also be related to turbulent eddy viscosity as follows:

$$\varepsilon_\mu = v\bar{S}_{ij}\frac{\partial \bar{u}_i}{\partial x_j} \tag{4a}$$

$$\varepsilon_t = -\tau_{ij}\frac{\partial \bar{u}_i}{\partial x_j} \tag{4b}$$

$$\tau_{ij} = -(C_s\Delta)^2\langle \bar{S} \rangle \bar{S}_{ij} \tag{4c}$$

$$\langle v_t \rangle = (C_s\Delta)^2\langle \bar{S} \rangle \tag{4d}$$

It follows then

$$\langle \epsilon_\mu \rangle = \frac{\langle \varepsilon_t \rangle v}{\langle v_t \rangle} \tag{4e}$$

Here, we have used the approximation $\langle \bar{S} \rangle \cong \langle \bar{S}^2 \rangle^{1/2}$ along the same lines of thinking as Lilly [20]. In Eqs. (3) and (4) C_s is the Smagorinsky constant; v_t is the SGS viscosity (analogous to the turbulent eddy viscosity); v is the molecular viscosity, and $\bar{S}_{ij}$ is the mean rate of strain tensor.

Substituting Eq. (4) into Eq. (2) yields

$$s \cong \frac{\langle v_t \rangle}{\langle v_t \rangle + v} = \frac{1}{(1 + v/\langle v_t \rangle)} \tag{5}$$

Since in most LES applications it is anticipated that $v_t \gg v$, Eq. (5) indicates that $s \cong 1.0$, and it is not sensitive to grid resolution. Thus, it will be difficult to use it as an assessment parameter.

Geurts and Froehlich [19] have suggested that the subgrid resolution parameter, $r=h/\Delta$, and s be regarded as independent indicators to classify and compare LES solutions. However, as we mentioned earlier, in most cases the filter width, $\Delta \approx h$, which makes $r \cong 1$. As observed by Geurts and Froehlich [19], with increasing r value, the numerical error increases. The evaluation of the activity parameter "s" is difficult; it requires calculation of the volume-averaged turbulent dissipation rate, which inherently includes both the modeled dissipation and the numerical dissipation; segregation of the two is necessary but not easy. On the other hand the modified activity parameter s^* given by Eq. (6) below can be used with relative ease, but its derivation involves many assumptions and is based on the Smagorinsky model.

The s values were calculated from Eq. (5), for the LES of the wake behind an Arleigh–Burke class destroyer (DDG51; see Sec. 4) cruising on a circular track on a relatively coarse grid resolution of 300 K and 1000 K nodes. The results (Fig. 1) indeed show $s \cong 1.0$. This is because in this case, as expected to be in many other cases, $\langle v_t \rangle \gg v$. To bring $\langle v_t \rangle$ down to the level of v would require huge computational resources. This again demonstrates that in a wide class of LES applications "s" is not sufficiently sensitive to grid resolution (in that it is fixed approximately at $s \cong 1.0$). Hence, some other measure needs to be found to assess the quality of LES results. For example, recognizing the importance of numerical dissipation in most LES applications, one could define a modified activity parameter as

$$s^* = \frac{\langle v_t \rangle + \langle v_{\text{num}} \rangle}{\langle v_t \rangle + \langle v_{\text{num}} \rangle + v} \tag{6}$$

where v_{num} is the numerical viscosity, and s^* is always less than 1.

3 Proposed LES_IQ

Following a similar line of thinking that is inherent in Eq. (6), one can formulate an LES index of quality based on grid resolution relative to the Kolmogorov length scale, η_κ, e.g.,

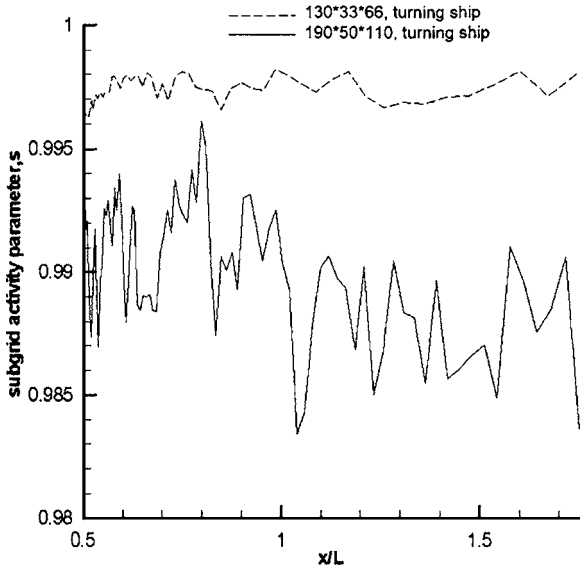

Fig. 1 The variation of subgrid activity parameter along the streamwise direction for LES of the wake of a turning ship (Cehreli, 2004 [31]).

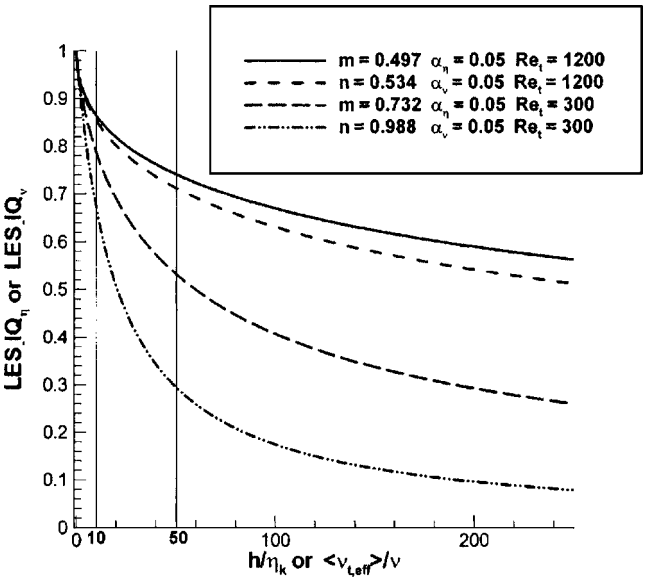

Fig. 2 Index of quality versus h/η_k or $\langle v_{t,\mathrm{eff}}\rangle/v$

$$\mathrm{LES\_IQ}_\eta = \frac{1}{1+\alpha_\eta\left(\frac{h}{\eta_\kappa}\right)^m} \tag{7}$$

where $\eta_k=(v^3/\varepsilon)^{1/4}$; if the dissipation rate ε is not known from DNS or experiments η_k should be calculated using its apparent value $\varepsilon^{\mathrm{eff}}=\varepsilon^{\mathrm{res}}+\varepsilon^{\mathrm{num}}$, i.e., the numerical dissipation should not be ignored.

An alternative index can be based on the ratio $\langle v_t+v_{\mathrm{num}}\rangle/v=\langle v_{t,\mathrm{eff}}\rangle/v$, e.g.,

$$\mathrm{LES\_IQ}_v = \frac{1}{1+\alpha_v\left(\frac{\langle v_{t,\mathrm{eff}}\rangle}{v}\right)^n} \tag{8a}$$

or

$$\mathrm{LES\_IQ}_v = \frac{1}{1+\alpha_v\left(\frac{s^*}{(1-s^*)}\right)^n} \tag{8b}$$

The parameters α_η, α_v, m, and n in Eqs. (7) and (8) can be determined using the rationale explained in Appendix A, that $h\cong\eta_k$ for DNS, $h\cong 25\eta_k$ for LES; the corresponding values are $\langle v_{t,\mathrm{eff}}\rangle/v\cong 1$ for DNS and $\langle v_{t,\mathrm{eff}}\rangle/v\cong 20$ (see Appendix A) for LES. In DNS simulations, the residual viscosity v_t is typically about twice the molecular viscosity (Ref. [11], p. 603). If we consider that an index of quality greater than 80% is a good LES, and that 95% and above is considered as DNS, this yields $m\cong 0.5$, $\alpha_\eta=0.05$, $n\cong 0.53$, $\alpha_v=0.05$. Concerning resolution of DNS and LES, Pope [11] suggests that 80% of the energy be resolved everywhere for LES with near-wall resolution. Moreover, in three-dimensional flow using the Kolmogorov spectrum for high Reynolds number homogeneous isotropic turbulence, it can be shown (Ref. [11], p. 577) that 80% of the energy is resolved when $\Delta\cong\lambda$, where λ is the integral length scale. To give an idea of the relative magnitude of subgrid viscosity v_t versus v_{num}, we refer to Froehlich and Rodi [14]. They reported that when the QUICK scheme was used, $v_t/v\cong 1.0$ and $v_{\mathrm{num}}/v\cong 180$ were typical values near the centerline of a channel flow simulated by employing a Smagorinsky model. The functions (7) and (8) are plotted in Fig. 2 for two values of the turbulence Reynolds number Re_t, one at the high end, $\mathrm{Re}_t=1200$ and one at the low end, $\mathrm{Re}_t=300$. These criteria demand that for sufficient LES resolution h/η_κ and $\langle v_{t,\mathrm{eff}}\rangle/v$ both be less than approximately 25. As shown in Appendix A, the model constants should actually be made functions of the turbulence Reynolds number and Δ/h, but as a first indicator, we believe that these values would be sufficient. We recommend these relations as an approximate quality measure everywhere for wall-resolved LES and away from the wall when LES is used with wall functions.

Equation (A3) (Appendix A) also indicates that for a good LES the grid size should be around $h\cong\lambda/8$, which fortifies the judgment that there should be at least 8 cells to resolve an eddy of size λ. It follows that, for example, in a channel flow the centerline flow is easy to resolve; however, near the wall $\lambda\to 0\Rightarrow h\to 0$, which makes it difficult to resolve wall-bounded flows appropriately. Note also that $\lambda=f(\mathrm{Re}_t)$; usually as Re_t decreases both the integral length scale λ and turbulent time scale τ increase, which in turn causes a moderate decrease in the velocity scale, $u=\lambda/\tau$ and an increase in the Kolmogorov length scale, η_k. It then follows that, at low Re_t, there is less restriction on the grid size h to obtain a good LES; i.e., with the same grid size, h, one can obtain a higher LES_IQ, as Re_t decreases. Similar arguments should apply to Eq. (8*a*) as well, noting that $\eta_k\sim v$ and $\lambda\sim v_t$.

In both Eqs. (7) and (8) the molecular viscosity is used [note that $\eta_k=(v^3/\varepsilon_{\mathrm{eff}})^{1/4}$] with the anticipation that LES are meaningful only when it is applied to viscous laminar or turbulent flows where the viscosity plays an important role in the generation of shear and turbulence. Cases where $v\equiv 0$ would be meaningless for LES; hence, these equations should not be applied.

In both of the above expressions the inherent difficulty is the calculation of $\eta_k=(v^3/\varepsilon_{\mathrm{eff}})^{1/4}$ and $v_{t,\mathrm{eff}}$ both including the effect of numerical dissipation. It seems more practical to make use of the resolved turbulent kinetic energy k^{res} versus the total $k^{\mathrm{tot}}=k^{\mathrm{res}}+k^{\mathrm{SGS}}+k^{\mathrm{num}}$, the latter two terms being the contribution from the SGS model and the numerical dissipation, respectively. If one can make the assumption that $k^{\mathrm{eff\_SGS}}=(k^{\mathrm{tot}}-k^{\mathrm{res}})$ scales with the mesh size h, then an index of quality similar to Eqs. (7) and (8) can be defined as [see also Eq. (18)]

$$\mathrm{LES\_IQ}_k = \frac{k^{\mathrm{res}}}{k^{\mathrm{tot}}} = \frac{k^{\mathrm{res}}}{k^{\mathrm{res}}+a_k h^p} \tag{9}$$

Here, k^{res} is the resolved kinetic energy, k^{tot} is the total kinetic energy, h is the grid size, a_k is a coefficient to be determined, and

p is the order of accuracy of the numerical scheme.

In the spirit of Richardson's extrapolation, the error in any continuous dependent variable ϕ can be expressed as a polynomial in h, i.e., $\phi_o - \phi_h = a_1 h + a_2 h^2 + \cdots$, here ϕ_h is the numerical solution on grid size h, and ϕ_o is the extrapolated solution as $h \to 0$ (see Roache, 1998 [3], for more details). The effective SGS kinetic energy can be approximated as

$$k^{\text{tot}} - k_1^{\text{res}} = k_1^{\text{eff\_SGS}} = a_k h_1^p \tag{10}$$

$$k^{\text{tot}} - k_2^{\text{res}} = k_2^{\text{eff\_SGS}} = a_k h_2^p \tag{11}$$

where subscripts (1) and (2) denote quantities obtained on mesh (1) and mesh (2), respectively. In the present application, $h = (\Delta x \Delta y \Delta z)^{1/3}$, where $\Delta x, \Delta y, \Delta z$ are the grid cell lengths in the x-, y-, z-directions, respectively. This relation can be used for calculating a local mesh size if the details of the grid are known. However, in cases where the local grid information is not available, a global grid index parameter can be defined as

$$h_{\text{eq}} = \left[\frac{1}{N} \sum \Delta \forall_i \right]^{1/3} \tag{12}$$

where $\Delta \forall_i$ is the volume of a computational cell, N is the total number of cells, and the summation is over all the cells. Equation (12) has been used in the literature (see Refs. [3,2,1]) successfully to characterize both structured and unstructured grids, but it is more suitable for structured and geometrically similar grids. In writing Eqs. (10) and (11), it is assumed that the leading term in the truncation error series is dominant; in other words, the grid resolution is in the asymptotic range (see Ref. [3]). We should also mention that Richardson extrapolation works well for monotonic grid convergence; if the convergence is oscillatory it should be used with caution (see Ref. [21]).

Equations (10) and (11) can be solved for a_k to yield

$$a_k = \frac{1}{h_2^p} \left[\frac{k_2^{\text{res}} - k_1^{\text{res}}}{\alpha^p - 1} \right] \tag{13}$$

where $\alpha = h_1/h_2 > 1$ is the grid refinement parameter.

Hence, the expression for LES_IQ$_k$ becomes

$$\text{LES\_IQ}_k = \frac{k^{\text{res}}}{k^{\text{res}} + \dfrac{(k_2^{\text{res}} - k_1^{\text{res}})}{\alpha^p - 1} \left(\dfrac{h}{h_2} \right)^p} \tag{14}$$

Rearranging Eq. (14) for both grid sizes yields

Fine-grid index:

$$\text{LES\_IQ}_k^f = \frac{1}{1 + \left(1 - \dfrac{k_1^{\text{res}}}{k_2^{\text{res}}} \right) (\alpha^p - 1)^{-1}} \tag{15}$$

Coarse-grid index:

$$\text{LES\_IQ}_k^c = \frac{1}{1 + \left(\dfrac{k_2^{\text{res}}}{k_1^{\text{res}}} - 1 \right) \alpha^p (\alpha^p - 1)^{-1}} \tag{16}$$

Furthermore, a relative index based on experimental or DNS results can be defined as

$$\text{IQ\_EX} = 1 - \frac{|k^{\text{exp}} - k^{\text{res}}|}{k^{\text{exp}}} \tag{17a}$$

$$\text{IQ\_DNS} = 1 - \frac{|k^{\text{DNS}} - k^{\text{res}}|}{k^{\text{DNS}}} \tag{17b}$$

The absolute value in Eq. (17) is necessary for cases where $\Delta k_{\text{exp}} = (k^{\text{exp}} - k^{\text{res}})$ or $\Delta k_{\text{DNS}} = (k^{\text{DNS}} - k^{\text{res}})$ is less than zero. Theoretically, both of these quantities should be larger than zero in the context of "incomplete resolution" in LES, meaning that velocity fluctuations that correspond to small scales are filtered out; hence, the turbulence field is not fully resolved. In other words, in LES it is expected that, in general, $\Delta k_{\text{LES}} > 0$ and monotonic convergence to "exact" solution is obtained, as far as the turbulent kinetic energy is considered. Unfortunately, this is not always the case (see for example Sreedhar and Stern's results [22]), where the coarse-grid simulations are in some regions closer to the DNS and experiments than the fine-grid simulations. In some cases, convergence seems to be oscillatory and DNS and experiments do not agree well. There are also such cases, for example channel flows, where it so happens that the coarse-grid kinetic energy values are higher near the wall compared to the fine-grid values or higher than the DNS or experiments (see Refs. [23,14,24,25]). It is not clear why such trends arise in LES. A discussion on this issue is presented in Appendix B. Nevertheless, in those situations Eq. (9) should be modified as

$$\text{LES\_IQ}_k = 1 - \frac{|k^{\text{tot}} - k^{\text{res}}|}{k^{\text{tot}}} \tag{18}$$

and $k^{\text{tot}} - k^{\text{res}} = k^{\text{eff\_SGS}} = a_k h^p$ be approximated in the same way as before.

In the above formulation it is assumed that the mesh size h and the filter width Δ are approximately equal to each other. Hence, the contributions from subgrid scale modeling and the discretization errors can be lumped together as in Eqs. (10) and (11). However, when the filter length is different than the grid size (see for example Ref. [18]), then the resolution index should be modified to account for these two major components separately

$$k^{\text{tot}} - k^{\text{res}} = k^{\text{eff\_SGS}} = a h^p + b \Delta^q \tag{19}$$

where p denotes the order of accuracy of the numerical scheme and q denotes the order of the modeling error, and a and b are the constants. Hence, the expression for LES_IQ$_k$ may be rewritten as

$$\text{LES\_IQ}_k = \frac{k^{\text{res}}}{k^{\text{res}} + a h^p + b \Delta^q} \tag{20}$$

If the order, p, of the discretization error is known and it is assumed that usually the SGS modeling introduces a second-order dissipation term (i.e., $q=2$), Eq. (20) can be evaluated with three sets of grids. If $q=p$ Eq. (20) reduces to Eq. (9) with a modified constant $a_k^* = (a r^p + b)$ (note: $r = h/\Delta$); then, two sets of calculations on sufficiently refined grids would suffice. It should be noted that the first term on the right-hand side of Eq. (19) represents the numerical/discretization error, and the last term represents essentially the modeling error. However, due to the convolution of these errors during an actual simulation, it is usually not possible to segregate the two from each other unless one is made dominant over the other by design.

4 Application and Results

The proposed quality index concept has been applied to six different cases, namely the LES of flow around a square cylinder [26], case 1; the turbulent mixing layer [27], case 2; channel flow [28], case 3; surface piercing flat-plate boundary layer [22], case 4; ship wake flow [29–31], case 5; and vertical buoyant jet flow [32]; case 6. The formal order of the schemes used in all six of these cases was second order both in space and time discretization. We also utilized the mixing layer simulations by Geurts and Froehlich [18] to study the effect of filter size versus grid size. In what follows we only briefly describe these cases taken from already published literature. The reader is referred to the original reference for more details.

For the first case, two calculations were used with $185 \times 105 \times 25$ (case 1.1) and $265 \times 161 \times 25$ (case 1.2) computational cells, where the grid distribution was uniform with a constant cell size, h. The resolved turbulent kinetic energy values [26] are presented in Fig. 3(a) for two different sets of grids. We applied Eqs. (15)

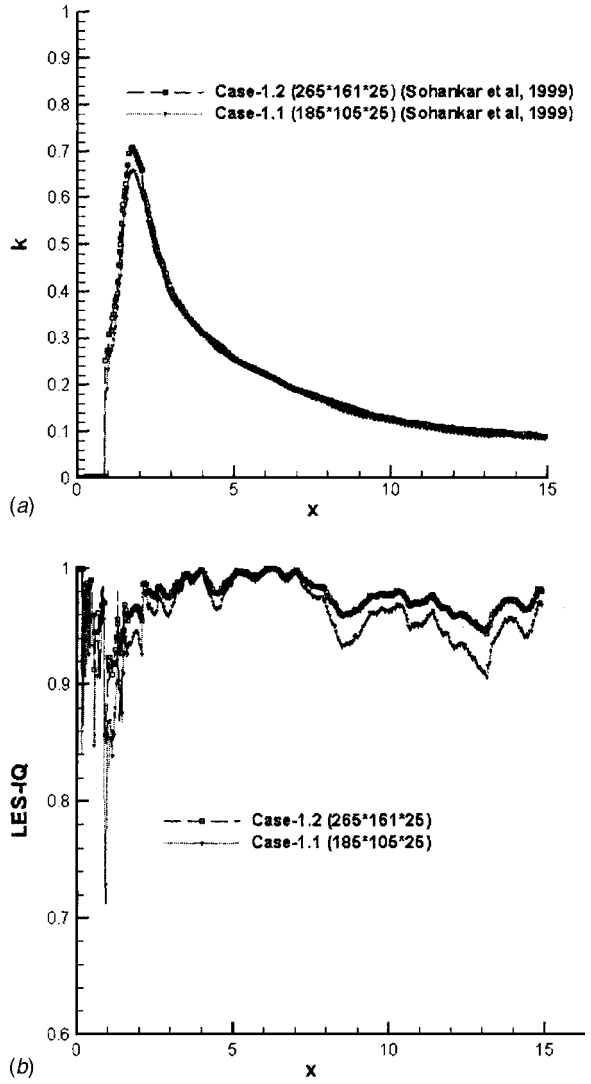

Fig. 3 (*a*) The resolved kinetic energy. (*b*) Large-eddy simulation index of quality (LES_IQ) [Eqs. (15) and (16)] for flow around a square cylinder (Sohankar et al., 1999 [26]). (The numbers in parentheses in the legend indicate grid nodes in the *x*-, *y*-, *z* directions, respectively).

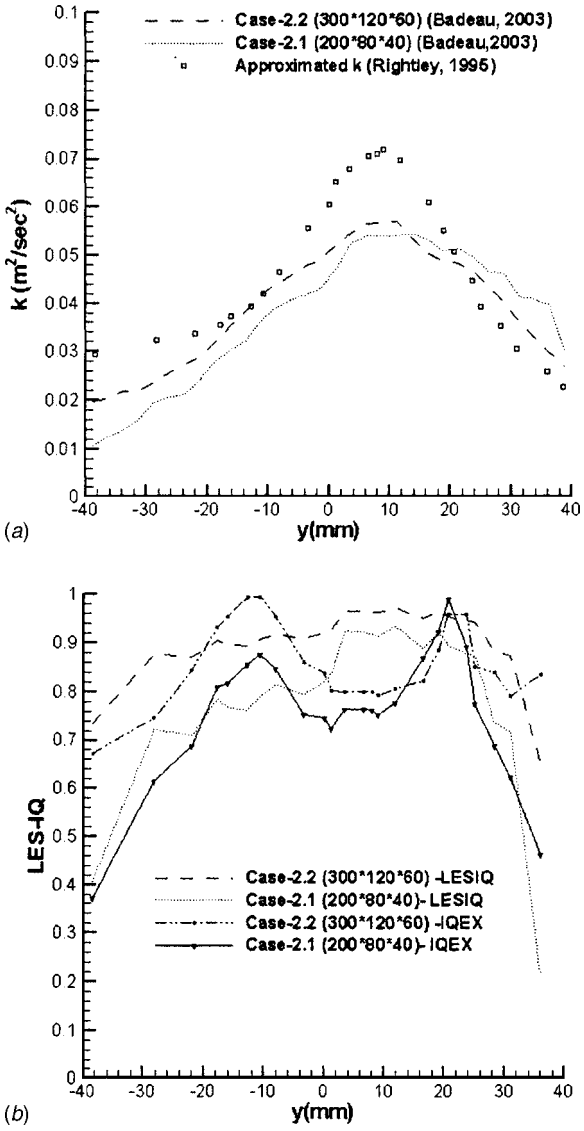

Fig. 4 (*a*) The resolved turbulence kinetic energy. (*b*) LES_IQ [Eq. (18)] and IQ_EX [Eq. (17)] for the mixing layer simulation (Badeau, 2003 [27]). (The numbers in parentheses in the legend indicate grid nodes in the *x*-, *y*-, *z* directions, respectively).

and (16); the calculated quality index for case 1.1 and case 1.2 is shown in Fig. 3(*b*). It is seen that for both grid resolutions, LES_IQ is approximately 95%. Sohankar et al. [26] have stated that their results with these two grid resolutions were in good agreement with experiments, reflecting the high LES_IQ we found.

The kinetic energy values for mixing layer flow simulations [27] with grids of $200\times80\times40$ (case 2.1) and $300\times120\times60$ (case 2.2) along with approximated experimental results [33] are shown in Fig. 4(*a*). Here, k^{exp} was calculated by assuming $v_{\text{rms}}=w_{\text{rms}}$; Rightley [33] reported only u_{rms} and v_{rms} values. The dimensions of the calculation domain used by Badeau were $0.55\times0.2\times0.2$ m, and uniform grid was used in all three directions. Using Eqs. (15)–(17), LES_IQ and IQ_EX are obtained for this case shown in Fig. 4(*a*), where Δk^{res} attains both positive and negative values. When the original formulation [Eq. (9)] suggested by Celik et al. [34] was used, the LES_IQ values in some locations were higher than 1.0, which is unrealistic. This can be due to the measurement errors or a high level of backscatter in the LES simulations (see also the discussion in Appendix A). It should be pointed out that in this case both LES results and experiments include the periodic fluctuations due to the coherent Kelvin–Helmholtz waves. This complicates the analysis further. It seems that Eq. (18) is more appropriate for this case. The calculated LES_IQ from Eq. (18) is depicted in Fig. 4(*b*) along with the true index IQ_EX calculated from Eq. (17). The proposed LES_IQ for both coarse- and fine-grid resolution follows closely the IQ_EX values based on experimental values of *k*. The observed LES_IQ values indicate the quality of LES is good in the middle section of the shear layer but it deteriorates considerably near the outer boundaries; the quality is particularly low (50%) for the coarse-grid resolution near the boundaries of the calculation domain.

For the channel flow (case 3), two calculations were carried out with 34^3 (case 3.1) and 66^3 (case 3.2) grids with a nonuniform grid distribution in the vertical direction [28]. The Reynolds number, based on the half-channel height, is 33 000. These calculations were performed with an imposed pressure gradient corresponding to Re=33 000; only the fluctuating part of the pressure was calculated. This practice, combined with the periodicity of the flow in axial and spanwise directions, makes the LES of channel flow easier. Hence, acceptable results can be obtained away from

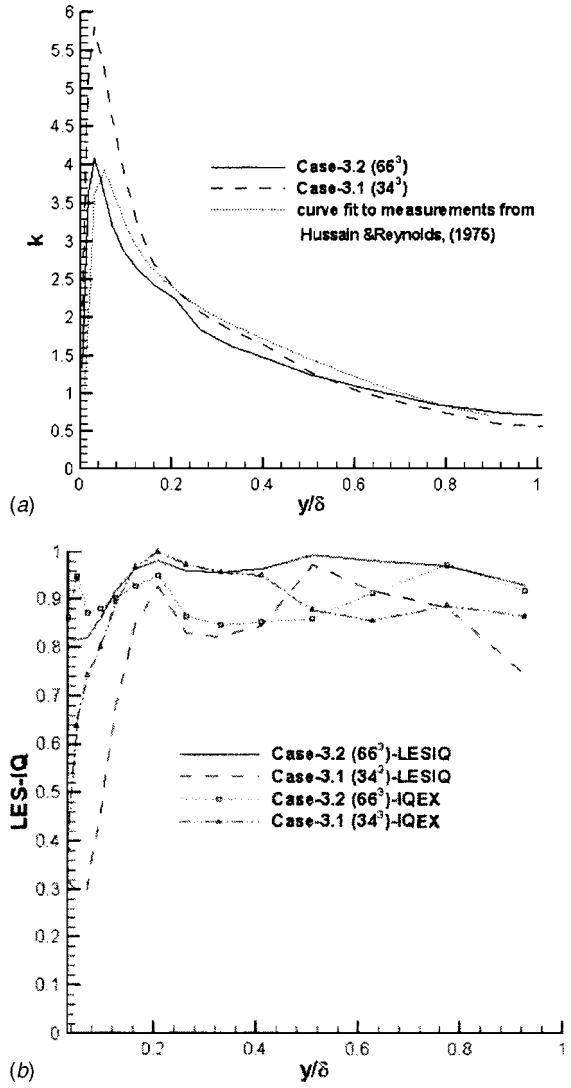

Fig. 5 (*a*) The resolved turbulence kinetic energy. (*b*) LES_IQ [Eq. (18)] and IQ_EX [Eq. (17*a*)] for the channel flow simulation (Shi, 2001 [28]): Curve fit to experiments was done by the present authors. (The numbers in parentheses in the legend indicate grid nodes in the *x*-, *y*-, *z* directions, respectively).

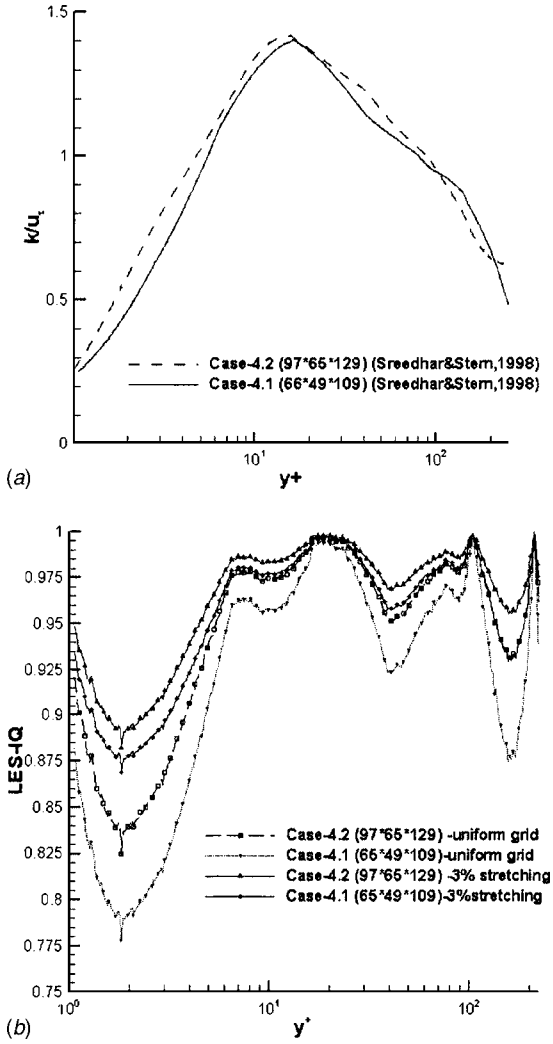

Fig. 6 (*a*) The resolved turbulence kinetic energy. (*b*) LES_IQ [Eqs. (15) and (16)] for surface piercing flat-plate boundary layer simulation (Sreedhar and Stern, 1998 [22]) for the uniform grid and 3% stretching in the transverse direction (The numbers in parentheses in the legend indicate grid nodes in the *x*-, *y*-, *z* directions, respectively).

the walls with relatively coarse grid resolutions. The computed turbulent kinetic energy and curve fit to the measurements of Hussain and Reynolds [35] are shown in Fig. 5(*a*). Equation (18) was used to compute LES_IQ; the results are shown in Fig. 5(*b*). Shown also in this figure is the quality index IQ-EX based on experimental results [Eq. (17*a*)]. Again, the suggested quality index is in good agreement with those obtained using the experiments. It is noteworthy to observe that the coarse-grid indices near the wall indicate less than 50%resolution, which is not surprising for wall boundary layers.

For case 4, two calculations with $65\times49\times109$ grids (case 4.1), and with $97\times65\times129$ grids (case 4.2) are studied and in all these simulations, the mesh size is taken to be uniform in all three directions; however, the actual grid was nonuniform in the transverse direction [22]. The dimensions of the calculation box are $(2\pi/\alpha)\delta$ in the streamwise direction, 40δ in the transverse wall normal direction, and 20δ in the spanwise direction, where δ is the reference length and α is the wave number of the linear stability wave explained briefly in Sreedhar and Stern [22]. The turbulent kinetic energy profiles are shown in Fig. 6(*a*). This case is used to illustrate the sensitivity of LES_IQ on variation of grid size, h, in space. Here, the details of the grid distribution are not known. We calculated the global grid index parameter from Eq. (12) and LES_IQ from Eqs. (15) and (16). It is seen from Fig. 6(*b*) that the calculated index of quality gives values in the range from approximately 80%–100%. This range is consistent with the conclusions drawn by Sreedhar and Stern [22]. When we used the 3% grid stretching in the transverse direction, the LES index increased by about 10% from 0.8 to 0.9. This shows that whenever possible, local grid refinement parameter should be used in calculation of LES_IQ.

The application of the quality index, LES_IQ, is also done for two more not as well resolved LES cases, case 5, namely the LES of the flow in the wake of a ship cruising on a straight track and that of a ship cruising on a circular track [29,30,21]. For brevity, we show here only the results from a ship cruising on a straight track. These studies examined the dynamics of turbulent flow in the wake of a surface ship using the LES technique with a three-dimensional incompressible Navier–Stokes solver, using nonorthogonal curvilinear coordinates. The LES technique has been applied throughout these studies in conjunction with a new random flow generation (RFG) technique originally developed at West

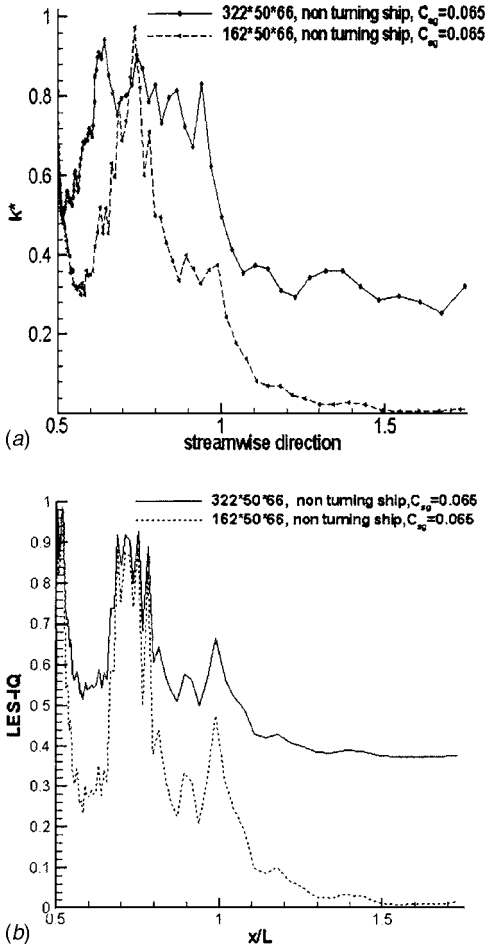

Fig. 7 (*a*) Resolved turbulence kinetic energy normalized with respect to its inlet value, $k_{\text{inlet}}=3.3E-0.3$ (ship cruising on a straight track). (*b*) LES_IQ [Eqs. (15) and (16)] along centerline of the wake. (The numbers in parentheses in the legend indicate grid nodes in the *x*-, *y*-, *z* directions, respectively).

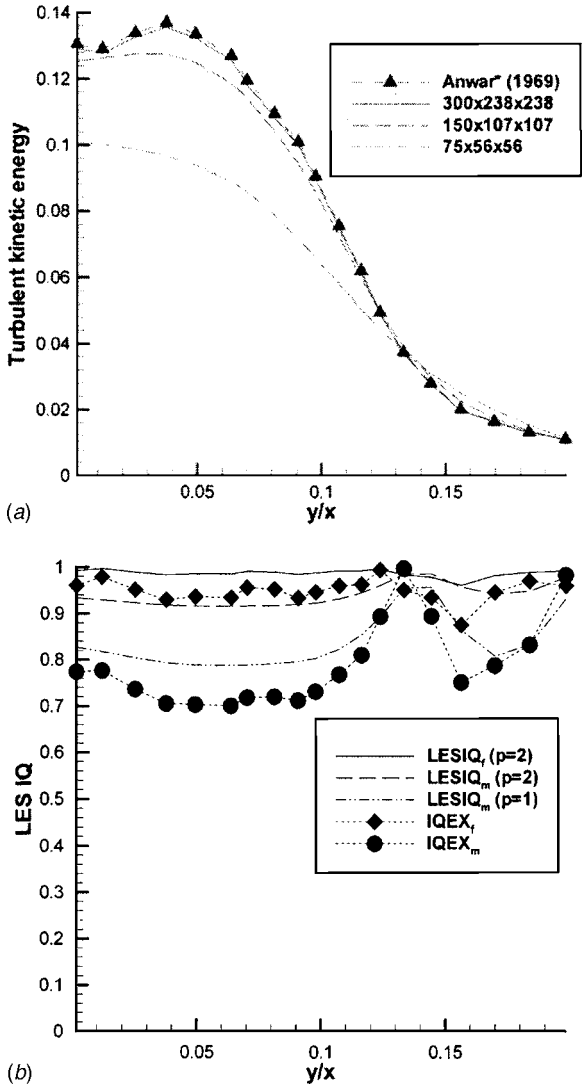

Fig. 8 Vertical buoyant jet. (*a*) Comparison of resolved TKE from DREAM® simulations (300×238×238; 150×107×107; and 75×56×56) to experiments (Anwar, 1969 [40]) at $x/D_{\text{in}}=20$ (normalized with respect to the square of the inlet velocity), (*b*). Corresponding LES_IQ and IQEX of the above data (* (w_{rms} for the experimental data was estimated by the authors as $w_{\text{rms}} \cong v_{\text{rms}}$).

Virginia University to provide unsteady inflow boundary conditions [36,37]. The formal order of the scheme is second order both in space and time discretization.

Shi [28] and Shi et al. [29] applied LES to the wake flow of the ship model DTMB 5512 [38,39]. A 3.048 m long unpropelled model of a modern U.S. Navy fleet ship, Arleigh-Burke class destroyer, DDG51, with a Reynolds number of 4.65×10^6 cruising on a straight track, has been investigated. The computational domain was $1.5\times0.3\times0.6$ (given in nondimensional units in ship length) in the *x*-, *y*-, *z*-directions, respectively, with a grid size of $162\times50\times66$ (~500 K) and $322\times50\times66$ (~1000 K). Nonuniform grid spacing with stretching less than 3% was used in both the *x*- and *y*-directions.

The resolved turbulent kinetic energy profile for the abovementioned ship wake simulation is shown in Fig. 7(*a*). We applied Eqs. (15) and (16) to the results of ship wake calculations. The calculated quality index with two different grid resolutions for the ship wake cruising on a straight track is shown in Fig. 7(*b*). For the fine grid, LES_IQ in the near-wake region is ca. 55% compared to a ca. 30% for the coarse grid. The quality deteriorates downstream where the grid resolution is coarser [see Fig. 7(*b*)]. The low LES_IQ values indicate that for this case more grid refinement is necessary.

The quality indices are also applied to a study conducted by Badeau and Celik [32], on Vertical buoyant jet plumes, case 6, that was investigated experimentally by Anwar [40]. Three different nonuniform grids were used, being $75\times57\times57$, $150\times107\times107$, and $300\times238\times238$. A uniform grid is used in the axial direction for all simulations, with a nonuniformity being imposed in the spanwise and transverse directions. The first grid size for the fine grid, away from $x=0$ and $z=0$, equaled 0.000 38 m; and the coarse grid equaled 0.000 68 m. The experiments by Anwar [40] ensured that the flow was turbulent after $x/D=5$, where x is the axial distance and D is the inlet diameter of the jet. The inlet mass flux of the primary water jet equaled 20.37 kg/s/m, which yields an inlet Reynolds number of 1892 for the primary stream. The inlet densimetric Froude number was 2.8.

Figure 8(*a*) shows the resolved turbulent kinetic energy, as compared to the experimental data. The simulation data have been time averaged over two flow-through times, as well as spatially averaged over eight nearest-neighbor cells on the centerlines. It is seen that the $75\times57\times57$ grid resolution clearly underpredicts the magnitude as compared to the experiments by as much as 50%. However, at the finer resolutions, agreement with experimental data is good. The LES_IQ and IQ_EX are presented in Fig. 8(*b*)

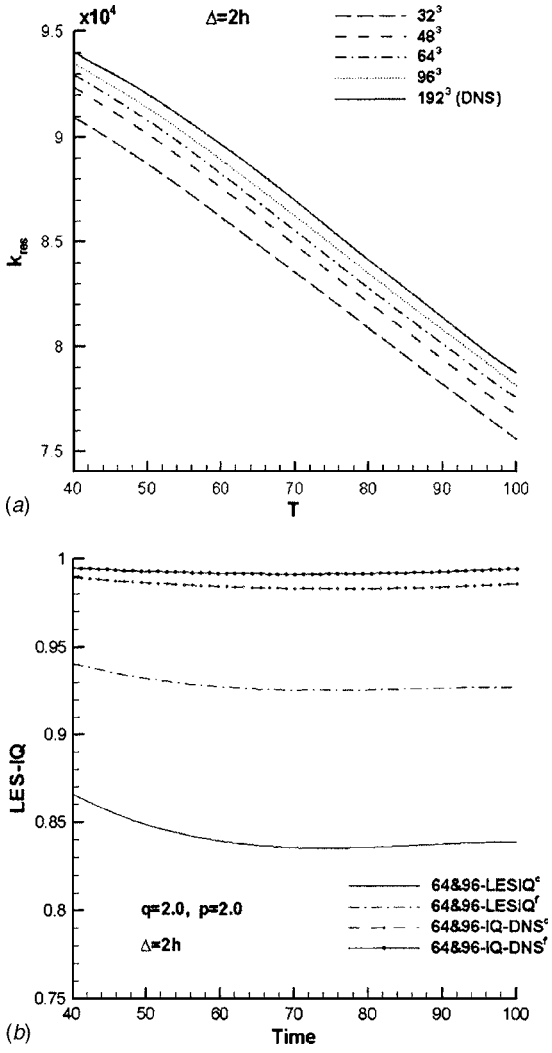

Fig. 9 (*a*) Resolved turbulence kinetic energy decay versus time for $\Delta/h=2$; (*b*) Calculated LES_IQ [Eq. (20)] and IQ_DNS [Eq. (17)]. A curve fit to the turbulent kinetic energy data from Geurts and Froehlich (2001) [18] was used in our analysis.

for this case. Although the index indicates a good LES when fine-grid distributions are used, it appears that the order of the monotonic scheme used by Badeau and Celik [32] reduces in the case of a coarse grid due to the use of the power-law scheme. When this is taken into account by letting $p=1.0$ the LES_IQ and IQ_EX agree quite well.

Influence of Filter Size versus Grid Size. Geurts and Froehlich [18] simulated turbulent flow in a mixing layer. DNS results with uniform grids that consisted of 192^3 nodes and LES results with grids that consisted of 32^3, 48^3, 64^3, 96^3 nodes were reported. The formal accuracy is second order in time, fourth order in space for convective terms, and second order for viscous and subgrid fluxes. The original study was completed for four cases with $\Delta/h=1,2,3,4$. However, grid convergence is not monotonic for the case $\Delta/h=1$. We calculated LES_IQ values for two cases with $\Delta/h=2,4$. The resolved kinetic energy profiles for these two cases are shown in Fig. 9(*a*) for a range of $\Delta/h=r$ values along with the DNS results.

The four sets of kinetic energy values from cases with $\Delta/h=2,4$ are used to calculate the values of p, q, a, and b described in Sec. 3. The order of the SGS contribution, q, is calculated to be approximately 2. This seems to be consistent with the general observation that the Smagorinsky model introduces a second-order contribution, dependent on the filter width. Although the spatial discretization scheme used by Geurts and Froehlich [18] for convective terms was fourth order, the current procedure yielded approximately second order, i.e., $p=2$, that is consistent with the order of the scheme they used for the viscous terms. The LES_IQ [Eq. (20)] and IQ_DNS [Eq. (17*b*)] have been calculated using the grids 64^3 (coarse) and 96^3 (fine) where $\Delta=2h$, and the results are shown in Fig. 9(*b*). The LES_IQ values fall in the range 85%–100%, and they follow the same trend as the IQ_DNS results; however, the coarse- and fine-grid indices are lower than the corresponding IQ_DNS results, which is desirable to assure some degree of conservatism in the calculated LES_IQ values. Calculations were also carried out for the case $\Delta=4h$. The results (not shown here) were similar to the case with $\Delta=2h$.

It may be thought that the suggested practice of $p=2$ and $q=2$ might lead to significant uncertainty if the actual p were to be much larger than the p used. To assess this, we did calculations with $p=4$. This resulted in ca. 10% improvement in the LES_IQ which can be absorbed into the conservatism of the proposed index.

5 Conclusions

Various indices to measure the quality of resolution measures for large-eddy simulations have been formulated and the underlying rationale is elucidated. The formulation given by Eq. (9) [or Eq. (18)] targets specifically those applications where the filter length and the mesh size are directly proportional to each other, and the numerical dissipation and subgrid scale contribution to dissipation of energy are both functions of mesh size. In such applications, Richardson extrapolation can be used to estimate the effective subgrid turbulent kinetic energy, including the contributions from both the modeling and discretization, hence leading to an estimate of the apparent total kinetic energy. The proposed index is a measure of the percentage of the resolved turbulent kinetic energy to the total. Equation (9) [or Eq. (18)] is recommended for those cases where $h\cong\Delta$ and the order of accuracy of the numerical scheme is approximately the same as that order implied of SGS modeling. On the other hand, for $\Delta>h$, LES_IQ formulation should be modified such that the effective subgrid turbulent kinetic energy is a function of both the filter width and the mesh size. Then, Eq. (20) should be used assuming that $p=\min(p,q)$. In situations where the values of p or q are not known, it is recommended that $p=q=2$ be used. This recommendation is based on the assumption that, on one hand, the numerical schemes used for LES must at least be second order both in time and space discretization, and on the other hand the quality or uncertainty measures should have some degree of conservatism. If more conservatism is desired the coarse-grid index rather than the fine-grid index can be used, or the fine-grid index can be used with $p=1.0$. We believe that the suggested quality index can be applied everywhere in the calculation domain, preferably using a local mesh size for LES with wall resolution; for LES with wall functions it should be applied away from the walls.

Applications of the proposed quality index to a range of case studies from the literature and comparison with DNS and experiments show that newly proposed LES_IQ is a good indicator of the resolution quality in LES. When possible, the proposed index of quality should be supplemented by providing additional information on relative mesh size [e.g., Eq. (7)], and relative magnitude of the subgrid viscosity [e.g., Eq. (8)] along with spectral information on resolved turbulent kinetic energy in frequency and wave number domains.

The reader must be warned against a misconception that "good grid resolution indicates a good model or a good accuracy!" The proposed LES_IQ is an indication of sufficient grid resolution so that the calculations can qualify as LES, and that the SGS model reveals its characteristics. In this regard LES_IQ should be con-

sidered as a verification index rather than a validation index; the latter necessarily requires comparison with DNS or physical experiments, and involves assessment of accuracy.

Acknowledgments

This work has been partially supported by the Office of Naval Research (ONR) as part of a DOD EPSCOR project. The technical program monitor is Dr. Patrick Purtel. We also acknowledge the partial funding kindly provided by the WVU Research Cooperation, National Research Center for Coal and Energy (NRCCE), and the College of Engineering and Mineral Resources (CEMR). We thank Lars Davidson of Chalmers University of Technology, Steve Jordan of Naval Undersea Warfare Center, and Ugo Piomelli of University of Maryland for their valuable discussions. We also thank B.J. Geurts and J. Froehlich for their kind help in providing references and data when needed.

Appendix A: Rationale for Eqs. (7) and (8) in the Main Text

It can be shown (Pope, 2000, [11]) that 80% of the turbulent kinetic energy can be resolved when $L/\Delta \cong 12$ for the sharp cutoff filter and $L/\Delta \cong 17$ for the Gaussian filter in case of high-Reynolds number homogeneous isotropic turbulence with the cutoff wave number $\kappa_c = \pi/\Delta$. Here, $L = k^{3/2}/\varepsilon$ is a length scale of turbulence and Δ is the filter width, k is the turbulent kinetic energy, and ε is the dissipation rate of turbulence. Noting that $\lambda \cong u^3/\varepsilon$ and $u \cong \sqrt{2/3k}$, we can relate the integral length scale λ to L by $\lambda = cL$, where $c \cong 0.55$. Taking an average value of $(12+17)/2 = 14.5$ yields

$$\lambda/\Delta \cong 8 \tag{A1}$$

The Kolmogorov length scale is given by

$$\eta_k = \lambda \, \mathrm{Re}_t^{-3/4} \tag{A2}$$

where $\mathrm{Re}_t = u\lambda/v$ is the turbulence Reynolds number.

Equations (A1) and (A2) can be used to rewrite (A1) as

$$\frac{h}{\eta_k} = \frac{\mathrm{Re}_t^{3/4}}{8(\Delta/h)} \tag{A3}$$

For a typically high $\mathrm{Re}_t \cong 1200$ and $\Delta \cong h$, Eq. (A3) yields $h/\eta_k \cong 25$ ($\mathrm{Re}_t \cong 300 \Rightarrow h/\eta_k \cong 9$). Moreover, in the context of the Smagorinsky SGS model, from the scaling of quantities in the inertial subrange the SGS residual viscosity is given by (Pope, 2000, [11])

$$v_t \cong C_s^2 \Delta^{4/3} \varepsilon^{1/3} \tag{A4}$$

A reasonable model for v_{num} is

$$v_{\mathrm{num}} \cong C_v h k_{\mathrm{num}}^{1/2} \tag{A5}$$

where C_v is a constant, and k_{num} is the residual kinetic energy caused by numerical dissipation.

Using the results mentioned above, i.e., $L/\Delta \cong 14.5$, when 80% of the turbulent kinetic energy is resolved, and $k^{\mathrm{res}} \cong 0.8k$, L can be related to k^{res} as

$$L = \frac{(k^{\mathrm{res}}/0.8)^{3/2}}{\varepsilon} = \frac{1.4(k^{\mathrm{res}})^{3/2}}{\varepsilon} \tag{A6}$$

One can then show that

$$v_t + v_{\mathrm{num}} = 1.12 C_s^2 \left(\frac{\Delta}{L}\right)^{4/3} L(k^{\mathrm{res}})^{1/2} + ch(k^{\mathrm{num}})^{1/2} \tag{A7}$$

Also, $C_s = 0.17$, $h \cong \Delta$, $c \cong 0.55$, $L/\Delta \cong 14.5$, and $k^{\mathrm{num}}/k^{\mathrm{res}} \cong 0.125$ (i.e., numerical dissipation contributes 50% of the unresolved energy budget; this is an intuitive approximation for a reasonably good quality LES); it follows that

$$\frac{v_t + v_{\mathrm{num}}}{v} = 0.014 \frac{(k^{\mathrm{res}})^{1/2} L}{v} \tag{A8}$$

Using the definition $\eta_k = (v^3/\varepsilon)^{1/4}$ and Eq. (A2) with $\lambda = 0.55L$, Eq. (A8) yields

$$\frac{v_t + v_{\mathrm{num}}}{v} = 0.017 \, \mathrm{Re}_t \tag{A9}$$

In deriving Eq. (A9), the assumed 50% contribution to the unresolved scales by numerical dissipation may be considered high, but most probably this is not an exaggeration when practical engineering applications of LES are considered. For a high turbulence Reynolds number of $\mathrm{Re}_t = 1200$ and low $\mathrm{Re}_t = 300$, Eq. (A9) gives v_{eff}/v to be approximately 20 and 5.

Appendix B: On The Consistence of LES With DNS

B.1 Celik's question. While reviewing literature on prediction of turbulent kinetic energy using large-eddy simulation, I have noticed that in some cases the calculated resolved turbulent kinetic energy is larger than DNS and/or experiments. This is particularly common in wall-bounded flows. Intuitively, I thought the resolved TKE and LES should always be smaller than (i.e., a fraction of) DNS results. Because there is usually higher energy dissipation in simulations of LES, I cannot explain the reverse trend. Could you provide your opinion on this?

B.2 Reply by L. Davidson. Often poor resolution in wall-bounded flows gives rise to too high resolved TKE. I think the reason is that the resolved strain $\bar{S}_{ij}$ gets too small and hence the resolved dissipation $\varepsilon_{\mathrm{SGS}} = 2v_{\mathrm{SGS}}\bar{S}_{ij}\bar{S}_{ij}$ gets too small. You're right when you say that one could expect the resolved dissipation to be larger in LES than in DNS (because $v_{\mathrm{SGS}} > v$), but then one forgets that the resolved dissipation is very dependent on the resolved strain rate tensor.

B.3 Reply by S. Jordan. This problem is a common occurrence when insufficient resolution is supplied in the spanwise direction. The peak turbulent intensities can be twice the correct values in the wake of bluff bodies if given poor spanwise resolution. This result can be easily seen in the coupled equation between pressure and velocity (dot product of momentum).

B.4 Discussion by I. Celik. Usually, the $\langle vv \rangle$ and $\langle ww \rangle$ are lower than DNS data, while $\langle uu \rangle$ is higher; the coarser the calculation the higher $\langle uu \rangle$ (see, e.g., Froehlich and Rodi, 2002 [14]). Froehlich and Rodi also observed that the discrepancy between LES and DNS diminished rapidly by improving the resolution in the streamwise and the spanwise directions. But, still the resolved turbulent kinetic energy in LES may attain higher values than that seen in DNS. If we assume that in the LES of channel flow the production $\langle uv \rangle \, dU/dy$ is predicted more or less correct, then the slope of the mean velocity profile should be more or less correct near the wall. The apparent dissipation rate $\varepsilon \cong u^3/\lambda$ should balance this production term. It appears that the apparent length scale in LES is usually too small near the wall, hence leading to large rms values in order to balance the correctly predicted production.

On the other hand, if the mean flow is not right, it is understandable that LES with a dissipative SGS model might give larger fluctuations. What might be the reason for not predicting the mean flow? The reason probably is that the grid resolution is not sufficient to capture the slope of the mean velocity profile correctly. This in effect will lead to inaccurate mean pressure gradient in the streamwise direction, which in turn, may lead to wrong strain rates that are used in SGS model. Then, the dissipation rate could be underpredicted, thus polluting the overall results. Also, when the grid is insufficient to resolve the near-wall energy carrying eddies, streaks, hairpins etc., an overshoot in turbulent kinetic energy may occur. As noted by Pope (2000 [11]),

for low Reynolds number flows there is considerable overlap between energy-containing eddies and dissipative ranges of scales. In LES of low Reynolds number flows the filter is likely to be placed in this overlapping region. This argument is also applicable to inherently low Reynolds number flows near a wall where the segregation of "large" and "small" scales is not possible.

Recent observations also indicate that bad SGS models cannot predict transition to turbulence at the proper Reynolds number and at the proper location. When this happens there is a phase shift in the profiles of turbulence quantities. For example, in LES of free-shear layers, if the location of transition in the axial direction is not predicted right, the peak rms values are not predicted at the right location; hence, at some points the LES results would show a higher turbulent kinetic energy than the corresponding DNS results. Similar phenomenon will occur in wall layers, where there is always transition from laminar (viscous sublayer) to turbulent flow. As long as the integral kinetic energy agrees well with DNS results, this is not necessarily a shortcoming of LES, other than the fact that the location of transition is not predicted accurately, which is in general a very difficult task.

References

[1] "Quantification of Uncertainty in Computational Fluid Dynamics," 1993, Celik, I., Chen, C. J., Roache, P. J., and Scheurer, G., eds. ASME Publ. No. FED-Vol. 158, ASME Fluids Engineering Division Summer Meeting, Washington, DC, 20–24 June.

[2] Celik, I., and Karatekin, O., 1997, "Numerical Experiments on Application of Richardson Extrapolation With Nonuniform Grids," ASME J. Fluids Eng., **119**, pp. 584–590.

[3] Roache, P. J., 1998, *Verification and Validation in Computational Science and Engineering*, Hermosa Publishers, Albuquerque.

[4] Stern, F., Wilson, R. V., Coleman, H. W., and Paterson, E. G., 2001, "Comprehensive Approach to Verification and Validation of CFD Simulations-Part 1: Methodology and Procedures," ASME J. Fluids Eng., **123**, pp. 793–802.

[5] Roache, P. J., Ghia, K. N., and White, F. M., 1986, "Editorial Policy Statement on Control of Numerical Accuracy," ASME J. Fluids Eng., **108**, Mach Issue.

[6] Freitas, C. J., 1993, "Journal of Fluids Engineering Editorial Policy Statement on the Control of Numerical Accuracy," ASME J. Fluids Eng., **115**, pp. 339–340.

[7] Freitas, C. J., Ghia, U., Celik, I., Roache, P., and Raad, P., 2003, "ASME's Quest to Quantify Numerical Uncertainty," AIAA, 41st Aerospace Sciences Meeting& Exhibit, 6–9 January 2003, Reno, NV.

[8] Speziale, C. G., 1998, "Turbulence Modeling for Time-Dependent RANS and VLES: A Review," AIAA J., **36**.

[9] Vreman, B., Geurts, B., and Kuerten, H., 1996, "Comparison of Numerical Schemes in Large-Eddy Simulation of the Temporal Mixing Layer," Int. J. Numer. Methods Fluids, **22**, pp. 297–311.

[10] Vreman, B., Geurts, B., and Kuerten, H., 1997, "Large-Eddy Simulation of the Turbulent Mixing Layer," J. Fluid Mech., **339**, pp. 357–390.

[11] Pope, S. B., 2000, *Turbulent Flows*, Cambridge University Press, Cambridge.

[12] Meneveau, C., 1994, "Statistics of Turbulence Sub-Grid-Scale Stresses: Necessary Conditions and Experimental Tests," Phys. Fluids, **6**, pp. 815.

[13] Rodi, W., Ferziger, J. H., Breuer, M., and Pourquie, M., 1997, "Status of Large Eddy Simulation: Results of a Workshop," ASME J. Fluids Eng., **119**, pp. 241–254.

[14] Froehlich, J., and Rodi, W., 2002, "Introduction of LES of Turbulent Flows," in *Closure Strategies for Turbulent and Transitional Flows*, B. Launder and N. Sandham, eds., Cambridge University Press, Cambridge, pp. 267–298.

[15] Choi, H., and Moin, P., 1994, "Effects of Computational Time Step on Numerical Solution of Turbulent Flows," J. Comput. Phys., **113**, pp. 1–3.

[16] Richardson, L. F., 1910, "The Approximate Arithmetical Solution by Finite Differences of Physical Problems Involving Differential Equations, with an Application to the Stresses in a Masonary Dam," Philos. Trans. R. Soc. London, Ser. A, **210**, pp. 307–357.

[17] Richardson, L. F., and Gaunt, J. A., 1927, "The Deferred Approach to the Limit," Philos. Trans. R. Soc. London, Ser. A, **226**, pp. 299–361.

[18] Geurts, B. J., and Froehlich, J., 2001, *Numerical Effects Contaminating LES; A Mixed Story*. Modern Strategies for Turbulent Flow Simulation, B. J. Geurts, ed., Edwards Publishing, pp. 317–347.

[19] Geurts, B. J., and Froehlich, J., 2002, "A Framework for Predicting Accuracy Limitations in Large Eddy Simulation," Phys. Fluids, **14**, pp. 41–44.

[20] Lilly, D. K., 1967, "The Representation of Small-Scale Turbulence in Numerical Simulation Experiments," Proceedings of the IBM Scientific Computing Symposium on Environmental Sciences, IBM-Form No. 320-1951, Yorktown Heights, NY.

[21] Celik, I. B., Li, J., Hu, G., and Shaffer, C., 2004, "Limitations of Richardson Extrapolation and Possible Remedies for Estimation of Discretization Error," HT-FE2004-56035, Proceedings of the ASME Heat Transfer/Fluids Engineering Summer Conference, 11–15 July, Charlotte, NC.

[22] Sreedhar, M., and Stern, F., 1998, "Large Eddy Simulation of Temporally Developing Juncture Flows," Int. J. Numer. Methods Fluids, **28**, pp. 47–72.

[23] Temmerman, L., Leschziner, M. A., and Hanjalic, K., 2003, "A Combined RANS-LES Strategy With Arbitrary Interface Location for Near-Wall Flows," 3rd International Symposium on Turbulence and Shear Flow Phenomena, Sendai, Japan.

[24] Stolz, S., Adams, N. A., and Kleiser, L., 2001, "An Approximate Deconvolution Model for Large-Eddy Simulation with Application to Incompressible Wall-Bounded Flows," Phys. Fluids, **13**, pp. 997–1015.

[25] Piomelli, U., 1993, "High Reynolds Number Calculations Using the Dynamic Subgrid-Scale Stress Model," Phys. Fluids A, **5**, pp. 1484–1490.

[26] Sohankar, A., Davidson, L., and Norberg, C., 1999, "A Dynamic One-Equation Subgrid Model for Simulation of Flow Around a Square Cylinder," in *Engineering Turbulence Modelling and Experiments 4*, W. Rodi and D. Laurence, eds., pp. 227–236.

[27] Badeau, A. E., 2003, "Simulation of Buoyant Flows Using Implicit Turbulence Modeling," Ph.D. dissertation, West Virginia University, Morgantown, WV.

[28] Shi, S., 2001, "Towards Large Eddy Simulation of Ship Wakes," Ph.D. dissertation, West Virginia University, Morgantown, WV.

[29] Shi, S., Celik, I., and Smirnov, A., 2006, "LES of a Spatially Developing Turbulent Wake Flows," J. Ship Res., (to appear)

[30] Yavuz, I., Cehreli, Z. N., and Celik, I. B., 2002, "Large Eddy Simulation of the Wake Behind a Turning Ship," 2002 Fluids Engineering Division Summer Meeting, 14–18 July 2002, Montreal, Quebec, Canada.

[31] Cehreli, Z. N., 2004, "Investigation of Ship Wakes Using LES With Various SGS Models," Ph.D. dissertation, West Virginia University, Morgantown, WV.

[32] Badeau, A. E., Jr., and Celik, I. B., 2004, "Simulation of Vertical Buoyant Flow Events Using ITM," J. Turbul. (submitted).

[33] Rightley, P., 1995, "Bubble Dispersion and Interphase Coupling in a Free Shear Flow," Ph.D. dissertation, University of California, San Diego, CA.

[34] Celik, I. B., Cehreli, Z., and Yavuz, I., 2003, "Index Of Quality For Large Eddy Simulations," 2003 ASME Fluids Engineering Division Summer Meeting, 6–10 July 2003, Honolulu, Hawaii.

[35] Hussain, A., and Reynolds, W., 1975, "Measurements in Fully Developed Turbulent Channel Flow," ASME J. Fluids Eng., **97**, pp. 568.

[36] Smirnov, A., Shi, S., and Celik, I., 2000, "Random Flow Simulations with a Bubble Dynamics Model," ASME Fluids Engineering Division Summer Meeting, No. 11215, FEDSM2000, Boston, MA.

[37] Shi, S., and Celik, I., 2000, "Random Flow Generation Technique in Large Eddy Simulations and Particle Dynamics Modeling," ASME J. Fluids Eng., **123**, pp. 359–371.

[38] Longo, J., Stern, F., and Toda, Y., 1993, "Mean-Flow Measurements in the Boundary Layer and Wake and Wave Field of a Series 60 CB=0.6 Ship Model-Part 2: Scale Effects on Near-Field Wave Patterns and Comparisons With Inviscid Theory," J. Ship Res., **37**, pp. 16–24.

[39] Gui, L., Longo, L., and Stern, F., 1999, "Towing Tank PIV Measurements System and Data and Uncertainty Assessment for DTMB Model 5512," 3rd International Workshop on PIV, Santa Barbara, CA, 16–18 September 1999.

[40] Anwar, H., 1969, "Experiment on an Effluent Discharging From a Slot Into Stationary or Slow Moving Fluid of Greater Density," J. Hydraul. Res., **7**, pp. 411–430.

Detached-Eddy Simulation of the Separated Flow Over a Rounded-Corner Square

Kyle D. Squires
Mechanical and Aerospace Engineering Department,
Arizona State University,
Tempe, AZ 85287-6106

James R. Forsythe
Cobalt Solutions, LLC,
4636 New Carlisle Pike,
Springfield, OH 45504

Philippe R. Spalart
Boeing Commercial Airplanes,
Seattle, WA 98124-2207

Detached-eddy simulation (DES) is used to study the massively separated flow over a rounded-corner square. The configuration is an idealization of the flow around a forebody cross section rotating at high angle of attack. Simulations are performed at sub- and supercritical Reynolds numbers, between which experimental measurements show a reversal of the side force. DES predictions are evaluated using experimental measurements and contrasted with unsteady Reynolds-averaged Navier–Stokes (URANS) results. The computations are also subjected to a moderate grid refinement, a doubling of the spanwise period, an enlargement of the domain in the other directions, and the removal of any explicit turbulence model. The sub- and supercritical flows are computed at Reynolds numbers of 10^5 and 8×10^5, respectively, and with the freestream at 10 deg angle of attack. Boundary-layer separation characteristics (laminar or turbulent) are established via the initial and boundary conditions of the eddy viscosity. Following boundary layer detachment, a chaotic and three-dimensional wake rapidly develops. For the supercritical flow, the pressure distribution is close to the measured values and both the streamwise and side forces are in adequate agreement with measurements. For the subcritical flow, DES side-force predictions do not follow the experimental measurements far enough to achieve reversal. [DOI: 10.1115/1.1990202]

1 Introduction

Knowledge of the spin and recovery characteristics of modern aircraft is crucial at a variety of levels, including maneuverability, control strategies, and ultimately design. One of the most significant factors affecting spin characteristics for modern fighters is the forebody, with its complex vortical flows and long moment arm. Laboratory measurements of spin characteristics are of limited utility since it is not possible to resolve important Reynolds number effects because of the range of available tunnels. Numerical simulation, therefore, provides an important tool that should ultimately provide higher-fidelity evaluations of rotary motion characteristics and aircraft spin than current approaches.

Unfortunately, numerical models are inadequate in many instances due to their inability to accurately predict the complex and unsteady effects associated with spin. Vortical flows, cross-flow separations, and sensitivity of forces and moments to Reynolds number greatly challenge modeling approaches. These factors also supply the overall motivation for the present fundamental investigations and the need to develop and assess improved techniques for predicting complex, separated flows at high Reynolds numbers.

Most predictions of high-Reynolds number turbulent flows encountered in applications are obtained from solutions of the Reynolds-averaged Navier–Stokes (RANS) equations. While the most popular RANS models appear to yield predictions of useful accuracy in attached flows as well as some with shallow separations, RANS predictions of massive separations have typically been unreliable. RANS models, calibrated in thin shear layers, appear unable to consistently represent to sufficient accuracy the geometry-dependent, chaotic, and unsteady features of massively separated flows. This is the case even with unsteady RANS (URANS), a technique most often applied in two-dimensional simulations and which is capable of producing vortex shedding, though the shedding is typically nonchaotic and exaggerated in amplitude [1]. In addition, predictions of quantities such as the mean drag using URANS can be quite large compared to measurements, though some studies have shown that URANS can yield relatively reasonable descriptions of separated flows [2,3].

The relatively poor performance of RANS models has motivated the increased application of large-eddy simulation (LES). Away from solid surfaces, LES is a powerful approach, providing a description of the large, energy-containing scales of motion that are typically dependent on geometry and boundary conditions. When applied to boundary layers, however, the computational cost of whole-domain LES does not differ appreciably from that of direct numerical simulation (DNS) [4]. The "large eddies" close to the wall are physically small in scale and, in high-Reynolds number boundary layers, LES may not sufficiently resolve near-wall structures. Inadequate resolution can severely degrade LES of separated flows if the location of boundary layer separation is not accurately predicted.

In the present contribution, predictions are obtained using detached-eddy simulation (DES), a hybrid method which has RANS behavior near the wall and becomes a large-eddy simulation in the regions away from solid surfaces provided the grid density is sufficient [4]. The formulation used here is based on a modification to the Spalart–Allmaras one-equation model [5] (referred to as S-A throughout) and is described in greater detail in the next section. DES is a nonzonal technique that is computationally feasible for high-Reynolds number prediction, but also resolves time-dependent, three-dimensional turbulent motions as in LES. Previous applications of the method have been favorable, yielding adequate predictions across a range of flows and also showing the computational cost has a weak dependence on Reynolds number, similar to RANS methods yet at the same time providing more realistic descriptions of unsteady effects [1,6,7].

The study described in this manuscript is part of a larger effort in which one of the main goals is development of simulation tools for prediction of the flight characteristics of full aircraft at application Reynolds numbers [8]. An area of particular interest is that of aircraft spin. These flow fields are massively separated, providing a regime suited for a "natural" application of DES–RANS prediction of the boundary layers and LES of the massively separated wake. Though a natural application for the model, calcula-

Contributed by the Fluids Engineering Division for publication in the JOURNAL OF FLUIDS ENGINEERING.

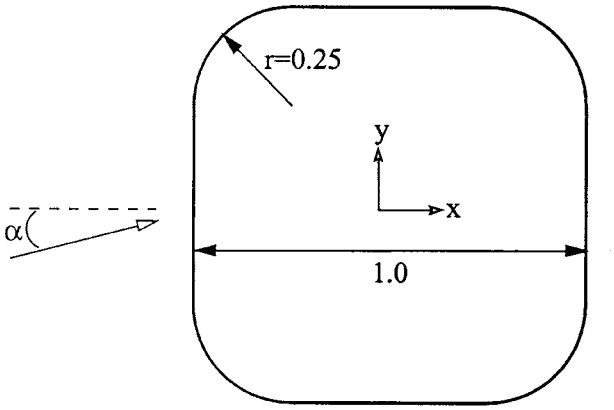

Fig. 1 Cross section of the rounded-corner square and angle of attack of the freestream flow. Corner radius is 1/4 the "diameter" *D* of the forebody. Angles are measured positive counterclockwise from the aft-symmetry stagnation point.

tions of complex configurations at high Reynolds numbers challenge the entire computational approach, including that of grid generation and flow solution. Unstructured grids form an integral component of the present computational approach; the solutions are obtained using the commercial flow solver COBALT in which the numerical method is stabilized via nonlinear dissipation. Related investigations have shown that the artificial dissipation associated with a numerical scheme used to solve the Navier–Stokes equations can be as large as that represented by the turbulence model; therefore, care must be exercised in application of these methods to LES (e.g., see Mittal and Moin [9]). This in turn motivates another goal of the work—to explore the current numerical approach on various grid topologies for DES applications. This is not a simple matter of verifying the order of accuracy, which is difficult to define and predict in LES and especially hybrid methods. The primary approach for such assessments remains grid refinement.

The flow considered in this work is that around a canonical forebody cross section, the rounded-corner square shown in Fig. 1. The corner radius is 1/4 of the width/height ("diameter," *D*) of the forebody, the angle of attack α is 10 deg. Numerical predictions are compared to the experimental measurements from Polhamus [10]. These investigators measured the forces and pressure distributions on a variety of forebody cross sections over a range of Reynolds numbers and angles of attack. Note that the angle of attack as considered by Polhamus [10] and indicated in Fig. 1 is that characterizing the idealized two-dimensional problem and would not represent the angle of attack of an airplane. In simplest terms the flow considered emulates that of a forebody at 90 deg angle of attack (an exactly flat spin), and rotating. The angle of attack considered in this study is then the arctangent of the ratio $\Omega D/V$, where Ω is the spin rate, *D* the distance from the nose to center of rotation of the spin, and *V* its sink velocity.

Pressure measurements indicate that, in the subcritical regime (Reynolds numbers below about 5×10^5 based on the freestream velocity and diameter *D*), boundary layer separation along the top surface (uppermost horizontal surface in Fig. 1) occurs near the upper-front corner of the forebody, while for the supercritical flows the boundary layer remains attached along the upper (and lower) surface. The changes in boundary layer separation characteristics have significant effects on the streamwise and lateral forces with Reynolds number (the lateral, or side, force acts along the *y* axis in Fig. 1). A reversal of the lateral force was measured in the experiments summarized by Polhamus [10], i.e., negative for subcritical flows and positive in the supercritical regime (for reference, the force is positive for an airfoil). Relevant to spin, the negative side force in the subcritical regime is spin propelling, while at the higher Reynolds numbers the positive side force is spin damping.

The main objectives of the work are to assess predictions of the separated flow over a rounded-corner square, especially as the predictions relate to the factors influencing side-force reversal. The response of DES predictions to changes in grid spacing is investigated, as well as other factors such as the dimension of the (statistically homogeneous) spanwise coordinate. DES predictions are also compared to results obtained from the unsteady Reynolds-averaged Navier–Stokes (URANS) equations (of both the two- and three-dimensional equations) and to simulations performed without an explicit turbulence model.

2 Computational Approach

2.1 Detached-Eddy Simulation. The DES formulation is based on a modification to the S-A model such that it reduces to its RANS form close to solid surfaces and a Smagorinsky-type subgrid viscosity away from the wall [4]. The S-A RANS model can be expressed as

$$\frac{D\tilde{\nu}}{Dt} = c_{b1}[1-f_{t2}]\tilde{S}\tilde{\nu} + \frac{1}{\sigma}[\nabla\cdot((\nu+\tilde{\nu})\nabla\tilde{\nu}) + c_{b2}(\nabla\tilde{\nu})^2] - \left[c_{w1}f_w - \frac{c_{b1}}{\kappa^2}f_{t2}\right]\left[\frac{\tilde{\nu}}{d}\right]^2 + f_{t1}\Delta U^2 \tag{1}$$

where $\tilde{\nu}$ is the working variable. The eddy viscosity ν_t is obtained from

$$\nu_t = \tilde{\nu}f_{v1}, \quad f_{v1} = \frac{\chi^3}{\chi^3 + c_{v1}^3}, \quad \chi \equiv \frac{\tilde{\nu}}{\nu} \tag{2}$$

where ν is the molecular viscosity. The production term is expressed as

$$\tilde{S} \equiv f_{v3}S + \frac{\tilde{\nu}}{\kappa^2 d^2}f_{v2} \tag{3}$$

$$f_{v2} = \left(1+\frac{\chi}{c_{v2}}\right)^{-3}, \quad f_{v3} = \frac{(1+\chi f_{v1})(1-f_{v2})}{\chi} \tag{4}$$

where *S* is the magnitude of the vorticity. The production term as written in (3) differs from that developed in Spalart and Allmaras [5] via the introduction of f_{v3} and redefinition of f_{v2}. These changes are advantageous for simulation of flows with laminar separation since spurious upstream propagation of the eddy viscosity into attached, laminar regions is more easily prevented. The function f_w is given by

$$f_w = g\left[\frac{1+c_{w3}^6}{g^6+c_{w3}^6}\right]^{1/6}, \quad g = r + c_{w2}(r^6 - r), \quad r \equiv \frac{\tilde{\nu}}{S\kappa^2 d^2} \tag{5}$$

The function f_{t2} is defined as

$$f_{t2} = c_{t3}\exp(-c_{t4}\chi^2) \tag{6}$$

The trip function f_{t1} is specified in terms of the distance d_t from the field point to the trip, the wall vorticity ω_t at the trip, and ΔU, which is the difference between the velocity at the field point and that at the trip

$$f_{t1} = c_{t1}g_t\exp\left(-c_{t2}\frac{\omega_t^2}{\Delta U^2}[d^2 + g_t^2 d_t^2]\right) \tag{7}$$

where $g_t = \min(0.1, \Delta U/\omega_t\Delta x)$, where Δx is the grid spacing along the wall at the trip. The wall boundary condition is $\tilde{\nu}=0$, and the inflow condition is discussed in Sec. 2.2. The constants are $c_{b1}=0.1355$,

Table 1 Simulation parameters. Grid size reported as surface-normal×surface-tangential ×spanwise; (baseline) is the smaller $x-y$ domain, (padded) the larger $x-y$ domain. URANS calculations performed using the Spalart–Allmaras one-equation model.

Case	Model	Grid Size	L_z	$x-y$ domain
1	DES	$100 \times 149 \times 151$	$3D$	baseline
2	DES	$100 \times 149 \times 301$	$6D$	baseline
3	DES	$150 \times 200 \times 151$	$3D$	baseline
4	DES	$120 \times 149 \times 151$	$3D$	padded
5	DES	unstructured, 3.55×10^6 cells	$3D$	padded
6	no model	$120 \times 149 \times 151$	$3D$	padded
7	2DURANS	200×400	–	baseline
8	3DURANS	$120 \times 149 \times 151$	$3D$	padded

$\sigma=2/3$, $c_{b2}=0.622$, $\kappa=0.41$, $c_{w1}=c_{b1}/\kappa^2+(1+c_{b2})/\sigma$, $c_{w2}=0.3$, $c_{w3}=2$, $c_{v1}=7.1$, $c_{v2}=5$, $c_{t1}=1$, $c_{t2}=2$, $c_{t3}=1.1$, and $c_{t4}=2$.

The DES formulation is obtained by replacing the distance to the nearest wall, d, by $\tilde{d}$, where $\tilde{d}$ is defined as

$$\tilde{d} \equiv \min(d, C_{\mathrm{DES}}\Delta) \tag{8}$$

In Eq. (8) for the current study, Δ is the largest distance between the cell center under consideration and the cell center of the neighbors (i.e., those cells sharing a face with the cell in question). In "natural" applications of DES, the wall-parallel grid spacings (e.g., streamwise and spanwise) are typically on the order of the boundary layer thickness and the S-A RANS model is retained throughout the boundary layer, i.e., $\tilde{d}=d$. Consequently, prediction of boundary layer separation is determined in the "RANS mode" of DES. Away from solid boundaries, the closure is a one-equation model for the subgrid viscosity. When the production and destruction terms of the model are balanced, the length scale $d=C_{\mathrm{DES}}\Delta$ in the LES region yields a Smagorinsky-type eddy viscosity $\tilde{\nu} \propto S\Delta^2$. Analogous to classical LES, the role of Δ is to allow the energy cascade down to the grid size; roughly, it makes the pseudo-Kolmogorov length scale based on the eddy viscosity proportional to the grid spacing. The additional model constant $C_{\mathrm{DES}}=0.65$ was set in homogeneous turbulence [11] and is used without modification in this work.

2.2 Approach and Simulation Overview. As reported in Polhamus [10], there are important Reynolds number effects in the flow around the forebody at angle of attack. These effects are analogous to that of the drag crisis occurring around cylinders and spheres and are linked to boundary layer transition and the nature of the flow separation. While predicting details of the transition process is beyond the scope of the methods used in the current simulations, it is possible to construct well-defined computations to investigate the effect of the type of boundary layer separation on the flow. In particular, simulations were performed in the sub- and supercritical regimes in which the type of boundary layer separation was controlled via the initial and boundary conditions on the eddy viscosity.

Following Travin [1], a "tripless" approach is employed for subcritical flows in which the inflow eddy viscosity is zero. Nonzero values of ν_t are seeded into the wake, and the reversed flow that is established in the recirculating region is sufficient to sustain the turbulence model downstream of separation. Boundary layer separation in this case is laminar, with the model active following separation. For the supercritical flows the inflow eddy viscosity is set to a small value (3ν), sufficient to ignite the turbulence model near solid surfaces as the fluid enters the boundary layers. The subsequent separation is then of a turbulent boundary layer.

The computations were performed using COBALT, an unstructured finite-volume method developed for solution of the compressible Navier–Stokes equations and described in Ref. [12]. The numerical method is a cell-centered finite volume approach applicable to arbitrary cell topologies (e.g., hexahedrals, prisms, tetrahdrons). The spatial operator uses the exact Riemann solver of Gottlieb and Groth [13], least-squares gradient calculations using QR factorization to provide second-order accuracy in space, and TVD flux limiters to limit extremes at cell faces. A point implicit method using analytic first-order inviscid and viscous Jacobians is used for advancement of the discretized system. For time-accurate computations, a Newton subiteration scheme is employed; the method is second-order accurate in time. For parallel performance, COBALT uses the domain decomposition library PARMETIS [14] to provide optimal load balancing with a minimal surface interface between zones. Communication between processors is achieved using message passing interface (MPI), with excellent parallel efficiencies.

Most of the calculations presented in the next section were performed on structured grids that were generated using the control technique of Hsu and Lee [15]. Using this technique, it was possible to control mesh spacing to the first point nearest the boundary (within one wall unit near solid surfaces), exert control over grid spacing tangent to the boundary, and also to maintain orthogonality of the mesh at all boundaries. Also evaluated in the next section is a DES prediction obtained on an unstructured mesh. The unstructured grid was generated using Gridgen [16], with prisms in the boundary layer and near-isotropic tetrahedra away from solid surfaces. The ability to exert greater control on cell distribution compared to the structured grids permitted generation of an unstructured mesh having 2.5×10^6 cells (of a total cell size of 3.55×10^6 cells) within two diameters of the forebody surface. The wall-normal spacing of the unstructured grid in the boundary layer was the same as that in the structured grid (geometric progression at a rate of 1.2). The streamwise and spanwise spacings of the unstructured grid near solid surfaces was also comparable to the structured grid, slightly finer due to grid topology (prisms) employed.

The parameters of the calculations are summarized in Table 1. Shown is the case number, model, grid size, spanwise period, and reference to the $x-y$ domain size. As summarized in the table, predictions are obtained using DES, URANS of both the two- and three-dimensional flow, and computations without any explicit turbulence model. As shown below, predictions of the flow experiencing turbulent boundary layer separation were obtained for each of the simulation cases in Table 1. Computations of the tripless solution were obtained for most of the simulation cases, as summarized below.

The majority of simulations was performed on domains in which the spanwise period was three times the diameter, i.e., $L_z=3D$. The influence of the spanwise dimension was investigated in case 2 via computations performed on a domain with a doubling of the spanwise period to $L_z=6$. Domain-size influences were also investigated in calculations with two domains having different outer-boundary placement. The smaller domain (referred to as "baseline" in the table) extended eight diameters down-

stream of the body and with a lateral extent also of $8D$. In calculations performed on the larger domains (referred to as "padded" in the table), the streamwise extent to the outflow boundary downstream of the body was at approximately $20D$, with the lateral dimension also approximately $20D$ from the model surface. As shown in the next section, there was a measurable effect of the baseline domain on the solutions, resulting in overpredictions of the stagnation pressure and axial force. Boundary conditions on the model surface were no-slip for the velocity components and with $\tilde{\nu}=0$. The normal momentum equation is used at solid walls to estimate the variation of pressure normal to the surface, while a one-sided, least-squares gradient method is used to estimate the variation of pressure tangent to the wall.

Grid resolution was investigated by refining the mesh in the $x-y$ plane by a factor of 2. For the coarse grid with the shorter spanwise dimension ($L_z=3D$), the structured-grid calculation was performed using approximately 2.2×10^6 points, the finer mesh calculation possessing about 4.5×10^6 grid points. In all computations the wall layer is resolved, i.e., the distance from the wall to the first cell center was within one viscous unit. For the turbulent separation cases the resolved wall layer is important to accurately predicting boundary layer properties. For the tripless case experiencing laminar boundary layer separation it would be possible to relax the near-wall spacing though that was not attempted in the current study—the same grids were used for both fully turbulent and tripless cases.

As shown by Eq. (8), the length scale Δ is determined by the largest of the three grid spacings. Near the surface of the forebody for the structured grids the spanwise mesh spacing is larger than either Δ_x or Δ_y and, consequently, the thickness of the "RANS region" (i.e., the wall-normal distance from the forebody surface to the interface where $\tilde{d}=C_{\mathrm{DES}}\Delta$) was $0.013D$ for each structured grid. The dimensionless time step, $\Delta t/(D/U_\infty)$ (U_∞ is the freestream speed), was 0.01, a value chosen based on preliminary calculations and other time-accurate computations of unsteady flows by the current investigators and other researchers [1,17]. These studies included computations performed using algorithms for solution of the Navier–Stokes equations different than the approach employed in COBALT, and the cross comparison of flow-field predictions has provided specific guidance on choice of time steps and an assessment of unsteady flow-field predictions using COBALT (e.g., see Forsythe [8]). With $\Delta t/(D/U_\infty)=0.01$, there are approximately 350 time steps per main shedding cycle. Far-field boundary values on the solution were obtained from the Riemann invariants; the freestream Mach number was 0.1.

From a given set of initial and boundary conditions for a particular flow type (tripless or fully turbulent), the governing equations were time advanced through a transient as the flow evolved to its equilibrium condition. Various initial conditions were used, e.g., specification of uniform properties or with perturbations applied to the initial conditions in order to accelerate the development of chaotic three-dimensional structure in the wake. Slight asymmetries in the initial state that arise from grid partitioning, ordering of the grid, machine round-off, etc., are amplified by the natural instabilities of the flow and, as will be shown in the next section, the numerical solutions develop strong lateral variations. The transient as the flow developed towards an equilibrium state was typically less than about $20D/U_\infty$. This transient was discarded and the simulations continued for an additional period of $\mathcal{O}(100D/U_\infty)$. This period was sufficient for adequate convergence of averaged quantities and capture of the long time scales in the flow.

3 Results

3.1 Solution Properties and Flow Visualization. The different structure of the sub-and supercritical flows is illustrated in Fig. 2. For the subcritical flow at $\mathrm{Re}=10^5$ the attached boundary layers are laminar and cannot sustain the development of the adverse pressure gradient in the upper-front corner with separation occurring around $\theta\approx135$ deg (note again that the angle θ is measured counterclockwise from the aft-symmetry point of the forebody). In the "tripless" mode, the turbulence model is dormant upstream of separation, with flow reversal sustaining the model downstream of separation. For the supercritical flow shown in the lower frame of Fig. 2, the fully turbulent boundary layers remain attached along the upper-front corner and over most of the upper surface, with flow separation taking place near the upper rear corner ($\theta\approx45$ deg).

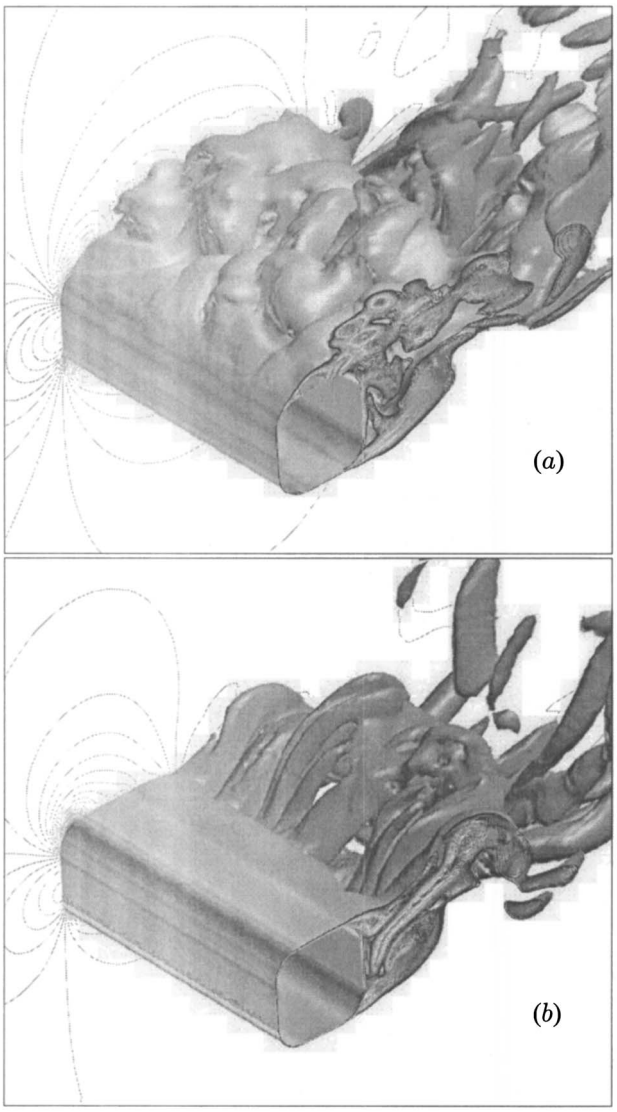

Fig. 2 Instantaneous vorticity isosurfaces colored by pressure. Pressure contours on the far plane; vorticity contours in the near plane. Subcritical flow at $\mathrm{Re}=10^5$ shown in (*a*); supercritical flow at $\mathrm{Re}=8\times10^5$ shown in (*b*).

Shown in Fig. 3 is a representative sample of pathlines in the vicinity of the upper-front corner of the forebody for the flow at $\mathrm{Re}=10^5$ (case 4 in Table 1). The pathlines in the figure are colored by the value of the viscosity ratio ν_t/ν (note that the pathlines cross in the view shown in the figure because the flow is three-dimensional). Upstream of separation the eddy viscosity is zero (as indicated by the dark color of the pathline). In the separated region the reversing flow sweeps turbulent fluid from downstream into contact with the separating flow producing a transition (in this case activation of the turbulence model) by contact of turbulent with nonturbulent fluid.

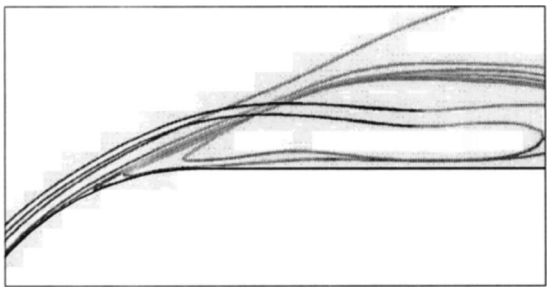

Fig. 3 Particle pathlines colored by ν_t/ν from tripless solution at Re=10^5. Threshold of ν_t/ν from 0 (dark) to 1 (light).

In "natural" applications of DES, the detached regions of the flow are modeled using LES, in this case with a one-equation model for the subgrid-scale eddy viscosity. An advantage of LES is that mesh refinement resolves more flow features, in turn lessening modeling errors. The effect of mesh refinement was investigated by doubling the $x-y$ grid in case 3 as compared to case 1 (cf., Table 1). Shown in Fig. 4 are contours of the instantaneous vorticity from Case 1 and Case 3 for a simulation with turbulent separation at Re=8×10^5. Cuts of the vorticity field from three spanwise planes are shown for each case and provide an example of the spanwise variation in the DES solution. As also the case for classical LES, Fig. 4 shows that the effect of the mesh refinement is to resolve smaller-scale eddies in case 3. This feature in the DES was also illustrated in the circular cylinder calculations of Travin [1].

3.2 Statistics for the Turbulent Separation Cases. Force coefficients C_x and C_y in the axial and lateral directions, respectively, are defined using the freestream density and velocity and frontal area of the forebody. Figure 5 shows the force coefficient time histories for the two-dimensional URANS solution at Re $=8\times10^5$. A fraction of the time history is shown in the figure, i.e., following the initial transient. The figure shows the 2D URANS solution is temporally periodic, with large swings in the side-force coefficient compared to the axial value as the flow undergoes a shedding cycle.

A representative force coefficient history for a DES case is shown in Fig. 6, for a turbulent separation run at Re=8×10^5 (case 2). Similar to Fig. 5, a transient of roughly 20 nondimensional time units has been excluded from the figure (note also the longer time integration for the DES). Unlike the 2D URANS, a strong modulation is apparent in the side-force coefficient C_y, similar to that in related studies of cylinders and other bluff bodies [1]. The side-force modulation is complex and seems to be an intrinsic feature of the chaotic, three-dimensional flow. For the forebody, the modulation develops via the interaction of spanwise and streamwise vorticity in the near wake. DES calculations on

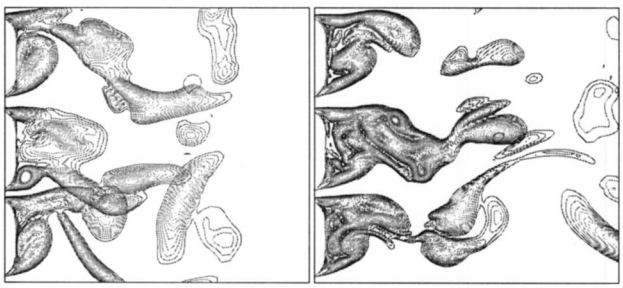

Fig. 4 Contours of the instantaneous vorticity in three spanwise planes for case 1 (on the left) and case 3 (on the right). Vorticity contours are from the turbulent separation cases at Re=8×10^5.

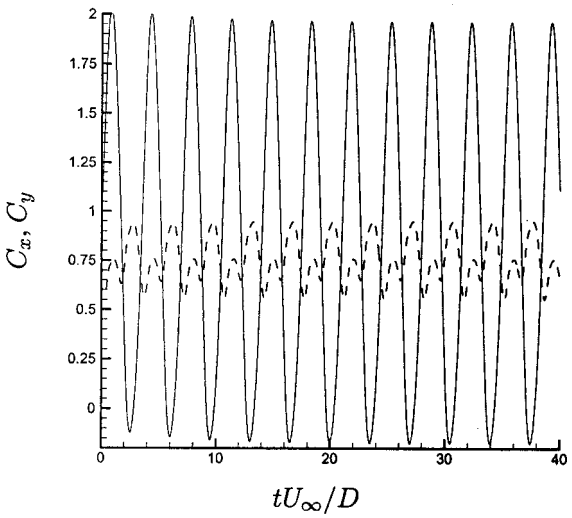

Fig. 5 Force coefficients C_x and C_y from two-dimensional URANS at Re=8×10^5, turbulent boundary layer separation. --- C_x; ——— C_y.

domains in which the spanwise coordinate L_z was $1.5D$ did not yield force modulation and suppressed three-dimensionality of the primary spanwise structure (although the solution did possess streamwise vorticity, albeit weak). Predictions on the domain with $L_z=1.5D$ yielded large overpredictions of the axial force. Though not shown here, force-coefficient histories for all of the three-dimensional turbulent separation cases—including the 3D URANS result—exhibited force modulation.

Time-averaged force coefficients for the turbulent separation cases are summarized in Table 2. The 2D URANS, which produces a periodic shedding and cannot accurately account for the force modulation, substantially overpredicts the mean axial force coefficient $\langle C_x\rangle$. This feature is analogous to the circular cylinder where two-dimensional URANS yields large drag [1]. For the DES, force coefficients from the smaller (baseline) domains are higher than the measured values and than those from calculations performed on the larger domain (cf., cases 1–3). A comparison of case 3 against cases 1–2 shows a trend towards lower axial force with grid refinement in the $x-y$ plane. In addition, the axial force slightly decreases in case 2, computed on the longer spanwise

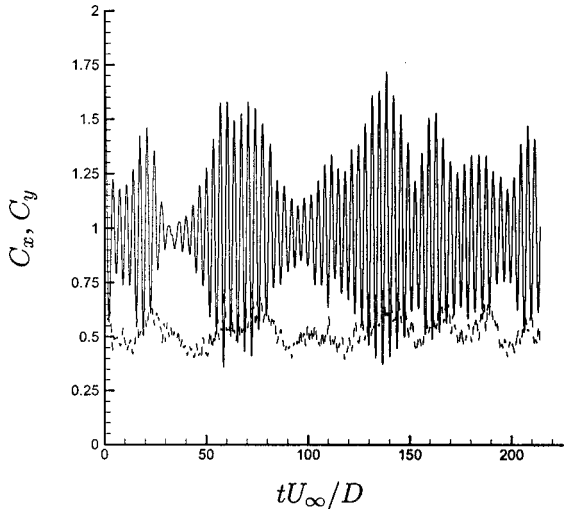

Fig. 6 Force coefficients C_x and C_y from case 2, DES prediction at Re=8×10^5, turbulent boundary layer separation. --- C_x; ——— C_y.

Table 2 Time-average force coefficients from turbulent separation cases at Re=8×10^5 (time averages denoted using $\langle\cdot\rangle$). Experimental measurements are from Polhamus et al. (1959) [10].

Case	Model	$\langle C_x \rangle$	$\langle C_y \rangle$
1	DES	0.57	0.92
2	DES	0.55	0.98
3	DES	0.51	0.96
4	DES	0.46	0.94
5	DES	0.43	0.83
6	no model	0.76	0.62
7	2D URANS	0.75	0.88
8	3D URANS	0.43	0.94
–	expts.	0.4	0.9

domain, compared to case 1. Nevertheless, $\langle C_x \rangle$ is too large and, as shown below, the overprediction arises from the influence of the computational domain, which effectively constrains the flow and raises the stagnation pressure coefficient by about 0.1 compared to results obtained on the larger domains (cases 4–5). DES predictions on the larger domain using both structured and unstructured grids are in quite good agreement with the measurements of Polhamus [10]. Interestingly, the 3D URANS also yields forces in good agreement with the measurements and padded-domain DES predictions. On the other hand, calculations without an explicit turbulence model (case 6) markedly overpredict the axial force due to the poor treatment of the attached boundary layers, as described in more detail below.

Pressure coefficients around the body for the fully turbulent runs (Re=8×10^5) are shown in Fig. 7. For the flow at 10 deg angle of attack, the maximum C_p occurs about 15–20 deg below the fore-symmetry point ($\theta\approx-160$ deg as shown in Fig. 7). For cases 1, 3, and 7, the stagnation C_p is overpredicted, an error introduced by the use of the smaller $x-y$ domain. For these cases the overprediction in the stagnation pressure is $\mathcal{O}(0.1)$, comparable to the overprediction of the mean axial force (cf., Table 2). Comparing the effect of the domain (case 1 and case 4) shows a reduction in the axial force coefficient on the larger domain, closer

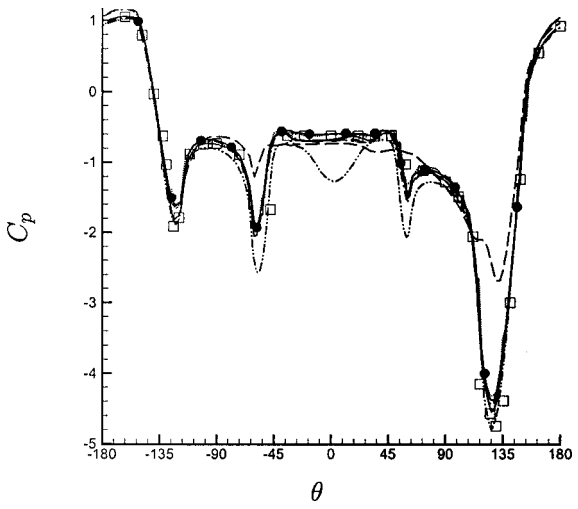

Fig. 7 Pressure coefficient distribution around the forebody. Turbulent separation cases, Re=8×10^5. Symbols are measurements from Polhamus et al. (1959) [10] ——— case 1; --- case 3; -·- case 4; ··· case 5; – – – case 6; -·-· case 7; ●———● case 8.

to the measured value of about 0.4 as also summarized in Table 2. The 2D URANS, with a finer $x-y$ grid compared to the three-dimensional runs, shows deeper minima in C_p in the vicinity of each corner, providing some insight into the effect of grid resolution on the pressure field. While finer grids would improve the description of the wake characteristics and therefore also the pressure distribution (especially in the aft region), other effects such as the domain size and treatment of the spanwise boundaries (periodic in this work) also contribute to differences between the simulations and experiment. Much deeper investigations than possible in this work could consider variations in these parameters and their influence on the accuracy of the predictions.

An effect of the Reynolds number reproduced in the fully turbulent solutions in Fig. 7 is that the boundary layers around the upper-front and lower-front corners ($\theta\approx\pm135$ deg) remain attached, as evidenced by the pressure minima in these regions, especially around $\theta\approx135$ deg. It is apparent that all of the simulations predict attached boundary layers around the upper-front corner, with the exception of case 6, i.e., the simulation performed without an explicit turbulence model in which the (effectively laminar) boundary layer separates. Without an explicit model in the boundary layers, accurate prediction of boundary layer growth and separation requires grids of sufficient density to resolve the small near-wall turbulent structures (as would also be required in whole-domain LES with an explicit SGS model). At high Reynolds numbers, however, boundary layer grids will not be sufficiently dense for accurate resolution of turbulent structures because of the prohibitively fine resolutions required. Figure 7 shows that the case 6 prediction separates (rather than remaining attached in the vicinity of $\theta\approx135$ deg) because of its nonturbulent character (i.e., without turbulent stress supplied by an explicit model or resolved Reynolds stresses captured by the grid).

Along the rear vertical surface (in the vicinity $\theta=0$ in Fig. 7) the 2D URANS (case 7) pressure distribution is far from the measured values, resulting in a large streamwise force (cf., Table 2) as also observed in other two-dimensional URANS predictions of bluff-body flows [1]. For all other cases shown in the figure, including the 3D URANS, predictions of the rear-surface pressures are reasonable, close to the measurements of Polhamus [10]. Consequently, for the DES and 3D URANS calculations on the padded domains (cases 4, 5, and 8), the overall pressure distributions are adequate and the axial and streamwise forces exhibit reasonable agreement with measurements. Because the peak suction is missed in the run without an explicit model (case 6), the axial force is too high, yielding a similar $\langle C_x \rangle$ to the 2D URANS, though the causes for the overpredictions by these two techniques are not the same. The accuracy of the 3D URANS result in Fig. 7 is surprising, though consistent with flow visualizations that indicate the wake is characterized by three-dimensional structure, albeit less fine-grained than obtained in the DES. The reader is referred to Shur [3] for more in-depth discussion of 3D URANS behavior applied to bluff body flows. The study reported by Shur [3] shows that 3D URANS, while capable of accurately predicting mean pressures and forces, yields unsteady forces that are sensitive to the turbulence model and parameters such as the spanwise period.

Mean side-force coefficients summarized in Table 2 show that the DES predictions of the lateral force coefficient $\langle C_y \rangle$ are in general not far from the measurements reported by Polhamus [10]. The lateral force prediction in case 6 provides another illustration of the error that can arise due to the boundary layer treatment without an explicit model. As also noted in the C_p distribution and axial force coefficient, the 3D URANS is again accurate and apparently able to resolve enough of the 3D variation important to accurate force predictions.

3.3 Statistics for the Laminar Separation Cases. Laminar separation cases in the DES were computed for most of the parameter combinations summarized in Table 1. The Reynolds num-

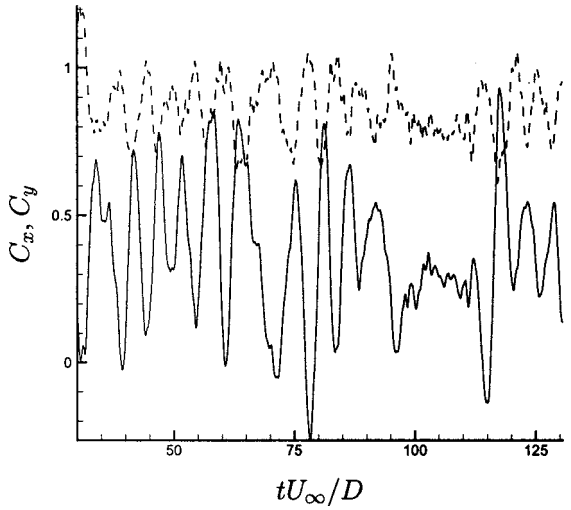

Fig. 8 Force coefficients C_x and C_y from case 4, DES prediction at Re=1×10^5, laminar boundary layer separation. --- C_x; ——— C_y.

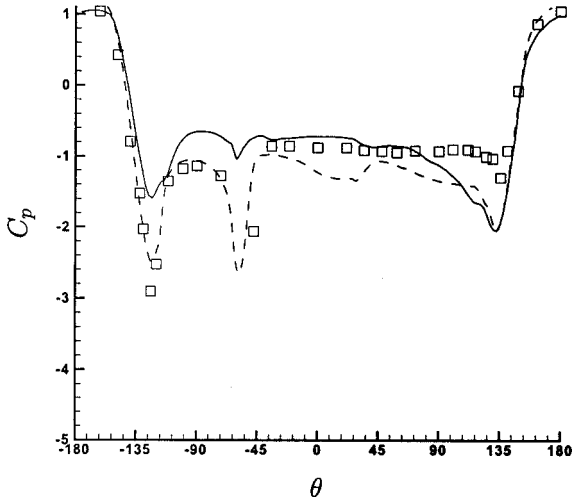

Fig. 9 Pressure coefficient distribution around the forebody. Laminar separation cases. Symbols are measurements from Polhamus et al. (1959) [10]. ——— case 4 (Re=1×10^5); --- case 7 (Re=4×10^5).

ber in the laminar separation runs was 1×10^5 for the DES (4×10^5 for the 2D URANS shown below), below the critical value found by Polhamus [10] of approximately 5×10^5. In the tripless mode, the upstream eddy viscosity was zero. The wake was initially seeded with eddy viscosity and the reversing flow established behind the forebody is sufficient to sustain the turbulence model following separation.

A representative force history from a laminar separation case is shown in Fig. 8. The simulation parameters for this case correspond to those of case 4 in Table 1. As shown qualitatively via Fig. 2, below the critical Reynolds number the flow separates in the vicinity of the upper-front corner of the forebody. The measurements of Polhamus [10] indicate that the boundary layer along the lower surface of the forebody remains attached. The pressure distribution then develops lower pressures along the lower forebody surface compared to the upper surface, which has the result of reversing the magnitude of the side force as compared to the values measured at higher Reynolds numbers, past the critical value.

The force histories shown in Fig. 8 show a higher axial force than in the fully turbulent runs. The mean axial force for the case shown in the figure is around 0.8, not far from the value reported in Table 2 for case 6 at Re=8×10^5, which also experiences flow detachment in approximately the same region near the upper-front corner of the forebody. More importantly, the side force C_y in Fig. 8, while chaotic, is only infrequently negative. Therefore, the mean side force will not be negative (the mean C_y is 0.38 for the trace in Fig. 8) and the simulation does not yield a reversal in the magnitude of the side force. Thus, changing the type of separation produces a very tangible move in the correct direction, but still an insufficient one.

The pressure coefficient distribution around the forebody for the laminar separation DES (case 4 parameters) is shown along with the experimental measurements of Polhamus [10] in Fig. 9. For comparison, the C_p distribution from the 2D URANS calculation at Re=4×10^5 is also shown. Consistent with the flow visualization shown in Fig. 2, flow detachment around $\theta\approx135$ deg results in a substantially higher C_p compared to the turbulent separation case in Fig. 7. Both the DES and 2D URANS have lower minima, indicative of delayed boundary layer separation as compared to the experiments. Near the lower front surface ($\theta\approx-135$ deg), measurements show a deeper minimum than predicted in the DES. The 2D URANS, on the other hand, comes closer to predicting the pressure minima along the lower surface. As with the fully turbulent solutions summarized above, in addition to the changes in the Reynolds number, part of the improvement for the improved prediction of the pressure distribution in the region $\theta\approx-135$ deg results from the finer $x-y$ grid compared to the three-dimensional runs.

Along the rear vertical surface ($\theta\approx0$ deg), DES predictions of the pressure distribution agree reasonably well with measurements. However, because of the deeper minima in the DES prediction of C_p near $\theta\approx135$ deg and higher C_p along the lower surface, side-force reversal cannot occur. Inspection of the instantaneous fields showed that along the lower surface (in the vicinity of $\theta\approx-135$ deg), a thin region of reversed flow occurs in the DES (in the mean, a view from a 2DURANS prediction is shown for reference in Fig. 10). This reversed flow region is one contributor to an effectively altered geometry that prevents development of a deep C_p minimum as apparently occurs in the experiments. To determine if the development of the thin region of reversed flow was caused by numerical and/or modeling errors, a calculation of the two-dimensional flow at Re=1×10^4 was conducted using a very fine grid of 1600×1200 points. Those results showed a similar thin region of reversed flow along the lower surface of the forebody, near the lower-front corner. Though not shown in Fig. 9, the C_p distribution for the fine-grid two-dimensional solution was similar to the tripless DES prediction at Re=1×10^5.

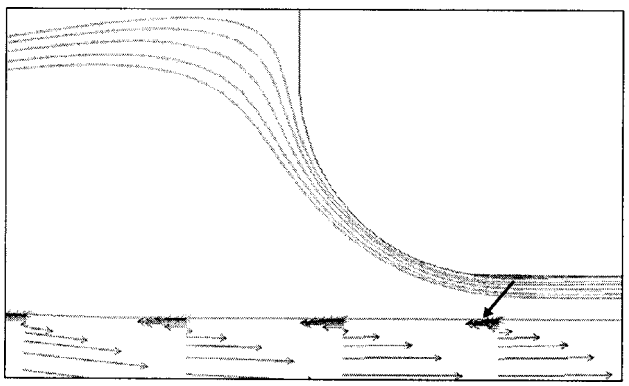

Fig. 10 Instantaneous streamlines around the lower-front corner of the square in the laminar separation case showing the thin region of reversed flow

4 Summary

DES was applied to prediction of the separated flow around a forebody cross section at 10 deg angle of attack. Influences of domain size, grid refinement, and turbulence model were investigated in cases in which boundary layer separation was either laminar or turbulent. The initial and boundary conditions on eddy viscosity set the type of boundary-layer separation, aimed at flows above or below the critical Reynolds number which controls a reversal of the side force in the experimental measurements of Polhamus [10].

DES predictions of the supercritical flow were successful at resolving the complex shedding process and modulation in the force histories. These features are consistent with circular-cylinder behavior and appear to be represented reasonably adequately, based on the agreement between simulation and measurement of the pressure distribution and forces. In the subcritical regime, no simulation technique applied during the course of this study (DES/LES, DNS of the two-dimensional flow, and preliminary calculations using vortex methods) yielded a sign change in the side force. Small differences in the geometry, hysteresis, and sidewall effects are three sources that might explain the differences between predictions of the subcritical flow and experimental measurements.

In addition, boundary layer treatment of the subcritical flow using the tripless approach makes no attempt to mimic the details of transition. The advantage of the tripless approach is that the simulation parameters are unambiguous (the results depend only on the model, and not on transition locations chosen case by case). In practice, there can be substantial regions of laminar flow and a prediction of boundary layer transition is required. Details of the processes of separation and transition to turbulence, especially if intermingled, continue to challenge simulation strategies. This point is worth emphasizing because failure to predict force reversal in the subcritical regime is likely connected to several factors, most of which are not directly related to the turbulence treatment of the wake.

In the present application, the attached boundary layers lie within the "RANS region" of the DES solution. As the flow detaches, in the separating shear layers the wake develops new instabilities that result in the rapid growth of a chaotic and three-dimensional wake. The lack of eddy content in the detaching boundary layers represents a relatively small error to the solutions presented here (its length scale would be several times smaller than that of the new instabilities). In other applications, e.g., flows with shallow separations, it will be advantageous and necessary to seed the upstream flow with "eddy content," considerably refine the grid to support these eddies, and initiate LES in the attached boundary layers prior to separation.

As shown above, the DES formulation is based on a modification to the length scale of the destruction term in the S-A RANS model. The DES limiter which acts to increase the magnitude of the destruction term compared to that obtained by the RANS model becomes active outside of the RANS–LES interface. Given that the S-A RANS model has very little sensitivity to the destruction term in the outer half the boundary layer, location of the interface above approximately half of the boundary layer thickness should not degrade boundary layer predictions (see also Spalart [4]).

The current study also provided an opportunity to assess various aspects of the numerical procedures. The algorithm was sufficient to capture the growth of instabilities in the wake on both structured and unstructured grids of reasonable density. Streamwise vortices were captured with between five and ten cells in both cases. Higher-order methods should be expected to retain a given solution quality while reducing the number of cells required. However, application of higher-order accurate methods on unstructured grids represents a more challenging exercise compared to the also difficult application of such methods on structured grids. A side-by-side comparison to a higher-order numerical method would provide important estimates of potential benefits from increased order of accuracy (and/or lower levels of numerical dissipation), in turn allowing one to determine the trade-offs between various approaches. DES predictions on the unstructured grid showed the potential benefit of the unstructured approach in guiding higher grid density into regions that benefit from finer meshes—in the near wake of the forebody. This study, however, is not a comprehensive testing of the numerics, since it only included experimental surface pressures for validation. More detailed comparisons, including quantities such as wake profiles and spectra, are needed to further assess the current approach.

Acknowledgments

The authors gratefully acknowledge the support of AFOSR Grant F49620-00-1-0050 (Program Manager: Dr. Tom Beutner). The bulk of the computations was performed at the Maui High Performance Computing Center (HPCC) and NAVO Major Shared Resource Center (MSRC). The support and CPU hours from each of these centers are gratefully acknowledged.

References

[1] Travin, A., Shur, M., Strelets, M., and Spalart, P., 2001, "Detached-Eddy Simulations past a Circular Cylinder," Flow, Turbul. Combust., **63**, pp. 293–313.

[2] Durbin, P. A., 1995, "Separated flow computations using the $k-\epsilon-v^2$ model," AIAA J., **33**, 4, p. 659.

[3] Shur, M., Spalart, P. R., Squires, K. D., Strelets, M., and Travin, A., "The Persistence and Effects of Three-dimensionality in Unsteady RANS Simulations of Two-dimensional Bluff Bodies," AIAA J. (to be published).

[4] Spalart, P. R., Jou, W.-H., Strelets, M., and Allmaras, S. R., 1997, "Comments on the Feasibility of LES for Wings, and on a Hybrid RANS/LES Approach," *Advances in DNS/LES, 1st AFOSR Int. Conference on DNS/LES*, 4–8 Aug. Greyden Press, Columbus, OH.

[5] Spalart, P. R., and Allmaras, S. R., 1994, "A One-Equation Turbulence Model for Aerodynamic Flows," Rech. Aerosp., **1**, p. 5.

[6] Spalart, P. R., 2000, "Strategies for Turbulence Modelling and Simulations," Int. J. Heat Fluid Flow, **21**, pp. 252–263.

[7] Constantinescu, S. G., and Squires, K. D., 2004, "Numerical Investigations of Flow over a Sphere in the Subcritical and Supercritical Regimes," Phys. Fluids, **16**, pp. 1449–1466.

[8] Forsythe, J. R., Squires, K. D., Wurtzler, K. E., and Spalart, P. R., 2004, "Detached-Eddy Simulation of the F-15E at High Alpha," J. Aircr., **41**, pp. 193–200.

[9] Mittal, R., and Moin, P., 1997, "Suitability of Upwind-Biased Finite Difference Schemes for Large-Eddy Simulation of Turbulent Flows," AIAA J., **35**, pp. 1415–1417.

[10] Polhamus, E. C., Geller, E. W., and Grunwald, K. J., 1959, "Pressure and Force Characteristics of Noncircular Cylinders as Affected by Reynolds Number with a Method Included for Determining the Potential Flow about Arbitrary Shapes," NASA TR R-46.

[11] Shur, M., Spalart, P. R., Strelets, M., and Travin, A., 1999, "Detached-Eddy Simulation of an Airfoil at High Angle of Attack," 4th Int. Symp. Eng. Turb. Modelling and Measurements, Corsica, 24–26, May.

[12] Strang, W. Z., Tomaro, R. F., and Grismer, M. J., 1999, "The Defining Methods of COBALT_{60}: A Parallel, Implicit, Unstructured Euler/Navier–Stokes Flow Solver," AIAA 99-0786.

[13] Gottlieb, J. J., and Groth, C. P. T., 1988, "Assessment of Riemann Solvers for Unsteady One-Dimensional Inviscid Flows of Perfect Gases," J. Comput. Phys., **78**, pp. 437–458.

[14] Karypis, G., Schloegel, K., and Kumar, V., 1997, "PARMETIS: Parallel Graph Partitioning and Sparse Matrix Ordering Library Version 1.0," University of Minnesota, Department of Computer Science, Minneapolis, MN.

[15] Hsu, K., and Lee, S. L., 1991, "A Numerical Technique for Two-Dimensional Grid Generation with Grid Control at All of the Boundaries," J. Comput. Phys., **11**, pp. 451–469.

[16] Steinbrenner, J., Wyman, N., and Chawner, J., 2000, "Development and Implementation of Gridgen's Hyperbolic PDE and Extrusion Methods," AIAA 00-0679.

[17] Morton, S. A., Forsythe, J. R., Mitchell, A., and Hajek, D., 2002, "Detached-Eddy Simulations and Reynolds-Averaged Navier-Stokes Simulations of Delta Wing Vortical Flowfields," ASME J. Fluids Eng., **124**, pp. 924–932.

Brian A. Edge[1]
e-mail: bae127@psu.edu

Eric G. Paterson
e-mail: eric-paterson@psu.edu

Computational Mechanics Division,
Applied Research Laboratory and Department of
Mechanical and Nuclear Engineering,
The Pennsylvania State University,
State College, PA 16804

Gary S. Settles
e-mail: gss2@psu.edu
Department of Mechanical and Nuclear
Engineering,
The Pennsylvania State University,
University Park, PA 16802

Computational Study of the Wake and Contaminant Transport of a Walking Human

The unsteady aerodynamic wake of a human is studied using a time-accurate computational fluid dynamics simulation. Transport of a scalar contaminant, which originates on the body, is also considered. An existing Reynolds-averaged Navier-Stokes solver is modified to include energy, scalar-transport, and thermal buoyancy effects. Structured overset grids are used to discretize the geometry and the flow field. Results indicate two distinct wake regions: an unsteady bluff-body wake behind the torso which is characterized by a mean recirculation zone, and a region of unsteady vortex shedding behind the legs which is dominated by a "jet" of air formed between the legs. A significant downwash occurs behind the body which has the effect of laterally spreading the lower portions of the wake. The magnitude of the scalar contaminant is shown to decay exponentially within the wake and is found to be highly dependent upon the source location.
[DOI: 10.1115/1.2013291]

1 Introduction

The aerodynamics of the human wake has received little attention in the engineering community. This work is intended to contribute to the physical understanding of the dynamics of the human wake using computational fluid dynamics simulations. The transport of a scalar contaminant from the surface of the body and the subsequent mixing by the wake is also studied. This information may be of interest to many areas of the engineering community such as homeland defense and cleanroom design, as well as the broader medical community. The current work focuses on the aerodynamic wake behind a simplified human form, neglecting the small scale details of the human body which tend to vary from person to person.

The flow about the human body can be classified as a bluff-body flow. Literature regarding bluff-body flows indicate that instabilities arising in the separating boundary layer will cause the wake to be unsteady [1–3]. Studies of three-dimensional bluff bodies, such as finite cylinders mounted on flat plates and the three-dimensional flow around tall buildings [4–7], can provide insight into the dynamics of the wake that may be expected from the human body. These studies indicate that a downwash occurs behind three-dimensional structures. The study of circular cylinders of various aspect ratios by Okamoto and Sunabashiri [4] show that cylinders with an aspect ratio of 3, which is similar to the human geometry of this study, will have a recirculation region extending four diameters downstream. Their results also show that a cylinder with an aspect ratio of 3 is at the transition between symmetric and anti symmetric vortex shedding. While the human form definitely differs from the geometries used in these studies, it is clear that we should expect a recirculation zone in the wake that is on the order of four body widths in length. No expectations regarding symmetric or anti symmetric vortex shedding can be drawn from the studies as our geometry is close to the aspect ratio associated with transition between these two modes.

The gap between the legs provides a significant geometrical difference with the three-dimensional bluff bodies studied in the literature. Several studies have been performed on two-dimensional circular cylinders in side-by-side configurations [8,9] which is similar to the two legs of our human model. These studies have identified three different regimes for the wake structure, with the first regime occurring when the cylinders are placed closely together. In a closely spaced configuration, the wake is similar to that of a single bluff body with a width equivalent to the two cylinders. This regime occurs for cylinder gaps of up to 20% of the cylinder diameters. Gap widths larger than 20% of the cylinder diameter are associated with the second regime and are characterized by individual wakes behind each cylinder. These wakes strongly effect one another until the gap width reaches 120% of the cylinder diamter. Gap widths greater than 120% of the diameter allow each cylinder to act as an independent bluff body, although some synchronization between the vortex streets was noted. These studies show us that the wake behind the legs, which have a gap width of 50% of the leg diameter, will likely behave similar to the wakes observed in the second regime of the previous studies. Each leg will likely have an independent wake that is heavily influenced by the neighboring wake. The actual

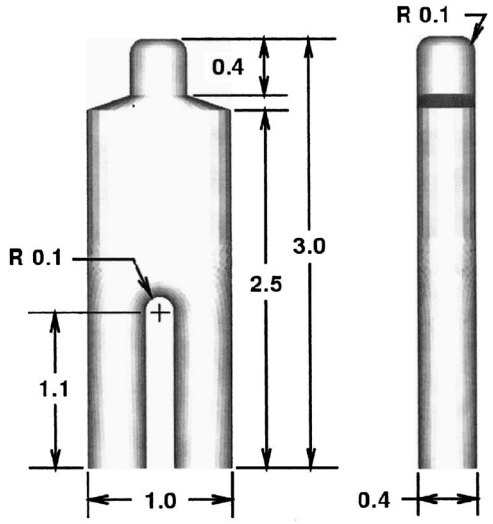

Fig. 1 Computational geometry shown with the nondimensional units (1.0 unit=0.58 m)

[1]Corresponding author.

Contributed by the Fluids Engineering Division for publication in the JOURNAL OF FLUIDS ENGINEERING. Manuscript received by the Fluids Engineering Division, November 11, 2004. Final Revision April 20, 2005. Associate Editor: Surya P Vanka.

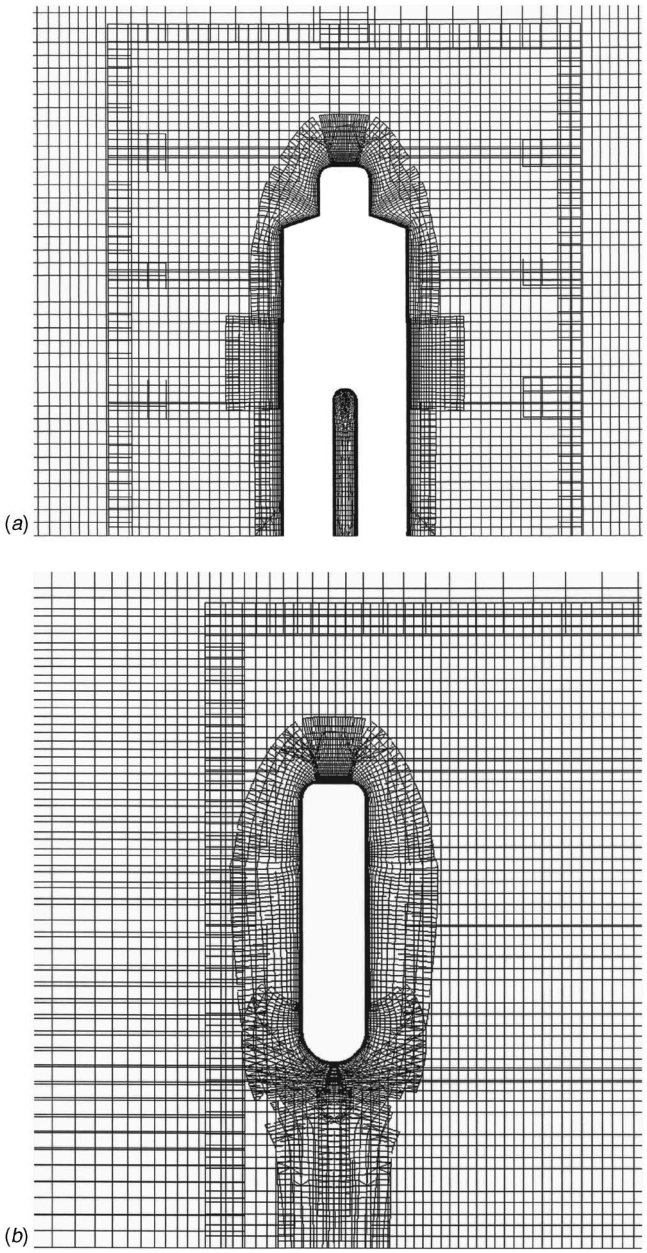

Fig. 2 Front (*a*) and side (*b*) details of the overset-grid system

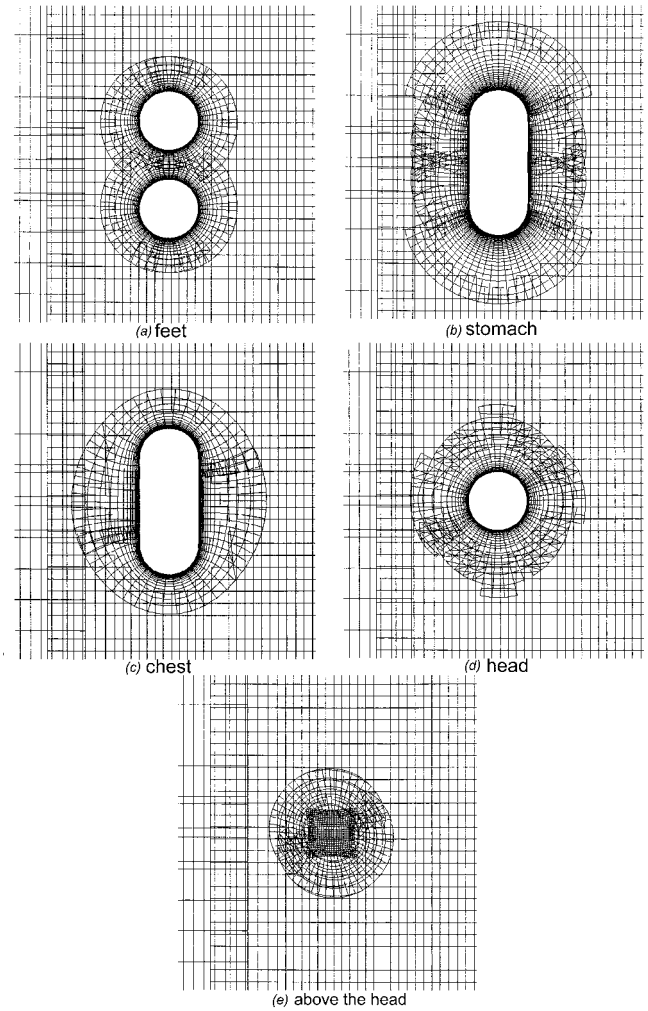

Fig. 3 Overset-grid layout: horizontal slices at various vertical elevations

behavior for this problem is difficult to determine in advance as the legs are not representative of the semi-infinite cylinders of the literature.

While the literature on bluff-body flows is quite numerous, there are also a few studies in the engineering literature regarding the human body. The flow about a stationary human in a quiescent environment was investigated decades ago by Lewis et al. [10] and Clark and colleagues [11,12], and more recently by Gowadia et al. [13], Settles and McGann; [14], Settles et al. [15], Gowadia and Settles [16], Gowadia [17], and Homma [18]. These works show the existence of a naturally occurring flow, known as the human thermal plume, with velocities of up to 1/4 m/s and volumetric flow rates of 50 l/s. When an external flow is combined with the buoyant human thermal plume, the relative importance of the buoyancy driven flow is deduced from the Richardson number Ri, which is the ratio of the Grashof number to the square of the Reynolds number, $\mathrm{Gr}/\mathrm{Re}^2$. The Reynolds number is defined as $\mathrm{Re}=U_0L/\nu$ where U_0 is the average velocity of the free stream flow, L is the characteristic length of the problem, and ν is the kinematic viscosity of the fluid. The Grashof number is $\mathrm{Gr}=g\beta\Delta TL^3/\nu^2$ where g is the gravitational constant, β is the volumetric thermal expansion coefficient, and ΔT is the temperature difference between the body and the free-stream air. When Ri is $\gg 1$, as it is for the human thermal plume, free convection dominates the flow. For a walking human, Re increases with walking speed which tends to reduce Ri. When Ri becomes much less than 1, forced convection dominates the flow and the free convection becomes negligible.

Research is quite limited for the aerodynamics of the human wake that develops under dominant external flow ($\mathrm{Ri}\ll 1$). Most studies of the human form have focused on thermal issues of the human body [19,18], measurement and prediction of the drag characteristic of a walking person [20], or lateral airflow studies motivated by air pollution control and reduction of worker exposure [21–23]. Murakami et al. [20] performed a three-dimensional steady-state computational simulation of the lateral flow about a human form under flow speeds of 0.25 and 2.5 m/s which correspond to Re (based upon body width) of 8×10^3 and 8×10^4, respectively. The authors, who were primarily focused upon predicting the thermal properties and drag, provide little discussion of the dynamics of the wake.

The human form used by Murakami et al. does not resolve separate legs with a gap between. While this geometry is quite acceptable for studies of lateral flow, ongoing experimental work

Table 1 Initial conditions and boundary conditions

Description	U	V	W	Φ	P	k	ω	ν_t
Initial conditions	0	0	0	0	0	10^{-7}	9.0	1.1
Inlet	1.0	0	0	0	0	1×10^{-7}	9.0	1.1×10^{-8}
Exit	$\frac{\partial^2 U}{\partial \xi_i^2}=0$	$\frac{\partial^2 V}{\partial \xi_i^2}=0$	$\frac{\partial^2 W}{\partial \xi_i^2}=0$	$\frac{\partial \Phi}{\partial \xi_i}=0$	$\frac{\partial P}{\partial \xi_i}=0$	$\frac{\partial k}{\partial \xi_i}=0$	$\frac{\partial \omega}{\partial \xi_i}=0$	$\frac{\partial \nu_t}{\partial \xi_i}=0$
Far-field	1.0	0	0	$\frac{\partial \Phi}{\partial \xi_i}=0$	$\frac{\partial P}{\partial \xi_i}=0$	$\frac{\partial k}{\partial \xi_i}=0$	$\frac{\partial \omega}{\partial \xi_i}=0$	$\frac{\partial \nu_t}{\partial \xi_i}=0$
Impermeable-slip, no force	See text	See text	See text	$\frac{\partial \Phi}{\partial \xi_i}=0$	$\frac{\partial P}{\partial \xi_i}=0$	$\frac{\partial k}{\partial \xi_i}=0$	$\frac{\partial \omega}{\partial \xi_i}=0$	$\frac{\partial \nu_t}{\partial \xi_i}=0$
No-slip	0	0	0	1	$\frac{\partial P}{\partial \xi_i}=0$	0	$\frac{60}{\mathrm{Re}\,0.075\Delta^2}$	0

by the Gas Dynamics Laboratory at The Pennsylvania State University indicates that the leg separation has a significant effect on the structure of the wake for flows in the primary walking direction [24]. This experimental work consisted of flow visualizations of the wake behind a walking person and measurement of the decay rate of a passive scalar originating from the surface of the human body. The Gas Dynamics Laboratory work shows the wake structure characterized by considerable intermittency at the boundaries and an obvious left-right vortex shedding which is characteristic of bluff-body wakes. The wake shows little lateral growth to a distance of about three body widths down-stream, followed by a quasilinear growth attributed to turbulent mixing. This work also indicates that the swinging of arms during walking has little significance in the formation of the wake. A passive scalar tracer, placed on the frontal midriff of a walking person, was found to decay rapidly in an exponential fashion.

The focus of the present work is to investigate the dynamics of the human wake and transport of a scalar surface contaminant using computational fluid dynamics simulation tools. This work involves the solution of the three-dimensional unsteady Reynolds-averaged Navier-Stokes equations with thermal buoyancy effects and scalar transport. The following sections will introduce the simplified human geometry, the governing equations, and the numerical methods that were used to solve the equations. A brief review of the computational uncertainty is presented, followed by results, conclusions, and recommendations for future work.

2 Model Equations

The flow about the human form is modeled with the nondimensional unsteady Reynolds-averaged Navier-Stokes (URANS) equations in the incompressible form.

$$\frac{\partial U_i}{\partial X_i}=0 \tag{1}$$

$$\frac{\partial U_i}{\partial t}+U_j\frac{\partial U_i}{\partial X_j}=-\frac{\partial P}{\partial X_i}+\left(\frac{1}{\mathrm{Re}}+\nu_t\right)\frac{\partial^2 U_i}{\partial X_j\,\partial X_j}+\frac{\partial \nu_t}{\partial X_j}\left(\frac{\partial U_i}{\partial X_j}+\frac{\partial U_j}{\partial X_i}\right)+\delta_{i3}\frac{\mathrm{Gr}}{\mathrm{Re}^2}\Theta \tag{2}$$

$$\frac{\partial \Theta}{\partial t}+U_i\frac{\partial \Theta}{\partial X_i}=\left(\frac{1}{\mathrm{Re\,Pr}}+\frac{\nu_t}{\mathrm{Pr}_t}\right)\frac{\partial^2 \Theta}{\partial X_j\,\partial X_j}+\frac{1}{\mathrm{Pr}_t}\frac{\partial \nu_t}{\partial X_j}\left(\frac{\partial U_i}{\partial X_j}+\frac{\partial U_j}{\partial X_i}\right)-\frac{2}{3}\frac{\partial k}{\partial X_i} \tag{3}$$

where the velocity terms are nondimensionalized by the free stream velocity ($U_i=u_i/U_0$), the Cartesian coordinates are nondimensionalized by the characteristic length ($X_i=x_i/L$), and the temperature values are nondimensionalized by the body temperature

$$\Theta=\frac{T(x,t)-T_\infty}{T_{\mathrm{body}}-T_\infty} \tag{4}$$

Pr is the Prandtl number defined as $\mathrm{Pr}=C_p\mu/k_t$ where C_p is the specific heat at constant pressure, μ is the dynamic viscosity, and k_t is the thermal conductivity. The contaminant is modeled using a scalar transport equation which assumes the mass and volume fractions are negligible, the contaminant is one-way coupled with the flow, and the contaminant has the same velocity as the local fluid. The contaminant is also assumed to have no effect on the turbulence in the carrier fluid.

$$\frac{\partial S}{\partial t}+U_i\frac{\partial S}{\partial X_i}=\left(\frac{1}{\mathrm{Re\,Sc}}+\frac{\nu_t}{\mathrm{Sc}_t}\right)\frac{\partial^2 S}{\partial X_j\,\partial X_j}+\frac{1}{\mathrm{Sc}_t}\frac{\partial \nu_t}{\partial X_j}\left(\frac{\partial U_i}{\partial X_j}+\frac{\partial U_j}{\partial X_i}\right)-\frac{2}{3}\frac{\partial k}{\partial X_i} \tag{5}$$

The Schmidt number, Sc is defined as $\mathrm{Sc}=\nu/D_{AB}$ where D_{AB} is

Table 2 Computational resources

Grid resolution	Number of blocks	Total points	Maximum points/block	Memory per processor (Mb)	Wall clock time per time step (s)
Fine	31	2.8 million	131,000	295	347
Intermediate	17	1 million	78,000	107 (est.)	60
Coarse	17	371,000	29,000	40 (est.)	11

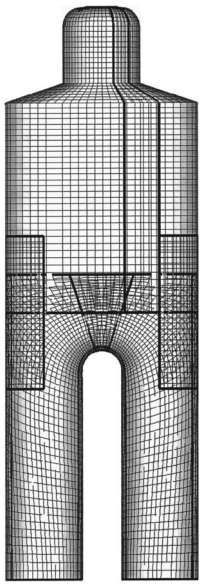

Fig. 4 Layout of the surface grids on the computational geometry

the mass diffusivity. The set of equations are closed by means of a linear stress-strain closure with an eddy viscosity computed by the two-equation blended k-ϵ/k-ω model of Menter [25]. While the k-ϵ model does a fine job predicting free stream turbulence quantities, the k-ω model has been shown to more accurately predict separation of boundary layer flows in adverse pressure gradients. Menter's model smoothly blends from the k-ω model near no-slip surfaces to the k-ϵ model in the free stream and wake.

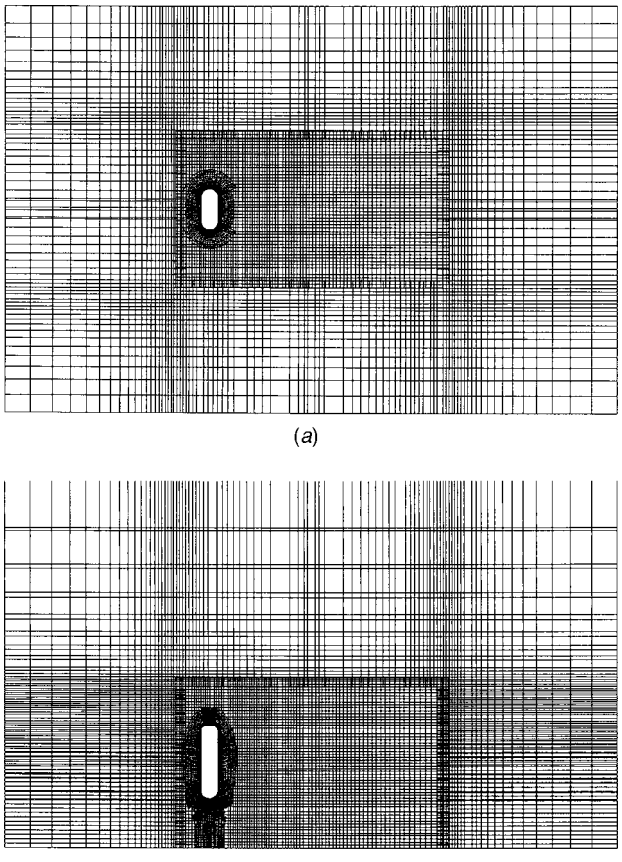

(*a*)

(*b*)

Fig. 5 Top (*a*) and side (*b*) views of the full overset-grid domain

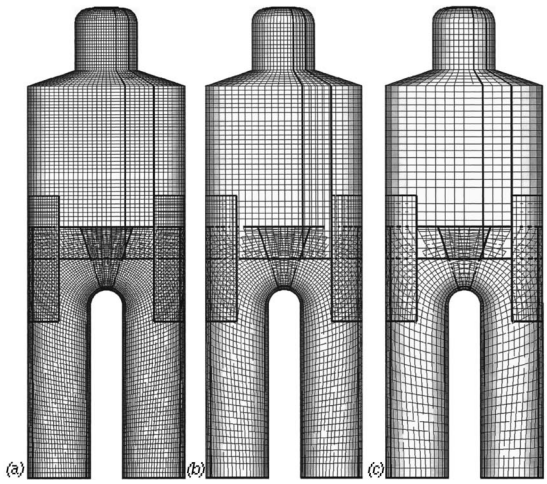

Fig. 6 a View of the fine (*a*), intermediate (*b*), and coarse (*c*) surface grids which were used in the grid refinement study

3 Geometry and Flow Conditions

The human body varies from person to person and can even change based upon the clothing worn. Considering all the variability, a simplified form, shown in Fig. 1, was chosen for this

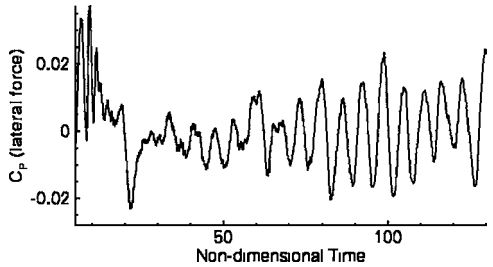

Fig. 7 Coefficient of pressure in the lateral direction versus nondimensional time as computed on the medium grid

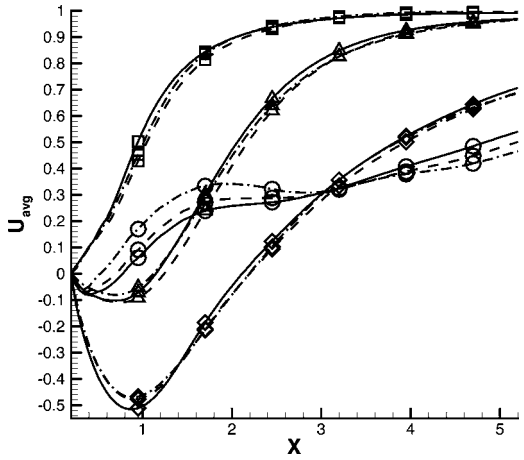

Fig. 8 Computed-mean *U* velocity for three different sample sizes versus downstream distance *X*. The line types define the sample set: — 150 time units, – – – 100 time units, and – - – 50 time units. The symbols define the location of the sample: □ head, △ chest, ◇ stomach, and ○ feet. U_{avg} is the nondimensional average velocity and *X* is the nondimensional distance downstream of the body.

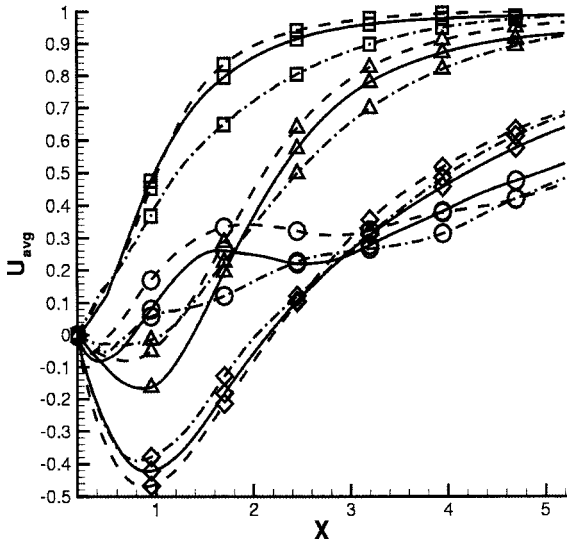

Fig. 9 Computed-mean *U* velocity of the three grid resolutions versus downstream distance at nondimensional time 50. The line types define the grid resolution: — fine grid, – – – medium grid, and – - – coarse grid. The symbols define the location of the sample: □ head, △ chest, ◇ stomach, ○ feet.

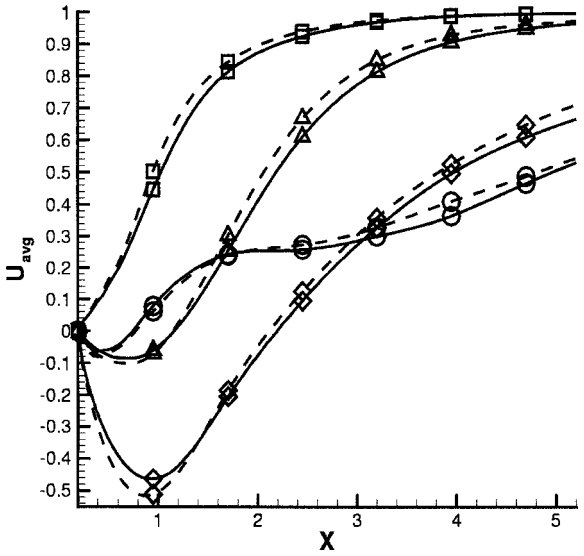

Fig. 11 Computed-mean *U* velocity at nondimensional time 50 for two different time step sizes. The line types represent the nondimensional time step size: — Δt=0.005, – – – Δt=0.01. The symbols represent the location of the sample: □ head, △ chest, ◇ stomach, and ○ feet.

computational work. The geometry is representative of a human with hands at the side and consists of a head, torso, and separate legs. The dimensions are derived from the human model used in the work of the Penn State Gas Dynamics Laboratory [24] and are nondimensionalized by the width of the shoulders (L=0.58 m).

The flow conditions are based upon a walking speed (U_0) of 1.34 m/s and a temperature difference between the body and the surrounding air of 10 K. This leads to Re=53,000 ($\nu=1.43\times10^{-5}$ m^2/s), and Gr=3.05×10^8 (g=9.81 m/s^2, β=0.0034 K^{-1}). The corresponding Ri of 0.109, indicates that the flow is dominated by forced convection. The flow is also assumed to have a Pr=0.693 [C_p=1.007 kJ/(kgK), $k=26\times10^{-3}$ W/(mK)] and Sc, for lack of experimental data, is assumed to have the same value as Pr.

4 Numerical Methods

Equations (1)–(5) are discretized in a grid-based coordinate system as outlined in Paterson et al. [26]. The temporal terms are discretized using the second-order backward difference for all but the first time step, where a first-order backward difference method is used. The spatial convective terms are discretized using a second-order upwind scheme while the diffusive terms are discretized using second-order accurate central-difference methods. The solver utilizes a segregated approach to the equations and handles the pressure and velocity coupling using the pressure-implicit with splitting of operators approach of Issa [27]. The Computational fluid dynamics code has been used and validated for many applications, e.g., complex bluff-body drag prediction [28], trailing-edge detached-eddy simulations [29], propulsion structural acoustics [30], jet cavitation [31], and Coanda-effect circulation control [32].

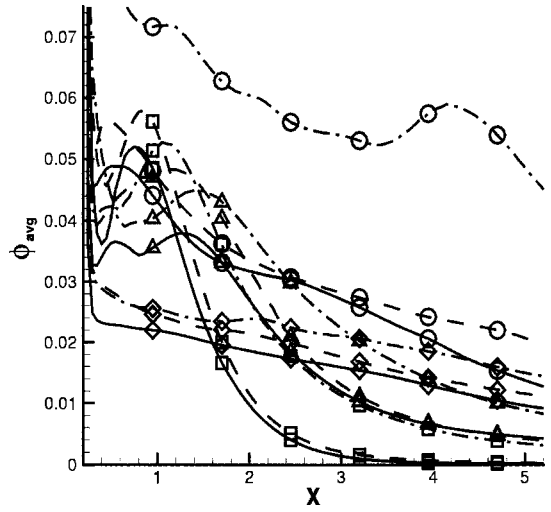

Fig. 10 Computed-mean scalar quantity for the three grid resolutions versus downstream distance at nondimensional time 50. The line types define the grid resolution: — fine grid, – – – medium grid, and – - – coarse grid. The symbols define the location of the sample: □ head △ chest, ◇ stomach, and ○ feet. The values of the computed-mean scalar quantities go to a limit of 1 at the body source *X*=0.

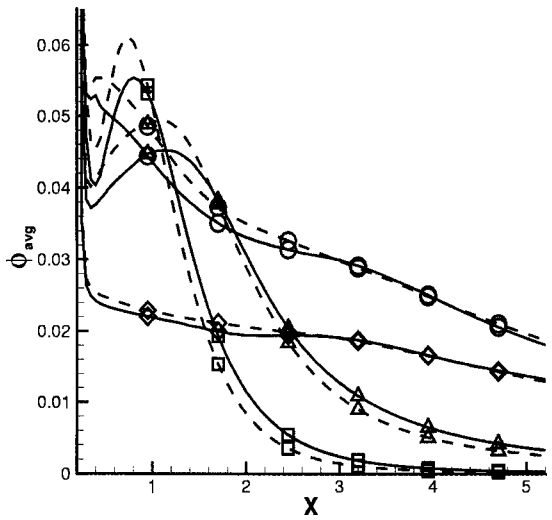

Fig. 12 Computed-mean scalar quantity at nondimensional time 50 for two different time step sizes. The line types represent the nondimensional time step size: — 0.005, and – – – Δt =0.01. The symbols represent the location of the sample: □ head, △ chest, ◇ stomach, and ○ feet.

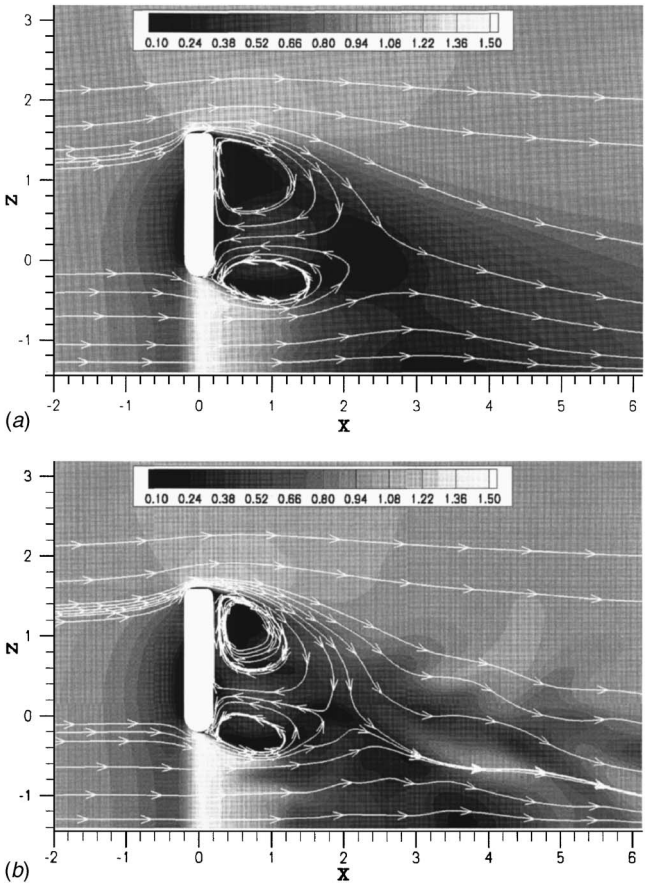

Fig. 13 Computed-mean (*a*) and instantaneous (*b*) total velocity magnitude with tangential streamlines in a vertical slice through the body centerline

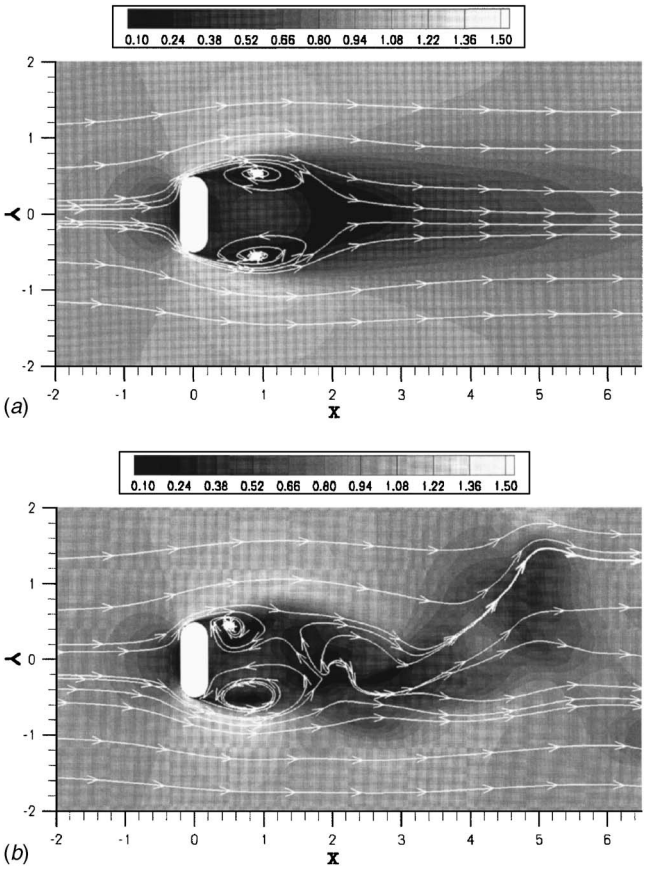

Fig. 14 Computed-mean (*a*) and instantaneous (*b*) total velocity magnitude with tangential streamlines in a horizontal slice through the stomach

The initial and boundary conditions for the dependent variables are listed in Table 1. The "impermeable-slip, no force" boundary condition is formulated using contravariant velocity components at one point off the boundary where the tangential components are computed assuming zero stress and the normal component is set to zero. This boundary condition is used on the bottom surface of the domain to approximate the ground below a walking person. Note that Δ, in the equation for ω, is defined as the distance to the first grid point off the no-slip surface. More details regarding the formulation of the boundary conditions can be found in Paterson et al. [26].

5 Grid Generation

The computational domain is an assembly of structured overset grids which are shown in Figures 2 and 3 [33,34]. The surface grids on the body, shown in Fig. 4, are extruded hyperbolically from the surface with an initial grid spacing of 1.43×10^{-4}, which corresponds to a y^+ value of less than 1. The y^+ term represents the viscous length and is defined as $y^+=u_\tau y/\nu$ where y is the dimensional distance to the wall, ν is the kinematic viscosity, and u_τ is the friction velocity defined as $u_\tau=\sqrt{\tau_w/\rho}$, where τ_w is the wall shear stress and ρ is the density [35]. Placing the first grid point at $y^+\leqslant 1.0$ ensures a sufficient number of grid points within the buffer layer, where turbulent production rapidly increases. This also ensures that the total number of grid points within the boundary layer are between 15 and 20 for these simulations.

The far-field boundaries are placed 4.8 units upstream, 4.5 units to the side, and 9.8 units downstream (one unit corresponds to the width of the body). The full domain is shown in Fig. 5. Notice the use of nested box grids, shown clearly in Fig. 5, to provide greater resolution in the near-wake regions of the flow.

Three different grid resolutions, depicted in Fig. 6, were used for a grid refinement study. The intermediate grid was generated from the fine grid by using linear interpolation to increase the grid spacing by a factor of $\sqrt{2}$ in all grid directions. The coarse grid is generated from the intermediate grid in the same manner. Table 2 lists the physical and computational sizes of each grid, where we see that the finest grid consists of more blocks than either the intermediate or coarse grids. This is a result of splitting the largest blocks for load balancing during parallel computations. The computer resource requirements are based upon an IBM SP system with 1024 Power3 processors running at 375 MHz. The computational fluid dynamics code is parallelized using the message passing interface standard which allows each individual block to be computed on a dedicated CPU.

6 Numerical Uncertainty

Numerical uncertainty is investigated through the comparison of results from three systematically refined grids and two different time step sizes. As the flow is naturally unsteady, the computed-mean quantities of the flow are used as the verification metrics. This method of comparison is not without difficulties since the exact mean quantities can only be obtained in the limit of an infinite sample. We can therefore expect the computed-mean to contain numerical sampling errors which can only be reduced by collecting a sample that is substantially longer than the lowest frequency fluctuations in the flow field, or by capturing an exact integer value of the fluctuations (assuming that they are repeating fluctuations, which is unlikely for a nonlinear problem with multiple length scales). Reducing the error to a value that is very

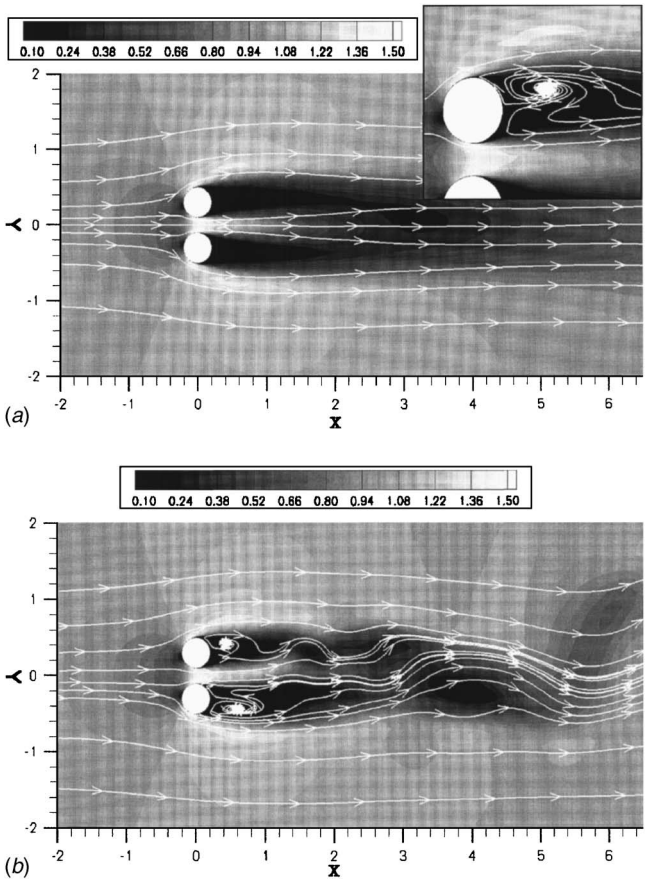

Fig. 15 Computed-mean (*a*) and instantaneous (*b*) total velocity magnitude with tangential streamlines in a horizontal slice through the ankles

small in comparison with the signal is quite expensive for these naturally unsteady flows, especially in regions where the mean velocity is small compared with the fluctuations.

The unsteady flow is started from a zero velocity field and a transient period exists where the flow transitions to the quasisteady, or stationary, flow state. Figure 7 shows the time history of the integrated surface pressure force coefficient C_p associated with lateral forces (i.e., perpendicular to the walking direction). This figure indicates that the solution does not reach its quasisteady state values until after a nondimensional time of 50. Ideally, the

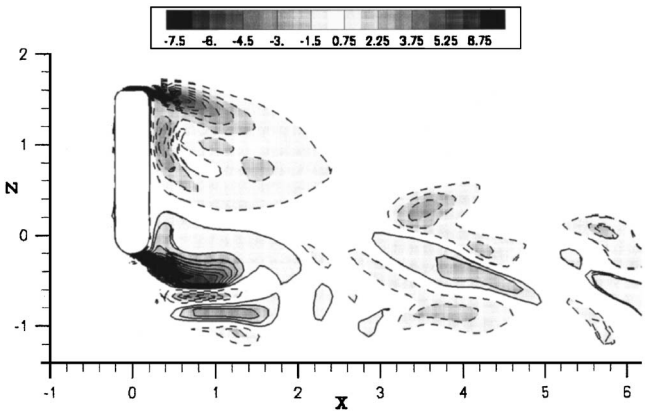

Fig. 16 Instantaneous vorticity for a vertical slice through the body centerline. Positive vorticity is bounded by solid lines and negative vorticity is bounded by dashed lines.

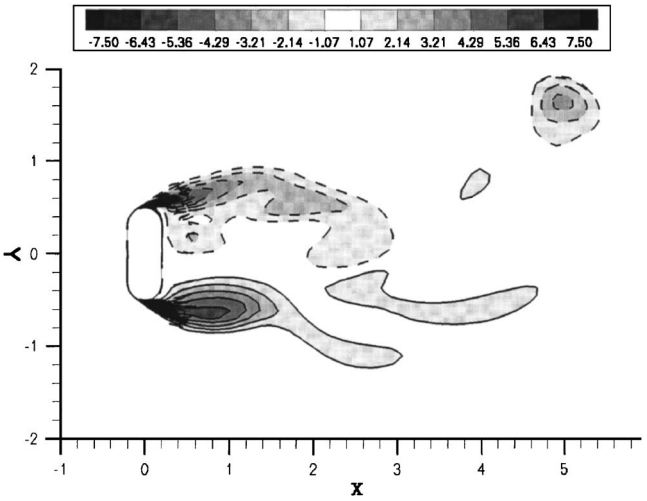

Fig. 17 Instantaneous vorticity for a horizontal slice through the stomach. Positive vorticity is bounded by solid lines and negative vorticity is bounded by dashed lines.

computed-mean sampling would begin after this point, however the computational expense associated with this simulation made it prohibitively expensive to rerun the simulations after obtaining this information. All time-averaged quantities presented in this paper represent samples taken from a starting time of zero through the specified ending time.

The computational expense for the finest grid is also substantial, requiring almost 350 (s) per time step. The computed-mean quantities from this grid are based upon a sample collected over a nondimensional time of 50, whereas the computed-mean samples from the other grids were collected over a nondimensional time of 150. Although the quasisteady state has not been reached for the body forces, some portions of the flow field have reached a quasisteady state as seen in Fig. 8. The computed-mean U velocity at several locations in the wake of the body are compared at nondimensional times of 50, 100, and 150. Figure 8 shows that the computed-mean solutions behind the head, chest, and stomach show little change between the 50, 100, and 150 time unit samples, whereas the solution behind the lower portion of the wake shows some variation. It is reasonable to conclude that the present grid study, which compares the time-averaged solutions for the upper wake, will provide reasonable assurances that grid convergence has been reached.

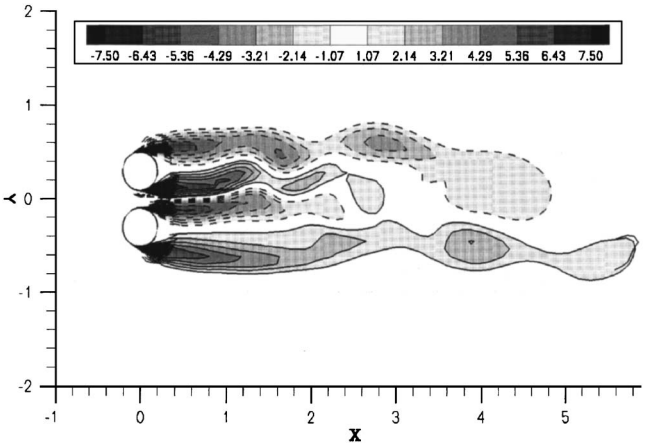

Fig. 18 Instantaneous vorticity for a horizontal slice through the ankles. Positive vorticity is bounded by solid lines and negative vorticity is bounded by dashed lines.

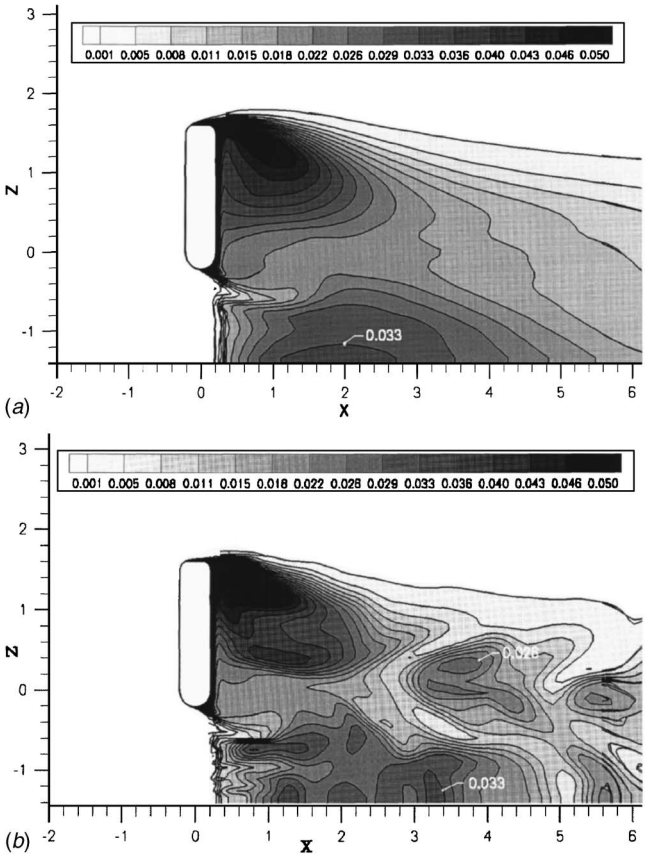

Fig. 19 Computed-mean (*a*) and instantaneous (*b*) scalar magnitude contours from a vertical slice through the centerline of the body

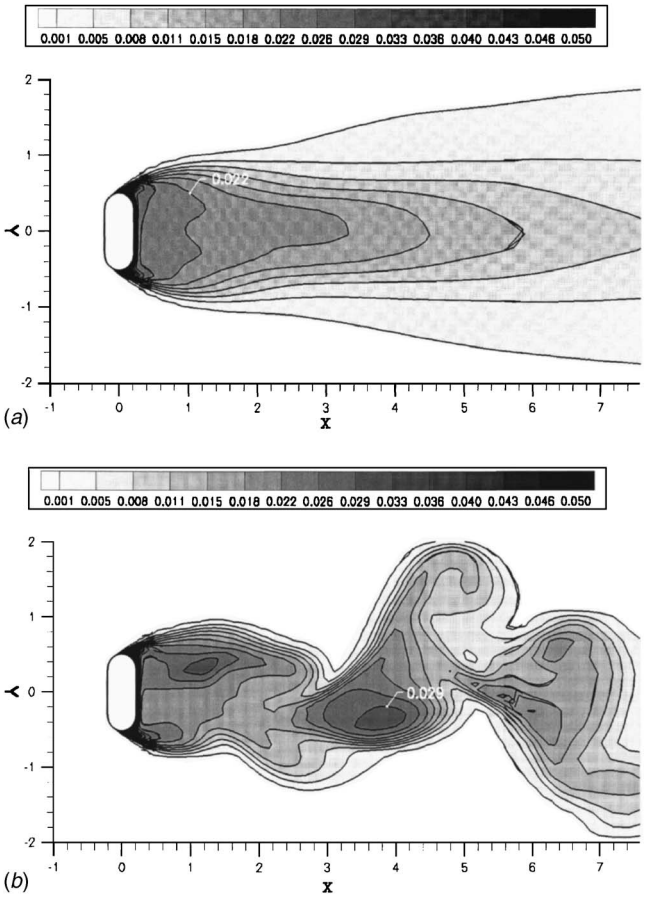

Fig. 20 Computed-mean (*a*) and instantaneous (*b*) scalar magnitude contours from a horizontal slice through the stomach

The grid study consists of three systematically refined grids where each successively refined grid reduces the mesh spacing by a factor of $\sqrt{2}$ in all directions. Comparing the results of the U velocity obtained from each grid, shown in Fig. 9, we see that similar results are obtained in the upper wake for all three grids and the solutions vary behind the lower wake, as anticipated. Although the solutions in the upper wake are similar, there is no consistency in the manner of convergence, i.e., the solutions converge in an oscillatory manner in some locations and in a monotonic fashion elsewhere. This is most likely due to the inclusion of the initial transient period in the time samples. While the results provide confidence that the grids are sufficiently refined to provide solutions to the governing equations, no quantitative estimates can be made regarding the magnitude of the numerical error. The computed-mean scalar concentration, shown in Fig. 10, leads to similar conclusions, except in the lower wake where the solutions are expected to differ. Although the sample size is not sufficiently large to obtain quantitative estimates of the numerical error, we feel confident in saying that the grids are sufficiently refined to provide plausible results for this problem.

While spatial discretizations account for part of the numerical error, temporal discretizations also contribute. Evaluation of these temporal contributions is performed through a time step study, the results of which are shown in Figs. 11 and 12. The nominal nondimensional time step size of 0.01 is represented by the dashed line and the finer time step size of 0.005 is shown in the solid line. While it is not possible to quantitatively evaluate convergence of the solutions, it is apparent from these figures that both solutions provide a similar estimate for the computed-mean velocity field, even in the lower wake region. The computed-mean scalar results also show good agreement.

Although a quantitative estimates of the numerical errors is not possible, these studies provide confidence that the medium grid resolution and finest time step size are appropriate choices for providing solutions to this problem. The solutions show convergence with grid refinement and little change is observed with the halving of the time step size.

7 Results and Conclusions

The numerical methods and grid presented in the previous sections are applied to two different cases of contaminant distribution at a single set of flow conditions as described in Sec. 3. The first part of this section will deal with the dynamics of the wake behind the human form and the second part will deal with transport of a scalar contaminant from the surface of the body. Two cases of contaminant distribution will be considered: a uniformly distributed contaminant over the entire surface of the body, and a localized patch of contaminant located on the frontal midriff of the body.

7.1 Fluid Dynamics. The fluid dynamics of the human wake are shown through plots of the velocity field. Figures 13–15 show contours of total velocity with tangential streamlines superimposed. The figures labeled as "*a*" show the computed-mean total velocity while the figures labeled as "*b*" show an instantaneous realization of the unsteady flow field. Figure 13 shows a slice of the flow field through the median plane of the body. This image shows a mean recirculation region in the upper wake (behind the torso) and a "jet" protruding from between the legs. The unsteady flow field also shows the recirculation zone, albeit with fluctuations in both the direction and magnitude of the velocity field. The recirculation region, as viewed from above, is shown in Fig. 14. This view represents a horizontal slice through the stomach at a constant elevation (i.e., Z=constant) and it confirms the existence

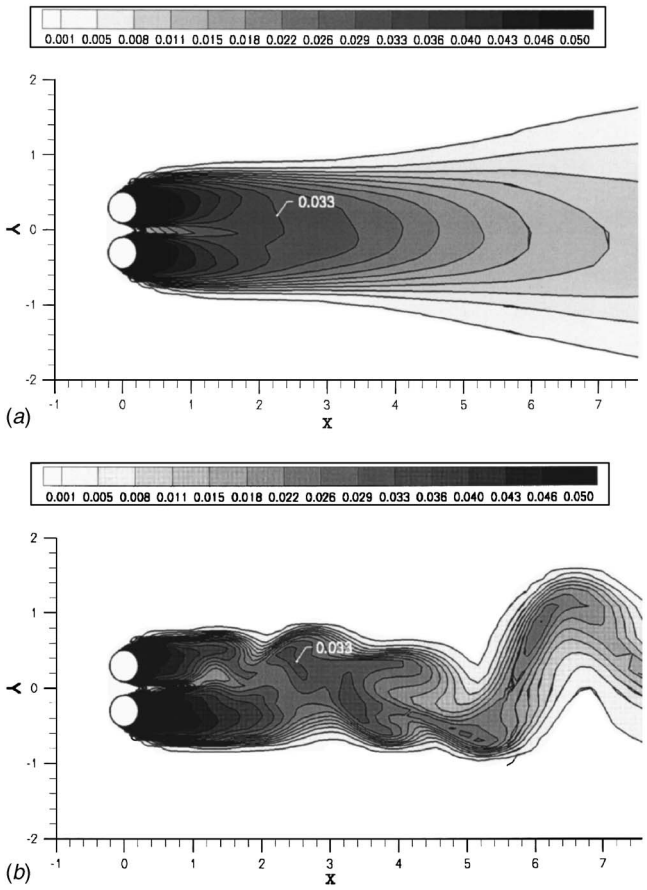

Fig. 21 Computed-mean (*a*) and instantaneous (*b*) scalar magnitude contours from a horizontal slice through the ankles

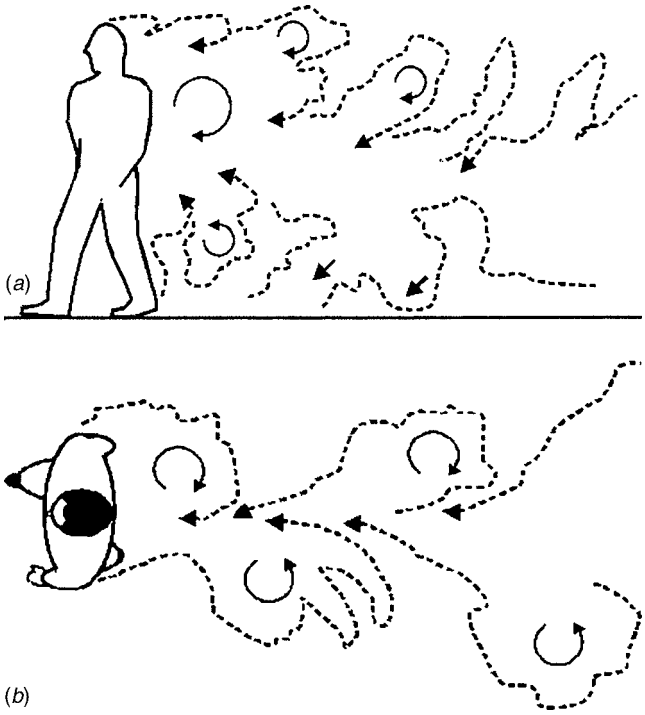

Fig. 22 Sketches of the significant physics observed in the flow visualization experiments performed by the Penn State Gas Dynamics Laboratory. (*a*) Vertical plane and (b) horizontal plane.

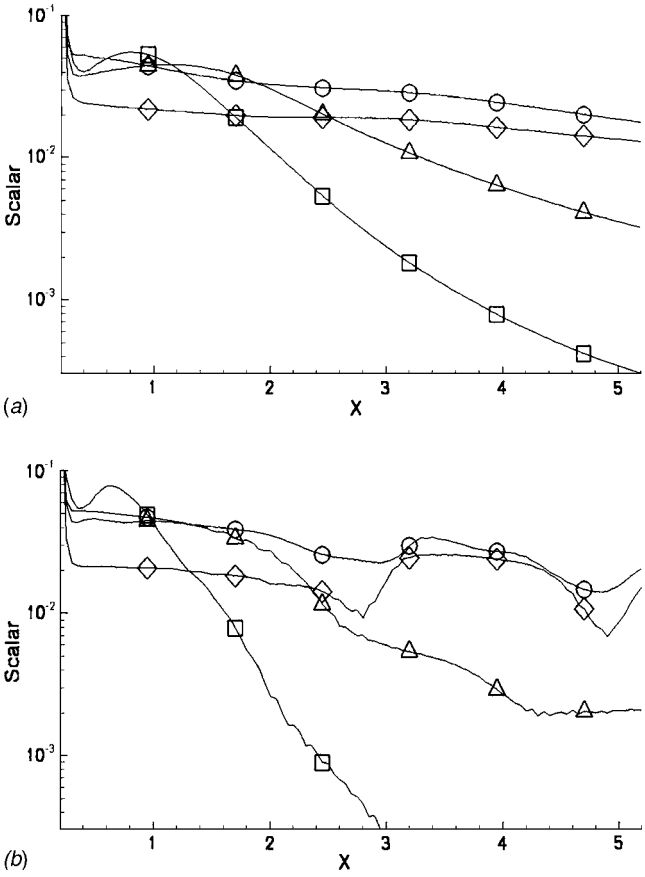

Fig. 23 Computed-mean (*a*) and instantaneous (*b*) scalar magnitude versus non-dimensional downstream distance *X* for the uniform contaminant source. Symbols define sample location: □ head, △ chest, ◇ stomach, and ○ feet.

of a mean recirculation region behind the torso. The instantaneous realization is considerably less symmetric, which suggests that the unsteady wake consists of asymmetric vortex shedding. Also note a large deviation in the wake velocity field 5 diameters downstream which indicates the existence of large-scale flow structures advecting downstream. The velocity field in the lower wake is presented in Fig. 15, which shows a horizontal slice through an elevation corresponding to the ankles. This figure clearly shows the "jet" between the legs with a magnitude that is roughly 30% greater than the free stream velocity. The computed-mean flow field (see the inset) shows the existence of a single recirculation in the wake region that is biased toward the outer side of the leg.

The vorticity within the wake region also provides some details of the wake dynamics. The instantaneous vorticity is presented in Figs. 16–18, with contours showing the magnitude of the out-of-plane vorticity. Figure 16, presenting the out-of-plane vorticity within the median plane, shows a strong negative vorticity concentration convecting off the head/shoulders and an even stronger vorticity concentration from the leg-body interface. Note that both vorticity concentrations follow the contour of the torso recirculation region and appear to be drawn downward as they are convected downstream. These observations, in conjunction with the observations of the velocity contours in Fig. 13, indicate the existence of a "downwash" behind the walking person in this Re regime.

Vorticity in the vertical direction ω_z is shown in Fig. 17, for the horizontal plane through the stomach. This plane shows the generation of strong vorticity regions along the side of the torso and the formation of left-right vortex shedding. Lateral spreading of the vorticity concentrations can be seen in the downstream wake (see the upper-right corner of Fig. 17). The lateral spreading is believed to occur by a combination of the asymmetric vortex

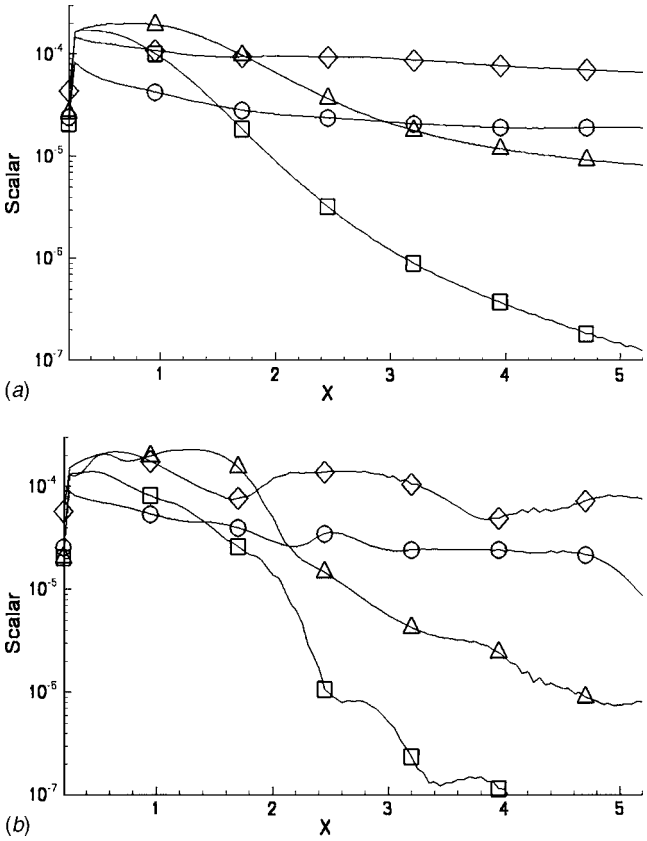

Fig. 24 Computed-mean (*a*) and instantaneous (*b*) scalar magnitude versus *X* for the localized contaminant source. Symbols define sample location: □ head, △ chest, ◇ stomach, and ○ feet.

shedding and the "downwash" noted earlier. The "downwash" causes lateral spreading as the fluid from the upper torso flows toward the ground where conservation of mass dictates that the lower wake region will expand. It should also be noted that the vortex in the upper right-hand corner corresponds with the large "hook" in the downstream wake of Fig. 14.

The vorticity in the lower wake behind the legs is presented in Fig. 18. The higher velocity of the "jet" tends to stretch the vorticity regions quite far when compared to the diameter of the legs before vortex shedding occurs two units downstream. Each leg appears to initiate left-right vortex shedding with the inner vortices quickly destroyed, leaving only the outer vortices to interact as vortex pairs. It is difficult to determine if the outer vortices pair in a symmetric or asymmetric manner.

7.2 Scalar Contaminant. The first contaminant boundary condition considered here consists of a uniform contaminant with a nondimensional magnitude of 1.0 over the entire surface of the body. The second boundary condition consists of a small localized patch of contaminant placed on the frontal midriff of the body.

The computed-mean and instantaneous contours of contaminant are shown in Figs. 19–21 for the first boundary condition. Figure 19 shows that the upper wake recirculation region contains higher levels of contaminant than the lower portion of the wake. This is a consequence of the surface area parallel to the flow on the shoulders and head. The lower portion of the recirculation region has much lower levels of contaminant due to the smaller surface between the legs which is the effective source of the contaminant.

A horizontal slice at the stomach is presented in Fig. 20. This figure shows the steady decay of the contaminant behind the body and the increased spreading of the wake around $X>2$. The increase in spreading of the contaminant is likely due to the combined effects of the left-right vortex shedding and the "downwash" effect. A horizontal slice through the ankles, Fig. 21, shows much higher concentrations of contaminant behind the legs, compared to the torso. This is due to the smaller recirculation zone and the increase in surface area supplying the contaminant. The computed-mean solution shows that the wake spreading does not become evident near the floor until $X>4$. The unsteady contaminant magnitudes seem to correlate well with the unsteady vorticity magnitudes of Fig. 18.

It is interesting to note that these computational results share many of the bulk flow structures that were observed in smoke visualization experiments performed at the Penn State Gas Dynamics Laboratory. Figure 22 shows artistic sketches of the bulk characteristics of the observed wake. The experiments showed considerable intermittency of the contaminant in the wake region and an observed lateral spreading of the wake around $X=3$ body widths downstream. These results are quite similar to the computational results depicted in Figs. 19 and 20.

The magnitude of the contaminant downstream of the body is shown in Figs. 23. It should be noted that the samples behind the ankle were taken directly behind the leg, not on the median plane of the flow. These figures highlight the exponential decay of the scalar quantity with downstream distance. This result is significant to applications that require sampling of the contaminant from the wake. The results imply that a sensor must be capable of detecting levels of the contaminant that are several orders of magnitude lower than the contaminant levels found at the surface of the body.

Results from the localized boundary condition are shown in Fig. 24. As we might expect from a drastically reduced surface area of the source, the contaminant magnitude in the wake is significantly lower than the levels observed in the previous case. From Fig. 24 we see that the exponential decay nature of the contaminant has not changed and its relative distribution throughout the wake remains surprisingly constant. This indicates that significant mixing is occurring between the various wake regions.

8 Summary and Recommendations

This paper has presented the results of an unsteady RANS simulation of the human aerodynamic wake and the transport of a scalar contaminant from the surface of the body. The results indicate the presence of a recirculation zone in the upper portion of the wake which persists from the head down to the legs. The recirculation region ends at the legs where it is broken up by the jet formed between the legs. The results also indicate a "downwash" that tends to spread the wake, and thus the contaminant, laterally behind the lower torso and legs.

Concentrations of a uniformly distributed contaminant within the wake are highest behind the shoulders and the legs. The higher concentrations correspond to locations where source areas are oriented parallel to the flow. Results of the localized contaminant show that the source location and size are important for determining the magnitude of the scalar throughout the wake, however, for the specific localized condition discussed here, these properties had little effect on the relative distribution of the contaminant.

Based on this work, several recommendations are provided for future studies. First, a wind tunnel experiment is currently in progress, the purpose of which is to acquire validation data. Near-term work should include comparing these experiments to the computational data with the goal of estimating model uncertainty. Second, a parametric study of walking speeds (i.e., Reynolds number), physiological body form, and clothing-related variability (i.e., robes and dresses) is recommended since these variables have potentially large impact on the wake dynamics.

Acknowledgment

This work was made possible by an Exploratory and Foundational grant from the Pennsylvania State University Applied Research Laboratory.

References

[1] Oertel, H., 1990, "Wakes Behind Blunt Bodies," Annu. Rev. Fluid Mech., **22**, pp. 539–564.

[2] Roshko, A., 1993, "Perspectives on Bluff Body Aerodynamics," J. Wind. Eng. Ind. Aerodyn., **49**, pp. 79–100.

[3] Williamson, C. H. K., 1996, "Vortex Dynamics in the Cylinder Wake," Annu. Rev. Fluid Mech., **28**, pp. 477–539.

[4] Okamoto, S., and Sunabashiri, Y., 1992, "Vortex Shedding from a Circular Cylinder of Finite Length Placed on a Ground Plane," ASME J. Fluids Eng., **114**, pp. 512–521.

[5] Park, C.-W., and Lee, S.-J., 2002, "Flow Structure Around a Finite Circular Cylinder Embedded in Various Atmospheric Boundary Layers," Fluid Dyn. Res., **30**, pp. 197–215.

[6] Park, C.-W., and Lee, S.-J., 2004, "Effects of Free-End Corner Shape on Flow Structure Around a Finite Cylinder," J. Fluids Struct., **19**, pp. 141–158.

[7] Song, C., and He, J., 1993, "Computation of Wind Flow Around a Tall Building and the Large-Scale Vortex Structure," J. Wind. Eng. Ind. Aerodyn., **46-47**, pp. 219–228.

[8] Sumner, D., Wong, S. S. T., Price, S. J., and Païdoussis, M. P., 1999, "Fluid Behaviour of Side-by-Side Circular Cylinders in Steady Cross-Flow," J. Fluids Struct. **13**, pp. 309–338.

[9] Meneghini, J. R., and Saltara, F., 2001, "Numerical Simulation of Flow Interference Between Two Circular Cylinders in Tandem and Side-by-Side Arrangements," J. Fluids Struct., **15**, pp. 327–350.

[10] Lewis, H. E., Foster, A. R., Mullan, B. J., Cox, R. N., and Clark, R. P., 1969, "Aerodynamics of the Human Microenvironment," Lancet, **322**(7609), pp. 1273–1277.

[11] Clark, R. P., and Cox, R. N., 1973, "The Generation of Aerosols from the Human Body," *Airborne Transmission and Airborne Infection: Concepts and Methods*, J. F. P. Hers and K. C. Winkler, eds., Wiley NY, pp. 413–426.

[12] Clark, R. P., and Edholm, O. G., 1985, *Man and his Thermal Environment*, E. Arnold, London.

[13] Gowadia, H., Strine, S., Johnson, T., and Settles, G., 1996. "The Natural Aerodynamic Sampling of Trace Explosives from the Human Body," *2nd FAA International Symposium on Explosives Detection Technology*, Atlantic City, NJ, Federal Aviation Administration, Washington, DC.

[14] Settles, G., and McGann, W., 2001, "Potential for Portal Detection of Human Chemical and Biological Contamination," *SPIE Aerosense Meeting*, Vol. 4394, paper 108, Orlando, FL, Society of Photo-Optical Instrumentation Engineers, Bellingham, WA.

[15] Settles, G., Ferree, H., Tronsky, M., Moyer, Z., and McGann, W., 2001. "Natural Aerodynamic Portal Sampling of Trace Explosives from the Human Body," *3rd International Symposium on Explosive Detection and Aviation Security*, Atlantic City, NJ, Federal Aviation Administration, Washington, DC.

[16] Gowadia, H., and Settles, G., 2001, "The Natural Sampling of Airborne Trace Signals from Explosives Concealed Upon the Human Body," J. Forensic Sci., **46**(6), pp. 1324–1331.

[17] Gowadia, H. A., 2000, "The Natural Sampling of Airborne Trace Signals Associated With the Human Body," Ph.D. thesis, The Pennsylvania State University.

[18] Homma, H., and Yakiyama, M., 1997, "Examination of Free Convection Around Occupant's Body Caused by it's Metabolic Heat," ASHRAE Trans., **103**(1), pp. 1–12.

[19] Murakami, S., Kato, S., and Zeng, J., 1997, "Flow and Temperature Fields Around Human Body with Various Room Air Distribution, CFD Study on Computational Thermal Manikin," ASHRAE Trans. **103**(1), pp. 1–12.

[20] Murakami, S., Zeng, J., and Hayashi, T., 1999, "CFD Analysis of Wind Environment Around a Human Body," J. Wind. Eng. Ind. Aerodyn., **83**, pp. 393–408.

[21] Rodel, C. E., Kamens, R. M., and Wiener, R. W., 1995, "Experimental Considerations for the Study of Contaminant Dispersion Near the Body," Am. Ind. Hyg. Assoc. J. **56**(6), pp. 535–545.

[22] Kim, T., and Flynn, M. R., 1991, "Airflow Pattern Around a Worker in a Uniform Freestream," Am. Ind. Hyg. Assoc. J. **52**(7), pp. 287–296.

[23] Flynn, M. R., and Miller, C. T., 1991, "Discreet Vortex Methods for the Simulation of Boundary-Layer Separation Effects on Worker Exposure," Ukr. J. Phys. **35**(1), pp. 35–50.

[24] Moyer, Z. M., 2003, The Human Aerodynamic Wake and the Design of a Portal to Sample It, Master's thesis, The Pennsylvania State University.

[25] Menter, F. R., 1994, "Two-equation eddy-viscosity turbulence models for engineering applications," AIAA J. **32**(8), pp. 1598–1605.

[26] Paterson, E. G., Wilson, R. V., and Stern, F., 2003, "General-Purpose Parallel Unsteady RANS Ship Hydrodynamics Code: CFDSHIP-IOWA, Technical Report 432, Iowa Institute of Hydraulic Research, April.

[27] Issa, R. I., 1985, "Solution of the Implicitly Discretized Fluid Flow Equations by Operator-Splitting," J. Comput. Phys. **62**, pp. 40–65.

[28] Edge, B., Trujillo, M., Paterson, E., and Peltier, L. J., 2004, "Prediction of Forces and Moments on a Sonobuoy Configuration Using Overset Grids and DES." *7th Overset Composite Grid and Solution Technology Symposium*, Huntington Beach, CA, The Boeing Company, Huntington Beach, CA.

[29] Paterson, E., and Peltier, L. J., 2004, Detached-eddy simulation of high Reynolds number trailing-edge flows and wakes, *Symposium on LES Advancements and Applications, ASME FED Summer Meeting*, Charlotte, NC, American Society of Mechanical Engineers, Fluids Engineering Division, New York, NY.

[30] Paterson, E., Poremba, J., Peltier, L. J., and Hambric, S., 2004, "A Physics-Based Simulation Methodology for Predicting Trailing-Edge Singing," *25th Symposium Naval Hydrodynamics*, St. Johns, Newfoundland and Labrador, Canada, Office of Naval Research, Washington, DC.

[31] Meyer, R., Zajackowski, F., Straka, W., Paterson, E.2004, "Experimental and Computational Study of Cavitation Inception in Co-Flow Nozzles, *25th Symposium Naval Hydrodynamics*, St. Johns, Newfoundland and Labrador, Canada, Office of Naval Research, Washington, DC.

[32] Paterson, E., and Baker, W., 2004, "Simulation of Steady and Pulsed Circulation Control for Marine-Vehicle Control Surfaces, *42nd AIAA Aerospace Sciences Meeting*, Reno, NV, American Institute of Aeronautics and Astronautics, Reston, VA.

[33] Suhs, N. E., Rogers, S. E., and Dietz, W. E., 2002. "Pegasus 5: An automated pre-processor for overset grid CFD," *32nd AIAA Fluid Dynamics Conference, AIAA 2002-3186*, St. Louis, MO, American Institute of Aeronautics and Astronautics, Reston, VA.

[34] Chan, W. M., III, Gomez, R. J. , Rogers, S. E., and Buning, P. G., 2002, "Best Practices in Overset Grid Generation," *32nd AIAA Fluid Dynamics Conference, AIAA 2002-3191*, St. Louis, MO, American Institute of Aeronautics and Astronautics, Reston, VA.

[35] Pope, S. B., 2000, *Turbulent Flows*, Cambridge University Press, Cambridge, England.

Investigation of the Large-Scale Flow Structures in the Cooling Jets Used in the Blown Film Manufacturing Process

Nan Gao[1]
e-mail: gaon@mcmaster.ca

Dan Ewing
e-mail: ewingd@mcmaster.ca

Department of Mechanical Engineering,
McMaster University, Hamilton, Ontario, Canada
L8S 4L7

The development of the flow field produced by concentric jets used in the blown-film manufacturing process was studied experimentally using hot wire anemometry. It was found that the inner jet was entrained into the outer jet before the outer jet attached to the wall. The inner shear layer of the outer jet attached to the surface 3*H to* 5*H downstream of the jet exit, and the outside shear layer of the outer jet attaches to the surface further downstream of the jet exit. The distribution and spectra of the fluctuating wall pressure was measured using microphones. The pressure fluctuations were largest where the outer jet attached to the surface, and had characteristic frequencies of* 100 to 900 Hz. *Measurements of two-point and two-time correlation of the fluctuating pressure were used to characterize the development of the large-scale structures that caused these pressure fluctuations. It was found that the structures were convected along the surface at 0.45 to 0.7 of the outer jet velocity for different ratios between inner and outer jet velocities. The convection velocity of the large scale structures in the region farther than* 10*H downstream of the jet exit was determined by the upper jet velocity.* [DOI: 10.1115/1.1989367]

Introduction

The blown film manufacturing process shown in Fig. 1 is used to produce thin plastic films in the polymer industry. In this process, a polymer melt is extruded through an annular die to form a thin-walled tube that is inflated into a bubble by the difference between the air pressure inside the tube and the exterior pressure caused by air being blown on the surface. The air blown over the bubble surface cools the polymer causing it to solidify at a distance above the die exit known as the freeze line height. The dynamics of the blown film process has been studied analytically in a number of investigations [1–6] that found the cooling air had a significant effect on the shape and the stability of the bubble. Increasing the air flow rates to increase the cooling on the bubble, but eventually causes flow induced instabilities in the blown film process.

The polymer bubbles in the blown film process were traditionally cooled using a single-lip air ring that directed a single jet of air over the bubble. Dual-lip air rings, such as the one shown in Fig. 2, were later developed to increase the heat transfer capability of the cooling jets while increasing the bubble stability [7]. In the dual lip air ring, the flow from the settling chamber is split into two jets by a forming cone. The inner jet, with a relatively low flow rate, passes through the lower lip gap and cools the bubble below the forming cone to increase the rigidity of the polymer. There is a gap between the lower lip and the die that can be adjusted to allow flow into the lower region and change the reference pressure for the flow below the forming cone. A second jet, with a larger flow rate, passes through the upper lip gap outside the inner jet and eventually attaches to the bubble, cooling the upper part of the bubble.

The flow field of cooling jets produced by single-lip air rings were studied analytically and experimentally by Campbell et al. [8] and numerically by Wolf et al. [9]. Campbell et al. [8] measured the pressure on a solid model and the mean velocity of the flow over the solid model. Sidiropoulos et al. [10] and Sidiropoulos and Vlachopoulos [11] numerically examined the flow fields produced by both single lip air rings and dual lip air rings. They found that the dual lip air ring produced smaller regions of large pressure so that bubble should be more stable. Li et al. [12] and Li [13] measured the static and fluctuating pressure on the surface of solid bubble models with two blow-up ratios for a dual lip air ring with a range of settings. They found that the pressure distribution below the forming cone was determined by the inner jet velocity, and the flow and the pressure distribution on the bubble above the forming cone was determined by the ratio of the outer and the inner jet velocities in the region where the two jets interact. After the outer jet attached to the surface, the flow and pressure distributions were determined by the outer jet velocity. They also found that the unsteady pressure on the bubble was a maximum at the location where the outer jet attached to the wall for both bubble shapes. The magnitude of the maximum depended on the velocity of the upper jet and, in many cases, was on the order of the static pressure.

The unsteady reattachment process of separated flows has been studied in a number of investigations. This includes investigations of the attaching offset jets [14–18], attaching separated flows from blunt bodies [19,20], and attaching separated flows from backward facing steps [21–23]. These investigations have found that the static wall pressure increases and reaches a maximum at the reattachment point, while the fluctuating pressure reaches a maximum at a location slightly upstream of the attachment point. The reattachment distance of offset jets, X_R, is approximately 4 step heights when the offset of the jet was on the order of the jet width [14,16].

The objective of this investigation is to further investigate and characterize the cooling jets from the dual-lip air ring in the region where the outer jet attaches to the wall. Li et al. [12] performed limited measurements in this region and did not characterize how the inner jet was entrained into the outer jet. A second objective was to characterize the development of the large-scale structures in the region up to 12 jet heights from the forming cone using measurements of the two-point and two-time correlation of

[1]Author to whom all correspondence should be addressed.

Contributed by the Fluids Engineering Division for publication in the JOURNAL OF FLUIDS ENGINEERING. Manuscript received by the Fluids Engineering Division, May 14, 2004. Final Revision: April 7, 2005. Associate Editor: Dennis Siginer.

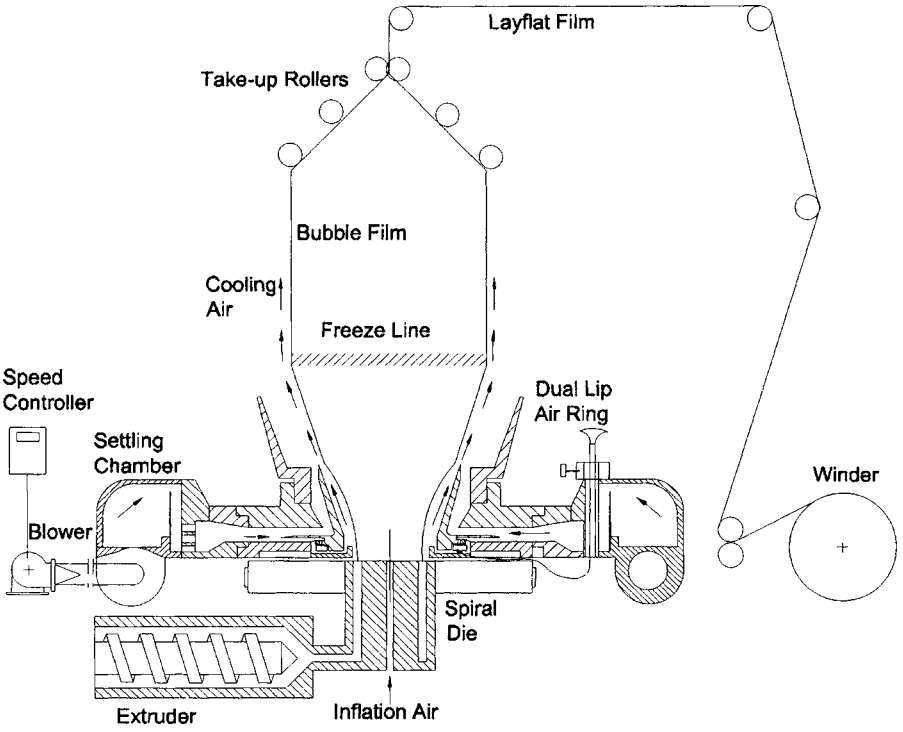

Fig. 1 Schematic of a typical blown film manufacturing process with a dual lip air ring

the fluctuating wall pressure. The measurements were performed for a rigid model designed to simulate the bubble formed by low-density polyethylene polymer in the blown film manufacturing process. The experimental facilities and methodology used in this investigation are outlined in the next section. The results are presented in the following section.

Experimental Methodology

The measurements were performed here for a typical dual lip air ring shown in Fig. 2. The air flow to the air ring was supplied by a high pressure blower. The bubble in this facility was a wooden model designed to model a plastic bubble with a blow-up ratio of 2.5 as shown in Fig. 2. The blowup ratio is the ratio of the bubble diameter at the freeze line to the bubble diameter at the die exit. The diameter of the model at the die exit was 10.2 cm and the diameter of the top was 25.4 cm. The height of the model is 40.9 cm. The bubble was modeled using a curved lower portion and a straight upper part. The angle of the straight upper part was 9° from the vertical direction. The minimum gap between the forming cone and the bubble was approximately 0.32 cm. The size of the outer jet at the exit, W, was approximately 0.8 cm, and the distance from the tip of the forming cone to the surface, H, was approximately 1 cm.

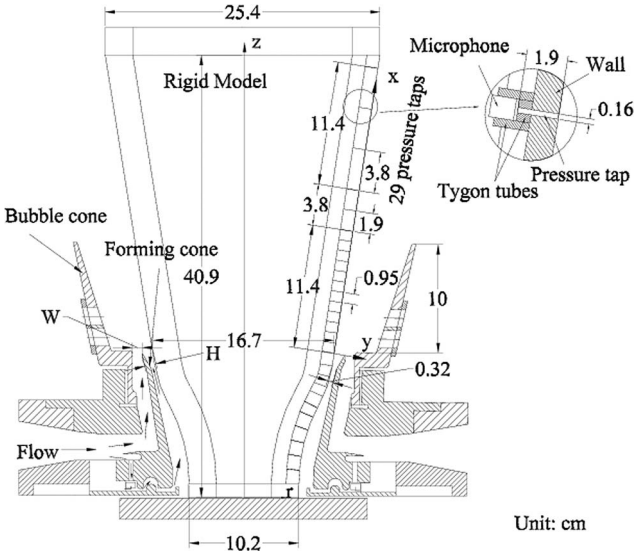

Fig. 2 Schematic of the dual-lip air ring and the rigid model used in this investigation

The static and fluctuating pressure on the bubble surface were measured using 29 pressure taps mounted flush with the surface of the model as shown in Fig. 2. The spacing between the pressure taps on the surface was 0.95 cm in the region $0\ \text{cm} \leqslant x \leqslant 11.4$ cm, 1.9 cm in the region $11.4\ \text{cm} < x \leqslant 15.2$ cm, and 3.8 cm beyond this region. The pressure taps were 0.16 cm diameter stainless steel tubes with a length of 1.9 cm. The static pressure was measured by Li et al. [12] using a multi-tube oil manometer bank that was inclined at an angle of 30°. The fluctuating pressure was measured using Sennheiser KE4-211-2 microphones. The microphone had a flat response for frequencies ranging from 20 to 10,000 Hz. The microphones were connected to the pressure taps using a 1 cm long Tygon tube. Li et al. [12] previously measured the fluctuating pressure using longer taps and longer tubes, but it was found that the natural frequency of that system was approximately 800–1000 Hz, on the order of the frequencies of interest here. The natural frequency of the modified assembly was determined by measuring the sound pressure level from a pink noise sound source with and without the microphone connected to the tube. It was found that the natural frequency of the measurement system was 2500 Hz, above the frequencies of interest here. The microphones were calibrated using a B&K piston phone type 4220 calibrator. The output of the microphone amplifier was filtered at 2048 Hz and sampled using a National Instrument 12 bit A/D board. The signals from microphone were acquired in 100 blocks of 8192 data points at a frequency of 32,768 Hz.

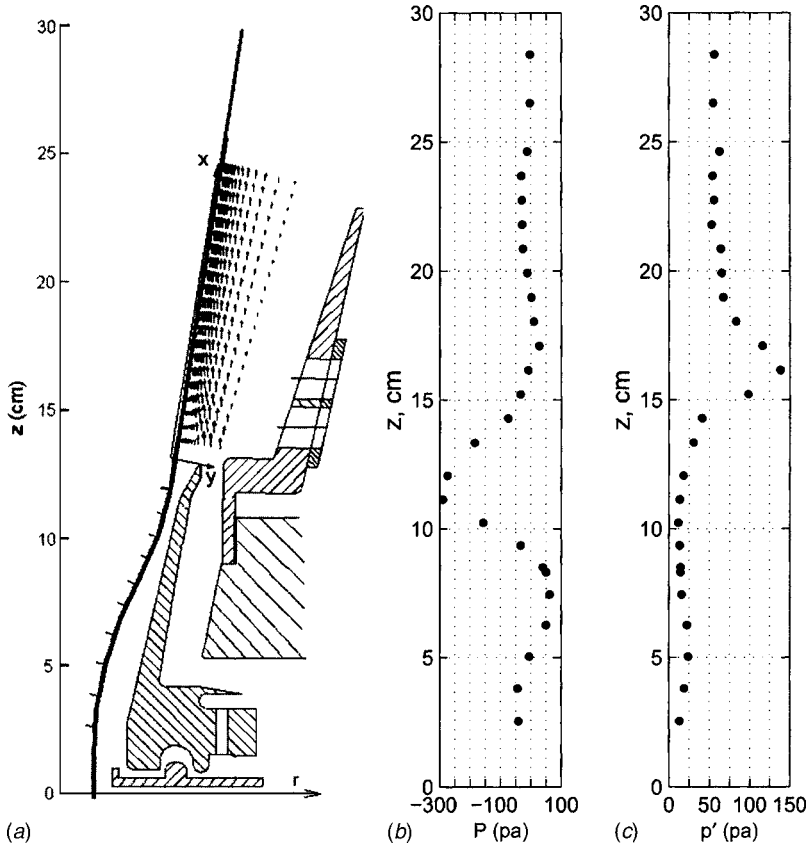

Fig. 3 Distributions of (*a*) the mean velocity vectors above the forming cone [12], (*b*) the static pressure, and (*c*) the fluctuating pressure measured on the bubble surface

The velocity field produced by the jets was measured using a single hot wire probe and an in-house anemometry system design based on the bridge proposed by Perry [24]. Sun [25] compared the performance of the in-house anemometry system with a Dantec DISA 55M system and a A.A. LAB AN-2000 system and found they were in good agreement. The wire had a diameter of 5 μm and a length of 1.25 mm. The hot wire probe was calibrated using a jet exiting a contoured nozzle that had a uniform velocity profile. The signal from the anemometry system was sampled using the A/D board at a sampling frequency of 4096 Hz for 40 s. A temperature sensor with a resolution of 0.1°C was used to measure the temperature during the test. The velocity measurements were modified to compensate for the changes in temperature using a technique proposed by Beuther [26]. The uncertainties for the reported mean velocity and rms velocity measurements were less than 2% and 5%, respectively. The flow field was measured by mounting the probes on an automated two-dimensional traversing system that could be used to move the probe through the field. The traverse could move the probe with an accuracy less than 0.05 mm. The profiles of the velocity were measured perpendicular to the wall and are presented in a *x*-*y* coordinate system referenced to the surface as shown in Fig. 2.

The measurements were performed here for an air pressure in the chamber of approximately 2 KPa. The baseline size of the channel leading to the upper lip, H_U, was 0.8 cm. The lower lip valve setting was 25% open. These produced an inner jet with a maximum velocity of 14 m/s at the jet exit that corresponded to a Reynolds number of 9000, based on the maximum velocity and the size of the inner jet. The mean velocity of the outer jet was approximately 40 m/s that corresponded to a Reynolds number of 25,500.

Results and Discussions

The distribution of the mean velocity vectors above the forming cone measured by Li et al. [12] and the static and fluctuating pressure measured on the bubble surface are shown in Fig. 3. The distribution of static and fluctuating pressure above the forming cone referenced to the coordinate system along the surface are also shown in Fig. 4. The results in this case are normalized by the dynamic head of outer jet. It is clear that the static pressure on the bubble surface increases and reaches a maximum at a height $z \approx 16-18$ cm, or $x/H \approx 4$ in good agreement with the measurements on the offset reattaching jets reported by Lund [14] and

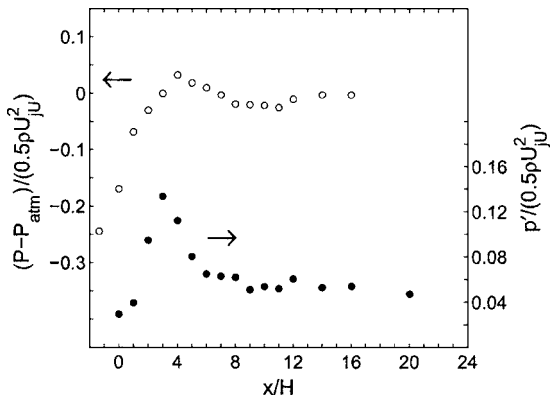

Fig. 4 Distributions of the normalized static and fluctuating pressure on the bubble surface above the forming cone

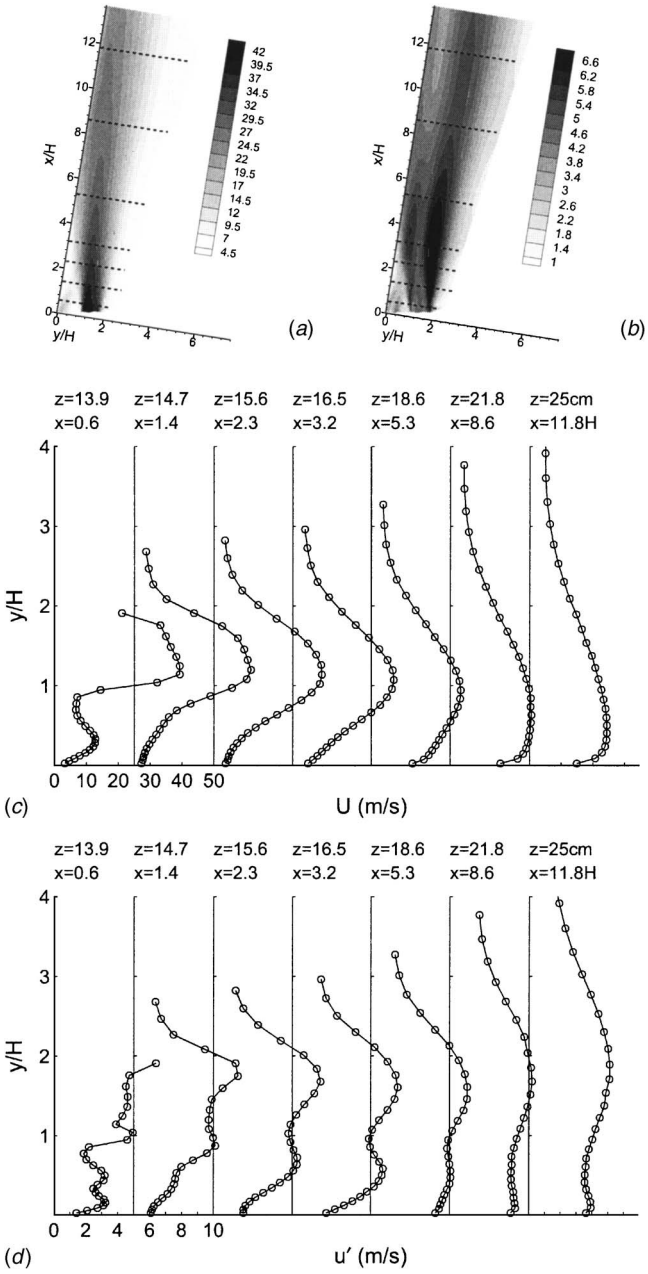

Fig. 5 Contours of (*a*) the mean streamwise velocity (in m/s) and (*b*) the rms streamwise velocity (in m/s) for a typical air ring setting, and profiles of (*c*) the mean streamwise velocity and (*d*) the rms streamwise velocity, measured at locations shown by the dash lines in the contour plots

Kim et al. [16]. The fluctuating pressure reaches to a maximum at $x/H \approx 3$, slightly upstream of the maximum in the static pressure. The maximum in the static pressure is caused by the streamline curvature as the outer jet turns parallel to the wall, while the maximum in the fluctuating pressure is associated with the attaching of the shear layer between the outer and inner jet. The static and fluctuating pressure decreased significantly in the region $x \approx 4H$ to $8H$, as the maximum velocity of the outer jet approaches the surface. The fluctuating pressure then decreases and became constant until $x/H \approx 12$, where the static and fluctuating pressure both increase. This may be due to the outside shear layer of the outer jet attaching to the wall.

The profiles of the mean streamwise velocity in the region where the outer jet attaches to the wall are shown in Fig. 5. The contours of the mean velocity are also shown in this figure. It is clear that the mean velocity of the flow from the inner jet decreases in the region $x/H \leqslant 4$ due to the adverse pressure gradient seen in Fig. 4 that was imposed by the outer jet. The location of the maximum inner jet velocity moves away from the surface as the flow evolves downstream, indicating that the inner jet is being entrained into the outer jet. The maximum outer jet velocity moves towards the wall as the outer jet attaches to the wall. The maximum of the outer jet velocity continues to approach the wall after the outer jet attaches to the wall even up to distances of $12H$.

The profiles of the turbulence intensity are shown in Fig. 5(*d*). The measurements at $x/H=0.6$ show evidence of four shear layers just downstream of the forming cone. In the inner jet, there is a shear layer near the wall as well as a shear layer on the inside of the forming cone. Similarly, there are shear layers on each side of the outer jet. At $x/H=1.4$, however, the shear layers produced by the inner jet are not apparent, suggesting these are suppressed or mixed into the outer jet shear layer as the inner jet is entrained into the outer jet. The attaching of the outer jet to the wall can be seen again in the profiles of the streamwise turbulence intensity. In particular, the local maximum in the turbulence intensity approaches the wall at $x/H=3-5$. The turbulence intensity near the wall increases as the jet core and the outside shear layer of the outer jet attaches to the surface in the region downstream of $x/H \approx 6$. The turbulence intensity has a wall-jet-like profile in the region $x/H \geqslant 12$.

Examples of the transient fluctuating wall pressure measured on the model surface at $x/H=3$, 6, and 12 during 50 ms are shown in Fig. 6. The pressure fluctuations, particularly the high-frequency components, decreases from $x/H=3$ to $x/H=12$. The pressure measured at $x/H=12$ is dominated by low-frequency fluctuations. The spectra of the fluctuating wall pressure are shown in Fig. 7. For $x/H<3$, before the outer jet attaches to the wall, the spectra of fluctuating pressure have peaks at 700–900 Hz that increase in magnitude as the flow evolves downstream. It should be noted that the peaks at 180 and 450 Hz in the spectrum measured at the jet exit, $x/H=0$, were caused by the resonance in the channel between the bubble surface and the forming cone. The magnitude of the spectra decrease rapidly in the region $3 \leqslant x/H \leqslant 6$, and a lower frequency peak emerges at 180 Hz. The spectra in the region $6<x/H<10$ decrease gradually everywhere except at 100 Hz, where the spectra increase. The spectrum then increase from $x/H=10$ to 12 at the 100 Hz peak due to the contribution from the upper shear layer. The peaks in the pressure spectra decrease in magnitude and shift slowly to lower frequencies as the flow evolves downstream beyond $x/H \approx 12$, similar to a fully developed wall jet. Similar results were also found for a range of air-ring settings and a second bubble with a blow-up ratio of 3.5. In all cases, these frequencies are much higher than those observed in the measurements of the film bubble instabilities [27]. Thus, in practical application, these fluctuations would likely cause localized disturbances on the bubble or flutter. If these disturbances occur, they would affect the flow near the wall and could increase or decrease both the local pressure fluctuations and the local heat transfer depending on the response of the film.

The characteristics of the pressure fluctuations can be examined further using the cross-spectra of the pressure between neighboring locations. The cross-spectra of the fluctuating pressure measured between $x/H=3$, $x/H=6$, $x/H=12$ and neighboring points are shown in Fig. 8. The cross-spectra measured for $x_1/H=3$ and $x_2/H<3$ have peaks at 700–900 Hz. The cross-spectra between $x_1/H=6$ and $3 \leqslant x_2/H<6$ have peaks at a frequency of approximately 180 Hz that increases in magnitude, suggesting there is a change in the dominant frequency in the flow. The cross-spectra measured for $x_1/H=6$ and $6<x_2/H \leqslant 9$ decrease in magnitude everywhere except at 180 Hz, while the peaks in the cross-spectra between $x_1/H=12$ and $6 \leqslant x_2/H<12$ increase in magnitude and shift to lower frequencies. This shift in the frequency continues

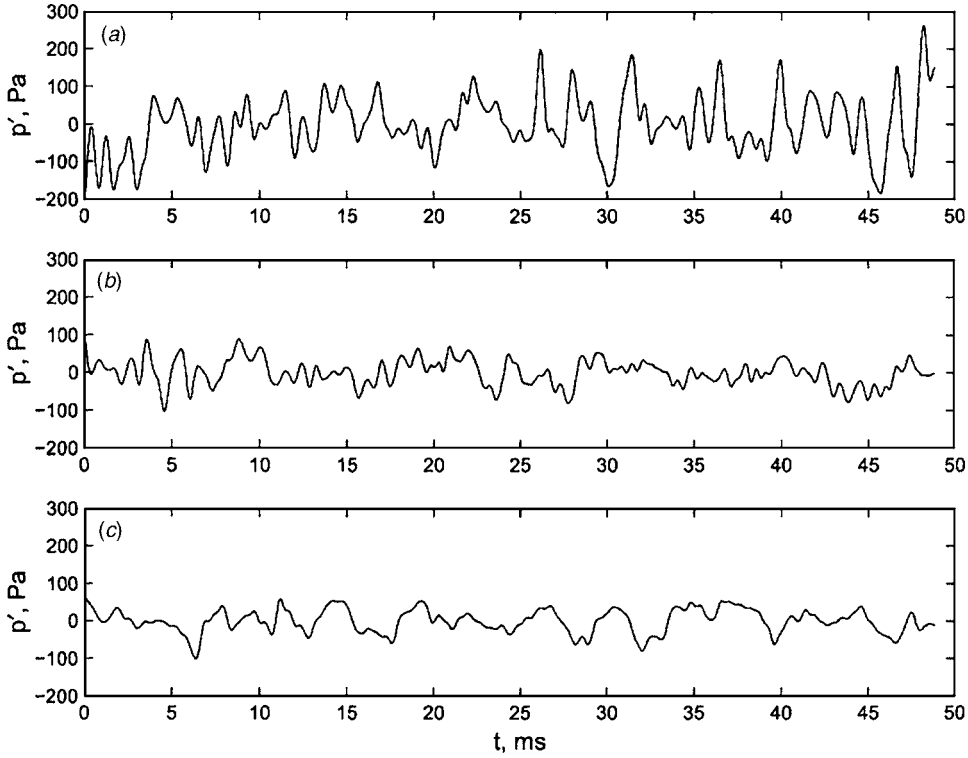

Fig. 6 Examples of the transient fluctuating wall pressure measured at (*a*) *x*/*H*=3, (*b*) *x*/*H*=6, and (*c*) *x*/*H*=12. The signals are low-pass filtered at 2048 Hz.

for $x_2/H>12$, suggesting the large scale structures are becoming larger or being convected more slowly as the flow evolves downstream.

The two-point and two-time correlation of the fluctuating pressure measured between $x/H=3$, $x/H=6$, $x/H=12$ and neighboring points are shown in Fig. 9. The fluctuating pressure in the region $3\leqslant x_2/H\leqslant 6$ is not that well correlated, indicating the large-scale structures are not simply convected along the surface. The fluctuating pressure between $x_1/H=6$ and $x_2/H>6$ are well correlated, indicating that there are large-scale structures being convected along the surface in this region. This is particularly true for $x/H>12$, suggesting the flow is dominated by the passage of large-scale structures so the pressure fluctuations are primarily a traveling wave on the surface.

The convection velocity of large-scale structures that contribute to the pressure fluctuations computed from the phase of the cross-spectra are shown in Fig. 10. The increase in the convection velocity in the regions $3\leqslant x/H\leqslant 5$ and $6\leqslant x/H\leqslant 8$ are likely associated with the attaching of the shear layer [21]. The convection velocity is relatively constant in the region $10\leqslant x/H\leqslant 12$, and decreases in the region $12\leqslant x/H\leqslant 14$ similar to a fully developed wall jet.

The effects of velocity ratio on the development of the large scale structures were studied by changing the size of the channel leading to the outer jet while keeping the static pressure in the chamber at 2 kPa. A comparison of the profiles of the mean velocity and rms velocity measured for these cases is shown in Fig. 11. It is clear that the velocity of the outer jet increased when the size of the channel was increased, while the inner jet velocity did not change significantly. The ratio between the maximum velocities of the inner and the outer jet at their exits decreased from 0.4 to 0.3 for these tests. This created a higher shear rate at the inner shear layer of the outer jet. The turbulence intensity of the outer jet was smaller at the jet exit when the outer jet velocity was increased. However, the turbulence intensity increases faster as the flow evolved downstream due to the large shear rate in the mean flow, and becomes larger than the cases with smaller outer jet velocity in the region $x/H>4$.

The normalized profiles of the static pressure and fluctuating pressure for these cases are shown in Fig. 12. The difference among the profiles in the region above the forming cone are significantly decreased after being normalized using the dynamic head of the outer jet. However, the normalized profiles of the static and fluctuating wall pressure do not collapse, suggesting that the outer jet velocity was not the only factor that determines the wall pressure as discussed in Li et al. [12].

The convection velocity of the large-scale structures for the three outer jet velocities are shown in Fig. 13(*a*), and the convection velocity normalized using the maximum outer jet velocity at the jet exit are shown in Fig. 13(*b*). It is clear that the convection velocity of large-scale structures increased as the outer jet velocity increased. The normalized convection velocity in the region $x/H<10$ seemed to decrease as the outer jet velocity increased. The normalized convection velocity in all three cases was approximately $0.45U_{jU}$ in the region $10\leqslant x/H<14$, indicating that the convection velocity was determined only by the maximum outer jet velocity in the region far downstream of the jet exit. The causes of the difference in the convection velocity in the near field are not known and need further investigation.

Concluding Remarks

The development of the flow in the near field of the cooling jets produced by a dual lip air ring used in the blown-film manufacturing process was investigated. It was found that the inner jet slowed down and was entrained into the outer jet before the outer jet attaches to the wall. The turning of the outer jet parallel to the surface caused a local maximum in the static pressure on the surface at $x/H\approx 4$. The fluctuating pressure reaches maximum upstream of this location at $x/H\approx 3$.

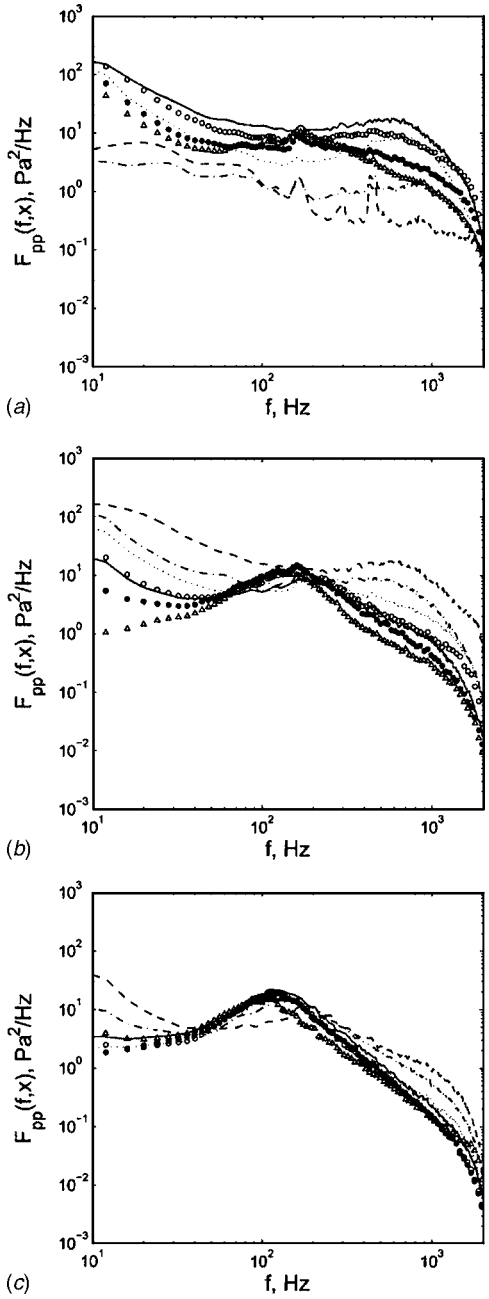

Fig. 7 Spectra of wall fluctuating pressure measured at (*a*) x/H=---0, ---1, ···2, ———3, ○ 4, ● 5, △ 6, (*b*) x/H=---3, ---4, ···5, ———6, ○ 7, ● 8, △ 9, and (*c*) x/H=---6, ---8, ···10, ———12, ○ 14, ● 16, △ 20

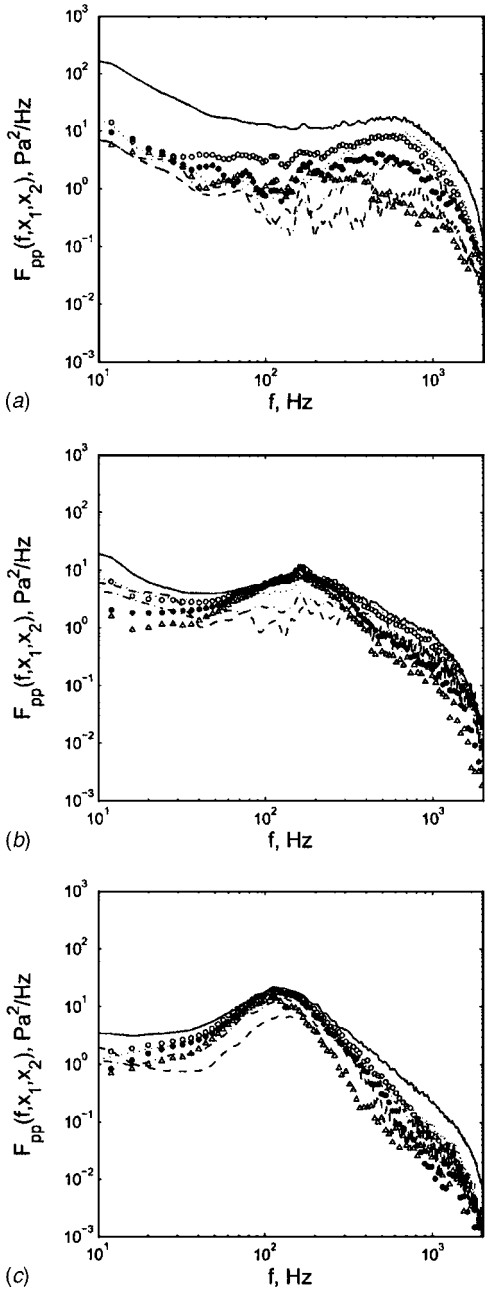

Fig. 8 Cross-spectra of fluctuating wall pressure measured for (*a*) x_1/H=3 and x_2/H=---0, ---1, ···2, ———3, ○ 4, ● 5, △ 6, (*b*) x_1/H=6 and x_2/H=---3, ---4, ···5, ———6, ○ 7, ● 8, △ 9, and (*c*) x_1/H=12 and x_2/H=---6, ---8, ···10, ———12, ○ 14, ● 16, △ 20

The inner shear layer of the outer jet attached to the surface at $x/H \approx 3-6$, where the dominant frequency in pressure spectra shifts from 700–900 Hz to approximately 180 Hz. The peak formed at 180 Hz shifts to a lower frequency as the flow evolves downstream in the region $x/H \geq 6$, where the large-scale structures are convected along the surface with the mean flow.

The convection velocity of the large-scale structures in the flow was also examined using measurements of the two-point cross spectra and two-point and two-time correlation of fluctuating pressure. The fluctuating pressure in the region $3 \leq x/H \leq 6$, where the outer jet attached to the wall, was as not well correlated, but the fluctuating pressure was well correlated in the region $x/H \geq 6$. The large-scale structures in this region were convected with a convection velocity that varied from $0.45U_{jU}$ to $0.7U_{jU}$ for different ratios between inner and outer jet velocities. The convection velocities of large-scale structures in the region $x/H > 10$ measured for different outer jet velocities were similar, indicating the convection velocity is determined by the outer jet velocity.

Acknowledgments

The authors wish to acknowledge the support of Materials and Manufacturing Ontario and McMaster Manufacturing Research Institute at McMaster University, Future Design Inc. and NSERC Canada. This paper was originally presented as HT-FED2004-56348 at the 2004 ASME Heat Transfer/Fluids Engineering Summer Conference at Charlotte, North Carolina, USA.

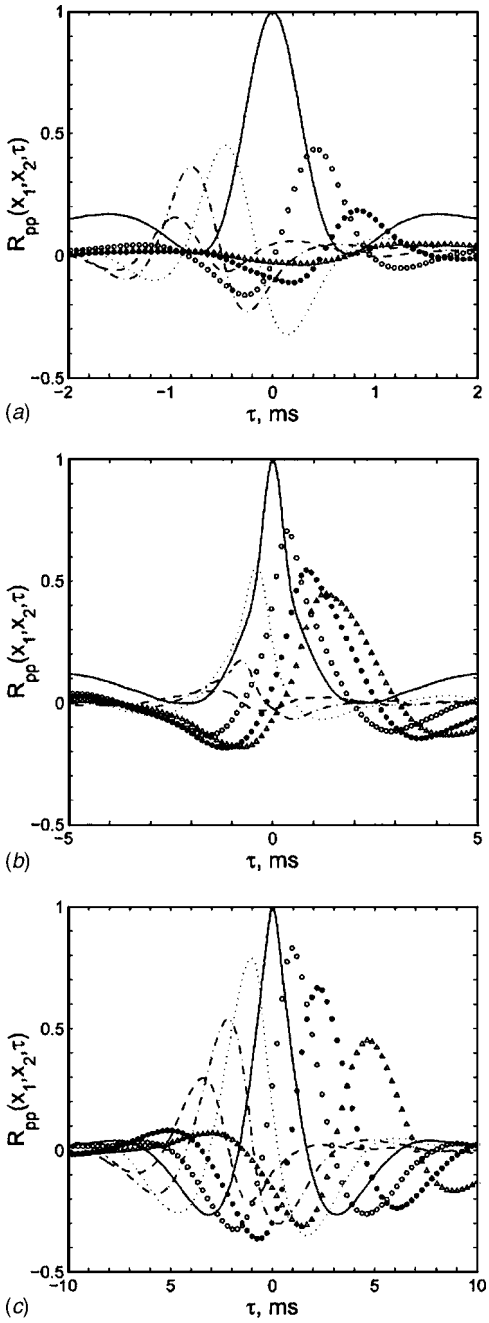

Fig. 9 Normalized cross correlation of fluctuating wall pressure measured between (*a*) x_1/H=3 and x_2/H=---0, ---1, ···2, ———3, ○ 4, ● 5, △ 6, (*b*) x_1/H=6 and x_2/H=---3, ---4, ···5, ———6, ○ 7, ● 8, △ 9, and (*c*) x_1/H=12 and x_2/H=---6, ---8, ···10, ———12, ○ 14, ● 16, △ 20

Nomenclature

F_{pp} = spectrum of fluctuating pressure, Pa^2/Hz
f = frequency, Hz
H = distance from the tip of the forming cone to the wall, m
H_B = bubble cone height, m
H_U = upper lip gap size, m
P = static pressure, Pa
P_{atm} = atmospheric pressure, Pa
p' = root mean square value of the fluctuating wall pressure, Pa

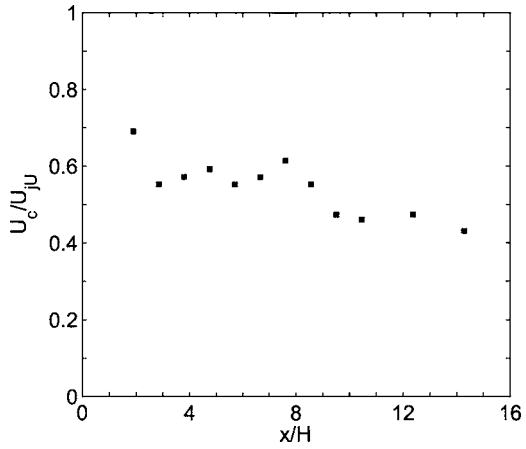

Fig. 10 Distribution of the convection velocity computed from the cross-spectra normalized by the maximum outer jet exit velocity

R_{PP} = normalized correlation of fluctuating wall pressure
rms = root mean square
r = spatial coordinate in the radial direction, m
t = time, s
U = mean velocity parallel to the bubble surface, m/s
U_c = convection velocity, m/s

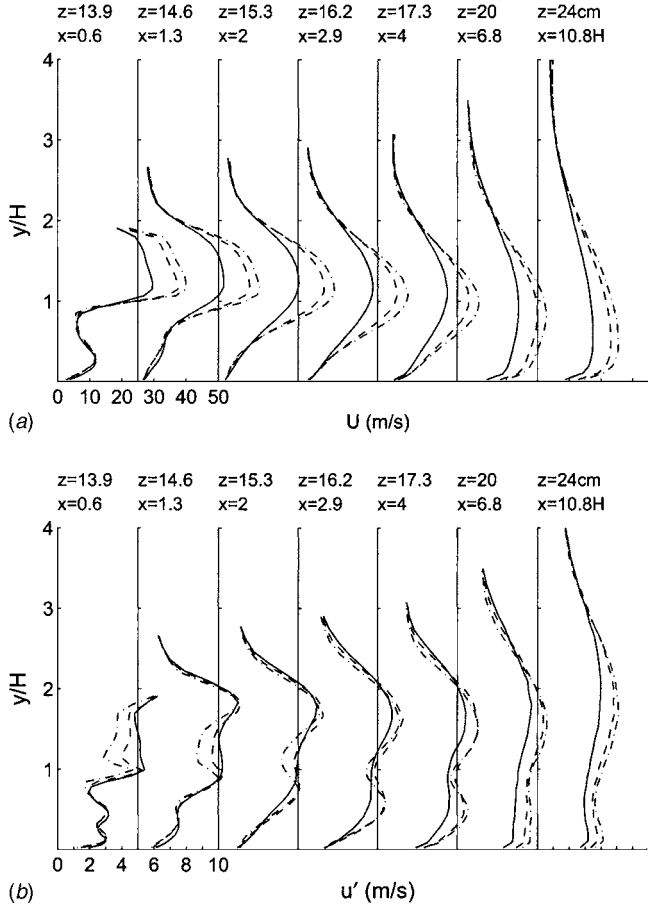

Fig. 11 Profiles of (*a*) the mean streamwise velocity and (*b*) the rms streamwise velocity for a maximum outer jet velocity of ———30.4 m/s, ---39.2 m/s, and -·-·-42.6 m/s

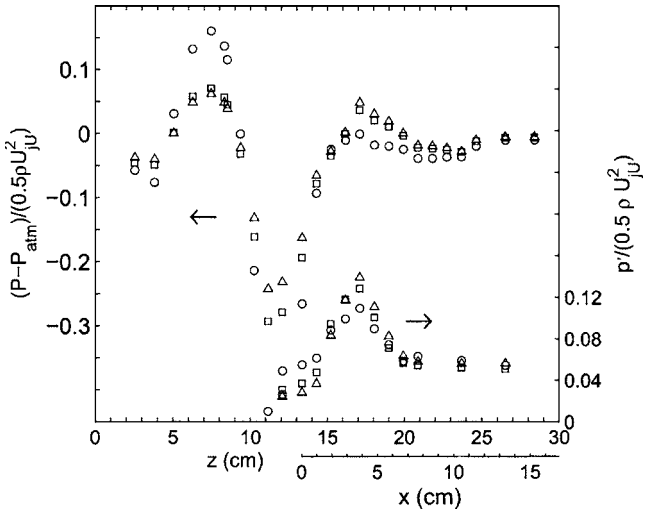

Fig. 12 Distributions of the static and fluctuating wall pressures normalized by the dynamic head of the outer jet for a maximum outer jet velocity of ○ 30.4 m/s, □ 39.2 m/s, and △ 42.6 m/s

U_{jU} = maximum velocity of the outer jet, m/s
u' = root mean square value of the fluctuating velocity, m/s
W = size of the outer jet exit, m

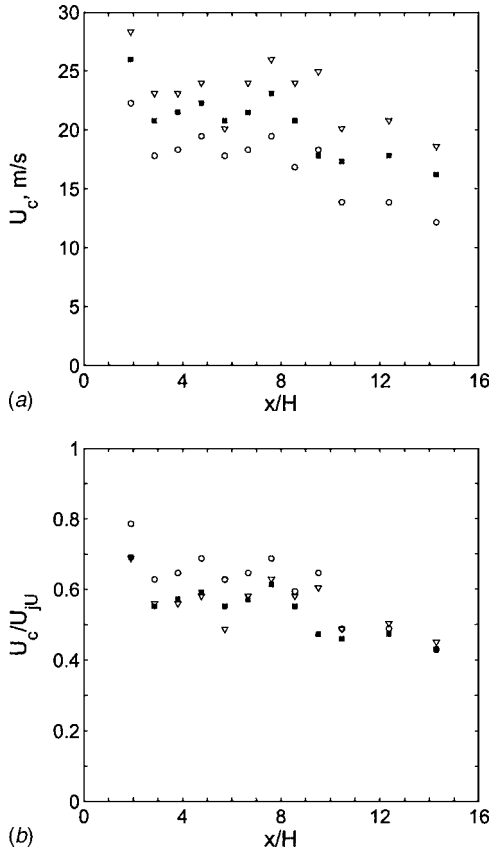

Fig. 13 Distributions of (*a*) the convection velocity of the large scale structures computed from the cross-spectra of the fluctuating wall pressure and (*b*) convection velocities for a maximum outer jet velocity of ○ 30.4 m/s, ■ 39.2 m/s, and ▽ 42.6 m/s

x = spatial coordinate parallel to the bubble surface, m
x_1 = location of the first pressure measurement, m
x_2 = location of the second pressure measurement, m
X_R = reattachment distance, m
y = spatial coordinate perpendicular to the bubble surface, m
z = spatial coordinate in vertical direction, m
ρ = density of air, kg/m^3
τ = time interval, s

References

[1] Pearson, J., and Petrie, C., 1970, "The Flow of a Tubular Film, Part 1. Formal Mathematical Representation," J. Fluid Mech., **40**, pp. 1–19.
[2] Pearson, J., and Petrie, C., 1970, "The Flow of a Tubular Film, Part 2. Interpretation of the Model and Discussion of Solutions," J. Fluid Mech., **40**, pp. 609–625.
[3] Yeow, Y., 1976, "Stability of Tubular Film Flow: A Model of Film-Blowing Process," J. Fluid Mech., **75**, pp. 577–591.
[4] Kanai, T., and White, J., 1984, "Kinematics, Dynamics and Stabilities of the Tubular Film Extrusion of Various Polyethylenes," Polym. Eng. Sci., **24**, pp. 1185–1201.
[5] Minoshima, W., and White, J., 1986, "Instability Phenomena in Tubular Film, and Melt Spinning of Rheologically Characterized High Density, Low Density and Linear Low Density Polyethylenes," J. Non-Newtonian Fluid Mech., **19**, pp. 275–302.
[6] Pirkle, J., and Braatz, R., 2003, "Dynamic Modeling of Blown-Film Extrusion," Polym. Eng. Sci., **43**, pp. 398–418.
[7] Cole, R., 1982, "Blown-Film Cooling: An Update," Plast. Eng. (Brookfield, Conn.), **38**, pp. 35–36.
[8] Campell, G., Obot, N., and Cao, B., 1992, "Aerodynamics in the Blow Film Process," Polym. Eng. Sci., **32**, pp. 751–759.
[9] Wolf, D., Feron, B., and Wortberg, J., 1997, "Numerical Analysis of Cooling Air Systems in Film Blowing," Int. Polym. Process., **12**, pp. 38–44.
[10] Sidiropoulos, V., Wood, P., and Vlachopoulos, J., 1999, "The Aerodynamics of Cooling of Blown Film Bubbles," J. Reinf. Plast. Compos., **18**, pp. 529–538.
[11] Sidiropoulos, V., and Vlachopoulos, J., 2000, "An Investigation of Venturi and Coanda Effects in Blown Film," Int. Polym. Process., **15**, pp. 40–45.
[12] Li, S., Gao, N., and Ewing, D., 2003, "Investigation of Cooling Jets Used in Blown-Film Manufacturing Process," IMECE2003-42747, ASME International Mechanical Engineering Congress and RD&D Expo, 15–21 November, Washington, DC.
[13] Li, S., 2003, "Investigations of the Cooling Jets Used in the Blown Film Manufacturing Process," MS thesis, McMaster University, Hamilton, Canada.
[14] Lund, T., 1986, "Augmented Thrust and Mass Flow Associated With Two-Dimensional Jet Reattachment," AIAA J., **24**, pp. 1964–1970.
[15] Pelfrey, J., and Liburdy, J., 1986, "Mean Flow Characteristics of a Turbulent Offset Jet," ASME J. Fluids Eng., **108**, pp. 82–88.
[16] Kim, D., Yoon, S., Lee, D., and Kim, K., 1996, "Flow and Heat Transfer Measurements of a Wall Attaching Offset Jet," Int. J. Heat Mass Transfer, **39**, pp. 2907–2913.
[17] Nasr, A., and Lai, J., 1997, "Comparison of Flow Characteristics in the Near Field of Two Parallel Plane Jets and an Offset Plane Jet," Phys. Fluids, **9**, pp. 2919–2931.
[18] Song, H., Yoon, S., and Lee, D., 2000, "Flow and Heat Transfer Characteristics of a Two-Dimensional Oblique Wall Attaching Offset Jet," Int. J. Heat Mass Transfer, **43**, pp. 2395–2404.
[19] Kiya, M., and Sasaki, K., 1983, "Structure of a Turbulent Separation Bubble," J. Fluid Mech., **137**, pp. 83–113.
[20] Kiya, M., and Sasaki, K., 1985, "Structure of Large-Scale Vortices and Unsteady Reverse Flow in the Reattaching Zone of a Turbulent Separation Bubble," J. Fluid Mech., **154**, pp. 463–491.
[21] Heenan, A., and Morrison, J., 1998, "Passive Control of Pressure Fluctuations Generated by Separated Flow," AIAA J., **36**, pp. 1014–1022.
[22] Lee, I., and Sung, J., 2001, "Characterics of Wall Pressure Fluctuations in Separated and Reattaching Flows Over a Backward-Facing Step, Part 1, Time-Mean Statistics and Cross Spectral Analyses," Exp. Fluids, **30**, pp. 262–272.
[23] Lee, I., and Sung, J., 2002, "Multiple-Arrayed Pressure Measurement for Investigation of the Unsteady Flow Structure of a Reattaching Shear Layer," J. Fluid Mech., **463**, pp. 377–402.
[24] Perry, A., 1982, *Hot-wire Anemometry*. Clarendon Press, Oxford.
[25] Sun, H., 2002, "The Development of Three-Dimensional Wall Jet," Ph.D. thesis, McMaster University, Hamilton, Canada.
[26] Beuther, P., 1980, "Experimental Investigation of the Axisymmetric Turbulent Buoyant Plume," Ph.D. thesis, The State University of New York at Buffalo, Buffalo, NY.
[27] Kim, S., Fang, Y., Lafleur, P., and Carreau, P., 2004, "Dynamics and Criteria for Bubble Instabilities in a Single Layer Film Blowing Extrusion," Polym. Eng. Sci., **44**, pp. 283–302.

Shin Hyung Rhee[1]
Lead Engineer
Member ASME
e-mail: shr@fluent.com
Fluent Inc.,
10 Cavendish Court,
Lebanon, NH 03766
Fax: 603-643-3967

Takafumi Kawamura
Assistant Professor
Department of Environmental and Ocean Engineering, University of Tokyo,
Tokyo, Japan

Huiying Li
Senior Engineer
Fluent Inc.,
Lebanon, NH 03766

Propeller Cavitation Study Using an Unstructured Grid Based Navier-Stoker Solver

The cavitating flow around a marine propeller is studied using an unstructured grid based Reynolds-averaged Navier-Stokes computational fluid dynamics method. A cavitation model based on a single-fluid multi-phase flow method is implemented in the Navier-Stokes solver. The proposed computational approach for cavitation is validated against a benchmark database for a cavitating hydrofoil as well as measured data for a cavitating marine propeller. The leading edge and mid-chord cavitation on the hydrofoil is reproduced well and shows good comparison with the well-known experimental data. The predicted noncavitating open water performance of the marine propeller geometry agrees well with the measured one. Finally, the cavitating propeller performance as well as cavitation inception and cavity shape are in good agreement with experimental measurements and observation. The overall results suggest that the present approach is practicable for actual cavitating propeller design procedures without lengthy preprocessing and significant preliminary knowledge of the flow field. [DOI: 10.1115/1.1989370]

Introduction

Marine propeller researchers and designers have made numerous efforts to reduce the effects of cavitation, which degrades propeller performance, erodes blade surfaces, produces noise, and causes vibration on the ship hull. However, with increasing demand for heavily loaded propellers, the occurrence of cavitation is unavoidable nowadays. Therefore, accurate prediction of cavitation is becoming more important than ever to ensure better propulsor designs.

Model tests provide valuable insights into the cavitation physics in various predetermined conditions, e.g., [1]. However, model tests cost a significant amount of money, sometimes tens of thousands of dollars per geometry, and are vulnerable to slight flow condition changes inside cavitation tunnels. Moreover, it is difficult to control the inflow, which is supposed to take the ship hull wake into account.

Computational methods for cavitation have been studied for over two decades. Lee [2] studied marine propeller cavitation in 1979, for example. The methods can be largely categorized into two groups: single-phase modeling with cavitation interface tracking and multi-phase modeling with an embedded cavitation interface.

The former approach, i.e., single-phase modeling with cavitation interface tracking, has been widely adopted for inviscid flow solution methods, such as potential flow boundary element methods [3] and Euler equation solvers [4]. These methods have evolved significantly and many successful application results have been presented, as reviewed in [5]. Still in many cases they require cumbersome iterative procedures and a considerable amount of preliminary knowledge, such as cavity closure conditions.

The latter approach, i.e., multi-phase modeling with an embedded cavitation interface, can be adopted for more general viscous flow solution methods, such as the Reynolds-averaged Navier-Stokes (RANS) equation solvers. Recently, it has become popular within the cavitation research community. This approach is more general for three-dimensional and unsteady flows. It can include the effects of compressible vapor and gas, turbulence fluctuations, and a bubbly phase within the mixture, although a closure equation is required to connect the density to the other variables. There are generally two types of methods available for this approach: a mixture fluid method, with separate continuity equations for multi-phase analysis [6–11], and a full multi-fluid method with separate conservation equations for each phase [12]. More recently, based on the existing methods, compressibility effects have been incorporated [13,14]. Many favorable results have been reported and various improvement efforts are underway; however, applications and validations of the methods for realistic marine propeller geometries are rare. The only presented results [15] found by the authors involve complex multi-block structured grid generation and show questionable cavity shapes for marine propeller cavitation.

This paper is concerned with a computational study of cavitating flow around a marine propeller, through solution of the RANS equations with a cavitation model. The objectives are to propose and verify a computational approach for propeller cavitation, which can complement the tunnel tests and existing numerical methods. For the present study, one of the mixture fluid methods mentioned above [11] was adopted for mass transfer between phases and extended for interphase slip velocity. For validation of this approach, simulations for the following problems have been carried out: (1) leading edge and mid-chord cavitation on a hydrofoil; (2) open water performance of a noncavitating propeller; and (3) open water performance and flow field analysis for a cavitating propeller. A full discussion of the results is presented below.

The present paper is organized as follows. The mathematical modeling and numerical method are described in the next section. Descriptions of the model geometry and grid generation follow. The computational results are presented for comparison and validation, and for flow field analysis. Lastly, some concluding remarks are made.

Mathematical Modeling and Numerical Method

The cavitation model employed in the present study is based on the so-called "full cavitation model" by Singhal et al. [11]. This model accounts for all first-order effects, i.e., phase change, bubble dynamics, turbulent pressure fluctuations, and noncondensable gases. However, unlike the original approach, which assumes single-phase and variable fluid density flows, the present

[1]Corresponding author.

Contributed by the Fluids Engineering Division for publication in the JOURNAL OF FLUIDS ENGINEERING. Manuscript received by the Fluids Engineering Division, December 9, 2003; Final revision: May 2, 2005. Associate Editor: Georges Chahine.

model is under the framework of multi-phase flows and has the capability of accounting for the effects of the slip velocities between liquid and gaseous phases.

For the multi-phase flow solutions, the single-fluid mixture model is employed. The mixture model solves the continuity and momentum (and energy, if necessary) equations for the mixture, and the volume fraction equation for the secondary phases, as well as algebraic expressions for slip velocities. The governing equations are written for the mass and momentum conservation of the mixture fluid, such that

$$\frac{\partial}{\partial t}(\rho_m) + \nabla \cdot (\rho_m \vec{v}_m) = 0 \tag{1}$$

$$\frac{\partial}{\partial t}(\rho_m \vec{v}_m) + \nabla \cdot (\rho_m \vec{v}_m \vec{v}_m) = -\nabla p + \nabla \cdot (\bar{\bar{\tau}}) + \nabla \cdot \left(\sum_{k=1}^{n} \alpha_k \rho_k \vec{v}_{dr,k} \vec{v}_{dr,k} \right) \tag{2}$$

where $\bar{\bar{\tau}}$ is the stress tensor given by

$$\bar{\bar{\tau}} \equiv \mu_m \left[(\nabla \vec{v}_m + \nabla \vec{v}_m^T) - \frac{2}{3} \nabla \cdot \vec{v}_m I \right] \tag{3}$$

In the above equations, ρ_m is the mixture density, $\vec{v}_m$ is mass-averaged velocity, μ_m is the mixture viscosity, I is the unit tensor, and $\vec{v}_{dr,k}$ is the drift velocity for the secondary phase k:

$$\vec{v}_{dr,k} = -\vec{v}_k - \vec{v}_m \tag{4}$$

where $\vec{v}_k$ is the kth phase velocity. The drift velocity is related to the slip velocity, $\vec{v}_{pq}$, as follows:

$$\vec{v}_{dr,p} = \vec{v}_{pq} - \sum_{k=1}^{n} \frac{\alpha_k \rho_k}{\rho_m} \vec{v}_{qk} \tag{5}$$

where the subscripts p and q refer to secondary and primary phases, respectively, and m refers to the mixture.

The present mixture model makes use of an algebraic slip formulation to calculate $\vec{v}_{pq}$. The basic assumption of the algebraic slip mixture model is that, to prescribe an algebraic relation for the relative velocity, a local equilibrium between the phases should be reached over short length scale. Following Manninen et al. [16], the form of the slip velocity is given by

$$\vec{v}_{pq} = \frac{(\rho_p - \rho_m) d_p^2}{18 \mu_q f_{drag}} \vec{a} \tag{6}$$

where d_p is the diameter of the particles of the secondary phase p, $\vec{a}$ is the secondary phase particle's acceleration of the form

$$\vec{a} = \vec{g} - (\vec{v}_m \cdot \nabla) \vec{v}_m - \frac{\partial \vec{v}_m}{\partial t} \tag{7}$$

and the default drag function f_{drag} is taken from Schiller and Naumann [17] as

$$f_{drag} = \begin{cases} 1 + 0.5\mathrm{Re}^{0.687} & \text{for } \mathrm{Re} \leqslant 1000 \\ 0.0183\mathrm{Re} & \text{for } \mathrm{Re} > 1000 \end{cases} \tag{8}$$

The value of d_p is problem dependent and set to 10^{-5} m or less when a secondary phase is assumed to consist of very small particles.

Once the Reynolds averaging approach for turbulence modeling is applied, the Reynolds stresses resulting from the process must be modeled to close Eq. (2). The k-ω turbulence model [18], which is based on the Boussinesq hypothesis and incorporates transport equations for the turbulent kinetic energy, k, and specific dissipation rate, ω, was used for the mixture. The specific dissipation rate can be thought of as the ratio of the turbulent kinetic energy dissipation rate to k. The turbulent viscosity μ_t is computed by combining k and ω as $\mu_t = \rho_m k/\omega$. The wall boundary conditions for the k-ω model are treated in such a way that when the wall-adjacent cells are located in the log-law region, the wall function approach, based on the law of the wall, is applied [18]. When the wall-adjacent cells are closer to the solid surface and inside the sublayer region, an alternative approach that ensures the no-slip condition on the solid surface is applied [19]. For cells in the buffer region, the above two are blended. The k-ω model is one of the most widely used turbulence models for external aero- and hydrodynamics and has shown good performance for highly skewed marine propeller cases [20] as well as for the complex flow field on both the sublayer level and wall function grids [19].

The mass transfer through cavitation is handled by the transport equation for the vapor mass fraction, $f_v \equiv \alpha_v \rho_v / \rho_m$, where α_v is the vapor volume fraction and ρ_v is the vapor density. The vapor transport equation is written as

$$\frac{\partial}{\partial t}(\rho_m f_v) + \nabla \cdot (\rho_m \vec{v}_v f_v) = \nabla \cdot \left(\frac{\mu_t}{\sigma_v} \nabla f_v \right) + R_e - R_c \tag{9}$$

where μ_t is the turbulent eddy viscosity, σ_v is the turbulent Prandtl number for the vapor, and R_e and R_c are the rates of vapor generation and condensation, respectively. The turbulent Prandtl number takes a value between 0.7 and 1.0 in most of the published studies, and is set to 1.0 in the present study. Note that, unlike the original model [11], the vapor phase velocity, $\vec{v}_v$, is used in Eq. (9) instead of the mixture velocity, $\vec{v}_m$, thanks to the present model extension that accounts for the slip velocity.

To solve Eq. (9), R_e and R_c need to be related to the bubble dynamics and volume fraction. To account for the bubble dynamics, the reduced Rayleigh-Plesset equation was employed, as for many other studies in the same modeling category. Following the approach used by Singhal et al. [11] and considering the limiting bubble size (i.e., assuming that the typical bubble diameter is the same as the maximum possible bubble size), the expressions for R_e and R_c are obtained as when $p < p_{sat}$:

$$R_e = C_e \frac{v_{ch}}{\gamma} \rho_l \rho_v \sqrt{\frac{2}{3} \frac{p_{sat} - p}{\rho_l}} (1 - f_v) \tag{10}$$

when $p > p_{sat}$:

$$R_c = C_c \frac{v_{ch}}{\gamma} \rho_l \rho_l \sqrt{\frac{2}{3} \frac{p - p_{sat}}{\rho_I}} f_v \tag{11}$$

where C_e and C_c are two empirical constants, p_{sat} is the liquid saturation pressure, p is the local far-field pressure, ρ_l is the liquid density, γ is the surface tension, and v_{ch} is the characteristic velocity, which reflects the effect of the local slip velocity and takes a value approximately equal to $\sqrt{k}$ with k being the local turbulent kinetic energy. Singhal et al. [11] used 0.02 and 0.01 for C_e and C_c, respectively, after careful studies of numerical stability and physical behavior of the solution. Their values are adopted in the present study.

The effects of turbulence-induced pressure fluctuations are taken into account by raising the phase change threshold pressure from p_{sat} to p_v, which is written as

$$p_v = p_{sat} + 0.5 p'_{turb} \tag{12}$$

where $p'_{turb} = 0.39 \rho k$ [21]. Singhal et al. [11] investigated the turbulence effects extensively and concluded that the present practice, Eq. (12), is much simpler, robust, and as good as the more rigorous practices, in which a probability density function was used to account for the effects [22]. In the present study, the influence of p'_{turb} was found to be negligible, thanks to the low turbulence level in the attached boundary layer type flow.

It is widely acknowledged that the effects of noncondensable gases need to be taken into account, as the operating liquid usually contains small finite amounts of such gases, e.g., dissolved gases and aeration. Even a very small amount of noncondensable gases can have significant effects on the cavitating flow field due to gaseous expansion at low pressures. In the present model, the working fluid is assumed to be a mixture of the liquid and gaseous

phases, with the gaseous phase being comprised of the liquid vapor and noncondensable gas. The mixture density is calculated as

$$\rho_m = \alpha_v \rho_v + \alpha_g \rho_g + (1 - \alpha_v - \alpha_g)\rho_l \tag{13}$$

where ρ_g is the noncondensable gas density, and α_l and α_g are the liquid and noncondensable gas volume fractions, respectively. The relationship between the mass fraction, f_ϕ, and the corresponding volume fraction, α_ϕ, is, for any given phase ϕ, is

$$\alpha_\phi = f_\phi \frac{\rho_m}{\rho_\phi} \tag{14}$$

With all of these effects considered, Eqs. (10) and (11) can be rewritten as when $p < p_v$:

$$R_e = C_e \frac{\sqrt{k}}{\gamma} \rho_l \rho_v \sqrt{\frac{2}{3}\frac{p_v - p}{\rho_l}}(1 - f_v - f_g) \tag{15}$$

when $p > p_v$:

$$R_c = C_c \frac{\sqrt{k}}{\gamma} \rho_l \rho_l \sqrt{\frac{2}{3}\frac{p - p_v}{p_l}} f_v \tag{16}$$

In summary, the solution procedure consists of the following steps:

1. Equation (2) is solved for the mixture velocity.
2. Equation (1) is satisfied with the mixture density and mixture velocity obtained in step 1.
3. Equation (9) is solved for the vapor mass fraction with source terms for the rates of vapor generation and condensation calculated by Eqs. (15) and (16).
4. The mixture density is updated by Eqs. (13) and (14) with the newly obtained vapor mass fraction and the predetermined noncondensable gas volume fraction.
5. Steps 1–4 are repeated until solution convergence is achieved.

The influence of slip velocity between the phases was found to be negligible in preliminary computations for the cavitation on a hydrofoil; therefore the last term in Eq. (2) was set to zero in the computations for the present study. For the noncondensable gas content in the mixture fluid, a typical value for air dissolved in water, 15 ppm, was used. A parametric study on the influence of the noncondensable gas content used in the same computational method was reported in [23]; however, the authors acknowledge the need for a more rigorous study, which is planned to be conducted in the not too distant future.

The computational fluid dynamics (CFD) code, FLUENT 6.1, employs a cell-centered finite-volume method that allows the use of computational elements with arbitrary polyhedral shape. Convective terms are discretized using the second-order accurate upwind scheme, while diffusive terms are discretized using the second-order accurate central differencing scheme. The velocity-pressure coupling and overall solution procedure are based on a SIMPLE type segregated algorithm adapted to unstructured grids. The discretized equations are solved using pointwise Gauss-Seidel iterations, and an algebraic multi-grid method accelerates the solution convergence. The convergence criteria in the present study were at least a three orders of magnitude drop in the mass conservation imbalance and momentum equation residuals, which are deemed sufficient for most steady flow solutions. A more detailed description of the numerical method is available in Kim et al.[24].

Model Geometry and Grid Generation

The leading edge and mid-chord cavitation on a hydrofoil is of particular interest for propeller cavitation studies, as it represents the two-dimensional characteristics of propeller blade cavitation. For the validation of leading edge and mid-chord cavitation on a hydrofoil, a modified NACA66 foil section with camber ratio of 0.02, mean line of 0.8 and thickness ratio of 0.09 was selected.

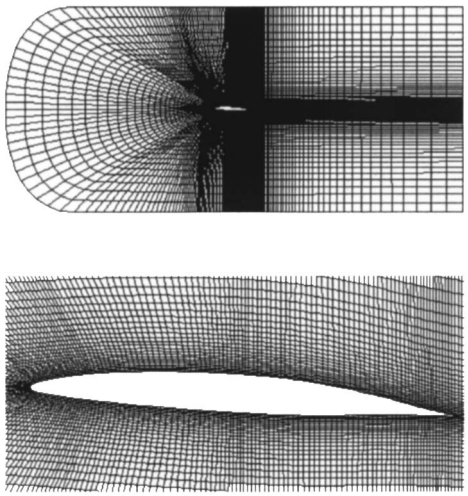

Fig. 1 Computational domain and grid for the leading edge hydrofoil cavitation case: full view (upper) and partial view (lower)

The same foil geometry was used for the experiments by Shen and Dimotakis [25]. A C-type structured grid consisting of 17,184 quadrilateral cells was generated in a computational domain with extent $-5C \leq x \leq 6C$ and $-2.5C \leq y \leq 2.5C$, where C represents the chord length, as shown in Fig. 1. Note that the tunnel walls were not modeled in the computational domain. Since verifying the present cavitation modeling approach for a propeller blade section was the main purpose of these hydrofoil computations, the grid was designed for the wall function based boundary conditions and thereby the first cell height off the solid surface was 25 to 200 in terms of y^+.

For the validation of noncavitating and cavitating marine propeller flows, a four bladed marine propeller, MP 017, was selected. The propeller geometry was designed at the University of Tokyo and the detailed experimental investigation was reported in [26]. The flow can be characterized by a flat pressure distribution on the backside and better cavitation characteristics than the conventional MAU type propeller on which it is based. The propeller geometry with hub and boss is shown in Fig. 2 and some of the model specifications are given in Table 1. Note that this is an open-water test configuration, so the flow direction is from the lower-left to the upper-right corner of the figure. The computational domain was created as one passage surrounding a blade: the inlet is 1.5D upstream, where D is the propeller diameter; the exit is 3.5D downstream; solid surfaces on the blade and hub are cen-

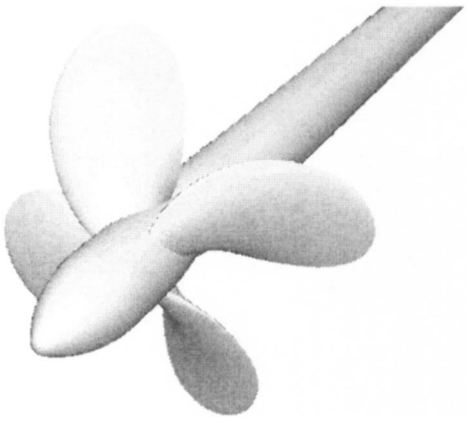

Fig. 2 MP 017 propeller geometry

Table 1 Specifications of MP 017 propeller

No. of blades	4
Diameter (m)	0.2143
Boss ratio	0.1800
Pitch ratio at 0.7R	0.8493
Expanded area ratio	0.6000
Skew (m)	0.01257
Rake (degree)	10.00

tered at the coordinate system origin and aligned with uniform inflow; the outer boundary is $1.4D$ from the hub axis; and two rotationally periodic boundaries subtending a 90° angle form the boundaries in between. Again the tunnel walls were not modeled, but its influence was reported to be insignificant [26].

A hybrid grid was generated using the FLUENT preprocessors GAMBIT and TGrid. First, the blade surface was meshed with triangles. The region around the root, tip, and blade edges was meshed with smaller triangles, i.e., with sides of approximately $0.001D$, while the inner region was filled with triangles of appropriately increased size. Once the blade surface was meshed, the other surfaces were meshed with larger triangles, i.e., with sides of up to $0.1D$. In order to resolve the turbulent boundary layer on the solid surfaces, the surface grid generated in GAMBIT was imported into TGrid, and four layers of prismatic cells were grown from the blade and hub surfaces. The first cell height off the solid surface was approximately $0.00001D$, which is 3 to 50 in terms of y^+, and the stretching ratio of the layers was 1.1. Finally the remaining region in the domain was filled with tetrahedral cells. The number of cells in this *baseline* grid was 186,637. For the grid dependence study, three more grids were generated with the same meshing strategy, but with systematically decreasing the element size on the edges, resulting in roughly doubling the number of cells. The numbers of cells in these grids were 403,748 *(medium-1)*, 782,665 *(medium-2)*, and 1,901,160 *(fine)*. Figure 3 shows the surface grid on the blade and hub surface for the *baseline* grid. Note that, due to the aspect ratio limit with triangular faces, the unstructured meshing approach generally results in a larger number of cells near the blade edges, compared to a structured meshing approach.

Results and Comparison with Data

Cavitation on Hydrofoil. Shen and Dimotakis [25] measured the static pressure on the foil surface at various angles of attack, α, and cavitation numbers, $\sigma=(p_\infty-p_v)/(\frac{1}{2}\rho_l V_\infty^2)$, where p_∞ and V_∞ are the reference pressure and velocity at the test section, respectively. The tunnel flow speeds and Reynolds numbers, $\mathrm{Re}=\rho_l V_\infty C/\mu_l$, where μ_l is the molecular viscosity of the liquid, were also varied with the reference velocity. Along the upstream and side boundaries, the undisturbed tunnel flow speed, V_∞, was imposed with a turbulence intensity of 1%. The pressure on these boundaries was obtained by a first-order accurate extrapolation. On the hydrofoil surface, a no-slip condition was imposed, i.e., the velocity is zero with pressure obtained by the first-order accurate extrapolation. On the downstream boundary, the constant exit pressure, p_∞, which is set to match the given σ, was imposed and all other variables were extrapolated with first order accuracy.

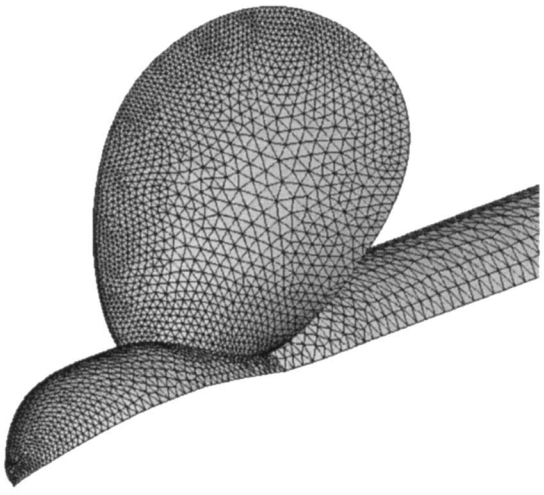

Fig. 3 Surface grid of the *baseline* grid for MP 017 propeller

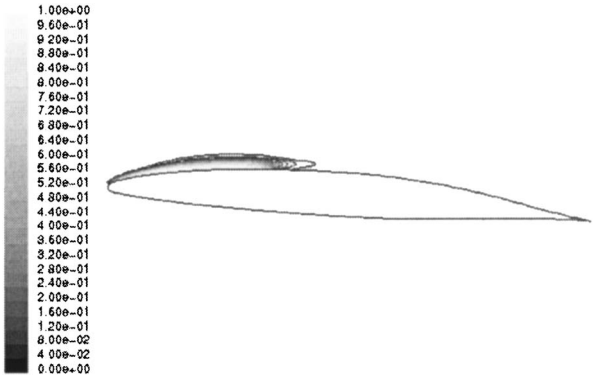

Fig. 4 Vapor volume fraction contours at $\alpha=4°$, $\sigma=0.91$

For the leading edge cavitation, the computational conditions were set to the experimental ones at $\alpha=4°$, $\sigma=0.84, 0.91, 1.0, 1.76$, and $\mathrm{Re}=2\times10^6$. By varying the constant exit pressure, the values of σ were controlled. Figure 4 displays contours of vapor volume fraction at $\sigma=0.91$, showing the typical leading edge sheet cavitation. Figure 5 presents a comparison of the computed and measured pressure distributions on the suction side of the foil surface in terms of the pressure coefficient, $C_p=(p-p_\infty)/(\frac{1}{2}\rho_l V_\infty^2)$. The flow does not cavitate at $\sigma=1.76$, as shown by the regular pressure distribution on the suction side. Once the flow cavitates at a lower σ, the cavity grows, as indicated by the increasing length of the constant pressure level. The overshoot of pressure at the cavity closure is obvious in the pressure distributions at $\sigma=0.84, 0.91, 1.0$. The agreement between the computed and measured C_p values is very good.

For the mid-chord cavitation, the computational conditions were again set to the experimental ones at $\alpha=1°$, $\sigma=0.34, 0.38, 0.43$, and $\mathrm{Re}=3\times10^6$. Figure 6 displays the contours of vapor volume fraction at $\sigma=0.38$, showing the well-reproduced mid-chord cavitation. Figure 7 presents the comparison of the computed and measured pressure distributions on the suction side of the foil surface. According to the experimental observation, the flow starts cavitating at approximately $\sigma=0.415$, as confirmed by the noncavitating pressure distribution at $\sigma=0.43$. At $\sigma=0.34$ and 0.38, the cavitation is clearly present and the agreement between the computed and measured C_p values is again very good. This good agreement also suggests that the present model predicts the initiation and termination points of the mid-chord cavitation well.

The authors acknowledge that there are certainly unsteady flow features in these hydrofoil cavitation cases, as stated in [25]. As a preliminary study, a representative case, i.e., the $\sigma=0.38$ case, was run in unsteady mode using the same grid and the time step size of 0.001 s, which correspond to the local Courant number of 0.049 to 1.3. Indeed, the unsteadiness was confirmed by the oscillating water volume fraction on the hydrofoil surface and the cavity shape. However, its time-averaged behavior coincides with the steady counterpart, and because the largely steady flow features are of primary concern here, only the steady flow results are presented. Obviously, running the solution in unsteady mode with the

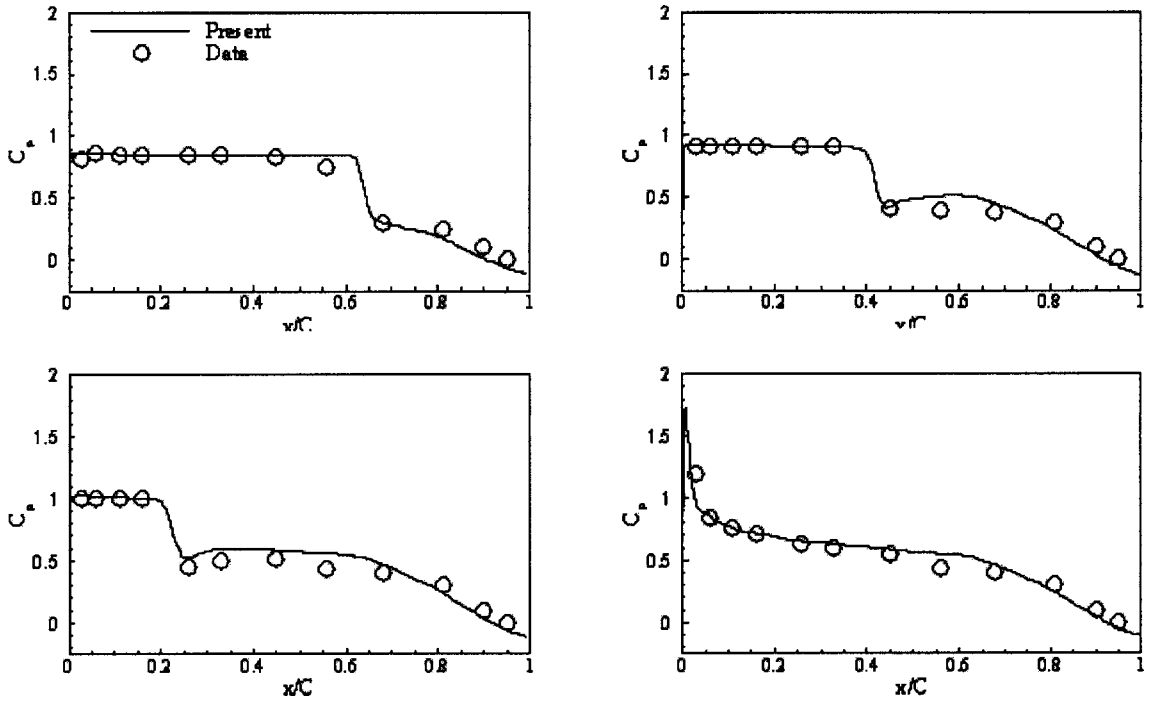

Fig. 5 Pressure coefficient distributions on the suction side of the foil surface: σ=0.84 (upper left), σ=0.91 (upper right), σ=1.00 (lower left), and σ=1.76 (lower right)

large eddy simulation (LES) or detached eddy simulation (DES) approach on much finer grids would illustrate the fine scale flow features better; but the authors believe that it is beyond the scope of the present study, which more or less focuses on the practical simulation method for the steady performance prediction of a cavitating marine propeller in open-water.

Noncavitating Marine Propeller. Validations for the noncavitating conditions were essential before proceeding to the propeller cavitation simulations, although detailed validations for another marine propeller geometry was reported in [20] using the same method, i.e., solving the RANS equations on an unstructured hybrid grid in a rotating reference frame. A wide range of advance ratios, $J=V_a/nD$, where V_a is the inflow speed and n is the number of revolutions per second, was considered, i.e., $0.23 \leqslant J \leqslant 0.9$. The values of J were varied by increasing/decreasing V_a, while n was kept constant at 25.

Boundary conditions were set to simulate the flow around a rotating propeller in the open water: on the inlet boundary, velocity components for a uniform stream with the given inflow speed, V_a, were imposed with a turbulence intensity of 1% and the pressure extrapolated from inside; on the blade and hub surface, a no-slip condition was imposed, i.e., zero velocity with extrapolated pressure; on the outer boundary, a slip boundary condition was imposed, i.e., a zero normal velocity component with extrapolated tangential velocity components and pressure; on the periodic boundaries, rotational periodicity was ensured, i.e., all variables at the same axial and radial coordinates were set equal on both of the periodic boundaries; and on the exit boundary, the pressure was set to a constant value, while all other variables were extrapolated. The first-order accurate scheme was used for the extrapolations. The inflow turbulence intensity was set based on the experimental setup in which the turbulence level was tightly controlled. The influence of this turbulence intensity level was found to be insignificant: the cavitating flow solution did not change with the intensity of up to 5%.

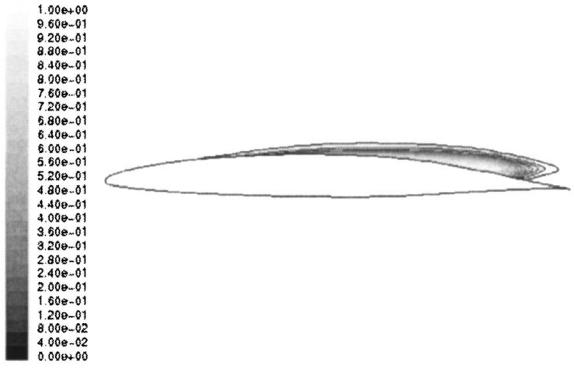

Fig. 6 Vapor volume fraction contours at α=1°, σ=0.38

A grid dependence study for the design condition, $J=0.55$, was carried out as a measure of numerical uncertainties. Four grids (as described in the grid generation section) were used. Table 2 presents the grid dependence study results in terms of the thrust, $K_T=\text{Thrust}/\rho_l n^2 D^4$, and torque, $K_Q=\text{Torque}/\rho_l n^2 D^5$, coefficients. The parameter ε is the relative difference in the solutions obtained at two grid levels considered and defined as $\varepsilon=(\varphi_{coarser}-\varphi_{finer})/\varphi_{finer}$, where $\varphi_{coarser}$ and φ_{finer} represent the solutions at coarser and finer levels of the two, respectively. The corresponding values of the grid convergence index (GCI) proposed by Roache [27] are also presented in Table 2. The GCI is defined as $|\varepsilon|/(r^p-1)$, where r is the grid refinement ratio and p is the order of accuracy of the numerical method. The values of r and p used to obtain the GCI's are $\sqrt[3]{2}=1.26$, the effective refinement ratio for the cell count doubling in three dimensions, and 2, the formal order of accuracy of the discretization schemes employed, respectively. For validation purposes hereafter, the *medium-1* grid was used.

Figure 8 shows the curves of K_T and K_Q vs. J along with the corresponding measured values. Overall, the agreement is good, with differences less than 2% and 7% for K_T and K_Q, respectively, and the trends with varying advance ratios are also well predicted. However, the CFD solutions slightly overpredict K_Q. This ten-

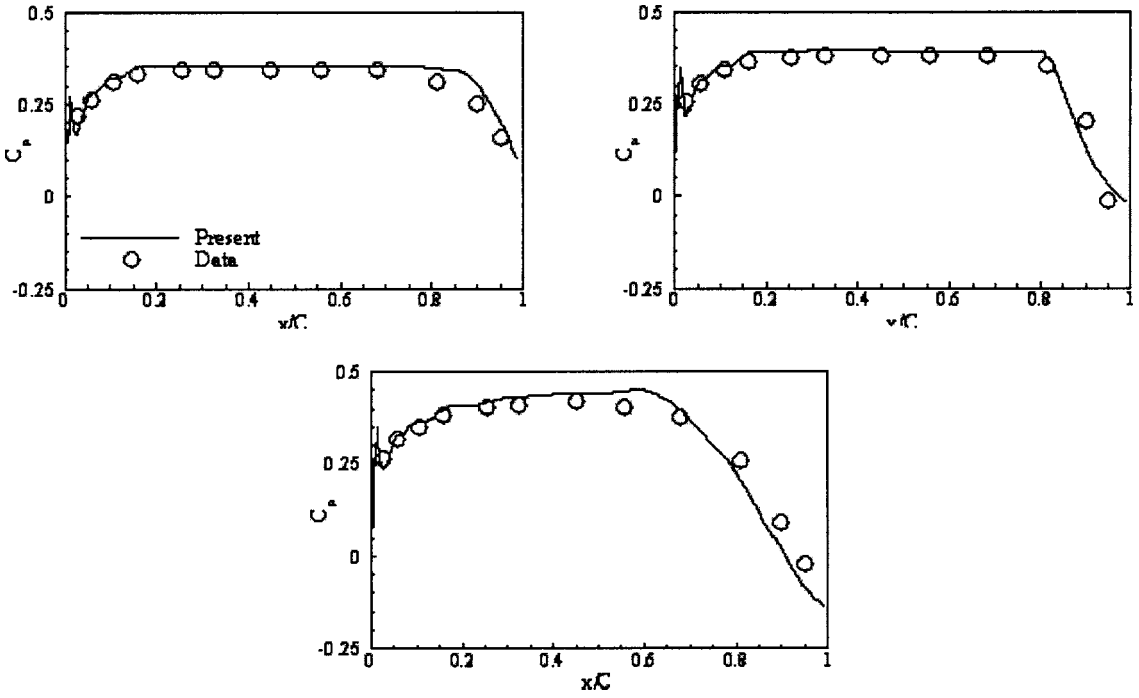

Fig. 7 Pressure distributions on the foil surface: σ=0.34 (upper right), σ=0.38 (upper left), and σ=0.43 (lower center)

dency seems to be prevalent in most of the RANS CFD simulations for marine propellers. It is due to, as Funeno [28] discussed, the viscous flow scale effect on the propeller performance prediction. In fact, a large, 50% to 60%, laminar flow region is known to exist and the turbulence transition takes place on the blade surface in model scale experiments. However, in numerical simulations, it is a general practice to assume that the flow around the propeller is fully turbulent whether in model scale or in full scale, because there is not a universally recognized method to handle the turbulence transition on the propeller blade surface. Therefore, without an ad hoc tuning of the turbulence quantities, it is very difficult to match the model scale experimental data. More detailed investigation results on this issue are available in [20]. Other causes might be that the experimental conditions do not conform perfectly to the CFD model. Insufficient grid resolution for the tip vortex could also give rise to the discrepancy observed.

Table 2 Grid independence study results for the design condition noncavitating case

No. of cells	K_T	$\|\varepsilon\|$	GCI	K_Q	$\|\varepsilon\|$	GCI
186,637	0.1677	0.0121	0.0206	0.02728	0.0727	0.1237
403,748	0.1657	0.0042	0.0071	0.02543	0.0188	0.0320
782,665	0.1650	0.0085	0.0144	0.02496	0.0073	0.0124
1,901,160	0.1636			0.02478		

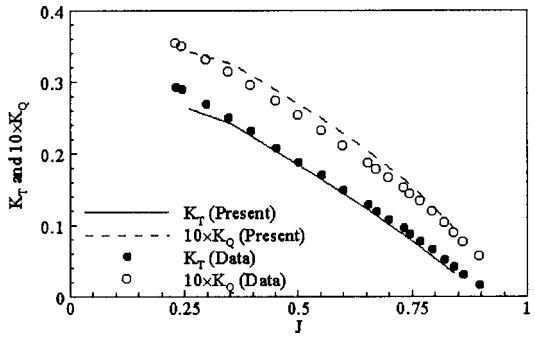

Fig. 8 K_T and K_Q vs. J for noncavitating conditions

Figure 9 compares contours of the backside pressure coefficient, $C_p=(p-p_\infty)/\left[\frac{1}{2}\rho_l(nD)^2\right]$ at three different J's: 0.2, 0.55, and 0.8. Cavitation occurs where the pressure is low, and it is obvious in Fig. 9 that the flow is more susceptible to cavitation at lower J's, where very low pressure in the tip area is observed. Based on these computational and experimental observations, only two J's, the high load J=0.2 and the design condition J=0.55, were considered for cavitating conditions.

Cavitating Marine Propeller. For the cavitating marine propeller cases, the cavitation model was activated. Boundary conditions for these cases were set in the same way as for the noncavitating cases. The only difference was at the exit boundary, where a constant exit pressure was set to match the given σ.

A grid dependence study for the representative cavitating propeller condition at J=0.2 and $\sigma=(p_\infty-p_v)/\left[\frac{1}{2}\rho_l(nD)^2\right]$=2 was carried out in a somewhat different way that is more focused on the cavitation feature. First, the results on two grids, i.e., the *baseline* and *fine* grids, were compared; $|\varepsilon|$'s for K_T and K_Q are 0.0292 and 0.0415, respectively. Next, the *baseline* grid was adapted, i.e., one tetrahedral cell is divided into eight tetrahedral cells, based on the gradient of the vapor volume fraction and named *adapted*. This grid adaption resulted in an approximate 8.5% increase in the number of cells and higher resolution around the cavity, which is comparable to that of the *fine* grid. The results on this *adapted* grid were compared with its counterpart on the *baseline* grid; $|\varepsilon|$'s for K_T and K_Q are 0.0220 and 0.0325, respectively. It was observed that these grid dependence study results for the cavitating cases were similar to those for the noncavitating cases. The authors are well aware of the importance of verification and validation of CFD results and more rigorous studies are recommended for future work.

Figure 10 presents the curves of K_T and K_Q vs. σ at J=0.2 and 0.55, along with corresponding measured values. The thrust breakdown is one of the major issues in cavitating propellers. At J=0.2, i.e., the high load and large angle of attack, both K_T and

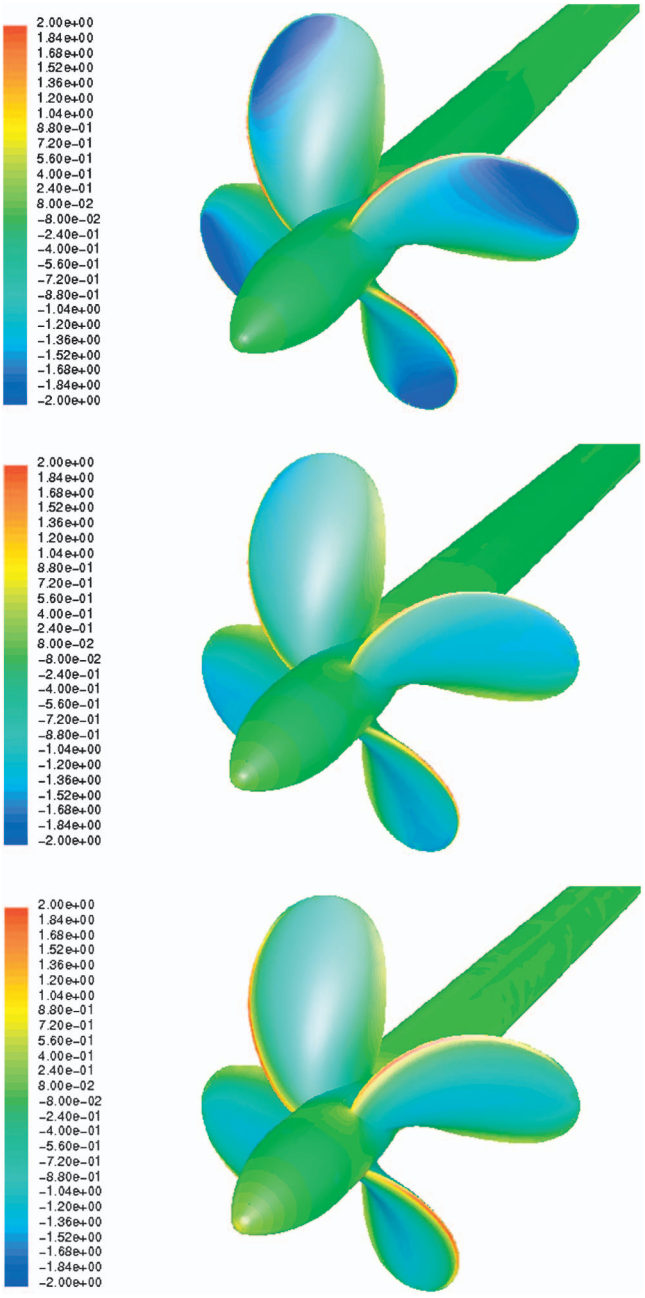

Fig. 9 (Color) Pressure coefficient contours on backside: J =0.2 (top), J=0.55 (middle), and J=0.8 (bottom)

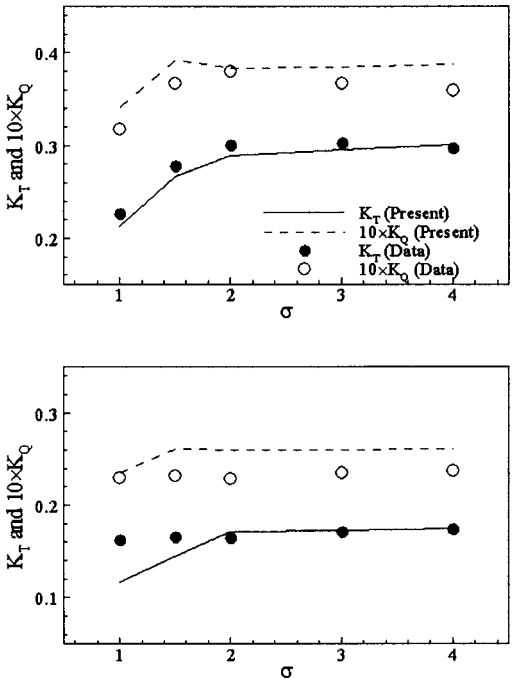

Fig. 10 K_T and K_Q vs. σ. J=0.2 (upper) and 0.55 (lower)

K_Q start decreasing upon the onset of cavitation at σ=2.0. This behavior is quantitatively well reproduced in the present simulation. However, at J=0.55, i.e., the design condition and small angle of attack, there is discrepancy between the measured and simulated values at lower σ's. The measured K_T and K_Q remain nearly constant, although the occurrence of cavitation is visually and acoustically apparent at σ values below 2.0: on the other hand, the simulated K_T and K_Q overpredict the decrease in this range. The authors believe that there are multiple issues contributing to this behavior. First of all, the viscous flow scale effect and the unavoidable nonconformity with the experimental conditions that are mentioned in the previous section must have an impact on the final solution. Second, at low load conditions, the cavitation is weak and in a different shape. A very thin leading edge cavitation combined with a relatively stronger mid-chord cavitation is observed, and its influence on the propeller performance is not as prominent as at high load conditions. The accurate prediction of this weak and somewhat different type of cavitation becomes more difficult, as discussed with Fig. 13 later.

Figure 11 shows the contours of the blade backside pressure coefficient at J=0.2 and σ=2.0. It is clearly seen that cavitation is to occur in the tip area, where the pressure is very low. Note that the pressure coefficient in the cavitating area is maintained constant at $-\sigma$, as expected from the general cavitation theory. This prediction of cavitation inception can be confirmed by the contours of vapor volume fraction on the backside of the blade, Fig. 12, in which the high vapor volume fraction area closely matches the low pressure area in Fig. 11.

The computed iso-surface of vapor volume fraction of 0.1 and observed cavity shapes are compared in Fig. 13 at several conditions: J=0.2 and σ=2.0, J=0.4 and σ=2.0, and J=0.5 and σ =1.0. The case at J=0.2 and σ=2.0 is representative of the cavitating propeller cases considered in the present study, while the case at J=0.4 and σ=2.0 represents a slightly low load condition and the case at J=0.5 and σ=1.0 represents the condition for which the thrust breakdown prediction shows discrepancy from

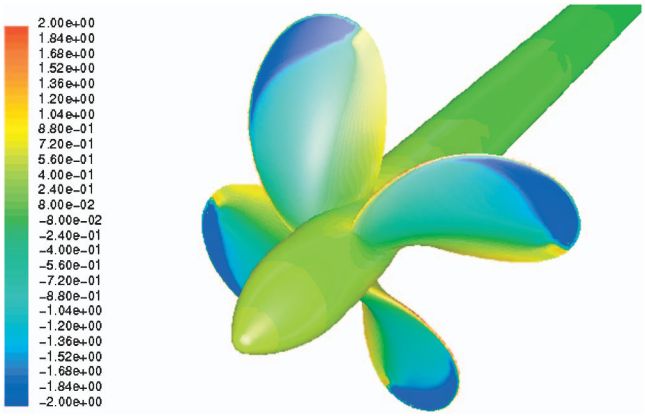

Fig. 11 (Color) Pressure coefficient contours on backside at J=0.2 and σ=2.0

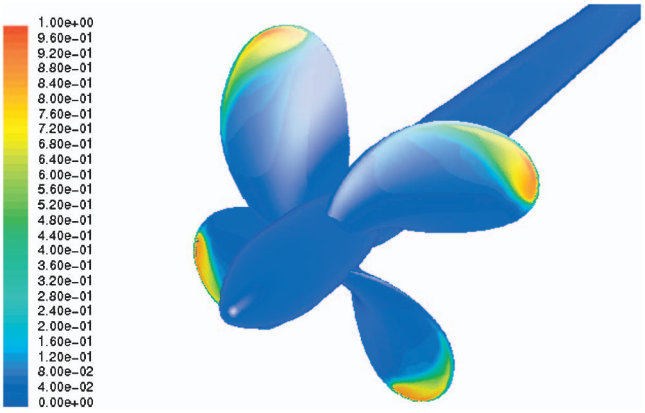

Fig. 12 (Color) Vapor volume fraction contours on back side at $J=0.2$ and $\sigma=2.0$

the measurement. Note that, at $J=0.5$, the measured K_T and K_Q remain nearly constant as for the cases at $J=0.55$. To explicate the discrepancy at low load conditions, the case at $J=0.5$ and $\sigma=1.0$ was selected instead of the case at $J=0.55$ and $\sigma=1.0$, because of the availability of experimental photographs that clearly show the cavity shapes at the corresponding conditions. Table 3 presents the comparison of K_T and K_Q for the three cavitating cases. The agreement is good at the two high load conditions; but the comparison shows the same behavior as in Fig. 10 for the low load condition. The cavity shapes on the blade are also in good agreement with each other at the two high load conditions, i.e., $J=0.2$ and $\sigma=2.0$, and $J=0.4$ and $\sigma=2.0$. It is observed, however, that the computed cavity shape shows an abrupt termination right behind the tip and the vortex cavity is missing. This is attributed mainly to the insufficient grid resolution in the region, which is entailed from the transition from the prismatic boundary layer

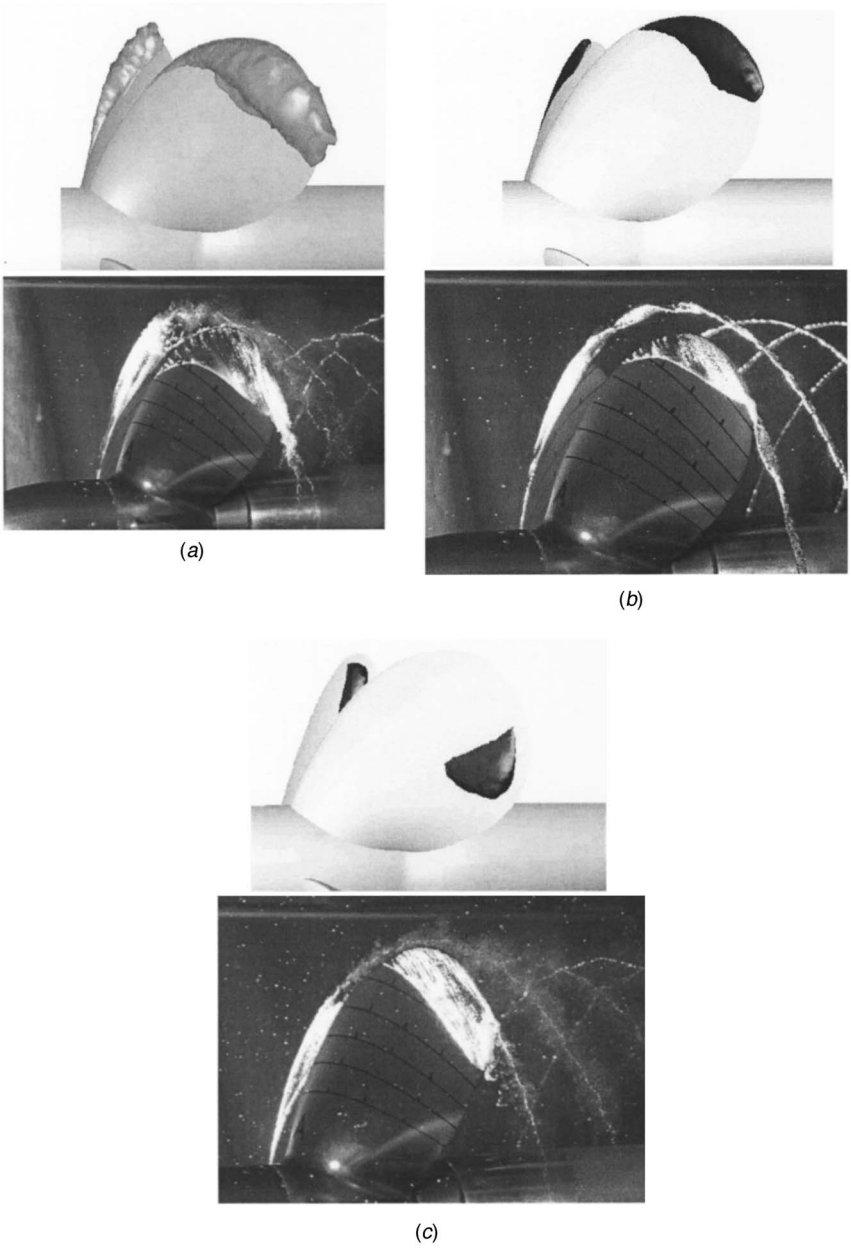

Fig. 13 (*a*) Cavity shape on blade at $J=0.2$ and $\sigma=2.0$ case: present (upper) and experiment (lower). (*b*) Cavity shape on blade at $J=0.4$ and $\sigma=2.0$ case: present (upper) and experiment (lower). (*c*). Cavity shape on blade at $J=0.5$ and $\sigma=1.0$ case: present (upper) and experiment (lower).

Table 3 Comparison of K_T and K_Q for three cavitating propeller cases

Condition	K_T (measured)	K_T (predicted)	K_Q (measured)	K_Q (predicted)
$J=0.2$, $\sigma=2$	0.297	0.289	0.0376	0.0384
$J=0.4$, $\sigma=2$	0.228	0.228	0.0295	0.0327
$J=0.5$, $\sigma=1$	0.176	0.139	0.0264	0.0293

cells to the tetrahedral outer cells. Note, however, that the resolution of the tip vortex cavity is not of primary concern in the present study, as it has less impact on the whole propeller performance. In any event, appropriate grid refinement approaches for this issue are recommended for future work. On the other hand, the cavity shapes at the low load condition, i.e., $J=0.5$ and $\sigma=1.0$, show clear disagreement. The predicted cavity is smaller and displays only the mid-chord cavitation. There are two issues that need to be considered here: (1) The leading edge sheet cavitation is usually accompanied by the laminar separation. At the two high load conditions, the laminar separation at the leading edge is predicted well, and the sheet cavitation there is well captured. However, at the low load condition, the laminar separation near the tip is more difficult to predict, since the region is smaller and the flow is more three-dimensional, and this improper prediction of laminar separation eventually leads to the unmatched cavity shapes. (2) The iso-surface of vapor volume fraction of 0.1 does not always correspond to the visible cavity observed in photographs. Apparently, more sophisticated modeling and numerical methods on refined grids seem to be required to appropriately capture this type of cavitation at low load conditions.

Concluding Remarks

Results of computational validations for cavitating flow around a hydrofoil and marine propeller have been presented. An unstructured grid based Reynolds-averaged Navier-Stokes method was used. The objectives were to propose and verify a computational approach for propeller cavitation that can complement tunnel tests and existing numerical methods.

A modified NACA66 foil section and conventional four-bladed marine propeller called MP 017 were selected for the validations. Computations were performed for various advance ratios and cavitation numbers following experimental conditions.

Computational results for both local and global flow quantities were discussed and compared with experimental data. The pressure distribution on the foil surface reproduced the physics of leading edge and mid-chord cavitation on a hydrofoil well. In the cavitating propeller case, the predicted global quantities, such as thrust and torque, were in good agreement with the measured values and the trend of the thrust breakdown was well captured. The cavity shape on the blade surface also matched the experimental observation, although the vortex cavity was missing due to the insufficient grid resolution.

The overall results suggest that the present approach is practicable for actual cavitating propeller design procedures without lengthy preprocessing and significant preliminary knowledge of the flow field. However, outstanding issues include a more refined approach for propeller cavitation at low load conditions, improvement in tip vortex cavitation prediction, an extensive investigation on the thrust identity conditions, and comparison of unsteady local flow quantities, if experimental data are available.

References

[1] Kerwin, J. E., Kinnas, S. A., Wilson, M. B., and McHugh, J., 1986, "Experimental and Analytical Techniques for the Study of Unsteady Propeller Sheet Cavitation," Proc. 16th Symposium on Naval Hydrodynamics, Berkeley, CA.

[2] Lee, C.-S., 1979, "Prediction of Steady and Unsteady Performance of Marine Propellers with or without Cavitation by Numerical Lifting Surface Theory," Ph.D. dissertation, Massachusetts Institute of Technology, Cambridge, MA.

[3] Kinnas, S. A., and Fine, N. E., 1993, "A Numerical Nonlinear Analysis of the Flow Around Two- and Three-Dimensional Partially Cavitating Hydrofoils," J. Fluid Mech., **254**, pp. 151–181.

[4] Deshpande, M., Feng, J., and Merkle, C. L., 1994, "Cavity Flow Predictions Based on the Euler Equations," ASME J. Fluids Eng., **116**(1), pp. 36–44.

[5] Kinnas, S. A., Choi, J.-K., Lee, H., Young, Y. L., Gu, H., Kakar, K., and Natarajan, S., 2002, "Prediction of Cavitation Performance of Single or Multi-Component Propulsors and Their Interaction with the Hull," Soc. Nav. Archit. Mar. Eng., Trans., **110**, pp. 215–244.

[6] Kubota, A., Kato, H., and Yamaguchi, H., 1992, "A New Modeling of Cavitating Flows: A Numerical Study of Unsteady Cavitation on a Hydrofoil Section," J. Fluid Mech., **240**, pp. 59–96.

[7] Chen, Y., and Heister, S. D., 1995, "Two Phase Modeling of Cavitated Flows," Comput. Fluids, **24**, pp. 799–809.

[8] Ahuja, V., Hosangadi, A., Ungewitter, A., and Dash, S. M., 1999, "A Hybrid Unstructured Mesh Solver for Multi-Fluid Mixtures," AIAA paper 99-3330, Proc. 14th AIAA Computational Fluid Dynamics Conference, Norfolk, VA.

[9] Kunz, R. F., Boger, D. A., Stinebring, D. R., Chyczewski, T. S., Lindau, J. W., Gibeling, H. J., Venkateswaran, S., and Govindan, T. R., 2000, "A Preconditioned Navier-Stokes Method for Two-Phase Flows with Application to Cavitation Prediction," Comput. Fluids, **29**, pp. 849–875.

[10] Senocak, I., and Shyy, W., 2002, "A Pressure-Based Method for Turbulent Cavitating Flow Computations," J. Comput. Phys., **176**, pp. 363–383.

[11] Singhal, A. K., Athavale, M. M., Li, H. Y., and Jiang, Y., 2002, "Mathematical Basis and Validation of the Full Cavitation Model," ASME J. Fluids Eng., **124**(3), pp. 617–624.

[12] Grogger, H. A., and Alajbegovic, A., 1998, "Calculation of the Cavitating Flow in Venturi Geometries Using Two Fluid Model," ASME paper FEDSM98-5295, Proc. 1998 ASME Fluids Engineering Division Summer Meeting, Washington, DC.

[13] Venkateswaran, S., Lindau, J. W., Kunz, R. F., and Merkle, C. L., 2002, "Computation of Multiphase Mixture Flows with Compressibility Effects," J. Comput. Phys., **180**, pp. 54–77.

[14] Lindau, J. W., Venkateswaran, S., Kunz, R. F., and Merkle, C. L., 2003, "Computation of Compressible Multiphase Flows," AIAA paper 2003-1285, Proc. 41st AIAA Aerospace Sciences Meeting and Exhibit, Reno, NV.

[15] Lindau, J. W., Medvitz, R. B., Boger, D. A., and Kunz, R. F., 2003, "Propeller Cavitation Breakdown Analysis," ASME paper FEDSM2003-45407, Proc. 4th ASME-JSME Joint Fluids Engineering Conference, Honolulu, HI.

[16] Manninen, M., Taivassalo, V., and Kallio, S., 1996, "On the Mixture Model for Multiphase Flow," VTT Publications 288, Technical Research Centre of Finland, Valtion Teknillinen Tutkimuskeskus, Espoo, Finland.

[17] Schiller, L., and Naumann, Z., 1933, "A Drag Coefficient Correlation," Z. Ven. Dtsch. Ing., **77**(12), pp. 318–320.

[18] Wilcox, D. C., 1998, *Turbulence Modeling for CFD*, 2nd ed., DCW Industries, Inc., La Canada, CA.

[19] Kim, S.-E., Rhee, S. H., and Cokljat, D., 2003, "Application of modern Turbulence Models to Vortical Flow Around a 6:1 Prolate Spheroid at Incidence," AIAA paper 2003-0429, Proc. 41st Aerospace Sciences Meeting and Exhibit, Reno, NV.

[20] Rhee, S. H., and Joshi, S., 2005, "Computational Validation for Flow around a Marine Propeller Using Unstructured Mesh Based Navier-Stokes Solver," accepted for publication in the JSME Int. J. Ser. B. Fluids Therm. Eng.

[21] Hinze, J. O., 1975, *Turbulence*, 2nd ed., McGraw-Hill, New York, NY.

[22] Singhal, A. K., Vaidya, N., and Leonard, A. D., 1997, "Multi-Dimensional Simulation of Cavitating Flows Using a PDF Model of Phase Change," ASME paper FEDSM97-3272, Proc. ASME FED Meeting, Vancouver, Canada.

[23] Watanabe, T., 2004, "Development of a Marine Propeller Simulator Considering Wake and Cavitation," M.S. thesis, University of Tokyo, Tokyo, Japan (in Japanese).

[24] Kim, S.-E., Mathur, S. R., Murthy, J. Y., and Choudhury, D., 1998, "A Reynolds-Averaged Navier-Stokes Solver Using Unstructured Mesh Based Finite-Volume Scheme," AIAA paper 98-0231, Proc. 36th AIAA Aerospace Sciences Meeting and Exhibit, Reno, NV.

[25] Shen, Y. T., and Dimotakis, P. E., 1989, "The Influence of Surface Cavitation on Hydrodynamic Forces," Proc. 22nd American Towing Tank Conference, St. John's, Canada.

[26] Yamaguchi, H., Kato, H., Kamijo, A., and Maeda, M., 1988, "Development of Marine Propellers with Better Cavitation Performance—2nd Report: Effect of Design Lift Coefficient for Propellers with Flat Pressure Distribution," J. Soc. Naval Architects Jpn, **163**, pp. 48–65.

[27] Roache, P. J., 1998, *Verification and Validation in Computational Science and Engineering*, Hermosa Publishers, Albuquerque, NM.

[28] Funeno, I., 2002, "On Viscous Flow around Marine Propellers—Hub Vortex and Scale Effect," J. Kansai Soc. Naval Architects, Jpn, **238**, pp. 17–27.

Jules W. Lindau
David A. Boger
Richard B. Medvitz
Robert F. Kunz

Applied Research Lab,
The Pennsylvania State University,
State College, PA 16804-0030

Propeller Cavitation Breakdown Analysis

A Reynolds-averaged Navier-Stokes computational model of homogeneous multiphase flow is presented. Cavitation driven thrust and torque breakdown over a wide range of advance ratios is modeled for an open propeller. Computational results are presented as a form of validation against water tunnel measured thrust and torque breakdown for the propeller. Successful validation of the computational model is achieved. Additional observations are made with regards to cavity size and shape as well as cavitation breakdown behavior. [DOI: 10.1115/1.1988343]

Introduction

A three-dimensional, multiphase Reynolds-averaged, Navier-Stokes (RANS) computational tool, UNCLE-M, is applied to propeller load breakdown, due to cavitation, via modeling of an open propeller, designated P4381. Thrust breakdown performance of P4381 has been documented in the open-literature [1,2]. This published data include breakdown at far off-design advance ratios, i.e., at both large positive and large negative rotor blade incidence. Model integrated results are presented, and compared with the available data. In addition, interesting numerical results are presented in a field form for comparison with experimental flow-field observations.

Previously, Kunz et al. [3] and Lindau et al. [4] have developed and demonstrated steady and unsteady large-scale cavity flow modeling capabilities of the flow solver. Those publications demonstrated that the numerical and physical modeling contained in the UNCLE-M code provide appropriate physics to properly model high Reynolds number flow fields dominated by attached cavities. The large scale of such cavities implies tractability by a homogeneous approach. Nonetheless, they are generally unsteady, and contain regions of separated flow. In flows modeled here, interface curvatures are small, and pressure and velocity are approximately continuous across the interface. Thus, it is presumed that nonequilibrium interface dynamics are of negligible magnitude, and the effect of surface tension is not incorporated. For cavitation inception, where physics of tiny bubbles is a significant contributor, this methodology would not be appropriate. For cloud cavitation, or cases where cavitation is sufficient to effect hydrodynamic performance, however, this approach is reasonable.

In liquid-vapor cavities of hydrodynamic engineering interest, degrees of unsteadiness are present. Typically the cavity or, at least, the *closure* region is unsteady with a wide range of significant scales in both time and space. The accurate simultaneous resolution of all such scales in the region of a turbulent cavity closure implies direct numerical simulation and is probably beyond the limit of known computational methods on current resources. The accurate modeling of one or a few of the modes of cavity closure may be feasible with homogeneous unsteady RANS methods and, for some cases, has been documented by Lindau et al. [4]. More scales may be feasible with Detached Eddy Simulation as documented by Kunz et al. [5]. However, in this investigation, only previously-reported time-averaged measurements are used for comparison, and only results of steady-state numerical computations are presented. Thus the vapor cavity and closure region in the presented results may be considered to be an average.

Contributed by the Fluids Engineering Division for publication in the JOURNAL OF FLUIDS ENGINEERING. Manuscript received by the Fluids Engineering Division, March 26, 2004; final revision: May 24, 2005. Associate Editor: Steven Ceccio.

Physical Model

The physical model equations solved here have been described previously [3]. In that presentation, the physically unsteady equations modeling a liquid, a vapor, and a third, noncondensable gas, phase were required. However, for the current work, only steady-state solutions consisting of liquid and vapor phases are considered. The basis of the model is the incompressible multiphase RANS equations in a homogeneous mixture form. Thus although the modeled solution at each point in space yields a single velocity vector, each field is treated as a separate species and requires the inclusion of a new continuity equation. Mass transfer between the liquid and vapor phases is achieved through a finite-rate model. Other researchers have applied similar models with a single species, barotropic, approach. However, with the ability to easily include more than one or two fields in a single control volume and discretely model mass transfer, the multiple species transport model of multiphase flow is presented as a more flexible physical approach. In addition, Senocak and Shyy [6] have suggested that the multiple species transport model provides a degree of freedom missing from the barotropic models required to capture the vorticity generation observed in regions of cavity closure. A high Reynolds number form of two-equation models with standard wall functions provides turbulence closure.

The governing differential equations, cast in Cartesian tensor form follow:

$$\left(\frac{1}{\rho_m \beta^2}\right)\frac{\partial p}{\partial \tau} + \frac{\partial u_j}{\partial x_j} = (\dot{m}^+ + \dot{m}^-)\left(\frac{1}{\rho_l} - \frac{1}{\rho_v}\right) \tag{1a}$$

$$\frac{\partial(\rho_m u_i)}{\partial \tau} + \frac{\partial(\rho_m u_i u_j)}{\partial x_j} = -\frac{\partial p}{\partial x_i} + \frac{\partial((\mu_{m,t} + \mu_m)t_{ij})}{\partial x_j} \tag{1b}$$

$$\left(\frac{\alpha_l}{\rho_m \beta^2}\right)\frac{\partial p}{\partial \tau} + \frac{\partial \alpha_l}{\partial \tau} + \frac{\partial(\alpha_l u_j)}{\partial x_j} = \left(\frac{\dot{m}^+ + \dot{m}^-}{\rho_l}\right) \tag{1c}$$

Shear tensor, mixture density, mixture viscosity, and turbulent eddy viscosity are defined in Eq. (2),

$$t_{ij} = \frac{\partial u_i}{\partial x_j} + \frac{\partial u_j}{\partial x_i} \quad \rho_m = \rho_l \alpha_l + \rho_v \alpha_v \quad \mu_m = \mu_l \alpha_l + \mu_v \alpha_v \tag{2}$$

$$\mu_{m,t} = \frac{\rho_m C_\mu k^2}{\varepsilon}$$

The density and molecular viscosity of each constituent is taken as a constant. Equation (1*a*) represents the mixture volume, Eq. (1*b*), the mixture momentum, and Eq. (1*c*), the liquid phase volume fraction conservation laws, respectively. Although not presented here, for unsteady computations, it is straightforward to include physical time derivatives [4]. The formulation incorporates preconditioned *pseudo*-time-derivatives ($\partial/\partial\tau$ terms), scaled

by parameter β, which provide favorable convergence characteristics for steady state and unsteady multiphase computations. This has been discussed in detail by Kunz et al. [3].

Two separate models are used to describe the transformation of liquid to vapor and the transformation of vapor back to liquid. These are given in Eq. (3). For transformation of liquid to vapor, $\dot{m}^-$ is modeled as being proportional to the product of the liquid volume fraction and the difference between the computational cell pressure and the vapor pressure. This model is similar to the one used by Merkle et al. [7] for both evaporation and condensation. For transformation of vapor to liquid, a simplified form of the Ginzburg-Landau potential [8] is used for the mass transfer rate, $\dot{m}^+$.

$$\dot{m}^- = \frac{C_{\phi 1}\rho_v \alpha_l \,\mathrm{MIN}[0, p - p_v]}{\frac{1}{2}\rho_l U_\infty^2 t_\infty} \quad \dot{m}^+ = \frac{C_{\phi 2}\rho_v \alpha_l^2 \alpha_v}{t_\infty} \tag{3}$$

$C_{\phi 1}$ and $C_{\phi 2}$ are empirical constants. Both mass transfer rates are nondimensionalized with respect to a mean flow time scale. For all work presented here, $t_\infty = 1$, $C_{\phi 1} = 100$, and $C_{\phi 2} = 0.2$. These values were arrived at by an investigation of average attached cavity lengths described in Kunz et al. [3] and Lindau et al. [4]. The sensitivity of multiphase results to the value of C_ϕ has been reviewed by Senocak and Shyy [9], and was found to be small over a large range of values bounding those chosen here. In Eq. (3), the mass transfer rates contain terms that represent a potential and other terms that scale the rate based on the available species volume per unit total volume. In the case of the liquid destruction, this potential is based on the static pressure. In the liquid production term, the potential is represented by the α_l^2. Similar behavior can be described by the van der Waals' equation of state. As is discussed by Hohenberg and Halperin [8], close proximity to equilibrium is implicit in this modeling.

A two-equation turbulence model with standard wall functions has been implemented to provide closure. The k-ε model is represented in Eq. (4). As with velocity, the turbulence scalars are interpreted as being mixture quantities.

$$\frac{\partial(\rho_m k)}{\partial t} + \frac{\partial(\rho_m k u_j)}{\partial x_j} = \frac{\partial}{\partial x_j}\left(\frac{\mu_{m,t}}{\mathrm{Pr}_{tk}}\frac{\partial k}{\partial x_j}\right) + P - \rho_m \varepsilon$$

$$\frac{\partial(\rho_m \varepsilon)}{\partial t} + \frac{\partial(\rho_m \varepsilon u_j)}{\partial x_j} = \frac{\partial}{\partial x_j}\left(\frac{\mu_{m,t}}{\mathrm{Pr}_{t\varepsilon}}\frac{\partial \varepsilon}{\partial x_j}\right) + [C_1 P - C_2 \rho_m \varepsilon]\left(\frac{\varepsilon}{k}\right) \tag{4}$$

Numerical Method

The described model equations are solved in the UNCLE-M code. This code has its origins as the UNCLE code, developed for incompressible flows [10]. Later this code was extended to multiphase mixtures, substantially revised, and named UNCLE-M [3]. The code is structured, multiblock, implicit and parallel with upwind flux-difference splitting for the spatial discretization and Gauss-Seidel relaxation for the inversion of the implicit operator. Primitive variable (MUSCL) interpolation with limiting is applied to retain higher order accuracy in flow fields containing physical discontinuities. In keeping with the finding of Kunz et al. [3], only those source terms associated with vapor production are linearized for inclusion in the implicit linear system left-hand-side. Terms associated with liquid production are treated explicitly and underrelaxed with a factor of 0.1. At each pseudo-time step, the turbulence transport equations are solved subsequent to solution of the mean flow equations.

During this investigation, attention was given to appropriate spatial discretization. As a requirement, to accommodate the use of wall functions, for regions of attached liquid flow, fine-grid near-wall points were established at locations yielding dimensionless, fine-grid wall spacing of $50 < y^+ < 300$. Strictly, in regions of separated flow, law-of-the-wall based wall functions are inappropriate. However, based on previous experience with RANS modeling of large vaporous cavities [3,4], the lack of conformity in separated regions is considered acceptable. The separated region is made largely of vapor with a molecular viscosity two orders of magnitude less than the main liquid flow. Presumably the shearing forces will be significantly less than in attached liquid regions. More significantly, the proper approach to wall modeling in this multiphase region is a research topic in itself. The supporting conjecture made here is that, for these massively separated, two-phase flows, the potential difference to be made with more accurate wall shear modeling is probably small. Further details regarding the numerical method are available in Kunz et al. [3].

The 3D multiphase RANS code was applied to the flow through an isolated blade row. Blade-to-blade azimuthal periodicity and uniform, steady far-field boundary conditions were assumed. In order to obtain the proper advance ratio, a rotor rotational speed was specified, and the free-stream velocity was held at a fixed value. For these computations, a fixed Reynolds number, based on the free stream velocity and the diameter, was applied, regardless of cavitation index or advance ratio. Thrust breakdown calculations obtained here involved an initial 3D solution of the single-phase flow at each desired value of advance ratio. To reduce computational effort and allow stable integration, it was necessary to obtain a converged solution based on these single-phase conditions. These single-phase solutions were then applied as initial conditions for multiphase computations. Results were obtained by specifying a large but finite cavitation number (based on free-stream conditions). By applying the flow solution method to each new condition with a successively reduced cavitation number, breakdown conditions were modeled. This procedure provided "nice" initial conditions for each pseudo-time marching effort, often a necessity to obtain CFD results. Using the current integration method, a more aggressive approach, led to computationally divergent results.

Results

A no-skew unducted propeller, designated P4381, was tested by Boswell [1] as part of a larger effort to parameterize ahead powering, blade-rate, fluctuating loads, cavitation inception, cavitation thrust breakdown, structural integrity, and backing performance with consideration of the effect of blade skew. The cavitation thrust breakdown performance of the propeller was determined in a water tunnel at a Reynolds number (based on relative incident velocity and chord at 70% of the span) ranging from 1.38 to 2.44×10^6. Measurements were taken at specific advance ratios while incrementally dropping the tunnel operating pressure. This process reduced the test cavitation index in a prescribed fashion. Thus, sufficient data were obtained to complete a map of thrust and torque over a range of advance ratios and cavitation indices.

For the modeled cases, the Reynolds number based on free stream velocity and diameter was held constant at 1.63×10^6. For the advance ratios modeled, this is equivalent to a range of Reynolds numbers based on relative incident velocity and chord at 70% span from 1.37 to 2.51×10^6. This range corresponds to advance ratios ranging from 0.6 to 1.0. The design advance ratio was given by Boswell [1] to be $J = 0.889$. At advance ratios less than approximately 0.6 and greater than 1.0, integrations of the steady form of the equations on the nominal computational grid failed to converge. Results presented here were integrated based on solution of the steady-state equations; i.e., physical time derivatives were set to zero. It is suspected that the lack of convergence to the steady-state equations is due to the large scale of unsteadiness inherent in multiphase and high angle-of-attack flows. When such inherent unsteadiness becomes too large to resolve with steady-state physics, it is typical that the solution method on these model equations [Eqs. (1)–(4)] will fail to converge to a steady state result but will converge with application of the time dependent formulation [4]. In addition to requiring unsteady integration, it is suspected that proper resolution of the large scale structure of

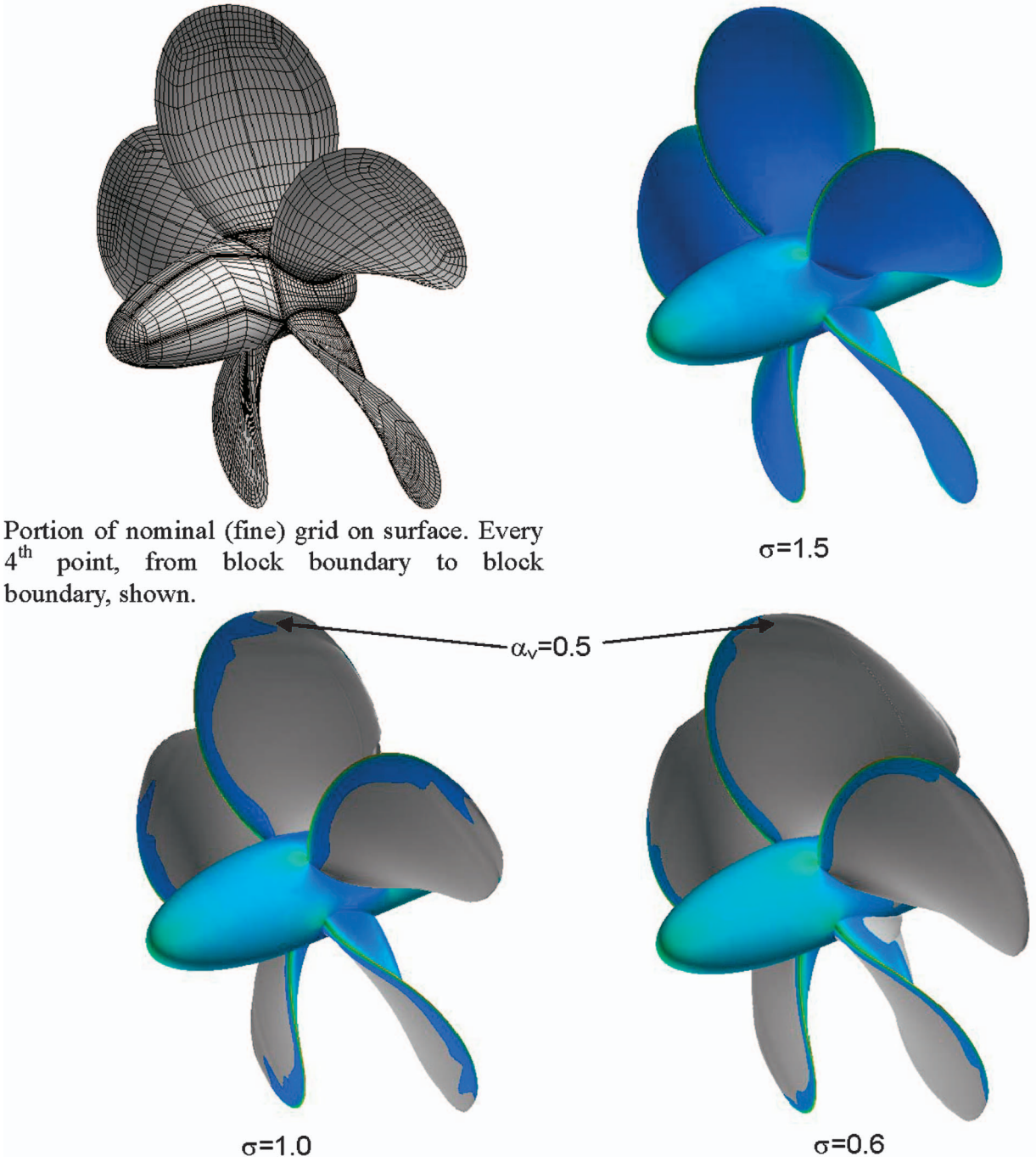

Fig. 1 Computed results. Grid and flow over P4381 at design advance ratio, J=0.889. Results at three cavitation indices with surface colored by pressure and a gray isosurface of liquid volume fraction.

such unsteadiness would necessitate additional and/or better placement of grid points. The nominal grid was designed with a topology conforming to low incidence flow without attempting the fine resolution of structures like leading edge separation eddies and tip vortices. These structures were only captured in some average sense and when the minimum pressure in such features became important, the overall results suffered. Such features are generally not significant for breakdown prediction at and around the design advance ratio.

In order to obtain thrust breakdown results with minimal difficulty, an incremental procedure was followed. For each advance ratio, results were first obtained assuming single phase flow. Then, the final, converged single phase flow solution was used as an initial condition for the pseudo-time marching procedure to obtain the subsequent two-phase flow solution. Initially a two-phase flow solution was sought at a large cavitation index. This cavitation index corresponded to a state where little or no cavitation was expected. A cursory examination of the suction surface pressure field based on the converged single-phase results would have yielded an approximate first cavitation index. However, for these results, the initial cavitation index was chosen based on the results given by Boswell. After a converged solution was obtained at this initial value of cavitation index, solutions at slightly smaller cavitation indices were obtained. This was done using the result based on the previous, slightly larger, cavitation index as initial flow conditions. The restart process was repeated until solution conver-

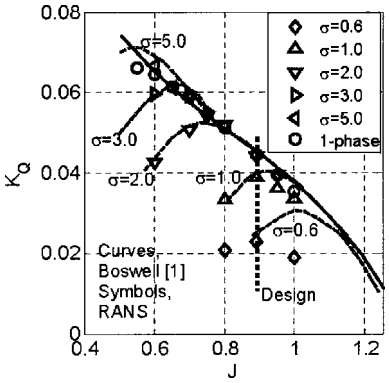

Fig. 2 Propeller torque coefficient $[Q/(\rho n^2 D^5)]$ versus advance ratio over a range of cavitation indices, experimental data [1] and computed results

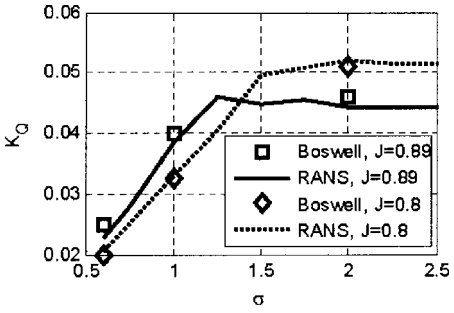

Fig. 4 Torque breakdown. Variation in propeller torque coefficient $[Q/(\rho n^2 D^5)]$ with cavitation index. Symbols indicate experimental data [1].

gence was obtained at the smallest cavitation index required to roughly complete the map presented by Boswell.

The nominal computational grid used to obtain breakdown results contained approximately 1.25 million control volumes and was distributed on 34 processors. A portion of the grid on the propeller surface is shown in Fig. 1. Although the computation was carried out over a single blade passage, taking advantage of azimuthal periodicity, here the grid has been replicated five times to give the appearance of a complete rotor. Due to the need to extend the domain out to a far-field condition and also due to the large degree of twist and variation in blade chord from the hub to tip, far more points were used than required by a typical, isolated, shrouded rotor passage computation. However, more judicious gridding will likely allow fewer points to be applied to analysis of future unducted propulsors. Results at design advance ratio and three significant cavitation indices are also shown in Fig. 1. This picture shows modeled flow with no significant cavitation, at $\sigma = 1.5$, with significant cavitation in breakdown, at $\sigma = 1.0$, and with significant cavitation and in severe thrust breakdown, at $\sigma = 0.6$. Note that at this low incidence angle, it appears that cavitation is initiated downstream of the leading edge, near the suction peak.

Results are summarized in Figs. 2 and 3. As seen in the figures, Boswell compiled the torque and thrust for the P4381 at a wide range of advance ratios and cavitation numbers. It should be noted that, during computations, surface shear forces were found to add approximately 5%–10% of the computed torque and remove 1%–4% from the computed thrust. These fractions were higher at more lightly loaded conditions. Integrated thrust and torque presented here include the shear forces.

Figures 4 and 5 present the torque and thrust breakdown comparison in a different form. Here the variation in torque, Fig. 4, and thrust, Fig. 5, is plotted with respect to cavitation index. This format is representative of the process of thrust breakdown testing done in a water tunnel and corresponds to the method of testing described in the original report by Boswell [1]. In addition to plotting the variation in integrated thrust and torque relative to significant parameters, at selected advance ratios and cavitation numbers, Boswell included pictures and diagrams depicting the extent of cavitation over the propeller. Similar presentation of computed results is given in Fig. 6(*a*), for flow at a high blade loading condition. Figure 6(*b*) includes a drawing and photograph from the original report by Boswell. Here the cavity size computationally predicted is seen to roughly coincide with the sketch due to Boswell. However, the exact cavity shape is somewhat different. Here, and at higher angles of attack, leading edge separation plays a larger role in cavity initiation than at the design incidence calculations shown in Fig. 1. Note the cavity extension into the tip vortex region. Although the grid used here is inadequate to resolve tip vortex induced cavitation, it is clear that the predicted, attached cavity persists in the initial region of the (poorly resolved) vortex.

In Fig. 2 the torque breakdown behavior versus advance ratio is plotted over a range of cavitation indices. Computed (UNCLE-M) results are represented with open symbols and data from the experiments conducted by Boswell are represented with faired curves. Due to the typical operating conditions of a vehicle, of primary interest is the behavior near the design point and at reduced values of the advance ratio. It is supposed that in the hypothetical case of an advance ratio greater than design, the situation would correspond to windmilling or an attempt to slow down or reverse. These represent transient events, not properly addressed here. Therefore, attention is called to the distribution of computationally generated results over the range of advance ratios equal to 0.9 and below. For this range, agreement of numerical prediction with experimental data is considered good. At every condition where a converged solution was obtained, torque pre-

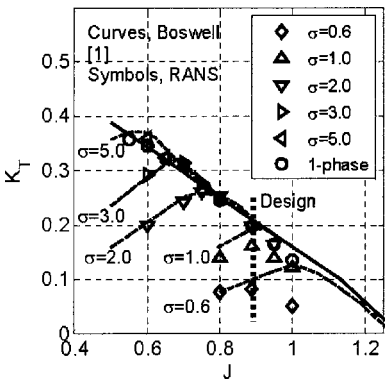

Fig. 3 Propeller thrust coefficient $[T/(\rho n^2 D^4)]$ versus advance ratio over a range of cavitation indices, experimental data [1] and computed results

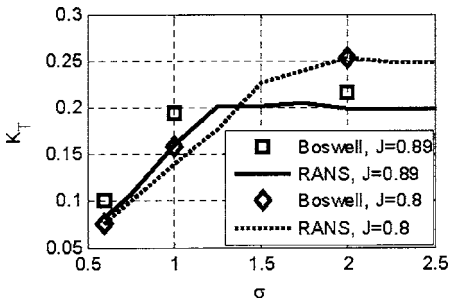

Fig. 5 Thrust breakdown. Variation in propeller thrust coefficient $[T/(\rho n^2 D^4)]$ with cavitation index. Symbols indicate experimental data [1].

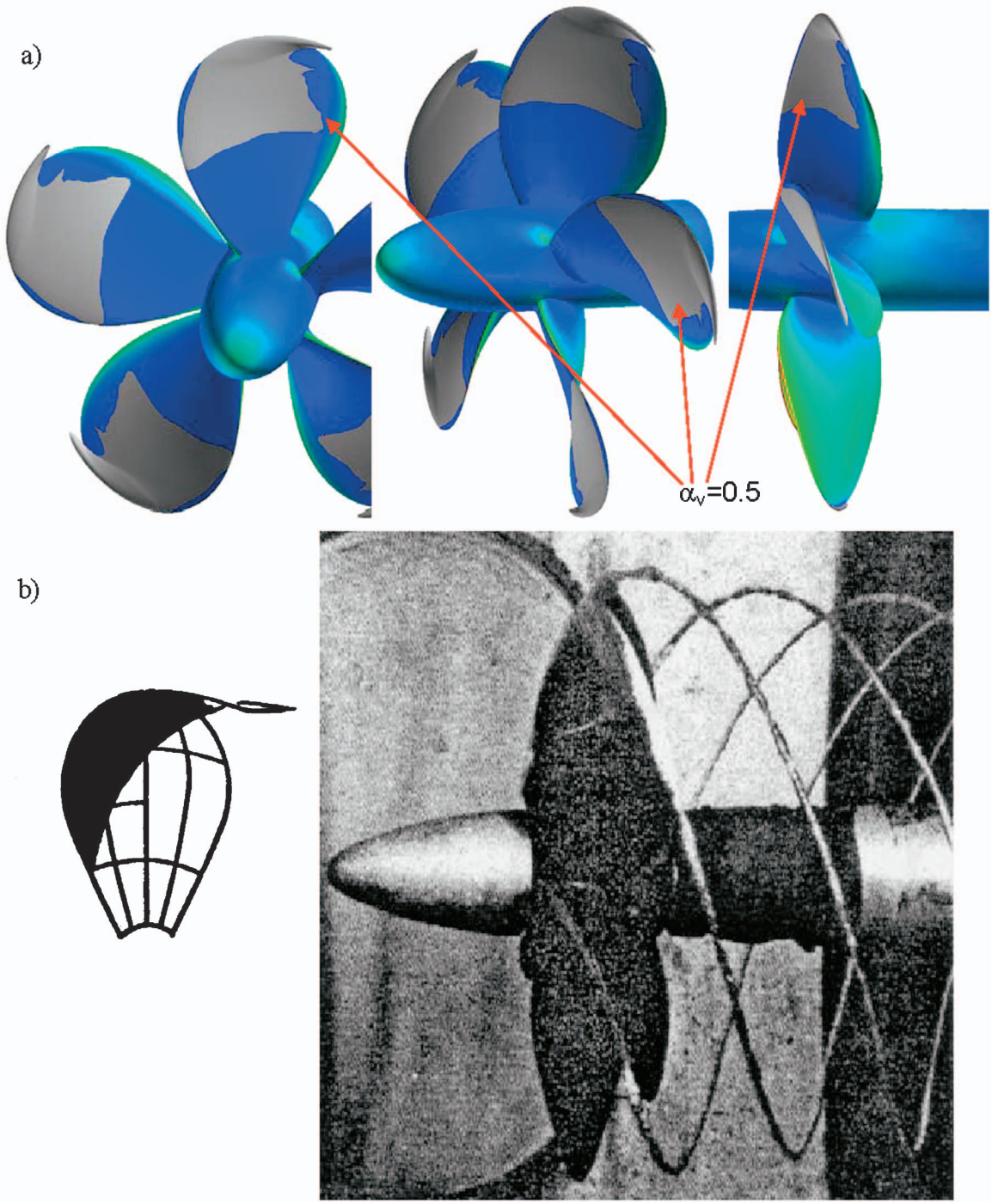

Fig. 6 Flow over P4381, J=0.7, σ=3.5. (*a*) Multiphase RANS solution, three views showing surface colored by pressure and a gray isosurface of liquid volume fraction. (*b*) Diagram and picture from Boswell [1] indicating extent of experimentally observed cavitation.

dictions appear to agree within 5% of the experimental results. Unfortunately, a presentation of the experimental uncertainty of original data is not included in the work by Boswell [1] or Cumming et al. [2]. Without a quantified estimate of the uncertainty, a precise statement of closeness to experimental results is difficult.

In Fig. 3, the thrust breakdown is plotted in a similar fashion to the torque breakdown in Fig. 2. Here, at the design and higher advance ratios, the agreement with actual values of thrust is not quite as good as in the case of torque. For more highly loaded cases, the agreement between computations and experiment is still good. It should be noted that the actual prediction of breakdown would be based on the prediction of a critical advance coefficient. This location is sometimes based on some fractional reduction in torque or thrust from the nominal design value. Typically this reduction is 2%–5% of the nominal value. It appears from Figs. 4 and 5 that the results from the flow solver, based on either integrated thrust or torque, were sufficiently accurate to make this prediction. Nonetheless, with proper application of a RANS solver, a high level of agreement should be attainable. The excellent agreement shown over most of the cases for both thrust and torque indicates that high fidelity predictions can be made, and

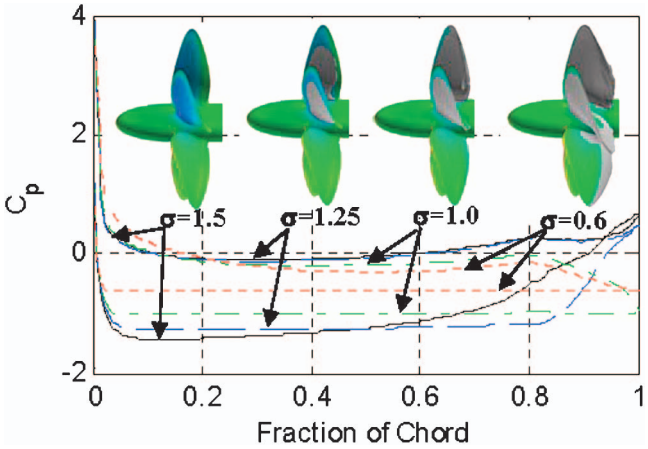

Fig. 7 Computed (UNCLE-M) pressure on both pressure and suction side at 30% of span and at selected cavitation numbers. Surface pressure also illustrated by color and cavity size indicated by gray surface of constant volume fraction, α_l=0.5. Design advance ratio, J=0.889.

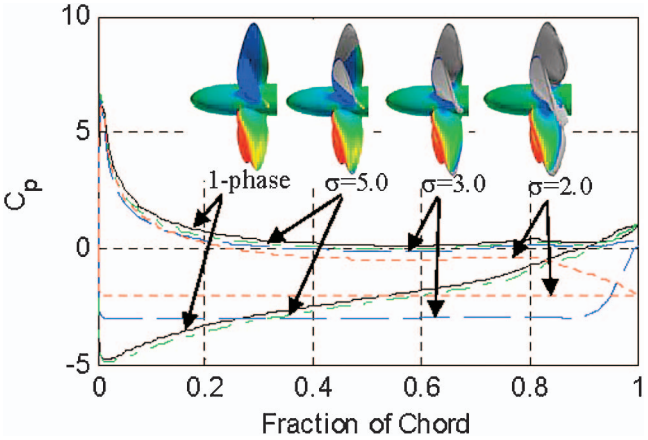

Fig. 9 Computed (UNCLE-M) pressure on both pressure and suction side at 30% of span and at selected cavitation numbers. Surface pressure also illustrated by color and cavity size indicated by gray surface of constant volume fraction, α_l=0.5. Highly loaded condition. Advance ratio, J=0.6.

with further refinement, reduction of the error in the thrust prediction at those few points where error was significant should be attainable.

Figures 7–10 give the computed blade pressure loading distribution at 30% and 70% of span. Results are shown from a fully wetted condition through breakdown at the design advance ratio, J=0.889, and also a more highly loaded condition, J=0.6. The loading is given in terms of the face and back side pressure coefficients distributed over chord. In addition, a rendering of propeller surface pressure and cavity shape, similar to Figs. 1 and 6, is given for each of the conditions. These pictures, identified with the blade loading distribution curves, serve to illustrate the cavity size and location and its effect on performance.

In Fig. 7, design advance ratio, 30% span blade loading curves are presented. Results are shown at cavitation indices equal to 1.5, 1.25, 1.0, and 0.6. Although the curves are labeled with cavitation indices in the figure, the value of the cavitation index (if cavitation is present) may also be inferred from the minimum suction side pressure. This value corresponds to the negative of the minimum pressure and a horizontal portion of the curve, indicating a region of separated, vaporous flow. As demonstrated in Fig. 2, these results span the breakdown event. In Fig. 8, results for the same conditions are shown at 70% of the span. Considered together, Figs. 7 and 8 illustrate how the cavity growth on the suction side of the blade affects the lift and eventually leads to a severe drop in torque and breakdown. At this design advance ratio, the suction side minimum pressure occurs somewhat downstream of the leading edge and initial, developed cavitation occurs there. It should be noted that the torque coefficient, K_Q, at σ=1.25 was computed to be 0.046, and at σ=1.5, the fully wetted condition, it was equal to 0.045. The mechanism for this slight increase in torque with the initial presence of cavitation is illustrated nicely in Fig. 7. Here, in the case of σ=1.25, even though the presence of cavitation separates the flow and effectively limits the minimum attainable value of suction pressure, the integrated area between the pressure and suction side pressure curves is larger, and, at this radius anyway, greater turning is accomplished. As the cavitation index is further reduced to σ=1.0 the presence of cavitation led to a reduced torque. This corresponds, at 30% span, to the extent of the cavity having reached the trailing edge. Thus, a portion of the separated, cavity displaced, flow never reattaches to the suction surface, and the pressure side must be severely unloaded as it approaches the trailing edge. At σ=0.6, the cavity has completely enshrouded the

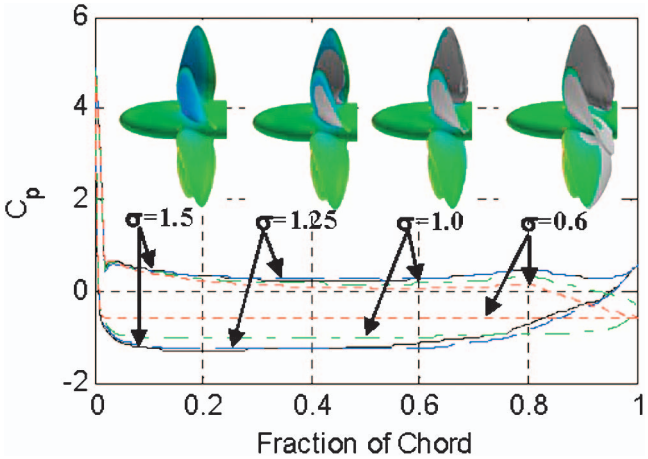

Fig. 8 Computed (UNCLE-M) pressure on both pressure and suction side at 70% of span and at selected cavitation numbers. Surface pressure also illustrated by color and cavity size indicated by gray surface of constant volume fraction, α_l=0.5. Design advance ratio, J=0.889.

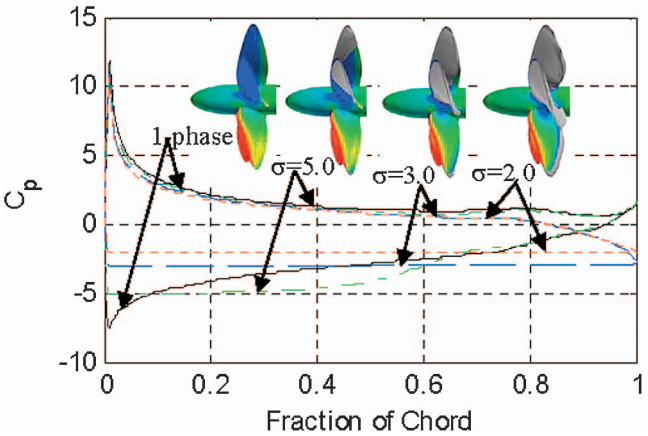

Fig. 10 Computed (UNCLE-M) pressure on both pressure and suction side at 70% of span and at selected cavitation numbers. Surface pressure also illustrated by color and cavity size indicated by gray surface of constant volume fraction, α_l=0.5. Highly loaded condition. Advance ratio, J=0.6.

trailing edge and severe breakdown is evident. At the 70% span section, the previously observed increase in lift from the $\sigma=1.5$ condition to $\sigma=1.25$ is not evident. In Fig. 8, examination of the curves corresponding to $\sigma=1.25$ shows that the presence of the cavity has had only a small effect on the pressure distribution. This can be partly explained by comparison of the fully wetted condition in Figs. 7 and 8. The 70% span minimum suction pressure, $C_p=-1.33$, is greater than the same quantity, $C_p=-1.45$, at 30% span. At this span, the higher relative total pressure level serves to reduce the presence of cavitation. However, cavitation is clearly present in both the pressure plot and the surface rendering beyond 70% span.

In Figs. 9 and 10, the advance ratio, $J=0.6$, blade loading results are presented. Figure 9 contains the results at 30% of the span, and Fig. 10 contains the results at 70%. At this higher loading condition, the fully wetted suction peak occurs very close to the leading edge and significant cavitation appears initially there. In contrast to the design conditions, the separation point is well defined and coincident to the leading edge. A finding similar to that at the design advance ratio is also apparent. The torque increase with the initial growth of suction side cavitation can be explained by comparison of the blade surface pressure at the fully wetted and initially developed cavitating conditions. Comparing the single phase and $\sigma=5.0$ results at this advance ratio, there is nearly equal loading at 30% span. However, at 70% span, the presence of cavitation increases the loading. Significant cavitation initially develops further out the span, closer to the leading edge. In addition, the maximum blade chord extent is at 70% span where the chord to diameter ratio is 0.347. At 30% span $c/D=0.229$. The wheel velocity also is greater at 70% than at 30% span. This leads to a more significant rise in torque than at the design advance ratio. For the integration over the entire surface (plotted in Fig. 2) the resulting increase in torque, at $J=0.6$, from fully wetted to $\sigma=5.0$, was from $K_Q=0.0645$ to 0.0665. In Figs. 9 and 10, in addition to results for the fully wetted and $\sigma=5.0$ conditions, $\sigma=3.0$ and $\sigma=2.0$ results are plotted. In these cases, from examination of Figs. 2 and 3, onset of torque and thrust breakdown due to cavitation is evident. At 70% span, for the case of $\sigma=3.0$, the cavity has reached the trailing edge on the suction side, but not at 30% span. However, at $\sigma=2.0$, the cavity has clearly reached the trailing edge at both radii and hence, severely altered the pressure side flow.

Computational Sensitivity

The numerical solutions presented here, based on modern discretization methods, are formally conservative with third order accuracy for construction of inviscid and convective flux terms and second order accuracy for viscous and diffusive terms. This order of accuracy is based on one-dimensional assessment of model scalar equations (e.g., Hirsch [11]). Solutions presented were determined to be converged based upon the magnitude of the reduction in residual error in solution of the model, discrete equations. Integration was continually pursued until further effort failed to reduce the residual error. Using this approach, applied to the results presented here, the residual error was reduced, during integration, by no less than three orders of magnitude.

The sensitivity of the solution to the level of computational gridding was investigated. In Fig. 11, plots indicating the sensitivity of the breakdown investigation to spatial discretization are shown for the design advance ratio. Here results are shown based on solutions obtained with three significantly different grids; the nominal grid, used to obtain results reported throughout this investigation is presented along with a similarly dense, "O" topology grid, and a coarsened version of the nominal grid. The nominal grid was constructed using an "H" topology and contained 1,258,320 computational volumes. The alternate, O-grid used in the study contained 1,516,560 control volumes. The coarsened grid was topologically similar to the nominal H-grid and contained 157,290 volumes. Figure 11 presents computed performance ranging from approximately single phase ($\sigma=2.0$) to severe breakdown ($\sigma=0.6$). Clearly the fine grid solutions appear to better predict the torque and thrust in single phase flow. Also, based on the reported torque alone, from single-phase to severe breakdown, there appears to be a dramatic trend with increasing grid resolution towards the measured data. However, the computed breakdown thrust at this advance coefficient is no better for the fine grids than the coarse grid. In fact solutions with each grid appear to predict the occurrence of breakdown (based on the significant drop in torque or thrust) at roughly the same cavitation coefficient. Thus it might be concluded that even the coarsened grid would be appropriate for predicting the onset of breakdown. However, resolution commensurate with the fine grid would be necessary to obtain on-design, pre-breakdown performance.

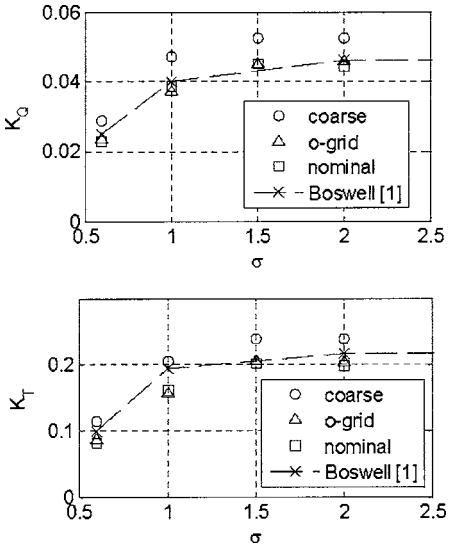

Fig. 11 Grid sensitivity data. Nominal grid, *o*-grid, and coarse grid results for cavitation breakdown. Comparison of performance predictions at design advance ratio ($J=0.889$). Coarse grid is topologically similar to nominal grid with exactly $\frac{1}{2}$ of the resolution in each of the computational dimensions. Nominal grid contains 1,258,320, *o*-grid 1,516,560, and coarse grid 157,290 control volumes.

Conclusions

Computational methodology and model results of propeller cavitation thrust breakdown based on a homogeneous, multiphase RANS formulation have been presented. In consideration of the large fraction of torque due to shear at the design flow coefficient and, also, the presence of large regions of separated, cavitating flow, it is concluded that viscous flow effects are significant. For the modeled propeller, the critical cavitation number leading to thrust and torque breakdown was predicted in agreement with the experimental data over a wide range of modeled flow coefficients. For flow coefficients greater than design, although the fully wetted computations compared well, agreement with absolute values of cavitating thrust and torque was poor. However, for the case of design or higher loading, the absolute value of torque coefficient tended to agree extremely well with the experiments. At the design advance ratio, the agreement with data for prediction of cavitating thrust was not as good as for torque, but, at lower than the design values of J, comparison was also excellent.

The usefulness and validity of the present modeling method, based on reliable physics (Reynolds-averaged Navier-Stokes Equations) and appropriate for high-fidelity turbomachinery design, has been shown for propeller cavitation thrust and torque breakdown prediction. Validation was achieved by comparison to experiment [1]. For vehicle design, it is useful to relate this break-

down condition to the effect it would have on *in situ* vehicle performance rather than water tunnel data. By coupling thrust and torque breakdown maps (such as Figs. 3 and 4) with data relating both vehicle drag to velocity and available shaft power to shaft speed, breakdown estimates may be so extended.

Acknowledgments

This work was supported by the Office of Naval Research, Contract No. N0039-97-D-0042, with Dr. Teresa McMullen as contract monitor and overseen by Mr. Leo Schneider, ARL Penn State Program Manager.

Nomenclature

Symbols

C_1, C_2 = turbulence model constants
C_ϕ = mass transfer model constants
C_p = pressure coefficient $\equiv (p_\infty - p)/(\frac{1}{2}\rho U_\infty^2)$
c = chord length
D = propeller diameter
J = advance ratio $\equiv U_\infty/(nD)$
K_Q = torque coefficient $\equiv Q/(\rho_l n^2 D^5)$
K_T = thrust coefficient $\equiv T/(\rho_l n^2 D^4)$
k = turbulent kinetic energy
$\dot{m}^-, \dot{m}^+$ = mass transfer rates
n = rotational frequency (revolutions/time)
P = turbulent kinetic energy production
$\mathrm{Pr}_{tk}, \mathrm{Pr}_{t\varepsilon}$ = turbulent Prandtl numbers for k and ε
p = pressure
p_v = vapor pressure
t, t_∞ = physical time, mean flow time scale
u_i = Cartesian velocity components
x_i = Cartesian coordinates
y^+ = dimensionless wall distance
α = volume fraction
β = preconditioning parameter
τ = pseudo-time
ε = turbulence dissipation rate
μ = molecular viscosity
ρ = density
σ = cavitation number $\equiv (p_\infty - p_v)/(\frac{1}{2}\rho U_\infty^2)$

Subscripts and Superscripts

l = liquid
m = mixture
t = turbulent
v = condensable vapor
∞ = free stream value

References

[1] Boswell, R. J., 1971, "Design, Cavitation Performance and Open-Water Performance of a Series of Research Skewed Propellers," Naval Ship Research and Development Center, Washington, D.C., Report No. 3339.
[2] Cumming, R. A., Morgan, W. B., and Boswell, R. J., 1972, "Highly Skewed Propellers," Trans. SNAME (Society of Naval, Architects, and Marine Engineers, **80**, pp. 98–155.
[3] Kunz, R. F., Boger, D. A., Stinebring, D. R., Chyczewski, T. S., Lindau, J. W., Gibeling, H. J., Venkateswaran, S., and Govindan, T. R., 2000, "A Preconditioned Navier-Stokes Method for Two-Phase Flows with Application to Cavitation Prediction," Comput. Fluids, **29**, pp. 849–875.
[4] Lindau, J. W., Kunz, R. F., Boger, D. A., Stinebring, D. R., and Gibeling, H. J., 2002, "High Reynolds Number, Unsteady, Multiphase CFD Modeling of Cavitating Flows," ASME J. Fluids Eng., **124**, No. 3, pp. 607–616.
[5] Kunz, R. F., Lindau, J. W., Kaday, T. A., and Peltier, L. J., 2003, "Unsteady Rans and Detached Eddy Simulations of Cavitating Flow Over a Hydrofoil," *Fifth International Symposium on Cavitation* (CAV2003), Osaka, Japan, November 1–4, 2003.
[6] Senocak, I., and Shyy, W., 2002, "Evaluation Of Cavitation Models For Navier-Stokes Computations," ASME Paper No. FEDSM2002-31011.
[7] Merkle, C. L., Feng, J., and Buelow, P. E. O., 1998, "Computational Modeling of the Dynamics of Sheet Cavitation," Third International Symposium on Cavitation, Grenoble, France.
[8] Hohenberg, P. C., and Halperin, B. I., 1977, "Theory of Dynamic Critical Phenomena," Rev. Mod. Phys., **49**, No. 3, pp. 435–479.
[9] Senocak, I., and Shyy, W., 2001, "A Pressure-Based Method for Turbulent Cavitating Flow Computations," AIAA Paper No. 2001-2907.
[10] Taylor, L. K., Arabshahi, A., and Whitfield, D. L., 1995, "Unsteady Three-Dimensional Incompressible Navier-Stokes Computations for a Prolate Spheroid Undergoing Time-Dependent Maneuvers," AIAA-95-0313.
[11] Hirsch, C., 1990, *Numerical Computation of Internal and External Flows*, Wiley, Chichester, England, Vol. 2.

Characterization of the Hydrodynamically Developing Flow in a Microtube Using MTV

B. R. Thompson

D. Maynes
e-mail: maynesrd@et.byu.edu

B. W. Webb

Department of Mechanical Engineering,
Brigham Young University,
435 CTB, Provo, UT 84602, USA

Micro-molecular tagging velocimetry (μMTV) *has been used to characterize the hydrodynamic developing flow in a microtube inlet with a nominal inner diameter of* 180 μm. *Velocity profile data at 11 axial locations within the hydrodynamic developing region were acquired using the* μMTV *approach and the results represent the first characterization of hydrodynamically developing pipe flow at the microscale. The uncertainty in measurements of time-averaged velocity profiles ranged from 6% to 7% of the centerline velocity. The uncertainty in instantaneous measurements is in the range 8%–16% of the peak maximum velocity. Data were taken at Reynolds numbers of 60, 100, 140, 290, and 350. The data suggest the formation of a vena contracta with either locally turbulent flow or unsteady laminar flow separation early in the tube for the larger Reynolds (Re) numbers, which is quite different from macroscale experiment or numerical simulation where a vena-contracta is not observed for* $\mathrm{Re} < 500$. *The velocity profiles obtained very near the tube entrance exhibited a uniform velocity core flow surrounded by regions of relatively stagnant fluid in the near wall regions. The size of the inferred recirculation zones, measured velocity rms, and maximum shear rates all exhibit increasing magnitude with increasing Reynolds number. The velocity profiles were observed to evolve in the downstream direction until the classical parabolic distribution existed. The total hydrodynamic entry length agrees well with values published in the literature for laminar flow with a uniform inlet velocity, despite the existence of the observed vena contracta.* [DOI: 10.1115/1.1989368]

Keywords: Microscale, MTV, Laminar, Developing Flow, Vena Contracta

Introduction

Fluid flow at the microscale is becoming increasingly important, driven by the miniaturization of many technologies. Applications that utilize fluid flow in either microtubes or microchannels are emerging at an increasing rate and the rapid development of microscale fabrication technologies has enabled the design and production of many novel microscale mechanical and thermodynamic systems. These advances may soon allow the production of complete energy systems capable of providing power, heating, and cooling. Such microscale devices may be used in integrated cooling of electronic circuits, reactors for modification and separation of biological cells, and purification of air or water from chemically contaminated sources [1].

With regard to fully developed pressure driven laminar flow of a liquid through long ($L/D_h > 1000$) microchannels several investigators have explored the frictional pressure drop and compared their results to fully developed laminar pipe-flow theory [2–6]. A recent paper by Judy et al. [7] shows that, at least for the Reynolds number ($\mathrm{Re} = \bar{u} D_h / \nu$) range from 8 to 2300, no statistically significant deviation from macroscale Stokes flow theory exists. $\bar{u}$, D_h, and ν are the average duct velocity, duct hydraulic diameter, and kinematic viscosity, respectively. Experiments were reported for both round and square channels, fabricated from both stainless steel and fused silica, and over a hydraulic diameter range from 15 to 150 μm. For all of these studies the channels were sufficiently long such that the pressure drop due to friction in the fully developed portion of the channel flow dominated the overall pressure drop, and entrance effects were neglected. Due to the length scales involved, Reynolds numbers based on hydraulic diameter in microchannel flows will typically be in the laminar range, although applications exhibiting much higher Reynolds numbers also exist (e.g., ink jet printing, fuel injectors, etc.).

There have been limited studies that have appeared in the literature addressing the hydrodynamically developing flow in the entrance region of channels with hydraulic diameters in the submillimeter range. Given that many microscale flows may involve channels of relatively short length, understanding the flow dynamics in the entrance region of a channel flow is critical. Characterization of the developing flow field is not possible, however, by measurement of the pressure drop across, and volume flow rate through channels as has been done for conditions where L/D_h is large. Instead, detailed local measurements of either the pressure distribution or velocity field are necessary. Because of the challenges associated with making measurements at this physical scale, few detailed studies have been reported in the open literature for hydrodynamically developing flow through microchannels. Lee and Kim explored the effect of inlet flow geometry on hydrodynamic development in a rectangular microchannel with a hydraulic diameter of 70 μm using a micro-PIV approach. In this study the Reynolds numbers were of order 10 [8].

Developing pipe flow at the macroscale is a classical problem that has received much attention, both analytically and experimentally. For laminar flow, Shah and London [9] give an extensive review. Early investigations considered the flow development of an initially uniform flow at the inlet plane to the classical parabolic distribution far downstream [10–13]. Experimental measurements of the developing streamwise velocity and excess pressure drop coefficient, K (the pressure drop not accounted for by fully developed laminar flow theory), showed good agreement with finite difference solutions of the full Navier-Stokes equations. The uniform flow imposed at the inlet plane, however, precludes any

Contributed by the Fluids Engineering Division for publication in the JOURNAL OF FLUIDS ENGINEERING. Manuscript received by the Fluids Engineering Division May 14, 2004; Final revision: May 5, 2005. Associate Editor: Sivaram Gogineni.

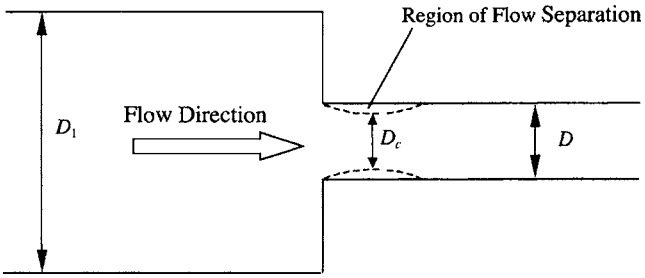

Fig. 1 Schematic illustration of flow through a sudden contraction

possibility of flow separation, which may exist in sharp-edged entrances and sudden contractions. For all available experimental data flow separation and the formation of a *vena contracta* are negligible at low values of the Reynolds number ($Re < 500$) [14]. Indeed, experiments conducted by Sylvester and Rosen [15] on a sharp-edged entrance flows with pipe diameters in the 1–2 cm range, reveal that, for $Re < 500$, there is no evidence in the static pressure distribution of a *vena contracta*. At $Re = 2000$ behavior was observed indicative of the existence of a *vena contracta*, and at $Re = 1100$ the behavior suggested a *vena contracta* existed, but to a much smaller extent than for the $Re = 2000$ condition. Others have conducted similar experiments that reveal the same behavior [16].

Perhaps the most detailed characterization of the laminar flow field in the inlet region of a macroscale pipe over the Re range from 40 to 2300 has appeared in work by Durst and Loy [17] and Bückle and Durst [18]. These authors considered flow through a sharp-edged contraction with a contraction ratio of $A/A_1 = 0.29$ and a downstream pipe diameter of $D = 1.02$ cm (see Fig. 1). A_1 and A are the upstream and downstream cross-sectional areas, respectively. The streamwise and wall-normal velocity distributions were measured in the developing region using LDV. These authors also conducted a numerical investigation of the same geometry and at dynamically similar conditions. Both the experimental data and the numerical simulations show similar results, namely, that for $Re < 550$ flow separation does not exist in the entrance region, which is similar to observations reported by others for sharp-edged entrance flows. As the magnitude of Re increased above about 550, regions of separated flow appeared. The radial extent of these regions, measured from the pipe wall, increased in nearly a linear manner with Reynolds number, from 0 at $Re \leqslant 550$ to a distance of about 5%–6% of the pipe diameter, D, at $Re = 2300$. Thus, the corresponding ratio of cross-sectional area without flow separation, A_c, to the pipe cross-sectional area, A, decreased from 1 to 0.77–0.81 over the same Re range. Another study detailed measurements of the developing flow in a sudden contraction with downstream diameter of 1.8 mm using nuclear magnetic resonance imaging for flows with $10 \leqslant Re \leqslant 20$ [19]. No flow separation or existence of a *vena contracta* was observed from these measurements.

For sharp-edged inlet/contraction flows in the turbulent regime numerous observations have shown that the size of the *vena contracta* is essentially independent of Re and depends almost exclusively on the area contraction ratio, A/A_1 [14,20]. The ratio of the cross-sectional area of the *vena contracta*, A_c (at the point where the size of the regions of flow separation is a maximum), to the downstream pipe area, for a turbulent flow is tabulated as a function of A/A_1 by Blevins [20], and is reproduced in Table 1. Note that for large contractions ($A/A_1 < 0.4$), A_c/A remains essentially constant and in the range 0.62–0.65. This ratio is significantly smaller than that observed by Durst et al. at the largest Re explored (2300) in laminar flow, indicating a much larger region of flow separation.

Based on the above macroscale experimental observations, one may expect similar behavior to exist for sharp entrance developing flows in microchannels, and since many flows will be in low-Re regime, flow separation at the inlet would not be expected. However, detailed measurements that will be presented in this work suggest that the dynamics of entrance flows can be significantly different and flow separation may exist at much smaller Re in microscale flows than expected based on previous macroscale observations. Detailed measurements that characterize the inlet flow field in circular tubes with diameters smaller than 1 mm have not previously appeared in the literature. This is the primary focus of the current paper. Specifically, this paper explores the developing streamwise fluid velocity in a circular microchannel (microtube) of diameter 182 μm, at five Re: 60, 100, 150, 290, and 350. A microscale adaptation of molecular tagging velocimetry (μMTV) was employed for the characterization. Velocity profile distributions were obtained at 11 axial locations in the developing region for each Re, where the dimensional average fluid velocities ranged from 0.3 to 1.9 m/s. The results from the investigation are compared with the observations and measurements of prior work noted above for macroscale conditions. Previously, velocity profile measurements in the fully developed region of a tube of diameter $D = 140$ μm [21] were reported using the μMTV approach, and an additional aspect of the current work is to further establish μMTV as a proven and robust technique for measuring fluid flow velocities at the micro-scale.

Methodology

Molecular Tagging Velocimetry. Molecular tagging velocimetry is a laser-based, nonintrusive method of measuring velocity profiles in fluid flows. MTV can be used to obtain spatially resolved velocity profiles over a planar domain of interest and is based on the ability to image the phosphorescence of a tracer molecule, dissolved in a test fluid. In water based flows, the molecular complex 1-BrNp·Gβ-CD·ROH is often used as the tracer molecule due to its superior characteristics [22]. Cyclohexanol was used here for the ROH with typical concentrations in the range 0.04 to 0.15 M. The concentration of the modified glucosyl-beta modified cyclodextrin, Gβ-CD, was in the range 1×10^{-4} to 2×10^{-4} M.

MTV for macroscale adaptation has been described in detail elsewhere [22,23]. The methodology and uncertainty analysis for the technique applied to a microscale flow has also been described in considerable detail [21,24] and is only summarized here. For velocity profile characterization in a flow dominated by a single velocity component a laser pattern consisting of a single line, positioned perpendicular to the streamwise flow direction, is adequate to quantify the entire axial flow behavior. Used in this fashion the approach is often called the "single line method." The molecular complex noted above is excited in a line pattern by a UV source at 308 nm and subsequently returns to the unexcited state by emitting visible phosphorescence. The line of phosphorescence (MTV line) represents a "tagging" of discrete molecules

Table 1 Ratio of the *vena contracta* flow area to pipe cross section area for turbulent flow in a sudden contraction (data from [20])

A/A_1	0.1	0.2	0.3	0.4	0.5	0.6	0.7	0.8	0.9	1.0
A_c/A	0.624	0.632	0.643	0.659	0.681	0.712	0.755	0.813	0.892	1.0

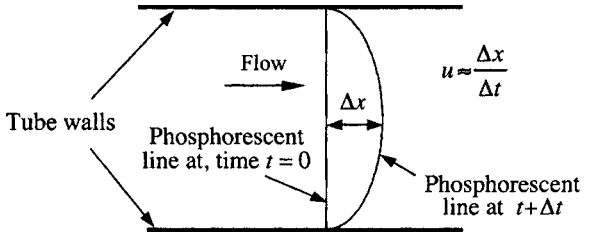

Fig. 2 Illustration of velocity determination from deformed and undeformed MTV lines

that are displaced with the flowing fluid. An intensified charge coupled device (ICCD) is placed normal to the MTV lines and is synchronized with a pulsed excimer laser. The opening of the camera shutter is controlled, via the intensifier, and images of MTV lines are acquired as the laser fires, resulting in undeformed MTV lines. Subsequently a time delay can be specified so that the camera shutter opens a short time interval after the laser excitation, resulting in the acquisition of deformed MTV lines. The images are then analyzed digitally using image analysis software, and the horizontal displacement, in pixels, of the MTV line is determined at each location using a correlation approach. The error associated with using the single line method in flows with nonzero wall-normal velocity components will be discussed in detail in a later section.

In summary, multiple images ($\sim$200) of undeformed lines are acquired and summed to form a robust average image. Subsequently, each acquired deformed image (representing instantaneous fluid displacement) is compared to the undeformed average image using a correlation algorithm. First, the spatial correlation between the undeformed average image and the deformed instantaneous image is computed for each wall normal location. Subsequently, the deformed image is offset by one pixel in the streamwise direction and the correlation is again determined. This procedure is repeated, sequentially offsetting the images by one pixel in the streamwise direction. The result is a distribution of the computed correlation with respect to the offset distance at each wall-normal locale. The offset where the maximum magnitude of the spatial correlation exists corresponds to the instantaneous streamwise fluid displacement, Δx, at the specified wall-normal position. Subpixel accuracy is obtained by performing a least-squares curve-fit to the correlation vs. offset distribution. For a steady laminar flow the rms of the Δx measurements from all images at a given wall-normal position is a measure of the uncertainty in determining Δx.

By dividing the local axial displacement, Δx, by the known time delay between acquisition of the undeformed and deformed MTV lines, Δt, the velocity of the fluid is then calculated. Figure 2 shows a representation of a typical velocity profile and illustrates the process described above. The Lagrangian velocity calculation is made with Eq. (1) below:

$$u(r) \approx c\frac{\Delta x}{\Delta t} \tag{1}$$

$u(r)$ is the axial velocity as a function of the radial location, Δx is the displacement at the r location of interest in camera pixels, and Δt is the time delay between acquisition of the deformed and undeformed line images. A conversion factor, c (μm/pixel), is necessary to convert the horizontal displacement value from imaged pixels to physical location in meters.

Two challenges exist when extending MTV to microscale scenarios; these are (1) directing a collimated UV beam of waist size small compared to the flow length scale, and (2) imaging the phosphorescent lines. To address the first challenge the UV beam is passed through a pinhole filter to ensure a beam of Gaussian distribution. The beam is then focused into the microtube using off-the-shelf optics. The beam waist size for the measurements presented here was about 30 μm and represents the smallest beam waist thus far achieved in our laboratory. The challenge of imaging the phosphorescent lines was addressed by utilizing a variable zoom lens with a 10$\times$ microscope objective on the CCD camera. This permitted visualization of the entire inner diameter of the microtube with an approximate resolution of 1 μm/pixel. The CCD array consisted of 640×480 elements with a total horizontal length of 12.5 mm.

The optical train employed is described as follows. First the laser beam was passed through a neutral density filter to reduce the total energy. The beam was then spatially filtered by focusing it with a 100 mm focal length lens and passing the beam through a 150 μm diameter pinhole precision-drilled through a 1 mm thick brass plate. Subsequently, the beam was recollimated by a second 100 mm focal length lens. The collimated beam was then focused and directed into the test section with a combination of a 25 mm focal length meniscus lens followed by a 12.5 mm focal length plano-convex lens.

Experimental Apparatus and Procedure. A flow facility was designed and constructed to permit velocity profile measurements in the developing region (nominal length 1 mm) of a microtube. A section of fused silica microtube with internal diameter of 182 μm was mounted that protruded into a reservoir pressurized with a precision pump. This facility was optically accessible on two sides: the top and front faces. A schematic illustration and a photograph of the flow facility are shown in Fig. 3. Through the top face the UV beam entered the test section, and through the front face the resulting phosphorescence was imaged with the CCD camera.

The reservoir was constructed from a single piece of brass. A hole about 10 mm in diameter was drilled down the axis of the part. Into this cavity the microtube protruded several mm and was sealed using a swagelock fitting with a nylon ferrule. The outer diameter of the microtube was about 312 μm (wall thickness, $\zeta = 65$ μm) and thus the ratio of flow areas was 3.2×10^{-4}. Consequently, the fluid velocity in the cavity, or reservoir, is essentially stagnant. Although the entrance is reentrant in form, published macroscale data [25] show that the entrance loss coefficient is independent of the ζ/D ratio if $\zeta/D \geq 0.05$. Here the wall thickness ratio is $\zeta/D=0.36$, and, thus, the entrance is essentially a sudden contraction with an area ratio $A/A_1 \rightarrow 0$.

Two slots were milled into the top and front side of the brass reservoir. These slots were covered with optical grade quartz windows allowing optical access for imaging and transmission in the UV range. The windows are flat and there is no distortion in the MTV lines and the laser beam remains thin as it enters the reservoir. Prior to mounting, the fused silica tubes were cut to length and the ends were carefully polished smooth in several steps, using successively finer abrasive for each step. The ends of the tube were then viewed via SEM imaging to ensure integrity, good surface quality, and no perceptible obstructions at the tube inlet.

Experiments were conducted in the following manner. First, flow was established in the microtube and the flow rate was measured by collecting a volume of water in a measured time as it exited the microtube. A deep graduated cylinder of small bore was used to collect the water and the elapsed time was measured by stopwatch. To minimize uncertainty, the volume collected was at least 160 times the least count of the graduated cylinder, and the minimum elapsed time was 152 s. From this measurement the average velocity and resulting Reynolds number were computed. Subsequently, the entrance length, L_e, could be estimated by $X_e = L_e/D = 0.05$ Re. With an estimate of the entrance length, length intervals were determined such that 11 velocity profile measurements could be made within the developing region. The microtube test apparatus was fixed to translational stages equipped with micrometer actuators that provided precision positioning to within ±0.5 μm. This enabled the microtube to be positioned relative to

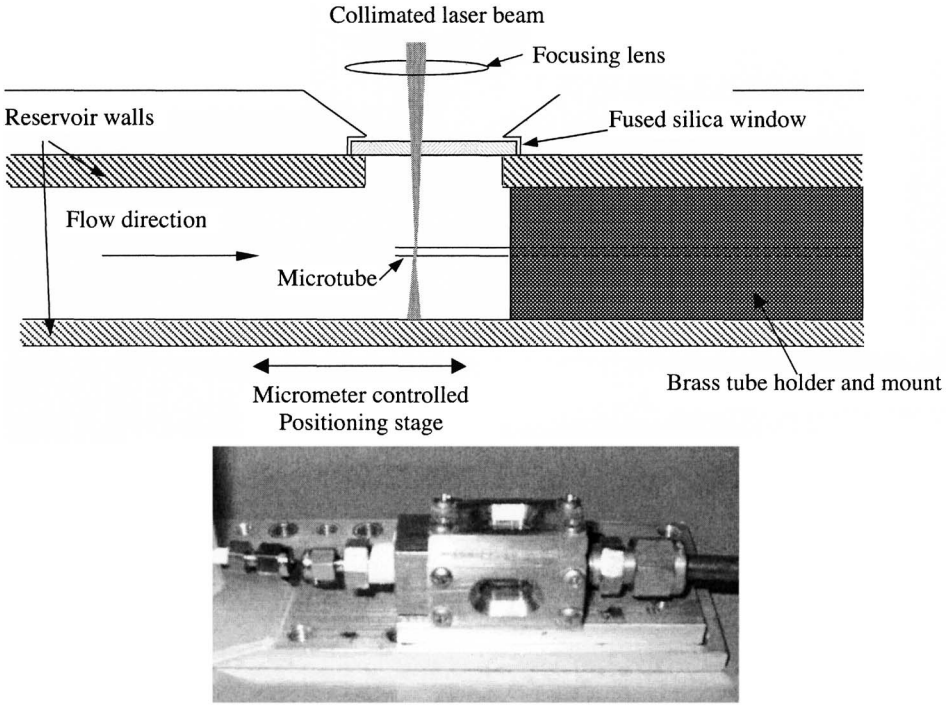

Fig. 3 Schematic illustration (top) and photograph of the entry length experimental test section and setup

the stationary laser beam, allowing the optical train to remain undisturbed as the measurement location changed. The offset from the initial measurement location was recorded for each subsequent measurement. Prior to measurements at each streamwise location the excitation beam was centered laterally in the microtube. This was accomplished by traversing the beam from one tube radial extreme to the other while maximizing the phosphorescing length parallel to the beam. The first axial measurement location corresponded to the locale where the excitation beam was just inside of the microtube entrance at the given Re. The flow facility was thereafter translated axially to permit measurements at all of the previously determined locations within the entrance region. Given the beam waist of ~ 30 μm achieved here, the uncertainty in the axial measurement location is approximately ± 15 μm and, further, the first axial location where measurements were possible is $x \approx 15$ μm. For all experiments the shutter time, or the time of CCD intensifier activation, was 15 μs. Also, the delay times between acquisition of deformed and undeformed lines were 37.2 μs (Re=350), 50.7 μs (Re=290), 89.7 μs (Re=150), 124.3 μs (Re=100), and 199.5 μs (Re=60). These delay and shutter times were selected to optimize the signal-to-noise ratio.

The steps described above were repeated at each axial location and for all five Reynolds numbers investigated. During the process, at a given Reynolds number, the laser beam, the camera settings, and the lens focus remained constant and were not adjusted. Consequently, only the position of the test apparatus was varied by use of the translation stages, and the image conversion factor, c, should be the same for all axial locations at a given Re. In macroscale flows the conversion factor is typically determined from imaging a length scale of known dimensions at the same camera focus and magnification settings used for the velocity measurements. Inserting an object of known length into a microtube is impossible. One physical length that is known is the tube diameter and the radial length of the MTV line in the radial direction is easily imaged. However, use of the tube internal diameter as the reference length scale introduces another complication. Because the tube is round, the curved surface acts as a cylindrical lens and the image is magnified in the radial direction. Thus, using the internal tube diameter as a reference scale for axial fluid displacement is not practical. However, in the streamwise direction the tube is straight and no curvature exists and, consequently, there is no magnification in this direction. Therefore, the tube curvature does not affect the streamwise displacement measurements. Total internal reflection can make it impossible to view the fluid near the wall. However, because the system consists of a liquid-glass-liquid interface, the effect will be small, but may not be completely negligible given the small radius of curvature.

The magnification that occurs in the MTV line is a linear function of radial location, since (1) the radius of curvature of the microtube is constant, (2) the CCD array and face of the camera lens are parallel to the MTV line, and (3) the entire tube is imaged by the camera. Furthermore, multiple inner diameter measurements vary by no more than ± 2 μm along different radial chords, based on scanning electron microscopy techniques calibrated with a traceable standard. Consequently, the magnification of the imaged MTV lines is spatially uniform. Thus, since the inner diameter of the microtube is known, and the inside edges of the tube can be found for each image, the actual radial location can be determined by a direct proportionality as shown below:

$$r = D\frac{y}{D_{im}} \tag{2}$$

D is the actual tube inner diameter, D_{im} is the imaged tube diameter in pixels, and y is the radial location from the mid-plane measured in pixels. The overall uncertainty in radial location, r, is comprised of contributions in the respective uncertainties in y, D, and D_{im}. As stated previously, the uncertainty in D is ± 2 μm (1.1%). The uncertainty in y is ± 1 pixel (0.5%) and D_{im} was measured to within ± 3 pixels (1.6%). The resulting composite uncertainty in the radial location is thus 2% of the microtube inner diameter.

The approach we employ to determine c utilizes global mass continuity. The volume flow rate through the microtube must equal the area integral of the velocity and must be a constant at every axial location for a given flow rate. Thus, the volume flow

rate as measured by the collection method described previously was compared with the area integral of the averaged (~190 images) streamwise velocity distribution as expressed below.

$$Q = \int_0^{D/2} 2\pi u(r) r dr = c 2\pi \int_0^{D/2} (\overline{\Delta x(r)/\Delta t}) r dr \tag{3}$$

Q is the volume flow rate (m^3/s) measured using the collection method, R is the known tube radius (m), r is the radial location (m), $\Delta x(r)$ is the obtained displacement of the MTV line as a function of radial location in pixels, and Δt is the time delay (s) between acquisition of deformed and undeformed lines. The total tube diameter was measured to be 182 ± 2 μm using a scanning electron microscope (SEM). The conversion factor, c, was determined using the above method at each axial location for each Re explored. The magnitude of c was nominally 0.94 μm/pixel with some slight variation with each different Re due to minor changes in camera position, settings, etc. For each of the five Re explored here c was found to be identical for all 11 axial locations to within ±6%.

Measurement Uncertainty. The uncertainty in the time-averaged, or mean, measured velocities, normalized by the centerline velocity at the fully developed state, may be expressed as

$$U_e = \sqrt{\left(\frac{c_e}{c}\right)^2 + \left(\frac{\Delta x_e}{\Delta x_{\max}}\right)^2 + \left(-\frac{\Delta t_e}{\Delta t}\right)^2} \tag{4}$$

where Δt_e, c_e, and Δx_e are the uncertainties in determining Δt, c, and Δx, respectively. $\Delta x_{\max}$ is the centerline MTV line displacement at the fully developed state. The device uncertainty in measuring Δt is 0.25 μs. The uncertainty in calculating the conversion factor depends on how accurately the location of the tube walls can be determined in each image, and the precision of the volume flow rate measurement. The ratio c_e/c was stated previously to be no worse than 6%. The uncertainty in the instantaneous local streamwise displacement, Δx_e, is determined at a location far downstream where a steady laminar flow is known to exist. This is done by computing the rms of the local Δx values for the N images acquired, termed Δx_σ. For a 95% confidence, $\Delta x_e = 2\Delta x_\sigma$. The composite uncertainties in instantaneous velocity measurements, normalized by the centerline fully developed velocity, were in the range 8%–16%. This corresponds to $\Delta x_e/\Delta x_{\max}$ values in the range 5.3%–14.3%. By time averaging multiple images, Δx_e is reduced significantly, expressed as $\Delta x_e = 2\Delta x_\sigma/\sqrt{N}$ for 95% confidence [26]. Thus, for time-averaged velocities $\Delta x_e/\Delta x_{\max}$ ranges from 0.4% to 1%, since for all data presented in this paper $N = 190$ images were acquired for each time-averaged measurement. Consequently, the composite uncertainty in the normalized time-averaged velocity measurements is less than 7%, with c_e/c being the largest contributor to this uncertainty.

The uncertainty analysis presented in the preceding paragraphs assumed uni-directional flow. For dynamical situations where there exists significant fluid velocity parallel to the MTV line of excitation, error in measuring the streamwise velocity can be introduced. This occurs due to motion of the tracer molecules normal to the primary flow direction which results in an inability to accurately track tagged molecules. It is only of concern, however, in regions where both nonzero wall-normal velocity component and large wall-normal gradients of the streamwise velocity exist. Hill and Klewicki [22] have shown that in a two-dimensional flow the deviation from the true velocity, normalized by the maximum streamwise velocity, can be expressed as

$$U_n = \frac{2\Delta t \hat{u}(r=0)}{D} V \frac{\partial U}{\partial R} \tag{5}$$

where V is the nondimensional wall-normal velocity, Δt is the time delay between the acquisition of deformed and undeformed lines, $R = 2r/D$, and $\partial U/\partial R$ is the nondimensional wall-normal gradient of the streamwise velocity. U_n, U, and V are dimensionless local velocities, normalized by $\hat{u}(r=0)$ which is the fully developed velocity at the tube centerline. Since in the present study profiles of U were obtained at several axial locations in the experiments, V can be estimated by use of the equation of continuity shown below.

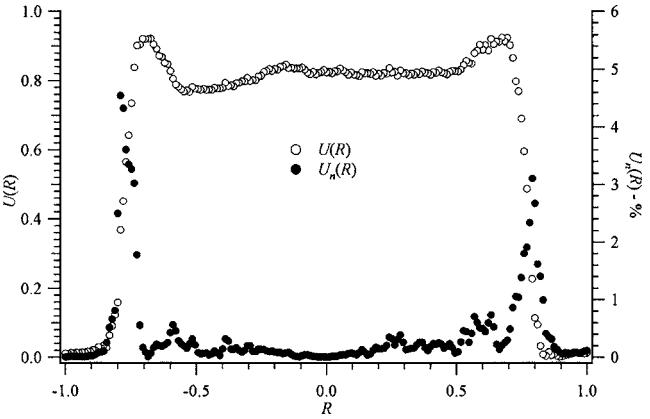

Fig. 4 Normalized measured velocity distribution, U, and induced error due to wall-normal fluid velocity, U_n, vs. R for Re = 350 and $X = 1.3$

$$\frac{\partial U}{\partial X} + \frac{2}{R}\frac{\partial}{\partial R}(RV) = 0 \tag{6}$$

Integrating with respect to R from $R=0$ to some variable location, R yields

$$V(R) = \frac{1}{2}\int_0^R \frac{\partial U}{\partial X} R' dR' + f(X) \tag{7}$$

Recognizing that $V = \partial U/\partial X = 0$ at $R=0$ requires that $f(X)$ be identically zero. Using the experimentally measured U velocity, Eq. (7) can be implemented to estimate V at each radial location across the tube cross section. Subsequently, Eq. (5) can be utilized to predict the error in U due to nonzero wall-normal velocity at all radial locations. It should be noted that this analysis gives only an estimate of the error since the measured U data were used in the estimation. As would be expected, this error is greatest for the highest Re explored here, 350, and at an axial location near the tube inlet, $X = x/D = 1.3$. The normalized velocity profile, and the corresponding induced error distribution, for this scenario are shown in Fig. 4. The error due to neglect of wall-normal velocity component is much less than 1% over almost the entire tube cross section and increases only in the regions of large $\partial U/\partial R$. The maximum error is less than 5% for the case shown in the figure, which represents the worst case of all experimental conditions. With the exception of the first three X locations for the Re=350 and 290 scenarios this maximum error was always less than 2%, and thus adds only marginally to the overall uncertainty to the time-averaged measurements.

Results and Discussion of Results

Figure 5 shows averaged images of deformed MTV lines for Re=350 at axial locations of $X=0.5$ ($x/D/\mathrm{Re}=0.0015$), $X=1.3$ ($x/D/\mathrm{Re}=0.0037$), and far downstream where the flow is fully developed, $X=23.2$ ($x/D/\mathrm{Re}=0.066$). The qualitative difference between the flow at these three locations can be observed. When fully developed, the flow profile is of the classical parabolic shape. At the entrance plane, however, the velocity is much more flat, or uniform, in the core. The tube walls are revealed in the images by the dark regions at the location where the phosphores-

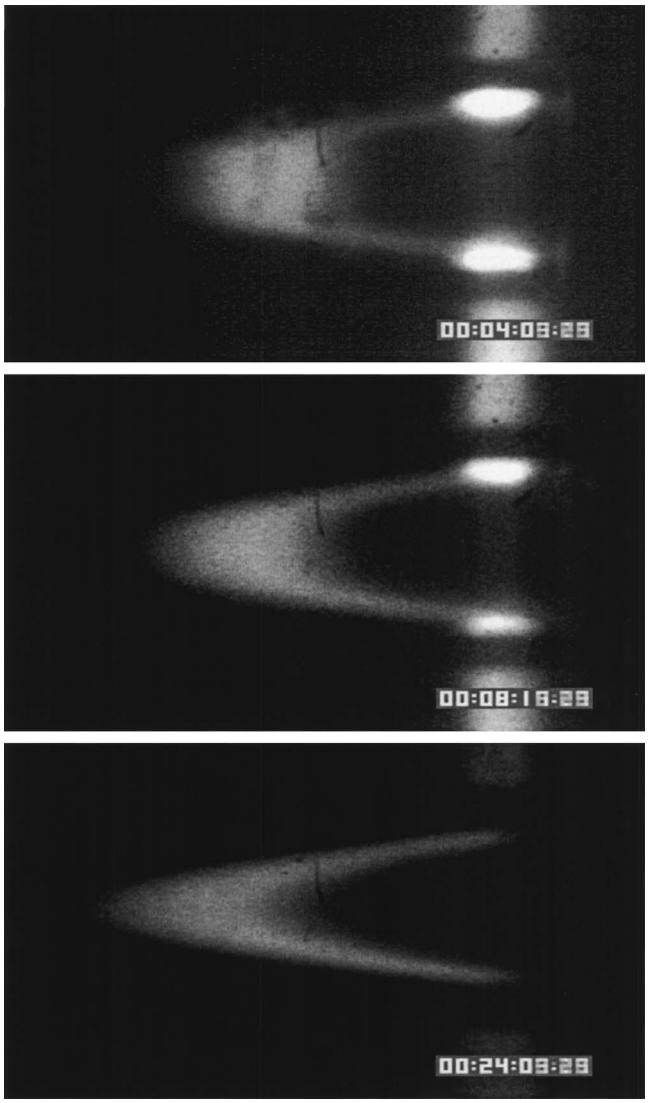

Fig. 5 Deformed MTV lines in a 180 μm diameter tube at X =0.5 (top), 2.1 (middle), and 23.2 (bottom) for Re=350. Flow is from right to left and each panel represents an average of 190 instantaneous images.

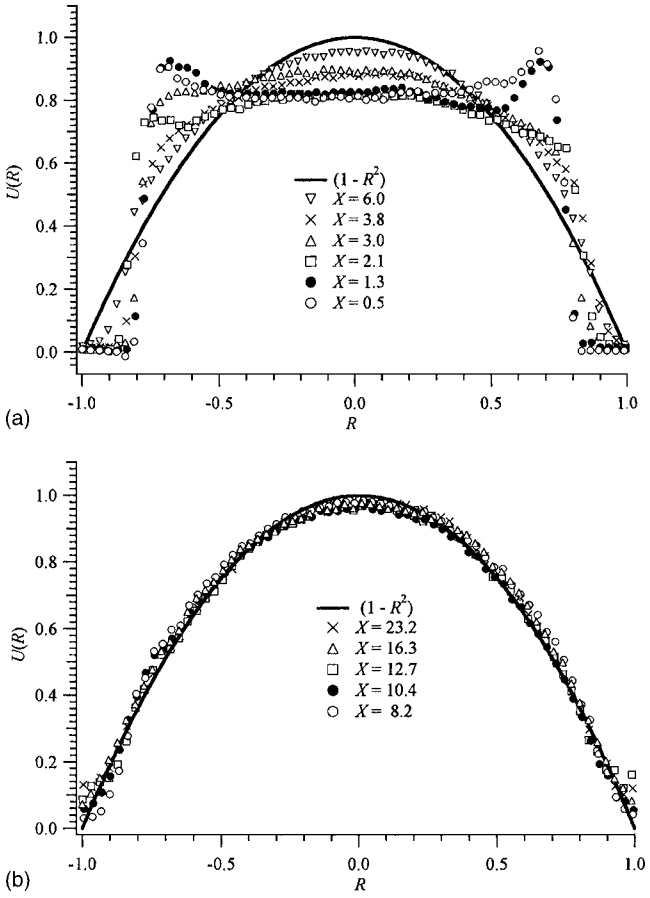

Fig. 6 Normalized time averaged velocity profiles at Re=350 and at X=0.5, 1.3, 2.1, 3.0, 3.8, and 6.0 in the top panel, and X =8.2, 10.4, 12.7, 16.3, and 23.2 in the bottom panel

cence vanishes. For the X=0.5 image, regions of more intense phosphorescence are observed near the walls. These regions are suggestive of fluid recirculation and a *vena contracta* that exists due to phosphorescing fluid that is trapped and circulating in the recirculation zone. As X increases, the size of these inferred recirculation zones, or bright regions, decreases. Because of the low quantum efficiency of the tracer molecule ($\sim$3%) and the small scale of the MTV lines, it becomes necessary to keep the camera shutter open longer than would normally be desirable. This is necessary so that a sufficient number of photons strike the CCD array for acceptable image quality. One effect of this is a broadening of the MTV lines. For our measurements the shutter time for acquisition of both the undeformed and deformed lines was the same, and use of the correlation approach described previously [21] is necessary to yield acceptable results.

Normalized time-averaged velocity profile results from the image analysis procedure are displayed in Fig. 6. In the upper panel $U=u(r)/\hat{u}(r=0)$ is plotted versus the normalized radial coordinate ($R=2r/D$) at the axial locations X=0.5, 1.3, 2.1, 2.9, 3.8, and 6.0 (corresponding entirely to entrance region results, x/D Re ranging from 0.0015 to 0.017) for a Reynolds number of 350. $\hat{u}(r)$ is the fully developed velocity profile based on Stokes flow theory corresponding to the measured volume flow rate. Each profile represents an average over 190 distinct deformed and undeformed line image sets, and symbol markers are shown on the figure corresponding to every third radial data point. Likewise shown in the bottom panel of Fig. 6 are velocity profile data at streamwise locations farther from the entrance, X=8.2, 10.4, 12.7, 16.3, and 23.2 (corresponding to x/D Re in the range 0.023 to 0.068), for the same Re. Included in both figures is the Stokes flow fully developed velocity profile for flow through a circular tube.

At $X(=x/D)$=0.5, the normalized core velocity is uniform and approximately equal to 0.8, 20% lower than the maximum (centerline) velocity for fully developed laminar flow in a circular tube. The flow is approximately stagnant near the tube wall, $|R| \geqslant 0.8$. At $|R| \approx 0.7$ there is a region of overshoot in the velocity where it exceeds the core velocity, which is further indicative of flow separation and corresponding local fluid acceleration. The relative velocity overshoot exhibits some asymmetry in the tube, and generally decreases with increasing X. The apparent asymmetry in the overshoot is perhaps due to unsteady flow phenomena at the microtube inlet. However, the magnitude of the asymmetry is very nearly within the experimental uncertainty in velocity.

At axial locations near the inlet the area comprising the zone where the flow is essentially stagnant is about 36% of the tube cross section and the ratio A_c/A is approximately 0.64. The transition between near-stagnant layers near the tube wall and the high-velocity core results in a region of extremely high fluid shear, with dimensional velocity gradients which reach magnitudes of order 10^5 s^{-1}. Although these gradients are large, an

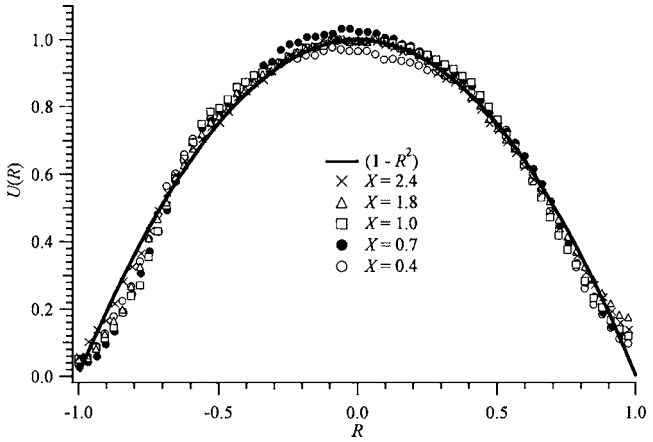

Fig. 7 Normalized time averaged velocity profiles at Re=60 and at *X*=0.4, 0.7, 1.0, 1.8, and 2.4

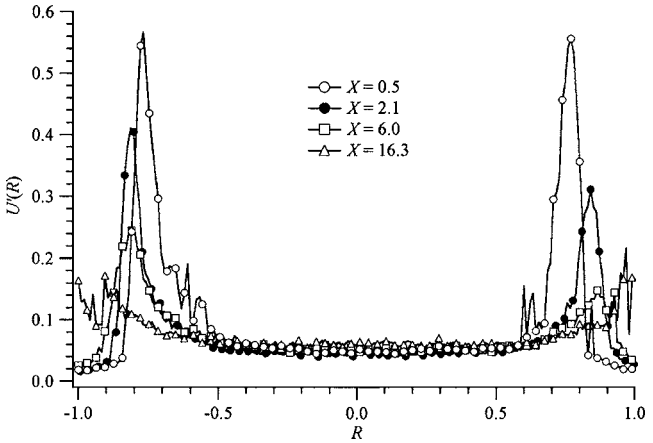

Fig. 8 Normalized profiles of the streamwise velocity rms for Re=350 at axial locations of *X*=0.5, 2.1, 6.0, and 16.3

analysis of the potential local viscous heating in a microtube flow indicates that such effects are negligible with regards to temperature dependence of the liquid properties. Although the *vena contracta* effect is expected to create a recirculation zone adjacent to the tube wall near the inlet with associated negative velocities, these velocities are too small to be detected using μMTV with the present experimental setup. It should be noted that the flow rate integral over the cross section of the velocity profile, Eq. (3), at Re=350 is modestly larger at small X as compared to the fully-developed condition. This may suggest that small negative velocities may exist in the separated flow region that are not detected. However, for no location is the deviation in the integration greater than 5%, indicating the magnitude of the velocities in the recirculation bubble, although possibly negative, are small.

At radial locations outside of the separation bubble (i.e., core flow), the flow accelerates from the stagnant reservoir environment and the centerline velocity in this region increases with increasing axial location. Thus, the flow is speculated to enter the microtube from the reservoir, separate at the sharp corner of the microtube, accelerate in the radial layer adjacent to the recirculation zone near the tube inlet, and reattach downstream when the separation bubble collapses. For the Re=350 data the reattachment occurs at approximately $X \approx 6-8$. Because of the nearly stagnant region near the tube wall, the core flow exceeds the microtube average fluid velocity, $U=u/\hat{u}(r=0)=0.5$, immediately upon entering the tube, and the centerline velocity approaches $U=1$ as X increases.

It is also observed that within experimental error, the velocity profile approaches the fully- developed profile as X increases. This is seen clearly in the bottom panel of Fig. 6 where velocity measurements are shown for axial positions that span the theoretical development length. This is further illustrated in Fig. 9, and will be discussed later. At these downstream axial locations there is little evidence of recirculation near the walls. The radial size of the recirculation zone, normalized by the tube radius, $(D-D_c)/D$, decreases from approximately 0.2 at $X \approx 0.5$, to approximately 0.15 at $X \approx 2.1$, to approximately 0.05 at $X \approx 6.0$. The velocity gradient at the wall also increases with increasing X, suggesting flow reattachment as well. Within the uncertainty of the data, the deviation of measured velocity profiles from the theoretical fully developed condition and the size of the recirculation region are both nearly indistinguishable beyond $X \approx 12.7$. It should be noted that very near the tube walls ($R \geq 0.98$) imaging limitations exist due to reflections arising from the mismatch in the indices of refraction of the microtube and test liquid, which may be the reason for the slightly anomalous velocities observed in Fig. 6.

Shown in Fig. 7 are time-averaged velocity profile measurements for the lowest Reynolds number explored, Re=60, at $X=0.4$, 0.7, 1.0, 1.8, and 2.4. At this Reynolds number the hydrodynamic development length is much shorter, and at the earliest axial measurement location the velocity profile is already very near the fully developed parabolic distribution. Also, little evidence of a *vena contracta* or recirculation regions exist for all X. Velocity profiles at Re=100, 150, and 290 are not presented here for the entire developing region. However, the results show qualitative behavior that lie between the Re=350 and Re=60 data.

The existence of a *vena contracta* at Re=350 is rather a surprising observation based on observed macroscale flow physics at similar Reynolds number values summarized in the Introduction. At a similar Re Durst and Loy observed no discernible flow separation [17] in macroscale experiments, which is the traditional assumption when considering the excess pressure drop in laminar flow inlets with Re$<$500 [14]. The observed value in this study of $A_c/A \approx 0.64$ is very nearly what one would predict if the flow was turbulent with a contraction ratio $A/A_1 \rightarrow 0$ (see Table 1). By contrast at Re=2300, Durst and Loy observed a *vena contracta* with $A_c/A \approx 0.8$, representing a significantly smaller region of flow separation even though the Reynolds number was greater by a factor of 7. If turbulent flow did prevail in our experiments for this condition, it would be manifest in the rms of the streamwise velocity profiles, u'. Profiles of the streamwise velocity rms, normalized by the theoretical centerline velocity at the fully developed state, $U'=u'/\hat{u}(r=0)$, are shown for Re=350 in Fig. 8 for $X=0.5$, 2.1, 6.0, and 16.3. Again, markers are shown for every third data point. It must be noted that both temporal fluctuations in the streamwise velocity at a fixed radial location and inherent measurement error contribute to the total magnitude of u'. Consequently, although the data do not provide an exact representation of the magnitude of the velocity fluctuations that exist, it does provide means for qualitative analysis. The data show that across the center portion of the tube U' is a minimum and of approximate magnitude 0.07 at all axial locations, likely due only to experimental uncertainty. Near the tube walls, and for $x/D=0.5$, U' increases significantly to a peak value of about 0.58 at $R \approx 0.8$, which corresponds to the region of high shear observed in the velocity profiles. As $R \rightarrow 1$, U' decreases from this peak value. The behavior is similar for increasing axial location, with the peak magnitude of U' decreasing and the location of the peak moving closer to the walls with increasing X. This behavior in U', and the velocity profiles of Fig. 6, suggest that for Re=350 the flow separates at the sharp entrance and either becomes locally turbulent or exhibits an unsteady laminar oscillation. Consequently, a peak in U' occurs at the interface between the core flow and the region of flow separation. The radial extent of this separated flow region

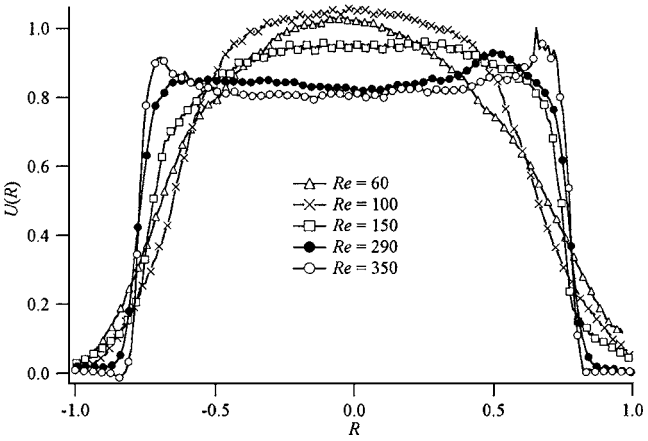

Fig. 9 Normalized time averaged velocity profiles for Re=60, 100, 150, 290, and 350, all obtained at the first axial measurement location for each data set, $X \approx 0.5$

then decreases for increasing streamwise distance from the inlet, with the rms of the velocity in the shear layer region decreasing due to dissipation until the flow eventually evolves to the classical laminar flow fully-developed state.

As noted previously there is no evidence of locally turbulent flow, unsteady laminar separation, or relatively large *vena contracta* in numerical simulation or in macroscale experiments conducted at similar Re. The behavior may exist at the microscale due to the sensitivity of the entrance flow to minute disturbances at the microtube inlet, despite the care exercised in the preparation of the microtube sections. Although wall surface roughness fabricated in a "drawn" process is likely to be small, characterization of such is a formidable task. As the physical scale decreases, the relative size of imperfections will increase and consequently, the relative surface roughness is significantly greater. This will be true of all microfabricated nozzles, channels, etc. Thus, despite care in fabricating flow apparatus, microscale flows may be inherently susceptible to imperfections caused by the manufacturing, preparation, or assembly process.

Shown in Fig. 9 are normalized time-averaged velocity profiles at the first measurement location $X \approx 0.5$ for Re=60, 100, 150, 290, and 350. These measurements provide a quantification of the size of the inferred recirculation region and general flow behavior at the inlet. Distinct variations in the flow physics are evident even though the Reynolds number remains nominally in the laminar flow regime. As Re increases the size of the stagnant regions near the wall also increases, as does the wall-normal velocity gradient in the shear layer. At the centerline the velocity is a minimum for the largest Re, and the velocity overshoot (above the centerline value), discussed previously, occurs at radial locations just inside of the region of high shear for the Re=290 and 350 data.

The deviation of measured velocity profiles from the fully developed limit may be further quantified by defining a normalized average velocity difference

$$\overline{\Delta U_D} = \frac{1}{N}\sum_N \frac{|u(r) - \hat{u}(r)|}{u\hat{u}(r=0)} \tag{8}$$

The summation represents a summation over the full radial extent of the velocity profile (from wall to wall). Likewise the maximum difference from the fully developed laminar flow theory is defined as

$$\Delta U_m = Max\left(\frac{|u(r) - \hat{u}(r)|}{\hat{u}(r=0)}\right) \tag{9}$$

These parameters vary with Re in a similar manner and both are plotted in Fig. 10 as a function of axial location x/D Re for the

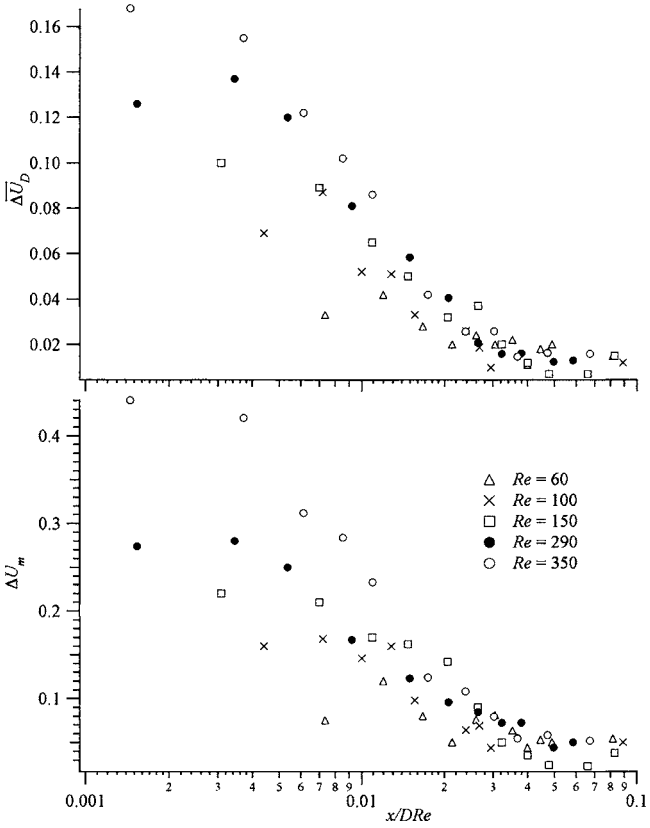

Fig. 10 Average difference from fully developed laminar pipe flow theory (top panel) and the maximum difference from fully developed laminar pipe flow theory (bottom panel) plotted as a function of x/D Re for all five Reynolds numbers explored

five Reynolds numbers investigated in this study. The figure illustrates that the difference between measured and fully developed profiles drops from a maximum near the tube inlet, vanishing near x/D Re ≈ 0.05 for all Re where the flow becomes fully developed. Further, the deviation from the fully developed profile behaves similarly for all Reynolds numbers investigated, when plotted against x/D Re as the normalized axial coordinate. The data suggest also a Reynolds number dependence, as noted in the velocity profiles of Fig. 9, with increasing deviation observed early in the microtube for increasing Re. For Re=60 the maximum value of $\overline{\Delta U_D}$ is approximately 0.05. Conversely, for Re=350 the maximum value of $\overline{\Delta U_D}$ is approximately 0.17, an increase of a factor of 3.4. The maximum values of $\overline{\Delta U_D}$ at the intermediate values of Re are approximately 0.07, 0.10, and 0.14 for Re=100, 150, and 290, respectively. As shown in Fig. 9 the corresponding velocity profiles for these intermediate Re cases show recirculation regions that increase in size with Re, which is the reason for the Re variation in $\overline{\Delta U_D}$ that exists in Fig. 10. The maximum magnitude of ΔU_m is approximately 0.44 at the first measurement location for Re=350 and decreases to approximately 0.09 for Re=60. It is also apparent that the development length x/D Re ≈ 0.05 matches the classically accepted value for circular tube flow with a uniform-velocity inlet for all Re, despite the separation and *vena contracta* observed for this entrance flow condition at higher Re.

Figure 11 shows the evolution of the normalized centerline velocity, U_{CL}, and the maximum value of the of the velocity rms (which occurs in the shear layer), $U'_{\max}$, at each axial location plotted as a function of x/D Re, for the five Reynolds numbers. The qualitative behavior in both panels is quite similar to the $\overline{\Delta U_D}$ and ΔU_m data. Again, the data approach an asymptotic value at large x/D Re indicating a fully-developed condition has been at-

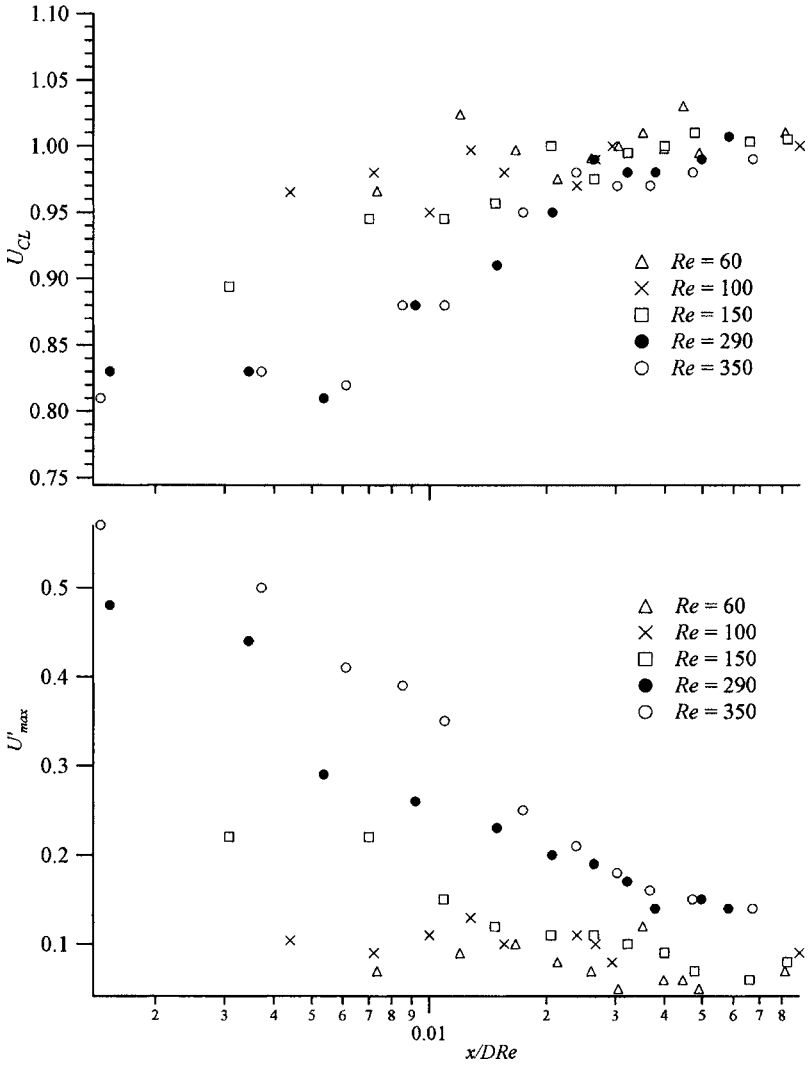

Fig. 11 Normalized centerline velocities (top panel) and normalized maximum in the streamwise velocity rms (bottom panel) plotted vs. $x/D\,\mathrm{Re}$ for all five Reynolds numbers

tained. $U'_{\max}$ is not identically zero at this downstream location, nor is U_{CL} identically unity, because of measurement uncertainty. $U'_{\max}$ is, however, a maximum at the first measurement location, exhibiting a decreasing magnitude with decreasing Re. This is indicative of a decrease in the local turbulence, or unsteady oscillations, in the region of flow separation with decreasing Re. The behavior of the centerline velocity also exhibits Re dependence as is exhibited in Fig. 11. For the lower magnitudes of Re the centerline velocity shows an increase of only about 5% from the inlet to the maximum value, whereas for the larger values of Re the increase is closer to about 20%. In the region $x/D\,\mathrm{Re} < 0.07$, and for $\mathrm{Re} \geqslant 290$, the centerline velocity is relatively unchanging. All of these observations are suggestive of the flow separation and recirculation bubble that is more pronounced for the larger values of Re.

Conclusions

Local velocities have been measured in the developing region of a circular microtube of diameter 180 μm using μMTV. Five different Reynolds numbers (60–350) in the nominally laminar regime were investigated. The results represent the first characterization of hydrodynamically developing pipe flow in tubes with diameters smaller than 1 mm. The uncertainty in the measured time averaged velocity ranges from 6% to 7% of the peak velocity. The uncertainty in instantaneous measurements is in the range 8%–16% of the maximum velocity. The data suggest the formation of a *vena contracta* with either locally turbulent flow or unsteady laminar separation early in the tube for larger Reynolds numbers. This behavior is quite different from macroscale experiment or numerical simulation, where the existence of a *vena contracta* in the laminar regime is typically not observed for $\mathrm{Re} < 500$. The area ratio of the *vena contracta* to tube cross section is Re dependent and approaches 0.64 for the largest value of Re explored, matching observations for macroscale experiments in the turbulent regime. Initially the tube core velocities are nominally flat, accelerating immediately to about 80% of the fully developed peak velocity for larger Re and closer to 100% for smaller values of the Reynolds number. At small axial locations a region of extremely high shear rate exists between a recirculation zone and the bulk tube flow. The size of the recirculation zones, measured velocity rms, and maximum shear rates also show dependence on the Reynolds number. Farther downstream of the inlet the velocity profile approaches the classical parabolic velocity distribution associated with laminar pipe flow. The hydrodynamic development length is nominally $x/D\,\mathrm{Re} = 0.05$ for all Re, which, despite the observed *vena contracta* that exists for some Re,

matches the classical entry length for a uniform flow inlet condition.

Nomenclature

A = area of small pipe in a sudden contraction or entrance, m^2
A_1 = area of large pipe in a sudden contraction, m^2
A_c = area of *vena contracta*, m^2
c = pixel to meter conversion factor, m/pixels
c_e = uncertainty in determining c, m/pixels
D = diameter of small pipe in a sudden contraction or inlet, m
D_1 = diameter of large pipe in a sudden contraction, m
D_c = diameter of *vena contracta*, m
D_{im} = imaged length of tube diameter, pixels
D_h = hydraulic diameter, m
K = entrance loss coefficient
L = microchannel length, m
L_c = entrance length, m
N = number of images
Q = measured volume flow rate, m^3/s
r = radial coordinate, m
R = normalized radial coordinate, m
Re = Reynolds number,
t = time, s
t_e = uncertainty in measuring time, s
u = streamwise velocity, m/s
u' = streamwise velocity rms, m/s
$\hat{u}$ = theoretical fully developed velocity profile, m/s
$\bar{u}$ = average streamwise velocity, m/s
U = normalized streamwise velocity
U' = normalized rms of the streamwise velocity
$U'_{\max}$ = normalized maximum rms of the streamwise velocity at a given axial location
U_{CL} = normalized centerline velocity at fully developed state
U_e = normalized uncertainty in normalized velocity measurement
U_n = normalized error due to flow normal to the MTV line
V = normalized wall-normal velocity component
x = streamwise coordinate, m
x_e = Uncertainty in determining displacement, m
x_σ = rms of the MTV line displacement, m
X = normalized streamwise coordinate, x/D
$\overline{y}$ = radial distance from tube centerline in pixels
ΔU_D = normalized average difference from the fully developed velocity profile, m/s
ΔU_m = normalized maximum difference from the fully developed velocity profile, m/s
Δx_e = rms of the local streamwise displacement for N images, m/s
ρ = fluid density, kg/m^3
μ = fluid viscosity, kg/m-s
ζ = wall thickness, m

References

[1] Jacobson, S. A., 1998, "Aerothermal Challenges in the Design of a Microfabricated Gas Turbine Engine," AIAA-98-2545, 29th AIAA Fluid Dynamics Conference, Albuquerque, NM, June 15–18.
[2] Urbanek, W., Zemel, J. N., and Bau, H. H., 1993, "An Investigation of the Temperature Dependence of Poiseuille Numbers in Microchannel Flow," J. Micromech. Microeng., **3**, pp. 206–209.
[3] Papautsky, I., Brazzle, J., Ameel, T. A., and Frazier, A. B., 1998, "Laminar Fluid Behavior in Microchannels Using Micropolar Fluid Theory," *Proceedings of 11th IEEE International Workshop on MEMS*, Heidelberg, Germany, Vol. 73, pp. 101–108.
[4] Mala, G. M., Li, D., and Dale, J. D., 1997, "Heat Transfer and Fluid Flow in Microchannels," Int. J. Heat Mass Transfer, **40**, pp. 3079–3088.
[5] Pfhaler, J., Harley, J., Bau, H., and Zemel, J., 1991, "Gas and Liquid Flow in Small Channels," in *Micromechanical Sensors, Actuators, and Systems*, ASME, New York, NY, DSC-Vol. 32, pp. 123–134.
[6] Webb, R. L., and Zhang, M., 1998, "Heat Transfer and Friction in Small Diameter Channels," Microscale Thermophys. Eng., **2**, pp. 189–202.
[7] Judy, J., Maynes, D., and Webb, B. W., 2002, "Characterization of the Frictional Pressure Drop for Liquid Flows Through Microchannels," Int. J. Heat Mass Transfer, **45**, pp. 3477–3489.
[8] Lee, S.-J., and Kim, G.-B., 2003, "Analysis of Flow Resistance Inside Microchannels With Different Inlet Configurations Using Micro-PIV System," *First International Conference on Microchannels and Minichannels*, ASME, New York, pp. 823–827.
[9] Shah, R. K., and London, A. L., 1978, *Laminar Flow Forced Convection in Ducts*, Academic, New York.
[10] Schmidt, F. W., and Zeldin, B., 1969, "Laminar Flow in the Inlet Section of Tubes and Ducts," AIChE J., **15**, pp. 612–614.
[11] Atkinson, B., Kemblowski, A., and Smith, J. M., 1967, "Measurements of Velocity Profile in Developing Flows," AIChE J., **13**, pp. 17–20.
[12] Shah, R. K., 1978, "A Correlation for Laminar Hydrodynamic Entry Length Solutions for Circular and Noncircular Ducts," ASME J. Fluids Eng., **100**, pp. 177–179.
[13] Berman, N. S., and Santos, V. A., 1967, "Laminar Velocity Profiles in Developing Flows Using a Laser Doppler Technique," AIChE J., **15**(3), pp. 323–326.
[14] Perry, R. H., Green, D. W., and Maloney, J. O., 1984, *Perry's Chemical Engineer's Handbook*, 6th ed., McGraw-Hill, New York.
[15] Sylvester, N. D., and Rosen, S. L., 1970, "Laminar Flow in the Entrance Region of a Cylindrical Tube," AIChE J., **16**, pp. 964–966.
[16] Astarita, G., and Greco, G., 1968, "Excess Pressure Drop in Laminar Flow Through a Sudden Contraction," Ind. Eng. Chem. Fundam., **7**, pp. 27–31.
[17] Durst, F., and Loy, T., 1985, "Investigations of Laminar Flow in a Pipe With Sudden Contraction of Cross Sectional Area," Comput. Fluids, **13**, pp. 15–36.
[18] Bückle, U., and Durst, F., 1993, "Investigations of Laminar Flow in a Pipe With Sudden Contraction of Cross Sectional Area," ASME Fluids Division, FED-Vol. 146, pp. 61–78.
[19] Xia, Y., Callaghan, P. T., and Jeffrey, K. R., 1992, "Imaging Velocity Profiles: Flow Through an Abrupt Contraction and Expansion," AIChE J., **38**, pp. 1408–1420.
[20] Blevins, R. D., 1984, *Applied Fluid Dynamics Handbook*, Van Nostrand Reinhold, New York.
[21] Thompson, B. R., Maynes, D., and Webb, B. W., 2002, "Micro-Scale Velocity Measurements Using Molecular Tagging Velocimetry: Methodology and Uncertainty," ASME Fluids Division Summer Meeting, Montreal, Canada, July 14–18.
[22] Gendrich, C. P., Koochesfahani, M. M., and Nocera, D. G., 1997, "Molecular Tagging Velocimetry and Other Novel Applications of a New Phosphorescent Supramolecule," Exp. Fluids, **23**, pp. 361–372.
[23] Hill, R. B., and Klewicki, J. C., 1996, "Data Reduction Methods for Flow Tagging Velocity Measurements," Exp. Fluids, **20**, pp. 142–152.
[24] Maynes, D., and Webb, A. R., 2002, "Velocity Profile Characterization in Sub-Millimeter Tubes Using Molecular Tagging Velocimetry," Exp. Fluids, **32**, pp. 3–15.
[25] Idel'chik, I. E., 1986, *Handbook of Hydraulic Resistance*, Hemisphere, New York.
[26] Taylor, T. R., 1982, *An Introduction to Error Analysis*, University Science Books, Mill Valley CA.

Ryuhei Yamaguchi
Department of Mechanical Engineering,
Shibaura Institute of Technology

Takeshi Mashima
Imabari Ship Building Co., Ltd.

Hideaki Amagai
Department of Mechanical Engineering,
Shibaura Institute of Technology

Hisashi Fujii
Department of Electrical System for Urban Engineering,
Shibaura Institute of Technology

Toshiyuki Hayase
Institute of Fluid Science, Tohoku University

Kazuo Tanishita
Department of System Design Engineering,
Keio University

Variation of Wall Shear Stress and Periodic Oscillations Induced in the Right-Angle Branch During Laminar Steady Flow

We report on flow phenomena such as wall shear stress and periodic oscillations that occur in the right-angle branch during laminar steady flow in the upstream trunk. The side-branch bifurcates from the trunk at a 90-deg angle, and both the upstream and the downstream corners of the entrance of the side-branch are square-edged. As the flow approaches the entrance of the side-branch through the trunk, the wall shear stress steeply increases along the near wall, and this stress at the upstream corner is comparable to that generated around the flow divider. Periodic velocity oscillations occur downstream in the separation region in the side-branch. The Strouhal number based on the flow conditions in the side-branch is independent of the flow division ratio for the side-branch radii ranging from 4 to 9 mm. Furthermore, it appears that the Strouhal number is weakly dependent on the Reynolds number. The periodic oscillation in the side-branch exhibits a characteristic flow behavior, which is a universally recognized phenomenon in the right-angle branch. [DOI: 10.1115/1.1852480]

1 Introduction

The right-angle branch is one of most important and fundamental components of pipeline networks and plant systems. Over the past 100 years, many researchers have studied the energy loss in asymmetrical branches, including the right-angle branch. A detailed investigation has been conducted on the flow structure and energy loss in the right-angle branch in a turbulent region of approximately $Re=10^5$ [1]. The energy loss coefficient for several area ratios of the trunk to the side-branch and several flow division ratios of the flow rate from the trunk to the side-branch have been established.

Lighthill [2] explained the flow pattern and the wall shear stress in the laminar flow region from the viewpoint of hemodynamics. Many arteries asymmetrically bifurcate from the abdominal aorta. The arterial site from the abdominal aorta to the renal artery or the mesenteric artery is a typical asymmetrical branch [3]. It is widely known that vascular diseases frequently occur at the arterial branch along the abdominal aorta [4–6]. With the exception of the aortic arch, the flow throughout the human body is generally a laminar flow. Therefore, when considering the flow structure in the right-angle branch, not only the turbulent flow, but also the laminar flow should be considered.

The hemodynamics of the right-angle branch in a laminar steady flow was investigated by Karino et al. [7], Liepsch et al. [8], and Hirose et al. [9]. Karino et al. [7] visualized the flow pattern around the corner in the right-angle branch, which showed how the helical flow in the side-branch results in recirculation. Based on flow visualization, Hirose et al. [9] showed the existence of a symmetrical pair of secondary flows in motion in the side-branch. Three-dimensional calculations were done for the flow pattern arising in the branch using the finite control volume and the finite element methods [10,11]. However, no details on the mechanism of the secondary flow in the side-branch such as the number of vortices, the symmetry, and the periodic change of the velocity have been reported. In the right-angle branch employed in various fluid power plants together with pipeline networks with turbulent flow, erosion is likely prone to be generated around a corner of the side-branch. It is thought that such erosion may be caused by the wall shear stress arising from the interaction between the fluid and the tube wall [12]. However, adequate information is not available with respect to the distribution of the wall shear stress around the corner of the entrance in the side-branch, even in a laminar steady flow. Recently, the present authors have suggested that the wall shear stress may abruptly change around the entrance corner of the side-branch and the flow in the side-branch may periodically oscillate [13,14]. However, details of this oscillation should be investigated and its dependence on the Reynolds number, flow division ratio, and the radius of the side-branch should be clarified. In the present study, measurements were conducted under flow conditions characterized by the variation of the wall shear stress and periodic oscillation induced in the right-angle side-branch during a laminar steady flow. In this experimental system, the trunk is 12.2 mm in radius and the side-branch bifurcates from the trunk at a 90 deg angle. Both the upstream and the downstream corners at the entrance of the side-branch are square-edged.

Consideration was given to the fact that the wall shear stress close to the upstream corner of the right-angle branch is much smaller than that close to the downstream corner which acts as a flow divider. It was observed that with the right-angle branch in question, the wall shear stress arising at a point immediately downstream of the upstream corner is much smaller than that at the flow divider. However, in the upstream trunk, the wall shear stress at the upstream corner is large, and the change in the wall shear stress around the upstream corner is thus comparable to that around the flow divider.

A pair of vortices appears within the region, immediately downstream of the upstream corner where the separation flow is also in motion. The flow moving through the upstream trunk in a laminar

Contributed by the Fluids Engineering Division for publication in the JOURNAL OF FLUIDS ENGINEERING. Manuscript received by the Fluids Engineering Division March 10, 2003; revised manuscript received August 17, 2004. Associate Editor: M. Otugen.

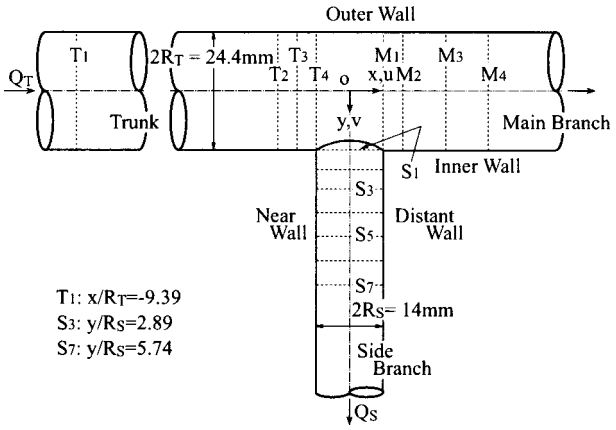

Fig. 1 System schematic of right-angle branch and typical measurement sections (typical case, $R_S=7$ mm)

steady state causes periodic velocity oscillation in the side-branch [13]. The frequency of this velocity oscillation depends on the Reynolds number, the flow division ratio from the trunk to the side-branch, and the radius of the side-branch [14]. This is due to the fact that the Strouhal number is independent of the flow division ratio and the radius of the side-branch, and it is weakly dependent on the Reynolds number.

2 Experimental Details

2.1 Branch Model. Figure 1 shows the configuration of the present branch model. A side-branch bifurcates from the trunk at 90 deg angle and with radius $R_T=12.2$ mm. To examine the effect of the side-branch radius R_S on the flow oscillation, measurements were made for $R_S=4$, 5, 6, 7, and 9 mm. Both the upstream and the downstream corners of the side-branch are square-edged. The point where the y axis of the side-branch intersects with the x axis of the trunk is defined as the origin. Both the x and y axes are defined on the common median plane where the measurements are made. Q_T and Q_S indicate the flow rate through the trunk and the side-branch, respectively.

From the viewpoint of hemodynamics, the renal artery with a diameter of about 2 mm bifurcates from the abdominal aorta at an angle of approximately 90 deg; the abdominal aorta has a diameter of about 6 mm [5]. Hence, the diameter ratio of the side-branch to the trunk is 1:3. From the viewpoint of geometry, this diameter ratio complies with the radius ratio of the side-branch $R_S=4$ mm to the trunk $R_T=12.2$ mm. In order to analyze the fundamental flow structure through the right-angle branch, the entrance shape is chosen to be a square-edged corner, although some detailed features of the flow structure may depend on the corner shape.

2.2 Velocity Measurement and Calculation of Wall Shear Stress. The velocity components and the measurement sections for $R_S=7$ mm are shown in Fig. 1. In the trunk and the main branch, u and v represent the axial and the transverse velocity components, respectively. On the other hand, v and u in the side-branch represent the axial and the transverse velocity components, respectively. The velocity profile was measured at several sections where the wall shear stress exhibited distinct behaviors. The site where the measurements were made are as follows: (1) sections $T_{1,2,3,4}$ in the trunk, (2) sections $M_{1,2,3,4}$ in the main branch, and (3) sections $S_{1,\ldots,7}$ in the side-branch. The coordinate of the typical measurement sections is also shown in Fig. 1. To obtain the fully developed flow in the upstream trunk, the inlet between the constant head reservoir and the measurement section was fixed at a length 100 times longer than the trunk diameter.

The velocity profile was measured by using two-component laser Doppler velocimetry (LDV). The LDV system is equipped with a 4 W Argon laser. The focal length of the convex lens is 122 mm, and the measurement shape is regarded to be a circular cylinder with a diameter of 0.04 mm and a length of 0.2 mm for the sake of easy measurement. The position of the LDV sensing volume was controlled within a three-dimensional spatial accuracy of 5 μm. Four beams enter the branch model from the direction perpendicular to the common median plane, and the measurement is made across the tube diameter at the common median plane. Velocity measurements are made every 0.5 or 1 mm across the tube diameter, except in the vicinity of the tube wall. The wall shear stress was estimated from the velocity gradient at the tube wall, that is, the velocity difference between the tube wall and the point 0.6 mm from the tube wall. Comparing the present estimation of wall shear stress with that of the Poiseuille flow at the tube wall, the wall shear stress obtained in this method is underestimated about 2.5%.

A saturated aqueous solution of sodium iodide NaI having the same refractive index as the acrylic channel material was used as the working fluid for the velocity measurements. The mass ratio of NaI to distilled water is 1.78:1. At a temperature of 295 K, the refractive index, the density, and the kinematic viscosity are $n=1.49$, $\rho=1.83$ g/cm^3, and $\nu=1.65\times10^{-6}$ m^2/s, respectively.

2.3 Spectrum Analysis. The velocity was measured every 2 ms while the LDV data rate was greater than 3 kHz. In a 40 s sampling interval, a 20 k data set was obtained. A spectral analysis was conducted for the velocity measurement since periodic velocity oscillations were observed in the side-branch.

2.4 Flow Visualization. The flow patterns both at the common median plane and in the circular cross section of the side-branch were visualized using suspended polystyrene particles with 100 μm in diameter, which were illuminated by a laser sheet. The working fluid employed in the flow visualization was the sodium iodide NaI solution with the same density, i.e., $\rho=1.04$ g/cm^3, as the polystyrene particles. The mass ratio of NaI to the distilled water was 1:10.

3 Results and Discussion

The measurements were primarily carried out for the case of $R_S=7$ mm, $\mathrm{Re}_T=800$, and $Q_S/Q_T=0.50$. Because flow oscillates in the side-branch, the velocity and the wall shear stress are calculated from ensemble averages of 20 k data sets.

3.1 Flow Structure

3.1.1 Velocity Profile. Figures 2(*a*) and 2(*b*) show the axial velocity profile at the common median plane in $Q_S/Q_T=0.25$ and 0.50 for $\mathrm{Re}_T=800$, respectively. The axial and the transverse velocities are normalized by the mean velocity, U_T, in the upstream trunk. In section T_1, the velocity profile is that for the Poiseuille flow. As it approaches the upstream corner in section T_4, the velocity increases along the near wall to the upstream corner. Furthermore, the velocity gradient at this corner becomes greater than that at the outer wall. The axial velocity decreases immediately downstream of the upstream corner, and a separation flow appears along the near wall of the side-branch. The reattachment points for $Q_S/Q_T=0.25$ and 0.50 are placed around in the vicinity of sections S_5 and S_3, respectively. The velocity gradient is large along the inner and the distant walls downstream of the flow divider. A reverse flow exists along the outer wall of the main branch.

3.1.2 Flow Visualization at the Common Median Plane and the Cross Section of the Side-Branch. The flow visualization at the common median plane for $\mathrm{Re}_T=800$, $Q_S/Q_T=0.25$ and 0.50 is shown in Fig. 3. R_p indicates the reattachment point of the separation region in the side-branch. The separation flow distinctly appears along the near wall. The flow generated in the

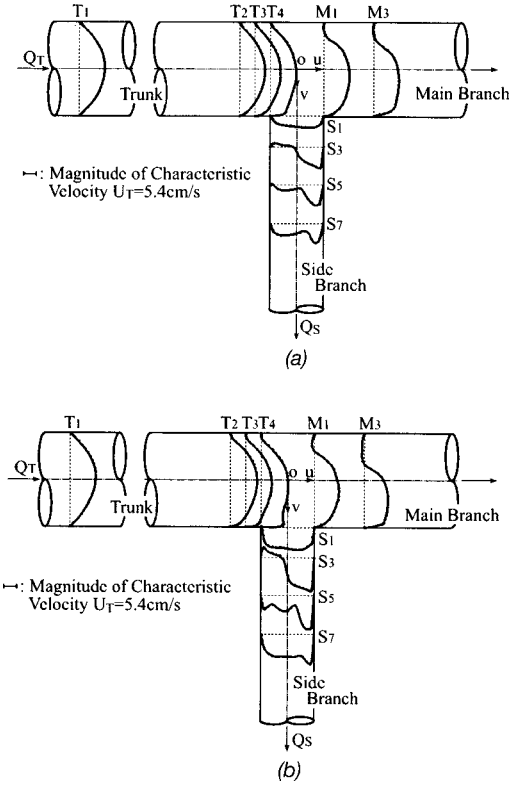

Fig. 2 Axial velocity profile at common median plane (Re_T = 800, R_S = 7 mm). (*a*) Q_S/Q_T = 0.25., (*b*) Q_S/Q_T = 0.50.

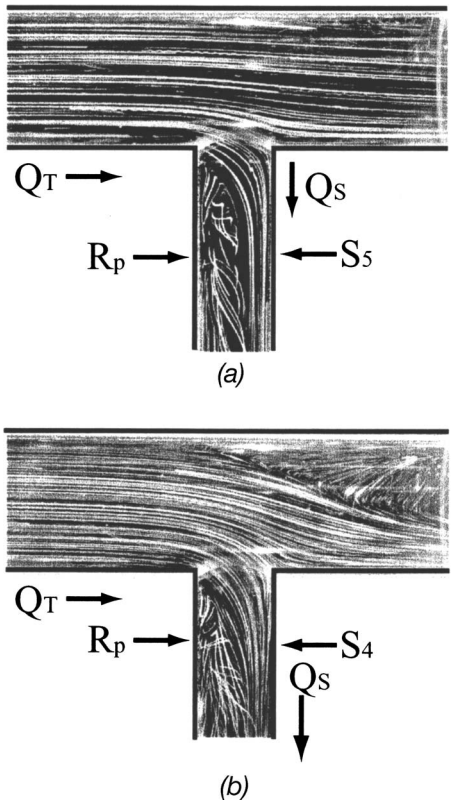

Fig. 3 Flow visualization at common median plane (Re_T = 800, R_S = 7 mm). (*a*) Q_S/Q_T = 0.25., (*b*) Q_S/Q_T = 0.50.

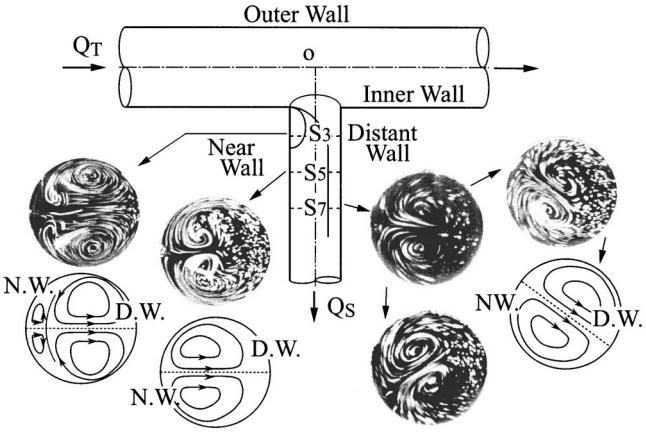

Fig. 4 Flow visualization and sketch of secondary flow at cross section in side-branch (Re_T = 800, Q_S/Q_T = 0.50, R_S = 7 mm)

separation region reverses with a peculiar helical movement. This helical movement within the separation flow is particularly prominent at $Q_S/Q_T = 0.25$ in Fig. 3(*a*). A strong shear layer is produced between the separation flow, resulting in reverse helical movement, and the main flow along the distant wall. The flow with the strong shear layer is unstable.

Figure 4 shows the secondary flow at the circular cross-section perpendicular to the common median plane in the side-branch. There are three types of secondary flows. First, in section S_3, including the separation region, there are two pairs of symmetrical vortices. One of these pairs of vortices appearing at a central point occupies a major portion of the cross section. The other pair is made up of smaller vortices and appears along the near wall. These two pairs of vortices result from two kinds of fluid motion. The core flow in the upstream trunk mainly impinges on the flow divider. After impinging, the fluid turns in the direction of the side-branch and helically flows along the peripheral tube wall from the distant wall to the near wall. This motion leads to the development of a large vortex at the center in the cross-section of the side-branch. On the other hand, the fluid with low velocity produced in the vicinity of the tube wall in the upstream trunk flows along both the top and the bottom peripheral tube walls starting from the trunk and moving towards the side-branch. This fluid produced in the vicinity of the peripheral tube wall in the upstream trunk is thought to flow into the separation region with a helical motion owing to lack of large momentum. Second, in section S_5 near the reattachment point, one pair of symmetrical vortices appears at the near wall with high velocity. Third, in section S_7 downstream of the reattachment point, there is one pair of symmetrical vortices. However, the symmetrical plane of this vortex in section S_7 does not coincide with the common median plane, although it inclines towards the common median plane. This inclination may depend on the flow condition in the upstream trunk.

3.1.3 Wall Shear Stress. The left side of Figs. 5(*a*) and 5(*b*) shows the distribution of wall shear stress τ_w in the trunk and in the main branch, respectively. The right side of the individual diagrams shows the distribution of τ_w in the side-branch. The τ_w is normalized by the wall shear stress in the upstream trunk. Therefore, $\tau_w = 1.0$ corresponds to the wall shear stress for the Poiseuille flow in the upstream trunk.

Along the outer wall of the trunk and along the main branch as shown in Fig. 5(*b*), τ_w (indicated by △) decreases from $\tau_w = 1.0$ in the upstream trunk. Along the near wall, τ_w (indicated by ○) rapidly increases as it approaches the entrance of the side-branch, reaching a maximum value of $\tau_w = 11$ in section T_4. The τ_w rapidly decreases and reaches a minimum negative value of $\tau_w =$

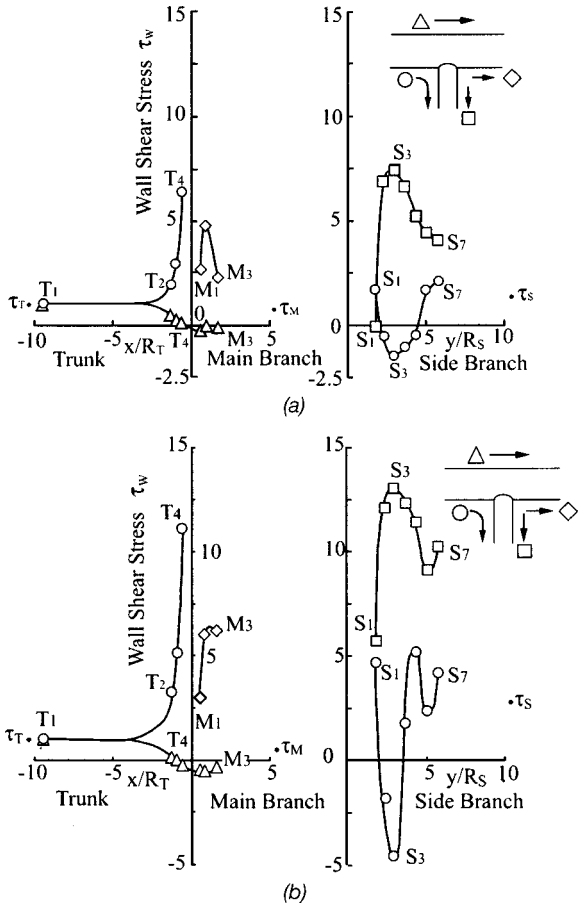

Fig. 5 Distribution of wall shear stress (Re_T=800, R_S =7 mm). (*a*) Q_S/Q_T=0.25. (*b*) Q_S/Q_T=0.50.

−5 in section S_3. Along the inner wall (indicated by ◇) and along the distant wall (indicated by □), τ_w becomes very large around the flow divider, and then rapidly decreases.

The variation of τ_w is one of the characteristics of the flow structure in the vicinity of the upstream corner, becoming very large in section T_4 and in section S_3. The change of τ_w in the vicinity of the upstream corner is comparable to that around the flow divider, and its magnitude is several times greater than that of the Poiseuille flow in the upstream trunk. The steep change of τ_w is thought to be related to the singularity of the upstream corner. In other words, the flow abruptly separates at a right angle in the upstream corner. Thus, acceleration might be quite large in the upstream corner. This singularity might be similar to that at the leading edge of a flat plate immersed in the parallel flow.

The variation of wall shear stress in the renal arterial branch might not be the same as that of the present model, as the entrance of the renal arterial branch is round. However, the increase of τ_w in sections T_3 and T_4 is related to the deflection of core flow starting from the upstream trunk into the side-branch. In the case of the arterial branch, the wall shear stress is thought to change in the vicinity of the upstream corner. Furthermore, the steep change of τ_w at the upstream corner might cause erosion to be experienced in the pipeline networks with turbulent flow.

3.2 Periodic Oscillation of Velocity

3.2.1 Time Variation. Figure 6(*a*) shows the time variation of axial velocity $2U_T$ at the tube axis in section T_1 for Re_T =800. The flow in section T_1 is a fully developed Poiseuille flow, although some noise is included. The maximum time-averaged velocity at the trunk axis is $2U_T$=0.108 m/s. The standard deviation is 0.0024 m/s, and the bias limit arising from the characteristic of the present LDV system is 0.0015 m/s. Thus, the uncertainty of axial velocity at the tube axis through the upstream trunk is approximately 0.0028 m/s. Figures 6(*b*)–6(*d*) show the time variation of axial velocity at the tube axis in section S_7 for Q_S/Q_T=0.25, 0.33, and 0.5, respectively. For Q_S/Q_T=0.25, 0.33, and 0.5, the axial velocity periodically oscillates, although each axial velocity includes random noise similar to that dealt with in Fig. 6(*a*).

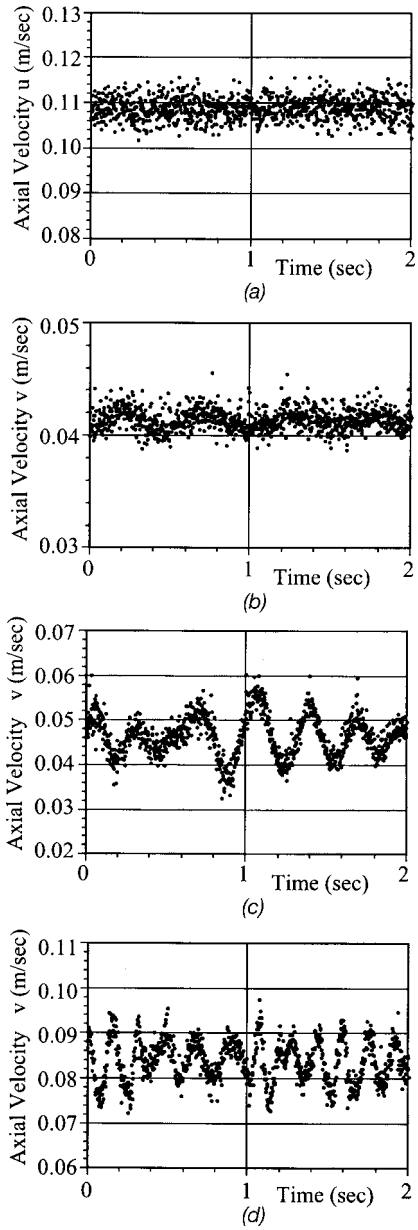

Fig. 6 Time variation of axial velocity along tube axis (Re_T =800, R_S=7 mm). (*a*) Section T_1. (*b*) Q_S/Q_T=0.25, section S_7, (*c*) Q_S/Q_T=0.33, section S_7, (*d*) Q_S/Q_T=0.50, section S_7.

3.2.2 Power Spectrum and Frequency. Figures 7(*a*)–7(*d*) show the distribution of the power spectrum corresponding to the time variation illustrated in Figs. 6(*a*)–6(*d*). Figure 7(*a*) tends to indicate that the random scatter in the axial velocity record at the tube axis is not caused by actual velocity fluctuations, but rather likely due to signal noise as illustrated in Fig. 6(*a*). The power spectrum in section T_1 is flat and does not have any peak frequencies. Figures 7(*b*) and 7(*c*) indicate the existence of a distinct

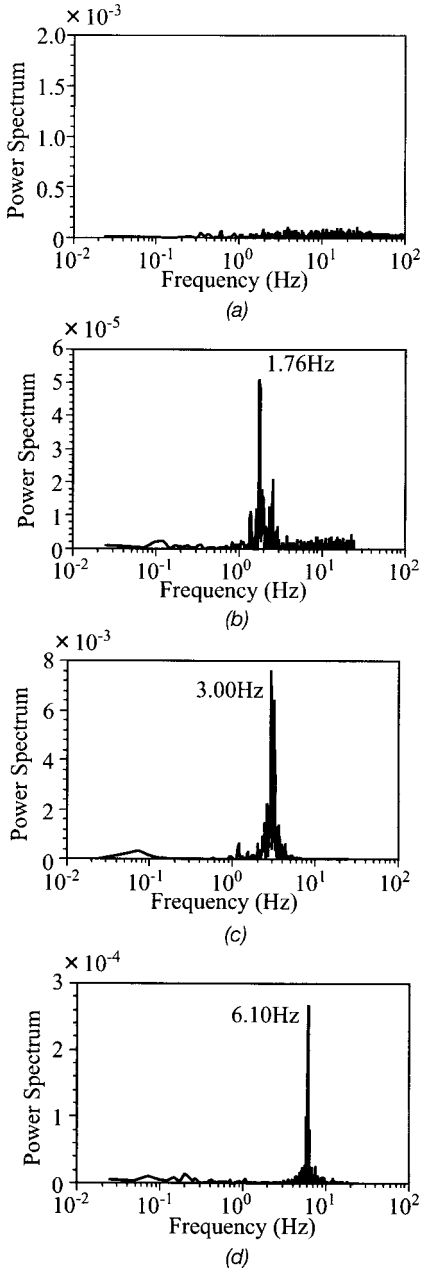

Fig. 7 Power spectrum of axial velocity along tube axis (Re_T = 800, R_S = 7 mm). (*a*) Section T_1, (*b*) Q_S/Q_T = 0.25, section S_7, (*c*) Q_S/Q_T = 0.33, section S_7, (*d*) Q_S/Q_T = 0.50, section S_7.

oscillation for $Q_S/Q_T = 0.25$, 0.33, and 0.5 in the side-branch. The velocity in the side-branch periodically oscillates at frequencies of $f = 1.76$, 3.00, and 6.10 Hz, respectively.

3.2.3 Periodic Oscillation in the Side-Branch. Periodic oscillations appear in the downstream direction of the separation region in the side-branch. To examine the distribution of the location with distinct oscillation of the velocity for $Re_T = 800$ and $Q_S/Q_T = 0.50$, the locations of periodic oscillation in sections S_3 and S_7 are shown in Figs. 8(*a*) and 8(*b*), respectively. For the side-branch with a radius of 7 mm, the axial and transverse velocities are measured every 1 mm in both x and y directions. The upper semicircle represents the transverse velocity, whereas the lower semicircle represents the axial isovelocity contours. The magnitude of the transverse velocity is given by the scale of the characteristic velocity U_T.

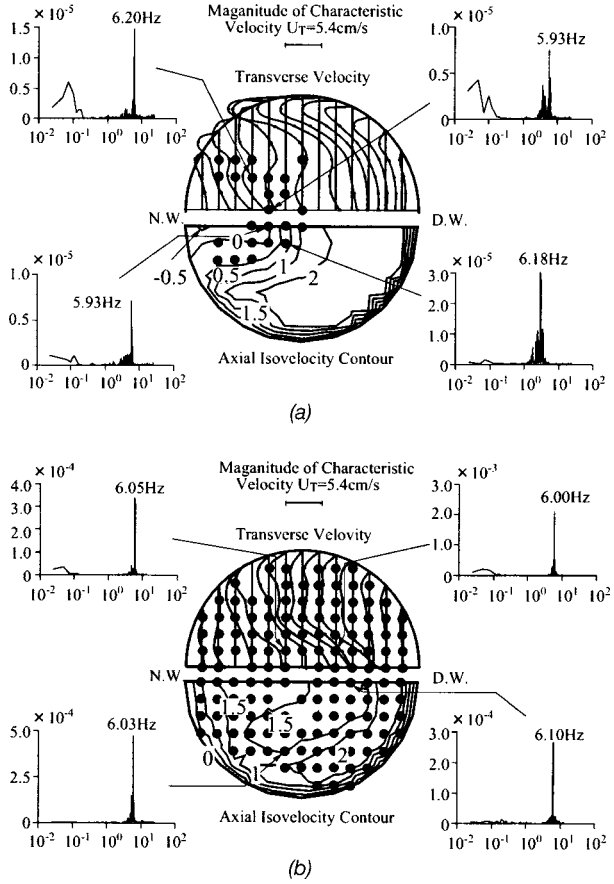

Fig. 8 Location with periodic oscillation ($Re_T = 800$, $Q_S/Q_T = 0.50$, $R_S = 7$ mm). The upper semicircle represents the transverse velocity contours and the lower semicircle represents the axial velocity contours. (*a*) section S_3, (*b*) section S_7.

In Fig. 8, the large solid circles represent the location where distinct oscillations are observed in the transverse and the axial velocities. The power spectrum at four typical locations is shown at the corners. From the axial isovelocity contours shown in lower semicircle in Fig. 8(*a*), it is apparent that the periodic oscillation forms in the separation region of section S_3. Further downstream, this region together with the periodic oscillation spreads across the entire cross section in section S_7 as shown in Fig. 8(*b*). The power spectra shown in Figs. 8(*a*) and 8(*b*) indicate that the peak frequency is about 6 Hz for the same value of Q_S/Q_T, and is independent of the location and the section in the side-branch. Thus, it can safely be said that this peak frequency is dependent on the Re_T and Q_S/Q_T.

From the results in sections S_3 and S_7, as well as section S_5 (which is not shown here), the mean frequency is 6.1 Hz and the standard deviation of the frequency is approximately 0.10 Hz. The bias limit cannot be estimated because it is basically considered that the flow within the side-branch in the right-angle branch is steady state in motion. Therefore, the uncertainty of the frequency is 0.10 Hz for the typical condition of Re=800, $Q_S/Q_T = 0.50$, and $R_S = 7$ mm as shown in Fig. 8.

3.3 Effect of Flow Division Ratio on Strouhal Number Figure 9 shows St_T versus Re_T for the flow conditions in the trunk. Figure 9 indicates that when the St and Re numbers are based on the trunk conditions, the Strouhal number, St_T, depends on both the flow division ratio Q_S/Q_T and the Reynolds number Re_T. Figure 10 shows the relation of St versus Re defined by the variables of the side-branch. For $300 < Re < 900$, $St \cong 1$ is independent of Q_S/Q_T, and is weakly dependent on the Reynolds number Re.

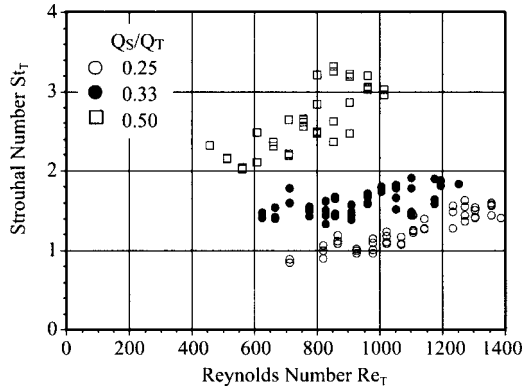

Fig. 9 Trunk Strouhal number, St_T, versus trunk Reynolds number, Re_T (R_S=7 mm)

3.4 Effect of Side-Branch Radius on Strouhal Number. To explain the independence of the Strouhal number St of the side-branch radius, measurements were also made for R_S=4, 5, 6, and 9 mm. For Re_T=800 and Q_S/Q_T=0.50, the power spectra are shown in Fig. 11. The figure clearly shows that the frequency depends on the side-branch radius. Figure 12 shows the relationship St vs. Re, and reveals that St is independent of Q_S/Q_T and R_S and is weakly dependent on the Reynolds number. As shown in Fig. 12, the mean value of St is 1.03, whereas the standard deviation (s.d.) is 0.26.

The uncertainties of the frequency with respect to the velocity oscillation in the side-branch and the velocity are 0.10 Hz and 0.0028 m/s, respectively. Using these uncertainties, in the typical condition of Re=800, Q_S/Q_T=0.50, and R_S=7 mm, the uncertainty of the Strouhal number St corresponds to 0.018 and 0.034 for the frequency and the velocity, respectively. Overall, the uncertainty of the Strouhal number is 0.052 for the Strouhal number St=1.03 under the typical conditions shown above.

3.5 Separation Flow and Universal Generality of Oscillation in the Side-Branch. Figure 8(*a*) shows that the periodic oscillation is generated along the separation region of the side-branch. In other words, the oscillation is generated along the zero axial isovelocity contour. The separation flow appears along the near wall in the side-branch, and two pairs of symmetrical vortices can be observed in section S_3, which includes the separation region. As can be inferred from the above, the mechanism of the secondary flow in section S_3 is quite complicated.

In Fig. 13, the upper semicircle indicates the secondary velocity in section S_3. In this section, which includes the separation region, one small vortex with low velocity manifests itself in the vicinity of the near wall. In addition to the above, another large high velocity vortex, which develops along the peripheral tube wall, is also manifested. As shown in Fig. 4, this secondary vortex coincides with the flow visualization in the configuration at section S_3. In section S_3, it is noted that two vortices rotate in the same direction. Strong shear flow is formed between these two secondary vortices. It is speculated that this strong secondary shear layer which runs in the opposite direction is likely to be quite unstable.

Furthermore, a strong axial shear layer between the separation flow moving helically in the reverse direction and the main flow moving along the distant wall is induced at the common median

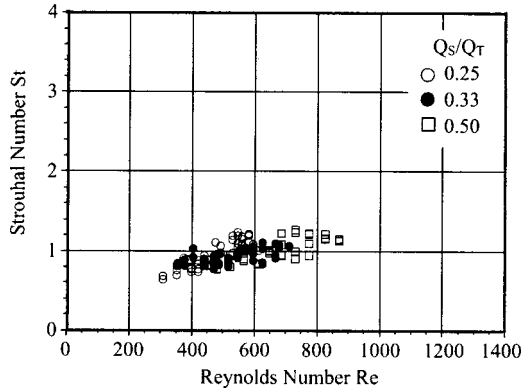

Fig. 10 Side-branch Strouhal number, St, versus side-branch Reynolds number, Re (R_S=7 mm)

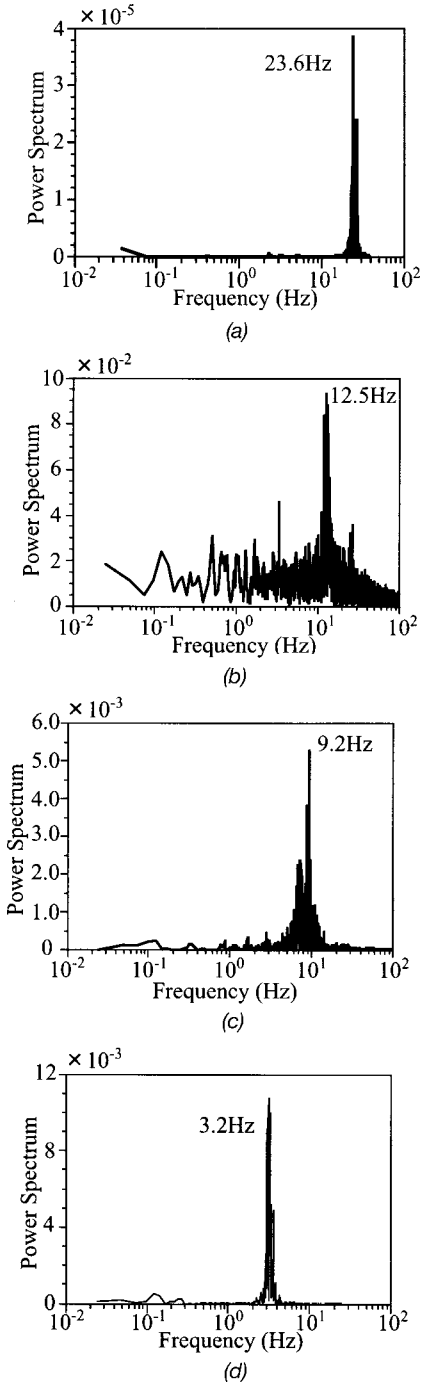

Fig. 11 Power spectrum of axial velocity along tube axis (Re_T=800, Q_S/Q_T=0.50). (*a*) R_S=4 mm, (*b*) R_S=5 mm, (*c*) R_S=6 mm, (*d*) R_S=9 mm.

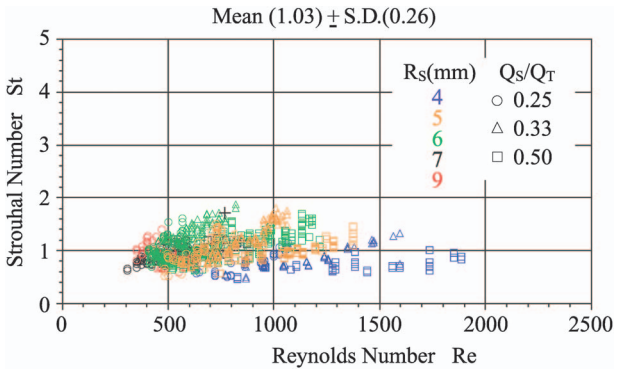

Fig. 12 Side-branch Strouhal number, St, versus side-branch Reynolds number Re for several radii of the side-branch

plane as shown in Fig. 3. Periodic oscillations are generated along both the strong secondary shear and the strong axial shear layers. It is speculated that the strong shear layer induced along both the axial separation flow and the secondary vortex in the side-branch might also be unstable, leading to the periodic oscillation observed along these strong shear layers.

As shown above, the Strouhal number St, which is independent of Q_S/Q_T and R_S, is weakly dependent on Re and the mean value of the Strouhal number is St≅1. Therefore, in the right-angle branch, the periodic oscillation induced in the side-branch exhibits a characteristic flow behavior, this periodic oscillation being a universally occurring phenomenon. It might be expected that the Strouhal number depends on the corner shape, the bifurcation angle, and the Reynolds number.

From the viewpoint of hemodynamics, it is possible that oscillations are generated in the arterial branch in the human body, although this would be dependent on the shape of corner of the entrance in the side-branch.

As for pipeline networks, the flow is turbulent for most applications; separation flow and periodic oscillations induced in the side-branch are likely to occur in these flows as well. In pipeline network and plant systems, such oscillations could lead to vibrations resulting in structural damage.

4 Conclusion

The variation of wall shear stress was characterized around the upstream corner. The change of wall shear stress around the upstream corner is comparable to that around the flow divider, and its magnitude is several times greater than that of the Poiseuille flow in the trunk. Basically, the steep change of wall shear stress in the vicinity of the upstream corner results from the flow deflection of core flow through the upstream trunk into the side-branch with the secondary flow. It is speculated that the drastic change of the wall shear stress is related to the erosion in the pipeline network where the flow state is in a turbulent state. The wall shear stress might also be expected to vary around the entrance corner of the arterial branch. This change of wall shear stress might affect the initiation and the development of vascular disease in human arteries.

The Strouhal number St in the side-branch is independent of both the flow division ratio Q_S/Q_T and the side-branch radius R_S, although the Strouhal number St is weakly dependent on the Reynolds number Re. The strong shear layer induced along both the axial separation flow and the secondary vortex in the side-branch is unstable, and a periodic oscillation results from this unstable region along the strong shear layers. This implies that the periodic oscillation induced in the side-branch is dependent only on the geometrical configuration of the right-angle branch and on the Reynolds number. Therefore, the periodic oscillation induced in the side-branch exhibits a characteristic flow behavior, which is a universally occurring phenomenon, in the right-angle branch having a square-edged corner at the entrance of the side-branch.

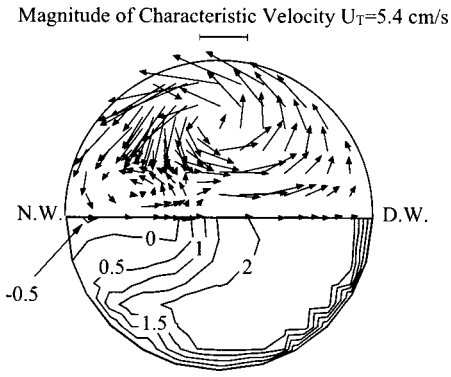

Fig. 13 Secondary velocity vectors (upper semicircle) and axial velocity contours (lower semicircle) in section S_3 in the side-branch (Re_T=800, Q_S/Q_T=0.50, R_S=7 mm)

Acknowledgments

This research was partially supported by the Japanese Ministry of Education, Science, Sports, and Culture, Grants-in-Aid for Science Research Nos. 09450083, 12650180, and 14550160. Furthermore, this research was supported by the Research Project "Fluid Mechanical and Biological Study for Clarification on Generation of Cardiovascular Disease and Medical Treatment" of Academic Frontier from the Japanese Ministry of Education, Science, Sports, and Culture.

Nomenclature

f = frequency of velocity oscillation
Q_S = flow rate through the side-branch
Q_T = flow rate through the trunk
Re = Reynolds number based on the variables of the side-branch, $=2R_SU_S/\nu$
Re_T = Reynolds number based on the variables of the trunk, $=2R_TU_T/\nu$
R_S = radius of the side-branch
R_T = radius of the trunk
St = Strouhal number based on the variables of the side-branch, $=2fR_S/U_S$
St_T = Strouhal number based on the variables of the trunk, $=2fR_T/U_T$
U_S = mean velocity in the side-branch
U_T = mean velocity in the trunk
u = velocity in the x direction
v = velocity in the y direction
ν = kinematic viscosity of the working fluid
ρ = density of the working fluid
τ_w = normalized wall shear stress

Subscripts

S = side-branch
T = trunk

References

[1] Oki, I., and Kawaguchi, T., 1951, "On the Losses of Head Due to Branch Pipes," Trans. Jpn. Soc. Mech. Eng., **17**(60), pp. 146–151 (in Japanese).
[2] Lighthill, M. J., 1972, "Physiological Fluid Dynamics," J. Fluid Mech., **52**, pp. 475–497.
[3] Houle, S., and Roach, M. R., 1981, "Flow Studies in a Rigid Model of an Aorta-Renal Junction: A Case for High Shear as a Cause of the Localization of Sudanophilic Lesions in Rabbits," Atherosclerosis, **40**, pp. 231–244.
[4] Yamaguchi, T., Hanai, S., Oyama, T., Mitsumata, M., and Yoshida, Y., 1986, "Effect of Blood Flow on the Localization of Fibrocellular Intimal Thickening and Atherosclerosis at the Young Human Abdominal Aorta-Inferior Mesenteric Artery Branching," Rece. Adv. Cardiovasc. Dis., **7**, pp. 97–108 (in Japanese).

[5] Yamamoto, T., Tanaka, H., Jones, C. J. H., Lever, M. J., Parker, K. H., Kimura, A., Hiramatsu, O., Ogasawara, Y., Tsujioka, K., Caro, C. C. G., and Kajiya, F., 1992, ''Blood Velocity Profiles in the Origin of the Canine Renal Artery and Their Relevance in the Localization and Development of Atherosclerosis,'' Arterioscler. Thromb., **12**, pp. 626–632.
[6] Yamaguchi, R., and Kohtoh, K., 1994, ''Sinusoidal Variation of Wall Shear Stress in Daughter Tube Through 45 Deg Branch Model in Laminar Flow,'' ASME J. Biomech. Eng., **116**, pp. 119–126.
[7] Karino, T., Kwong, H. H. M., and Goldsmith, H. L., 1979, ''Particle Flow Behavior in Models of Branching Vessels: I. Vortices in 90° T-Junctions,'' Biorheology, **16**, pp. 231–248.
[8] Liepsch, D., Poll, A., Strigberger, J., Sabbah, H. N., and Stein, P. D., 1989, ''Flow Visualization Studies in a Mold of the Normal Human Aorta and Renal Arteries,'' ASME J. Biomech. Eng., **111**, pp. 222–227.
[9] Hirose, T., Tanabe, A., and Tanishita, K., 1992, ''Fluid Flow and Wall Shear Stress Profiles in Model Branch of Abdominal Aorta,'' Biomechanism, **11**, pp. 99–109 (in Japanese).
[10] Perktold, K., and Peter, R., 1990, ''Numerical 3D-Simulation of Pulsatile Wall Shear Stress in an Arterial T-Bifurcation Model,'' J. Biomed. Eng., **12**, pp. 2–12.
[11] Yung, C. N., De Witt, K. J., and Keith, Jr., T. G., 1990, ''Three-Dimensional Steady Flow Through a Bifurcation,'' ASME J. Biomech. Eng., **112**, pp. 189–197.
[12] Kastner, W., and Riedle, K., 1986, ''Empirical Model for the Calculation of Material Losses due to Corrosion Erosion,'' VGB Kraftwerkstechnik, **66**(12), pp. 1023–1029.
[13] Yamaguchi, R., Mashima, T., and Takahashi, Y., 1997, ''Separated Secondary Flow and Wall Shear Stress in Side Branch of Right Angle Branch,'' ASME FEDSM'97, #3303.
[14] Yamaguchi, R., Shigeta, M., Kudo, S., and Hayase, T. Y., 2000, ''Wall Shear Stress and Periodical Oscillation Induced in Side Branch at Right Angle Branch in Laminar Steady Flow,'' ASME FEDSM'00, #11085.

Theoretical Analysis of Experimentally Observed Perplexing Calibration Characteristics of Ball-in-Vortex Flow-Meter

S. P. Mahulikar[1]
Faculty Member
A. von Humboldt Fellow
e-mail: spm@aero.iitb.ac.in

S. K. Sane
Faculty Member

Department of Aerospace Engineering, IIT Bombay, P.O. IIT Powai, Mumbai-400076, India
Fax: ++91 (0)22 2572-2602
Phone: ++91 (0)22 2576-7122

This investigation analyzes the calibration nonlinearity of the ball-in-vortex flow-meter, designed to work on the principle of a rotating sphere in and due to a vortex flow. The comparison of this flow-meter reading with the standard flow-meter indicates the existence of different calibration regimes, bifurcated by a sharp change in slope of the calibration curve. Based on the governing mechanics of this flow-meter, this paper explains this nonlinearity, and proposes its mathematical form. In particular, the bifurcation in calibration characteristics is attributed to the change in the surface contact frictional force, due to translation of the ball. The mathematical model captures the various calibration regimes associated with this translation, from one plane of rotation in the flow-meter to another, or from one periphery to another. Thus, calibration nonlinearity of this flow-meter can be fully comprehended through its governing mechanics, and harnessed for flow measurement. [DOI: 10.1115/1.1988342]

1 Introduction and Necessity

The need for development of instruments for the measurement of process variables is exponentially increasing, due to global industrialisation. Flow is one of the most important process variables; and by its accurate measurement, it is possible to check/monitor the system performance. Flow measurement serves as the basis in agriculture, ballistics, biomedical, combustion, explosion studies, heat transfer, hydraulics, and magneto-hydrodynamics.

1.1 Background and Literature Survey. Based on consideration of pressure drop through the flow-meter, the various flow-meters can be classified in to two types: (i) in which the flowing fluid comes in direct contact with the flow-meter, "contact type," e.g., orifice-meter and turbine-meter, hence, the flow-meter causes a pressure loss in flow; (ii) in which the flowing fluid does not come in direct contact with flow-meter, "noncontact type," e.g., ultrasonic-meter and electromagnetic flow-meter, hence, the flow-meter does not cause a pressure loss in flow. Various contact and noncontact flow-meters are used depending upon the application, cost, and accuracy. The principles of flow measurement and their classification are discussed, e.g., in [1]. An ideal flow-meter should have the following characteristics—coverage of a wide flow range, low initial and maintenance cost, should not be bulky, and should produce a low pressure-loss. In the contact-type of flow-meters, the rotary type flow-meters are popular due to their reasonable pressure drop performance; as compared to the pressure loss characteristics of other contact type flow-meters, e.g., orifice-meter (especially with high sensitivity). Amongst the rotary type, turbine type [2] and ball type [3] have the most superior pressure drop performance. Turbine-meters are extensively used, because they are well known, fully-understood, accurate, and cheap. However, turbine-meters do not maintain their original calibration over a long period, because their calibration changes gradually with wear or fouling of surface. Hence, if their accuracy is to be maintained, periodical recalibration is mandatory. Due to relatively greater bearing contact friction losses than fluid friction losses, the pressure-loss performance of turbine-meters suffers; especially for gas flow measurement. For fixed discharge and flow cross-sectional area, smaller sized turbine-meters have lesser fluid friction losses, due to reduced flow blockage and reduced interference with flow; but about the same bearing contact friction losses as the larger sized turbine-meters. Consequently, smaller-sized turbine-meters perform only marginally better than larger sized turbine-meters, with respect to pressure loss characteristics.

The ball-type flow-meter has been less popular in the flow community, mainly because its nonlinear calibration characteristics, especially for gas flows, have not been comprehended. The ball in Ball-in-Vortex-Flow-Meter (BiVFM) is a sphere in a decaying swirl flow; experiencing viscous driving force (and not viscous drag, as for a stationary sphere in a flow), surface contact frictional resistance, gravity, buoyancy, centrifugal, and Magnus lift [4,5] forces. The basic drag characteristics of a sphere are provided by Roshko [6]. Floberg [7] theoretically considered the case of a ball in a tube filled with liquid, and generalized it to apply to cases when a ball is in a moving liquid. It was shown that the rotational speed of the ball depends on the eccentricity, which was derived from equilibrium conditions of the ball. This theory was found to be concordant with experiments.

Kwok et al. [8] presented a momentum exchange analysis for a flow-meter comprised of a ball driven by swirling water flow in a thin chamber; their analytical model is based on flow visualization. The angular momentum accompanying water introduced in the vortex chamber (VC) was assumed to be used up to impart momentum to the fluid contained in the boundary layers. The inviscid core (ball) spinning in the middle of the chamber was considered to consume a negligible part of incoming momentum. Based on these assumptions, their analytical model predicted that for liquid flow, the frequency of revolution of the ball varies almost linearly with discharge, i.e., linear calibration of their BiVFM, for liquid flow measurement. Further, the frequency of rotation of the contained ball was shown to depend mainly on the mass of the ball. Komarov et al. [9] reported design procedures

[1]Corresponding author.

Contributed by the Fluids Engineering Division for publication in the JOURNAL OF FLUIDS ENGINEERING. Manuscript received by the Fluids Engineering Division, March 2, 2004. Final revision May 5, 2005. Associate Editor: Sivaram Gogineni.

adopted during construction of ball flow-meters for tachometric industrial instruments, to optimize shapes of the block containing the balls. Bourrier et al. [10] described the "pop-off" effect of a light ball in water, starting from acceleration from rest of a buoyant sphere rising freely in water. The acceleration included a contribution due to the flow of the fluid induced by the motion of the sphere. Ivanov and Zolotarevskii [11] reported a tachometric flow-meter with hydrodynamic suspension of ball rotors, for the measurement of water flow, at temperatures up to 285 °C, in the discharge (Q) range 8–50 m^3/h. They analyzed its operation by considering forces acting on the ball rotors under hydrodynamic suspension. Arenas et al. [12] designed and constructed a laboratory instrument for measuring small flows (3–100 ml/s) of transparent fluids. As the fluid passes, a polypropylene ball inside the polystyrene housing moves. The housing entrance and exit are arranged in such a way that the direction of flow favors the rotation of the ball in one particular way, and the greatest range of measurement is obtained. An infrared reflective opto-switch, mounted perpendicular to the housing is activated by this ball. At each passage of the ball, the sensor sends a pulse that is amplified and raised to logical levels by a trigger, whose output is connected to a block counter-decoder. Kurose and Komori [13] estimated the effect of rotational speed of sphere on the drag and lift forces. Their results showed that the drag force on a rotating sphere in a uniform unsheared flow increases with increasing rotational speed. They also found that the lift force on a rotating sphere in a uniform unsheared flow, acts in the same direction, and is independent of particle Reynolds number (Re).

An inherent disadvantage of BiVFM especially for measuring gas flows, is its calibration nonlinearity, which is hitherto neither captured by an appropriate analytical model, nor explained physically. The BiVFM can be best utilized, if its calibration nonlinearity is comprehended by theoretical model that captures the governing mechanics of motion of the moving ball in the fluid.

1.2 Objectives and Scope. Based on the survey, it is concluded that there is a lack of reported literature on the performance of a spinning and translating sphere in a vortex flow of gas. In this paper, experimental data on BiVFM is generated with the objective of comprehending the calibration nonlinearity. The calibration model is derived from basic force balance equations, and superimposed over the experimental data.

2 Experimental Setup of BiVFM and Calibration of Bell-Mouth

In the BiVFM (Shonin et al. [14]), whole or part of the gas flow in a duct is admitted through a number of tangentially located holes, ports or passages, at one end of an annular VC, with properly shaped center body (Fig. 1). The outlet is at the other end of this chamber, from which, the flow exits to the duct outlet.

2.1 BiVFM Operation. A ball made of suitable material, size, and weight, is placed inside the VC. Due to tangential fluid motion, the ball experiences a rolling motion in the flow. The frequency of rotation of the ball in VC is calibrated, to provide a measure of discharge. This rotational speed of the ball can be measured using an optical sensor (like stroboscope), or by a pickup coil, if the ball is ferromagnetic. Hence, this flow-meter can also be calibrated while in service. The other advantages of this flow-meter include its simplicity in design, elimination of bearings (unlike turbine-meter), ease of fabrication, low cost, less fouling of the device, and its applicability for measurement of flow rates of abrasive fluids. Most importantly, this device produces one of the lowest pressure-loss amongst contact flow-meters, mainly because fluid friction losses associated with flow blockage and flow interference effects due to the device, is one of the least.

2.2 Experimental Setup. The model of BiVFM used for experimentation has a volute casing and six tangential ports in the form of aerofoils (Fig. 2). The VC and tangential ports of BiVFM are made of teakwood, and BiVFM casing is made of marine plywood. The BiVFM has a circular sleeve as its center body (around which the ball rotates), made of mild-steel, which allows the working fluid to be discharged downward; and a commercially available table tennis ball (of diameter, $D=37$ mm, and mass, $m_b=2.4$ gm) rolls about the circular sleeve. The circularity and eccentricity of the annular spacing in which the ball rotates, are confirmed as well within the acceptable limits for the experimentation. The VC is covered with a lid of Perspex sheet, and the rotational speed of the ball is measured by a photoelectric sensor. A bell-mouth, made of marine plywood, is at the flow inlet (upstream of BiVFM entrance). A bent duct with appropriate inner and outer radius of curvature to minimise the loss, and also made of marine plywood, connects the axial discharge from BiVFM model outlet to a suction blower. By changing the blower speed, the suction pressure (measured at the bell-mouth) and hence the discharge to the VC, is varied. The straight pipe connecting bell-mouth and BiVFM, is of mild-steel. Figure 3 shows the schematic layout of the experimental setup.

2.3 Bell-Mouth Calibration. The bell-mouth (due to its specially designed shape) has the highest discharge coefficient, C_d, in contact type flow-meters. Before investigating the calibration characteristics of BiVFM, the bell-mouth is calibrated against standard pitot tube and Hot Wire Anemometer (HWA). The pitot tube has diameter, ϕ 4 mm, and the bell-mouth exit plane has ϕ 12 cm: the ratio of these diameters is, 1:30. Hence, the blockage effect due to the pitot tube is small and acceptable.

While calibrating bell-mouth against HWA and pitot tube, the bell-mouth exit plane is divided into 16 concentric rings; and the pitot tube is traversed along the radius. The wall static gauge pressure at these different radial locations is measured in mm of water using micromanometer, and converted in to mean axial flow velocity at the radial location; using incompressible Bernoulli's equation. The Q thus obtained for each ring is added to give the total Q, which is the theoretical discharge, Q_{th}. The cross-sectional area of the bell-mouth exit plane, A_{ex}, is calculated from the mean diameter of the pipe; which is obtained as the arithmetic mean of measurements of the four diameters of the cross section at approximately equal angle of 90 deg to each other. From HWA reading of mean flow velocity at the bell-mouth exit plane (V_{ex}), the actual discharge is obtained ($Q_{\text{act}}=A_{\text{ex}}\cdot V_{\text{ex}}$). Thus, C_d ($=Q_{\text{act}}/Q_{\text{th}}$), is obtained for each velocity. Six readings for C_d are taken by changing the suction pressure at the pipe exit. For each velocity, Re is obtained, and a graph of C_d versus Re is plotted (Fig. 4).

As seen from Fig. 4, C_d for the bell-mouth is close to unity over the range of operation, and its uncertainty is insignificant: $U(C_d)=0.0279$ (with respect to unity). Hence, C_d (=1) is practically independent of Re (and hence, an independent variable); thereby justifying the use of bell-mouth as datum. The slight decrease in C_d with increasing Re that results in $U(C_d)$, is due to increasing losses resulting from flow separation; which also increases the blockage effect due to the pitot-tube.

3 Theoretical Analysis of Mechanics of BiVFM

Figure 5 shows the free body diagram of the ball in BiVFM, which has a tangential flow velocity, V_t, along positive Y-direction (Y-axis in direction of tangential motion of ball), and X-axis passes through the radius of rotation of the ball. The F_c is centrifugal force acting on the rotating ball, $F_{f,1}$ is the surface contact frictional force on the ball from lower surface of BiVFM, and $F_{f,s}$ is the surface contact frictional force on the ball from the peripheral surface of BiVFM. The ball rotates about the axis in clockwise direction when viewed along the Z-axis (axis parallel to axis of rotation of ball). The $R_{\text{rot},o}$ is radius of rotation when the ball is

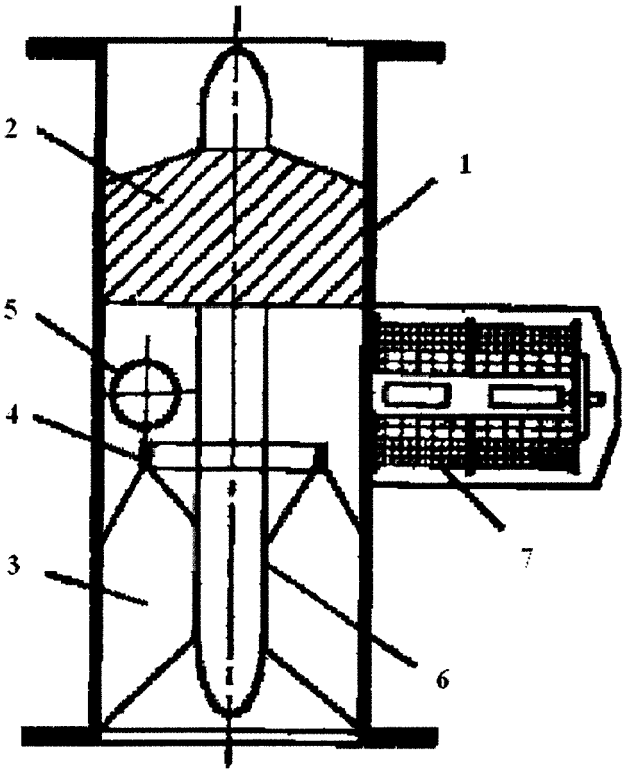

1 – housing (length of pipe fitted with flanges at its ends, for attachment in flow line)

2 – stationary assembly made of flow guide

3 – multi-thread screw or helix, and flow straightener

4 – race ring (mounted by spider of flow straightener)

5 – ball (free to revolve in annulus formed by race ring and flow guide)

6 – hub

7 – ball rpm pickup

Fig. 1 Schematic of typical ball-in-vortex flowmeter [3]

rubbing against the outer peripheral wall of BiVFM. The tangential driving force, F_{dr}, for the motion of the ball, is due to viscous fluid flow, and is given as,

$$F_{dr} = (1/2)\rho_f \cdot S \cdot C_D \cdot (V_t - R_{rot,o} \cdot \omega_{rot})^2, \quad (1)$$

where, ρ_f is density of air in flow-meter, S is reference area of the ball for drag estimation, C_D is drag coefficient of the ball, and ω_{rot} is rotation angular velocity of ball about vortex axis; and $V_t > R_{rot,o} \cdot \omega_{rot}$. Equation (1) states that the viscous driving force, is due to the difference in the tangential velocities of the flow, V_t, and the ball ($=R_{rot,o} \cdot \omega_{rot}$). The maximum tangential velocity of the ball is the same as, V_t, in which case, there is no driving force and pressure loss. For the practical case, "F_{dr}" is necessary to

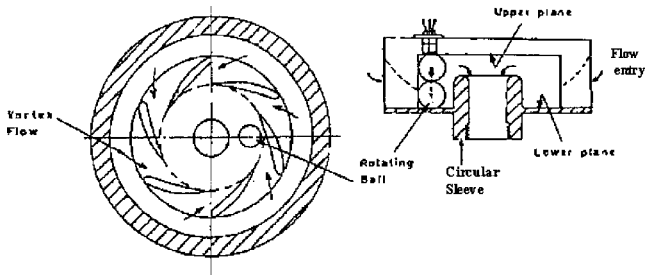

Fig. 2 Schematic sketch illustrating operation of BiVFM

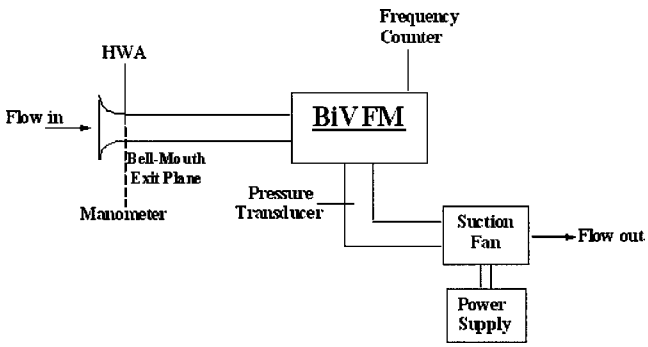

Fig. 3 Block diagram of experimental rig

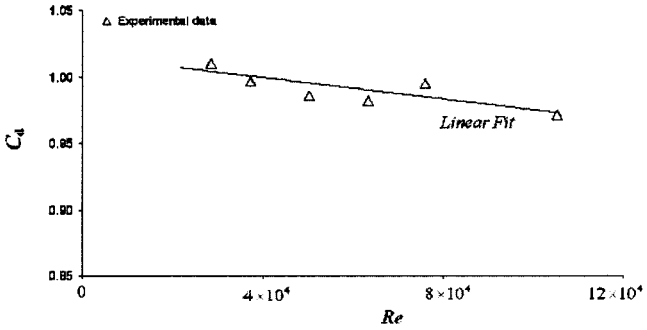

Fig. 4 Plot of C_d versus Re, for the bell-mouth

balance the surface and viscous friction forces; hence, the friction losses are embedded in F_{dr}, and manifests as a difference in the tangential velocities of flow and ball.

3.1 Analysis of Governing Mechanics of BiVFM. As illustrated in Fig. 2, the ball can rub against the lower or upper planes of BiVFM, placed horizontally; at low velocities, the ball rubs against the lower plane. Due to friction, the ball spins about its own axis (through its center) in a clockwise sense and in a vertical plane, as illustrated in Fig. 5. The spin angular velocity (in vertical plane), $\omega_{\mathrm{sp},v}$, is related to the rotational velocity as (assuming no slip),

$$\omega_{\mathrm{sp},v} = (R_{\mathrm{rot}}/R_b) \cdot \omega_{\mathrm{rot}}, \tag{2}$$

where, R_b is radius of the ball. Equation (2) is obtained by equating the distances traversed in spin and rotation for a given time, assuming no slip. For $\omega_{\mathrm{sp},v}$, the point of contact is at a distance, R_{rot}, from axis of rotation. The spinning ball in fluid flow experiences Magnus lift force (in vertical direction) [4,5] given as,

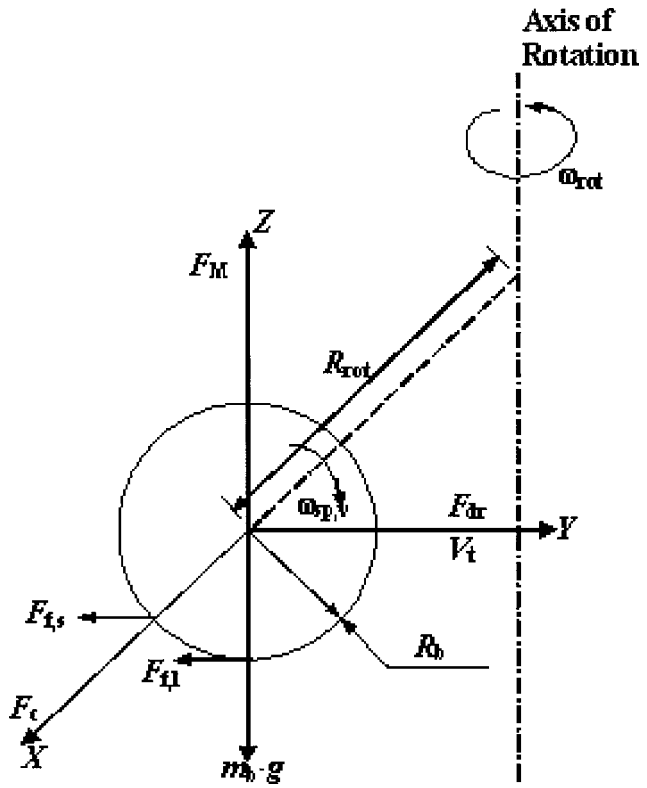

Fig. 5 Free body diagram of moving ball in BiVFM

$$F_{M,v} = \rho_f \cdot \Omega_b \cdot (V_t \times \omega_{\mathrm{sp},v}), \tag{3}$$

where, Ω_b is volume of the ball; from Eq. (2), $F_{M,v} = \rho_f \cdot \Omega_b \cdot (R_{\mathrm{rot}}/R_b) \cdot V_t \omega_{\mathrm{rot}}$. For the spinning ball in Fig. 5, this Magnus lift force acts vertically upward (as per the right hand screw rule), when the ball spins rubbing against the lower plane. The ball lifts-up when the sum of Magnus force and buoyancy force equals the weight. Thus, the dimensionless criterion for vertical lift-off ($\Pi_{v,\mathrm{LO}}$) is given as, $\Pi_{v,\mathrm{LO}} > 1$, where,

$$\Pi_{v,\mathrm{LO}} = (F_{M,v} + \rho_f \cdot \Omega_b \cdot g)/(m_b \cdot g), \tag{4}$$

where, g is acceleration due to gravity (=9.806 m/s^2). Equation (4) reduces to,

$$\Pi_{v,\mathrm{LO}} = (\rho_f \cdot \Omega_b/m_b) \cdot [(R_{\mathrm{rot}}/R_b) \cdot (V_t \omega_{\mathrm{rot}}/g) + 1]. \tag{4.1}$$

When the ball encounters the upper plane, it rubs against its surface, and spins in the anticlockwise, $-\hat{i}$, sense (Fig. 5). The Magnus force is now in the direction of gravity; hence, the ball is not in equilibrium rubbing against the upper plane, since the upward buoyancy force is insufficient to balance the total of weight and the Magnus force. Thus, the ball oscillates between the upper and lower planes, i.e., in a vertical plane, which is experimentally observed. During these oscillations, the resistance to motion is in periodic impacts.

Due to the centrifugal force, the ball also rubs against the peripheral wall of BiVFM, because of which, the ball spins in a horizontal plane in a clockwise sense as seen from the top, i.e., this axis of spin is in the $-\hat{k}$ direction (Fig. 5). This spin velocity in horizontal plane, $\omega_{\mathrm{sp},h}$, is given as,

$$\omega_{\mathrm{sp},h} = [1 + (R_{\mathrm{rot}}/R_b)] \cdot \omega_{\mathrm{rot}}. \tag{5}$$

The resulting Magnus force is in $-\hat{i}$ (radially inward) direction, i.e., opposite to the direction of the centrifugal force, and is given as,

$$F_{M,h} = \rho_f \cdot \Omega_b \cdot (V_t \times \omega_{\mathrm{sp},h}). \tag{6}$$

From Eq. (5), $F_{M,h} = \rho_f \cdot \Omega_b \cdot [1 + (R_{\mathrm{rot}}/R_b)] \cdot V_t \omega_{\mathrm{rot}}$. Hence, the ball spins rubbing against the outer periphery, so long as this radially inward Magnus force is lower than the centrifugal force. The dimensionless criterion for this horizontal detachment from the outer peripheral plane is given as, $\Pi_{h,\mathrm{PD}} > 1$, where,

$$\Pi_{h,\mathrm{PD}} = [F_{M,h}/(m_b \cdot R_{\mathrm{rot}} \cdot \omega_{\mathrm{rot}}^2)] = \{\rho_f \cdot \Omega_b \cdot V_t/(m_b \cdot \omega_{\mathrm{rot}})\} \cdot [(1/R_{\mathrm{rot}}) + (1/R_b)]. \tag{7}$$

When, $\Pi_{h,\mathrm{PD}} > 1$, is satisfied, the ball moves towards the inner periphery, and attempts to rub against the inner peripheral wall. Upon rubbing against this wall, the spin velocity is in an anticlockwise sense when viewed from top, i.e., the spin axis is in the $+\hat{k}$ direction (Fig. 5). The resulting Magnus force is in the $+\hat{i}$ (radially outward) direction, i.e., in the direction of the centrifugal force. Thus, the ball is not in equilibrium rubbing against the inner peripheral wall of the device, and it oscillates between the inner and outer peripheral walls, i.e., in a horizontal plane. These radial oscillations have also been experimentally observed in conjunction with the vertical oscillations. From Eqs. (2), (3), (5), and (6), $(F_{M,h}/F_{M,v}) = (\omega_{\mathrm{sp},h}/\omega_{\mathrm{sp},v}) = (R_b/R_{\mathrm{rot}}) + 1$. Hence, for fixed V_t and ω_{rot}, $F_{M,h} > F_{M,v}$.

To obtain the condition deciding whether the ball first translates vertically or radially, the condition, $\Pi_{v,\mathrm{LO}} = 1$, is substituted in Eq. (7). From Eq. (4.1), when $\Pi_{v,\mathrm{LO}} = 1$,

$$[m_b/(\rho_f \cdot \Omega_b)] = (R_{\mathrm{rot}}/R_b) \cdot (V_{t,\Pi_{v,\mathrm{LO}}=1} \cdot \omega_{\mathrm{rot},\Pi_{v,\mathrm{LO}}=1}/g) + 1. \tag{8}$$

From Eqs. (7) and (8), this dimensionless criterion is given as,

$$\Pi_{h,\mathrm{PD},\Pi_{v,\mathrm{LO}=1}} = [(V_t/\omega_{\mathrm{rot}})_{\Pi_{v,\mathrm{LO}=1}}/R_{\mathrm{rot}}] \cdot \{1 + (R_b/R_{\mathrm{rot}})/[(V_t \cdot \omega_{\mathrm{rot}})_{\Pi_{v,\mathrm{LO}=1}}/g] + (R_b/R_{\mathrm{rot}})\};$$

where $\Pi_{h,\mathrm{PD},\Pi_{v,\mathrm{LO}=1}}$, $V_{t,\Pi_{v,\mathrm{LO}=1}}$, and $\omega_{\mathrm{rot},\Pi_{v,\mathrm{LO}=1}}$, are the values of $\Pi_{h,\mathrm{PD}}$, V_t, and ω_{rot}, respectively, when $\Pi_{v,\mathrm{LO}}=1$. Thus, if $\Pi_{h,\mathrm{PD},\Pi_{v,\mathrm{LO}=1}}>1$, then radial translation of the ball occurs before vertical translation, and if $\Pi_{h,\mathrm{PD},\Pi_{v,\mathrm{LO}=1}}<1$, radial translation of the ball occurs after vertical translation.

The above analysis illustrates that the calibration of rotation of the ball (ω_{rot}) with the flow (V_t), changes depending upon the regimes dictated by $\Pi_{v,\mathrm{LO}}$ and $\Pi_{h,\mathrm{PD}}$. Consider the case when, $\Pi_{v,\mathrm{LO}}<1$, and $\Pi_{h,\mathrm{PD}}<1$, which is the case for low values of V_t. The resistance to motion due to surface contact friction, F_{res}, is given as

$$F_{\mathrm{res}} = \mu \cdot \{m_b \cdot (g + R_{\mathrm{rot}} \cdot \omega_{\mathrm{rot}}^2) - \rho_f \cdot \Omega_b \cdot (V_t \cdot \omega_{\mathrm{rot}} \cdot [(2R_{\mathrm{rot}}/R_b) + 1] - g)\}, \quad (9)$$

where, μ is the coefficient of dynamic friction between ball and surfaces of flow-meter. As seen from Eq. (9), the weight of the ball and the centrifugal force add to the normal force exerted by the surface on the ball, and the buoyancy and Magnus forces in the vertically upward and radially inward directions, respectively, relieve the normal force exerted by the surface on the ball. The calibration form is now obtained by force equilibrium, which was also the approach of Floberg [7], for obtaining the rotational speed of a ball in a moving liquid. The force equilibrium is obtained by equating the viscous driving force given by Eq. (1), with the frictional resistance given by Eq. (9) as, $(\frac{1}{2})\rho_f \cdot S \cdot C_D \cdot (V_t - R_{\mathrm{rot}} \cdot \omega_{\mathrm{rot}})^2 = \mu \cdot \{m_b \cdot (g + R_{\mathrm{rot}} \cdot \omega_{\mathrm{rot}}^2) - \rho_f \cdot \Omega_b \cdot (V_t \cdot \omega_{\mathrm{rot}} \cdot [(2R_{\mathrm{rot}}/R_b) + 1)] - g)\}$, which is simplified as,

$$V_t^2 = R_{\mathrm{rot}} \cdot [2\mu \cdot m_b/(\rho_f \cdot S \cdot C_D) - R_{\mathrm{rot}}] \cdot \omega_{\mathrm{rot}}^2 + 2\{R_{\mathrm{rot}} - [(2R_{\mathrm{rot}} + R_b) \cdot \mu \cdot \Omega_b]/(S \cdot C_D \cdot R_b)\} \cdot V_t \cdot \omega_{\mathrm{rot}} + [2\mu \cdot (m_b + \rho_f \cdot \Omega_b) \cdot g]/(\rho_f \cdot S \cdot C_D). \quad (10)$$

The dependent variable is the flow velocity, V_t, and the independent variable is, ω_{rot} (which is measured). Hence, the objective is to calibrate BiVFM, so that measurement of ω_{rot} yields V_t. As evident from Eq. (10), even for low values of V_t, the calibration is nonlinear, which could not be predicted by the theoretical model of Kwok et al. [8]. Further, the above theoretical analysis reveals that the frequency of rotation of the contained ball depends not just on the mass of the ball (m_b) as reported by Kwok et al. [8], but also on several other geometric and flow parameters that appear in Eq. (10).

When the ball lifts-up, $\Pi_{v,\mathrm{LO}}>1$, and Eq. (10) cannot be used for calibration. When the ball rubs against the upper plane, prior to the spin velocity changing its sign due to surface contact friction, the roles of weight, buoyancy, and Magnus forces in determining surface contact friction, change. The vertically upward buoyancy and Magnus forces now add to the surface contact friction, and the weight reduces the friction. The role of radial Magnus force in determining friction remains unchanged. Hence, the force balance equation reduces to

$$(\tfrac{1}{2})\rho_f \cdot S \cdot C_D \cdot (V_t - R_{\mathrm{rot}} \cdot \omega_{\mathrm{rot}})^2 = \mu \cdot \{m_b \cdot (R_{\mathrm{rot}} \cdot \omega_{\mathrm{rot}}^2 - g) + \rho_f \cdot \Omega_b \cdot (g - V_t \cdot \omega_{\mathrm{rot}})\},$$

which is simplified as,

$$V_t^2 = R_{\mathrm{rot}} \cdot [2\mu \cdot m_b/(\rho_f \cdot S \cdot C_D) - R_{\mathrm{rot}}] \cdot \omega_{\mathrm{rot}}^2 + 2[R_{\mathrm{rot}} - \mu \cdot \Omega_b/(S \cdot C_D)] \cdot V_t \cdot \omega_{\mathrm{rot}} + 2\mu \cdot g/(\rho_f \cdot S \cdot C_D) \cdot [\Omega_b - (m_b/\rho_f)]. \quad (11)$$

Comparing Eqs. (10) and (11), it is seen that their forms are exactly identical, but they differ in their coefficients. When the spin direction changes due to friction on the upper plane, the Magnus force acts downward, and the ball moves from the upper plane and hits the lower plane. It continues rubbing against the lower plane until its spin direction changes, and while rubbing on the lower plane, the force balance is given as

$$(\tfrac{1}{2})\rho_f \cdot S \cdot C_D \cdot (V_t - R_{\mathrm{rot}} \cdot \omega_{\mathrm{rot}})^2 = \mu \cdot \{m_b \cdot (g + R_{\mathrm{rot}} \cdot \omega_{\mathrm{rot}}^2) - \rho_f \cdot \Omega_b \cdot (V_t \cdot \omega_{\mathrm{rot}} + g)\},$$

which is simplified as,

$$V_t^2 = R_{\mathrm{rot}} \cdot [2\mu \cdot m_b/(\rho_f \cdot S \cdot C_D) - R_{\mathrm{rot}}] \cdot \omega_{\mathrm{rot}}^2 + 2[R_{\mathrm{rot}} - \mu \cdot \Omega/(S \cdot C_D)] \cdot V_t \cdot \omega_{\mathrm{rot}} + [2\mu \cdot g/(S \cdot C_D)][(m_b/\rho_f) - \Omega_b]. \quad (12)$$

Comparing Eqs. (11) and (12), it is seen that there is a change, only in the sign of the constant term. Now, consider that $\Pi_{h,\mathrm{PD}}>1$, is satisfied, and the ball moves radially inward, and the radius of rotation changes to R'_{rot} ($R'_{\mathrm{rot}}<R_{\mathrm{rot}}$). When the ball rubs against the inner peripheral wall of BiVFM and the lower plane, the force equilibrium is given as,

$$(\tfrac{1}{2})\rho_f \cdot S \cdot C_D \cdot (V_t - R'_{\mathrm{rot}} \cdot \omega_{\mathrm{rot}})^2 = \mu \cdot \{m_b \cdot (g - R'_{\mathrm{rot}} \cdot \omega_{\mathrm{rot}}^2) + \rho_f \cdot \Omega_b \cdot [V_t \cdot \omega_{\mathrm{rot}} \cdot (1 - 2R'_{\mathrm{rot}}/R_b) - g]\},$$

which is simplified as,

$$V_t^2 = -R'_{\mathrm{rot}} \cdot [2\mu \cdot m_b/(\rho_f \cdot S \cdot C_D) + R'_{\mathrm{rot}}] \cdot \omega_{\mathrm{rot}}^2 + 2\{\mu \cdot \Omega/(S \cdot C_D) + [1 - 2\mu \cdot \Omega/(S \cdot C_D \cdot R_b)] \cdot R'_{\mathrm{rot}}\} \cdot V_t \cdot \omega_{\mathrm{rot}} + [2\mu \cdot g/(S \cdot C_D)] \times [(m_b/\rho_f) - \Omega_b]. \quad (13)$$

In all the calibration forms given by Eqs. (10)–(13), ω_{rot} depends on the radius of rotation, for given V_t. This observation is in agreement with Floberg [7], who reported that the rotational speed of the ball is a function of eccentricity, for the case of a ball in a moving liquid in a tube. Comparing Eqs. (10)–(13), the universal calibration form for BiVFM is categorized as,

$$V_t^2 = a_1 \cdot \omega_{\mathrm{rot}}^2 + a_2 \cdot V_t \cdot \omega_{\mathrm{rot}} + a_3, \quad (14)$$

where, a_1, a_2, and a_3, are dimensional coefficients. Thus, calibration forms for different regimes dictated by $\Pi_{v,\mathrm{LO}}$ and $\Pi_{h,\mathrm{PD}}$ are obtained by changing the coefficients in Eq. (14). These coefficients are obtained from a regression analysis of error between mathematical calibration form and experimental data.

4 Analysis of Experimental Data for Calibration

The theoretical calibration form arrived at, is now validated using experimental data. Figures 6(*a*) and 6(*b*) show the nonlinear experimental data, for calibration of BiVFM, where, $Q_{\mathrm{act}} \propto V_t$, and the calibrated discharge, $Q_{\mathrm{cal}} \propto \omega_{\mathrm{rot}}$. Hence, Eq. (14) can be rewritten as,

$$Q_{\mathrm{act}}^2 = a_1 \cdot Q_{\mathrm{cal}}^2 + a_2 \cdot Q_{\mathrm{act}} \cdot Q_{\mathrm{cal}} + a_3, \quad (15)$$

where, the coefficients, a_1, a_2, and a_3, in Eqs. (14) and (15), are identical in form, but differ by a constant. The change in the rotation plane (when $\Pi_{v,\mathrm{LO}}>1$), segregates the data in two sets, I and II. The data point of change of rotation plane is common to both sets. The coefficients, a_1, a_2, and a_3, for the two sets are obtained by minimizing the square of the calibration error, ε^2, obtained from Eq. (15) as,

$$\varepsilon^2 = \sum_{i=1}^{N_d} (a_1 \cdot Q_{\mathrm{cal},i}^2 + a_2 \cdot Q_{\mathrm{act},i} \cdot Q_{\mathrm{cal},i} + a_3 - Q_{\mathrm{act},i}^2)^2, \quad (16)$$

where, i is the ith experimental data point, and N_d is the number of experimental data points. By differentiating Eq. (16) with respect to the three coefficients, and equating them to zero, the following three linear simultaneous equations are obtained:

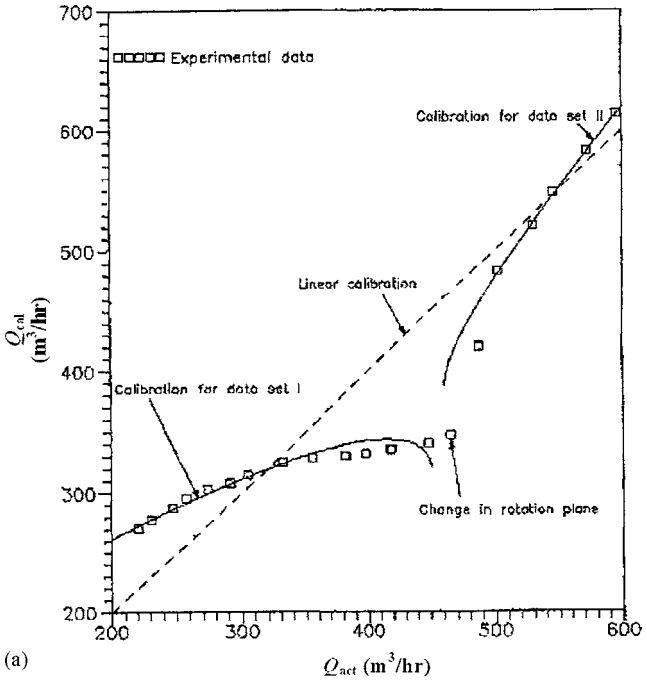

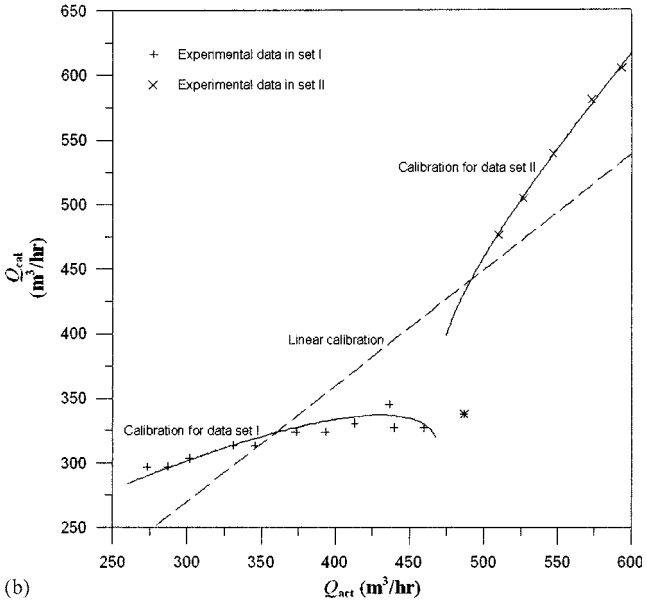

Fig. 6 Illustration of BiVFM calibration based on theoretical analysis. (*a*) Calibration for observation set No. 1. (*b*) Calibration for observation set No. 2.

$$\left(\sum_{i=1}^{N_d} Q_{\mathrm{cal},i}^4\right)\cdot a_1+\left(\sum_{i=1}^{N_d} Q_{\mathrm{act},i}\cdot Q_{\mathrm{cal},i}^3\right)\cdot a_2+\left(\sum_{i=1}^{N_d} Q_{\mathrm{cal},i}^2\right)\cdot a_3 = \left(\sum_{i=1}^{N_d} Q_{\mathrm{act},i}^2\cdot Q_{\mathrm{cal},i}^2\right), \quad (16.1)$$

$$\left(\sum_{i=1}^{N_d} Q_{\mathrm{act},i}\cdot Q_{\mathrm{cal},i}^3\right)\cdot a_1+\left(\sum_{i=1}^{N_d} Q_{\mathrm{act},i}^2\cdot Q_{\mathrm{cal},i}^2\right)\cdot a_2 + \left(\sum_{i=1}^{N_d} Q_{\mathrm{act},i}\cdot Q_{\mathrm{cal},i}\right)\cdot a_3=\left(\sum_{i=1}^{N_d} Q_{\mathrm{act},i}^3 Q_{\mathrm{cal},i}\right), \quad (16.2)$$

and

$$\left(\sum_{i=1}^{N_d} Q_{\mathrm{cal},i}^2\right)\cdot a_1+\left(\sum_{i=1}^{N_d} Q_{\mathrm{act},i}\cdot Q_{\mathrm{cal},i}\right)\cdot a_2+N_d\cdot a_3=\left(\sum_{i=1}^{N_d} Q_{\mathrm{act},i}^2\right). \quad (16.3)$$

Equations (16.1)–(16.3) are solved for the two independent data sets in Figs. 6(*a*) and 6(*b*), and the nonlinear calibration results are summarized in Table 1. From Eqs. (10) and (11), $a_{1,\mathrm{I}}=a_{1,\mathrm{II}}$, which is validated from the experimental data in Table 1 ($a_{1,\mathrm{I}}\approx a_{1,\mathrm{II}}$). The negative value of this coefficient implies, $R_{\mathrm{rot}}>2\mu\cdot m_b/(\rho_f\cdot S\cdot C_D)$. Comparing the coefficient a_2 in Eqs. (10) and (11), it is seen that $a_{2,\mathrm{I}}<a_{2,\mathrm{II}}$, since, $[R_{\mathrm{rot}}-(2R_{\mathrm{rot}}+R_b)\cdot\mu\cdot\Omega_b/(S\cdot C_D\cdot R_b)]<[R_{\mathrm{rot}}-\mu\cdot\Omega_b/(S\cdot C_D)]$, which is also validated from the processed experimental data in Table 1.

The calibration curves for the two data sets in Figs. 6(*a*) and 6(*b*) are superimposed with the experimental data. These curves are obtained by solving the quadratic in Q_{cal} for a given Q_{act} in Eq. (15), and then determining the physically feasible root. The solutions are given as, $Q_{\mathrm{cal}}=(-a_2\cdot Q_{\mathrm{act}}\pm\sqrt{\Delta})/(2a_1)$, where the discriminant, $\Delta=(a_2\cdot Q_{\mathrm{act}})^2-4a_1\cdot(a_3-Q_{\mathrm{act}}^2)$. The values of Q_{cal} are thus determined for $\Delta>0$. It is noteworthy that $\Delta<0$ for both sets I and II, in the vicinity of the point of change of rotation plane, i.e., real solution does not exist, thereby indicating bifurcation of experimental data points. Table 1 gives the experimental data point ($Q_{\mathrm{act,bif}}$) that indicates the bifurcation of the two data sets, and the predicted bifurcation point based on $\Delta=0$. It is noteworthy that this bifurcation of experimental data is also predicted by the theory. This bifurcation leaves a narrow band for Q_{act}, 451–461 m^3/h in Fig. 6(*a*), and 470–475 m^3/h in Fig. 6(*b*), for which no real solution exists. Flow calibration points in such narrow band may be obtained by linear interpolation within this band.

To quantitatively compare this new calibration form with the otherwise used linear calibration (Kwok et al. [8]), the root mean square (rms) errors for the experimental data, δ, for both the linear and nonlinear calibration are obtained as,

$$\delta=\left[\sum_{i=1}^{N_d}\sqrt{(\omega_{\mathrm{rot}}-\omega_{\mathrm{rot},i})^2}\right]\Big/ N_d.$$

Both, linear and proposed nonlinear calibration curves are in Fig. 6, and the respective rms errors, δ_{lc} and δ_{nlc}, are in Table 1. Thus, using the proposed nonlinear calibration form, the rms error reduces to less than half of that for linear calibration.

In summary, as seen from Fig. 6 and Table 1, the proposed nonlinear calibration form fits well for most of the experimental data, except close to the point of change in rotation plane, which is primarily responsible for the rms error. Hence, away from such bifurcation points, the proposed calibration form works well and also explains the nonlinear calibration behaviour of BiVFM.

Table 1 Nonlinear calibration coefficients and calibration errors for experimental data

Fig. No.	Set	N_d	a_1	a_2	a_3	$Q_{\mathrm{act,bif}}$		δ_{lc} (m^3/h)	δ_{nlc} (m^3/h)
6(*a*)	I	14	−1.72209	2.410307	+31903.15	465.6	451.4	11.7	3.7
	II	7	−1.63189	2.737004	−31369.54	(Expt.)	(Predicted)		
6(*b*)	I	12	−1.940377	2.551445	+35581.98	486.7	469.9	12.6	5.6
	II	6	−2.071428	3.283491	−67055.48	(Expt.)	(Predicted)		

Table 2 Uncertainty in experimentally derived quantities

Quantity	A_{ex} (cm^2)	P_∞ (Pa)	ρ_∞ (kg/m^3)	V_{ex} (m/s)	C_d	Q_{act} (m^3/h)	$\dot{m}_{act}$ (g/s)
Value	113.1	99983	1.148	0.13–17.2	1	5.3–700	1.69–223.22
U (Quantity)	1.9	10	0.002	0.029–0.7	0.0279	1.19–36.0	0.379–11.5
%	1.6	0.01	0.16	22.0–4.0	2.79	22.0–5.0	22.0–5.0

5 Uncertainty Analysis of Experimental Data

This section presents details of uncertainty analysis of experimentally measured and derived quantities, obtained from an analysis of variance. The comparison of these uncertainties with the range of experimental observations is in Table 2.

5.1 Bell-Mouth Exit Cross-Sectional Area. The diameter of the bell-mouth exit is measured as, $D=12$ cm, where, $U(D)=1$ mm. Since, bell-mouth exit cross-sectional area, $A_{ex}=(\pi/4)\cdot D^2=113.1$ cm^2; $U(A_{ex})=\pi\cdot D\cdot U(D)/2=1.885$ cm^2 (1.67%).

5.2 Atmospheric Properties. The atmospheric pressure, P_∞, is measured in mm of water as, $P_\infty=10334$ mm$=99983$ Pa, where the uncertainty is, $U(P_\infty)=1$ mm of $H_2O=10$ Pa (0.01%); which is the same as the uncertainty in static pressure at bell-mouth exit $[U(P_{ex})]$. The ambient temperature, $T_\infty=30.5$ °C, was measured using an alcohol thermometer, whose least count, i.e., $U(T_\infty)=0.5$ °C (1.6%).

The ambient density, $\rho_\infty=P_\infty/(R_a\cdot T_\infty)=1.148$ kg/m^3 [where, R_a is gas constant for air (=287 J/kg K)], is a function of two measured variables, which have their uncertainties. Hence, uncertainty in ρ_∞ is obtained as, $U(\rho_\infty)=\{[(\partial\rho_\infty/\partial P_\infty)\cdot U(P_\infty)]^2+[(\partial\rho_\infty/\partial T_\infty)\cdot U(T_\infty)]^2\}^{1/2}$; where, $(\partial\rho_\infty/\partial P_\infty)=1/(R_a\cdot T_\infty)$, and $(\partial\rho_\infty/\partial T_\infty)=-P_\infty/(R_a\cdot T_\infty^2)$; based on which, $U(\rho_\infty)=0.0019$ kg/m^3 (0.17%).

5.3 Mass-Flow-Rate through Bell-Mouth. The bell-mouth exit velocity, V_{ex}, is obtained as,

$$V_{ex}=[2(P_\infty-P_{ex})/\rho_\infty]^{0.5}=[2R_a\cdot(P_\infty-P_{ex})\cdot T_\infty/P_\infty]^{0.5};$$

hence, the uncertainty is obtained as,

$$U(V_{ex})=\{[(\partial V_{ex}/\partial P_\infty)\cdot U(P_\infty)]^2+[(\partial V_{ex}/\partial P_{ex})\cdot U(P_{ex})]^2+[(\partial V_{ex}/\partial T_\infty)\cdot U(T_\infty)]^2\}^{1/2},$$

where,

$$(\partial V_{ex}/\partial P_\infty)=[P_{ex}/(\sqrt{2}P_\infty^2)]\cdot[R_a\cdot P_\infty\cdot T_\infty/(P_\infty-P_{ex})]^{0.5},$$

$$(\partial V_{ex}/\partial P_{ex})=-[2\rho_\infty\cdot(P_\infty-P_{ex})]^{-0.5},$$

and

$$(\partial V_{ex}/\partial T_\infty)=[R_a\cdot(P_\infty-P_{ex})/(2P_\infty\cdot T_\infty)]^{0.5}.$$

Since,

$$Q_{th}=A_{ex}\cdot V_{ex}=(\pi D^2/4)\cdot[2R_a\cdot T_\infty\cdot(P_\infty-P_{ex})/P_\infty]^{1/2},$$

$$U(Q_{th})=\{[(\partial Q_{th}/\partial P_\infty)\cdot U(P_\infty)]^2+[(\partial Q_{th}/\partial P_{ex})\cdot U(P_{ex})]^2+[(\partial Q_{th}/\partial T_\infty)\cdot U(T_\infty)]^2+[(\partial Q_{th}/\partial D)\cdot U(D)]^2\}^{1/2},$$

where,

$$(\partial Q_{th}/\partial P_\infty)=(\pi D^2/4)\cdot(P_{ex}/P_\infty)\cdot[2\rho_\infty\cdot(P_\infty-P_{ex})]^{-1/2},$$

$$(\partial Q_{th}/\partial P_{ex})=-(\pi D^2/4)\cdot[2\rho_\infty\cdot(P_\infty-P_{ex})]^{-0.5},$$

$$(\partial Q_{th}/\partial T_\infty)=(\pi D^2/4)\cdot[R_a\cdot(P_\infty-P_{ex})/(2P_\infty\cdot T_\infty)]^{1/2},$$

and

$$(\partial Q_{th}/\partial D)=\pi D\cdot[(P_\infty-P_{ex})/(2\rho_\infty)]^{1/2}.$$

Since,

$$Q_{act}=C_d\cdot Q_{th},$$

$$U(Q_{act})=\{[(\partial Q_{act}/\partial P_\infty)\cdot U(P_\infty)]^2+[(\partial Q_{act}/\partial P_{ex})\cdot U(P_{ex})]^2+[(\partial Q_{act}/\partial T_\infty)\cdot U(T_\infty)]^2+[(\partial Q_{act}/\partial D)\cdot U(D)]^2+[(\partial Q_{act}/\partial C_d)\cdot U(C_d)]^2\}^{1/2};$$

where,

$$(\partial Q_{act}/\partial P_\infty)=C_d\cdot(\partial Q_{th}/\partial P_\infty),$$

$$(\partial Q_{act}/\partial P_{ex})=C_d\cdot(\partial Q_{th}/\partial P_{ex}),$$

$$(\partial Q_{act}/\partial T_\infty)=C_d\cdot(\partial Q_{th}/\partial T_\infty),$$

$$(\partial Q_{act}/\partial D)=C_d\cdot(\partial Q_{th}/\partial D),$$

and

$$(\partial Q_{act}/\partial C_d)=Q_{th}.$$

Since, the actual mass flow rate through the device is given as,

$$\dot{m}_{act}=\rho_\infty\cdot Q_{act}=(\pi D^2/4)\cdot C_d\cdot[2(P_\infty-P_{ex})\cdot P_\infty/(R_a\cdot T_\infty)]^{0.5},$$

$$U(\dot{m}_{act})=\{[(\partial\dot{m}_{act}/\partial P_\infty)\cdot U(P_\infty)]^2+[(\partial\dot{m}_{act}/\partial P_{ex})\cdot U(P_{ex})]^2+[(\partial\dot{m}_{act}/\partial T_\infty)\cdot U(T_\infty)]^2+[(\partial\dot{m}_{act}/\partial D)\cdot U(D)]^2+[(\partial\dot{m}_{act}/\partial C_d)\cdot U(C_d)]^2\}^{1/2},$$

where,

$$(\partial\dot{m}_{act}/\partial P_\infty)=(\pi D^2/4)\cdot C_d\cdot(2P_\infty-P_{ex})/[2(P_\infty-P_{ex})\cdot P_\infty\cdot R_a\cdot T_\infty]^{0.5},$$

$$(\partial\dot{m}_{act}/\partial P_{ex})=-(\pi D^2/4)\cdot C_d\cdot\{\rho_\infty/[2(P_\infty-P_{ex})]\}^{0.5},$$

$$(\partial\dot{m}_{act}/\partial T_\infty)=-(\pi D^2/4)\cdot(C_d/T_\infty)\cdot[\rho_\infty\cdot(P_\infty-P_{ex})/2]^{0.5},$$

$$(\partial\dot{m}_{act}/\partial D)=\pi D\cdot C_d\cdot[\rho_\infty\cdot(P_\infty-P_{ex})/2]^{0.5},$$

and

$$(\partial\dot{m}_{act}/\partial C_d)=(\pi D^2/4)\cdot[2\rho_\infty\cdot(P_\infty-P_{ex})]^{0.5}.$$

5.4 Implication of Uncertainty Analysis. The uncertainties presented in Table 2 are objectively interpreted, considering the aim of theoretically understanding the experimentally observed qualitative calibration characteristics, and not final calibration of BiVFM. Hence, it is concluded that the uncertainties are insignificant over most of the experimental observation range: $200\ \text{m}^3/\text{h}\leqslant Q_{act}\leqslant 700\ \text{m}^3/\text{h}$ (Fig. 6), since placing the uncertainty band does not alter the qualitative trend. The high uncertainty values of ~22% in V_{ex}, Q_{act}, and $\dot{m}_{act}$ are at $\dot{m}_{act}=1.7$ g/s (=5.3 m^3/h, which is less than the lowest Q_{act} that matters, by a factor of 38); these uncertainties reduce as $\dot{m}_{act}$ increases.

6 Summary and Conclusions

(i) The nonlinear calibration characteristics of the Ball-in-Vortex Flow-Meter (BiVFM) is mainly due to the change

in the rotation plane of the ball, from horizontal to vertical, and/or the change in the peripheral bounding surface, from outer periphery to inner periphery. This translation of the ball alters the role played by its weight, Magnus lift, buoyancy and centrifugal forces, in determining surface contact friction.

(ii) The nonlinear calibration form for the different combinations of plane of rotation and peripheral bounding surface of BiVFM, is obtained by force equilibrium in the tangential direction of flow, and is given in form as, $Q_{act}^2 = a_1 \cdot Q_{cal}^2 + a_2 \cdot Q_{act} \cdot Q_{cal} + a_3$; where, Q_{act}, is the actual discharge, and Q_{cal}, is the discharge measured by BiVFM. The coefficients (a_1, a_2, a_3) take different values for the different data sets, demarked by bifurcation. These bifurcation points are determined by transition in plane of rotation of the ball, or transition in peripheral bounding surface.

(iii) The proposed nonlinear calibration qualitatively explains the calibration behavior of the flow-meter, and quantitatively justifies its incorporation over the earlier linear calibration. Since this flow-meter has significantly lower pressure loss as compared to other contact-type flow-meters, it can now be effectively used for accurate flow measurement, especially for gas flows, using the derived nonlinear calibration form.

(iv) In summary, this essentially theoretical investigation, demonstrates that the calibration nonlinearity of BiVFM, can be understood and harnessed for appropriate nonlinear calibration, from the governing mechanics of the flow-metering principle.

Acknowledgments

The authors thank the Industrial Research and Consultancy Centre, Indian Institute of Technology-Bombay, for the financial support provided through seed grant Project No. 00IR007. The authors thank the staff and students of their Propulsion Laboratory, for fabrication of the experimental rig and measurements. The authors are grateful to the A. von Humboldt Foundation—Germany, for the rich exposure to research.

References

[1] Arndt, R. A., 1983, "What do we Measure and Why?" in *Fluid Mechanics Measurements*, R. J. Goldstein, ed., Hemisphere, Washington.

[2] Lee, W. F. Z., Blakeslee, D. C., and White, R. V., 1982, "A Self-Correcting and Self-Checking Gas Turbine Meter," ASME J. Fluids Eng., **104**(2), pp. 143–149.

[3] Preobrazhensky, V. P., 1980, *Measurements and Instrumentation in Heat Engineering*, Mir, Moscow, Vol. 2, pp. 178–181.

[4] Barkla, H. M., and Auchterlonie, L. J., 1971, "The Magnus or Robins Effect on Rotating Spheres," J. Fluid Mech., **47**, pp. 437–447.

[5] Oesterle, B., and Dinh, T. B., 1998, "Experiments on the Lift of a Spinning Sphere in a Range of Intermediate Reynolds numbers," Exp. Fluids, **25**(1), pp. 16–22.

[6] Roshko, A., 1954, "On the Development of Turbulent Wakes from Vortex Streets," NACA Report No. 1191.

[7] Floberg, L., 1968, "On the Ball Flowmeter and the Ball Viscosimeter," Acta Polytech. Scand., Ser.ME, p. 28.

[8] Kwok, C. K., Lee, P. M., and Lin, S., 1975, "An Analytical Investigation of a Vortex Flowmeter," ISA Trans., **14**(2), pp. 167–171.

[9] Komarov, Y. A., Shonin, L. N., Veyalis, N. P., and Fomina, V. I., 1981, "Industrial Ball Flowmeters for General Use, of the Types 'Saturn' and SHRT," Prib. Sist. Upr., **6**, pp. 13–15.

[10] Bourrier, P., Guyon, E., and Jorre, J. P., 1984, "The 'Pop Off' Effect: Different Regimes of a Light Ball in Water," Eur. J. Phys., **5**(4), pp. 225–231.

[11] Ivanov, I. N., and Zolotarevskii, S. A., 1985, "Tachometric Flowmeter with Hydrodynamic Suspension of Ball Rotors," Prib. Sist. Upr., **12**, pp. 17–18.

[12] Arenas, A., Victoria, L., and Luna, T., 1989, "A Digital Circuit for Measuring Small Flows," Am. J. Phys., **57**(12), pp. 1153–1154.

[13] Kurose, R., and Komori, S., 1999, "Drag and Lift Forces on a Rotating Sphere in Laminar Shear Flows," J. Fluid Mech., **384**, pp. 183–206.

[14] Shonin, L. N., Konoplev, J. S., Komarov, J. A., Ivanov, I. N., Slin, M. D., Vevalis, N. P., and Karpinskaya, V. B., 1969, "Flowmeter," U.S. Patent No. 3 443 432 [Original USSR Patent No. 1 065 760].

Experimental Investigation and Modeling of Inertance Tubes

L. O. Schunk

G. F. Nellis[1]
e-mail: gfnellis@engr.wisc.edu
Phone: (608) 265-6626
Fax: (608) 265-2316

J. M. Pfotenhauer

Cryogenic Engineering Laboratory,
Room 1339 Engineering Research Building,
1500 Engineering Drive,
University of Wisconsin,
Madison, WI 53706

Growing interest in larger scale pulse tubes has focused attention on optimizing their thermodynamic efficiency. For Stirling-type pulse tubes, the performance is governed by the phase difference between the pressure and mass flow, a characteristic that can be conveniently adjusted through the use of inertance tubes. In this paper we present a model in which the inertance tube is divided into a large number of increments; each increment is represented by a resistance, compliance, and inertance. This model can include local variations along the inertance tube and is capable of predicting pressure, mass flow rate, and the phase between these quantities at any location in the inertance tube as well as in the attached reservoir. The model is verified through careful comparison with those quantities that can be easily and reliably measured; these include the pressure variations along the length of the inertance tube and the mass flow rate into the reservoir. These experimental quantities are shown to be in good agreement with the model's predictions over a wide range of operating conditions. Design charts are subsequently generated using the model and are presented for various operating conditions in order to facilitate the design of inertance tubes for pulse tube refrigerators. These design charts enable the pulse tube designer to select an inertance tube geometry that achieves a desired phase shift for a given level of acoustic power. [DOI: 10.1115/1.1989369]

1 Introduction

The pulse tube is among the simplest of all cryocoolers and has the advantage over the Stirling cryocooler of having no moving parts in the cold region, resulting in high reliability, long life, and low vibration at the cold tip. However, the thermodynamic efficiency of early versions of the pulse tube was less than the Stirling cryocooler. The Stirling cryocooler generally showed better performance because the phase between the oscillating mass flow and pressure in the expansion space is easily adjustable using the low-temperature displacer. The optimal phase shift produces the maximum refrigeration effect per unit of working fluid mass; the working fluid mass must be processed by the regenerator and, after the compressor, most of the losses in the cryocooler are related to the regenerator and scale directly with the amplitude of the mass flow rate. Therefore, optimizing the refrigeration effect per unit of working fluid mass corresponds approximately to optimizing the thermodynamic efficiency of the cryocooler.

The introduction of the orifice pulse tube by Mikulin [1] and the double inlet pulse tube by Zhu et al. [2] have allowed pulse tubes configurations to approach, and in some cases exceed [3], the performance of a Stirling cryocooler. The orifice in the orifice pulse tube provided a convenient method of controlling the phase between the mass flow rate and pressure and led directly to the increase in efficiency. A limitation of the orifice pulse tube is that the mass flow rate must always lead the pressure; in the limiting case of a zero-volume pulse tube, the mass flow rate and pressure ratio may be in phase with one another. This limitation does not allow the thermodynamically optimal phase to be achieved in which the pressure leads the mass flow rate at the inlet to the expansion space.

An alternative means of adjusting the phase between the pressure and mass flow rate is with an inertance tube, as reported by Kanao et al. [4]. The inertance tube does not suffer from the same limitation as the orifice; through proper selection of the inertance tube geometry it is possible to force the mass flow rate to either lead or lag the pressure. Therefore, proper implementation of an inertance tube with a pulse tube has the potential to improve the performance of the cryocooler. Inertance is the dynamic characteristic associated with the inertia of a rapidly moving fluid. The inertance, together with the tube's resistance and compliance as well as the compliance of the terminating reservoir, provides a complex impedance at the warm end of the pulse tube. Through proper selection of the inertance geometry it is possible to adjust this complex impedance and therefore achieve the phase between flow and pressure that is consistent with maximum system performance.

The use of an inertance tube in a pulse tube cryocooler has been discussed previously by Gardner and Swift [5] in the context of a model that uses an electrical analogy to generate phasor diagrams representing the mass flow rates within a pulse tube with various types of acoustic networks, including an inertance tube. Gardner and Swift present experimental measurements of the behavior of a system in which an inertance and resistance is placed in parallel with a second resistance in order to provide independent control of the magnitude and phase of the impedance of the acoustic network. However, the characteristics of the inertance tube are not separated from the system level behavior. De Boer [6] presents a detailed analytical model of an inertance pulse tube refrigerator which solves the linearized governing equations explicitly for a sinusoidal driving pressure. Ju et al. [7] present a series of measurements of the resistance and inertance of small (0.6 to 2.0 mm) diameter tubes at relatively high frequency (40 to 70 Hz). These measurements are presented, normalized against the expected values for an oscillating, laminar flow in the limit of small acoustic amplitude.

This paper is divided into five sections in addition to this Introduction. In the second section of the paper, a distributed component inertance tube model is described that is capable of predicting the inertance effect as well as the pressure variation and mass flow rate along the length of the inertance tube. In the third section, the model's predictions are compared to a transmission line model developed by Luo et al. [8] which has been experimentally verified for operating conditions associated with low levels of acoustic power. In the fourth section, the distributed component model is verified at high levels of acoustic power through careful comparison with measurements of magnitude and phase (relative to the inlet pressure) of the pressure along the inertance tube

[1]Corresponding author.

Contributed by the Fluids Engineering Division for publication in the JOURNAL OF FLUIDS ENGINEERING. Manuscript received by the Fluids Engineering Division, June 25, 2004. Final revision: April 27, 2005. Associate Editor: Malcolm J. Andrews.

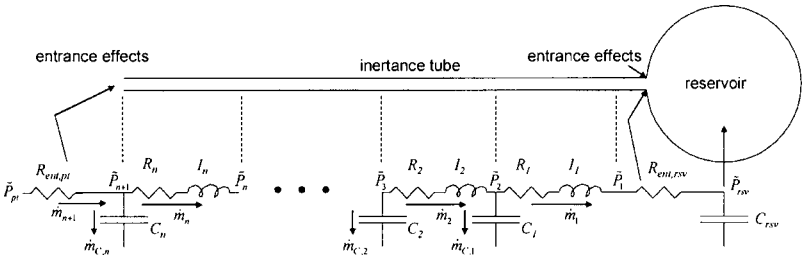

Fig. 1 Schematic of the distributed component model of the inertance tube/reservoir system. Note that the inertance tube is broken into discrete segments that are represented using a capacitance, resistance, and inertance.

length and the mass flow rate into the reservoir. These measurements were obtained in experiments over a wide range of operating conditions and geometry. Design charts are generated using the model and presented in the fifth section of the paper. These design charts, presented in both dimensional and nondimensional form, can be used to conveniently select inertance tube geometry (length and diameter) for a given acoustic power and desired phase shift. The sixth section summarizes the paper and presents the important conclusions.

2 Distributed Component Model

The distributed component model breaks the inertance tube into a large number (n) of segments. Each differential section of tube is represented by a fluid resistance (R_i), compliance (C_i), and inertance (I_i). The reservoir is represented by a fluid compliance (C_{rs}) and a resistance that represents the entrance effects (R_{ent}) associated with the contraction/expansion of the fluid at the reservoir inlet and the pulse tube side of the inertance tube, as shown in Fig. 1. The distributed component model will limit to the transmission line model [8] if n is taken to infinity. This implementation of the distributed component model has the advantage of allowing the consideration of entrance effects associated with the expansion/contraction of the gas as it enters/leaves the reservoir and pulse tube and also explicitly accounting for the spatial variation in the flow conditions along the tube by varying the characteristics of the impedance components according to the local conditions.

The resistance of each increment may be calculated independently based on the local mass flow rate along the tube. The pressure gradient in the inertance tube is nominally proportional to the mass flow rate squared and therefore the resistance, which is a linearization of the slope of the pressure gradient with mass flow rate, must vary according to the local mass flow rate. The distributed model can explicitly account for this effect through an iterative, relaxation procedure wherein the resistance values are updated based on the local mass flow rate. The Fanning friction factor of each increment of the inertance tube (f_i) is calculated assuming turbulent flow in a smooth tube [9]:

$$f_i = 0.046\,\mathrm{Re}_i^{-0.2} \tag{1}$$

where Re_i is the local Reynolds number in each increment, calculated based on the rms value of the mass flow through that element. The resistance of each increment (R_i) is given by

$$R_i = \frac{64 f_i \dot{m}_i (L/n)}{\pi^3 \bar{\rho} D^5} \tag{2}$$

where $\dot{m}_i$ is the amplitude of the mass flow rate though the corresponding increment, L is the total length of the inertance tube, $\bar{\rho}$ is the average density of the gas enclosed in the inertance tube, and D is the inner diameter of the inertance tube. The variation in the mass flow rate along the tube also causes the Reynolds number to change and therefore leads to a different friction factor in each element. Note that the oscillating flow in the inertance tube is likely to be characterized by a resistance per unit length that is larger than predicted by Eqs. (1) and (2) based on the ratio of the viscous penetration depth to the boundary layer thickness. The compliance (C_i) and the inertance (I_i) of each increment are given by

$$C_i = \frac{\pi D^2 (L/n)}{4\gamma R g \bar{T}} \tag{3}$$

$$I_i = \frac{4L}{n\pi D^2} \tag{4}$$

where γ is the heat capacity ratio, Rg is the gas constant, and $\bar{T}$ is the mean temperature of the gas in the tube which is assumed to be room temperature. The general time-dependent equation for the pressure drop across a segment of tube (Δp_i) can be written as

$$\Delta p_i = \dot{m}_i R_i + C_i \frac{d\dot{m}_i}{dt} + I_i \int \dot{m} dt \tag{5}$$

Therefore, the impedance associated with the compliance, inertance, and resistance of any segment ($Z_{C,i}$, $Z_{L,i}$ and $Z_{R,i}$) are given by Eqs. (6)–(8), respectively:

$$Z_{C,i} = \frac{1}{j\omega C_i} \tag{6}$$

$$Z_{I,i} = j\omega I_i \tag{7}$$

$$Z_{R,i} = R_i \tag{8}$$

where j is the square root of negative one and ω is the operating frequency. The impedance of the resistance associated with contraction or expansion at the reservoir inlet (Z_{ent} associated with R_{ent}) can be significant in some conditions and may either be experimentally determined or, as in this paper, modeled through the use of an orifice equation with a discharge coefficient.

The distributed component model may be represented as a set of cascaded impedances; the reservoir is represented by the innermost impedance and the total inertance tube/reservoir system is represented by the outermost impedance. Integer subscripts are used to indicate the position of the mass flow rate, pressure, or impedance value within the network; the subscript 1 indicates the discrete element that is adjacent to the reservoir and the subscript n indicates the element adjacent to the pulse tube. The entire network, as considered, can be divided into discrete components of impedance that are connected in parallel and in series; the subscripts s and p denote impedances that are in series and in parallel, respectively. These impedances in array notation are given by Eqs. (9) and (10) and can conveniently be computed sequentially, starting with the innermost impedance and working towards the outermost:

$$Z_{rsv} = Z_{R,ent,rsv} + Z_{C,rsv} \tag{9}$$

$$Z_{s,1} = Z_{rsv} + Z_{R,1} + Z_{I,1} \tag{10}$$

$$Z_{s,i} = Z_{p,i-1} + Z_{R,i} + Z_{I,i}, \quad i = 2, \ldots, n \tag{11}$$

$$Z_{p,i} = \left[\frac{1}{Z_{s,i}} + \frac{1}{Z_{C,i}} \right]^{-1}, \quad i = 1, \ldots, n \tag{12}$$

The total impedance of the network Z_{total} is the sum of the nth impedance in parallel ($Z_{p,n}$) and an additional impedance related to the entrance effect on the pulse tube side:

$$Z_{total} = Z_{R,ent,pt} + Z_{p,n} \tag{13}$$

The magnitude of the mass flow rate at the inertance tube entrance ($\dot{m}_{n+1}$) is calculated from the ratio of the pressure amplitude applied to the inertance tube inlet ($\tilde{P}_{pt}$) to the magnitude of the total impedance (Z_{total}):

$$\dot{m}_{n+1} = \frac{\tilde{P}_{pt}}{|Z_{total}|} \tag{14}$$

The phase shift between the mass flow rate and pressure (θ_{pt}) is related to the angle of the total impedance:

$$\theta_{pt} = - \angle Z_{total} \tag{15}$$

In addition to the total impedance of the network, the variation of the mass flow rate and pressure amplitude along the inertance tube can be determined using this model. Having carried out the overall system analysis described above, these intermediate values can most conveniently be calculated sequentially starting with the outermost impedance and working inwards towards the reservoir:

$$m_{C,i} = \frac{\tilde{P}_{i+1}}{Z_{C,i}}, \quad i = n, \ldots, 1 \tag{16}$$

$$\dot{m}_i = \dot{m}_{i-1} - \dot{m}_{C,i}, \quad i = n, \ldots, 1 \tag{17}$$

$$\tilde{P}_i = \tilde{P}_{i+1} - \dot{m}_i (Z_{R,i} + Z_{I,i}), \quad i = n, \ldots, 1, \tag{18}$$

Note that the mass flow rate entering the reservoir is equal to the mass flow rate leaving the inertance tube, $\dot{m}_1$. The acoustic power ($\dot{W}_{ac}$) flowing through a pulse-tube is

$$\dot{W}_{ac} = \frac{\dot{m}_{n+1} \tilde{P}_{pi}}{2\bar{P}} R T_h \cos \theta_{pt,h} \tag{19}$$

where $\bar{P}$ is the mean operating pressure. Substituting Eq. (14) into Eq. (19) leads to

$$\dot{W}_{ac} = R T_h \frac{\tilde{P}_{pt}^2}{2\bar{P}|Z_{total}|} \cos \theta_{pt,h} \tag{20}$$

The model is implemented using the Engineering Equation Solver (EES) software [10]. Sensitivity studies indicate that the predicted impedance is insensitive to n, the number of components used to model the inertance tube, provided n is at least 10; this value is used for all subsequent predictions.

3 Comparison of the Distributed Component Model Against Published Results

Luo et al. [8] present an inertance tube model based on transmission line theory that has been verified against experiments performed at low acoustic powers (1–40 W) and high frequencies (30–90 Hz); therefore it is worth comparing the predictions of the distributed component model, described in the previous section, against the transmission line model. The results reported in [8] are presented in terms of the dimensionless diameter ($\bar{D}$), length ($\bar{L}$), and acoustic power ($\bar{\dot{W}}_{ac}$). The dimensionless diameter is defined as

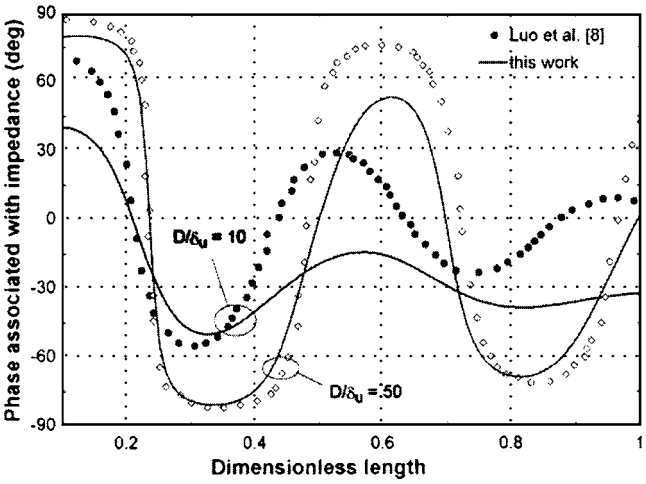

Fig. 2 Comparison of the phase predicted by the distributed component model with the transmission line model predictions presented by Luo et al. [8]

$$\bar{D} = \frac{D}{\delta} \tag{21}$$

where δ is the viscous penetration depth, given by the square root of the kinematic viscosity (ν) over the operating frequency (ω). The dimensionless length is defined as

$$\bar{L} = \frac{L}{\lambda} \tag{22}$$

where λ is the wavelength, given by the ratio of the speed of sound (a) to the operating frequency. The dimensionless acoustic power is defined as

$$\bar{\dot{W}} = \frac{4\dot{W}_{ac}}{\pi D^2 \bar{P} a} \tag{23}$$

Figure 2 illustrates the phase angle ($\theta_{pt,h}$) as a function of the dimensionless length for two different dimensionless diameters, assuming an infinite reservoir volume and a pressure ratio, defined as the ratio of the highest to the lowest pressure experienced during a cycle, of 1.1. Note that in Fig. 2 a negative value of the phase angle corresponds to pressure leading the mass flow rate whereas the phase reported in [8] has the opposite convention. For short dimensionless lengths the two models agree well whereas there is some discrepancy for the longer dimensionless lengths, particularly for the smaller dimensionless diameter case. This discrepancy is possibly related to the fact that the transmission line model, as implemented in [8], does not adjust the local resistance based on the local mass flow rate, an effect that becomes more pronounced at longer lengths and smaller diameters. Figure 3 illustrates the dimensionless acoustic power as a function of the dimensionless length for two different dimensionless diameters, assuming an infinite reservoir volume and a pressure ratio of 1.3.

4 Experimental Verification of the Distributed Component Model

The distributed component model has been verified through careful comparison with experimental measurements of the pressure along the inertance tube and the mass flow rate into the reservoir at higher acoustic power levels (up to 2.5 kW) and lower frequency (less than 20 Hz). Figure 4 illustrates a schematic of the

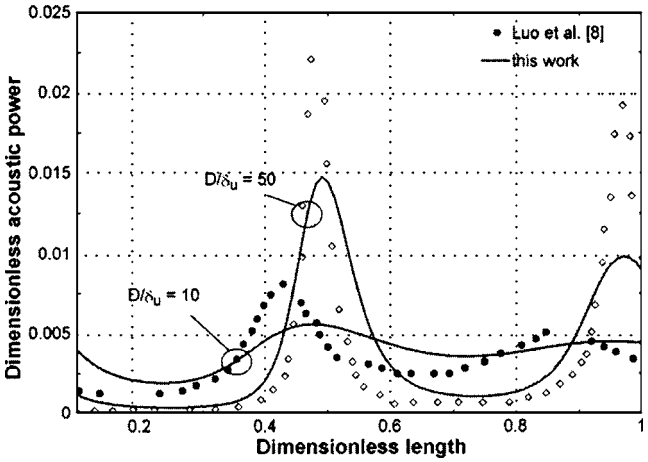

Fig. 3 Comparison of the dimensionless acoustic power predicted by the distributed component model with the transmission line model predictions presented by Luo et al. [8]

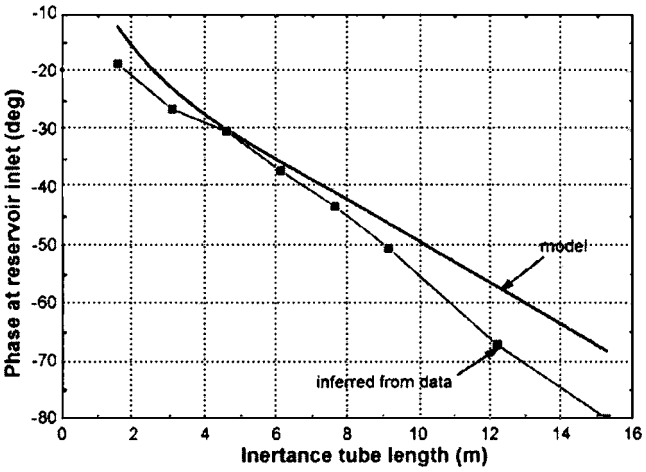

Fig. 5 Phase between the pressure in the reservoir and the mass flow rate at the reservoir end of the inertance tube as a function of inertance tube length for a 7.9 mm i.d. tube (15.3 Hz) predicted by model and inferred from measurements

experimental setup. Pressures are measured at the inertance tube inlet and exit, at various positions along the inertance tube, and in the reservoir. The mass flow rate into the reservoir can be inferred by assuming ideal gas behavior, an adiabatic reservoir, and also that the gas enters the reservoir always at the ambient temperature as described by Ju et al. [7] who verified that this technique yields results that are within 3.3% of mass flow rates measured directly using a hot wire anemometer. These assumptions allow the amplitude of the reservoir mass flow rate ($\dot{m}_{rsv}$) to be computed based on the amplitude of the pressure variation measured in the reservoir ($\tilde{P}_{rsv}$).

Figure 5 illustrates the phase between the pressure in the reservoir and the mass flow rate at the reservoir end of the inertance tube predicted by the model and inferred from the data for an inertance tube with an inner diameter of 7.9 mm. Figure 6 illustrates the magnitude of the mass flow rate at the reservoir end of the same inertance tube predicted by the model and inferred from the data. Figures 7 and 8 illustrate the same quantities for an inertance tube with an inner diameter of 11.1 mm. All data presented are for a compressor frequency of 15.3 Hz using helium at nominally 20 °C. Reasonable agreement for the mass flow rate at the reservoir end of the inertance tube is seen for both the 11.1 mm id and 7.9 mm id tubes for inertance tube lengths larger than about 3 m. The prediction of the phase is also good; the maximum deviation between predicted and measured phase is 15°.

Figures 9 and 10 illustrate the predicted and measured pressure variation for a 6.1 m long inertance tube with an 11.1 mm inner diameter operating at 15.3 Hz. Figure 9 presents data and model predictions half-way along the inertance tube length (i.e., at 3.05 m) while Fig. 10 illustrates the same information at the inlet to the reservoir. Notice that the predicted pressure and measured amplitude and phase (with respect to the inertance tube inlet pres-

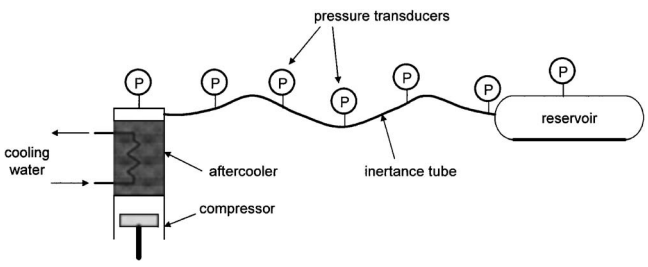

Fig. 4 Schematic of the experimental setup

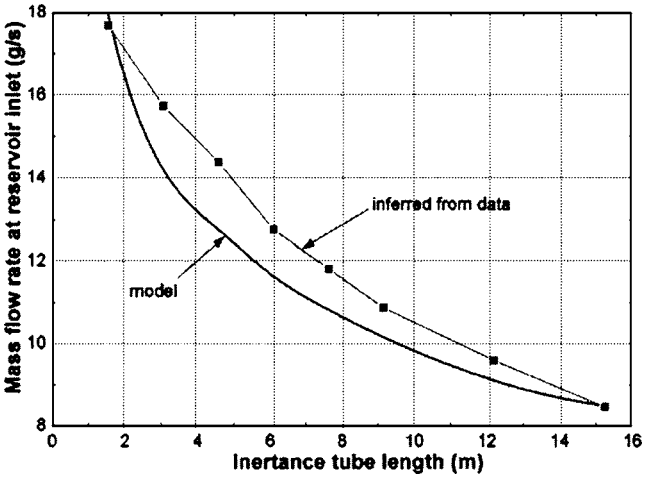

Fig. 6 Mass flow rate at the reservoir end of the inertance tube as a function of inertance tube length for a 7.9 mm i.d. tube (15.3 Hz) predicted by model and inferred from measurements

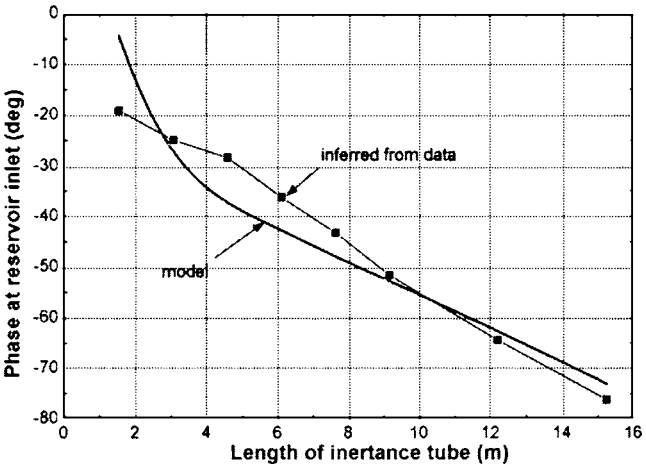

Fig. 7 Phase between the pressure in the reservoir and the mass flow rate at the reservoir end of the inertance tube as a function of inertance tube length for a 11.1 mm i.d. tube (15.3 Hz) predicted by model and inferred from measurements

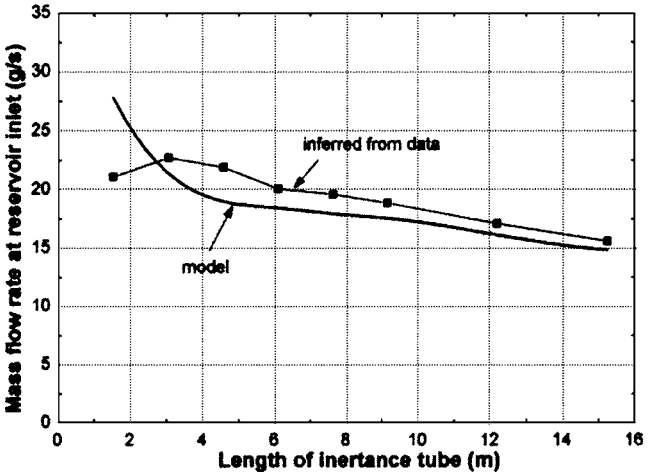

Fig. 8 Mass flow rate at the reservoir end of the inertance tube as a function of inertance tube length for a 11.1 mm i.d. tube (15.3 Hz) predicted by model and inferred from measurements

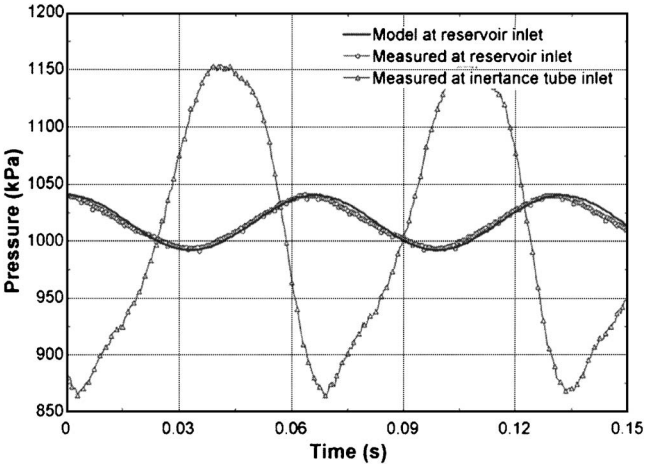

Fig. 10 Measured and predicted pressure variation at the reservoir inlet for a 6.1 m long inertance tube with an 11.1 mm inner diameter (15.3 Hz). Also shown is the measured pressure variation at the inertance tube inlet.

sure) agree extremely well. This close agreement was observed for other diameters, lengths, and operating frequencies. A more interesting demonstration of the fidelity of the model would be between predicted and measured mass flow rate and phase at the pulse tube end of the inertance tube; unfortunately, these measurements were not available.

5 Design Charts

The agreement between the predictions and measurements described in the previous section is considered partial validation of the distributed component model and therefore the model is used as a potential design tool and exercised in order to develop design charts for inertance tubes. These are convenient graphical representations of modeling results that can be used by a pulse tube designer in order to determine the length and diameter of an inertance tube that will provide a given acoustic power and a desired phase shift. In this section, design charts are presented in dimensional and nondimensional form for several, typical operating conditions.

Figures 11 and 12 illustrate the phase between the mass flow rate and pressure at the inlet of the inertance tube and the acoustic power entering the inertance tube, respectively, as a function of

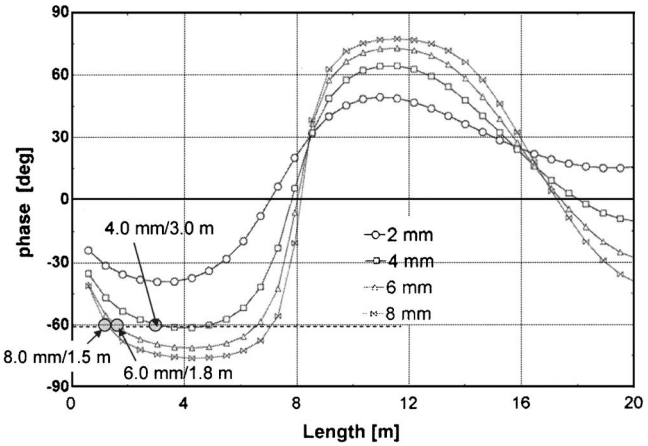

Fig. 11 Phase between the mass flow rate and pressure at the inertance tube inlet as a function of length for various diameters (at 30 Hz, a pressure ratio of 1.1, and a mean pressure of 25 bars). Also shown are three combinations of diameter and length that yield a desired phase of –60°.

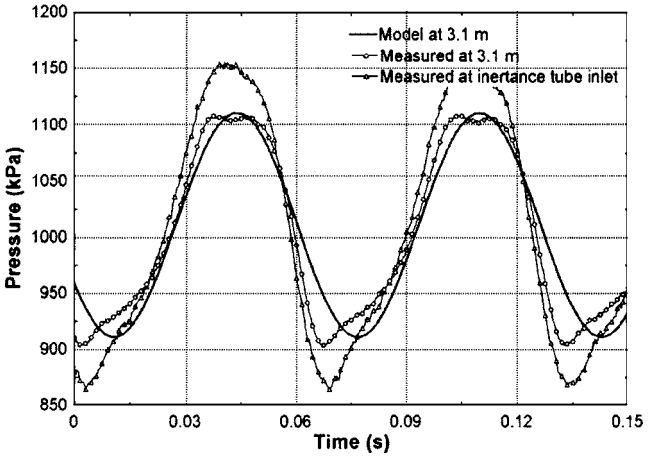

Fig. 9 Measured and predicted pressure variation half-way along (i.e., at 3.05 m) a 6.1 m long inertance tube with an 11.1 mm inner diameter (15.3 Hz). Also shown is the measured pressure variation at the inertance tube inlet.

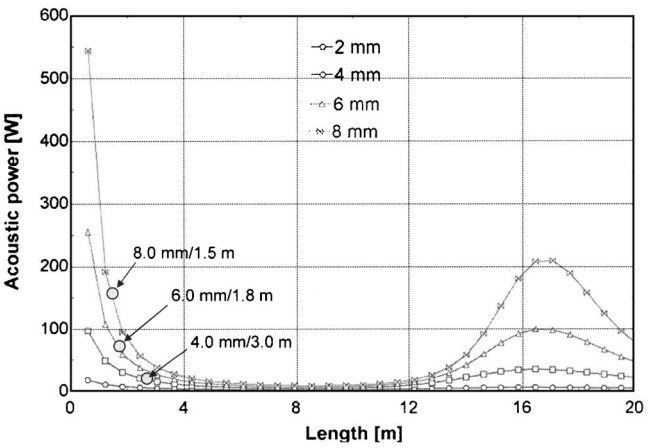

Fig. 12 Acoustic power as a function of length for various diameters (at 30 Hz, a pressure ratio of 1.1, and a mean pressure of 25 bars). Also shown are three combinations of diameter and length that yield a desired phase of –60°.

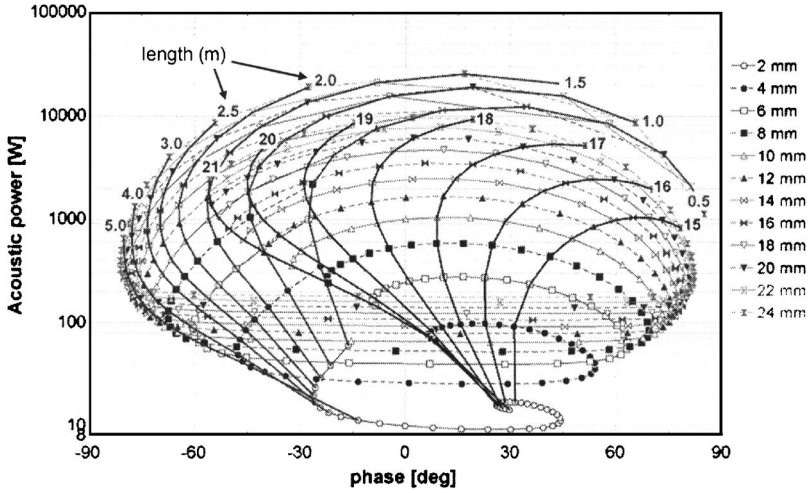

Fig. 13 Contours of constant length and constant diameter shown in the space of acoustic power and phase (assuming an operating frequency of 30 Hz, a pressure ratio of 1.2, 25 bar mean pressure, and a 7.6 liter reservoir volume)

the inertance tube length for several values of inertance tube diameter. These figures were generated assuming an operating frequency of 30 Hz, a pressure ratio of 1.1, and a mean pressure of 25 bars with helium gas. Figures 11 and 12 together can be used to select an inertance tube geometry for a desired phase shift and a given acoustic power. However, this is not a convenient method of presenting this information. For example, if the desired phase shift is −60° and the acoustic power is 75 W, then Fig. 11 provides at least three different diameter/length combinations that satisfy the phase requirement, including 4.0 mm/3.0 m, 6.0 mm/1.8 m, and 8.0 mm/1.5 m. These combinations must subsequently be evaluated using Fig. 12 in order to determine which combination provides the correct acoustic power; it can be seen that only the 6.0 mm/1.8 m combination provides the desired acoustic power. Considerable iteration between Figs. 11 and 12 might be necessary when interpolation between diameters and lengths is required in cases where the desired phase and acoustic power do not line up precisely with the curves.

A more convenient presentation format would show both acoustic power and phase information on the same figure. Figure 13 illustrates contours of constant length and constant diameter in the space of acoustic power (plotted on a logarithmic scale) and phase. Diameters (inner diameter) ranging from 2 to 24 mm in 2 mm increments are indicated in Fig. 13 as the lighter curves and lengths ranging from 0.5 to 21.0 m in 0.5 m increments are indicated by the heavy, solid curves. The numbers indicated on the constant length curves indicate the length in meters.

There are a few interesting things to notice in Fig. 13. The cyclic nature of the phase as a function of the length (see Fig. 11) shows up in Fig. 13 in the way that the constant length contours progress back-and-forth across the figure as the length is increased. As a result of this oscillating behavior, there are regions of acoustic power and phase that are unattainable to the pulse tube designer. With a very low power pulse tube, for example, a pulse tube designer requiring 30 W of acoustic power could not expect the pressure to lead the mass flow rate by more than about 45°. The phase achievable by smaller power pulse tubes would be even more limited. While there are some combinations of acoustic power and phase that are unattainable for any inertance tube geometry, there are others that can be obtained using more than one

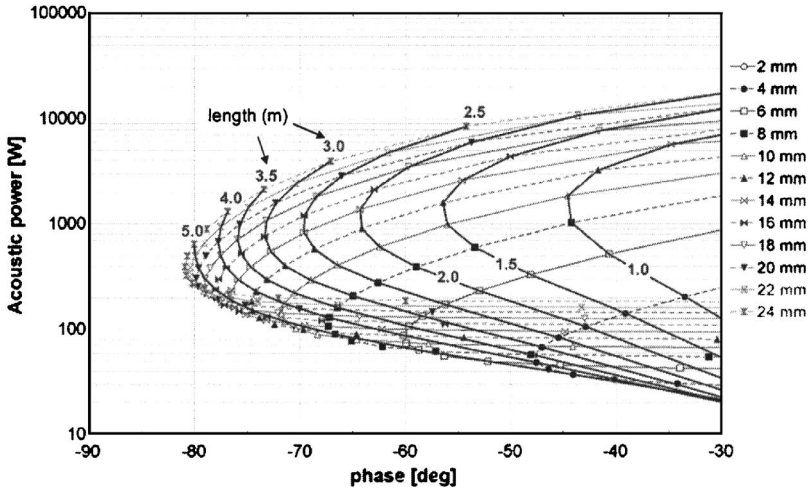

Fig. 14 Inertance tube design chart at 30 Hz and 1.2 pressure ratio, 25 bar mean pressure, and 7.6 liter reservoir volume for short inertance tubes. Bold lines represent various lengths (m).

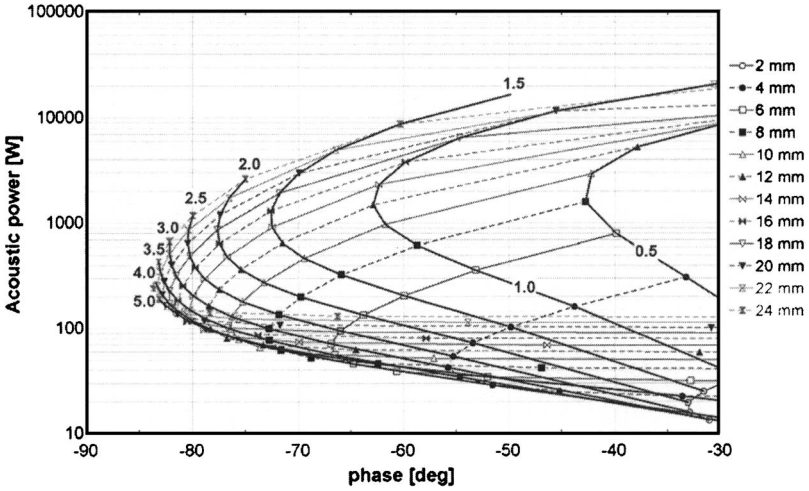

Fig. 15 Inertance tube design chart at 40 Hz and 1.2 pressure ratio, 25 bar mean pressure, and 7.6 liter reservoir volume for short inertance tubes. Bold lines represent various lengths (m).

combination of diameter and length. Figures 14 shows an expanded view of Fig. 13 in the range of phase angle that is most relevant for pulse tube designs; inner diameter contours are shown from 2 to 24 mm in 2 mm increments and only the short tube length contours, those lengths which represent the first oscillation of the phase with respect to length, are illustrated for clarity with relevant lengths spaced in 0.5 m increments. The smallest diameter corresponds to the smallest acoustic powers; with increasing diameter, the acoustic power increases. Lines of constant lengths and diameters seem to mesh a surface that corresponds to half of an oblate ellipsoid of revolution. Figure 15 shows a design chart for short inertance tubes operating at 40 Hz, a pressure ratio of 1.2, 25 bar mean pressure, and a 7.6 liter reservoir volume. Figure 16 shows a design charts for short inertance tubes operating at 50 Hz, a pressure ratio of 1.2, 25 bar mean pressure, and a 7.6 liter reservoir volume. Figures 14–16 are strictly valid only for a 7.6 liter reservoir volume. Under most of the conditions considered this is essentially equivalent to an infinitely large reservoir volume; however, for the small length and large diameter inertance tubes this is not true and the results are very sensitive to the size of the reservoir. Therefore, caution should be used when applying these design charts to regions corresponding to small phase and high acoustic power.

Dimensionless design charts can be used to consolidate the large number of design charts that would otherwise be required for varying mean pressure and frequency. The dimensionless groups suggested by Luo et al. [8] and introduced in the previous chapter are shown for pressure ratios of 1.1 and 1.3 in Figs. 17 and 18, respectively, for a 7.6 liter reservoir volume. Dimensionless inner diameter contours are shown from 5 to 70 in increments of 5. Bold lines represent contours of constant dimensionless length (their labels indicate their dimensionless length). Parametric analysis has shown that the dependence of the dimensionless charts on mean pressure or frequency is negligible.

6 Conclusions

The distributed component model of an inertance tube, described in this paper, divides the inertance tube into discrete increments, each represented by a resistance, compliance, and iner-

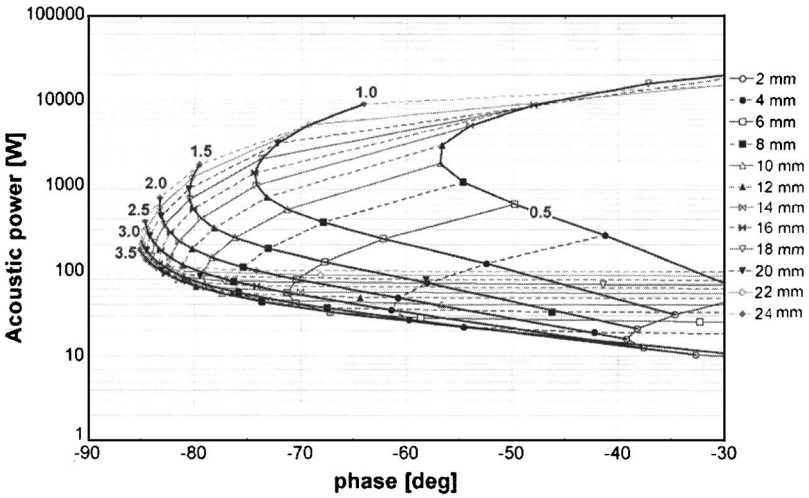

Fig. 16 Inertance tube design chart at 50 Hz and 1.2 pressure ratio, 25 bar mean pressure, and 7.6 liter reservoir volume for short inertance tubes. Bold lines represent various lengths (m).

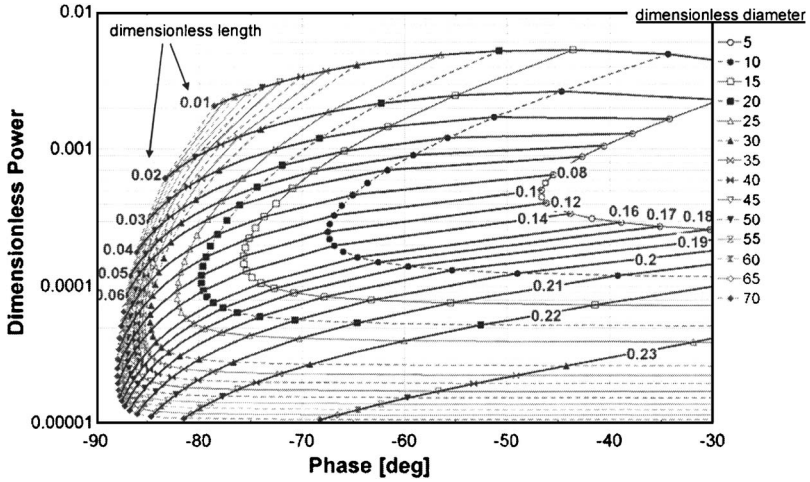

Fig. 17 Dimensionless inertance tube design chart at 1.1 pressure ratio and 7.6 liter reservoir volume for short inertance tubes. Bold lines represent various dimensionless lengths.

tance. If enough increments are used and the variation of the flow resistance is ignored, the distributed component model yields the same predictions as the transmission line model. However, the advantage of the distributed model over the transmission line model is its ability to model the axial variation in the resistance of the inertance tube and the associated variation in the mass flow rate amplitude along the tube, as well as its physically intuitive nature. Also, the distributed component model is capable of including the fluid resistance associated with contraction/expansion at the interface between the reservoir and the inertance tube. The distributed component model was verified through an extensive comparison with the predicted and measured values of the time varying mass flow rate into the reservoir (inferred from the reservoir pressure) and the measured and predicted pressure along the line and in the inertance tube.

The distributed component model was used to develop design charts showing contours of constant inertance tube length and diameter as a function of phase and acoustic power for compressor frequencies of 30, 40, and 50 Hz at a pressure ratio of 1.2, a reservoir volume of 7.6 liter, and a mean pressure of 25 bar. A complete set of design charts would require a comprehensive variation of pressure ratio, reservoir volume, and mean pressure. However, the dependence of the dimensionless length, diameter, and acoustic power on mean pressure and frequency was found to be negligible. Therefore, dimensionless design charts are presented for pressure ratios of 1.1 and 1.3 and a fixed reservoir volume of 7.6 liter. Together, these charts allow the pulse tube designer to conveniently specify the inertance tube geometry that will yield a desired acoustic power and phase. Examination of the design curves shows that there are regions of operation, specifically very small acoustic powers and large, negative phase angle, which cannot be obtained by any combination of inertance tube diameter and length. There are other regions where multiple combinations of length and diameter can be used to obtain a given phase and acoustic pressure.

Nomenclature

a = speed of sound, m/s
C = compliance, s^2-m
D = diameter of inertance tube, m
$\bar{D}$ = dimensionless diameter of inertance tube
f = Fanning friction factor
I = inertance, 1/m

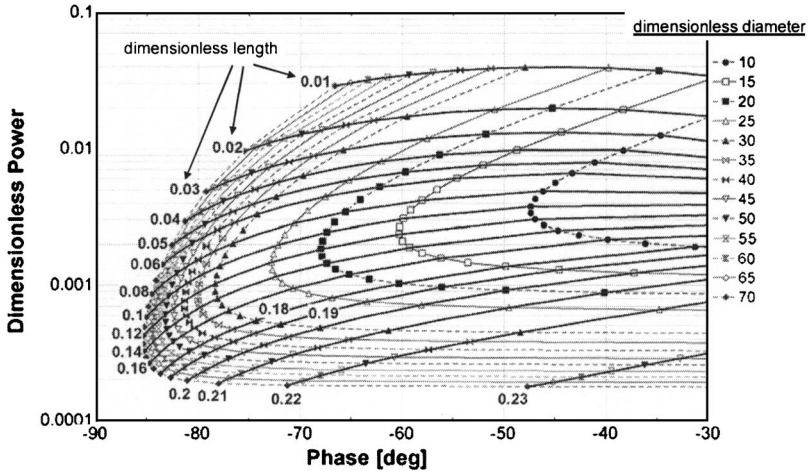

Fig. 18 Dimensionless inertance tube design chart at 1.3 pressure ratio and 7.6 liter reservoir volume for short inertance tubes. Bold lines represent various dimensionless lengths.

L = length of inertance tube, m
$\bar{L}$ = dimensionless length of inertance tube
$\dot{m}$ = amplitude of mass flow rate, kg/s
n = number of increments used in model
P = pressure, Pa
$\bar{P}$ = average pressure, Pa
$\tilde{P}$ = amplitude of pressure variation, Pa
R = fluid resistance, 1/m-s
Re = Reynolds number
Rg = gas constant, N-m/kg-K
T = temperature, K
V = volume, m^3
$\dot{W}$ = power, W
Z_C = impedance associated with compliance, 1/m-s
Z_I = impedance associated with inertance, 1/m-s
Z_R = impedance associated with resistance, 1/m-s
δ = viscous penetration depth, m
Δp = pressure drop, Pa
γ = ratio of specific heat capacities
λ = wavelength, m
ν = kinematic viscosity, m^2/s
θ = angle, rad
$\bar{\rho}$ = nominal density, kg/m^3
ω = operating frequency, rad/s

Subscripts

ac = acoustic
c = cold end temperature
ent = entrance
h = hot end temperature
i = subscript of inertance tube increment
pt = pulse tube
rsv = reservoir
s = impedances in series
total = total impedance of reservoir/inertance tube system
p = impedances in parallel

References

[1] Mikulin, E. I., Tarasov, A. A., and Shrebyonock, M. P., 1984, "Low-Temperature Expansion Pulse Tube," Adv. Cryog. Eng., **29**, pp. 629–637.
[2] Zhu, S., Wu, P., and Chen, Z., 1990, "Double Inlet Pulse Tube Refrigerators: An Important Improvement," Cryogenics, **30**, pp. 514–520.
[3] Marquardt, E. D., and Radebaugh, R., 2001, "Pulse Tube Oxygen Liquefier," Adv. Cryog. Eng., **45**, pp. 457–464.
[4] Kanao, K., Watanabe, N., and Kanazawa, Y., 1994, "A Miniature Pulse Tube Refrigerator for Temperature Below 100 K," Cryogenics, **34**, (supplement) p. 167.
[5] Gardner, D. L., and Swift, G. W., 1997, "Use of Inertance in Orifice Pulse Tube Refrigerators," Cryogenics, **37**(2), pp. 117–121.
[6] de Boer, P. C. T., 2002, "Performance of the Inertance Pulse Tube," Cryogenics, **42**, pp. 209–221.
[7] Ju, Y. L., He, G. Q., Hou, Y. K., Liang, J. T., and Zhou, Y., 2003, "Experimental Measurements of the Flow Resistance and Inductance of Inertance Tubes at High Acoustic Amplitudes," Cryogenics, **43**, pp. 1–7.
[8] Luo, E., Radebaugh, R., and Lewis, M., 2004, "Inertance Tube Models and Their Experimental Verification," Adv. Cryog. Eng., **49**, pp. 1485–1492.
[9] Incropera, F. P., and DeWitt, D. P., 2002, *Introduction to Heat Transfer*, 4th Edition, John Wiley and Sons, New York.
[10] Klein, S. A., and Alvarado, F. L., 2002, "EES-Engineering Equation Solver," F-Chart Software.

Journal of Fluids Engineering

Technical Briefs

Two-phase Flow in Jet Pumps for Different Liquids

S. Mikhail
Ph.D.
Mechanical Power Engineering Department, Cairo University, Cairo, Egypt

Hesham A. M. Abdou
Ph.D.
Agiba Petroleum Co., Cairo, Egypt

1 Introduction

This research was performed to determine the performance of a jet pump when the viscosity and density of the primary (or power) liquid are different from the viscosity and density of the secondary (or pumped) liquid. Engineers face this problem in several engineering applications [1,2]. Using one-dimensional assumptions, a theory has been developed [3,4] and validated [5,6] for jet pumps for water–water flow. The one-dimensional theory has been used [7–9] for two-phase flow in jet pumps. However, little research has investigated the use of two different liquids [10]. The second objective of this research is to study the mixing process analytically and experimentally. The one-dimensional theory, was altered to account for difference of the viscosities and densities of the two liquids. Experimental verification of the theoretical results was carried out by tests to measure the performance of the jet pump and the wall static pressure variation along the mixing chamber.

2 One-Dimensional Equations for the Jet Pump Performance

The one-dimensional flow assumptions are

1. Streams are one-dimensional at the entrance and exit of the mixing chamber.
2. Mixing is completed in the mixing chamber area.
3. Spacing between the nozzle exit and inlet of mixing chamber is zero, which is attainable due to the small nozzle diameter, relative to the large diameter of the mixing chamber.

Momentum and continuity equations [3] were applied to different sections of the jet pump, namely the suction, inlet, and outlet of the mixing chamber and the outlet of the diffuser. From this, the relationships between M, N, and η and the performance of the jet pump were determined.

N=numerator/denominator, where

$$\text{numerator} = A + B - C \tag{1}$$

$$\text{denominator} = D - A - E \tag{2}$$

Where

$$A = [1 - K_{\text{diff}} - (A_t/A_{\text{diff}})^2]$$

$$B = 2[(1+M)^{-1}\{R^{-1}(1+\Gamma M)^{-1} - 1\} + M(1+M)^{-1}\{\Gamma M(1-R)^{-1}(1+\Gamma M)^{-1} - 1\}] - K_t$$

$$C = \Gamma M^2[(1+M)^{-1}(1-R)^{-2}(1+\Gamma M)^{-1}\text{Cd}_s^{-2}]$$

$$D = (1+\Gamma M)(1+M)^{-1}[R^{-2}\{\text{Cd}_n(1+M)\}^{-2}]$$

$$E = 2[(1+M)^{-1}\{R^{-1}(1+\Gamma M)^{-1} - 1\} + M(1+M)^{-1}\{\Gamma M(1-R)^{-1}(1+\Gamma M)^{-1} - 1\}] - K_t$$

The coefficient of loss in the mixing chamber, K_t, is set as a function of Reynolds number in the form

$$K_t = \zeta/\text{Re}^{\beta} \tag{3}$$

where $\text{Re}=(\rho_m V_t D_t)/\mu_m$, $V_t=(Q_p+Q_s)/A_t$, $\rho_m=(\rho_p Q_p+\rho_s Q_s)/Q_d$, $\mu_m=\alpha\mu_o+(1-\alpha)\mu_w$, and ($\zeta$ and β) are constants, derived from the experimental data.

Calculation of M versus N and η were carried out for the cases of water–water flow and water–oil flow, assuming $\text{Cd}_n=0.96$, $\text{Cd}_s=0.9$, and $K_t=377.5/\text{Re}^{0.63}$ to estimate the impact of the velocity and density on performance.

Figure 1 shows the changes in M, N, and η, under differing density ratios, γ holding viscosity ratio, R_v constant. Figure 2 shows that, at the highest efficiency, both M and η are increased by increasing γ, but the pressure ratio, N, does not change appreciably. Further, at constant (γ) and differing R_v, Figs. 3 and 4 show that, at the highest efficiency points, both M and η decrease appreciably as R_v increases, while N does not change much.

3 Test-rig and Experimental Results

A diagrammatic sketch of the test loop is shown in Fig. 5. It consists of a transparent Perspex jet pump and a water pump driven by a 1.5 horsepower electric motor. The pump has a duty of 1.33×10^{-3} m^3/s at 33.5 m head of water and is connected to a lower sheet-metal water tank. A 235l sheet-metal suction tank for the secondary liquid is elevated 1 m above ground level, and a 290l "accumulating and separator" liquid reservoir is used. Two orifice meters were used, one to measure the flow rate of the power fluid and the other to measure the flow rate of the secondary fluid from the suction tank. Mercury and water differential manometers are used to measure the differential heads across the orifice meters. The pump dimensions were calculated according to the best ratios developed by previous research [3] for $R=0.34$ in a similar system. Calibrated pressure gauges measured pressure heads in the suction chamber, P_n, and at the outlet point of the jet pump, P_d. Static pressures across the mixing chamber and diffuser section were measured by a pressure gauge at four points, equally spaced along the mixing chamber and at the midpoint of the diffuser. The power liquid was always water, while three types of liquids were used as suction fluid: (1) water; (2) light crude oil (Sp.Gr.=0.85 and ν=29.4 centistokes at 25°C); and (3) very

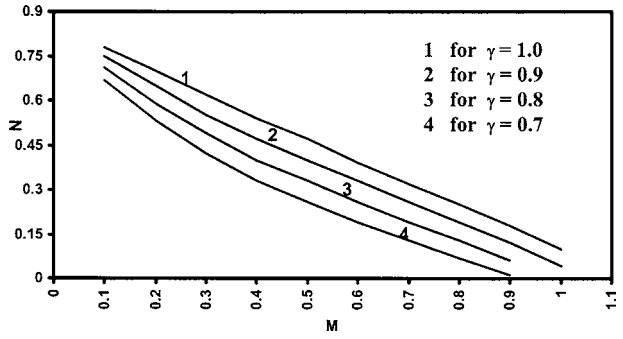

Fig. 1 M versus N at constant viscosity ratio and variable density ratio

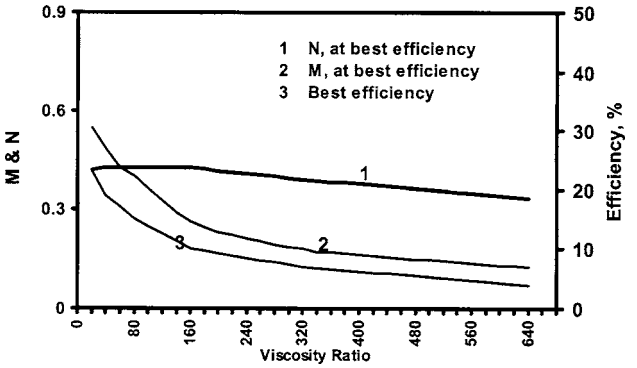

Fig. 4 Variation of M, N, and best efficiency with different viscosity ratio

viscous crude oil (Sp.Gr. =0.98 and ν=357 centistokes at 25°C). The jet pump efficiency curves are plotted in Fig. 6, for the water/water flow, water/light oil flow, and water/heavy oil flow. The theoretical results plotted against experimental results in Fig. 7, for the cases of water/water flow and water/light oil flow. Uncertainty analysis was carried out using the method developed by Kline and McClintock [11] and gave the results shown in Table 1.

4 Two-dimensional Analytical Study of the Mixing Process

A computer program was used to solve the Navier–Stokes equations for the axially symmetric two-phase turbulent flow [12] based on the finite-difference method, together with a two-equation turbulence model. The flow is bubbly, so the coefficient of drag (F) is taken as

$$F = -\mathrm{CD}(\rho_w d'/\mu)|v-u| \tag{4}$$

where CD is the drag coefficient, calculated by an empirical correlation [13], ρ_w is the density of the continuous phase, and d' is the droplet diameter.

Turbulent correlations appearing in the equations of the mean motion of both phases and the kinetic energy of turbulence and its dissipation rate for the carrier fluid are modeled through turbulent exchange coefficients and mean gradients.

The interaction between the phases was accounted for by including interfacial drag in the corresponding momentum equations. The parameters to be determined were the pressure, velocity component of each phase, the void fraction of each phase, and the turbulence energy and its dissipation.

The solution domain is subdivided into a number of finite cells, each of which encloses an imaginary grid node, at which all of the dependent variables are calculated with the exception of the velocities, which are caused to lie on the cell boundaries where they are used for mass flux computations. Algebraic finite difference counterparts of the differential equations were derived for each cell by a combination of formal integration and approximation.

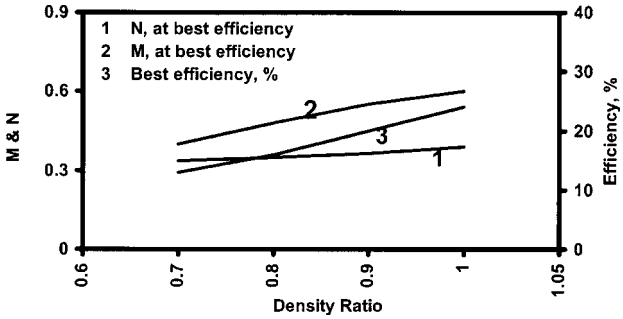

Fig. 2 Variation of M, N, and best efficiency with different density ratio

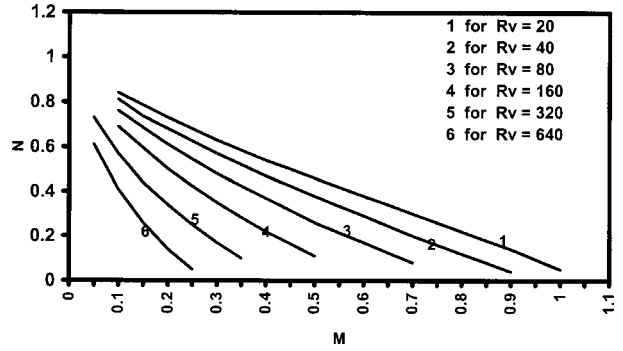

Fig. 3 M versus N at constant density ratio and variable viscosity ratio

5 Static Pressure Distribution Along the Jet Pump and Determination of the Pressure Loss Coefficient, K_t, Inside Mixing Chamber

Static pressure was measured along the mixing chamber and diffuser, and in the outlet of the diffuser. The measured pressure distributions are plotted in Fig. 8 for the three secondary liquids. The pressure distribution is negative in the inlet of the mixing chamber due to the acceleration of velocity in the mixing zone, and begins to rise near the middle of the mixing chamber due to the decrease of total momentum. The mixing process is begun in the mixing chamber and is completed in the diffuser. K_t is experimentally derived by applying following equations:

The actual pressure rise in the mixing chamber:

$$(\Delta P_{\mathrm{ms}}) = (P_d - P_s) - 0.5\rho_m \eta_{\mathrm{diff}}(V_t - V_{\mathrm{diff}}) \tag{5}$$

The theoretical pressure rise in the mixing chamber (ΔP_{th}):

$$\Delta P_{\mathrm{th}} = [(1/A_t)\{m_p V_n + m_s V_s - V_t(m_p + m_s)\}] \tag{6}$$

and the coefficient of pressure losses:

$$K_t = (\Delta P_{\mathrm{th}} - \Delta P_{\mathrm{ms}})/(0.5\rho_m V_t^2) \tag{7}$$

Reynolds number (Re) plotted versus K_t in Fig. 9.

6 Main Observations and Discussion

The validity of the theoretical analysis is proved by comparing the experimental performance curves with the theoretical curves (Fig. 7). At a constant viscosity ratio and variable density ratio, it is observed that there is no appreciable change for N with increas-

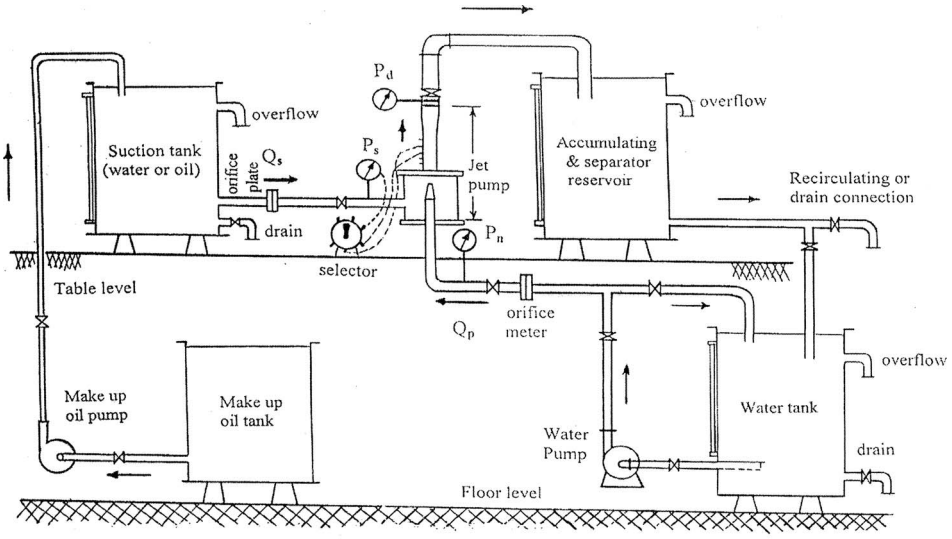

Fig. 5 Diagrammatic sketch of test rig

ing density. At best efficiency, both M and η increase gradually with increasing density ratio. This is probably related to the fact that, as the density ratio increases, Reynolds number increases. However, the coefficient of pressure loss in the mixing chamber (K_t) decreases slightly at high Reynolds number and consequently has only a small influence on the pressure ratio N. At constant density and varying viscosity ratio, N decreases slightly with an increase in the viscosity ratio. At best efficiency, both M and η decrease sharply with an increasing viscosity ratio. The reason for this is probably the same as for the effect of the density ratio, but the change is limited, especially at higher Reynolds numbers. Consequently, N changes only slightly.

7 Conclusions

A one-dimensional theoretical equation for the performance of the jet pump is developed when the viscosity and density of the

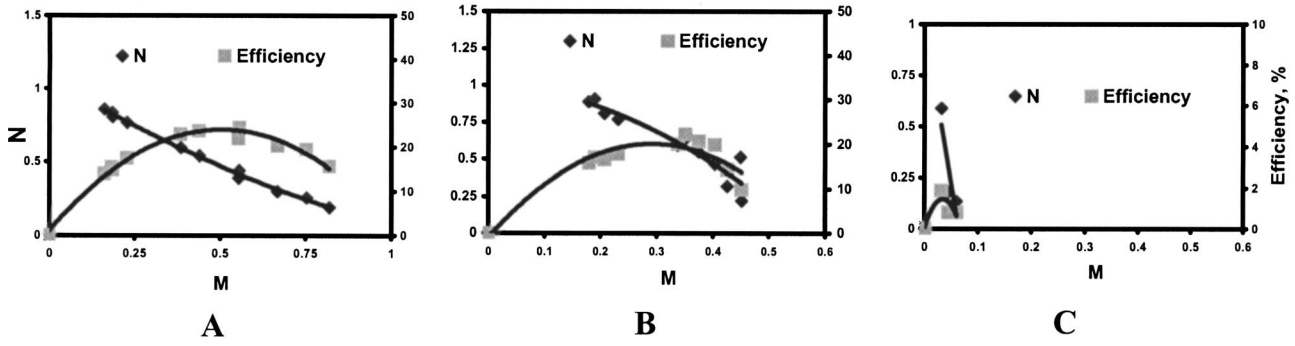

Fig. 6 Experimental jet pump performance: (*A*) water/water; (*B*) water/light oil; (*C*) water/heavy oil

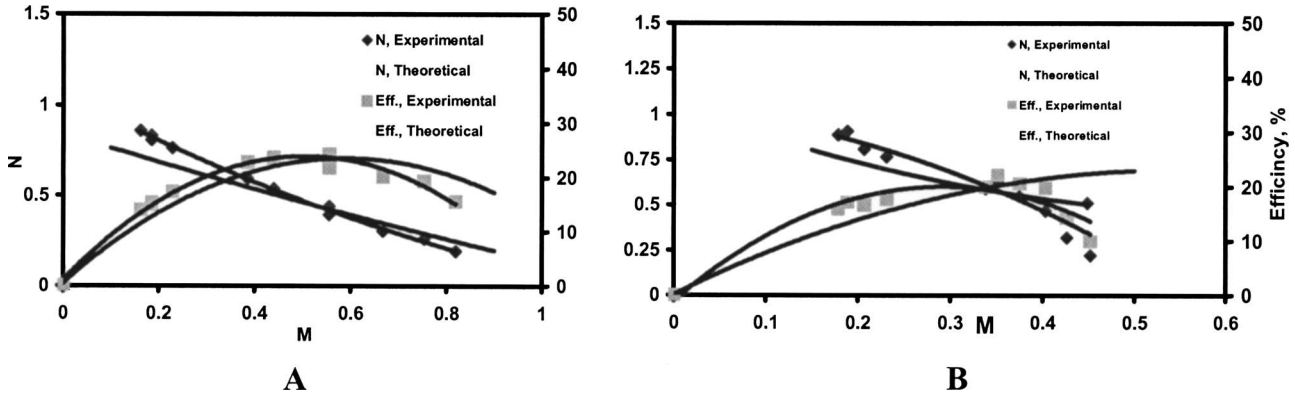

Fig. 7 Experimental against theoretical jet pump performance: (*A*) water/water and (*B*) water/light oil

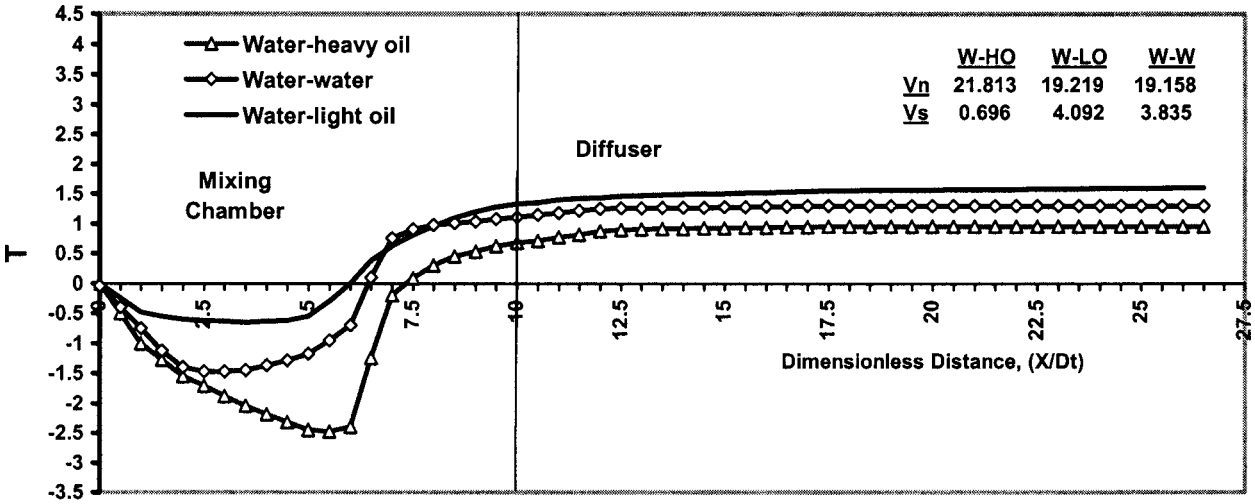

Fig. 8 Pressure distribution along the jet pump

primary liquid are different from those of the secondary flow. Comparison between the results of the theoretical equations and experimental results shows close agreement.

The empirical formula: $K_t=379/\mathrm{Re}^{0.63}$, is obtained experimentally by relating the pressure loss coefficient in the mixing chamber (K_t), to the Reynolds number calculated from the density, viscosity, and velocity of the mixture inside the mixing chamber ($K_t-\mathrm{Re}$). To pump an extremely viscous crude oil, a longer mixing chamber is needed to get a good mixing between this oil and the powered water flow.

Acknowledgment

The authors wish to express their gratitude to all who provided help and guidance in various ways at the different stages of this research. Our deepest appreciation is conveyed to cosupervisor, Professor Mohsen Abou Elleial, for his guidance in overcoming problems occurring during this research. Thanks also to Dr. Mostafa El-Sallak, for his valuable help in supplying some references.

Table 1 Results of Uncertainty Analysis

Item	Uncertainty for water–water flow, %	Uncertainty for water–oil flow, %
M	0.893	2.965
N	1.31	0.822
η	0.115	0.174

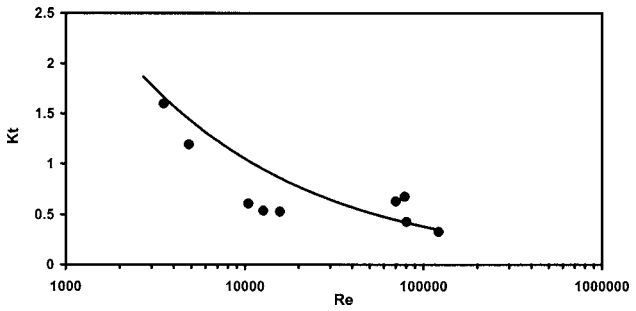

Fig. 9 Re versus Kt

Nomenclature

Symbol	Meaning	Unit
A	area	m^2
Cd	discharge coefficient	—
D	diameter	mm
K	pressure loss coefficient	—
m	mass flow rate	Kgm/s
M	mass ratio$=m_s/m_p=(\rho_s Q_s)/(\rho_p Q_p)$	—
N	pressure ratio$=(P_d-P_s)/(P_n-P_d)$	—
P	pressure	Pa
Q	flow rate	L/s$=10^{-3}$ m^3/s
R	area ratio$=A_n/A_t$	—
Re	Reynolds number$=\rho_m V_t V_t/\mu_m$	—
R_v	viscosity ratio$=\mu_s/\mu_p$	—
Sp.Gr.	specific gravity	
T	dimensionless pressure$=[2(P-P_s)/\rho_m V_t^2]$	—
u	velocity of the dispersed phase (light oil or heavy oil)	m/s
v	velocity of the carrier phase (water)	m/s
V	velocity	m/s
W-HO	water–heavy oil	—
W-LO	water–light oil	—
W-W	water–water	—
X	distance from inlet to mixing chamber	mm
ρ	density of fluid	Kgm/m^3
γ	density ratio$=\rho_s/\rho_p$	—
Γ	$=\rho_p/\rho_s$	—
η	efficiency$=100[Q_s(P_d-P_s)/Q_p(P_n-P_d)]$ $=100\ M\times N$	%
α	void fraction$=Q_s/(Q_s+Q_p)$	—
μ	dynamic viscosity of the fluid	pa s
ν	viscosity of the fluid	centistokes
Subscripts		
d	delivery	
D	drag	
m	mixture	
ms	measured	
n	nozzle or normal	
o	oil	
s	suction	
t	mixing chamber	
diff	diffuser	
th	theoretical	

References

[1] Villa, M., De Ghetto, G., Paone, F., Giacchetta, G., and Bevilacqua, M., 1999, "Ejectors for Boosting Low-Pressure Oil Wells," SPE Prod. Facil., **14**, 229–234.

[2] www.nrc.gov/reactors/bwrs.html

[3] Gosline, J. E., and O'Brine, M. P., 1934, "The Water Jet Pump," *Publications in Engineering*, University of California, 3, pp. 167–190.

[4] Cunningham, R. G., Hansen, A. G., and Na, T. Y., 1970, "Jet-Pump Cavitation," ASME J. Basic Eng., **94**, pp. 483–494.

[5] Mueller, N. H. G., 1964, "Water Jet Pump," *Proceedings of the ASCE*, 90, pp. 83–112.

[6] Reddy, Y. R., and Kar, S., 1968, "Theory and Performance of Water Jet Pump," ASCE J. Hydrol., **94**, pp. 1261–1281.

[7] Jiao, B., Bials, R. N., and Schmidt, Z., 1990, "Efficiency and Pressure Recovery in Hydraulic Jet Pumping of Two-phase Gas/Liquid Mixtures," SPE Prod. Eng., **5**, pp. 361–364.

[8] Noronha, F. A. F., Franca, F. A., and Alhanati, F. J. S., 1988, "Improved Two-Phase Model for Hydraulic Jet Pumps," SPE J., No. 50940, pp. 227–231.

[9] Zandi, I., and Govatos, G., 1970, "Jet Pump Slurry Transport," in *Hydrotransport 1, First International Conference on the Hydraulic Transport of Solids in Pipes (BHRA)*, University of Warwick, Warwick, U.K., pp. L2.17–L2.32.

[10] Corteville, J. C., Ferschneider, Hoffmann, F. C., and Valentin, E. P., 1987, "Research on Jet Pumps for Single and Multiphase of Crudes," in 62nd Annual Technical & Exhibition—SPE 16923, Dallas, TX, 27–30 Sep., pp. 437–448.

[11] Holman, J. P., 1978, *Experimental Methods for Engineers*, 3rd ed., McGraw-Hill, New York.

[12] Warda, H. A., and Abou-Ellail, M. M. M., 1984, "Computer Simulation of Two-phase Flow in Oil Wells Using Gas-Lift," in *International Conference on Engineering Software for Microcomputer*, Bineridge Press, Venice, Italy, pp. 567–582.

[13] Haberman, W. L., and Morton, R. K., 1955, David Taylor Model Basin Report 802, Naval Research Center, Bethesda, MD.

Comments on Reynolds Number Definition for the Discharge of non-Newtonian Liquids from Tanks

Marek Dziubiński
e-mail: dziubin@wipos.p.lodz.pl

Andrzej Marcinkowski

Faculty of Process and Environmental Engineering,
Lodz Technical University,
Wolczanska 213, 93-005 Lodz, Poland

[DOI: 10.1115/1.1989374]

Introduction

The discharge of non-Newtonian liquids from tanks is a subject of very few publications, e.g. Refs. [1,2]. In Ref. [1], the correlation equation for the coefficient of gravitational discharge of non-Newtonian liquids from tanks is proposed in the form

$$\phi = \left[0{,}101 - 0{,}0164\left(\frac{L}{d}\right)^{0{,}48}\right]\mathrm{Re}_{\mathrm{MR}}^{0{,}426} \tag{1}$$

where

$$\mathrm{Re}_{\mathrm{MR}} = \frac{v^{2-n}d^n\rho}{k\left(\frac{3n+1}{4n}\right)^n 8^{n-1}} = \frac{vd\rho}{k\left(\frac{3n+1}{4n}\right)^n\left(\frac{8v}{d}\right)^{n-1}} \tag{2}$$

Equation (1) has a general character because it describes a discharge coefficient depending on the Reynolds number $\mathrm{Re}_{\mathrm{MR}}$ and discharge orifice geometry. Equation (1) describes a broad range of experimental data obtained in Ref. [1] with mean error 5.7%. It holds for $0.005m < d < 0.017m$; $0 < L/d < 3$; $1.45\ \mathrm{Pa\,s}^n < k < 15.1\ \mathrm{Pa\,s}^n$; $0.474 < n < 0.606$; $0.0495 < \mathrm{Re}_{\mathrm{MR}} < 100$.

In the case of non-Newtonian liquids discharged from tanks there is a problem of a correct definition of the Reynolds number in the orifice. The Metzner-Reed Reynolds number applied to correlate experimental data [3] refers to the steady-state flow of non-Newtonian liquids in pipes. It is based on the nominal value of shear rate γ at the pipe wall equal to $8v/d$. In the case of liquid discharge through a short orifice, the flow is usually not fully developed (inlet region of the pipe), so the rheological properties of the liquid are determined by the mean value of shear rate in the whole cross section of the orifice which was defined by the equation

$$\gamma = \frac{Fv}{d} \tag{3}$$

where F is the constant dependent on liquid rheological properties and the orifice geometry L/d. Thus the definition of Metzner-Reed Reynolds number does not reflect fully the character of liquid flow in the orifice.

The aim of this study is to propose a definition of the Reynolds number based on the mean shear rate γ in the entire volume of the discharge orifice.

To specify the mean value of shear rate for the flow of non-Newtonian liquid in the orifice, a series of numerical simulations were performed using FLUENT® software. Results were discussed in Ref. [1]. Figure 1 shows examples of the simulation of velocity and pressure distribution in the discharge orifice.

In order to refer to changes in the velocity profile formed in the orifice, simulations were made for a dozen of cases of liquid discharge to determine velocity profiles in several cross sections of the orifice at different distances z from the tank bottom. The simulations for different geometries of the orifice L/d were carried out for the discharge of non-Newtonian liquids with the rheological parameter of power-law model n ranging from 0.47 to 0.76 and for Newtonian liquid (starch syrup) of viscosity $\eta = 0.1$ Pa s. Figure 2 shows examples of changes in the liquid velocity profiles during its discharge. As follows from the analysis of these diagrams, the velocity profiles assumed different shapes depending on the ratio of the distance from the tank bottom to orifice diameter z/d. The diagrams reveal that on the plane of the tank bottom ($z/d=0$), the shape of velocity profiles is flattest, while with an increase of the distance from this surface, the flow becomes more formed. The most formed velocity profile occurs at the outlet of the orifice $z/d = L/d$.

On the basis of velocity profiles the mean values of shear rates were calculated from the equation

$$\dot{\gamma}_{\mathrm{av}} = \frac{\sum_{i=1}^{j-1} \frac{|v_{z_i} - v_{z_{i+1}}|\pi(x_{i+1}^2 - x_i^2)}{x_{i+1} - x_i}}{\pi x_j^2} \tag{4}$$

where v_z is the local flow velocity in direction z and x is the distance from the pipe axis. The values of constant F in Eq. (3) were also determined. Parameter F for mean shear rates at several dimensionless distances from the tank bottom z/d for different orifice geometries L/d and different liquids is shown in Fig. 3. As follows from this figure, the values of F depend on the type of discharged liquid and z/d ratio. For a growing value of z/d parameter F also increases tending to a constant value.

To determine mean values of shear rates, in the entire discharge orifice mean values of constant F characterizing the tested liquid and a given orifice geometry L/d were determined. To accomplish this, the values of constant F were integrated numerically by the trapezoid method. The following equation was used in the algorithm of calculations:

$$F_{\mathrm{av}} = \frac{\sum_{i=1}^{j-1} \frac{F_i + F_{i+1}}{2}(z_{i+1} - z_i)}{L} \tag{5}$$

where j is the number of values of parameter F for the given orifice geometry L/d.

Next, coefficient F_{av} was approximated by the correlation equation that made dependent its value on L/d ratio and rheological parameter of power-law model n of the liquid tested. The following form of the proposed equation was obtained by means of data correlation

$$F_{\mathrm{av}} = 4.74 + 0.395\left(\frac{L}{d}\right)^{0.113} - 3.15(1-n)^{4.2}. \tag{6}$$

Figure 4 presents a comparison of constant F_{av} obtained on the basis of numerical calculations and correlation equation (6). The mean relative error of this approximation for 24 calculation points did not exceed 0.4%.

Table 1 gives the values of constant F_{av} obtained for the discharge of different non-Newtonian liquids through an orifice of geometry $L/d=3$ and value of coefficient $F_{\max}$ corresponding to the maximum shear rate $\gamma_{\max}$ at the pipe wall of the same diameter in the conditions of formed flow of the same non-Newtonian liquids. The value of constant $F_{\max}$ was determined from the relation

Contributed by the Fluids Engineering Division for publication in the JOURNAL OF FLUIDS ENGINEERING. Manuscript received by the Fluids Engineering Division, June 8, 2004. Final revision: May 20, 2005. Associate Editor: Dennis Siginer.

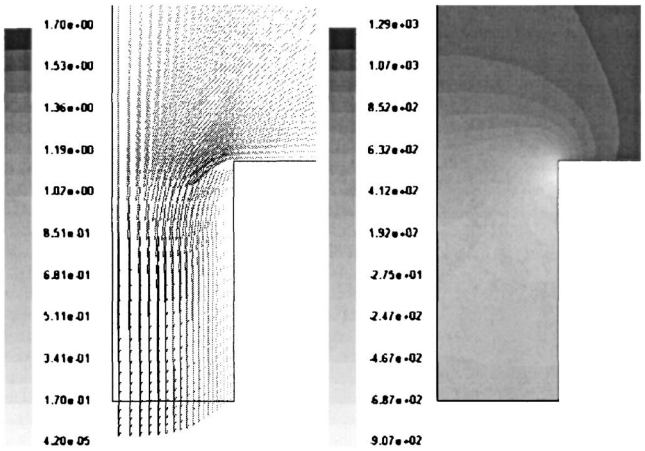

Fig. 1 Distribution of local velocities (m/s) and pressure (Pa) in the orifice region for the discharge of 1.6% CMC solution, $L/d=1$, $d=17$ mm, $H=0.13$ m

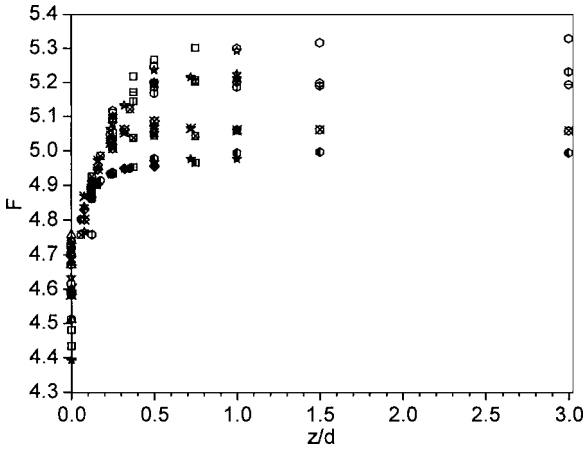

Fig. 3 Constant F in Eq. (3) in different cross sections of the discharge orifice at different distances z/d. Symbols as in Fig. 5.

$$F_{\max} = \frac{d}{v}\dot{\gamma}_{\max} \tag{7}$$

where

$$\dot{\gamma}_{\max} = \frac{3n+1}{4n}\frac{8v}{d} \tag{8}$$

is the value of corrected shear rate at the pipe wall that occurs during the non-Newtonian flow of liquid described by the power-law model with rheological parameter n [4].

As follows from Table 1, the values of coefficient F_{av} are much lower than the values of coefficient $F_{\max}$. This confirms the statement that in the case of discharge of non-Newtonian liquids from a tank through a short orifice, the mean shear rate in the discharge orifice does not correspond to the shear rate at the orifice wall which occurs in the definition of Metzner-Reed Reynolds number. So, the value of the Metzner-Reed Reynolds number does not correspond to the real value of the Reynolds number in the discharge orifice. A similar character of changes in the value of F_{av} was obtained for other orifice geometries L/d.

In view of the above conclusions, the following definition is proposed for Reynolds number that takes into account the mean shear rate in the entire orifice volume:

$$\mathrm{Re}_F = \frac{vd\rho}{k\left(\frac{F_{av}v}{d}\right)^{n-1}} \tag{9}$$

with F_{av} determined by Eq. (6).

The equation $F_{av}v/d$ determines the mean value of shear rate for the whole orifice.

Figure 5 shows the same experimental values of discharge coefficient ϕ that were used when deriving correlation equation (1) as a function of the Reynolds number Re_F calculated from Eq. (9) and orifice geometry L/d for non-Newtonian liquids with different rheological parameters. For the Reynolds number $\mathrm{Re}_F < 100$ the values of discharge coefficient ϕ are defined by the equation

$$\phi = \left[0.108 - 0.02\left(\frac{L}{d}\right)^{0.417}\right]\mathrm{Re}_F^{0.428} \tag{10}$$

Curves described by Eq. (10) are illustrated in Fig. 5 as solid lines.

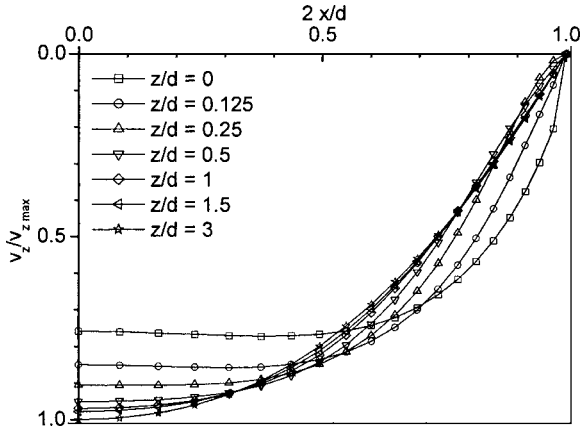

Fig. 2 Formation of liquid velocity profiles during discharge of 1.6% CMC solution from a tank through the orifice of $L/d=3$, $d=8$ mm. Rheological liquid parameters $k=0.115$ Pa s^n, $n=0.756$.

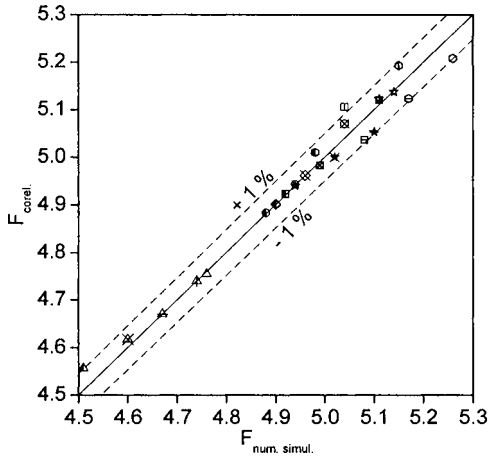

Fig. 4 Comparison of constant F_{av} obtained on the basis of numerical calculations and correlation equation (6) for different orifice geometries L/d and different liquids. Symbols as in Fig. 5.

Table 1 Constant F_{av} for $L/d=3$ and constant F_{max} in Eq. (8) for liquids with different rheological properties

n	1	0.756	0.592	0.528	0.474
F_{av}	5.208	5.193	5.124	5.070	5.010
F_{max}	8.000	8.644	9.376	9.787	10.22

Figure 6 shows a comparison of discharge coefficient ϕ obtained experimentally and calculated from Eq. (10). The correlation coefficient for 241 experimental points obtained in the investigations was $R=0.993$, and the mean relative error was equal to 5.1%.

Equation (10) proposed in this study, that describes discharge coefficient ϕ in a wide range of changes in the non-Newtonian liquid discharge velocity and geometry of the orifice, has not been presented in literature so far. It holds for $0.005\ \mathrm{m} < d < 0.017\ \mathrm{m}$; $0 < L/d < 3$; $1.45\ \mathrm{Pa\,s}^n < k < 15.1\ \mathrm{Pa\,s}^n$; $0.474 < n < 0.606$; $0.0490 < \mathrm{Re}_F < 100$.

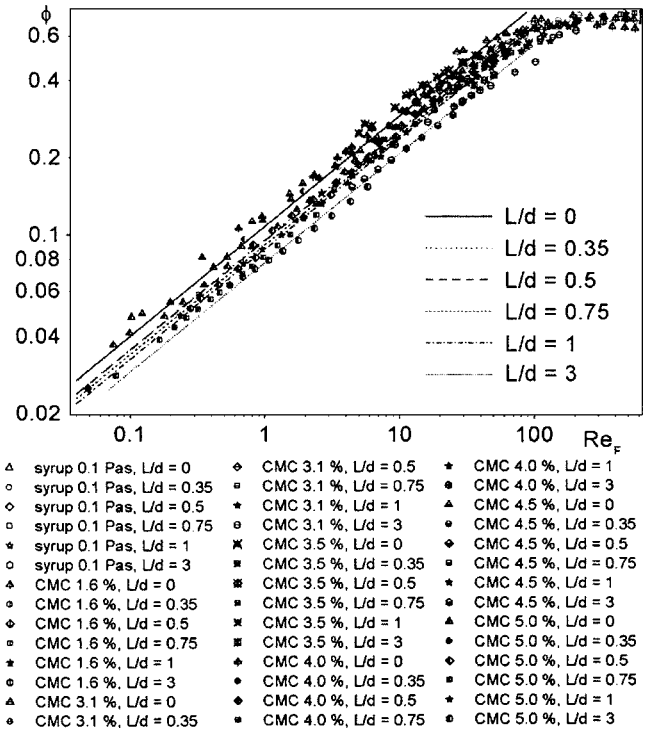

Fig. 5 Dependence of discharge coefficient on the Reynolds number (9) for selected orifice geometries L/d

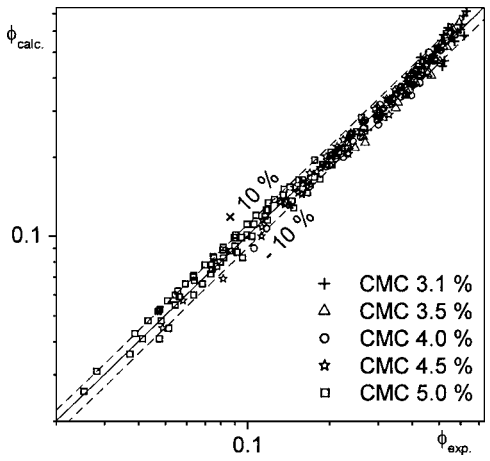

Fig. 6 Correlation of experimental data by Eq. (10)

While analyzing similarity of Eqs. (1) and (10) that describe the coefficient of discharge of non-Newtonian liquids from a tank which use different definitions of Reynolds number Eqs. (2) and (9), it can be found that they do not differ significantly from one another. Constants in these equations assumed very similar values. The exponent of Reynolds number is almost the same in both cases. This confirms that the slope of curves which illustrate the graphical form of the discussed equations in the log-log system of coordinates remained unchanged. It is worth stressing that the correlation equations prepared using the classical definition of the Metzner-Reed Reynolds number (2) and the Reynolds number definition (9) taking into account the averaged shear rate along the whole length of the discharge orifice, give a slightly better accuracy of experimental data description related to the discharge coefficient ϕ of non-Newtonian liquid. Differences in the flow mechanism are most probably contained in different values of constants in the correlation equation.

Conclusions

On the basis of numerical simulations an attempt has been made to determine the mean shear rate in the whole orifice and to apply this value in the definition of Reynolds number Re_F that takes into account flow conditions in the inlet region of the discharge orifice, Eq. (9).

An original correlation equation (10) was proposed to describe the discharge coefficient of non-Newtonian liquids in a broad range of Reynolds number (9).

The numerical simulations appeared to be very useful in modeling of non-Newtonian liquid discharge from a tank.

Acknowledgments

This study was financed by the Polish State Committee for Scientific Research with Grant No. 4 T09C 019 23.

Nomenclature

d = orifice diameter, m
F = constant in Eq. (3)
k,n = rheological parameters of Ostwald–de Waele power-law model, $\mathrm{Pa}\cdot\mathrm{s}^n, -$
L = length of an orifice, m
Re_F = Reynolds number taking into account velocity profile formation
Re_{MR} = Metzner-Reed Reynolds number
v = liquid velocity in the orifice, ms^{-1}
x = horizontal coordinate, m
z = distance from surface of the vessel bottom, m
ϕ = discharge coefficient

γ = shear rate, s^{-1}
ρ = liquid density, kg m^{-3}

Subscripts

av = average value
max = maximum value

References

[1] Marcinkowski, A., and Dziubiński, M., 2004, "Discharge Coefficient for Discharge of Non-Newtonian Liquids From Vessel," Inż. Chem. Proc., **25**, pp. 1297–1302.

[2] Dziubiński, M., and Marcinkowski, A., 2003, "The Discharge of Non-Newtonian Liquids From Tanks," 4th European Congress of Chemical Engineering, Grenada, Paper No. P.5.5-014.

[3] Metzner, A. B., and Reed, J. C., 1955, "Flow of Non-Newtonian Fluids—Correlation of the Laminar, Transition and Turbulent Flow Regions," AIChE J., **1**, pp. 434–440.

[4] Ferguson, J., and Kembłowski, Z., 1991, *Applied Fluid Rheology*, Elsevier Applied Science, London.

Separation of Condensation Jet Image Using Filter Effect of Wavelets Transform

Motoaki Kimura
e-mail: kimura@mech.cst.nihon-u.ac.jp

Masahiro Takei

Department of Mechanical Engineering,
College of Science and Technology, Nihon University,
1-8-14 Kanda Surugadai, Chiyoda-ku,
Tokyo, 101-8308, Japan

Yoshifuru Saito
Department of Electronic Engineering,
College of Technology, Hosei University,
Tokyo, Japan

Atsushi Saima
Department of Mechanical Engineering,
College of Science and Technology, Nihon University,
1-8-14 Kanda Surugadai, Chiyoda-ku,
Tokyo, 101-8308, Japan

The present paper describes the application of discrete wavelet transform to the analysis of condensation jets in order to clarify the fluid and heat transfer phenomenon. The condensation jets in the nozzle vicinity are experimentally visualized via the laser light sheet method to obtain condensation particle density images of the jets. The image of the condensation particle density in the jet is decomposed to mean and fluctuation images via wavelet multiresolution. The dominant temperature boundary and the mean component outside the boundary were obtained from wavelet separation images. The boundary was compared to the experimentally obtained temperature distribution.
[DOI: 10.1115/1.1989373]

Introduction

Condensation jets are typically generated by adiabatic expansion of a vapor or by injection of one fluid into another. Condensation jets formed by adiabatic expansion have been studied [1] in supersonic Laval nozzles. In terms of the condensation jets formed by injection, Vatazhin et al. [2] analyzed the structure of the condensation zone when a steam jet is submerged into an ambient air atmosphere. Kimura et al. [3] investigated experimentally condensation jets that formed when cold dry air is discharged downward from a round nozzle into a high-humidity environment. This experimental study indicated that the condensation particles in the free shear layer during the jet diffusion process affect the condensation jet behavior. This previous study provided visual data on condensation jet behavior, details of the jet structure remain to be clarified.

Based on these previous studies, the authors proposed the possibility of the detailed analysis of jet diffusion based not only on the velocity distribution of the condensation jet, but also on the image information processed by wavelet transform. Wavelet image processing allows feature extraction from the original image to obtain the frequency characteristic without removing time and space information. Pioneered by the Li application of the wavelets in experimental fluid dynamics was started as application for the turbulent jet analysis [4]. Li et al. visualized the multiscale of turbulence structure from an LIF image of a lobed mixing jet using the discrete wavelet [5].

The originality of the present study lies in the application of discrete wavelet image processing to two-dimensional condensation particle density images of the condensation jet, and, in order to further clarify the jet characteristics, the applicability of this method with respect to temperature distribution is discussed. In the following section, an experiment is described in which a cold, dry air jet is injected from a round nozzle into a high-humidity atmosphere. Next, the image of the condensation particle density in jet diffusion is analyzed by multiresolution discrete wavelet transform in order to separate the large-scale component and the small-scale component. Finally, the temperature distribution of the condensation particle in the nozzle vicinity is used to verify the image analysis results.

Experimental Apparatus and Procedures

The test section was 300×300 mm^2 in cross section and 500 mm in length below the nozzle exit. The test section was built from Plexiglas in order to allow good visualization. The high-humidity atmosphere in the test section is assumed not to be affected by the laboratory air because the length from the nozzle outlet to the test section bottom is of sufficient length. For the jet, a desiccant-type dryer with active alumina was used to maintain the air from a compressor at a relative humidity of $\phi=1.0\%$. A filter removed particles of greater than 0.01 μm diameter, and a refrigerator was used to control the jet inlet temperature. The jet issued into the test section from a nozzle of diameter $d=10$ mm. The mean jet temperature at the nozzle exit, T_0, was 0°C, and the mean exit velocity, U_0, was 4.5 m/s. Reynolds number based on the jet diameter is 3300. The flow axis is z, and the cross axis is r.

For the surrounding high-humidity atmosphere, air was supplied from a compressor. The temperature of the surrounding atmosphere, T_e, was maintained at 40°C by heating this air supply prior to release into the test section. The relative humidity was adjusted to 100%. In addition, compared to the condensation jets, a noncondensing jet was produced air.

During the tests, the air jet was injected downward into the high-humidity atmosphere and visual images were obtained via the laser light sheet (LLS) method. The laser light beam generated by a Spectra Physics model SP2016-04S Argon laser was focused onto a sheet of 1.0 mm in thickness by means of convex and cylindrical lenses. The digital image was captured using a charge-couple device (CCD) camera (Chori-America, XC-003, 1/3 inch 768×494 pixels) having an exposure time of 1.0 s. The image processing area is 100×50 mm^2, and the space resolution is 0.20 mm^2/pixels. A chromel-alumel thermocouple of 50 μm in diameter was used to measure the temperature. The time constant of the thermocouple was 50 ms.

Experimental Results

Figure 1 shows a photograph of the condensation jet obtained via the LLS method and the CCD camera. The condensation zone clearly becomes wider with axial distance from the nozzle exit. Because the air jet undergoes only minimal mixing with the high-humidity atmosphere very close to the nozzle exit, the potential core down to approximately five diameters is not illuminated. Figure 2 shows the time mean temperature distribution for 10 s as measured using a thermocouple, where *(a)* is $\phi=100\%$ and *(b)* is a noncondensing jet. The vertical axis is the mean temperature T normalized as $(T-T_e)/(T_e-T_0)$. The temperature distribution of

Contributed by the Fluids Engineering Division for publication in the JOURNAL OF FLUIDS ENGINEERING. Manuscript received by the Fluids Engineering Division, December 24, 2003. Final revision: May 12, 2005. Associate Editor: Sivaram Gogineni.

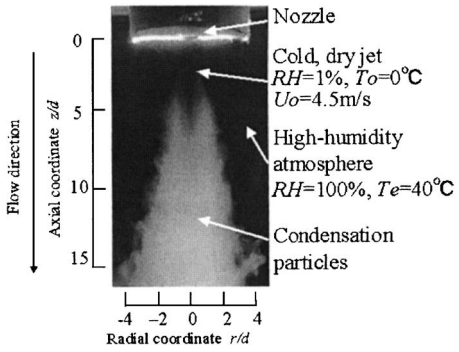

Fig. 1 Original image of condensation jets

Table 1 Relationship between wavelet level and representative frequency in the *z* direction

	Representative Spatial frequency	Wavelength
Level 0	1.30×10^{-2} [mm^{-1}]	76.92[mm]
Level 1	4.68×10^{-2}[mm^{-1}]	21.37[mm]
Level 2	8.00×10^{-2}[mm^{-1}]	12.5[mm]
Level 3	1.54×10^{-1}[mm^{-1}]	6.45[mm]
Level 4	3.00×10^{-1}[mm^{-1}]	3.32[mm]
Level 5	5.88×10^{-1}[mm^{-1}]	1.70[mm]
Level 6	1.62×10^{0}[mm^{-1}]	0.62 [mm]

the condensation jet is higher than that of a noncondensing jet at the downstream side from $z/d=4$. For $\phi=100\%$, the mean temperature downstream from the nozzle at $z/d=4$, 6, 8, and 10, i.e., the radius point, at which the circumference temperature becomes equal to condensation jet temperature (indicated by an arrow for $z/d=4$), is moving toward circumference, at $r/d=1.4$, 2.0, 2.5, and 3.0.

Decomposition Method

The condensation jet image obtained in the present experiments is decomposed via wavelet multiresolution in order to separate the large-scale component image and the small-scale component image. The two-dimensional wavelet spectrum S is obtained by

$$S = W_n D W_m T \tag{1}$$

where D is the original image consisting of $n=256$ pixels $\times m=512$ pixels elements, W_n is $n\times n$ elements analyzing wavelet matrix and W_m^T is the transpose matrix of W_m ($m\times m$ elements). The inverse wavelet transform of Eq. (1) is

$$D = W_n^T S W_m \tag{2}$$

when Daubechies 16th-order orthonormal function is used to analyze the wavelets and the image data D is resolved with 256 $\times 512$ data over the region (8 nozzle diameters $\times 16$ nozzle diameters), the original image can be decomposed to

$$D = W_n^T S W_m = W_n^T S_0 W_m + W_n^T S_1 W_m + W_n^T S_2 W_m + W_n^T S_3 W_m + W_n^T S_4 W_m + W_n^T S_5 W_m + W_n^T S_6 W_m \tag{3}$$

$W_n^T S_6 W_m$ is referred to as wavelet level 6 and has the highest space resolution, while $W_n^T S_0 W_m$ is referred to as wavelet level 0 and has the lowest spatial resolution. In this study, the relationship between level and wavelength when using the Daubechies 16th order are listed in Table 1.

Assumptions for Images and Decomposed Images

In order to simplify the discussion of the condensation jet images shown in Fig. 1 we assume that the nucleation rate of the condensation nuclei is extremely high, thus, condensation nuclei are assumed to grow to condensation particles instantaneously, and the number of condensation particles generated depends on the temperature at the position in question. Based on this assumption, the physical model for submerged condensation jets was developed in order to simplify the following qualitative discussion, as shown in Fig. 3. In this figure, "a temperature dominant boundary" between a mean dominant area and a fluctuating dominant area is indicated by solid line (b). In the mean dominant area, the condensation particles appear by high probability because the local vapor saturation temperature has decreased to the dew-point temperature by jet-atmosphere mixing. The number of condensation particles generated at the observation point is higher than that arriving from upstream. In the fluctuating dominant area, the large-scale image intensity is dramatically decreased by the dominated temperature fluctuation and transport phenomenon. The number of condensation particles generated intermittently from the fluctuation at the jet outer observation point is lower than that arriving from upstream.

Dotted line (d) shows the position of greatest circumference, and condensation particles do not exist in outside of this area. A cold, dry jet is mixed with a high-humidity atmosphere by entrainment, and a condensation particle is formed in the free shear layer, which is then transported downstream by the jet.

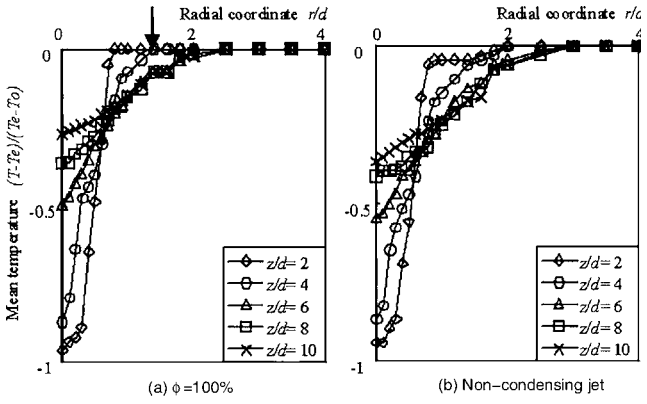

Fig. 2 Mean temperature distribution

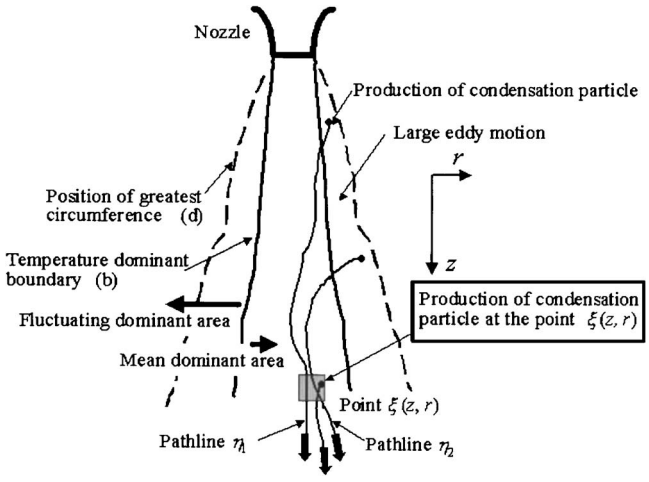

Fig. 3 Model of submerged condensation jet

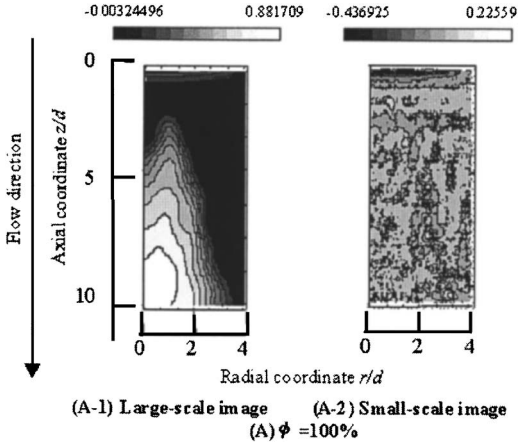

Fig. 4 Large-scale images and small-scale images decomposed from condensation original images

A typical point, $\xi(z,r)$ is pointed out in a condensation jet image in Fig. 3. The brightness of the ξ point is the product of the exposure time ($t=1$ s), the condensation particle which nucleates at the ξ point, and the path line η of the condensation particle which nucleates upstream of the ξ point. In other words, brightness $C(z,r)$ of a condensation jet image in Fig. 1 is expressed as

$$C(z,r) \approx k(JV_{\xi}t_1 + \eta_n) \tag{4}$$

where V_{ξ} is the volume of 1 pixel$\times$1 pixel$\times$1 mm (laser sheet thickness), k is a fixed number for the sensitivity of the CCD camera to the exposure, η_n is the number of path lines from point ξ over t_1 seconds, and t_1 is the exposure time. J is the nucleation rate per unit time and unit volume [6].

In Eq. (4) the brightness of the condensation jet image can be decomposed into a large-scale component and a small-scale component

$$C(z,r) = \overline{C(z,r)} + c'(z,r) = k(\bar{J}V_{\xi}t_1 + \overline{\eta_n}) + k(J'V_{\xi}t_1 + \eta_n') \tag{5}$$

In words, the condensation particle density of the condensation jet is dependent on the average nucleation rate and fluctuating nucleation rate at the ξ point, and the ξ point upstream.

Considering the above-mentioned condensation jet model, the condensation jet image, Fig. 1, is decomposed into a large-scale component image and a small-scale component image. The length scale of large eddy motion in the free boundary layer of the jet is estimated to be approximately 20 mm. If this value is the threshold between the large-scale component image and the small-scale component image, from Table 1, then $\overline{C(z,r)}$ is assumed to be equivalent to the summation of wavelet levels 0 and 1, and $c'(z,r)$ is taken to be equivalent to the summation of wavelet levels 2 through 6. Figure 4(A-1) shows the large-scale component image of the condensation jet image calculated from the summation of wavelet levels 0 and 1. Figure 4(A-2) shows the small-scale component image from the summation of wavelet levels 2 through level 6. The condensation particle density is indicated by a 10-level gray scale from black (low density) to white (high density).

Discussions

Figure 5 shows the brightness distribution, cross-sectional slices of the two-dimensional image of the normalized steady intensity component from Fig. 4 which is the large-scale component image at four axial positions. The radius position (position of greatest circumference) at which the brightness distribution change rate becomes zero is $r/d=2.0$ at $z/d=4$. As the position of the cross section increases, $z/d=6$, $z/d=8$, and $z/d=10$, the position of greatest circumference moves outward, $r/d=2.4$, $r/d=3.0$, and $r/d=4.0$.

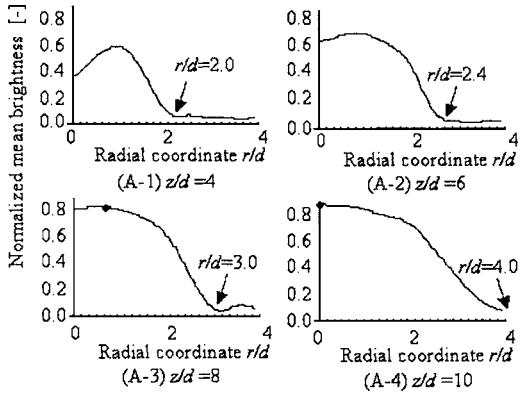

Fig. 5 Normalized mean brightness distribution

Figure 6 shows the brightness distribution formed by cross-sectional slices of the two-dimensional image of the normalized fluctuation intensity component from Fig. 4(A-2), which is the small-scale component image at four axial positions, $z/d=4$, 6, 8, and 10. The radius position of maximum value of $z/d=4$ is $r/d=1.59$. As the position of cross section increases, $z/d=6$, $z/d=8$, and $z/d=10$, the radius position of maximum value moves outside the jet, $r/d=2.17$, $r/d=2.52$, and $r/d=3.05$. These peak positions are equivalent to the above-mentioned "temperature dominant boundary" position. More than one peak is regarded as either image noise or a change in space scale inside the jet.

Figure 7 shows the average differences in temperature distribution for a condensation jet and a noncondensing jet is shown in Fig. 2. *Tc* and *Ts* are the condensation jet temperature and the noncondensing jet temperature, respectively. The large-scale image and the small-scale image of Figs. 5 and 6 are compared to the average difference in temperature distribution of Fig. 7 in the free shear layer of condensation jet using this difference.

In Fig. 7 (a) is the radius position at which the dew point temperature of Fig. 2 was reached, (b) is the temperature dominant boundary position in Fig. 6, (c) is the position at which the average temperature of the condensation jet and the noncondensing jets of Fig. 7 becomes equal, and (d) is the position of greatest circumference in Fig. 5.

The temperature dominant boundary position (b) is located outside the dew point position (a). This is thought to be because the

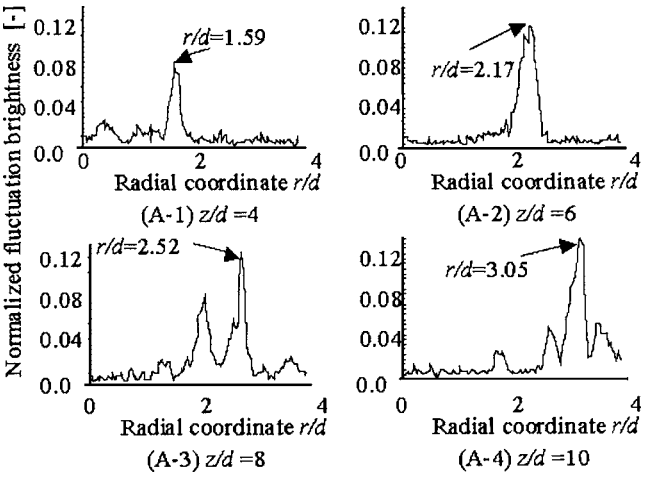

Fig. 6 Normalized fluctuation brightness distribution

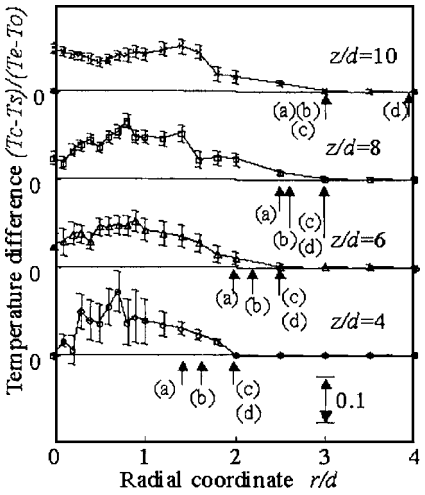

Fig. 7 Mean temperature distribution in the radial direction

dew point position (a) shows the position of time average to reach the dew point temperature, when actually, a fluctuation of intermittent flow by coherent structure is produced in the free shear layer. Accordingly, through the mixture of high-humidity circumference air and cold air, condensation particles form by falling below the dew point temperature intermittently at a positions outside the dew point position (a).

In addition, the temperature dominant boundary position (b) is located inside the circumference temperature arrival position (c). This is thought to be because in the region outside the temperature dominant layer position (b) "sensible heat" is discharged intermittently by the creation of an intermittent condensation particle, and this sensible heat causes the region to reach the circumference temperature arrival position (c).

Furthermore, the position of greatest circumference (d) is located at or outside the circumference temperature arrival position (c). The creation of a condensation particle is not possible outside the circumference temperature arrival position (c) of Fig. 7. However, it is thought that the pathline of the condensation particle was recorded as an image because the condensation particle which occurred upstream was guided by a vortex structure in the free shear layer and was transported to the circumference region downstream.

Conclusions

Cold, dry air was discharged from a circular nozzle into a high-humidity atmosphere. Two-dimensional images of the condensation jet were resolved via wavelet multiresolution. As a result, the following findings were obtained:

(1) Two-dimensional images of a condensation jet in which a mean value and a fluctuating value coexisted were divided into a large-scale image and a small-scale image.
(2) A temperature dominant boundary position was analyzed from a decomposed small-scale component image. The position is located outside the radius position reached the dew point temperature. The position was located inside the radius position at which the average temperature distribution reached the circumference temperature from the jet central temperature.
(3) The position of greatest circumference obtained from the decomposed large-scale component image is the circumference temperature arrival position and is in the neighborhood of the nozzle. Downstream, the position of greatest circumference was located outside the circumference temperature arrival position.

References

[1] Schnerr, G. H., Bohning, R., Breitling, T., and Jantzen, H. A., 1992, "Compressible Turbulent Boundary Layers With Heat Addition by Homogenous Condensation," AIAA J., **30**, pp. 1284–1289.
[2] Vatazhin, A. B., Klimenko, A. Y., Lebedev, A. B., and Sorokin, A. A., 1991, "Effect of Turbulent Fluctuations on Homogeneous Condensation in a Turbulent Isobaric Submerged Jet," Fluid Mech.-Sov. Res., **20**(2), pp. 1–11.
[3] Kimura, M., Itho, K., and Saima, A., 1995, "The Study of Cold Jet Issuing Into High Humidity Environment," *Proc. ASME/JSME Thermal Engineering*, pp. 165–170.
[4] Li, H., and Nozaki, T., 1995, "Wavelets Analysis for the Plane Turbulent Jet (Analysis of Large Eddy Structure)," JSME Int. J., Ser. B, **38**(4), pp. 525–531.
[5] Li, H., Hu, H., Kobayashi, T., Saga, T., and Taniguchi, N., 2001, "Visualization of Multi-Scale Turbulent Structure in lobed Mixing Jet Using Wavelets," J. Visualization, **4**(3), pp. 231–238.
[6] Volmer, M., 1939, *Kinetik der Phasenbildung*, Stienkopff-Verlag, Leipzig, Germany.

Journal of Fluids Engineering

Errata

Erratum: "Boundary-Layer Transition Affected by Surface Roughness and Free-Stream Turbulence" [Journal of Fluids Engineering, 2005, 127(3), pp. 449–457]

S. K. Roberts and M. I. Yaras

Tables 3 and 4 were inadvertently substituted with Table 1. The correct Tables for 3 and 4 are as follows:

Table 3 Streamwise location of transition inception (mm) Re_L=350,000

$k_{rms} \setminus Tu_{ref}$	0.4-0.9%	2.2-2.6%	3.4-4.8%
0.7 μm	567	569	537
31 μm	559	551	529
53 μm	561	541	523
107 μm	545	539	521*
185 μm	537	529	499*

* test case with attached-flow transition

Table 4 Streamwise location of transition inception (mm) Re_L=470,000

$k_{rms} \setminus Tu_{ref}$	0.4-0.9%	2.2-2.6%	3.4-4.8%
0.7 μm	567	558	539
31 μm	555	545	450*
53 μm	555	450*	450*
107 μm	535	525*	509*
185 μm	521	505*	450*

* test case with attached-flow transition

The original published article has been updated online to include the correct tables.

Erratum: "Limitations of Richardson Extrapolation and Some Possible Remedies" [Journal of Fluids Engineering, 2005, 127(4), pp. 795–805]

Ismail Celik, Jun Li, Gusheng Hu, and Christian Shaffer

This paper should have been the fourth paper under the Special Section on CFD Methods.

